

LIBRARY
Department of Metallurgy
University of Cambridge

Light Blue

A Study of the
Microstructure and stress relaxation of
spring steels

by

Stefan Paetke

Darwin College

Cambridge.

A dissertation submitted for the
degree of Doctor of Philosophy
at the University of Cambridge.

March 1980

A study of the microstructure and stress relaxation in spring steels

Summary

A detailed literature survey and critique of previous investigations into stress relaxation and spring steels has been used to initiate significant new work and to develop accurate microstructural and mechanical testing techniques with special reference to patented steel spring wire and its service replacement, 17- 7PH stainless steel wire. Changes in the microstructure, both in phase and dislocation distribution, and in solute segregation which take place during low temperature heat treatment in these spring steels, have been observed by means of high resolution transmission electron microscopy, field-ion microscopy and atom-probe techniques and have been correlated with concomitant changes in mechanical properties, notably stress relaxation. This has enabled a deeper understanding of the relaxation resistance in such complex materials to be formulated.

Preface

This dissertation, which is submitted for the degree of Doctor of Philosophy at the University of Cambridge, describes an investigation carried out under the supervision of Dr. D.V. Edmonds in the Department of Metallurgy and Materials Science, Cambridge between October 1975 and October 1978. Except where acknowledgement and reference to previous work has been made, the work is original and has been carried out without collaboration. Neither this dissertation nor any one substantially similar to it has been, or is in the process of being, submitted for a degree, diploma or any other qualification at any other University. The length of this thesis does not exceed 60,000 words.

S. Paetke

March 1980

Acknowledgements

It is a pleasure to thank Dr. D.V. Edmonds for his helpful advice and encouragement during the course of this work and Professor R.W.K. Honeycombe for the provision of laboratory facilities. I am also indebted to many members, both past and present, of the Department of Metallurgy and Materials Science, particularly in the Alloy-Steels research group, for the essential benefit of their wide experience and expertise. Also I would like to acknowledge the great help and assistance of Dr. A.W. Waugh, Mr. P. Mills, Dr. P. Sargent.

In addition my ability to carry out this programme has been made possible by many members of our Departmental staff, in particular Mr. J. Leader, Mr. D. Ackland, Mr. B. Barber, Mr. S.D. Charter and Mr. R. Turkentine and, of course Mr. J. Hurlock. A special mention of gratitude must go to my typists, Mrs. E. Palmer, Mrs. H. Thomson, Mrs. C. Bishop and Mrs. P. Summerfield, whose skill and encouragement have been of great help.

This programme of research has been generously funded by the Royal Armaments Research and Development Establishment (Fort Halstead). The staff at RARDE deserve considerable credit for their patience, help and understanding of the problems in this type of research. In particular I would like to express my sincere gratitude to Dr. R. Warren, Mr. P. Jones, Dr. R. Hawkins and Mr. D. Palmer.

Finally, I owe a particular debt of gratitude to many non-metallurgical friends for their active help and support since the start of my research, in particular to Polly J. Fahnestock. It is difficult to realise their importance in this way until such a project is undertaken.

Contents

	page
1. Introduction	1
1:1 Background to present work	1
1:2 Experimental approach	1
1:3 Plan of the documentation of the present work	2
2. Patented wire: its production, microstructure and strengthening mechanisms	5
2:1 Introduction	5
2:2 The structure and properties prior to drawing	5
2:2.1 Introduction	5
2:2.2 Effects of process variables on morphology and properties	6
2:2.2.1 General comments	6
2:2.2.2 Interlamellar spacing	6
2:2.2.3 Grain size	6
2:2.2.4 Directionality in the structure	6
2:2.2.5 Effects of composition	7
2:2.3 Nucleation and growth of pearlite	7
2:2.4 Commercial practice and its effects on the transformation	9
2:3 The deformation of pearlite and the process of cold drawing	9
2:3.1 Introduction	9
2:3.2 Wire drawing	10
2:3.2.1 Introduction	10
2:3.2.2 General description	11
2:3.2.3 Stock material requirements	11
2:3.2.4 Process variables	12
2:3.2.5 The effects of heating during wire drawing	12
2:3.3 Deformation mechanisms	13
2:3.3.1 Deformation and the strength of cementite	13
2:3.3.2 Plastic deformation of pearlite during drawing	15
2:3.3.3 Strengthening mechanisms and work hardening in drawn pearlite	16
2:3.4 Dislocation substructures and related topics	20
2:3.4.1 Introduction	20
2:3.4.2 Substructures formed from cold working - basic concepts	21
2:3.4.3 Substructures in deformed polycrystals	21
2:3.4.4 Post deformation phenomena - general comments	24
2:3.4.5 The effects of strain ageing with particular reference to annealing patented wire	26
2:3.4.6 Comments on dislocation substructures produced by other deformation modes	29
2:3.4.7 The effects of dislocation substructures on mechanical properties	29
2:3.4.7.1 Flow initiation in materials possessing dislocation substructures	29
2:3.4.7.2 Other mechanical properties	34

3.	Microstructural studies of patented wire	35
3:1	Introduction	35
3:2	Transmission electron microscopy studies (TEM)	35
3:2.1	Introduction	35
3:2.2	A/R microstructure	36
3:2.3	A/R + LTHT "A" microstructure	39
3:2.4	A/R + LTHT "B" microstructure	40
3:2.5	A/R + LTHT "C" microstructure	40
3:3	Field-ion microscopy (FIM) and atom-probe studies	40
3:3.1	Introduction	40
3:3.2	Previous FIM and atom-probe work on pearlitic steels	43
3:3.3	Present studies on patented wire	44
3:3.3.1	Introduction	44
3:3.3.2	A/R patented wire	45
3:3.3.3	A/R + LTHT "A" patented wire	48
3:3.3.4	A/R + LTHT "B" patented wire	50
3:4	Comments and Summary	50
4.	Stress relaxation	52
4:1	Introduction	52
4:2	Stress relaxation of commercial spring wires	55
4:3	Analytical stress relaxation testing	57
4:3.1	Introduction	57
4:3.2	Uses of analytical stress relaxation testing	58
4:3.3	Theoretical considerations	59
4:3.3.1	Introduction	59
4:3.3.2	Dislocation dynamics	59
4:3.3.3	Phenomenological approach	61
4:3.4	Basic theory and practice of stress relaxation tests	62
4:3.4.1	Introduction	62
4:3.4.2	Initial comments on the analysis of the test	62
4:3.4.3	Consideration of possible dislocation interactions during stress relaxation	67
4:3.4.4	Summary of analyses and comments	68
4:3.4.4.1	Introduction	68
4:3.4.4.2	Li's analysis	69
4:3.4.4.3	Sleeswyk's analysis	71
4:3.4.4.4	Guiu & Pratt's analysis	72
4:3.4.4.5	Comments	74
4:3.5	The relationship between creep and stress relaxation	75
4:3.6	Measurement of activation parameters by stress relaxation	75
4:3.7	Measurement of internal stress by stress relaxation tests	76
4:3.8	Stress relaxation prior to yield	76
4:3.8	Machine problems	77
4:3.10	Summary of stress relaxation on some specified materials	80
4:3.10.1	Introduction	80
4:3.10.2	Cu and Cu alloys	80
4:3.10.3	Al and Al alloys	81
4:3.10.4	Fe and Fe alloys	82
4:3.10.5	Other materials	83
4:3.11	Anisothermal stress relaxation testing	84

5.	Mechanical testing	86
5:1	Introduction	86
5:2	High accuracy tensile testing	86
5:3	Spring testing	87
5:3.1	Introduction	87
5:3.2	Experimental results	88
5:4	High resolution stress relaxation testing	89
5:4.1	Introduction	89
5:4.2	100 kN, servo-hydraulic Mand behaviour	91
5:4.3	Consistency evaluation	92
5:4.4	Preliminary investigation into the nature of the stress relaxation test	93
5:4.5	Effect of relaxation on the material under test	94
5:4.5	Effects on subsequent relaxations of ageing specimens at room temperature	95
5:4.7	Changes in magnitude of relaxation with stress	96
5:4.8	Relaxations of patented wire specimens over periods exceeding 400 seconds	96
5:4.9	Variation of dislocation parameters during relaxation in patented wire, with various initial loads and heat treatments	97
5:4.9.1	Introduction	97
5:4.9.2	Variation in dislocation velocity exponent, m^* , with test variables	98
5:4.9.2.1	Introduction	98
5:4.9.2.2	Behaviour of patented wire	99
5:4.9.3	Variation in behaviour of $\ln(\sigma)$ vs $\Delta\sigma$ graphs, with test variables	100
5:4.9.3.1	Introduction	100
5:4.9.3.2	Behaviour of patented wire	101
5:4.9.4	Variations in behaviour of $\Delta\sigma$ vs. $\ln t$ graphs, with test variables	102
5:4.9.4.1	Introduction	102
5:4.9.4.2	Behaviour of patented wire	103
5:4.9.5	Determination of σ_i and σ^* values	103
5:5	Comments and summary	104
5:5.1	Techniques	104
5:5.2	Information obtained	105
5:5.2.1	Tensile testing	105
5:5.2.2	Spring testing	106
5:5.2.3	High resolution stress relaxation testing	106
6.	Preliminary observations on the microstructure and stress relaxation of 17-7PH stainless steel	108
6:1	Introduction	108
6:2	Previous investigations on controlled transformation and precipitation hardenable stainless steels	108
6:2.1	Introduction	108
6:2.2	Controlled transformation steels	108
6:2.3	Wrought precipitation hardenable stainless steels	109
6:2.3.1	Austenitic steels	109
6:2.3.2	Semi-austenitic steels	110
6:2.3.3	Martensitic steels	111

6:3	The microstructure and properties of 17-7PH stainless steels	111
6:3.1	Introduction	111
6:3.2	Previous work on the microstructure and properties of 17-7PH stainless steel	111
6:3.3	Present investigation into the microstructure and properties of 17-7PH stainless steel	116
6:3.3.1	Introduction	116
6:3.3.2	Microstructural information	116
6:3.3.3	Mechanical testing information	118
6:3.3.3.1	Stress/strain behaviour	118
6:3.3.3.2	General comments on the relaxation behaviour of 17-7PH stainless steel	118
6:3.3.3.3	Variations in dislocation parameters during relaxation, with initial load	120
6:4	Comments and summary	120
6:4.1	Techniques	120
6:4.2	Information obtained	121
7.	General discussion	123
7:1	Introduction	123
7:2	Patented wire and 17-7PH stainless wire: their microstructures, strengthening mechanisms and their general stress relaxation behaviour	123
7:3	Analytical stress relaxation	127
7:3.1	Introduction	127
7:3.2	Testing problems	127
7:3.3	Comments on stress relaxation analyses and the concepts introduced by them	129
7:3.4	Particular comments on the work of Okazaki et al. - a case study	135
7:4	Previous research on the concepts of rate controlling deformation processes - general examples	136
7:5	Previous research on the concepts of rate controlling deformation processes - with particular reference to the present work	137
7:6	Summary of the present work	139
7:7	Conclusions from the present work	142
8.	Further work	144
8:1	Introduction	144
8:2	Microstructural work	144
8:3	Mechanical testing	145
8:4	Theoretical work	146
A.I	Appendix I: Experimental techniques	147
A.I:1.1	High resolution testing	147
A.I:1.1.1	Introduction	147
A.I:1.1.2	Design of the tensile specimens	147
A.I:1.1.3	Design of the inner grips	148
A.I:1.1.4	Design of the outer grips	149
A.I:1.1.5	Evaluation of tensile machines for high resolution stress relaxation testing	149

	A.I:1.1.6	Description and use of 100kN, 4-post Mand, with specific reference to tensile stress relaxation tests	150
	A.I:1.1.6.1	General description of a closed-loop servo-hydraulic testing machine	150
	A.I:1.1.6.2	Mand 100kN machine	150
	A.I:1.1.6.2.1	General comments	150
	A.I:1.1.6.2.2	Modifications and improvements introduced to Mand 100kN machine	151
	A.I:1.1.6.2.3	Procedure for tensile relaxation tests	152
	A.I:1.2	Lower resolution testing (spring testing)	160
	A:I.1.2.1	Introduction	160
	A:I.1.2.2	Experimental details	160
A.I:2	Structural Investigations		161
	A.I:2.1	Transmission electron microscopy (TEM)	161
	A.I:2.2	Field-ion microscopy (FIM) and atom probe analysis	163
	A.I:2.2.1	Introduction	163
	A.I:2.2.2	Time-of-flight atom-probe	163
	A.I:2.2.3	Imaging atom-probe	164
	A.I:2.2.4	Preparation of FIM specimens	165
	A.I:2.2.5	Selected details of operation of atom-probes	166
A.II.	Appendix II:	Mechanical testing data reduction	163
	A.II:1	Introduction	168
	A.II:2	How to make it work	169
	A.II:2.1	Program Intgo	169
	A.II:2.2	Programs Subgo and Subgo2	169
	A.II:2.3	Program Forxlib	170
	A.II:2.4	Program Interp	170
	A.II:2.5	Program Subtract	171
	A.II:3	The data formats	172
	A.II:3.1	The data file calib	172
	A.II:3.2	The data file data	173
	A.II:4	Calibrating several machines	174
A.III.	Appendix III:	Nomenclature	175
A.IV.	Appendix IV:	References	184

1. Introduction

1:1 Background to present work

This work originated in service failures of patented wire steel springs which suffered a loss in free length when subjected to compressive loads. Such failure is caused by stress relaxation. It was found that replacement of the patented wire by other materials of similar UTS brought about a dramatic improvement in this property: in particular, a 17-7PH stainless steel was selected as being the best available spring steel. It was, however, not clear why the stainless steel showed superior performance or, indeed, what the mechanisms of plastic deformation were in the case of the patented wire. Service failures of this type are, in fact, well known in the spring industry (e.g. engine valve springs), where work to determine the suitability of component materials under wide varieties of operating environments has occupied considerable time and effort. Little attempt has been made, however, to elucidate the failure mechanisms and the significance of the data which has been collected.

The materials studied in this work have not been studied in detail before in the context of this failure mode. However, patented wire has been manufactured for many years and its qualities, such as the high tensile strength, have been put to use in a wide range of products, e.g. high tensile cable, tyre cord, springs. The deformation behaviour is not well understood and neither is the detailed microstructure nor the strengthening mechanisms involved. A brief study of the material's industrial development shows that these inadequacies have held back, to some degree, its recent improvement which has been obtained by expedient means. The 17-7PH stainless steel, although having a shorter development period, has again suffered from similar maladies, in this case the steel being superseded by other stainless steels of modified composition. Again little has been discovered of the detailed microstructure in such transformable, precipitation hardened, materials.

1:2 Experimental approach

Microstructural studies were undertaken on both drawn patented steel wire and drawn 17-7PH stainless steel wire in various heat treated conditions. Optical techniques were shown to be inadequate in this investigation and the main thrust of research was with transmission electron microscopy (TEM), field-ion microscopy (FIM) and atom-probe microscopy. TEM was used to study the microstructure of the as drawn and

heat treated wires which were used in the tensile testing programme (see later). FIM and atom-probe microscopy enabled a microstructural study, in particular the dislocation substructure, of the patented wire on an extremely fine scale. Wire of the same type used in the TEM study was examined but drawn to a higher degree (which resulted in a finer scale microstructure more suited to these techniques). By means of atom-probe microscopy, an ultra-high resolution study of the distribution of elements across the microstructure was undertaken. In particular the segregation of C to the dislocation substructure was found to be of importance. Mechanical tests on springs of patented wire were undertaken to simulate service conditions and to extend the higher resolution work. The most concentrated effort was given to the development and use of an extremely high resolution, tensile testing apparatus, to enable controlled relaxation tests, along with a flexible data reduction system. These developments allowed a confident comparison to be made with relaxation data obtained on simpler materials in previous work (see Ch.4) in addition to the application of theoretical models to the present materials.

It has been observed (see Ch.4: 2) in patented wire that a significant improvement in the relaxation resistance could be obtained by low temperature heat treatment (LTHT) of the wire or springs before use. It was therefore decided to investigate the microstructure and mechanical properties of as drawn patented wire and wire LTHT to various degrees. In a similar manner the 17/7PH stainless steel was examined in the as-drawn and the precipitation hardened condition.

1:3 Plan of the documentation of the present work

An initial report on the present work (1) largely contains extensive reviews on background information not reproduced in this thesis. Springs and spring materials were reviewed in a broad manner. The types of springs together with the importance of materials selection and quality control were explained, along with production features and their effects on the properties of the final article. The subject of wire drawing was also reviewed, giving not only theoretical aspects of the process but also practical considerations (e.g. the concept of "cold" drawing) which are of particular interest in the case of spring wires. Appendices were included to cover an analysis of the elastic deformation of springs and also a review of residual stresses and their relevance to spring materials and stress relaxation phenomena.

A summary of the work included in the present thesis is given below.

(a) Chapter 2 is an extensive review of patented wire and covers: the structure and properties of the patented bar stock before drawing; the deformation of the pearlite during drawing; strengthening mechanisms and work hardening in the drawn structure; dislocation substructures their properties and their particular relevance to patented wire; strain ageing phenomena in carbon steels.

(b) Chapter 3 presents the microstructural studies undertaken in the present work and covers: TEM studies on longitudinal and transverse sections of as drawn patented wire in several conditions; field-ion microscopy and atom-probe studies on comparable patented wire (along with a brief review on the development and use of these techniques in similar materials).

(c) Chapter 4 is an extensive review on the field of stress relaxation. Topics discussed include: the types of relaxation (and their relation to other deformation modes) and the type involved in the present failure; the fields in which relaxation is important; previous studies of the relaxation of spring wires; a concise review and critique of analytical stress relaxation work; an in-depth analysis of the theoretical basis for stress relaxation testing; a similar analysis of the techniques of stress relaxation testing; a summary of analytical stress relaxation tests which have been undertaken on a wide range of materials.

(d) Chapter 5 presents the results of the present work in mechanical testing. Techniques employed include: high accuracy tensile testing of materials; a spring testing programme; a programme of high resolution, tensile stress relaxation testing with comparative details between the various conditions of the patented wire and the use of analytical techniques described and evaluated in the proceeding chapter.

(e) Chapter 6 details the work performed to date with 17-7PH stainless steel. Information includes: a review of controlled transformation and precipitation hardenable stainless steels; the microstructure of 17-7PH stainless steel; the mechanical properties of 17-7PH stainless steel in both tensile failure and tensile stress relaxation failure.

(f) Chapter 7 gives comments and an overall summary of the work included in this thesis.

(g) Chapter 8 includes suggestions where further work will be most profitable.

(h) Appendix I is a detailed account of the experimental techniques developed and used in the present work. Topics covered are: the choice of a suitable tensile testing machine and its development to give the required resolution; the design and treatment of the grips and specimens for mechanical testing; the detailed procedure for the undertaking of relaxation tests on the wire specimens to give optimum performance; the technique for spring testing; the procedures involved in transmission electron microscopy; the history, development and present use of field ion microscopy and atom-probe analysis.

(i) Appendix II gives information on the data handling and reduction techniques employed in the mechanical testing programme.

(j) Appendix III is a list of symbols used in the present thesis (they are identical to those employed in reference 1 except where stated).

(k) Appendix IV is a list of the references given in the present thesis (the reference numbers are not identical to those in reference 1).

2. Patented wire: its production, microstructure and strengthening mechanisms

2:1 Introduction

The term patented wire is applied to a high carbon steel wire of particularly high tensile strength. In fact, except for filamentary whiskers, high quality patented wire (often known as music wire) gives the highest known tensile strength while retaining considerable ductility: in the UK its manufacture is controlled under BS 5216:1975 (replacing BS 1408:1964). Patented wire can be supplied to various standards classified under normal or high duty and static or dynamic duty. It is also graded in five strength categories, 5 being the highest. The wire is generally supplied bright, i.e. as cold drawn, and has to pass torsion, bend, wrapping and dimensional tolerance tests. The tensile strength has to fall within narrow limits corresponding to the wire diameter, the strength increasing with decreasing wire diameter. There are in addition a number of further requirements (2), including a maximum amount of surface decarburization for the music wire grades. The specified chemical composition is given below:

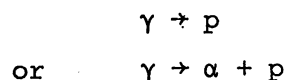
<u>Element</u>	<u>Min.</u> (wt. %)	<u>Max.</u> (wt. %)
Carbon	0.55	0.85
Silicon	-	0.35
Manganese	0.30	1.00
Sulphur	-	0.030
Phosphorous	-	0.030
Nitrogen	-	0.008

The exceptional mechanical properties of this material have caused it to come into general use in a wide variety of fields, from springs to tyre cord and high tensile cables. The term "patented" refers to the process by which an extremely fine pearlitic structure is produced before cumulative cold drawing to high deformations is carried out, the strength increasing progressively with drawing.

2:2 The structure and properties prior to drawing

2:2.1 Introduction

In essence a patented wire is produced from a eutectoid or hypoeutectoid steel which is austenitized and transformed to give a fine pearlitic structure (sometimes with proeutectoid ferrite) thus:



Hypereutectoid compositions are generally avoided as the probability of producing proeutectoid cementite films is increased, which significantly

reduces drawability. Extensive work has been carried out on the morphology and transformation kinetics of pearlite (3 to 10). During the decomposition, the pearlitic nuclei develop in nodular fashion, either from the prior austenite grain boundaries or from ferrite allotriomorphs.

2:2.2 Effects of process variables on morphology and properties

2:2.2.1 General Comments

Considerable research has been undertaken over many years into relating the transformation conditions to the ferrite/pearlite morphology and thus the mechanical properties of the material (usually in uniaxial tensile conditions). Extensive surveys exist (e.g. McNeill (11), Gladman et al (12)) the salient points being given below.

2:2.2.2 Interlamellar spacing

Early work (Gensamer et al (13, 14)) suggested that the spacing was a function of the transformation temperature for a given composition (confirmed by Mellor (15) and Marder and Bramfitt (16)), decreasing with undercooling. It was also shown that the tensile strength of an isothermally transformed eutectoid steel increases linearly with reduction in transformation temperature and logarithmically with the reduction in interlamellar spacing. As reiterated by Gladman et al (12) and Pickering (17), the presence of proeutectoid ferrite complicates the analysis due to other factors discussed below. McNeill (11) has pointed out, there is conflicting evidence on the effect of spacing on toughness. Clearly, increasing the pearlite content of the steel increases the transition temperature (17) to some degree, but the transition range is also increased (18). It appears, though (11, 12) that the fracture stress of a eutectoid steel increases with decreasing transformation temperature, other factors being constant (the reasons for this not being clear).

2:2.2.3 Grain Size

A number of investigations have shown that the ductile/brittle transition temperature is lowered by a reduction in the pearlite colony size, e.g. Gladman et al (12), but it is worth noting that the colony size decreases with pearlite spacing (i.e. with the transformation temperature). This relationship gives an indication of the problems involved in distinguishing between interrelated mechanisms contributing to a macroscopic property.

2:2.2.4 Directionality of the structure

Miller et al (19) noted that cracking in a pearlite colony occurred in shear bands at 45° to the tensile axis and was most prevalent for those colonies with lamellae aligned along the axis. A number of successful attempts to produce directional pearlites have been made, e.g. Mellor

(15 , 20 , 21) and McNeill (11). Mellor suggested that such cracking could be explained on a fibre loading model. Similar alignment of the pearlite lamellae occurs during the cold crawling of patented wire and it has been suggested (15) that such failure of the structure can be elucidated by work with directionally transformed material. The validity of this concept is not clear, particularly when considering the variations of failure mode between fine (drawn wire) and coarser (directionally transformed material) structures.

2:2.2.5 Effects of composition

It has been widely noted, e.g. Gladman et al (12), that as the carbon content, i.e. the cementite content, is increased, the tensile strength increases even after taking into account changes in the proeutectoid ferrite grain size. In fact the proeutectoid ferrite was shown to make a significant contribution up to 90% pearlite by volume. Above this figure its effect fell rapidly, especially when the continuity of the ferrite on the prior austenite boundaries was lost, fig. (2:1). Burns and Pickering (18) showed that increasing the carbon content in hypoeutectoid steels increased the ductile/brittle transition temperature, while noting that reducing the ferrite grain size decreased it. Gladman et al (12), studied in detail the effects of various additions to the mechanical properties of these steels. Nitrogen was found to have little strengthening effect while excess nitrogen was found to drastically reduce the toughness and should be avoided by the addition of nitride-forming grain refiners. Manganese provided solid solution hardening and also increased the strength by reducing the ferrite grain size, pearlite colony size, interlamellar spacing and by increasing the volume fraction of pearlite. It appeared, however, to have little effect on toughness. Silicon was found to increase the tensile strength but was detrimental to toughness. Grain refiners, e.g. aluminium, raised the strength by reducing the grain sizes while niobium and titanium also gave some dispersion strengthening. Bramfitt and Marder (22) have confirmed the effects of alloying elements in improving the hardenability, the ferrite stabilizers (molybdenum and silicon) being far more effective than the austenite stabilizers (manganese, nickel and cobalt).

2:2.3 Nucleation and growth of pearlite

The nucleation and growth of pearlite has been studied for many years. The nucleation problem appears to have been elucidated through crystallographic work, summarized by Dippenaar and Honeycombe (23), who made use of the

stability of austenite in a 13% Mn, 0.8% C steel. They showed that the Bagaryatski relationship:

$$(100)_{\text{Fe}_3\text{C}} // (0\bar{1}1)_{\alpha}$$

$$(010)_{\text{Fe}_3\text{C}} // (1\bar{1}\bar{1})_{\alpha}$$

$$(001)_{\text{Fe}_3\text{C}} // (211)_{\alpha}$$

occurs in cases where nucleation does not take place on a clean austenite grain boundary, in this case on cementite allotriomorphs. Thus the pearlitic cementite is crystallographically related to the adjacent austenite grain.

In the case where the pearlite nodule nucleates on a clean austenite grain boundary, it was shown that the pearlitic cementite and ferrite are Pitsch related:

$$(100)_{\text{Fe}_3\text{C}} \quad 2.6^\circ \text{ from } (13\bar{1})_{\alpha}$$

$$(010)_{\text{Fe}_3\text{C}} \quad 2.6^\circ \text{ from } (113)_{\alpha}$$

$$(001)_{\text{Fe}_3\text{C}} // (5\bar{2}\bar{1})_{\alpha}$$

In addition it has been shown that the cementite habit plane (the ferrite/ Fe_3C interface in this case) exhibits 2 distinct orientation relationships with respect to each other:

$$\begin{aligned} & (001)_{\text{Fe}_3\text{C}} // (\bar{2}\bar{1}5)_{\alpha} \quad \text{Pitsch (24)}, \\ \text{or} \quad & (001)_{\text{Fe}_3\text{C}} // (2\bar{1}\bar{1})_{\alpha} \quad \text{Pitsch and Schrader (25)}. \end{aligned}$$

The significance of these 2 possibilities is not, as yet, clear.

The mode and kinetics of growth of the pearlitic noduli has also been closely studied. This work has been extensively surveyed by Mellor (15) who went on to generalize previous studies to give a growth law of the form:

$$v_p (\bar{d}_e)^{n_p} \exp \left\{ \frac{Q}{RT} \right\} = \text{const.} \quad 2:1$$

where:

- v_p is the growth velocity
- \bar{d}_e is the mean pearlite spacing
- n_p is an exponent corresponding to the diffusion mode of carbon
- $n_p = 2$ for bulk diffusion
- $n_p = 3$ for interfacial diffusion
- Q is the activation energy.

This combined the work on bulk diffusion of carbon in the austenite which gives a rate law of the form:

$$v_p \propto (T_e - T)^2 \exp \left\{ \frac{-Q}{RT} \right\} \quad 2:2$$

or with interface diffusion:

$$v_p \propto (T_e - T)^3 \exp \left\{ \frac{-Q}{RT} \right\} \quad 2:3$$

where: T_e is the eutectoid temperature (in Kelvin)
and the interlamellar spacing is given by:

$$(\bar{d}_\epsilon) \propto \left\{ \frac{1}{T_e - T} \right\}$$

2:2.4 Commercial practice, and its effects on the transformation

The above laboratory work has involved the isothermal transformation of eutectoid and hypoeutectoid steels near the nose of the TTT diagram, fig. (2:2), or if a coarser pearlite is required for experimental reasons, above the nose. The effect of continuous cooling during the transformation (which is closer to the industrial situation) has also been investigated (26 , 27) and industrial practice of producing a suitable pearlitic structure in the bar stock by the patenting process is well documented (28 , 29 , 30). The effect of industrial processing variables has been shown to be critical, and it is clear that although the transformation can be reasonably well controlled in the laboratory the industrial situation is far more complex. Commercial practice is designed to austenitise the rod or wire and transform it to as fine a pearlite as possible (some upper bainite may be present in addition) thus giving good drawability and maximum increase in strength on drawing. There are several types of commercial patenting, basically varying in the environment in which the material is transformed. It is common to use air patenting for the initial wire drawing reductions, while to obtain the finest and most uniform microstructures for the final reductions, lead patenting is used. Research into these techniques, which have been in general use for over 100 years, has been sparse and incomplete (as noted in the CPGS 1), but detailed work has increased in recent years. Cahill and Jones (26) have studied the effects of patenting variables on the structure and properties of the transformed rod. They commented on the best possible combination of austenitising and lead bath temperatures for use in commercial situations. Payne and Smith (27) have considered the transformation kinetics of the decomposition in industrial environments. There is interest at present in attempting to improve the patenting process, both to give higher quality material and also to reduce production costs by the reduction of energy and process material requirements, e.g. Armstrong and Taylor (31).

2:3 The deformation of pearlite and the process of cold drawing

2:3.1 Introduction

The majority of studies concerning the deformation of pearlite have considered that which occurs during uniaxial tension. The modes of deformation and failure of various aggregates of ferrite/pearlite and pearlite (as well as hypereutectoid steels) although extensively investigated are as yet not fully understood; a summary of the work to date is given later. It is not clear

how closely the tensile testing investigations can be applied to the deformation which occurs during wire drawing. Clearly, the processes involved in the tensile case are extensively modified by the high hydrostatic pressure which is set up within the die region (see CPGS 1). It has been pointed out by many workers in this field, that although in a eutectoid steel the cementite occupies only 14% by volume, the deformation and strength of the structure is critically controlled by its presence. For example, the work hardening of a drawn pearlitic steel increases exponentially with the true strain, (28) fig. (2:3), and increases with decreasing lamellae spacing. This is in contrast to iron wire which work hardens linearly (32 , 33 , 34). Thus at a true strain of 4, the pearlitic wire is 4 to 5 times stronger than ferritic wire (35). In addition, the dislocation substructure which is formed on this cold deformation is considerably affected by the pearlitic structure.

Yamada (36) has reviewed the investigations which have been undertaken to investigate the remarkable ductility that patented wire shows on cold drawing (reductions of >99% are possible). It has always been assumed that coarse grained materials gave better drawability and mechanical properties to the finished wire than fine grain stock. However, the modern use of Al-killed steels has shown these materials to be superior, at least when considering drawability. Work has shown that this may be due either to the presence of aluminium reducing the free nitrogen content or by its effect on the austenite grain size. Yamada concluded that a reduction in free nitrogen at constant austenite grain size improves the ductility of as-patented eutectoid steel. A similar improvement was obtained by reducing the austenite grain size (by decreasing the austenitising temperature) at constant free-nitrogen content. Both these effects were most marked for fine pearlitic structures. He suggested that the effect of free nitrogen may be due to a reduction in fracture strain although it might improve the tensile strength.

2:3.2 Wire Drawing

2:3.2.1 Introduction

The techniques of wire drawing have tended to develop through industrial experience rather than through scientific practice. It is only in recent years, with more stringent requirements being placed on the process, that an analytical treatment has been required to give the necessary improvements. Surveys of this field have been given by Wistreich (37), Maclellan (38) and Sutton (39): A general account of the deformation involved along with the practice and results of wire drawing have been given previously in the CPGS (1), a summary of which is given below.

2:3.2.2 General description

The principal function of wire drawing is to produce, from a given bar stock, a wire of a specified size and strength. In the case of patented wire the requirement usually specifies the latter, so stock of sufficient diameter has to be available to allow for adequate reduction. Drawing is normally achieved by successive reductions through hardened steel or carbide dies on a draw bench. This is a continuous process, the wire being wound a number of times about a rotating capstan between each die. The reduction at each die is controlled by, amongst other factors, the tensile strength of the work hardened material at each die exit. Two basic drawing processes have evolved: the "wet" and the "dry" methods. The former involves immersing the dies in a liquid lubricant bath, e.g. mineral oil: it is usually employed for fine wires and non-ferrous materials. "Dry" drawing is accomplished with solid or semi-solid lubricants, e.g. greases or soaps, and is generally used for drawing ferrous materials.

2:3.2.3 Stock material requirements

As can be shown (detailed in the CPGS 1) the failure condition during drawing is that of necking at the die exit when:

$$\epsilon_{\max} = \eta (n'+1) \quad 2:5$$

where

ϵ_{\max} is the maximum true strain at one pass

η is a drawing efficiency term

n' is the strain hardening coefficient (from $\sigma = k\epsilon^{n'}$).

This is to be compared with the theoretical value of ϵ'_{\max} in a tensile test, when:

$$\epsilon'_{\max} = n' \quad 2:6$$

Thus a high value of n' aids drawability. In addition, however, the material must show stable ductility, i.e. failure by brittle fracture modes must not occur (an example of a possible failure mode is shown by the phenomenon of cupping or internal fracture). These parameters are a strong function of the thermomechanical history of the material and consequently many materials are annealed before drawing, e.g. pure metals such as high conductivity copper. An exception is that of patented wire, the process of patenting conferring great drawability along with work hardening capacity on the material. It is common for intermediate anneals and air-patenting to be undertaken to allow greater reduction. The stock bar has to be free from piping, segregation and surface cracks and shivers and it is essential that size and shape control is of the highest order. Surface scale has to be removed before drawing the patented bar as it has a high coefficient of friction. This may be done mechanically (e.g. by shot blasting) or chemically (with dilute mineral acid and inhibitor) or by a combination of the two.

2:3.2.4 Process variables

Before drawing, the patented bar is usually given a borax or phosphate coating to aid adherence of the lubricant, usually a soap. The design of drawing machines varies considerably: in the case of patented wire a non-slip machine with water-cooled capstans is used. It is also common, with modern high-speed drawing machines, to cool the dies (see CPGS 1). Although relatively little heat is removed, such cooling is necessary to reduce die wear as this can cause scoring of the wire, making it unfit for many purposes. This heat production, due to redundant deformation and friction, is a function of (amongst other variables) the draw rate and reduction.

2:3.2.5 The effects of heating during wire drawing

The effects of heat produced during drawing on the wire are not well understood, but it is clear that severe impairment of the mechanical properties occurs if the temperature of the wire reaching a capstan is greater than 120°C (approximately) (see comments in CPGS 1). One of the problems in ^{the} investigation, is the measurement of the wire surface temperatures (being greater than those at the wire core). However, some recent work indicates that instantaneous temperatures of 400°C are possible during normal cold wire drawing (Bridon 40). Theoretical work has substantiated these figures (see CPGS 1) but has indicated that consideration of cooling need necessarily only consider the mean wire temperature.

The rapid, non-uniform increase in the wire temperature has a number of consequences. Die lubrication can fail causing impairment of wire finish, die wear and breakages. In addition such heat treatment can affect the pearlitic microstructure, giving dislocation substructure refinement, strain ageing and spheroidization. The last effect will be considered here while the first two are discussed later in this chapter.

The large ferrite/cementite interfacial area to volume of carbide ratio makes it surprising that pearlite does not spheroidize more rapidly than is in practice observed. In fact complete spheroidization occurs extremely slowly even at just below the eutectoid temperature, showing that the structure is very stable. This has been explained in terms of a low interfacial energy, indicated by the preferred orientation relationships (see CPGS 1). It has been known for many years that deformation increases the rate of spheroidization of pearlite. This was initially attributed to fracture of the cementite (see CPGS 1), but it was later shown that the initial waisting of the cementite plates during spheroidization initiated at kinks, i.e. deformed regions. It has also been noted that concurrent deformation accelerates spheroidization still further, suggesting strain induced

mobility of carbon, possibly by the formation of C/vacancy complexes.

Chojnowski and McG Tegart (41) performed various types of deformation on eutectoid steels to gain an insight into the relative effectiveness of promoting degradation of the structure. It was noted that 50% cold work prior to a 700°C anneal increased the spheroidization by a factor of 100 over that of a straight anneal. Lupton and Warrington (42) performed annealing experiments with cold deformed pearlite. They noticed a high dislocation density in the cementite, which refined to a cell structure on annealing for 1 minute at 580°C. In addition the cementite plates were given a "rippled" appearance by this treatment. They concluded that at high plastic strains the formation of dislocation cell boundaries in both phases increased the rate of spheroidization by enhanced carbon diffusion in addition to the dissolution of cementite in areas of high dislocation density. Ho and Weatherly (43) have considered the spheroidization to be controlled by the motion of triple-points in the cementite dislocation structure leading to "pinching-off" of the lamellae. This agrees with work by Paqueton and Pineau (44) who suggested that spheroidization initiated at sites related to the dislocation structures in both the cementite and ferrite. In addition to investigating the effects of deforming after transformation they considered deforming the austenite (producing grain refinement, and having no effect on the pearlite lamellae) and deforming during transformation (which appeared to be equivalent to deforming both the austenite and ferrite/pearlite).

2:3.3 Deformation mechanisms

2:3.3.1 Deformation and the strength of cementite

In order for pearlite to work harden at a rate greater than that of ferrite, the cementite's role must be critical. Langford (35) has pointed out that for this to occur the lamellae must deform plastically. He correlated data on the plasticity of cementite, fig. (2:4), with reference to the lamellar thickness, although he tended, as many other workers have, to assume that similar ductile behaviour will occur under all deformation modes. Evidence for the presence of crystallographic defect studies in cementite, indicating the possibility of plastic flow, has been summarized elsewhere (see CPGS 1 , 35, 45). Dislocations in this material have been observed in lightly deformed cementite particles in both spheroidized and pearlitic steels. Pickering, (17), has observed cracking in the pearlitic carbide, mainly in the thicker lamellae, while Maurer and Warrington (46), Keh (47) and Inoue et al (48 , 49) (also see CPGS 1), have made further investigations. Both (001) and (010) appear to be possible slip

planes, while incipient cracks were found on (100) planes. To explain these cracks it was suggested that dislocation locks of $\frac{1}{2}\langle 111 \rangle$ type occurred so dislocations of the $\langle 100 \rangle$ type on (010) planes can cause cracking on (100) planes,

$$\text{e.g.} \quad [010] + [001] \rightarrow \frac{1}{2}[111] + \frac{1}{2}[\bar{1}\bar{1}\bar{1}] \quad 2:7$$

It was suggested that [100] and [010] dislocations did not interact in this manner and could therefore cause the majority of plastic deformation. Keh (47) has observed stacking faults on (001) planes in the pearlitic carbide and also noted that room temperature deformation did not appear to increase the defect structure concentration in the cementite, in contrast to that in the ferrite. Koréeda and Shimizu (50) observed tilt boundaries in pearlitic cementite indicating dislocations of the type [0b0]. Little work appears to have been carried out considering the effect of hydrostatic pressure, as exists in the wire drawing die (see CPGS 1) on the deformation of cementite and thus the pearlite. Davidson and Ansell (51), however, have shown the relationship to be complex, but the ductility of a pearlitic sample tends to increase with pressure indicating a general improvement in ductility of the cementite. It has been concluded (11) from the above work that deformation of pearlitic cementite can be accommodated, within limits, by processes of slip and cracking.

Langford has pointed out that if the flow stress of the cementite is assumed to be controlled by the movement of dislocations in the lamellae then the flow stress is considerably underestimated: it was therefore suggested that the controlling factor is the generation of dislocations as no evidence of substructure had been found in the cementite. His comment in fact implies that when considering the deformation of pearlite, the cementite can be regarded as a perfect crystal when considering its resistance to plastic deformation. Thus the yielding of pearlite can be modelled on a Hall-Petch approach considering dislocation pile-ups in the adjacent ferrite. This model (see later) is also supported by the work of Karashima and Sakuma (52) and Takahashi and Nagumo (53) who have measured strain rate sensitivities in pearlite and found them to be the same as in ferrite. There is evidence, in fact, for the existence of dislocation substructures, e.g. Paqueton and Pineau (44) and Lupton and Warrington (42) although they have not been well documented. Inoue et al (48) have suggested that these form only at deformation temperatures greater than 300°C.

McNeill (11) has detailed work which suggests, at least in the drawing process, that kinking of cementite lamellae is common in addition to concurrent thinning due to homogeneous plastic flow. Cracking of pearlitic cementite,

however, has been frequently observed particularly in tensile deformation. It appears to occur, even at low strains due to localised slip in the ferrite on planes intersecting the cementite lamellae. At higher strains cracking can, in addition, be explained on a fibre loading theory (54). It appears, however, that under deformation with a high hydrostatic pressure, e.g. Pepe (55), Embury and Fisher (28), that these defects tend to "heal" and the possibility of void formation and subsequent failure is reduced.

2:3.3.2 Plastic deformation of pearlite during drawing

Langford (35), has distinguished two types of deformation that may occur in a pearlitic structure. The first he termed homogeneous, which involves the operation of many slip systems in both the ferrite and cementite and causes a macroscopic homogeneous reduction in the lamellae widths: the second is inhomogeneous and is often called "deck of cards slip", where one highly stressed slip system in the ferrite, which is more or less parallel to the habit plane, is operative fig. (2:5). In addition a twinning mechanism may operate at extremely high strain rates, e.g. shock loading (56). There is recent evidence (57) to suggest that in fine pearlite deformed in tension, the dominant mode is that of inhomogeneous slip except for colonies accurately aligned with the tensile axis. The effects of work hardening on the deformation mode has not been investigated in detail for this system. It is in this field that orientated pearlitic structures have been employed, e.g. Langford (35), McNeill (11), in order to simplify the possible deformation behaviour. This appears to be a justified simplification: for example the strain hardening rate and the maximum attainable strain is similar to that found in a patented wire of otherwise identical specification (35).

Early work to investigate the deformation of fine pearlite was undertaken on patented wire or patented rolled strip, details of which have been previously given (see CPGS 1). Initial work to elucidate the deformation structure includes that by Kardonskii et al (58) who reported what they termed as a "block-structure" in the ferrite with a 10 to 15 nm scale: the ferrite and cementite plates had thicknesses of the order of 25 to 50 nm and 6 to 12 nm respectively. They suggested that the inherent strength could be due to either the pearlitic structure or to the "block-structure" in the ferrite (the latter related to a Petch type equation).

Embury and Fisher (28) greatly improved on previous work and also investigated the dislocation cell structure in the ferrite which was elongated in the drawing direction. They also noted that the interlamellar spacing was

a constant fraction of the wire diameter, indicating homogeneous, axisymmetric deformation. This last point has been disputed by Dewey and Briers (59) and Langford (60) who attribute the "wavy" transverse microstructure to plane strain elongation. However, Langford's original assumption that the apparent failure of this plane strain to effect the rate of lamellae refinement being due to the cementite fragmentation, has been shown to be erroneous. He has considered in detail (35) the apparent paradox between macroscopically homogeneous deformation, indicated by the relationship:

$$\left\{ \frac{\bar{d}_1}{\bar{d}_\epsilon} \right\} = \left\{ \frac{D_o}{D_\epsilon} \right\} \quad 2:8$$

where: \bar{d}_1 is the initial mean interlamellar spacing
 \bar{d}_ϵ is the mean interlamellar spacing at a true strain ϵ
 D_o is the initial wire diameter
 D_ϵ is the wire diameter at strain ϵ ,

and local plane strain deformation caused by the <110> wire texture (the latter giving rise to the typical "wavy" microstructure). It appears that this local mode is defeated by redundant deformation of various types resulting in a nett deformation giving the impression that the wire texture had had no effect. The "wavy" appearance of the transverse section is apparently due to subunits deforming from an equiaxed form to a lenticular shape in wire drawing. Work by Hosford (61), Peck and Thomas (62) and Meiran and Thomas (63) has helped to explain the deformation modes leading to this structure and the <110> bcc wire texture.

It is interesting to compare other deformation modes with wire drawing (see CPGS 1 for details). Aernoudt and Gil Sevillano (63) have examined torsion of patented wire where the strain hardening rapidly falls to zero during testing. This was attributed to there being a constant dislocation free path in the ferrite in this case. Langford (35) has compared wire drawing to strip rolling and has shown that a similar strain hardening equation to that given by Embury and Fisher (28) (for wire drawing) can be applied, although the derivation is not the same.

2:3.3.3 Strengthening mechanisms and work hardening in drawn pearlite

As previously noted (Ch. 2:2.2.1) the tensile strength of as transformed eutectoid steel increases logarithmically with the reduction of interlamellar spacing. This is only the first reason for high quality patenting to obtain a fine structure, the second being the enhanced ductility so obtained. Embury and Fisher noted that the dislocation cell size formed in the ferrite by cold drawing was proportional to the wire diameter, the initial cell size being controlled by the interlamellar

spacing. In fig. (2:6) is presented their plot of proof stress versus reduction in area. They gave considerable thought to the possible dominant mode of strengthening. A simple fibre strengthened composite model was suggested, i.e.:

$$\sigma_c = \sigma_f V_f + \sigma_m (1 - V_f) \quad 2:9$$

where:

- σ_c is the composite failure stress
- σ_f is the fibre failure stress
- σ_m is the matrix failure stress
- V_f is the fibre volume fraction

The failure of this model to predict the material's strengthening characteristics has been discussed elsewhere (see CPGS 1). Another fibre model (see CPGS 1) postulating a work hardening matrix with a non-plastic second phase, predicts a relationship of the form:

$$\sigma_c \propto (\epsilon_p)^{\frac{1}{2}} \quad 2:10$$

where: ϵ_p is the plastic strain.

Embury and Fisher, however, did not find this, instead they showed that the flow stress could be related to the mean transverse ferrite cell size, thus:

$$\sigma_{fl} = \sigma_o + K' (\bar{d}_b)^{-\frac{1}{2}} \quad 2:11$$

where:

- σ_o is the apparent friction stress in ferrite
- K' is the Petch slope
- \bar{d}_b is the mean transverse barrier

intercept, where the barrier could be either cementite lamellae or dislocation cell walls. Their results of proof stress versus \bar{d}_b is reproduced in fig. (2:7). Although they did express caution in accepting too strong an analogy with the normal Petch plot, it was assumed that the cell structure was the dominant strengthening mechanism.

The use of transverse intercept values in the above and later work, as opposed to the dislocation slip distance in the ferrite may, at first sight, be unacceptable. McNeill, however, has shown that the errors so introduced are negligible.

Chandok et al (65) continued the investigation (see CPGS, 1 , for details) and noted the effects of drawing at various temperatures on the wire strength (fig. (2:8)) which is of relevance when considering industrial drawing practice. Embury, Keh and Fisher, (66), made a study of substructural strengthening in a number of materials including patented wire (fig. (2:9)). They concluded that in general no simple relationship existed between the substructure scale and the plastic strain (fig. (2:10)). It appeared,

however, that the relationship:

$$\sigma_{fl} \propto (\bar{d}_0)^{-1/2} \quad 2:12$$

held for each material (c.f. Petch). Langford (60) pointed out that the Embury and Fisher relationship (equation 2:13) appeared to be more accurately obeyed by drawing at low temperatures (fig. (2:11)). As noted above, he stated that the deformation is locally plane strain (as opposed to Embury and Fisher who concluded it was homogeneous) although for the incorrect reason. It can be shown (see CPGS 1) that Embury and Fisher's theory leads to the relationship:

$$\sigma_{fl} = \sigma_o + \frac{k'}{(2\bar{d}_0)^{1/2}} \exp \left\{ \frac{\epsilon_p}{4} \right\} \quad 2:13$$

whereas Langford predicted:

$$\sigma_{fl} = \sigma_o + \frac{k''}{(\beta\bar{d}_0)^{1/2}} \exp \left\{ \frac{\epsilon_p}{2} \right\} \quad 2:14$$

where: $1 < \beta < 2$, \bar{d}_0 is the initial mean barrier intercept.

It appears from Langford's later comments (35) that he now believes that the failure of equation 2:14 is the result of a complicated interaction between deforming subunits in the microstructure.

From the above comments it is clear that there has been some inconsistency in considering whether the slip distance in the ferrite lamellae is controlled by the interlamellar spacing or by a dislocation substructural spacing (the pearlite colony size not affecting the flow characteristics, (11)). It is not obvious why the Hall-Petch approach to yielding should necessarily apply if the slip distance is limited by the lamellar width. Both Takahashi and Naguro (53) and Chadwick (67) have expressed doubts that a stress field caused by a dislocation pile-up on one side of a cementite lamella should act through it to activate a dislocation source in the adjacent ductile (ferrite) lamella. Similarly it is not clear whether a Hall-Petch type of relationship, typically of the form:

$$\tau_{fl} = \tau_o + K' (d)^{-\psi} \quad 2:15$$

where: $\psi = 1/2$ in the Hall-Petch case, applies to plastic deformation within a dislocation substructure. This latter point is dealt with in more detail later in this chapter.

An alternative approach in the situation where the lamellar spacing controls the slip distance, is to consider the nucleation of a dislocation in the cementite (the existence of which has been shown by empirical studies) at the tip of a dislocation pile-up in the ferrite. Langford (35) has stated that dislocations probably do not interact with the ferrite/cementite interface due to the phases elastic moduli being similar.

This is oversimplifying the situation at the interface. As continuity there is generally maintained and as, in the general case:

$$\begin{aligned} \vec{b}_{cm} &\neq \vec{b}_{\alpha} & 2:16 \\ \text{where: } \vec{b}_{cm} &\text{ is a burgers vector in cementite} \\ \vec{b}_{\alpha} &\text{ is a burgers vector in ferrite} \end{aligned}$$

dislocations are required to be generated in the interface if deformation is to proceed into the cementite. Such extrinsic dislocations would be present in the interface in addition to 3 sets of intrinsic dislocations. The latter are present to allow for mismatch at the energetically favourable orientation relationships which exist in this structure. Thus considerable work will need to be done to propagate plastic flow, and strain hardening will occur by this mechanism in addition to others. Clearly for generalised plastic flow, as^{is} observed in practice, extrinsic dislocations must find sinks, such as points where dislocations can be forced into cementite and ferrite again. A further complication to this concept is the observation that dislocations can be emitted from grain and phase boundaries under low strains without the necessity of pile-ups (see later).

The consideration of the work-hardening behaviour of this material, during a tensile test for example, has been considered by a number of workers, although the comments made in the previous paragraph concerning dislocation dynamics have not been taken into consideration. Empirical investigations have produced conflicting results. Takahashi and Nagumo (53) derived an expression for $(\partial\sigma/\partial\epsilon)_{tr}$ by considering dislocation densities which could develop between lamellae:

$$\left(\frac{\partial\sigma}{\partial\epsilon}\right)_{tr} = \frac{\alpha, \mu b_{\alpha}}{2} \left[\rho_o (1+\beta' \epsilon_t) + \frac{\epsilon_t}{b_{\alpha} \lambda_{\alpha}} \right]^{-\frac{1}{2}} \left[\rho_o \beta' + \frac{1}{b_{\alpha} \lambda_{\alpha}} \right] \quad 2:17$$

$$\begin{aligned} \text{where: } \alpha, \beta' &\text{ are constants} \\ \mu &\text{ ferrite shear modulus} \\ \lambda_{\alpha} &\text{ ferrite mean free path} \\ \rho_o &\text{ initial dislocation density} \end{aligned}$$

Clearly this is a complicated relationship and in fact their results did not support it (showing a $\lambda_{\alpha}^{\frac{1}{2}}$ dependence). Karlsson and Linden (68) suggested that $(\partial\sigma/\partial\epsilon)_{tr}$ was not a function of the inter-lamellar spacing, while McNeill's results (11) indicate that the function increases with decreasing interlamellar spacing. In addition he noted a reduction of the dependency of $(\partial\sigma/\partial\epsilon)_{tr}$ with increasing ϵ_p and suggested that the Ludwig relationship:

$$\left(\frac{\partial\sigma}{\partial\epsilon}\right)_{tr} = k, n' \epsilon_p^{(n'-1)} \quad 2:18$$

$$\text{where: } k, n' \text{ are a function of } \epsilon_p, \text{ is reasonably well obeyed.}$$

Reasons for the dependence of the strain hardening function on ϵ_p were suggested in terms of back stresses making dislocation sources inoperative at high ϵ_p , while its dependence on lamellar spacing was assumed to be consistent with dislocation generation at the ferrite/cementite interface (as observed by Pickering, (17)).

2:3,4 Dislocation substructures and related topics

2:3.4.1 Introduction

The production, behaviour and properties of dislocation substructures have been subject to considerable investigation in recent years, mainly in response to industry's requirements for stronger, tougher materials. Such substructures are commonly produced by thermomechanical working, and the term substructure strengthening has, as a result, come into general use. The most common method of such strengthening involves cold deformation, i.e. at $<0.4T_m$ (c.f. cold drawing), to introduce a high dislocation density, which may be followed by a recovery heat treatment to allow solute pinning or to rearrange the dislocations into a more stable configuration. The strength of a metal whose grains contain subgrains or dislocation cells (the latter be defined as formed at low homologous temperature) produced by such a technique, is greater at both ambient and elevated temperatures than one with recrystallised grains of the same size (69). Such substructures can, in fact, be produced by cold work with recovery, fatigue, creep or hot working, only the first being considered here in detail. It is worth noting, however, that in each type of deformation a cellular dislocation substructure is formed which apparently does not affect the well known dependence of the flow stress on the square root of the dislocation density. It has also been observed that the cells become larger with fewer interior dislocations and more regular boundaries as the deformation temperature and/or time are increased or if the strain rate and/or amplitude are decreased (69).

An extremely thorough review of this field has been given by McElroy and Szkopiak (70) and further useful reviews are due to McQueen (69) and in the CPGS (1). The work reviewed includes many other types of deformation other than that present in cold drawing, however the following comments are restricted to this problem. It has become conventional to refer to the non-homogeneous dislocation structures that can be produced by cold working as tangles or cells, to distinguish

them from typically higher temperature deformation structures such as subgrains which show cleaner, more regular substructure boundaries (71).

2:3.4.2 Substructures formed from cold working

Basic concepts

Considerable work has taken place (70) to investigate dislocation substructures in crystalline materials and has revealed 2 basic types of dislocation arrangement:

- (a) 3 dimensional networks - Frank nets;
- (b) planar dislocation arrays - low angle boundaries.

The first is a network of intersecting dislocations with the vector sum at any node being zero: they often possess a high thermal stability. Planar arrays are often divided into tilt, twist or hybrid boundaries and can arise in a number of ways, the basic factor being an excess concentration of one sign of dislocation in a region of the lattice. The general form for the relation governing the dislocation spacing, h , is:

$$|\underline{b}|/h = \theta, \text{ for } \theta < 5^\circ \quad 2:19$$

where: θ is the twist or tilt misorientation
 \underline{b} the burgers vector.

An important feature of such planar networks is that long-range internal stresses due to the dislocations are approximately eliminated by their mutual interaction, while their short-range stress fields remain (72). The effect of solute on such dislocation configurations manifests itself mainly through its effect on the stacking fault energy (SFE). It is considered (70) that the most important effects are those due to the interaction of extended dislocations at nodes and the reduction in cross-slip, the latter reducing the likelihood of dislocation rearrangement so promoting the formation of cell walls (which can be regarded as 3-dimensional arrays of dislocations as opposed to planar arrays). Theoretical work on the behaviour of dislocations in forming planar arrays (nets) of various types have been produced frequently noting the effects of the thermo-mechanical regime and microstructure. Many analyses are due to Li (e.g. 72 , 73) along with reviews by other workers e.g. Thompson (71), McQueen (69). It is not clear how closely these analyses can be applied to practical cases but they have been of use in postulating the fundamental causes behind experimental observations.

2:3.4.3 Substructures in deformed polycrystals

Dislocation substructures are basically a function of one material variable, the SFE, and 3 experimental variables, the values of ϵ_p and $\dot{\epsilon}_p$ and the deformation temperature. Their main effects are similar in

both fcc and bcc structures provided the material has a SFE value greater than approximately 0.03 Jm^{-2} . In such cases cross-slip is relatively easy, ferrite being an example (see CPGS 1 and McElroy and Szkopiak (70) list values of SFE). In the case of cold deformation dynamic recovery is slight (74) and the dislocation density and flow stress increase monotonically with ϵ_p (69): the flow stress is proportional to $\sqrt{\rho}$ (ρ the dislocation density) with the dislocation distribution varying from uniform to cellular. The main features of the structure developing with ϵ_p (fig. 2:12) are:

- (a) $\epsilon_p < 0.01$ - little interaction between generated dislocations;
- (b) $\epsilon_p < 0.1$ - dislocation density increases and clusters are formed which develop into tangles;
- (c) $\epsilon_p \approx 0.1$ - the tangles link to form a fairly well defined cell structure (the cell wall being, in effect, a Frank network);
- (d) on further deformation there is little reduction in cell size but a gradual increase in wall dislocation density;
- (e) at high strains (as is found in wire drawing) elongation of the cells, along with transverse cell size refinement, coupled with the development of a texture is often noted (e.g. 69) (this is particularly obvious in bcc materials 66).

The initial cell size formed in a single phase material is dependent not only on the material SFE and the test conditions but also on the grain size. Conrad et al (75) obtained a relationship:

$$\bar{d} \propto \bar{d}_g^{-1/3} \quad 2:20$$

where: \bar{d}_g is the mean grain diameter.

Often, however, a relationship of the form:

$$\bar{d} \propto \bar{d}_g^{-1} \quad 2:21$$

$$\text{or} \quad \bar{d} \propto \bar{d}_g^{-1/2} \quad 2:22$$

is found, e.g. (76). The strain necessary to produce a cellular structure decreases with increasing deformation temperature, fig. (2:13), while the limiting cell size increases with deformation temperature, fig. (2:14). Alloying additions to bcc materials, particularly carbon and nitrogen in the case of ferrite, have considerable effect on the substructure. In general the tendency is to increase dislocation generation and multiplication rates along with accelerating tangle and cell formation. Also a finer limiting cell size has been noted (77). At somewhat higher temperatures (180°C to 300°C in the case of ferrite) it appears that alloying elements may hinder cell formation by dynamic strain ageing effects (see later). (The effects of alloying additions

on fcc materials are generally more severe, cell formation only being found at much higher strains.) Schlaubitz et al (78) have considered the changes in the relative mobilities of edge and screw dislocations in a bcc structure with temperature. They postulated the existence of a transition temperature (T_t) above which the yield stress is approximately constant and below which it increased with decreasing temperature. It was suggested that above T_t a cell structure could be formed due to the enhanced mobility of screw dislocations. The process was related to the development of textures and it was proposed that cells only formed in grains with non-stable orientations.

The effects of a dispersed second phase, such as carbides in steels, is in many ways similar to those of solutes: by increasing the rate of cross-slip, dislocation interactions are increased. It appears (66) that the initial cell size formed in a variety of materials is often a function of the microstructural scale of the second phase (clearly of relevance to drawn pearlite). In general the cell structure formed with a dispersed second phase in a bcc matrix reduces continuously in size during deformation (66), fig. (2:15). Thus a fine initial dispersion, as is found in a patented eutectoid steel, allows cold drawing to form an extremely fine cell structure (28), fig. (2:16).

Theoretical work has been carried out on the formation and behaviour of dislocation cells. Karashima et al (79) considered the stability of uniform dislocation distributions by means of an energy analysis. They assumed that, either:

- (a) dislocations arrange themselves to minimise the shear stresses at constant strain rate, for tensile deformation; or,
- (b) dislocations arrange themselves so the strain rate is maximised, for creep deformation. They derived formulae for each case defining a critical dislocation density (ρ_c) above which a cell structure would form (see CPGS 1).

Holt, (80 , 81) has considered alloys where the prior thermomechanical history is not significant in the building of a cell structure (not in pearlite or ferrite but, for example, in the fatigue of high SFE alloys). He looked for situations where the initially uniform dislocation density was unstable to periodic fluctuations (c.f. spinodal decomposition) due to a lowering of the elastic energy by clustering. He showed that fluctuations of certain wavelengths grew most rapidly, this wavelength being identified with the cell size. The

wavelength also corresponded to the scale of dislocation interactions, implying the cell size was determined by the distance at which the elastic stresses of the dislocation walls became too small to effect the motion of free dislocations.

Bergström (82 , 83) has advanced a model describing the dynamic equilibrium of dislocation generation and recovery in a material of constant grain size. He examined in the post-Lüders stage of deformation by which point cells (which were assumed to be stable) had been formed. It was suggested that strain hardening occurred due to the increase in density of immobile dislocations. The model is summarised in fig. (2:17).

2:3.4.4 Post-deformation phenomena—

General comments

The effects of annealing cold-worked materials, at progressively higher temperatures, on the defect density and distribution, phase dispersion and physical and mechanical properties, is of considerable importance. Following McElroy and Szkopiak's definitions, the commercial heat treatments that can be given to patented wire after forming can be defined as low or intermediate recovery. It is generally accepted (69) that during annealing the material's strength decreases as a result of static recovery which takes place by processes of cross-slip, climb and combination or annihilation of dislocations, e.g. fig. (2:18). The activation energy for recovery is usually the same as for volume diffusion and the processes show no incubation period, proceeding with decreasing driving force and rate as the substructure approaches lower energy states.

During low temperature recovery (70) considerable elimination of point defects occurs, by annihilation or clustering or by segregation of other atomic species to such sites. At these temperatures ($<0.2T_m$) only slight rearrangement of dislocations can occur, the major cause of changes in mechanical properties being due to static strain ageing effects (see later). At intermediate annealing temperatures ($0.2T_m$ to $0.4T_m$) dislocation interactions (such as those detailed later) can occur, the result being some reduction in the cell interior dislocation density along with a reduction in the thickness and complexity of the cell walls (70): these substructural rearrangements relieve residual, internal stresses. Given extensive annealing, particularly at higher temperatures, the cells develop into subgrains

with well defined dislocation nets as boundaries. It has been noted (69) that the rate of recovery can be increased by imposing an external stress (essentially a form of creep). Recovery may also be promoted by solid solution additions since the solute can pin the cell walls: however, it may hinder recovery by reducing the SFE. A dispersion of a second phase stabilizes a dislocation substructure by inhibiting cell wall migration and growth.

Sandström (84 , 85) has considered the mechanism and kinetics of subgrain and cell growth and coalescence, and of dislocation recovery in these structures. Expressions were derived for the retarding behaviour of a dispersion of a second phase and mechanisms for subgrain recovery were summarised as:

- (a) pair annihilation of dislocations in the walls;
- (b) pair annihilation of dislocations in subgrain interiors;
- (c) transfer of dislocations to the cell interiors by emission from the walls;
- (d) transfer of dislocations from the cell interiors for absorption in the walls;

Subgrain growth mechanisms were suggested to be:

- (a) extraction of wall dislocations;
- (b) emission of wall dislocations;
- (c) migration of dislocations in the boundaries;
- (d) migration of boundaries.

McQueen has pointed out some of the advantages of annealing after cold working. Annealing can be carried out so that there is no significant dimensional change nor a change in the surface condition (both of which are usually important where cold working processes are employed). The reduction in residual stresses can itself lead to an improvement in dimensional stability and corrosion resistance. The main effect is often an improvement in the mechanical properties by a reduction in the mobile dislocation density. In many cases it is not clear how this is brought about: strain-ageing (see later) and dislocation interaction and annihilation are possible causes. (Work by Myshlayaev et al (86) for example has shown an increase in the cell wall stability by the formation of loops and stacking-fault tetrahedra on quenching.) In the case of low temperature mechanical properties it is the effect of post deformation annealing on the work-hardening rate and the tensile strength which is most significant.

2:3.4.5 The effects of strain ageing with particular reference to annealing of patented wire

Considerable work has been undertaken on the phenomena of interstitial and substitutional strain ageing and there exist a number of extensive reviews, the most relevant being those due to Baird (87 to 91, and 92) In addition, Brindley and Worthington (93) have reviewed the effects of substitutional solid solution on yield-points and dynamic strain ageing. Baird (92) has considered the main features of this phenomenon with particular reference to the effects of interstitials in steels. It manifests itself mainly by an increase in the flow stress on ageing after or during deformation: ageing after deformation being termed static strain ageing, while that during deformation being dynamic strain ageing. Other properties may also change, e.g. a return of a yield drop (particularly in low carbon steels); a rise in the ductile/brittle transition temperature; a rise in the tensile strength; a reduction in tensile ductility and a decrease in the internal friction peaks. It has been explained by the segregation of solute atoms to form a Cottrell atmosphere around dislocations which have been produced during deformation (92), in the case of steels this being mainly due to carbon and nitrogen. Strain ageing is commercially important in a number of ways: it can give an undesirable decrease in the cold-formability, reduce the toughness or cause problems associated with yield point phenomena (e.g. stretcher strains). In addition, dynamic strain ageing can cause ductility troughs at certain working temperatures. There can be attendant advantages (Baird (92)) such as the significant improvement in strength of cold-worked steels and the improvement of fatigue and creep properties.

The static strain ageing of a ferritic steel can be divided into several stages with ageing time: initially the yield stress rises but the work hardening rate remains constant; later the work hardening exponent, n' , increases; finally the properties degrade. The main effect of increasing the ageing temperature is to make this sequence more rapid. It is now thought that an interstitial atmosphere is initially formed around dislocations and this produces an increase in K' , the Petch slope (equation 2:15). Later an increase in τ_0 is apparent which is thought to be due to pinning of dislocations by other dislocations or by fine precipitates. Most investigations into these effects have been made with rapidly cooled and aged samples to ensure supersaturation of solute. It is not clear how closely the above work can be applied to situations more approaching equilibrium (further comments are made later). The comparative effectiveness of carbon and nitrogen as strain ageing agents

has been reviewed by Baird (92). For a given solute concentration their effect appears to be similar, however their solubilities vary differently with temperature (92). At low temperatures (less than 100°C say) the equilibrium solubility of carbon in ferrite is very low and it has been suggested that as a result its strain ageing capabilities are insignificant. At higher temperatures, however, it has been suggested (92) that fine carbides can redissolve at a rate which can supply sufficient solute to give the observed effects. In contrast, below 100°C the nitrogen in such steels, which has a higher solubility, can cause strain ageing, although the situation is complicated by the possibility of interaction between free nitrogen and precipitated carbides. Further complications occur with the addition of other alloying elements. Those in solid solution only have an effect on the rate of strain ageing if they interact with carbon or nitrogen. Carbide and nitride formers, for example aluminium, zirconium, titanium, vanadium, boron, chromium and niobium, slow the ageing by reducing their equilibrium concentration, while such elements as manganese also retard strain ageing by means of a complicated interaction.

Dynamic strain ageing normally occurs at typical process deformation rates in the 100°C to 300°C temperature range, although the lower limit may be decreased by an increase in the free interstitial concentration. Typically as dynamic strain ageing becomes effective the tensile strength and the work hardening rate increase and serrated flow (the Portevin-Le Chatelier effect) may be noticed. These are accompanied by a reduction in toughness. The causes behind these changes and the effects of other alloying elements are similar to those of static strain ageing, although it is thought that nitrogen is generally more important than carbon pinning in the role of dislocation pinning in most steels (92). It has been noticed that the dislocation density increases rapidly, being nucleated to maintain the applied strain rate. The effects of strain ageing during low temperature creep is of particular interest in the present work. Baird (92) has reported on the conflicting evidence concerning the effects in ferritic steel. It appears, however, that solute pinning, e.g. by carbon and nitrogen, has little effect on the creep rate whereas creep at higher temperatures (450°C to 650°C) in steels with further alloying additions^{it} appears to be somewhat retarded, possibly by substitutional segregation or by the pinning by alloy carbides (although the latter may be produced prior to creep).

In general strain ageing mechanisms which can be applied to the case of patented wire have been developed from quench ageing studies,

e.g. Phillips (94), Vyhna1 and Radcliffe (95) and Kleemola and Kuusisto (96). The way in which the supersaturated ferrite (with interstitials and vacancies) decomposes has been shown to be a complicated function of both the quench rate and ageing temperature (95). Phillips (94) showed that the mode of decomposition (e.g. whether a precipitate was formed and on what scale) was a function of the dislocation density: the higher the density the less likely was precipitation to occur, the carbon and nitrogen segregating to the dislocations as interstitials. This last result was in contradiction to some earlier work by Doremus (97). The crystallography of such precipitation was studied, e.g. Phillips (94) and Leslie (98), and appears to vary with ageing temperature and alloying content. The effects of certain alloying additions were described by Kleemola and Kuusisto (96) and Leslie (98), chromium, manganese and nickel apparently affecting the solubility and precipitation of carbides and nitrides.

Strain ageing work on pearlitic steels has been considerably less frequent: Peterson (99) has studied a range of hypoeutectoid steels and noted that such a post-deformation heat treatment is of considerable value in the case of medium and high carbon, cold drawn steel bars. He concluded that atmosphere locking along with some precipitation could explain the noted increase in strengths in such materials. Yamada (100) has specifically considered the static strain ageing of eutectoid steel wires and suggested that the processes can be considered in 3 stages with increasing temperature (for constant annealing time).

- (a) Below 150°C: supersaturated carbon and nitrogen lock dislocations, in patented pearlite he considered that the amount of supersaturated carbon was insignificant as compared with nitrogen.
- (b) In severely cold worked specimens annealed between 150°C and 250°C, further locking of dislocations occurred by interstitial carbon from the dissolution of cementite.
- (c) Above 250°C it appeared that although the dislocations were pinned by carbon, or possibly carbides, recovery and recrystallization occurred, causing a degradation in mechanical properties.

Szombatfalvy's investigations (101) with patented wire considered the effects of annealing on the mechanical and magnetic properties. He considered that the effects below 100°C were due to a reduction in the internal stress levels, while between 100°C and 250°C segregation phenomena were important. He found that optimum mechanical properties were obtained with a 200°C heat treatment.

2:3.4.6 Comments on dislocation substructures produced by other deformation modes

It has been pointed out, earlier in this chapter, that the term cold deformation often disguises the fact that significant heating can occur. Previous work on patented wire has not noted any effects of this heating and it has been assumed that if adequate cooling is applied during drawing, the structure and properties of the wire were not significantly affected.

Hot working has been defined (69) as that at greater than $0.5T_m$ and at $\dot{\epsilon}_p > 10^{-4} s^{-1}$: the term has been subdivided to acknowledge the various mechanical behaviour differences that have been noted. It is generally true to say that a subgrain structure is formed at an early stage and, due to a rapid rate of dynamic recovery, a steady state is soon attained with little change in the subgrain size or shape or the dislocation density. (This is to be contrasted with the grains containing these subgrains which elongate at high strains.) This behaviour, which should be contrasted with that of cold deformation, is depicted in fig. (2:19). Creep at temperatures greater than $0.5T_m$ and $\dot{\epsilon}_p < 10^{-4} s^{-1}$ can produce similar subgrains. Details of both situations are given by McQueen (69): He has also summarised dislocation theories which have been suggested for the formation of subgrain boundaries and their behaviour. Solute additions in general appear to retard recovery (c.f. cold working) and it appears that a fine second phase dispersion stabilizes the substructure and frequently determines its dimensions. A review of flow stress and subgrain size and stability at elevated temperatures has been carried out by Sherby et al (102).

2:3.4.7 The effects of dislocation substructures on mechanical properties

2:3.4.7.1 Flow initiation in materials possessing dislocation substructures

A considerable amount of research has been undertaken on the effects of dislocation substructures on material properties and in formulating models for yielding and flow related to observed substructures. Li and Chou (103) have considered in detail the role of dislocations in flow stress/grain size relationships. They distinguished between several types of model:

- (a) dislocation pile-up models, both single layer and more complex situations, along with the effects of second phases etc.;
- (b) non-pile-up models, e.g. work hardening theories, grain boundary source theories and dislocation dynamic theories.

They showed that the observed Hall-Petch observance with grain size can

be accounted for by any of the models with varying degrees of success and plausibility. Since the Li and Chou review further work has been undertaken to formulate more advanced flow models, e.g. Hirth (77,104), Ashby (105) and Thompson et al (106): it is obvious that further clarification is required.

McElroy and Szkopiak (70) noted that several methods of producing dislocation substructures have been employed to allow mechanical property theories to be elucidated. They can adequately be subdivided thus:

- (a) cold working,
- (b) cold working and annealing,
- (c) cold and warm working followed by annealing,
- (d) hot working followed by a quench to suppress recrystallization,
- (e) growth of single crystals from the melt.

Methods (b) and (c) have been the most versatile, the annealing "sharpening-up" the substructures and producing a more uniform value of internal stress. Wire drawing has been employed to great effect in these studies (see CPGS,1) the degree of drawing being used to vary the cell size.

Early work (70) suggested that the flow behaviour of such materials could be modelled by a Hall-Petch relationship, e.g.:

$$\sigma_{fl} = \sigma_o + K' \bar{d}^{-\frac{1}{2}} \quad 2:23$$

where:

σ_{fl} is the flow stress

σ_o is the friction stress

K' the Petch constant

\bar{d} the mean subgrain/cell size

McElroy and Szkopiak (70) gave details of this work along with a summary of values for σ_o and K' for various situations.

More recently the value of the exponent of the cell size (\bar{d}) has come into question and a more general relationship has been suggested:

$$\sigma_{fl} = \sigma_o + K' \bar{d}^{-\Psi} \quad 2:24$$

At high homologous test temperatures, experimental data indicates $\Psi \sim 0.5$ (McQueen and Hockett(107), Miller and Sherby (108), Young et al (109)), the room temperature flow behaviour, however, does not in most cases appear to follow this dependence. Young and Sherby's work (110) with iron alloys gives a value of $\Psi = 0.79$ and other workers (Abson and Jonas(111), Abson and Jonas (112), Annand and Gurland (113, 114)) have obtained $0.5 < \Psi < 1$. A considerable amount of experimental data if plotted with $\Psi = 0.5$ gives a very small or negative value of σ_o : this appears to be unrealistic (c.f. grain size dependence, Li and Chou (103)). Data obtained by Langford and Cohen (32, 115) using iron wires drawn to high strains ($\epsilon_p \sim 7$) clearly shows a relationship with $\Psi = 1$, fig. (2:20). By using a

model with dislocation loops bowing from a boundary net (115), they have derived a relationship of the form:

$$\sigma_{fl} = \sigma_o + k_2 G |b_{\alpha}| (\bar{d})^{-1} \quad 2:25$$

where: k_2 is a bulk material constant (~ 2.5)

G the bulk modulus

b_{α} the burgers vector in ferrite

More recent, extensive reviews of this field are due to Young and Sherby (110) and Thompson (71). Young and Sherby used the generalized Hall-Petch relationship (equation 2:24) and attempted to explain the variation of Ψ by postulating that below a given size, cells are a more effective strengthening mechanism than the grains, for given test conditions, as represented in fig. (2:21). Annand and Gurland's work (113, 114) indicated a value of $\Psi = 0.5$. They suggested that other values of Ψ may be due to large numbers of mobile dislocations in the interior of the cells, a high "redundant" density in the walls, elongated cells and texture effects. Their cells were found to be equiaxed with few interior dislocations with well defined cell walls.

Staker and Holt's work (116) showed that the flow stress, τ_{fl} , associated with a cell structure in a single phase material could be represented by (fig. 2:22):

$$\tau_{fl} = \alpha_2 G |b| \sqrt{\rho_w} \quad 2:26$$

where α_2 is a material constant (~ 0.5)

ρ_w is the dislocation density in the walls.

This is a well known relationship (e.g. see Li and Chou (103)) for uniform dislocation arrays. In Holt's analysis (81), which applies to the cell substructure case (71), the cell size should vary:

$$\bar{d} = \frac{k_4}{\sqrt{\rho_w}} \quad 2:27$$

where k_4 is a material constant, although it appears to vary with strain, alloying content, strain rate and temperature (66). Combining equations 2:27 and 2:26.

$$\tau_{fl} = \alpha_2 k_4 G |b| \bar{d}^{-1} \quad 2:28$$

One advantage with Holt's energy analysis is that it is not concerned with specific dislocation source or barrier models, although its validity is still not proved. Thompson (71) has suggested that equation 2:28 could be modified to:

$$\tau_{fl} = \tau_o + k_3 G |b| \bar{d}^{-\Psi} \quad 2:29$$

(c.f. Langford and Cohen (32, 115)) and has suggested that a value of τ_o ought to be obtained from single crystal work rather than by extrapolation

of polycrystalline data to infinite cell size. A plot of $\tau_{fl}/G|b|$ versus \bar{d} due to Staker and Holt (116) for pure materials is given, fig. (2:23), and for iron alloys, fig. (2:24), indicating a value of $\Psi = 1$. Care has to be taken when attempting to obtain a value of Ψ and the range $0.5 < \Psi < 1$ can often be shown to be acceptable for a given set of data (77, 71): one problem is, in many cases, a restricted range of \bar{d} values. McElroy and Szkopiak (70) considered $\Psi = 0.5$ is generally valid, although most of their data appears to be for recovered material. Rack and Cohen's work (33) on drawn iron wires (quoted by Thompson (71)) apparently showed that Ψ decreased progressively from 1 to 0.5 as the recovery treatment proceeded (see later). It appeared, however, that for most materials with a predominantly cellular structure $\Psi = 1$. A consideration of the variation in the values of σ_o and K' in equation (2:24) was given by McQueen (69). There appeared to be a very wide scatter in the values of σ_o (unlike those of K') for any one alloy including negative values. McQueen dispensed with this anomaly by the use of an Abson and Jonas (111) relation of the form:

$$\sigma_{fl} = \sigma_o + K'' \bar{d}^{-p_d - \frac{1}{2}} \quad 2:30$$

indicating that the boundary became stronger as the substructure scale decreased. This argument appears now to be unnecessary due to later work described here.

The theoretical reasons behind this dependence are not altogether clear (see Thompson (71), Bassin and Kuhlmann - Wilsdorf (117), Li (72, 73) for theoretical reviews). The main problem is the consideration of how a dislocation source in a wall, e.g. a segment of the network, behaves under both internal and applied stresses. Such models appear to work quite well for cells, whether the movement of dislocation segments are considered or (after high deformation) if the wall is considered as a tilt boundary (73), the latter concept being rather more dubious (71). Another interesting possibility, also commented on by Thompson (71), is the penetration of walls by mobile dislocations, which is more likely for cell walls than for subgrain boundaries.

The flow behaviour of subgrains at room temperatures is generally accepted to be more like that of grains with high angle boundaries, i.e. $\Psi = 0.5$. Such planar arrays of dislocations can be produced by either dynamic recovery or by post-deformation heat treatment, as has been discussed earlier in this chapter. It is clear, however, that even the empirical behaviour of these structures is not well understood. In addition, as previously noted, no universally accepted model for the Hall-Petch effect is available. It is also clear, that the degree of

refinement of the substructure boundary which predominates in a single phase material, can control the value of Ψ .

There is also the problem, as raised by Young and Sherby (110) of the dependence of Ψ on the value of \bar{d} alone: the concept is shown in fig. (2:21) and experimental data is given in fig. (2:25) for a tungsten steel supports this, in this case implying that an intrinsic value of $\Psi = 0.5$ does not exist below $\bar{d} \sim 1\mu\text{m}$. Thompson (71) has quoted work on pure nickel supporting the idea that cell structures can be stronger than comparably sized grains (or presumably subgrains), fig. (2:26), although other work indicates the reverse may be true (111). The basic reasons why this appeared to be valid was not clear, but it is likely that the causes will only be found when yielding behaviour itself is understood more fully.

In most practical situations it is likely that a mixed cell/subgrain structure will be produced. It seems reasonable to postulate that the Ψ dependence will be characteristic of the stronger boundaries present. Thus for a small substructure size $\Psi = 1$ until a significant fraction of the cells are recovered, otherwise $0.5 < \Psi < 1$.

A considerable proportion of the experimental work in this field has been undertaken on iron and iron alloys. Effort has been given to understanding the strain ageing effects (e.g. Embury et al (66), Warrington (118), also see section (2:3.4.5)) which were thought to be due to interstitial pinning. However, Rack and Cohen (33) have apparently shown that this behaviour is not dependent on the presence of mobile interstitials. Thompson (71) suggested, although with little substantiating evidence, that this may be due to the possibility, in a bcc structure as opposed to an fcc one, of "mopping-up" free dislocations in the cell interiors. Dynamic recovery processes which remove mobile dislocations also appear to be unlikely according to Thompson (71) who pointed out that similar amounts occur in both pure iron and copper while no strain ageing effects are noted in the latter. A further possibility is the recovery of redundant dislocations which are included in the cell structure during deformation, due to the presence of the $\langle 110 \rangle$ bcc wire texture (Hosford (61)).

The above review indicates the complexity and lack of understanding in this field, even in the case of single phase materials. The problems are more severe for the case of two phase structures such as patented wire, e.g. see Embury et al (66), and isoformed steel, e.g. see Irani (119).

Some workers, e.g. Thompson (71) apparently feel that the above analyses probably do not apply. It is possible, however, that it is the interpretation of such models when applied to two phase structures which is the key step in understanding their mechanical behaviour.

2:3.4.7.2 Other mechanical properties

Dislocation structures, whether cells as initially formed or subgrains when recovered, also have effects on other properties: some examples are improvements in toughness, maintaining the strength levels, of isoformed steel; or the improved properties, notably in the relaxation resistance, imparted by stabilized dislocation structures in drawn aluminium wire, Chia and Starke (120). Also McQueen (69) noted the improvement in creep resistance of many alloys imparted by such structures, although the behaviour is complex.

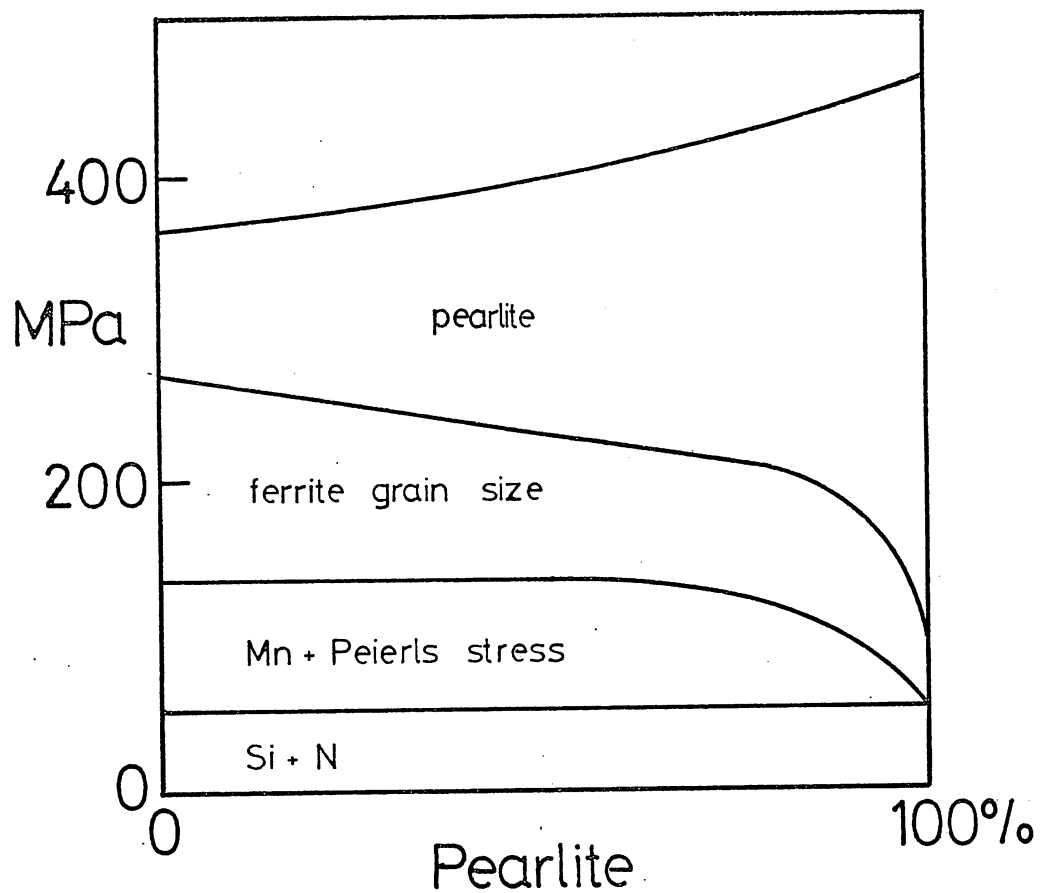


Fig. (2:1) Components of yield strength (12)

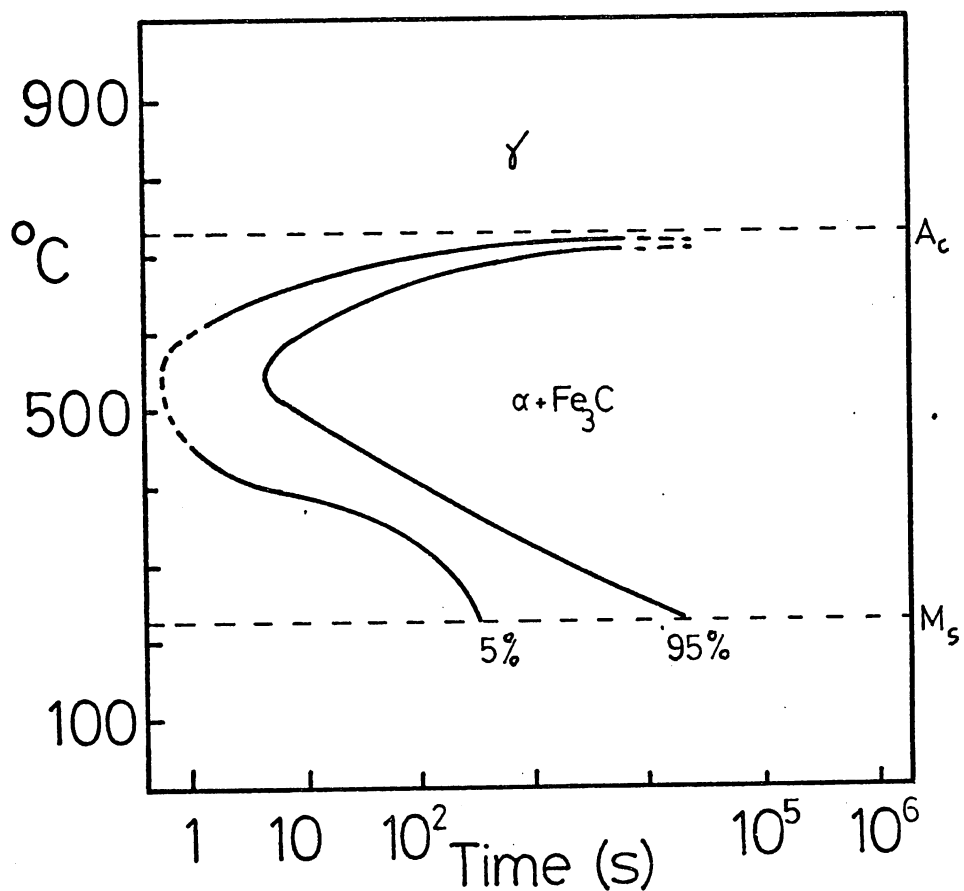


Fig. (2:2) TTT diagram for a eutectoid plain carbon steel (292)

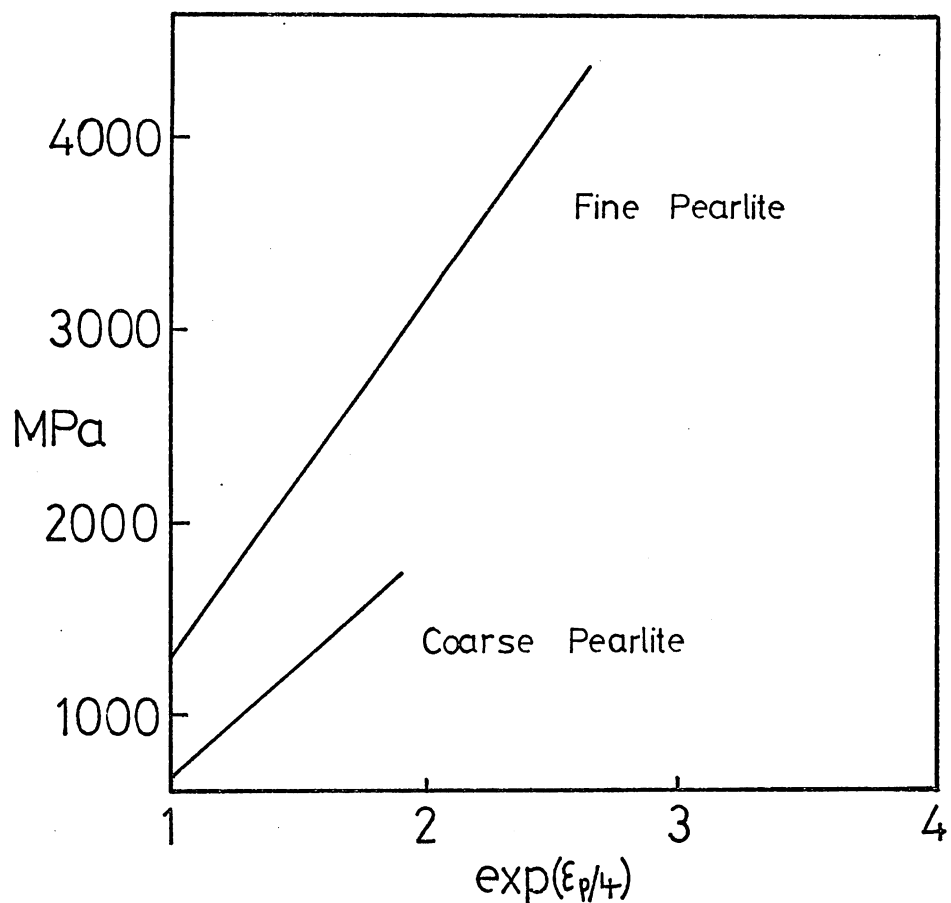


Fig.(2:3) Increase in proof stress with wire drawing strain (28)

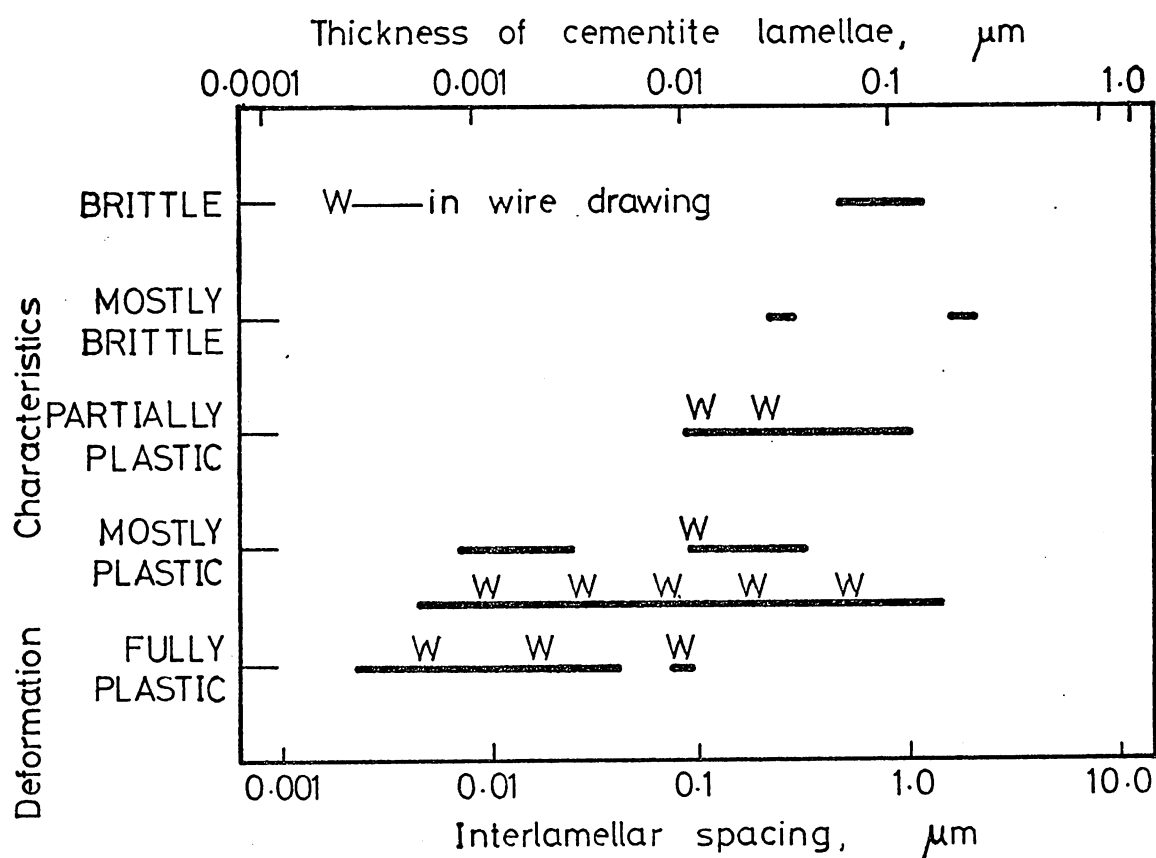


Fig. (2:4) Evidence of a size effect of the plastic deformability of pearlitic cementite (35).

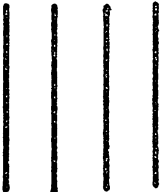


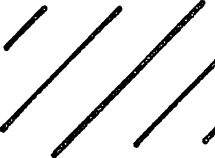
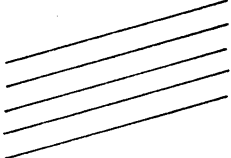

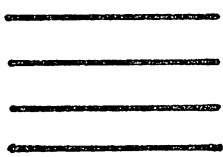
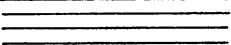
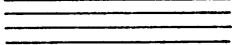
Original colony	Expected result	Actual result	Type of deformation
			homogeneous
			inhomogeneous
			homogeneous

Fig. (2:5) Modes of deformation in pearlite (35)

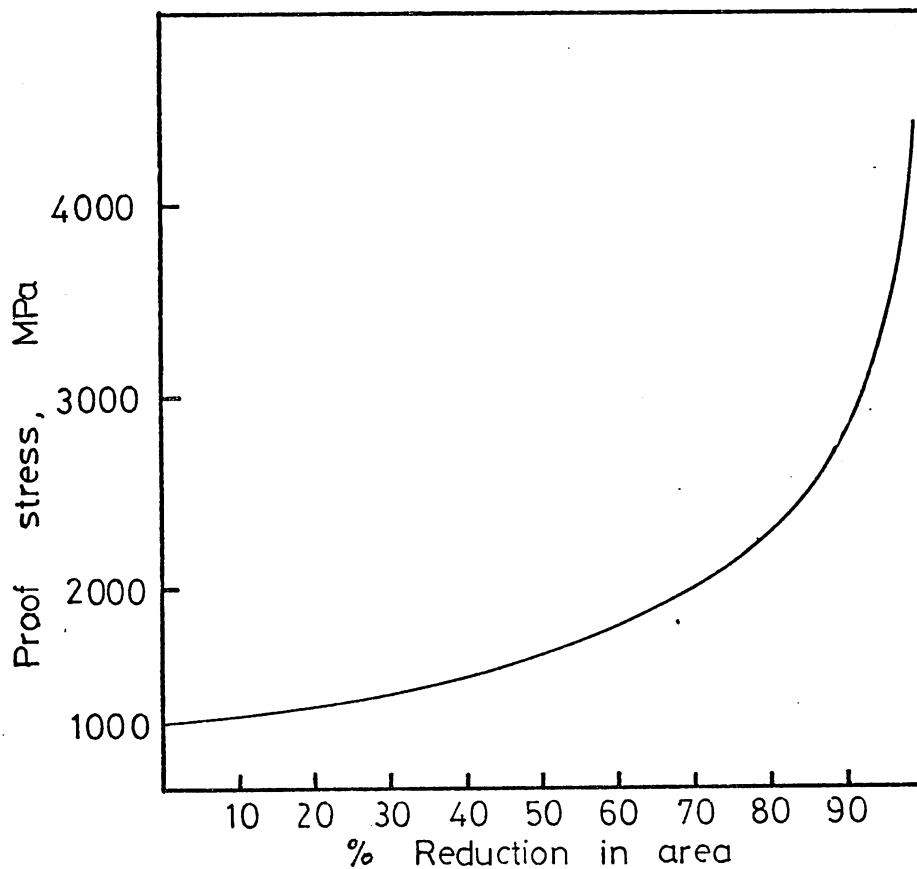


Fig. (2:6) Increase in proof stress of drawn pearlite with drawing reduction (28).

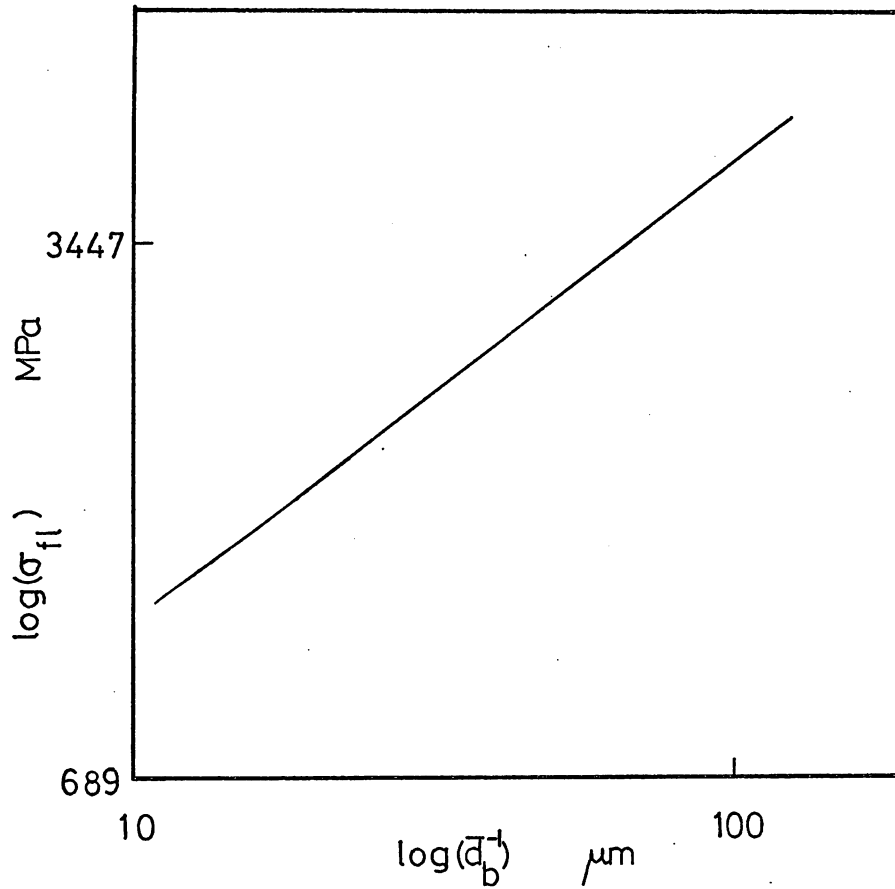


Fig. (2:7) Relationship between flow stress and substructure spacing in drawn pearlite

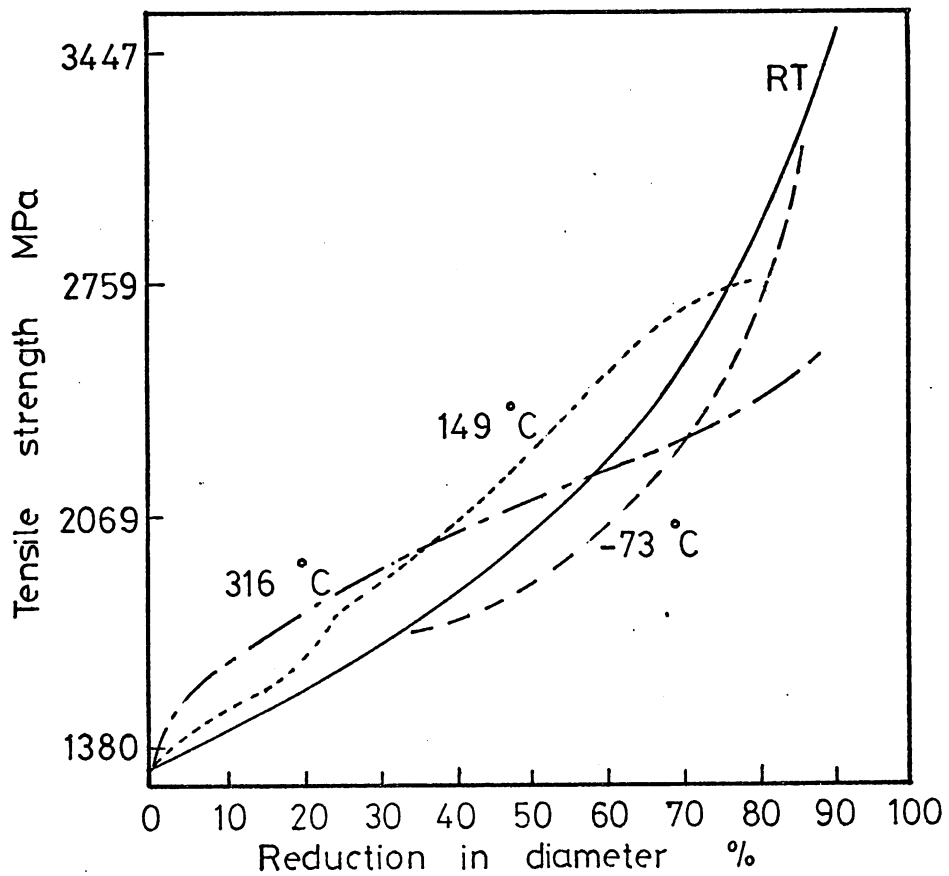


Fig. (2:8) Effects of wire drawing temperature on tensile strength (65)

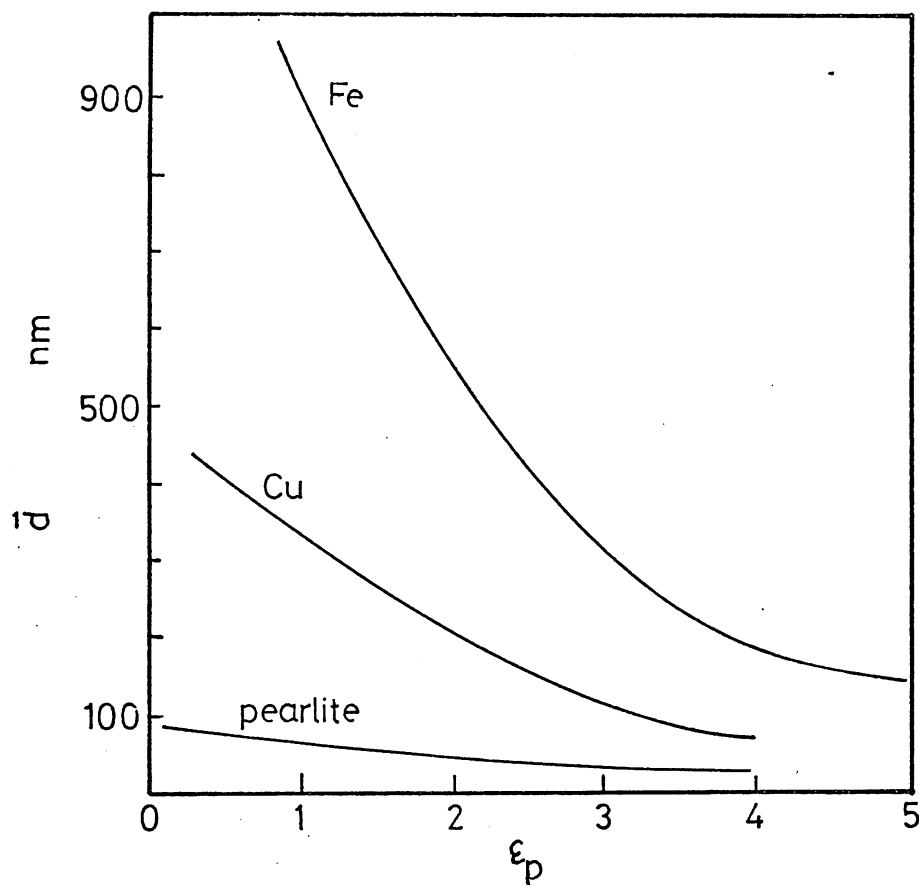


Fig. (2:10) Observed cell diameter with true drawing strain in the absence of dynamic recovery (66).

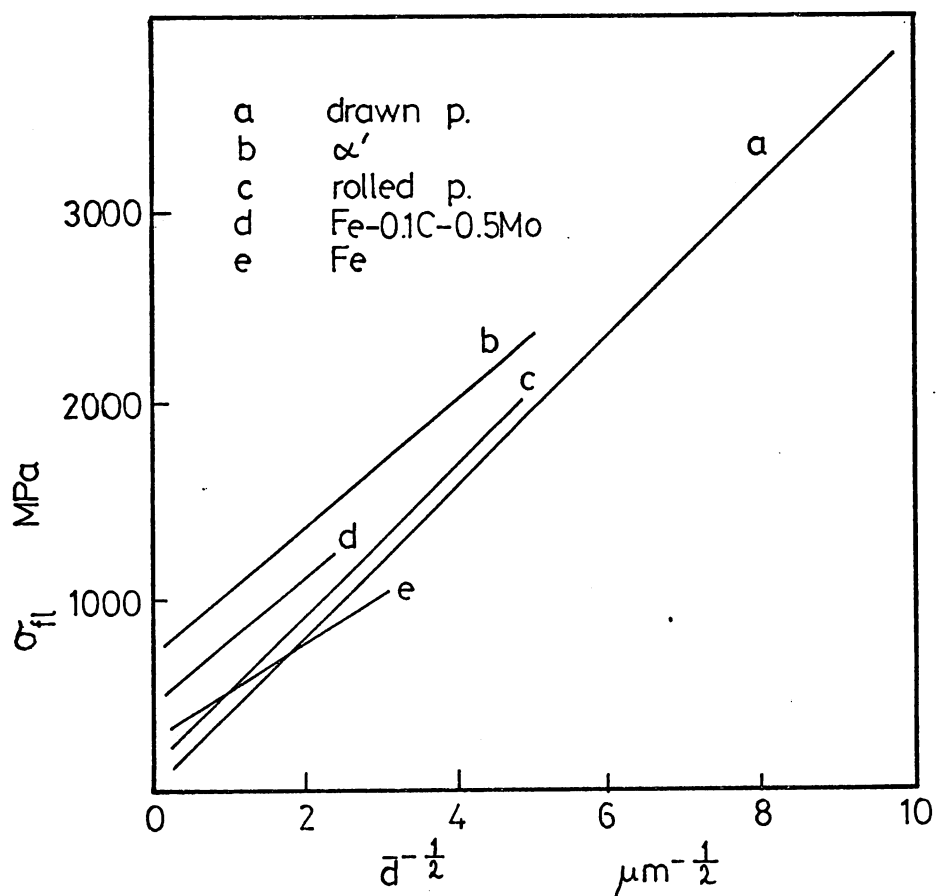


Fig. (2:9) Flow stress of drawn materials with cell diameter (66)

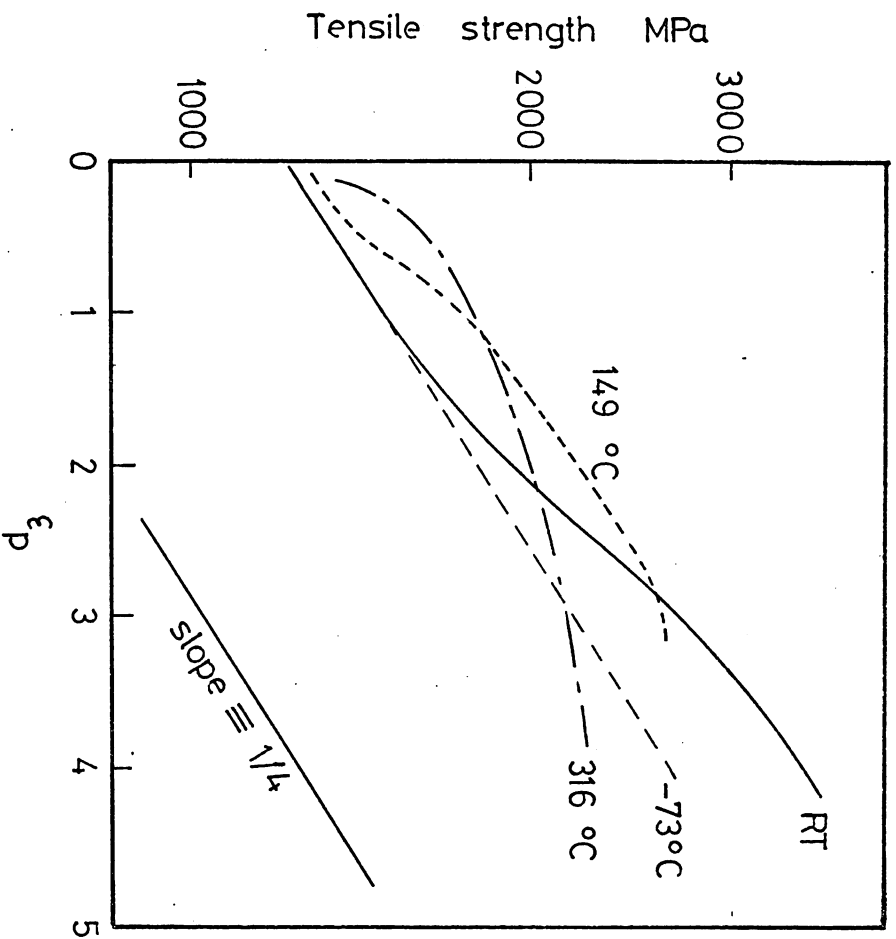


Fig. (2:11) Effect of wire drawing temperature on tensile strength (60)

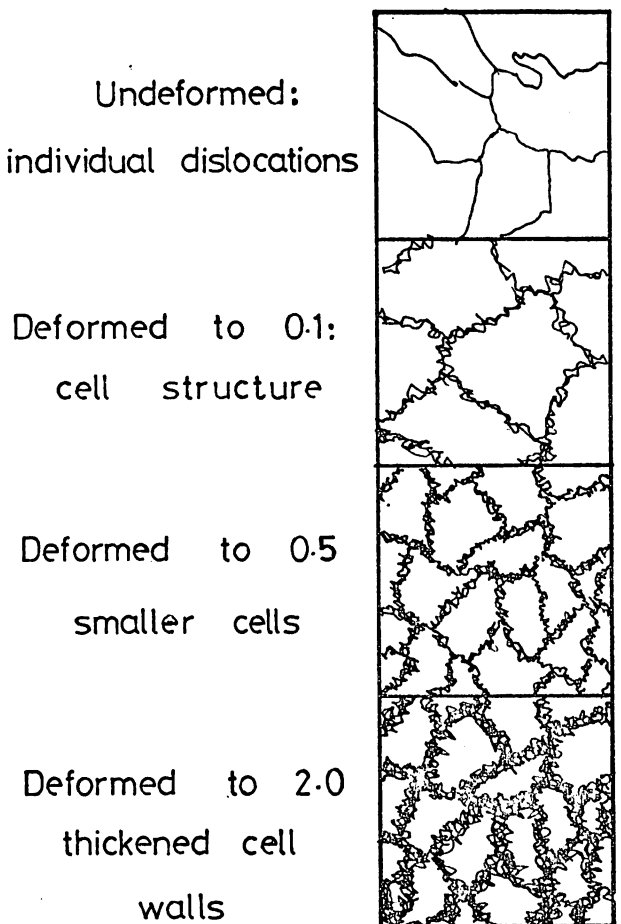


Fig. (2:12) Development of a dislocation cell structure under cold work with true strain.

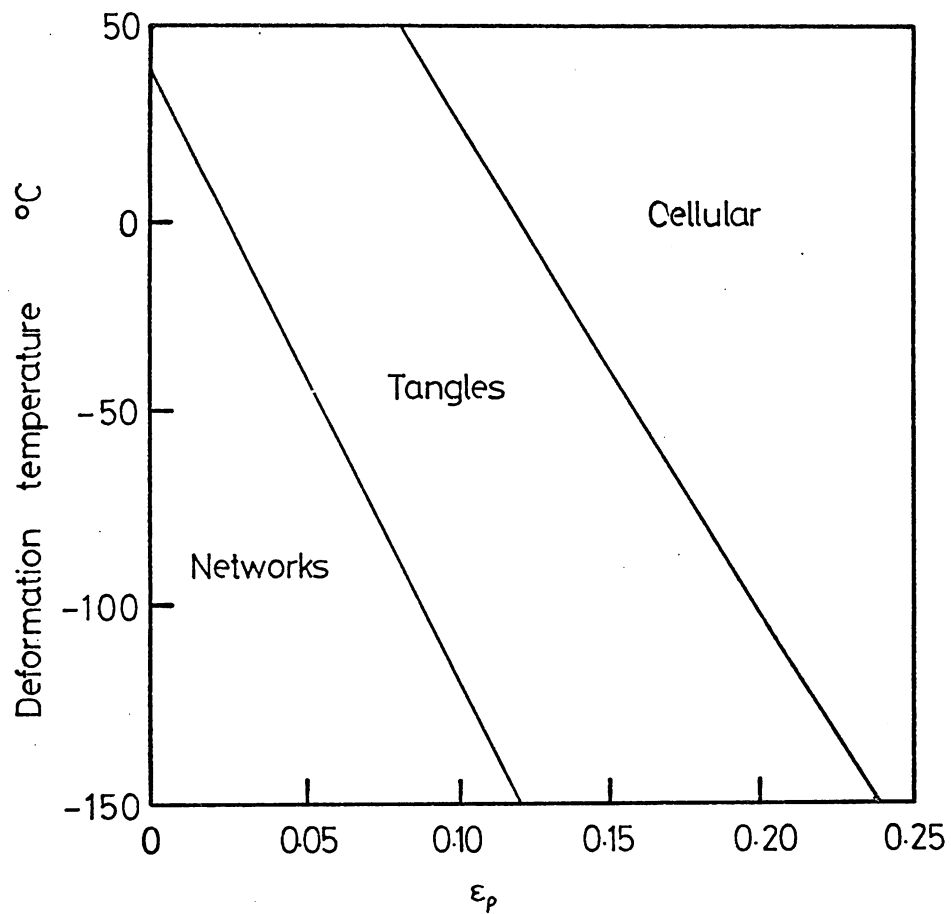


Fig. (2:13) The true strain necessary to produce a cellular substructure in α (70)

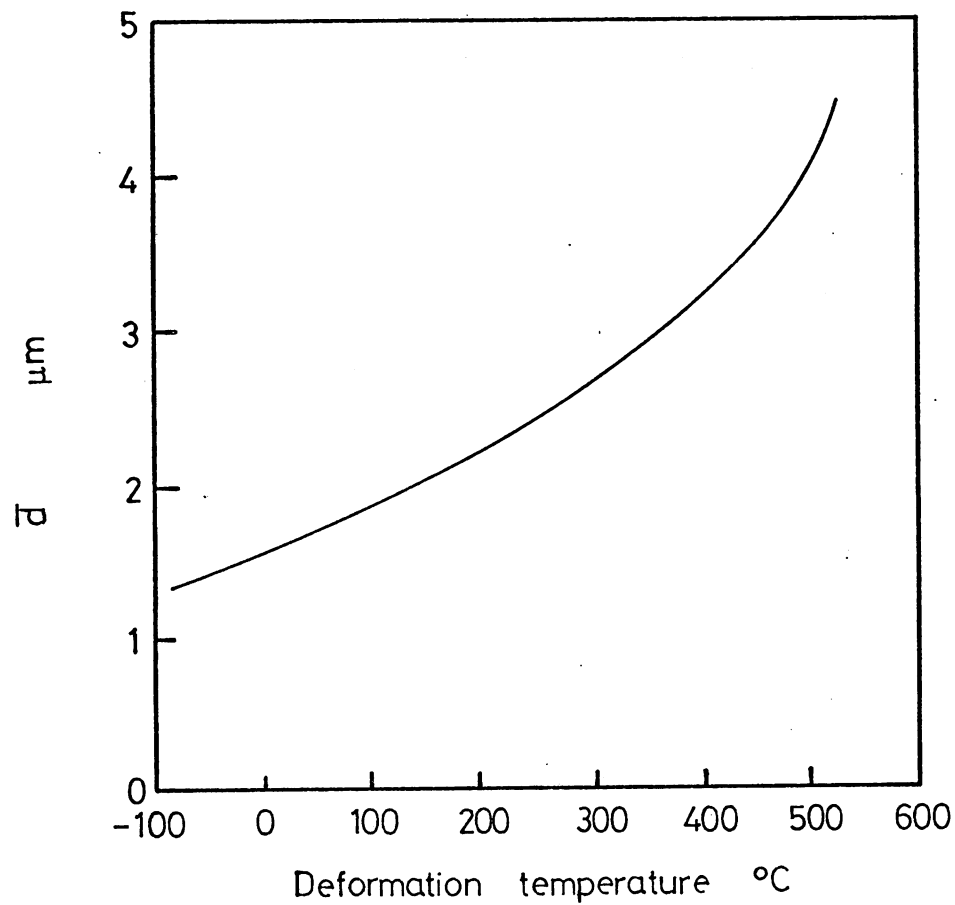


Fig. (2:14) The dependence of limiting cell size on deformation temperature in α (70).

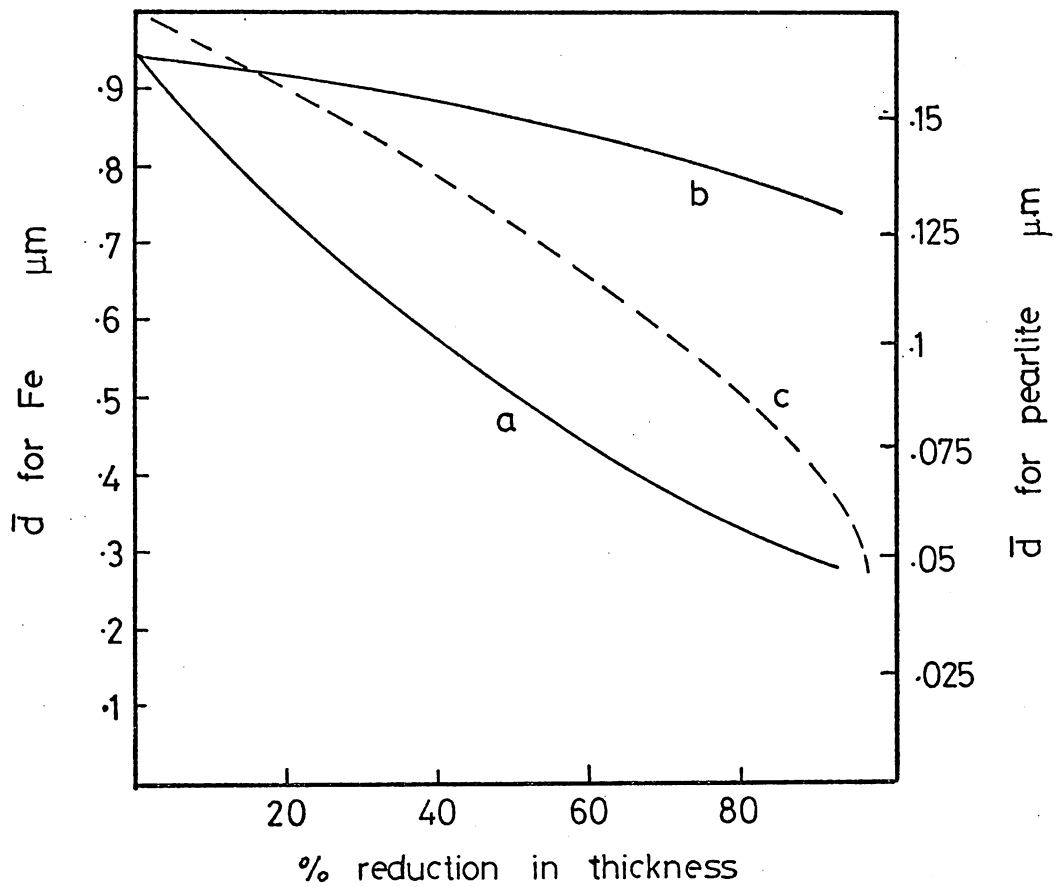


Fig. (2:15) Cell size as a function of rolling deformation for (a) edge section (b) face section (Fe), (c) pearlite (66)

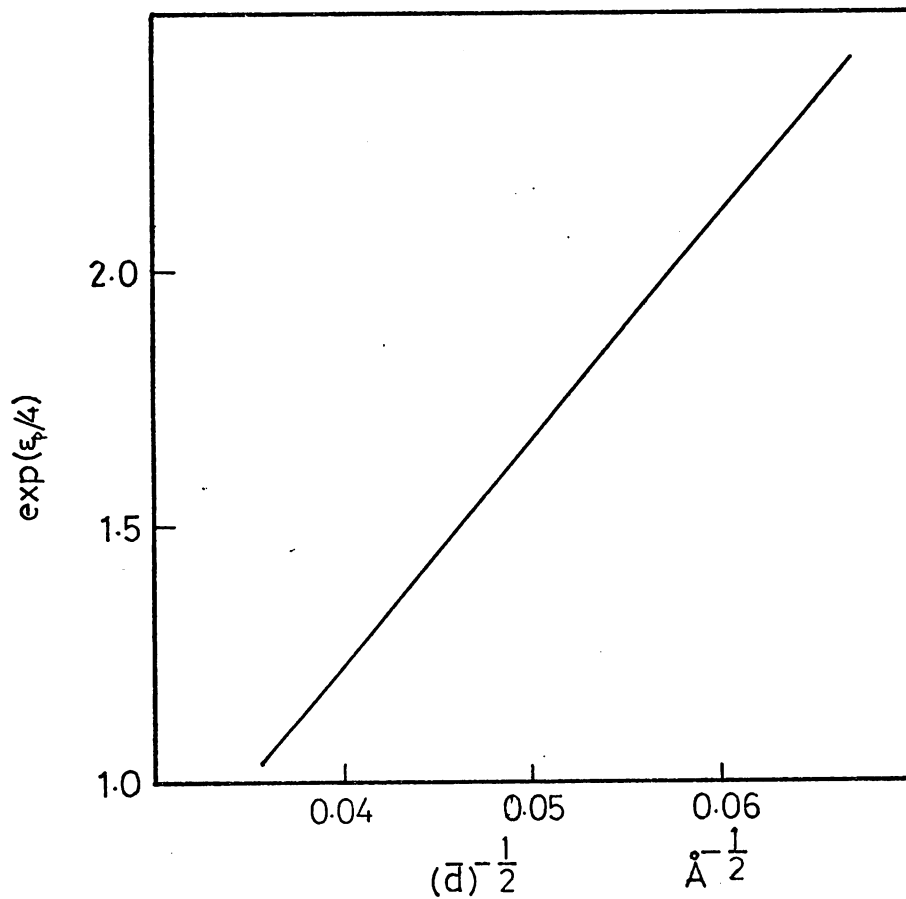


Fig.(2:16) Cell diameter as a function of true strain in patented wire (28).

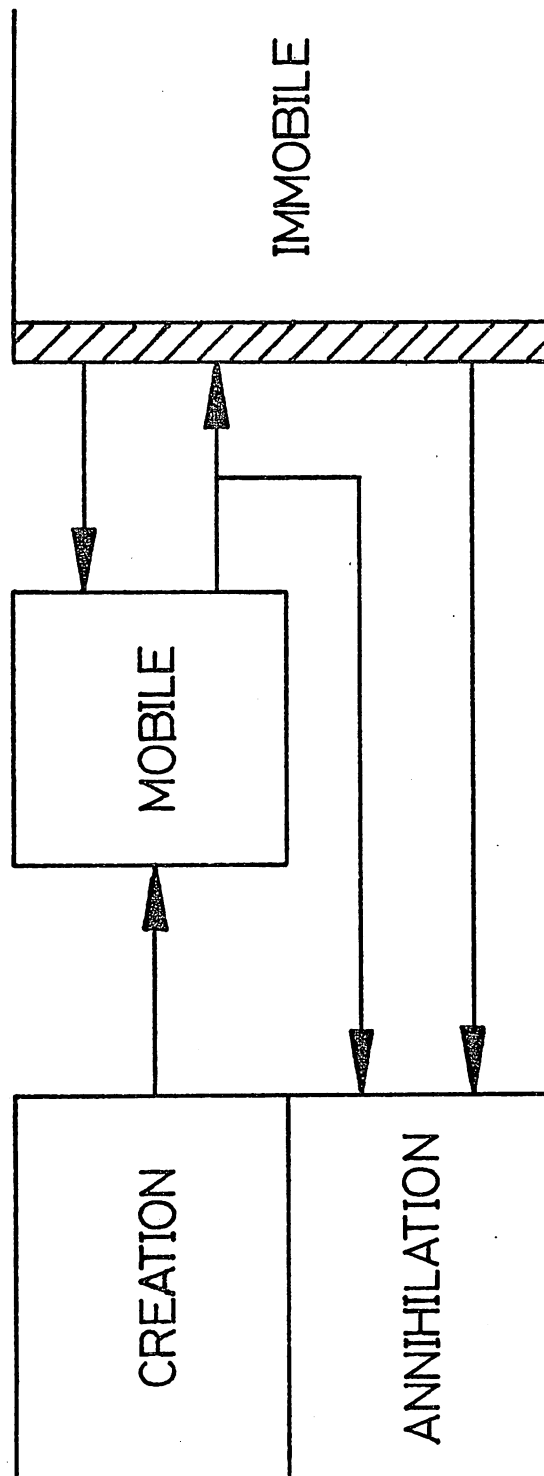


Fig. (2:17) Bergstrom's dislocation model (82, 83).

Fig. (2:19) Development of dislocation subgrain structure on hot work with true strain (69)

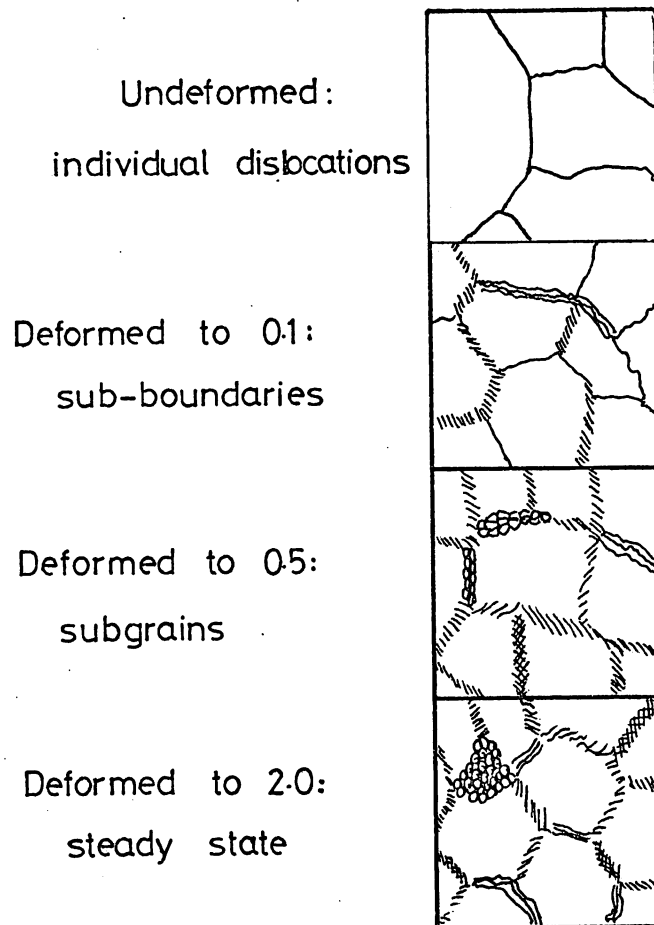
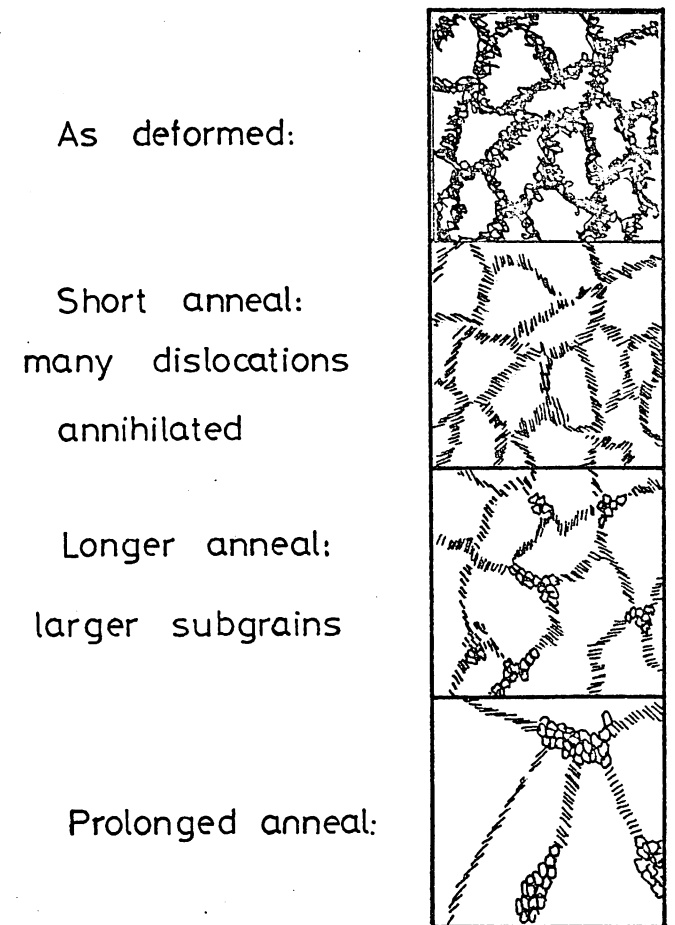


Fig. (2:18) Behaviour of cell structure during recovery (69)



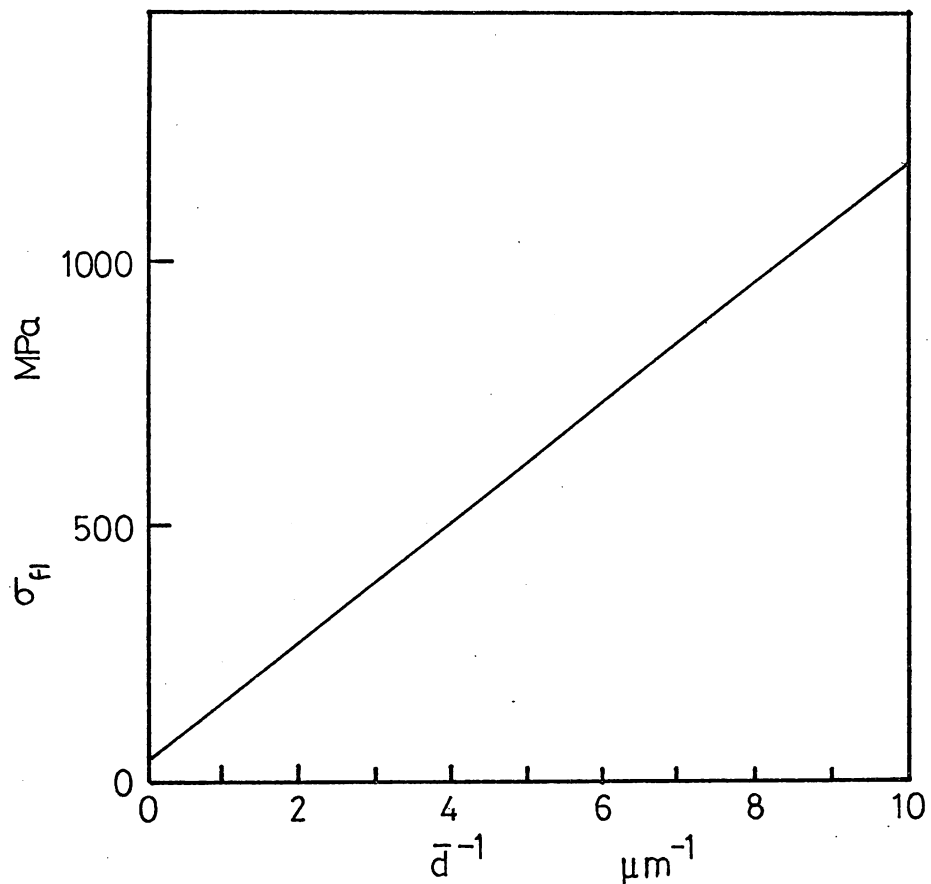


Fig. (2:20) Change in flow stress with cell diameter for iron wire: $\psi = 1$ (32, 115).

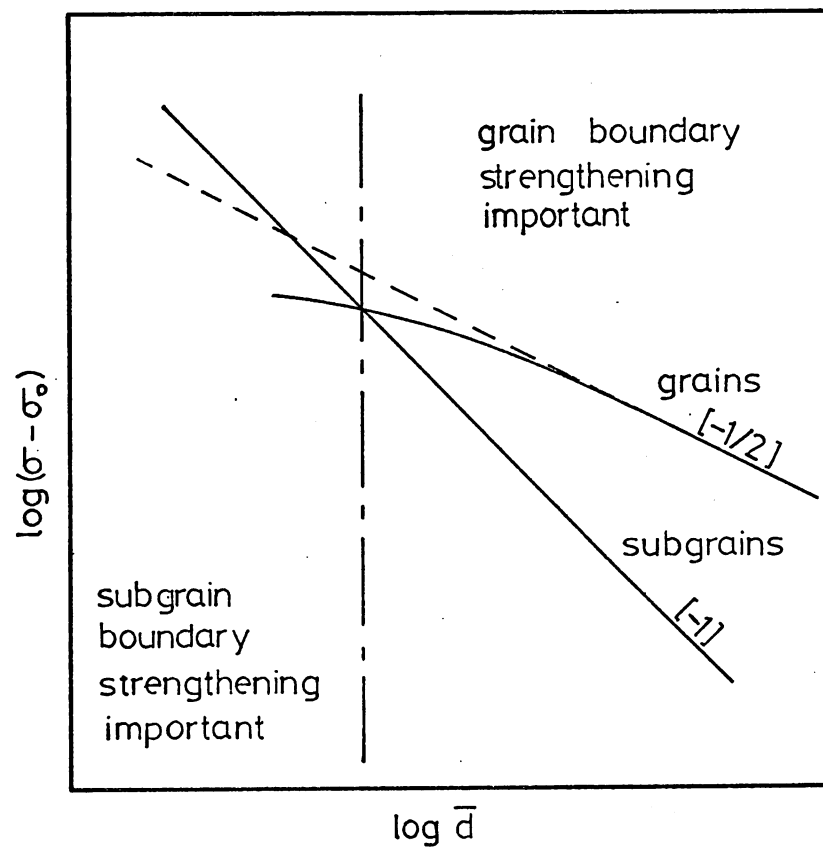


Fig. (2:21) Schematic representation of the trends predicted by grain and subgrain strengthening for a given material and test conditions (110).

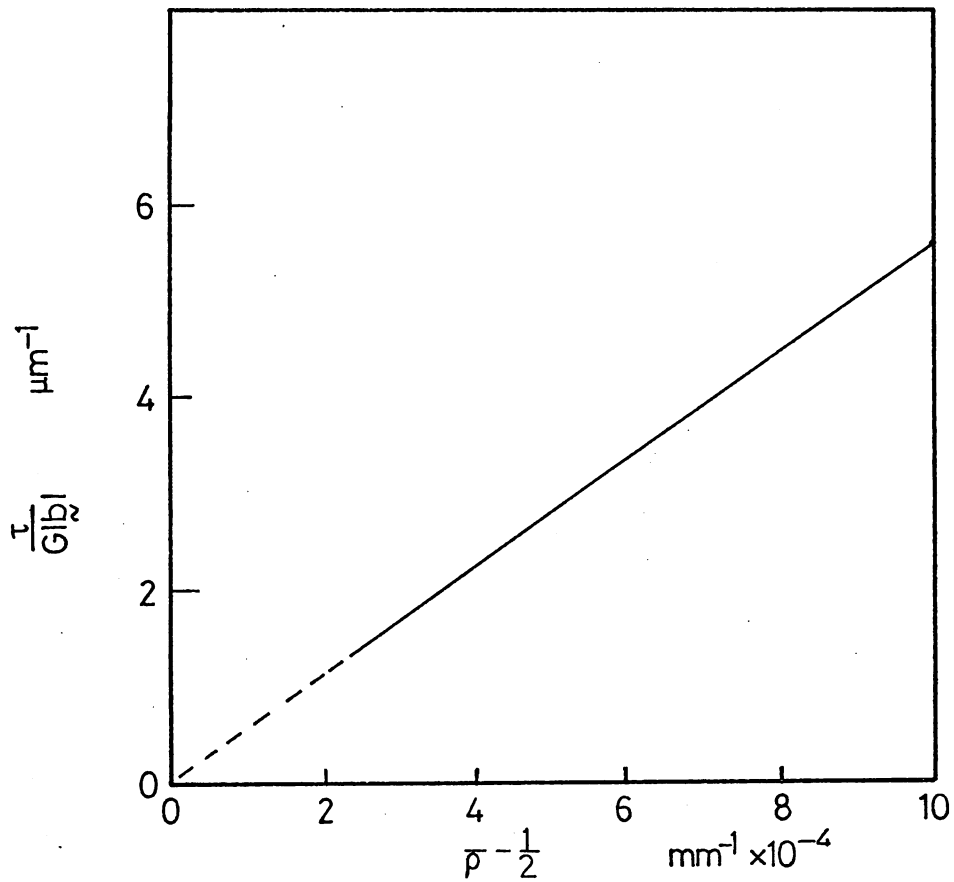


Fig. (2:22) Variation of flow stress with wall dislocation density (116), $\tau/G|b|$ standardized to room temperature

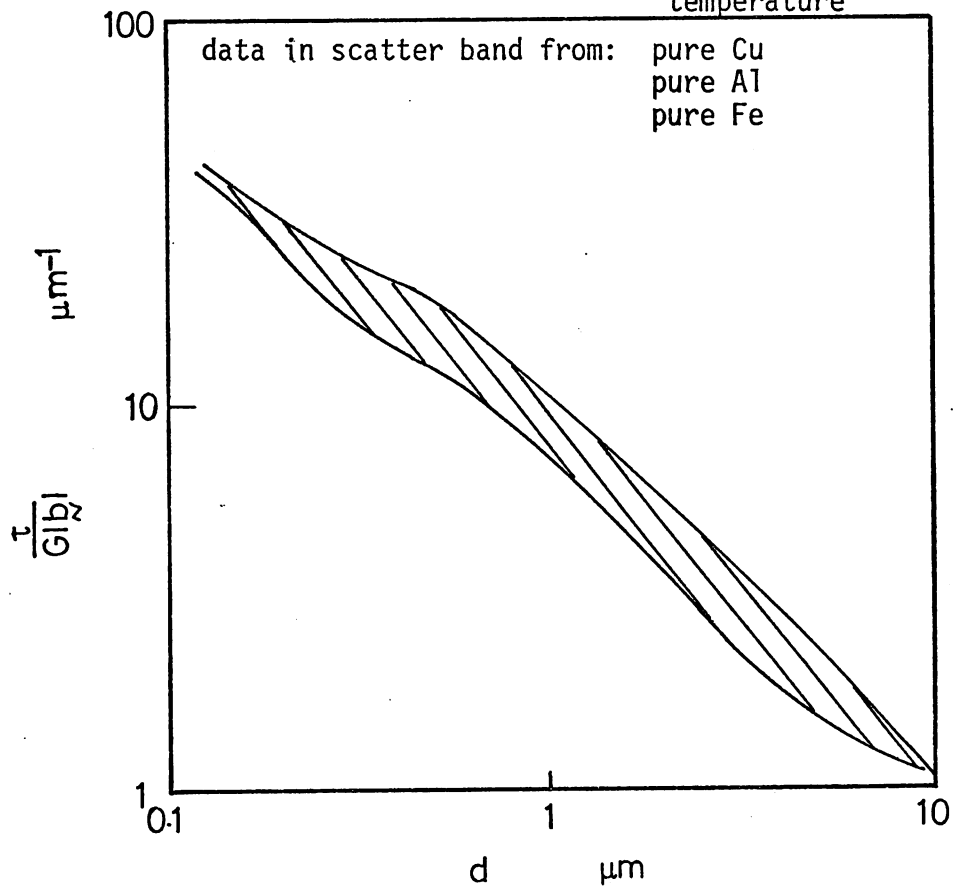


Fig. (2:23) Variation of $\tau_f/G|b|$ with \bar{d} (116) for selected pure metals

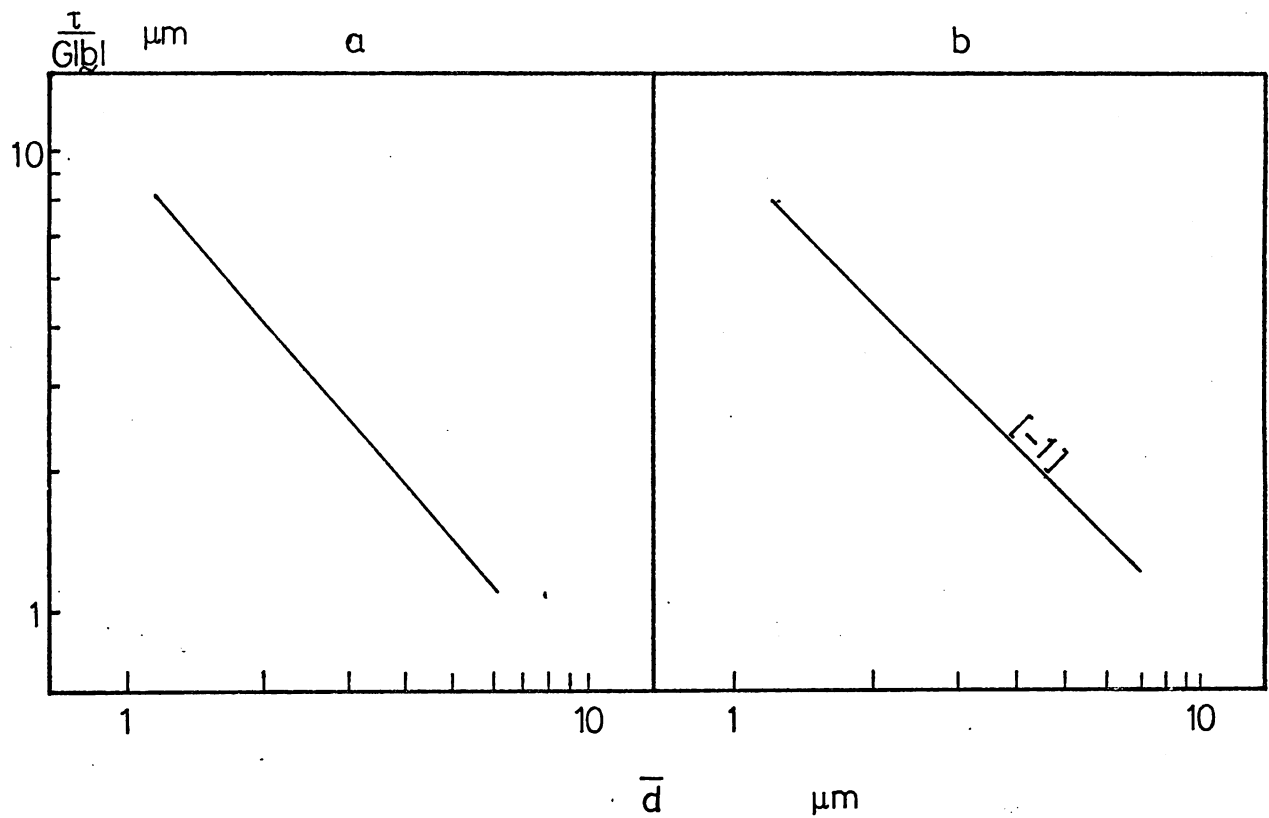


Fig. (2:24) Variation of $\tau_{f1}/G|b|$ with \bar{d} for selected iron alloys (116).

- a) $\tau/G|b|$ is at the test temperature
- b) $\tau/G|b|$ is standardized to its value at room temperature by dividing by the Cottrell-Stokes factor.

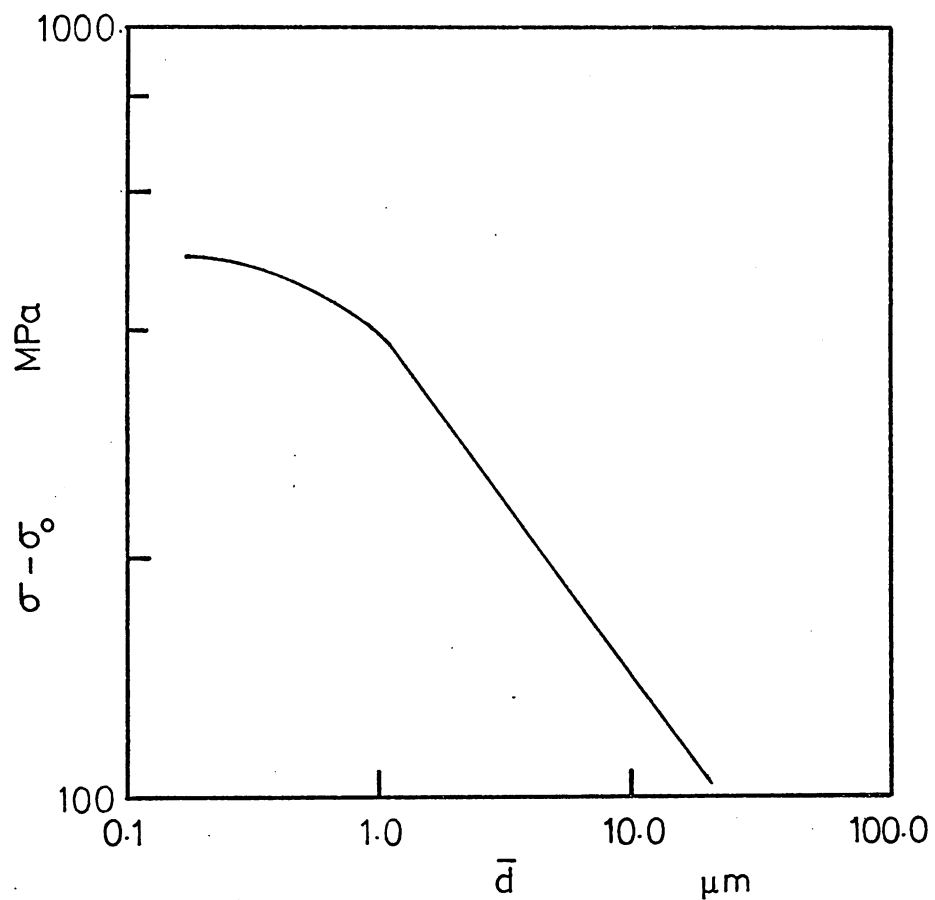


Fig. (2:25) Variation of parameter ψ with \bar{d} for a tungsten steel (110).

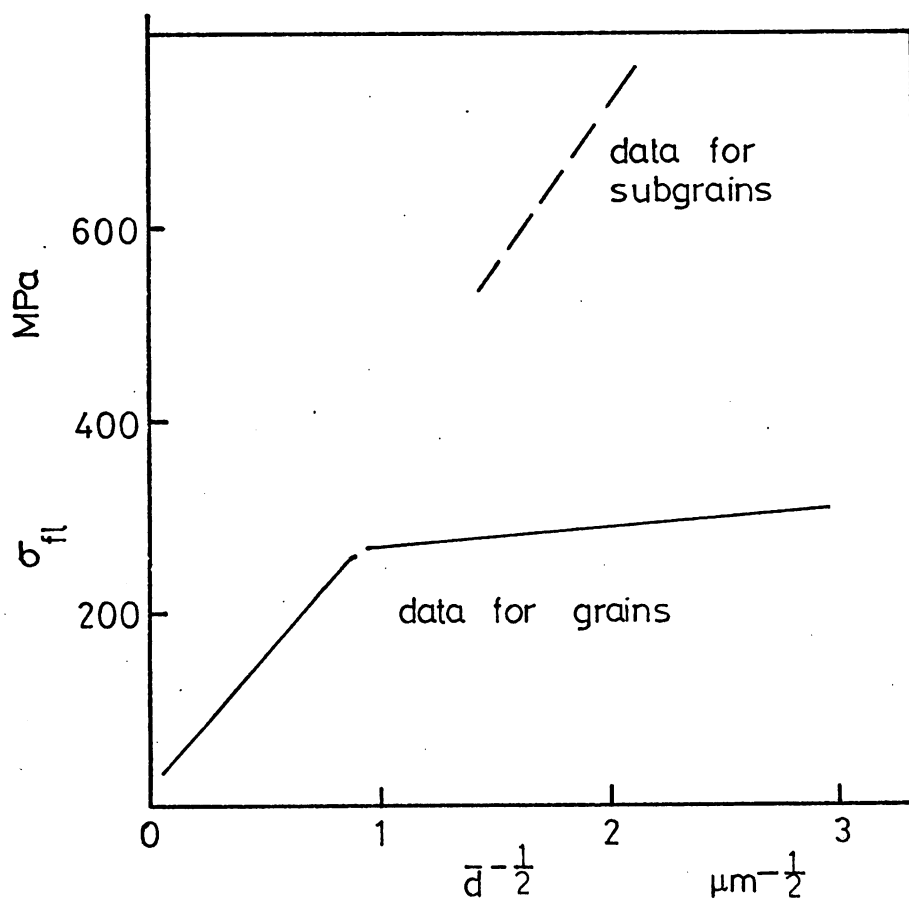


Fig. (2:26) The relative strength of grains and subgrains in pure nickel (71)

3. Microstructural studies of patented wire

3:1 Introduction

The microstructural studies undertaken in the present work were directed towards an improved understanding of the mechanical properties of patented wire, particularly the nature of stress relaxation. As relaxation could not be investigated in situ in any available microscope, the research philosophy, as detailed previously, made use of the industrial practice of annealing the wire before use, thus obtaining significant improvements in yield strength and relaxation resistance. Examination of the wire in the following conditions was undertaken:

- (a) As received (i.e. as drawn), A/R;
- (b) A/R + LTHT "A" (30 mins at 200°C);
- (c) A/R + LTHT "B" (300 mins at 200°C);
- (d) A/R + LTHT "C" (30 mins at 300°C).

Industrially, material (b) is found to exhibit the optimum combination of yield strength and relaxation resistance; material (c) was examined in an attempt to exaggerate the microstructural changes which improve the mechanical properties while material (d) is known to have further improved relaxation resistance, although the yield properties deteriorate (see chapters 2 and 4 for further details). A high resolution transmission electron microscopy (TEM) study was undertaken (for practical details see A.I:2.1) to extend previous work on the as drawn wire and to attempt to characterise the microstructural changes: this study was essential as optical work was shown to lack the necessary resolution fig.(3:1). Scanning electron microscopy was briefly employed to record the fracture of the wire, fig.(5:1). Extensive field-ion microscopy (FIM) and atom probe work was used to give extremely high resolution structural data and to study segregation phenomena in the first 3 materials listed (details in A.I:2.2).

As discussed in detail in chapters 2 and 4, the mechanical behaviour of the ferrite is the critical influence on the yield and relaxation properties of patented wire. This proved fortunate, as work on the cementite phase would have been far more difficult to accomplish with any of the available techniques.

3:2 Transmission electron microscopy studies

3:2.1 Introduction

TEM was employed to study the dislocation substructure present in the wires: the same initial as drawn wire was used as in the mechanical testing programme (Ch.5) i.e. 4.25 mm or 4.0 mm diameter music wire: details of the problems encountered and the practical solutions evolved

are given in A:1. The essential difficulties in thinning and observing this type of material are due to both the very fine microstructure and the rapidly varying internal stress levels due to the cold work involved in drawing. It was found difficult to thin the two phases at the same rate, which left the cementite lamellae proud of the surface, examples are noted later, and also to produce what is normally regarded as a reasonable amount of thin area. The latter problem was, in fact, often not important owing to the fine scale of the microstructure. Despite these problems a knowledge of the material superior to that of previous work has been obtained.

3:2.2. A/R microstructure

As described in the experimental details, each material was examined in both transverse (T/S) and longitudinal section (L/S) and where possible examinations were made at various distances from the wire surface. The appearance in the 2 sections was essentially similar, except that in the latter the alignment of the lamellae along the wire axis was more evident. A typical appearance of the T/S is shown in fig. (3:2): it can be seen that the cementite lamellae in this region, although having undergone severe plastic deformation, show little sign of fragmentation, however they are strongly aligned with the wire axis. The rapid variation in contrast conditions in the ferrite is indicative of variations on a similar scale of its orientation: in some cases this change in contrast is abrupt while in others it is more gradual. In this area the typical ferrite lamellae width (which is not subject to the normal magnitude of sectioning errors because of its alignment) is of the order of 16 nm to 80 nm while that of the cementite varies from 7 nm to 15 nm. Fig.(3:2b) shows an area where the lamellae are more aligned in the section, although not necessarily along the wire axis as shown by the cementite lamellae in the centre. In this case the field of view contains 2 colonies and shows an interesting zone of higher deformation (indicated by contiguous kinks in the cementite lamellae, rather than by their fracture). The inhomogeneous effects of plastic deformation on the pearlitic cementite is well shown in fig.(3:2c) where the cementite lamellae thickness varies from approximately 25 nm to less than 1nm. Shear zones which pass through successive lamellae can also be seen and in some cases the cementite, where kinked in such regions, has extensively plastically thinned. It was generally observed that in regions of high plastic deformation, cementite coarsening was frequent, again such areas are visible on this micrograph. Another example

of this last point is shown in fig.(3:2d) in a region of severe bending. The axis of rotation has been such that in some areas bending and rotation of the lamellae has occurred while in others fracture of the cementite followed by coarsening is evident. Further examples which indicate the severe plastic deformation which can occur in certain regions during wire drawing are given in fig. (3:3a,b): in certain favourable regions dislocation substructure in the ferrite lamellae can be identified. The majority of areas examined retained the basic lamellar structure, but some regions, however, showed rather greater fragmentation of the cementite. This is shown in fig. (3:3c), which also gives examples of the rotation of the cementite enabling internal structure to be made visible. Occasionally extensive spheroidization of the cementite was observed fig. (3:3d): this type of effect could not be correlated to the position in the wire. Further examples of contrast observed in the ferrite are given in fig.(3:4). Sharp boundaries were often noted across ferrite lamellae along with linear features: in a bright-field examination, however, it was not, in general, possible to estimate the extent of the dislocation cells present or to examine the cell wall structure. An exceptional specimen is shown in fig. (3:4d) where the cementite thinned at a similar rate to the ferrite: this allows contrast to be seen in the former indicating the presence of a dislocation substructure in this phase in addition to that present in the ferrite.

This last observation was confirmed by using a centred cementite reflection to obtain a dark-field image. The typical result is that shown in fig.(3:5), the particular reflection chosen illuminating certain cells in the substructure. This substructure is clearly on a very fine scale, much finer than that in the adjacent ferrite, and was of the order of 1 nm to 10 nm in transverse size. Ferrite centred dark-field micrographs, a typical example being shown in fig.(3:6), allowed an accurate estimation of the ferrite cell size to be obtained. As can be observed the cell (i.e. ferrite of similar orientation) extends over several lamellae and is bounded by either a cementite lamellae or a distinct cell wall. Linear features, due to dislocation nets, can be seen in the cell walls and the variation in contrast in the cells is due to poorly resolved dislocations present: particularly strong variations were frequently noted near the ferrite/cementite interface indicating a higher dislocation density in these regions. The most favourable situation for the observation of the

cell wall structure is in situations where it is at a shallow angle to the foil surface: a good example is shown in fig.(3:6c) from a transverse section. The arrangement of the dislocations visible in the cell wall can be seen to be complex and is not easily resolved: the typical feature spacing is of the order of 1 nm and it is likely that many dislocations present are not visible.

The SADP's given in fig.(3:6) are exceptional in that they are from areas with few sub units, i.e. little orientation change. A more typical example is that given in fig.(3:7) with the corresponding bright-field image. Characteristic arcing of the reflections can be seen indicating a gradual change in ferrite orientation, (the smallest selected area aperture available, 10 μ m, was always used) although the individual reflections show that the orientation variation takes place in discrete steps, i.e. at cell walls, not continuously.

It was found that the normal techniques for magnetic and objective astigmatism correction were not adequate for this material due to its fine 2 phase structure and high dislocation content. A technique was evolved where after the normal magnetic correction techniques had been applied in dark-field a further correction could be made at high magnification by ensuring the single cell under investigation, whether it was ferrite or cementite, showed no image movement on going through focus. This having been achieved, a more accurate objective astigmatism adjustment could be attempted although this was always made difficult by cementite and ferrite requiring different corrections.

Longitudinal sections of the A/R wire were examined in an analogous manner. Similar features to those seen in the transverse section were observed in both the ferrite and cementite lamellae although, as might be expected by the deformation mode, the lamellae were strongly aligned along the wire axis. Examples of the general microstructure are given in fig.(3:8), the incremental change in the ferrite orientation being again shown in the given SADP and in areas of favourable contrast the evidence of dislocation networks can be observed in the ferrite. Micrographs of a centred dark-field ferrite reflection (again using the smallest objective aperture available to restrict the observation to a single cell) are given in fig.(3:10). Contrast variations due to dislocations within the cell are clearly apparent and, where the cell walls are inclined to the foil surface dislocation, nets can be seen, fig. (3:10c). Attempts were made to improve the resolution of dislocations by means of weak-beam

techniques: this proved difficult although in some cases single dislocations in cell interiors were resolved fig.(3:11). It was considered that although dislocations in cell walls are effectively pinned during thinning of the TEM specimen, dislocations within a ferrite cell (whose dimensions were often greater than the foil thickness) could be lost as they are securely pinned only at their ends at cell walls or at ferrite/cementite interfaces.

Estimates were made of the transverse and longitudinal dimensions of the ferrite cells from a large number of TEM specimens: no significant variations in cell size were found with position in the wire. The distributions are given in fig.(3:12).

3:2.3 A/R + LTHT "A" microstructure

It is in this condition that the patented wire shows the optimum combination of strength and relaxation resistance. The TEM was therefore used in an attempt to characterise any changes which may have occurred in both the T/S and L/S. An extensive survey of the material, however, failed to show unambiguous trends brought about by the annealing process. No spheroidisation of the cementite was obvious and the size distribution of the ferrite cells was not significantly changed. A general impression was gained of a slight reduction in the dislocation density which was indicated both in the lowering of contrast variations in the ferrite, and by improving resolution at cell walls. Fig.(3:13) shows a number of areas in T/S: with similar features to those described in the previous section. In some areas the cementite lamellae can be seen at a shallow angle to the specimen: in such areas substructure in this phase can be seen although resolution is poor due to its thickness. In fig.(3:13e) is shown an area of cementite coarsening at a colony boundary: it is thought that this occurred prior to the LTHT as it was also observed in the A/R material.

A weak-beam image of dislocations within a ferrite cell in L/S is given in fig.(3:13f): typical spacings are of the order of 0.5 to 3 nm. Attempts were made to use the $g \cdot b = 0$ criterion to characterise the dislocations present. As the strain fields of the dislocations present would usually interact (due to their close spacing) it was known that the invisibility criterion with any given g reflection would not necessarily be valid. This proved to be the situation in the few cases where other observational problems, e.g. variations in orientation within a cell, allowed an attempt at such a determination. An example is given in

fig.(3:14) from a L/S where the cell walls were inclined to the specimen. Image quality using most g reflections were poor, the best being shown in fig.(3:14b). However, as the linear features retained the same direction with varying g reflection, it was clear these were dislocation images rather than moire fringes. The dislocation structure in another cell wall (also from a L/S) is shown in fig.(3:14d) the typical spacing being of the order of 2 nm. The cell structure in the cementite could also be revealed where the lamellae were sufficiently thin. As noted previously, the cementite cells retained a similar orientation over a relatively wide area, which is to be contrasted, in most cases, with the variation of orientation of the ferrite cells in the same area.

3:2.4 A/R+ LTHT "B" microstructure

The prolongation of the LTHT at 200°C produced little observable change in the microstructure an example of the T/S being given in fig.(3:15). The effects of a slower polishing rate on the inclined cementite lamellae is clearly shown in fig.(3:16a,b): high shear regions can easily be identified. Occasionally the proximity of ferrite and cementite reflections allowed a simultaneous dark-field micrograph to be obtained fig.(3:17): the complex nature of the diffraction pattern does not allow a full interpretation. Details of this micrograph, fig.(3:17c,d) show contrast features similar to those observed elsewhere. In certain instances the dislocation networks in the ferrite were particularly well shown fig.(3:17,e,f,g). Areas of localised shear were also observed, fig.(3:17 h,i) indicated by apparent twisting of the cementite lamellae.

3:2.5 A/R + LTHT "C" microstructure

This material was examined in a similar manner to those above: again, no significant microstructural changes could be found.

3.3. Field-ion microscopy (FIM) and atom-probe studies

3:3.1 Introduction

The development of the field ion microscope began over 30 years ago when Müller recognized that the resolution of a field-emission microscope could be improved by using an ionized gas as the imaging medium (121). Considerable improvements were made following this initial work and wide ranging reviews have been published (122, 123, 124, 125). It is generally true that the resolution and magnifications obtained on the majority of materials is less than the theoretical maximum, however it has still proved itself to be an extremely powerful structural technique. In addition to the

resolution and magnification obtainable, FIM when used under the correct conditions can determine crystallographic data and also "micro-dissect" the observed area of the specimen by removing material atomic plane by atomic plane.

In its simplest form the field-ion microscope consists of a vacuum chamber in which the material to be examined, in the form of a needle shaped specimen, is spot welded to a fine nickel tube connected to an EHT supply. The specimen tip faces an earthed phosphor screen and is cryogenically cooled. The chamber is evacuated to a high vacuum (e.g. 10^{-9} torr) and a suitable pressure of imaging gas is introduced into the system (10^{-4} torr). The imaging gas atoms are polarized by the high electric field at the tip and are attracted towards it. If the field is high enough selective ionization will occur radially from the tip and these ions are allowed to strike the phosphor screen. It is found that the protruding atoms on low index planes form concentric rings and give rise to a characteristic ring structure on the FIM graph.

The background pressure in the microscope is kept low to avoid specimen contamination and image degradation while the image gas pressure must be high enough to give adequate image brightness but not so high as to impair resolution. The relationship between tip radius r_{tip} , the applied voltage V_{EHT} and the specimen ionization field E_c was given by Drechsler & Wolf (126):

$$V_{\text{EHT}} = k_{\text{FIM}} r_{\text{tip}} E_c \quad 3.1$$

where k_{FIM} is a material constant between 5 and 10. Generally voltages below 3 kV do not give useful image quality while above 30 kV insulation breakdown usually occurs. The image magnification is the ratio of the tip radius to the tip-screen distance. Typically tip radii are between 200 nm and 50 nm and the tip-screen distance is of the order of 100 mm.

Field evaporation of the material at the tip can occur if V_{EHT} is increased sufficiently. This process can be used to "clean" the tip after insertion into the microscope and to remove, in a controlled manner, material from the tip to investigate the 3 dimensional structure present. The process can be observed by the low index planes shrinking in the image. Details of this process are summarized by Dury (125). In principle, it is possible to produce FIM images of a metal if its evaporation field is greater than the imaging field of the image gas used. In practice, however, the situation is complicated by a number of factors, notably the ability of the tip to withstand the high stresses produced by the

electric field. (This problem is increased if field-etching at grain boundaries, for example, producing stress concentrations has taken place, or if the material is multiphase.)

Initial drawbacks in operating these microscopes on other than refractory metals were mainly due to poor image intensity. This problem stemmed from both the high field strengths required and also low phosphor efficiencies of imaging gases other than hydrogen and helium. The problem has been successfully overcome, largely by the use of channel plates (127). Improvements in specimen cooling have also enhanced image quality. By reducing the pressure over the liquid nitrogen in the cryostat, temperatures of 65K, can be obtained. For some studies the use of liquid helium (down to 4K) has been used, but is expensive. A more common method, is to transfer cold helium gas from a Dewar and temperatures of 10K to 20K are commonly achieved.

The choice of imaging gas is controlled by the requirement that for the tip material under investigation the gas ionization potential must be significantly less than the field evaporation potential. These potentials are dependent on the specimen temperature and the structure at the tip. Thus with multiphase materials, e.g. patented wire, it is often possible to image only one phase adequately. Early work on imaging iron alloys tended to use hydrogen (125). The image quality was, however, poor and considerable etching occurs. In addition, in stainless steel microscopes hydrogen is strongly adsorbed, necessitating frequent baking out. The best imaging has been obtained with neon at low temperatures. However, high field strengths are required tending to cause frequent specimen failures. Details of imaging techniques and the imaging characteristics of iron and iron alloys have been given by Youle (128) and Dury (125). In general it can be said that {110} poles are well defined but {111} poles are field-etched and are not well developed. As the alloy content or the dislocation density of the iron is increased, the resolution rapidly deteriorates. Precipitation studies were undertaken in several steels with particular reference being made to precipitate coarsening kinetics in its early stages.

The applications of FIM to metallurgical studies have become widespread, and Ralph (124) has listed the following categories:

- (a) The study of atomic scale defects, e.g. dislocations and vacancies;
- (b) Crystallographic defects e.g. stacking faults and slip steps;

- (c) The structure and crystallography of grain boundary and interfaces;
- (d) Atomic scale ordering;
- (e) Surface films;
- (f) Precipitation phenomena in the size range 1-100 nm;
- (g) Compositions on the atomic scale.

Youle (128) has given further details of each.

It is in the last category that the use of FIM and atom-probe microscopy has recently shown the most significant developments. The atom-probe allows quantitative compositional determination on an extremely fine scale. Other quantitative techniques, e.g. those based on X-ray fluorescence, cannot match the atom-probe's resolution and also they often cannot determine distributions of low atomic weight species, e.g. C, N. The atom-probes used in this work and their mode of operation are described in detail in A:I.2.2. Details of imaging characteristics and interpretation of FIM graphs have been collated by Dury (125), with particular reference to the study of pearlitic steels.

Considerable use is now being made of computer techniques in the analysis of FIM and atom-probe data: Youle (128) & Dury (125) have given information on these. Such techniques allow the relatively easy generation of 3-D information from experimental data, e.g. particle size and shape distributions. In addition they allow the reduction of data from the time-of-flight atom-probe to give spectra of numbers of ions with given mass/charge ratios: it is this last application which has been used in the present work.

3:3.2. Previous FIM and atom-probe work on pearlitic steels

The first systematic work using these techniques was that due to Morgan & Ralph (129) who imaged pearlite in hypereutectoid and eutectoid steels and were able to determine a $\alpha/\text{Fe}_3\text{C}$ orientation relationship. Dury (125, 130) extended this work on plain carbon hypereutectoid steels along with commercial grade patented wire. In addition he studied the deformation of pearlite and the pearlite reaction in the Fe-N system. Dury summarized the FIM work as follows:

- (a) The orientation relationship between α and Fe_3C in pearlite were found to be within 10° of either the Pitsch or Bagaryatsky relationships;
- (b) The habit planes for the Pitsch relationship were found to be within 20° of $(001)_{\text{Fe}_3\text{C}}$. The habit planes for the Bagaryatsky relationship showed a larger scatter but tended to be grouped about the $(010)_{\text{Fe}_3\text{C}}$ zone;
- (c) For steels near the eutectoid composition, the proportion of colonies exhibiting the Pitsch relationship increased with the Mn content or the total alloy content of the steel. (Two possible mechanisms for this were

suggested: the first considered the effect of Mn on the lattice parameter of Fe_3C and the second concerned the effect of alloying elements on the interfacial energies of the 3 phases involved).

Dury's work showed that deformation of pearlite causes deformation of the Fe_3C plates perpendicular to the wire axis and lattice rotation, with respect to the ferrite, may occur. Slip steps and dislocation pile ups in the Fe_3C were noted although the observation of individual dislocations was inconclusive. Dury also noted the presence of dislocation "sub-boundaries" in the ferrite with misorientations in the 1° to 5° range and it appeared that the majority of the boundaries were roughly parallel to the wire axis.

Recent work using a time of flight atom-probe has been undertaken by Miller & Smith (131), Smith et al (132) Miller et al (133). These workers have used a commercial patented wire to investigate the partitioning of substitutional solute atoms between the phases present. The machine employed was similar to that used in the present work. The probe hole was initially aligned and re-aligned during use by the regular admission of an imaging gas and the specimens were nitrogen cooled. It was noted that in the steel studied the silicon content of the ferrite matrix was twice that of the cementite while Mn enrichment was found near the interface, Cr, Ni and Cu was also found to segregate to the interfaces. It is interesting to note that they did not detect any sign of dislocation cell walls in the ferrite matrix, although this might be due to poor image quality. They were also unable to image the cementite laths adequately which they observed in their specimens, due to the choice of Ne as the imaging gas. The cementite laths in their micrographs had the appearance of deeply field-etched, non-imaging areas and this is discussed later.

3:3.3. Present Studies on patented wire

3:3.3.1. Introduction

In the present study, it was necessary to characterise the dislocation substructure and segregation of substitutional and interstitial solutes in the ferrite matrix, particularly with varying LTHT in order to elucidate the behaviour of patented wire in simple tensile testing and tensile relaxation. A plausible explanation of the dramatic improvement of mechanical properties is a strain ageing effect (see section (2:3.4.5)) on LTHT of interstitial solutes C & N. The atom-probes with their unique characteristics have proved ideally suited to this problem. Experimental details of this work are summarised in section (A.1:2.2). The material investigated was BS 1408, 0.6 mm diameter wire with batch composition (in wt%):

C	Si	S	P	Mn
0.82%	0.23%	0.025%	0.015%	0.68%

which is similar to the 1408M wire used in the mechanical testing programme.

The wire was studied in 3 conditions:

- (a) A/R
- (b) A/R + LTHT "A" (30 mins @ 200°C)
- (c) A/R + LTHT "B" (300 mins @ 200°C)

LTHT "A" is typical of that used by the wire industry in the production of wire or manufactured articles (e.g. springs) from the wire. It is regarded as being the optimum treatment for the improvement of relaxation resistance and tensile strength. LTHT "B" was used in an attempt to accentuate any segregation processes which may occur.

3:3.3.2. As received Patented Wire (A/R)

Basic characterisation of the ferrite structure was carried out using the atom-probes merely as field-ion microscopes with the specimen usually held at ~70K. The use of a patented wire drawn to a large reduction ensured a fine microstructure which was an advantage considering the restricted field of view of these machines. An example of the microstructure is given in fig.(3:18). With neon gas the ferrite images quite well showing some well developed poles: the two cementite lamellae do not image well, as has been noted above. In the central ferrite lamella can be seen in two cell walls, the misorientation across one can be seen in its effect where it crosses a prominent pole. In this case it is estimated that the thickness of the ferrite lamella is of the order of 50 nm while that of the cementite is approximately 10 nm. A more common appearance of a specimen is that shown in fig. (3.19) where the field of view was completely composed of one ferrite lamella. This behaviour was apparently due to selective chemical polishing during specimen preparation. In fig.(3.19a) can be seen a number of cell walls imaging as dark lines in the micrograph. This poor imaging in such areas is due to field-etching causing local changes in the specimen radius of curvature. These variations cause focussing of ions when the imaging atom-probe is used to produce an Fe²⁺ desorption image fig.(3:19b). It was generally found that such a desorption image was the most sensitive test of the presence of cell walls. A further example of the substructure in a ferrite lamella is given in fig.(3:20). The misorientation across a cell wall can best be seen when it intersects prominent poles. The 3 micrographs included in this example are part of an evaporation sequence with approximately 5 atom planes removed between each. Use of this technique enabled a measure of the typical 3 dimensional nature of the

substructure to be obtained. This specimen showed well, the random nature of the substructure in the as received material. There was a wide variation in the dislocation cell size : a histogram of transverse cell sizes in this material is given in fig.(3:2 1.) which was constructed from the examination of 18 specimens by a linear intercept method. As can be seen the most common transverse cell size range was 25 to 30 nm. It was not possible to complete a comparative study in the longitudinal direction, although in the few examples where a specimen remained stable through a long evaporation sequence the longitudinal size of individual cells was greater than their transverse size.

A measure of the misorientation across the dislocation cell walls present can be obtained if both cells show sufficiently well developed poles to allow indexing. Not only must the micrograph quality be good but also each cell must cover sufficient of the specimen tip to show the poles. The latter problem has limited the applicability of this technique: an example of its application is given in fig.(3:22). All the misorientations observed were in the range 5° to 10° , the sample size being too small to comment further. A montage of a particular specimen is given in fig.(3:23): such exercises allowed a more representative view of the microstructure to be made, although its accuracy was limited by reason of the necessary projection of an approximately spherical cap onto a flat plane montage. This example shows the presence of a large number of randomly orientated boundaries which have been field-etched. Also present are a number of small non imaging areas which may have been carbides: it proved impossible however to check if this was correct as the tip disintegrated after transfer between atom-probes. A further example of the differing imaging characteristics of ferrite and cementite are given in fig.(3:24): in this case the upper part of the field of view is poorly imaging cementite while the lower ferrite shows well developed poles. To the left in the ferrite is shown a boundary which moved to the right during the evaporation sequence indicating that the wall was not accurately aligned with the wire axis. Fig.(3:25) shows another example of a specimen with ferrite and cementite at the tip.

The imaging atom-probe was employed to identify cell walls and to give a spatial indication of chosen ionic species. In all cases when a suitable specimen was produced, an iron (Fe^{2+}) desorption image was obtained in order to identify cell walls and also to give an indication of the focussing behaviour of the field-etching effect at such high energy sites. Clearly

similar behaviour will also occur with all other ionic species limiting the resolution of the technique. The easily obtained Fe^{2+} peak also enabled the gating pulse to the channel plate to be accurately calibrated. An example of the images so obtained from the A/R wire are shown in fig.(3: 26). The field-ion micrograph is at a higher magnification than those referred to above and shows a single cell wall in ferrite (a): this can also be seen on the Fe^{2+} desorption image (b). The segregation of interstitials were of particular interest in this study and the C^+ and C^{2+} images (c,d) are given indicating that there is strong segregation of C to certain areas of the boundary and most of the C is evaporated as C^{2+} . An image for mass to charge ratio 14 is given (e): this includes both N^+ and Si^{2+} ions which cannot be distinguished. There is, however, no significant segregation of these species to the cell wall: a similar conclusion can be drawn from the S^+ and P^+ image (f). From the observation of a number of such specimens it was shown that the segregation of C and not N was common, and in addition the C segregation was not uniform along the observed cell walls.

To obtain quantitative information suitable specimens were transferred to the time-of-flight atom-probe, and spectra were obtained from the ferrite matrix and from various points along selected boundaries. This procedure did not prove entirely satisfactory, however, (complicated machine improvements would have been necessary to alleviate the problem) as specimens transferred in this manner proved considerably more liable to disintegrate when in the second atom-probe. Also it was not possible to predict with complete success the high C areas along a cell wall network. For each analysis an ion count of greater than 1000 was used, the Ne imaging gas was maintained to ensure constant alignment of the probe hole over a particular area. Examples of spectra, after processing, from a cell interior fig.(3:27a) and from a cell wall, which showed a high C segregation fig.(3:27b), are included: the former showed a C concentration of less than 0.1 atomic % while the latter showed a mean concentration of approximately 12 at%. By repeating these analyses on further specimens it was shown that these values are typical of the as received material.

Observations of the A/R patented wire were hindered by its fragility: the high internal stress levels along with the stress concentrators at the surface were a severe enough problem to cause many specimens to fragment on increasing the EHT. This proved to be less of a problem with the heat treated samples.

3:3.3.3 As received with LTHT "A"

An analysis of the ferritic microstructure of patented wire given a LTHT of 30 mins at 200°C (the typical industrial heat treatment to optimise the wire's mechanical properties) was undertaken to ascertain whether significant changes could be detected which could explain the observed changes in the mechanical properties (Ch.2). This was carried out as above except that the occasional availability of liquid helium allowed specimen cooling to lower temperatures, thus improving resolution.

An observed ferritic microstructure is given in fig.(3:28), which shows cell walls and non-imaging areas which were possibly carbides. A common appearance, however, is that shown in fig.(3:29), where the boundaries have become aligned in the ferrite over a relatively wide area and were approximately parallel to the adjacent lamellae. The spacing between cell walls in this particular example was approximately 12 nm. With this type of microstructure, few prominent poles were visible in each cell: thus it was found difficult in many specimens to obtain values for the misorientation. In those cases where a determination was possible the values were again between 5° and 10°. Determination of the transverse cell size in specimens not generally showing this strong alignment showed a most likely value in the 25 nm to 30 nm range, fig.(3:30). The spacing between boundaries in aligned specimens varied between 3nm and 30 nm in the examples studied, the transverse length often being greater than the field of view. A montage of an annealed specimen is given in fig.(3:31). As can be seen there are areas which show aligned boundaries (in the upper part of the plate the spacing is of the order of 6 nm, while in the lower part it is approximately 20 nm), other areas show a more random arrangement and, again, there were dark imaging areas. As in the case of the A/R material the imaging atom-probe was highly successful in giving a spatial distribution of segregating species in the ferrite. Fig.(3:32a) depicts an area of ferrite containing several non-aligned boundaries clearly marked by field etching: this effect is clearly shown in the Fe²⁺ desorption image. From the C²⁺ image it can be seen that C has segregated only to certain sections of the boundaries, a behaviour also noted in the A/R material. The last image indicates, as before, no significant segregation of N⁺ or Si²⁺ to the substructure. Fig.(3:33) shows a specimen where a single cell wall is evident: again no segregation of N⁺ + Si²⁺ occurred and also C²⁺ ions were only detected at the edge of the field of view. A typical specimen with aligned cell walls, at higher magnification than fig.(3:29),

is shown in fig.(3:34). The spacing in this example is approximately 5 nm and the walls which pass through the prominent pole which is visible appear to have a misorientation of approximately 15° : the adjacent walls appear, however, to have a lower misorientation. An adjacent area of the same specimen is shown in fig.(3:35): it is again clear that not all of the cell walls, as seen in the field-ion micrograph and the Fe^{2+} image, are decorated by C to a significant extent. The aligned walls shown in fig.(3:36) are particularly regular and closely spaced (approximately 2nm to 3nm): as can be seen by the effects on the poles visible, the misorientation across each wall varies but is generally of the order of 5° to 10° . The improvement in image quality and resolution which is obtained by cooling with cold He gas is clear by comparing fig.(3:36) with fig.(3:37) which is approximately of the same area. Field evaporating the specimen at lower temperatures showed a noticeable reduction in the field-etching at

boundaries as can be seen from the field-ion micrograph (particularly shown by the wall passing through the pole): however, the effect persists as shown in the Fe^{2+} desorption image. The C^{2+} image is, as seen in other specimens, localized to certain areas of the cell wall network. An example of aligned cell walls from another area is given in fig.(3:38). The field ion micrograph fig.(3:38a) was obtained with what is normally taken to be the optimum imaging potential: because of the variation in curvature the optimum potential for areas at the cell walls is approximately 5% higher as shown in fig.(3:38b). This ensures imaging up to the cell wall with extremely high resolution: however, it causes defocussing between them. Of particular interest in this example is the step shown in the central wall which is most clearly seen in the Fe^{2+} image. It is interesting to note that this step corresponds to an area of C segregation unlike the remainder of this particular cell wall in the field of view.

Specimens of this material were examined in the time-of-flight atom probe, as described in the previous section, to obtain quantitative data. Examples of spectra from a cell interior and from a cell wall with high C concentration are shown in figs.(3:39a,b). The former areas showed a mean concentration of again less than 0.1 atomic %, while the latter had a mean of approximately 14 atomic %. A further analytical technique was applied to such specimens using the data from the time-of-flight atom-probe. The IBM 370 was again used to record the sequence of ion species (in the form of mass /charge ratio) and to plot running means of atomic % of chosen atomic species: in this case Fe and C. Typical traces from initially a high C region of a cell wall are given, fig.(3:40). This trace gives a

profile of the composition as the specimen is field evaporated, allowing for a scaling factor due to the number of atoms covered by the probe hole (which was estimated to be 100 ± 10 atoms). The composition profile varies between approximately 5 atomic %C and 25 atomic %C (to be compared with that of cementite of 25 at%C). The frequency of variation between these two limits was irregular, the profile including one period of low (5 to 10 at%) C concentration, but the variations themselves were significant considering the high resolution of the technique.

3:3.3.4. As received + LTHT "B" (300 mins at 200°C).

This second heat treatment was chosen in an attempt to exaggerate any segregation obtained during LTHT "A". Similar cell walls and dark imaging areas as seen in the previous two materials were found, fig.(3:41) gives a low magnification example. A higher magnification series of images of a cell wall is given in fig.(3:42). A more thorough examination of a dark imaging area was found to be possible in this material: a low magnification image being given in fig.(3:43a) showing such an area along with cell walls. Fig.(3:43b) is a higher magnification micrograph of the central portion of (3:43a), and there follows the relevant Fe^{2+} and C^{2+} desorption images. It is clear that the dark imaging area has a much higher C concentration than the visible ferrite. A subsequent quantitative analysis gave a composition of 25 atomic %C for this dark region.

3:4. Comments and summary

The present work has shown that present microstructural techniques can be used to obtain further information on patented wire. Due to the reasons already described, the present investigations were limited by resolution and manipulation problems: a deeper study of the deformation during drawing and the dislocation, microstructural changes on LTHT could possibly be made with available techniques if a systematic survey using a higher pearlite transformation temperature were employed. The segregation investigation showed considerable success indicating the power of FIM and atom-probe microscopy in this type of complex material. Conclusions of this study can be summarised as follows:

(a) No significant microstructural changes were observed through the section of the wire: surface decarburization was limited to 5 μm in depth.

(b) The TEM study of the A/R 4.25 mm wire showed no general fragmentation of the cementite lamellae, indeed there were many signs of considerable ductility under this deformation mode e.g. at shear bands, kinking and necking:

no voids at sites of fragmentation were observed. An extensive dislocation substructure was observed in the cementite with a scale of the order of 1 nm to 10 nm.

(c) A clear cell structure was present in the ferrite: in the 4.25 mm patented wire it typically extended over several adjacent ferrite lamellae and was found to be slightly larger in the longitudinal rather than transverse direction. These cells consisted of interiors of relatively low dislocation density bounded by well defined walls of dislocation nets with typical spacing of 2 nm: these dislocations could not be fully characterized. The structure in these walls was often obscured by dislocation contrast from overlying cell interiors.

(d) No major changes in microstructure were observed on LTHT except that it was observed, that dislocation contrast from within cells showed a significant decrease.

(e) The patented wire used in the FIM/atom-probe studies (drawn to a higher reduction) showed a typical ferrite cell size considerably less than the ferrite lamellar width. With this cell configuration a noticeable transverse alignment of the cell walls was noted on LTHT "A": no change was observed on further LTHT. A typical cell wall misorientation of 5° to 10° was noted on specimens examined.

(f) Segregation studies using atom-probes have shown the segregation of C to the cell walls: this segregation was not uniform along each boundary and the same feature was shown in concentration profiles down a particular boundary at a chosen point. The concentration at such a boundary varied between 1 at% and 25 at%. Segregation of N (or Si) and other impurities to these features was not significant. There was no significant change in the segregation profiles during any of the LTHTs used.

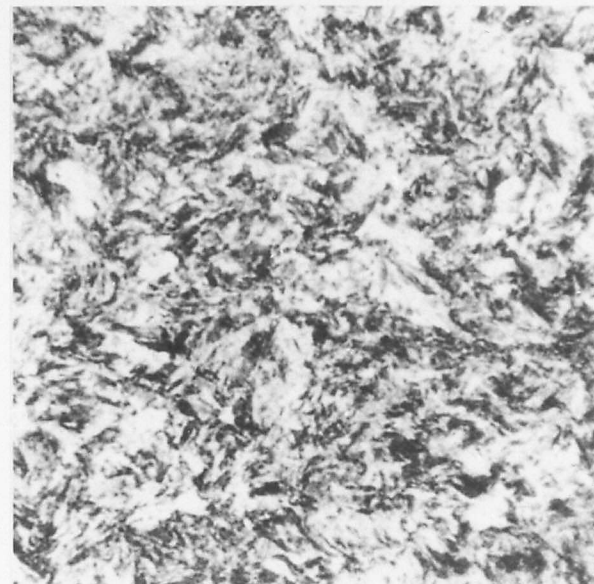


Fig.(3:1a) Optical micrograph of T/S of
A/R patented wire (2% nital etch). X2200

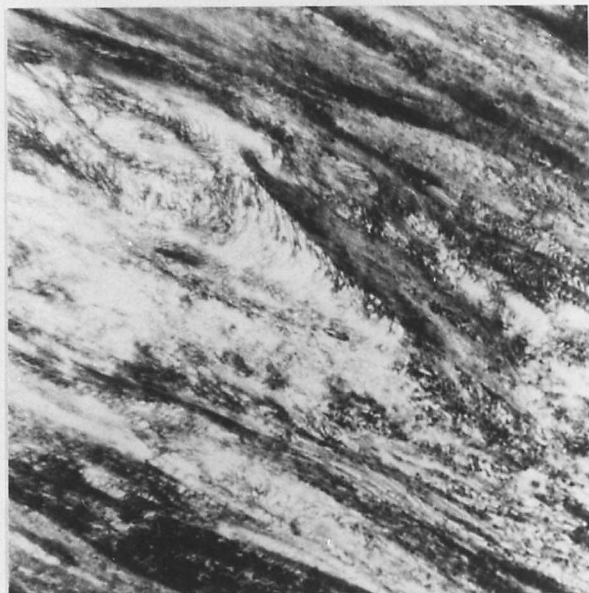


Fig.(3:1b) Optical micrograph of L/S of
A/R patented wire (2% nital etch). X2200

(N.B. Wire in the other examined conditions appeared essentially similar)

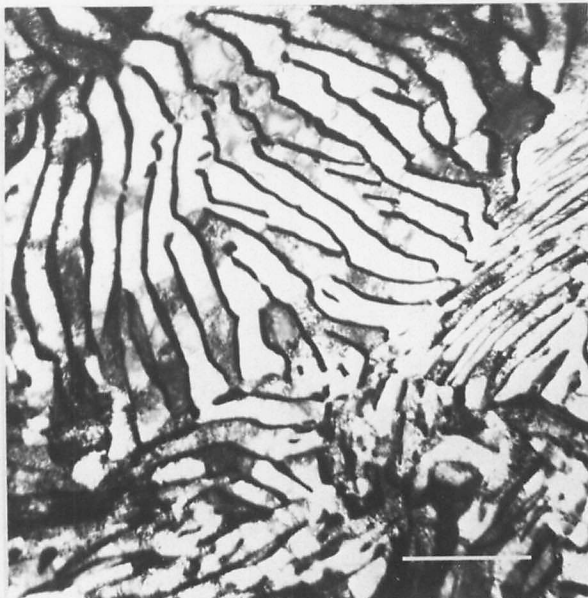


Fig. (3:2a) TEM of T/S of A/R patented wire
(BF) X110,000

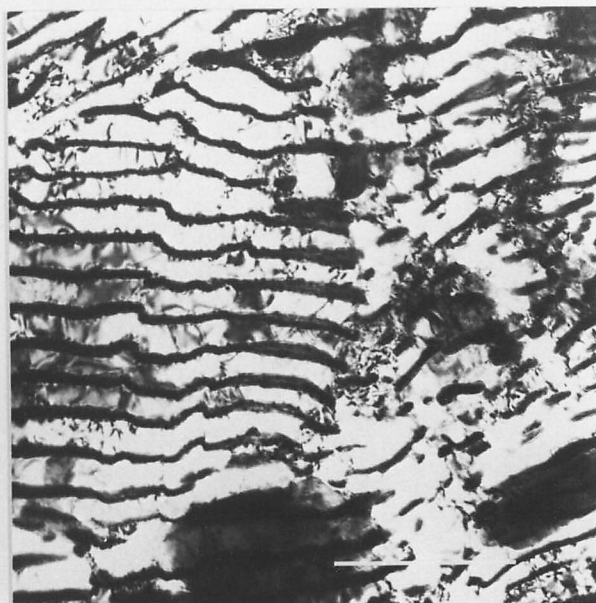


Fig. (3:2b) TEM of T/S of A/R patented wire
(BF) X155,000



Fig. (3:2c) TEM of T/S of A/R patented wire
(BF) X120,000



Fig. (3:2d) TEM of T/S of A/R patented wire
(BF) X250,000

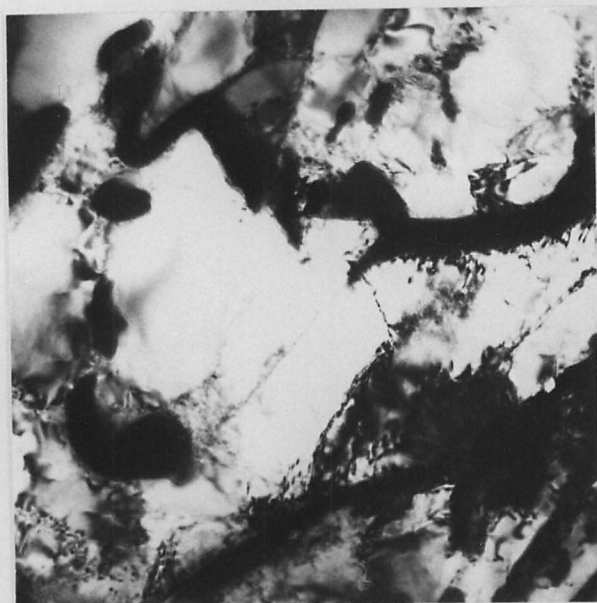


Fig.(3:3a) TEM of T/S of A/R patented wire
(BF) X185,000

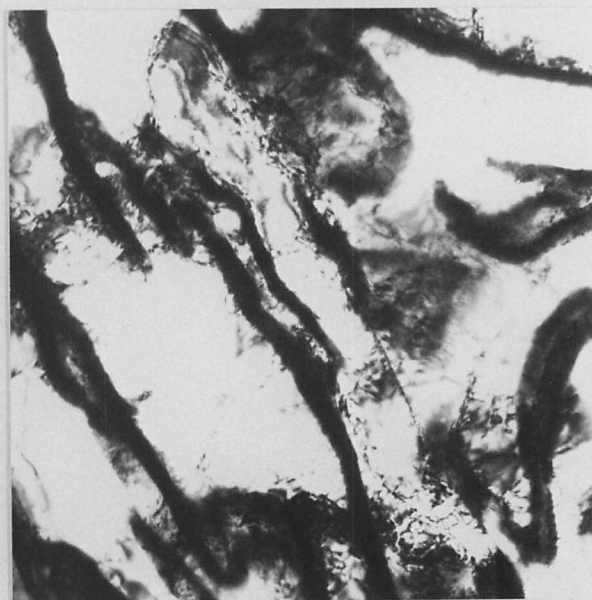


Fig.(3:3b) TEM of T/S of A/R patented wire
(BF) X185,000

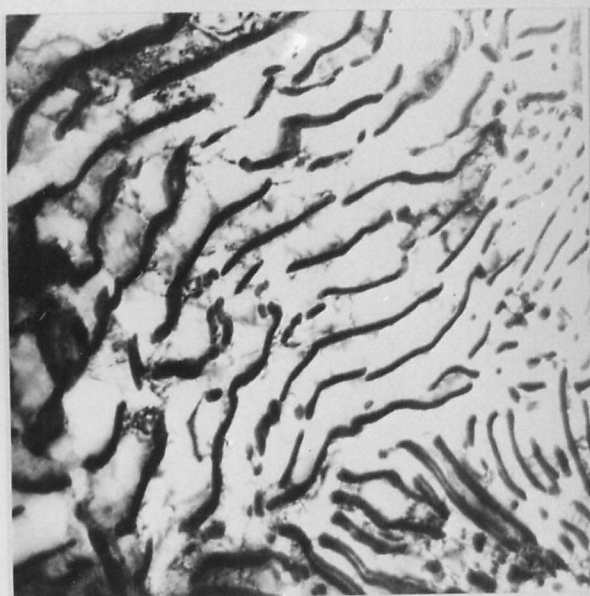


Fig.(3:3c) TEM of T/S of A/R patented wire
(BF) X48,000

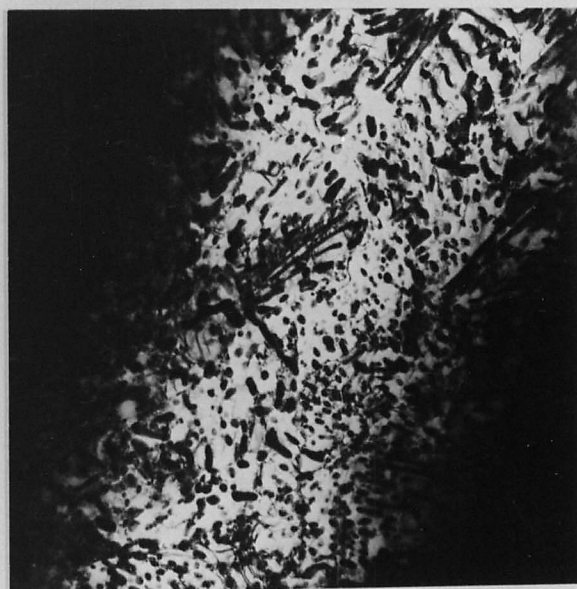


Fig.(3:3d) TEM of T/S of A/R patented wire
(BF) X22,000



Fig. (3:4a) TEM of T/S of A/R patented wire
(BF) X185,000



Fig. (3:4b) TEM of T/S of A/R patented wire
(BF) X260,000



Fig. (3:4c) TEM of T/S of A/R patented wire
(BF) X150,000



Fig. (3:4d) TEM of T/S of A/R patented wire
(BF) X270,000

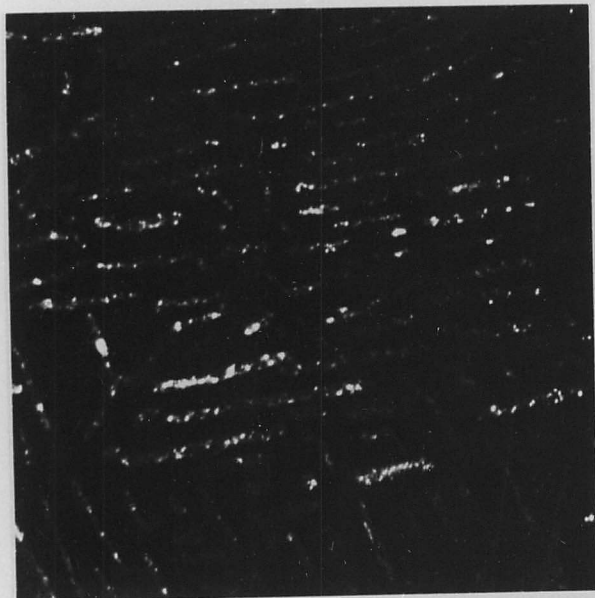


Fig. (3:5a) TEM of T/S of A/R patented wire
(Fe_3C CDF) X150,000

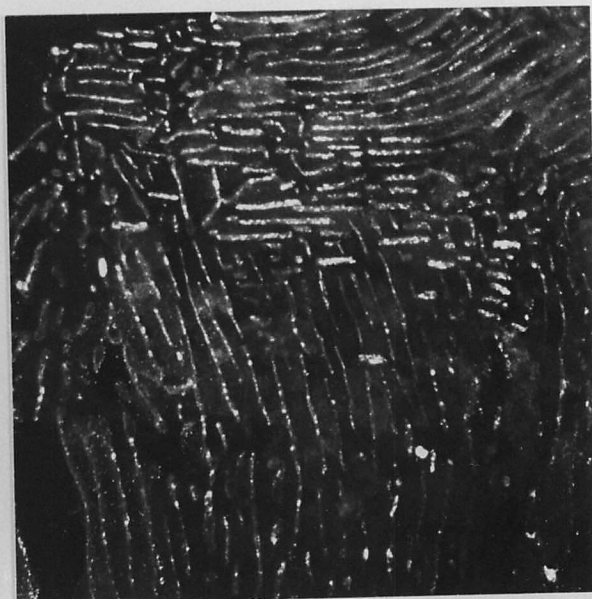


Fig. (3:5b) TEM of T/S of A/R patented wire
(Fe_3C CDF) X70,000

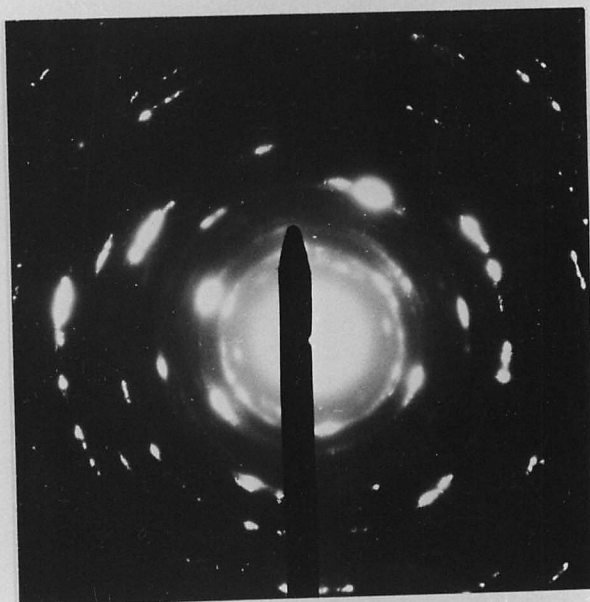


Fig. (3:5c) TEM of T/S of A/R
patented wire (SADP)

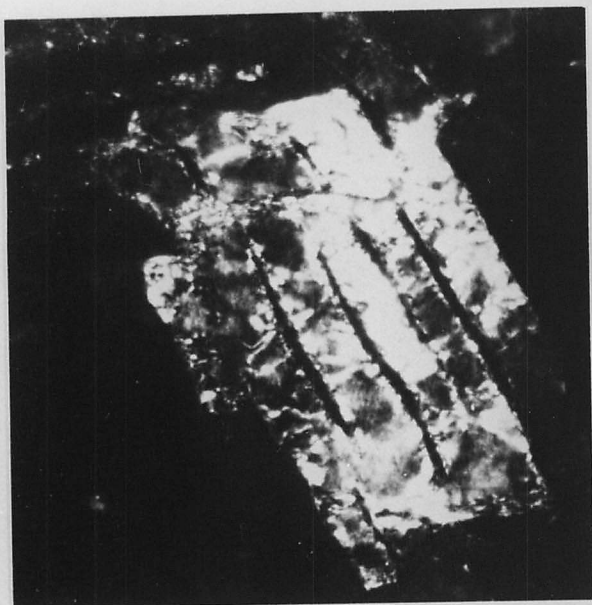


Fig.(3:6a) TEM of T/S of A/R patented wire
(α CDF) X25,000

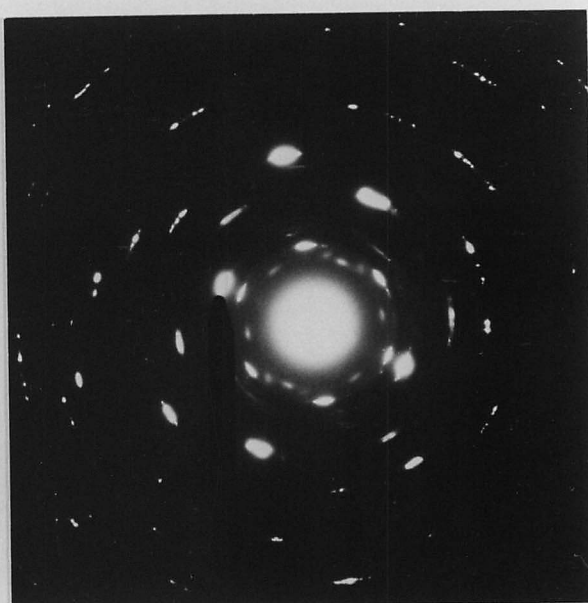


Fig.(3:6b) TEM of T/S of A/R patented wire
(SADP for (3:6a))

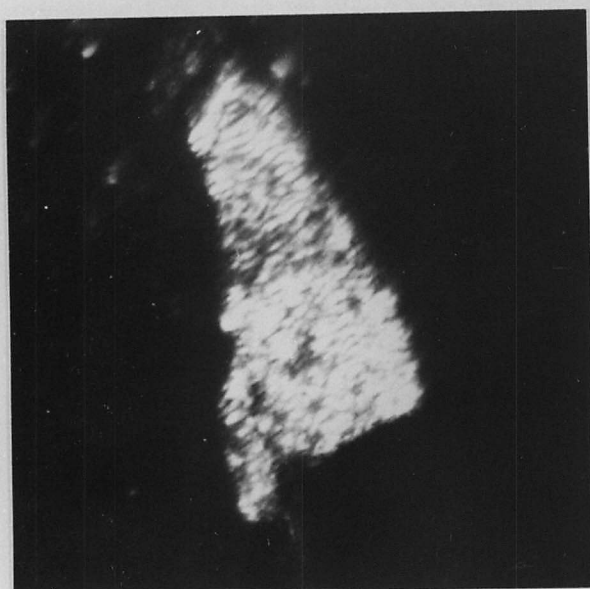


Fig.(3:6c) TEM of T/S of A/R patented wire
(α CDF) X600,000

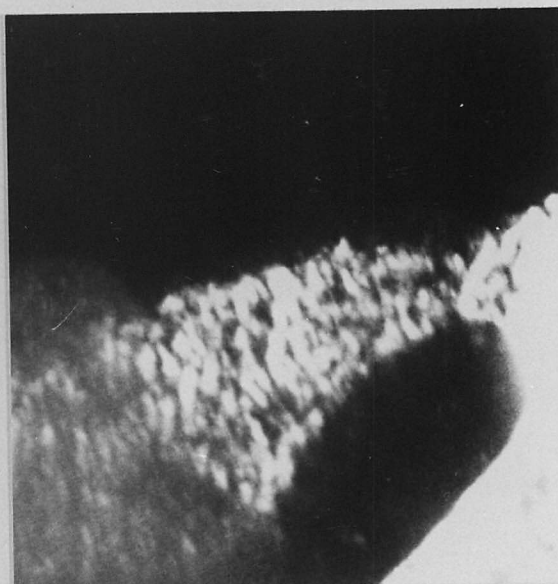


Fig.(3:6d) TEM of T/S of A/R patented wire
(SADP for (3:6c)) (α CDF)

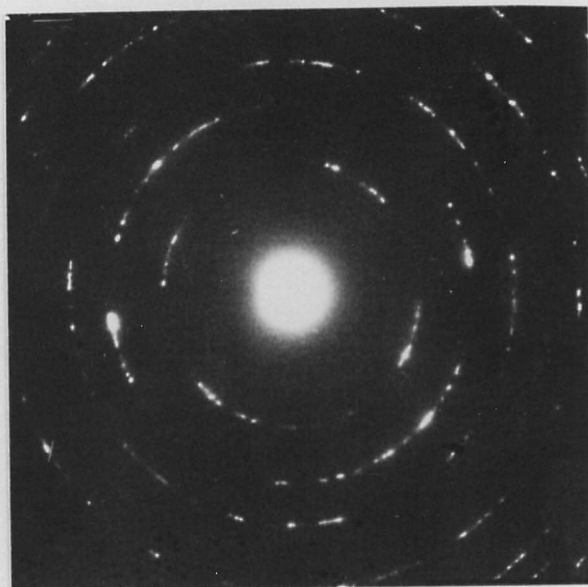


Fig.(3:7a) TEM of T/S of A/R patented wire. (SADP for (3:7b))



Fig.(3:7b) TEM of T/S of A/R patented wire. (BF) X135,000



Fig. (3:8a) TEM of L/S of A/R patented wire
(BF) X48,000



Fig. (3:8b) TEM of L/S of A/R patented wire
(BF) X86,000



Fig. (3:9a) TEM of L/S of A/R patented wire
(BF) X38,000



Fig. (3:9b) TEM of L/S of A/R patented wire
(SADP for (3:9a))



Fig. (3:10a) TEM of L/S of A/R patented wire
(SADP for (3:10b))

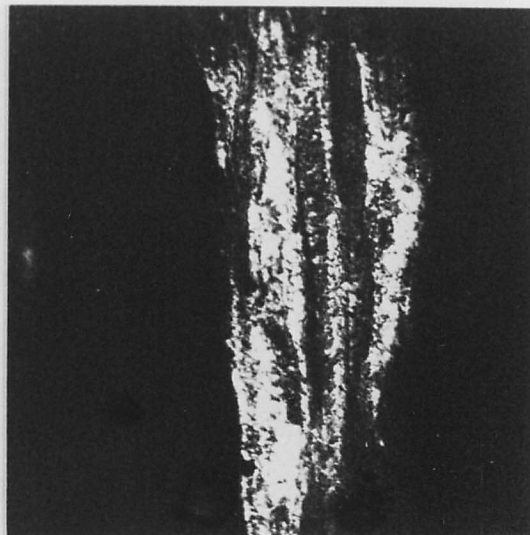


Fig. (3:10b) TEM of L/S of A/R patented wire
(α CDF) X110,000



Fig. (3:10c) TEM of L/S of A/R patented wire
(SADP for (3:10d))

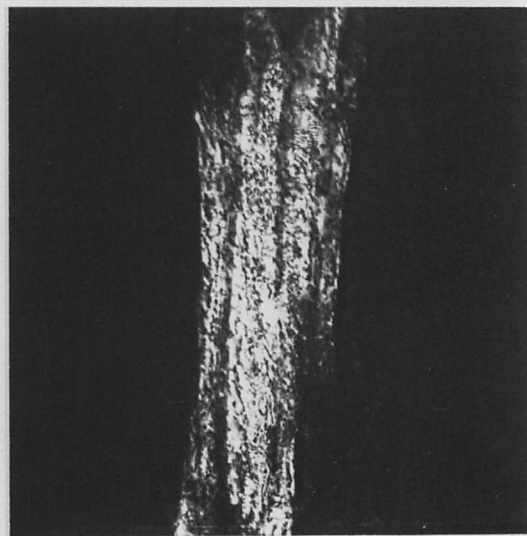


Fig. (3:10d) TEM of L/S of A/R patented wire
(α CDF) X110,000

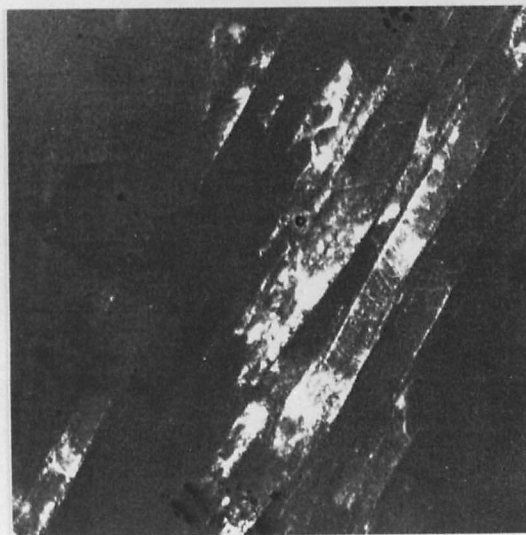


Fig. (3:11) TEM of L/S of A/R patented
wire (α WB) X48,000

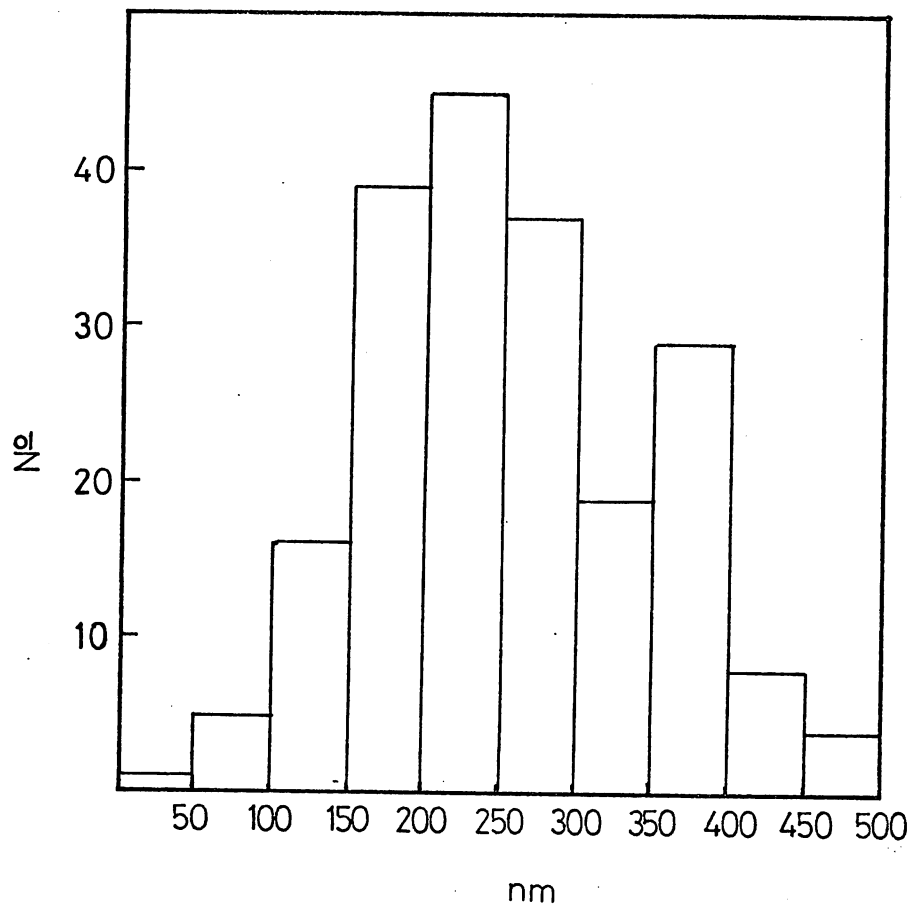


Fig. (3:12a) Distribution of T/S ferrite cell size (A/R patented steel wire, reduction $\approx 70\%$).

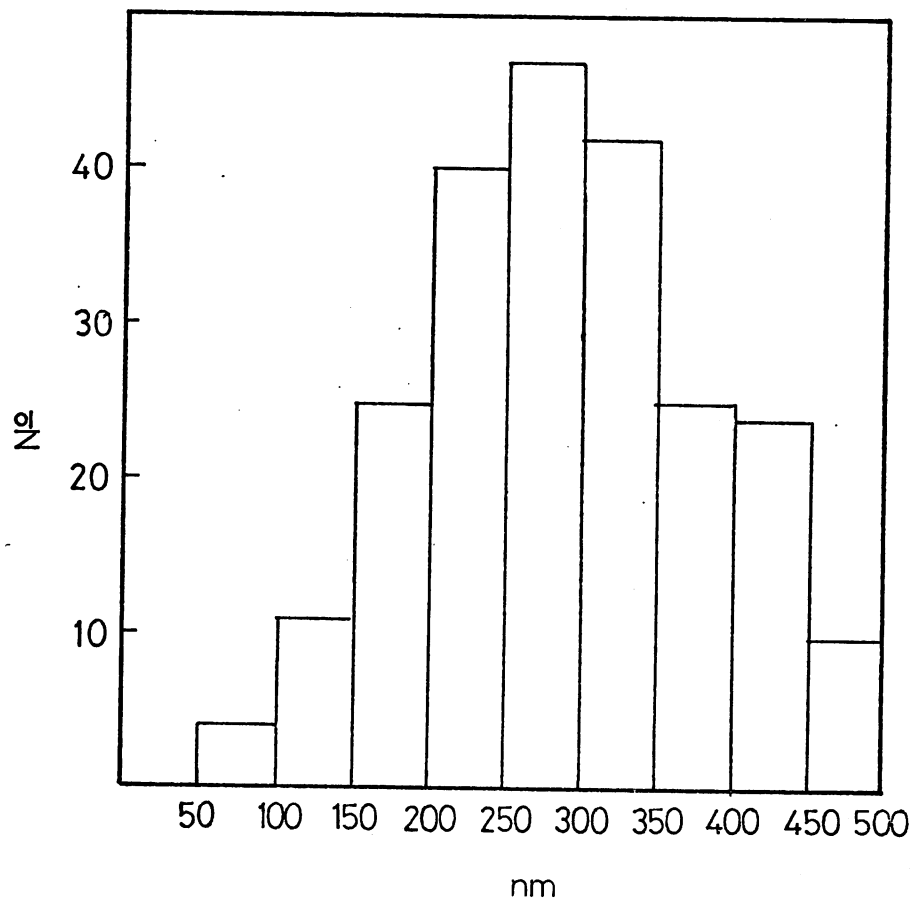


Fig. (3:12b) Distribution of L/S ferrite cell size (A/R patented steel wire, reduction $\approx 70\%$).



Fig. (3:13a) TEM of T/S of A/R + LTHT "A"
patented wire
(BF) X60,000



Fig. (3:13b) TEM of T/S of A/R + LTHT "A"
patented wire
(BF) X60,000

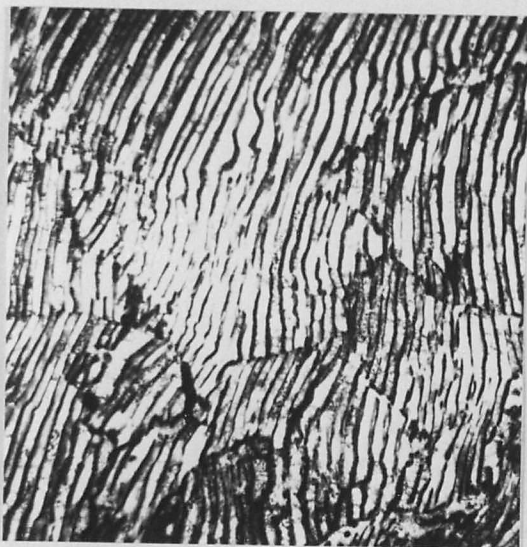


Fig. (3:13c) TEM of A/R + LTHT "A"
patented wire
(BF) X50,000



Fig. (3:13d) TEM of T/S of A/R + LTHT "A"
patented wire
(BF) X50,000

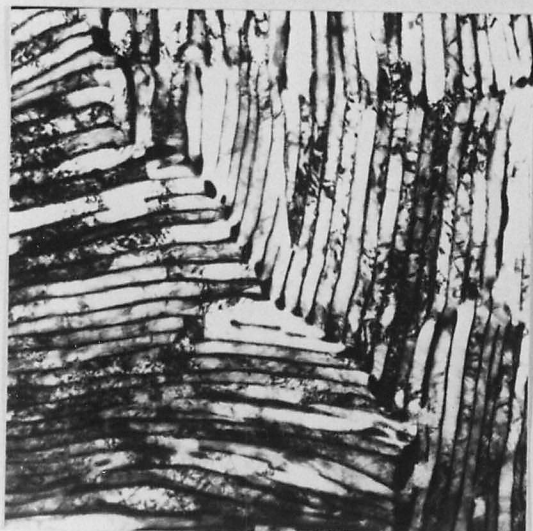


Fig. (3:13e) TEM of T/S of A/R + LTHT "A"
patented wire
(BF) X60,000

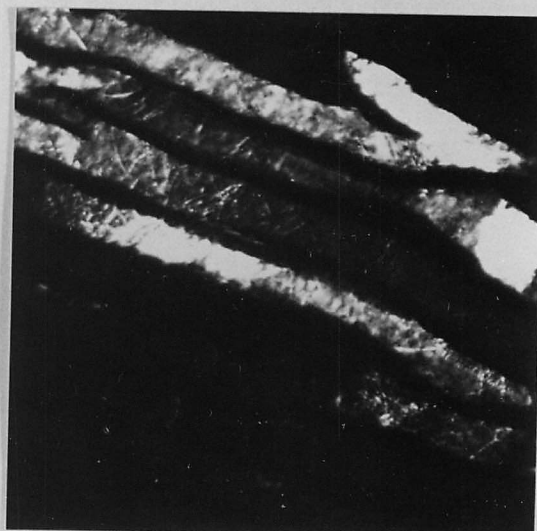


Fig. (3:13f) TEM of T/S of A/R + LTHT "A"
patented wire
(BF) X350,000

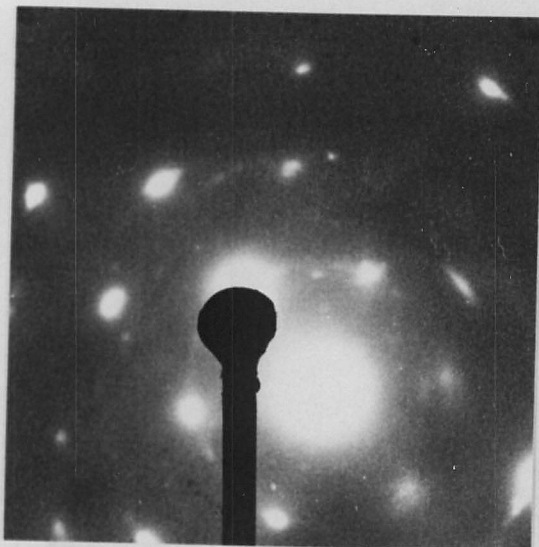


Fig. (3:14a) TEM of L/S of A/R + LTHT "A"
patented wire
(SADP for (3:14b,c))



Fig. (3:14b) TEM of L/S of A/R + LTHT "A"
patented wire
(α CDF)

X110,000

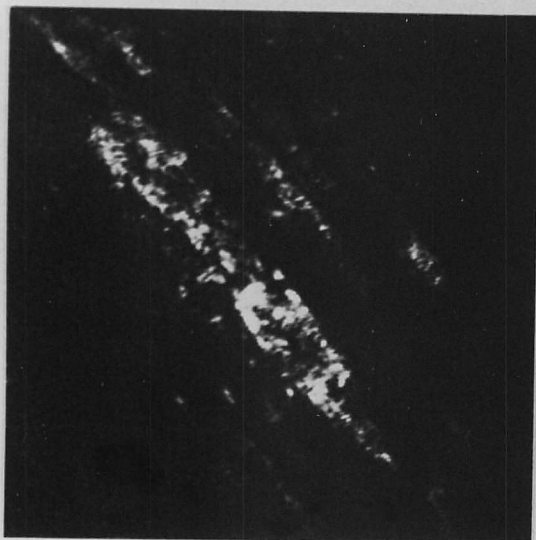


Fig. (3:14c) TEM of L/S of A/R + LTHT "A"
patented wire
(α CDF)

X110,000

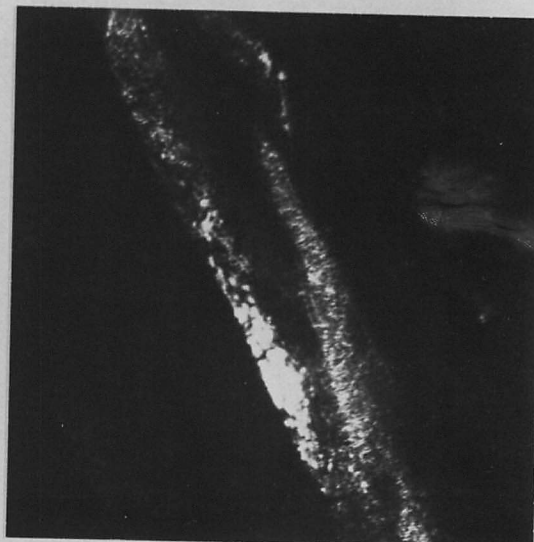


Fig. (3:14d) TEM of L/S of A/R + LTHT "A"
patented wire
(α CDF)

X330,000

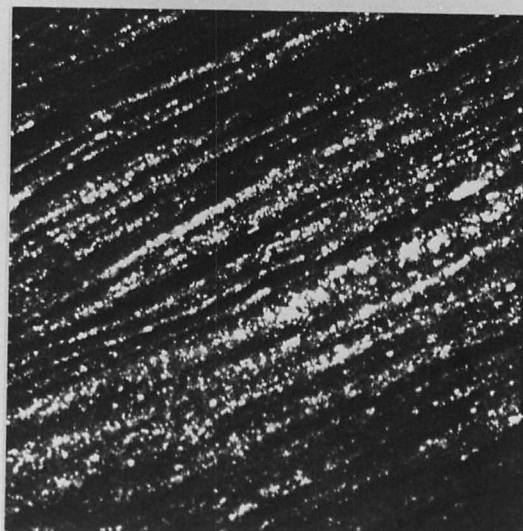


Fig. (3:14e) TEM of L/S of A/R + LTHT
"A" patented wire
(Fe₃C CDF)

X65,000

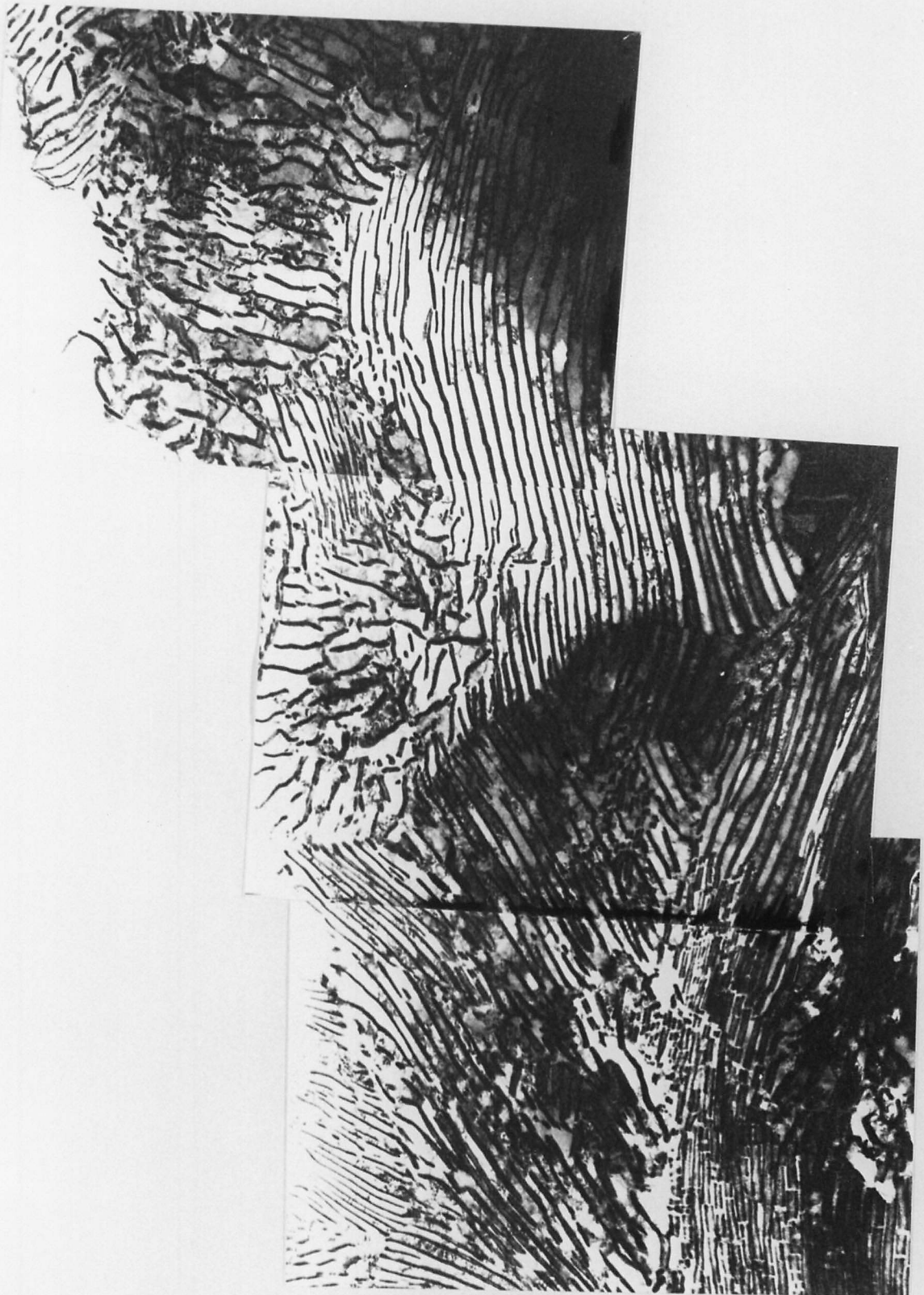


Fig. (3:15) TEM of T/S of A/R + LTHT "B"
patented wire
(BF)

X48,000

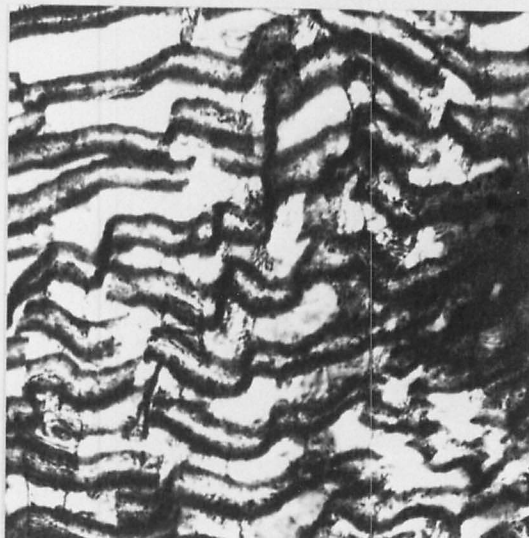


Fig. (3:16a) TEM of T/S of A/R + LTHT "B"
patented wire
(BF) X63,000



Fig. (3:16b) TEM of T/S of A/R + LTHT "B"
patented wire
(BF) X110,000

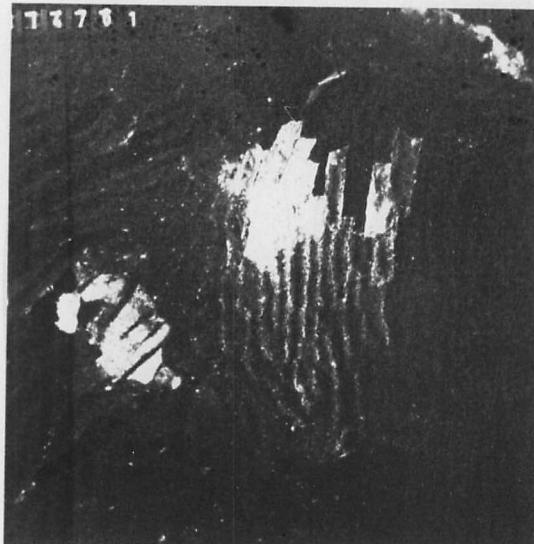


Fig. (3:17a) TEM of T/S of A/R + LTHT "B"
patented wire
(α and Fe_3C CDF) X60,000

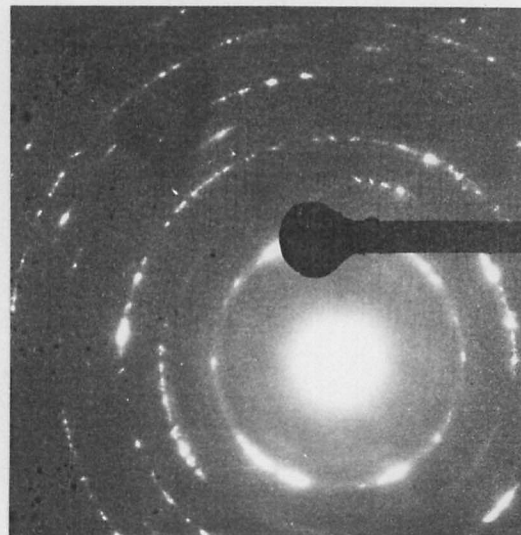


Fig. (3:17b) TEM of T/S of A/R + LTHT "B"
patented wire
(SADP for 3:17)



Fig. (3:17c) TEM of T/S of A/R + LTHT "B"
patented wire
(detail of (3:17a)) X300,000

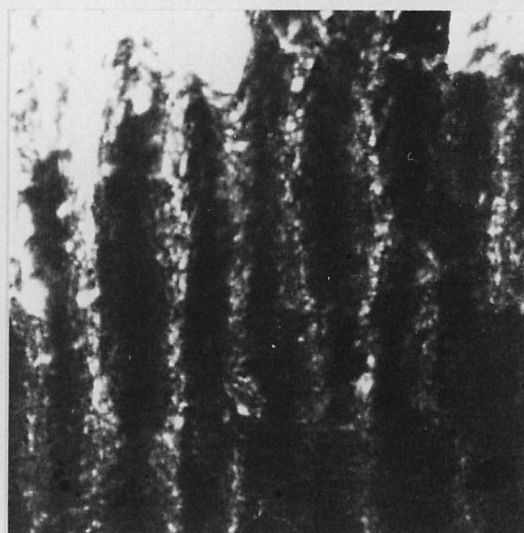


Fig. (3:17d) TEM of T/S of A/R + LTHT "B"
patented wire
(detail of (3:17b)) X300,000



Fig. (3:17e) TEM of T/S of A/R + LTHT "B"
patented wire
(α CDF) X200,000

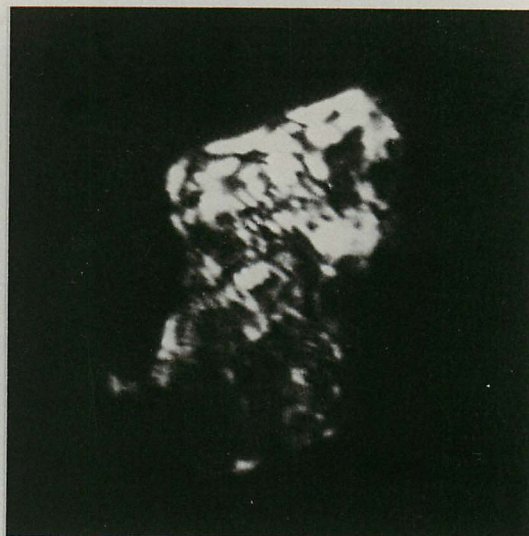


Fig. (3:17f) TEM of T/S of A/R + LTHT "B"
patented wire
(α CDF) X360,000

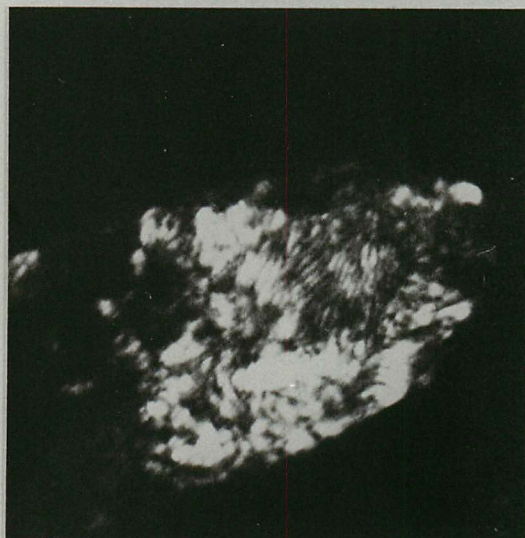


Fig. (3:17g) TEM of T/S of A/R + LTHT "B"
patented wire
(α CDF) X360,000

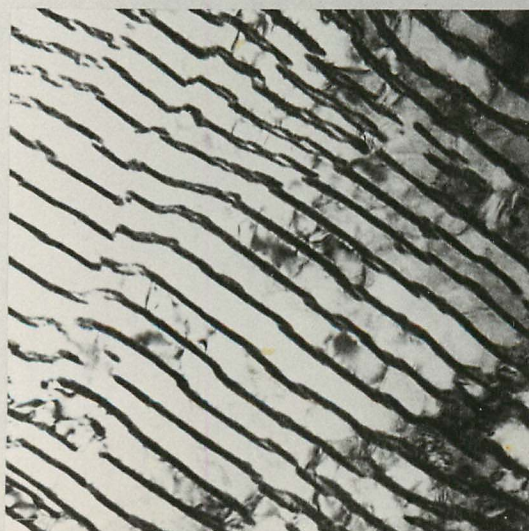


Fig. (3:17h) TEM of T/S of A/R + LTHT "B"
patented wire
(BF) X90,000

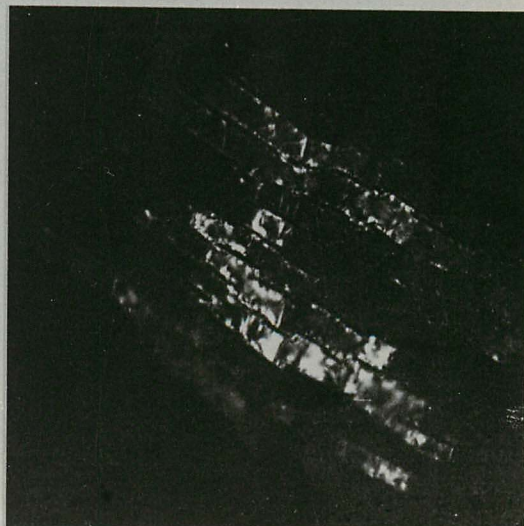


Fig. (3:17i) TEM of T/S of A/R + LTHT "B"
patented wire
(α CDF of (3:17h)) X90,000

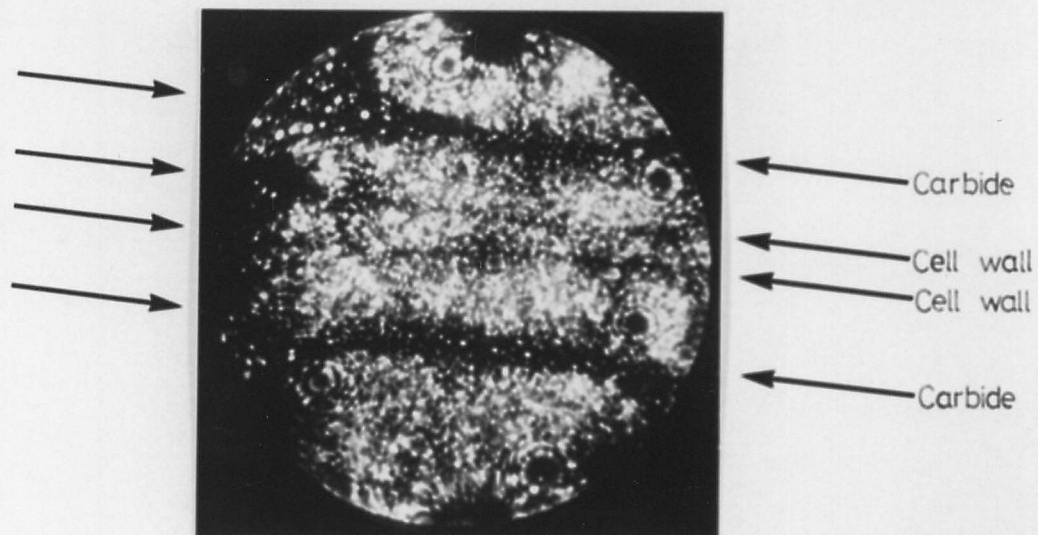


Fig. (3:18a) FIM of A/R patented wire (Ne)



Fig. (3:19a) FIM of A/R patented wire (Ne)

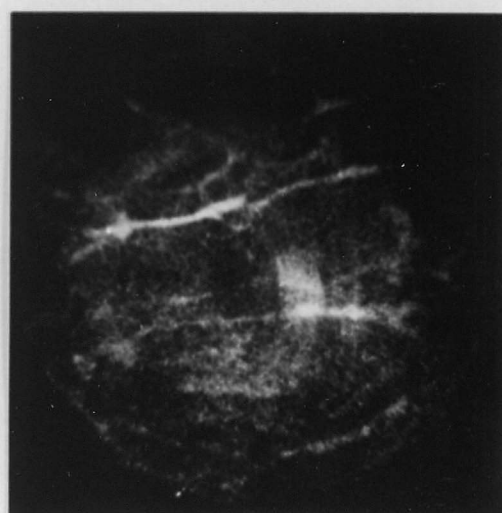


Fig. (3:19b) Fe^{2+} desorption image of area in (3:18b)

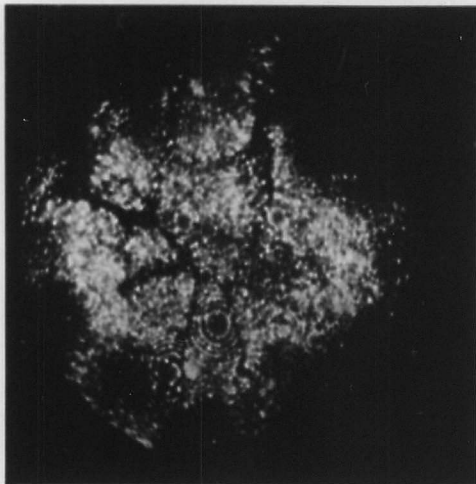


Fig. (3:20a) FIM of A/R patented wire (Ne)

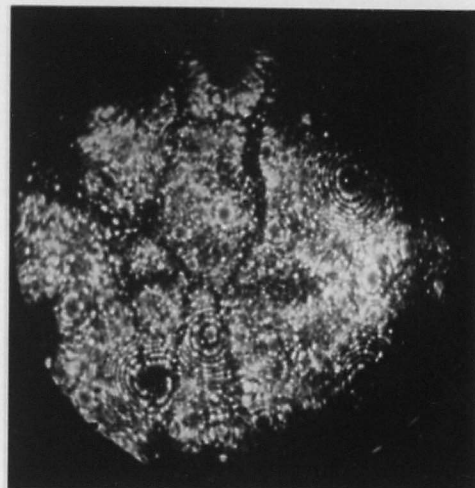


Fig. (3:20b) as for (3:20a) after field evaporation

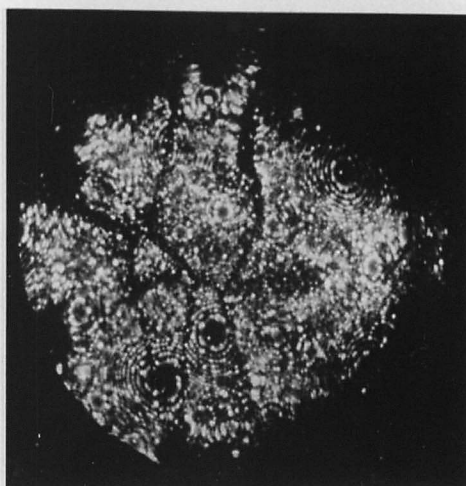


Fig. (3:20c) as for (3:20b) after further field evaporation

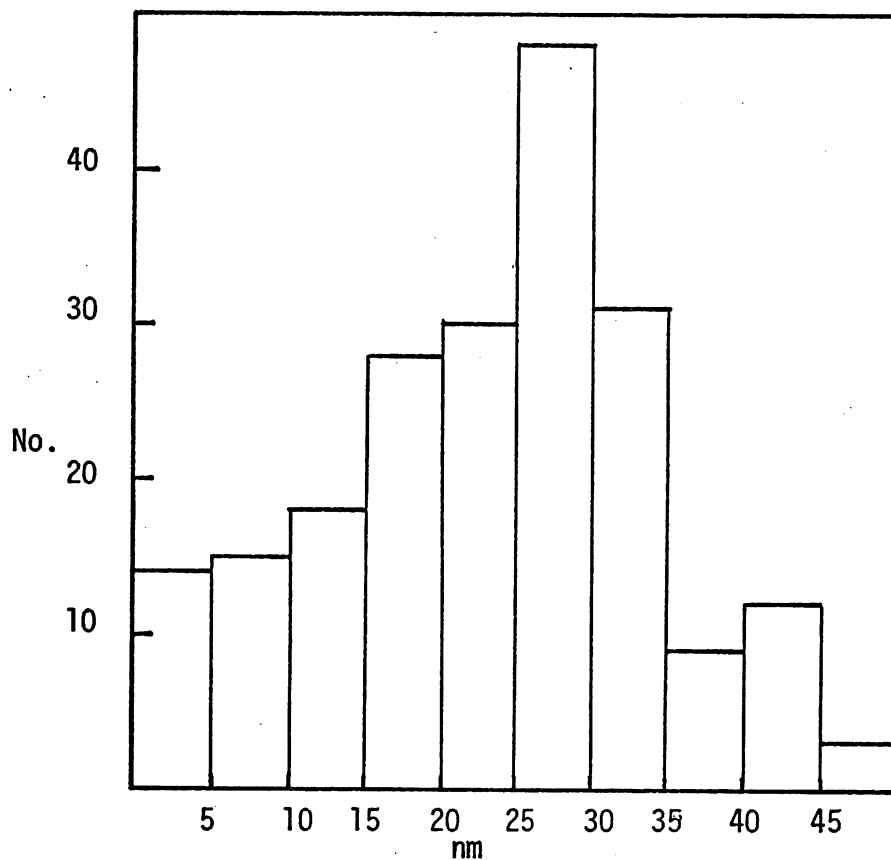


Fig. (3:21) Distribution of T/S ferrite cell sizes (A/R patented steel wire reduction $\approx 98\%$).

[Fig. (3:12), Fig. (3:21) and Fig. (3:30)
 Note: all cell sizes were measured by intercept method.]

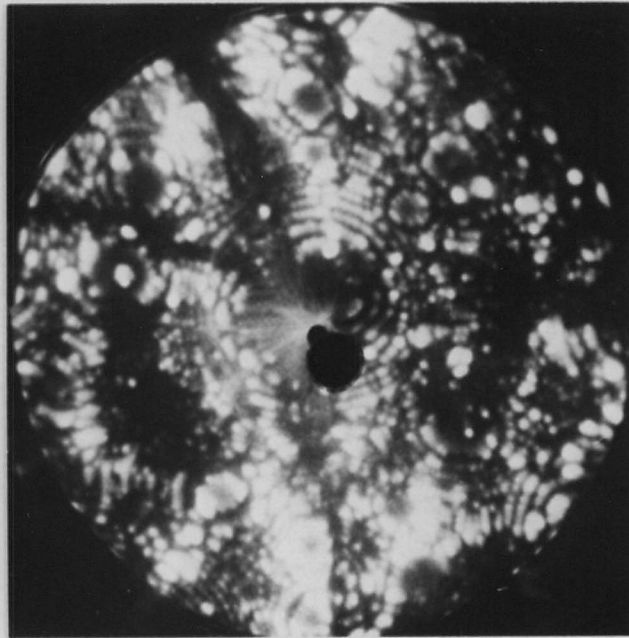


Fig. (3:22a) FIM of A/R patented wire (Ne)

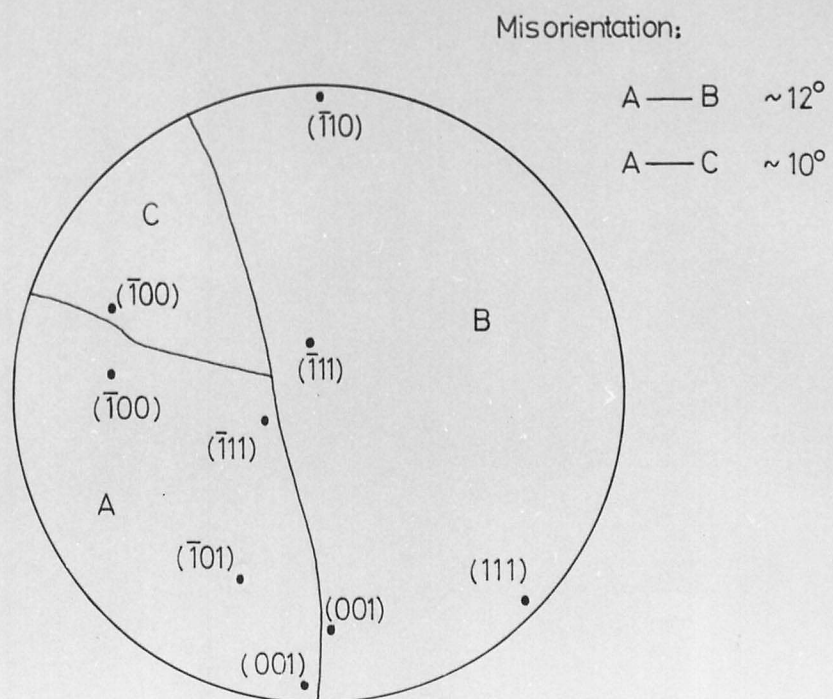


Fig. (3:22b) approximate analysis of (3:22a)

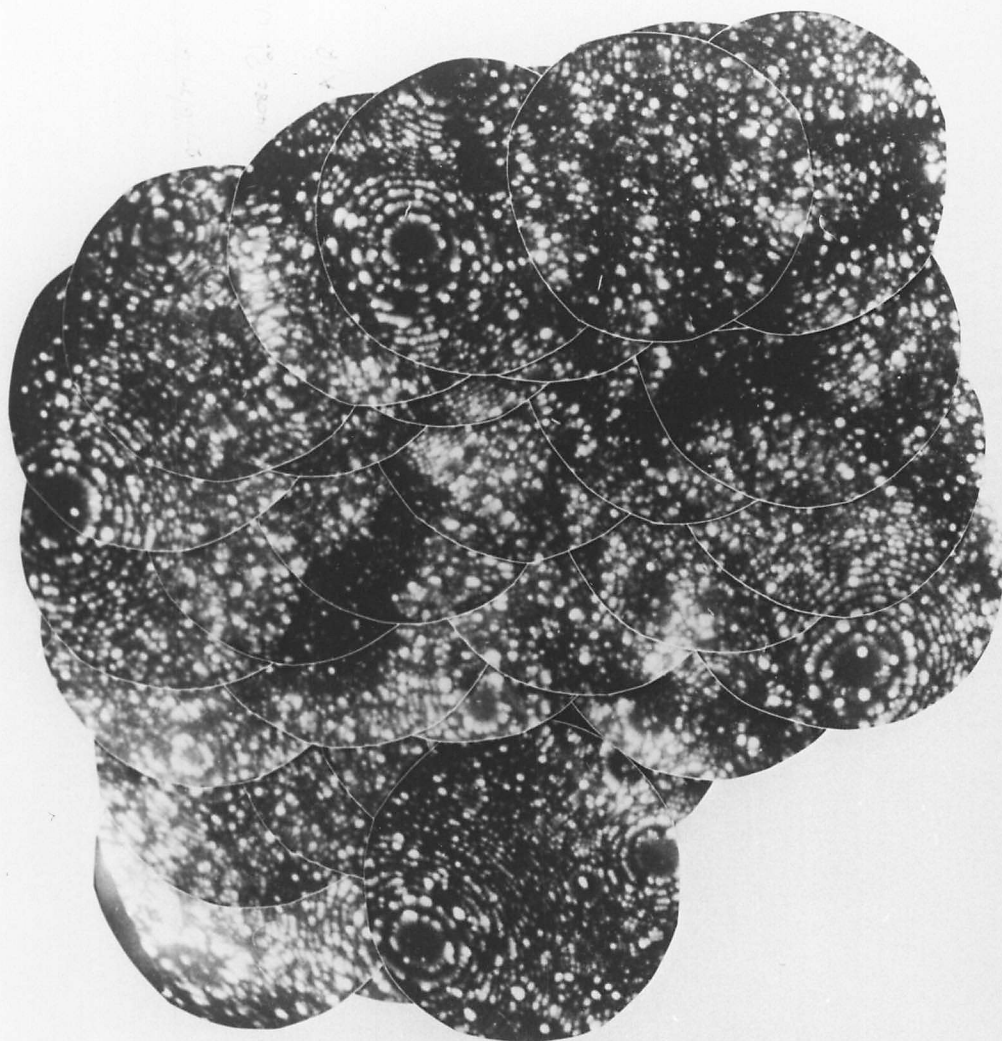


Fig. (3:23) FIM montage of A/R patented wire (Ne)

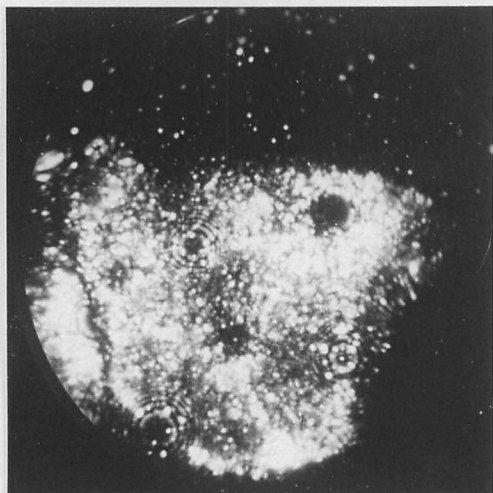


Fig.(3:24a) FIM of A/R patented wire (Ne)

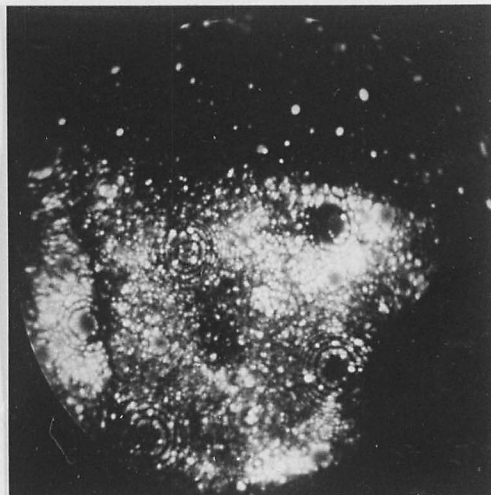


Fig.(3:24b) as for (3:24a) after field evaporation.

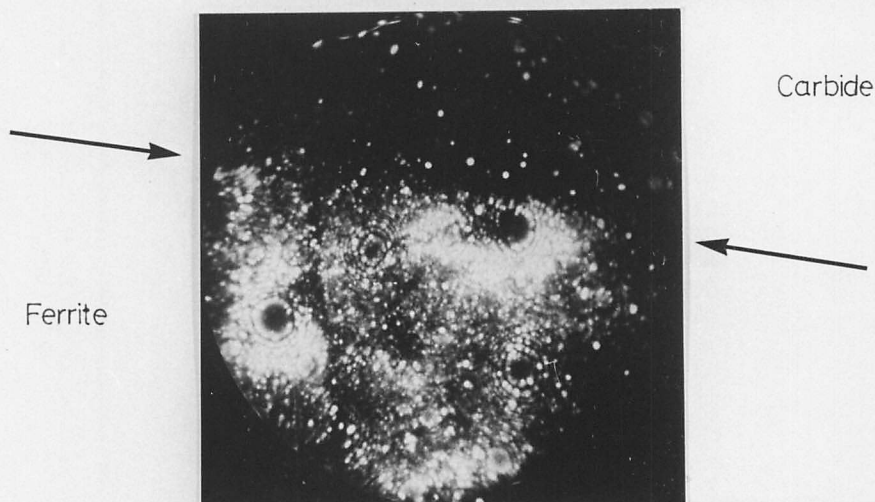


Fig.(3:24c) as for (3.24b) after further field evaporation

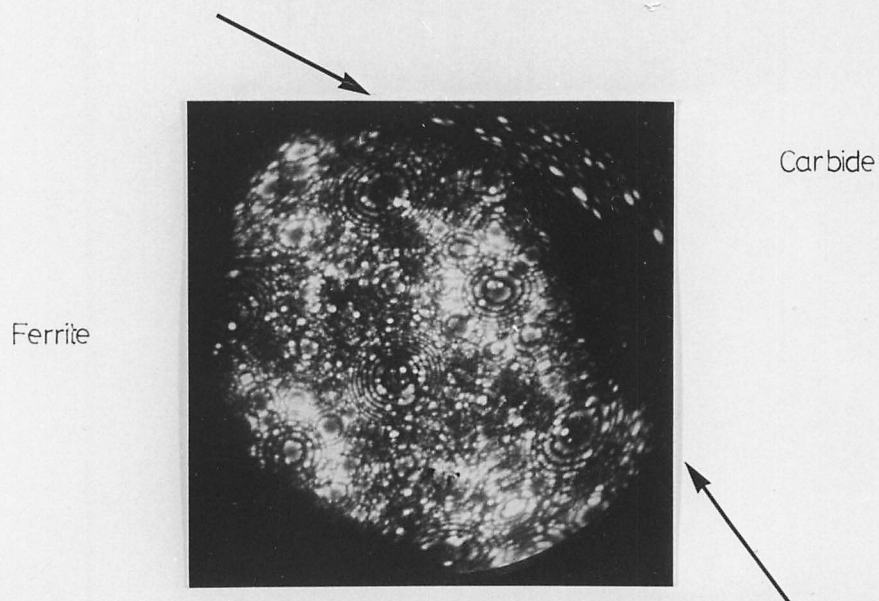


Fig.(3:25) FIM of A/R patented wire (Ne)

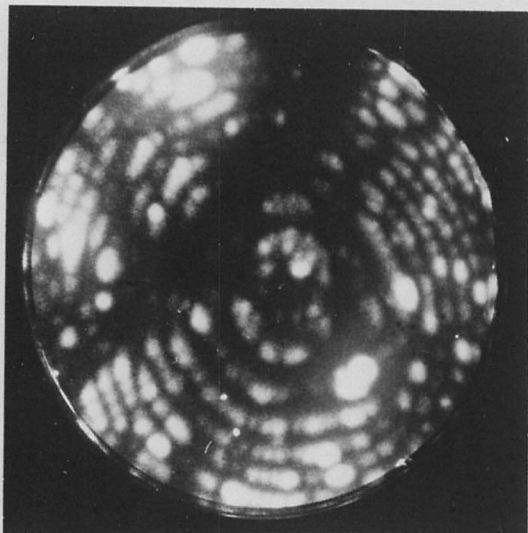


Fig. (3:26a) TEM of A/R patented wire (Ne)

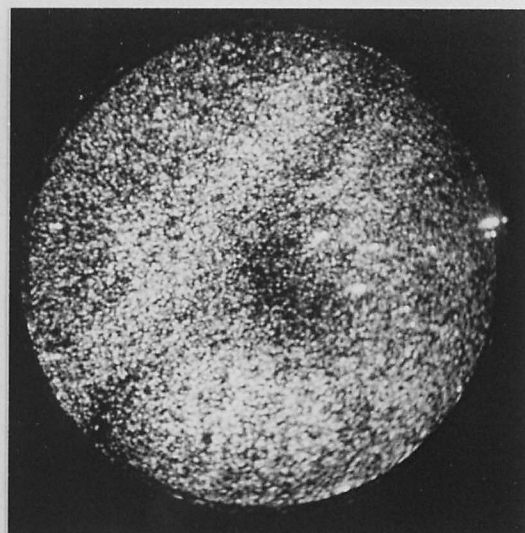


Fig. (3:26b) corresponding Fe^{2+} desorption image



Fig. (3:26c) corresponding C^+ desorption image



Fig. (3:26d) corresponding C^{2+} desorption image



Fig. (3:26e) corresponding $\text{N}^+ + \text{Si}^{2+}$ desorption image



Fig. (3:26f) corresponding $\text{S}^+ + \text{P}^+$ desorption image

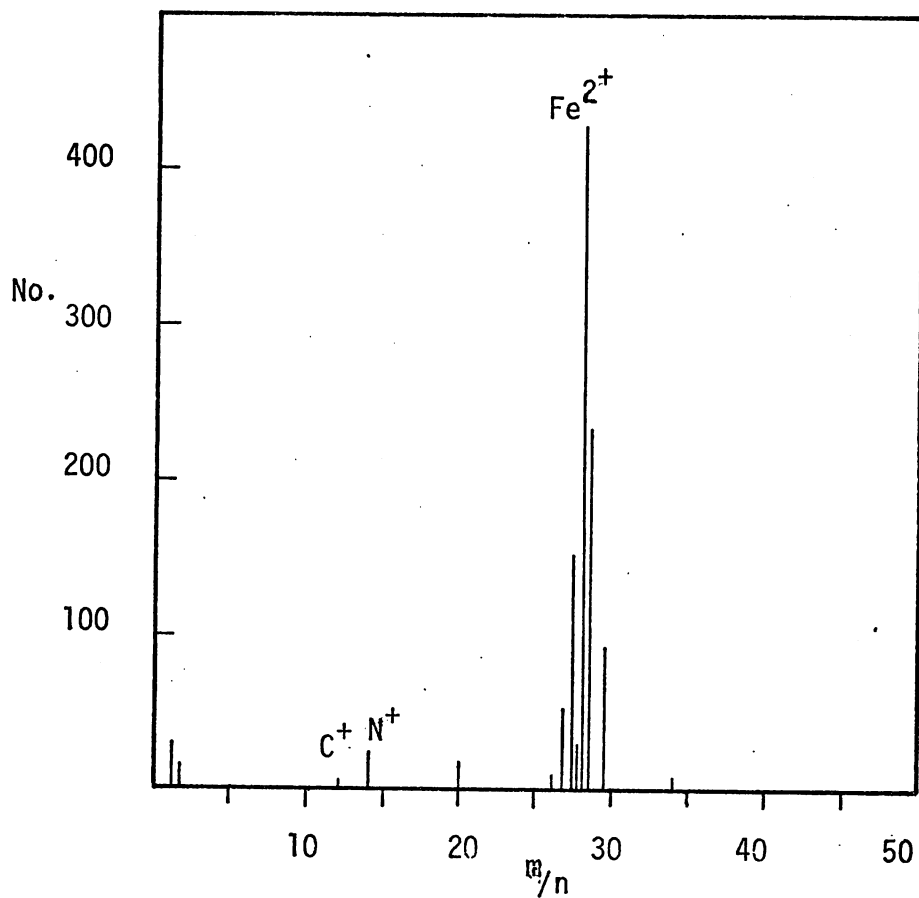


Fig. (3:27a) Spectra from ferrite cell interior (A/R patented steel wire, reduction $\approx 98\%$).

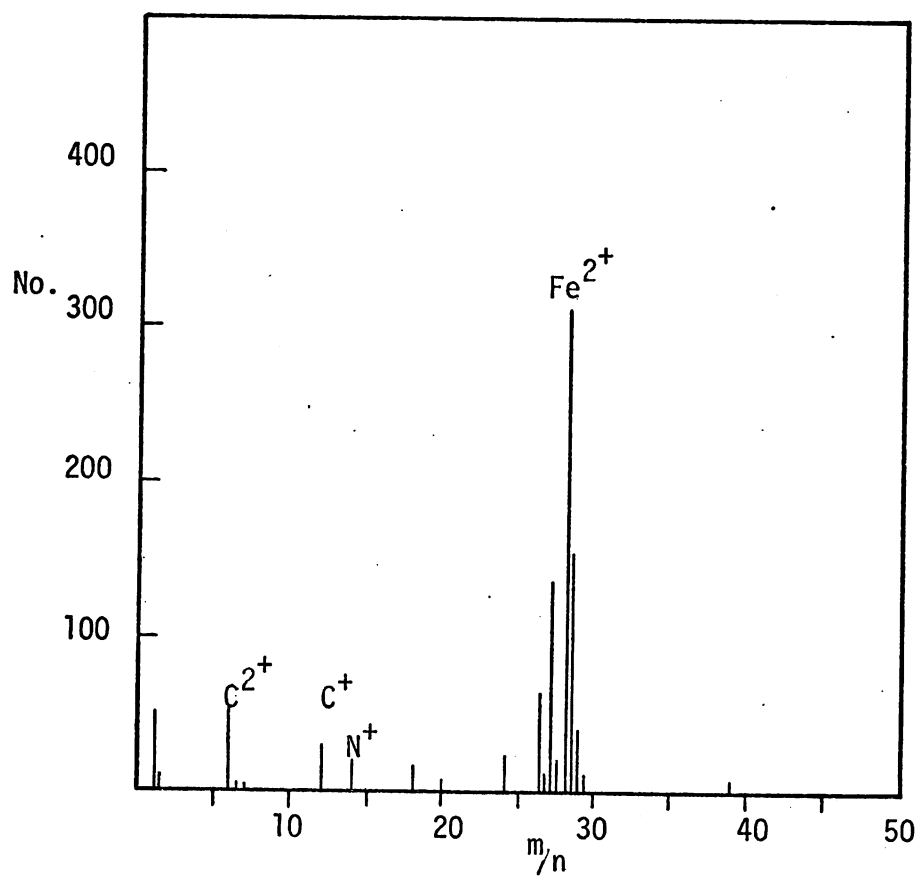


Fig. (3:27b) Spectra from cell wall (A/R patented steel wire, reduction $\approx 98\%$).

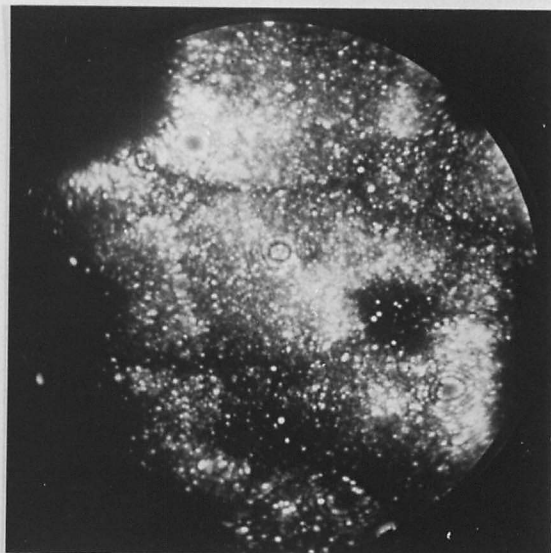


Fig.(3:28) FIM of A/R + LTHT "A"
patented wire (Ne)



Fig.(3:29) FIM of A/R + LTHT "A"
patented wire (Ne)

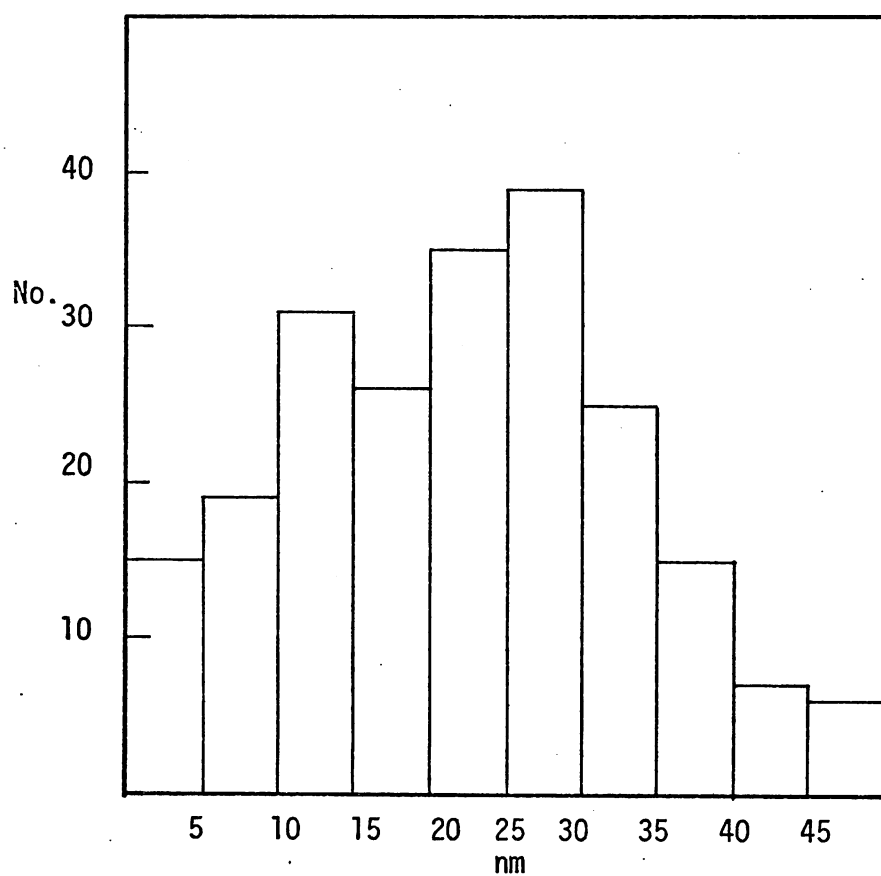


Fig. (3:30) Distribution of T/S ferrite cell sizes (A/R + LTHT "A" patented steel wire, reduction \approx 98%).



Fig. (3:31) FIM montage of A/R + LTHT "A"
patented wire (Ne)

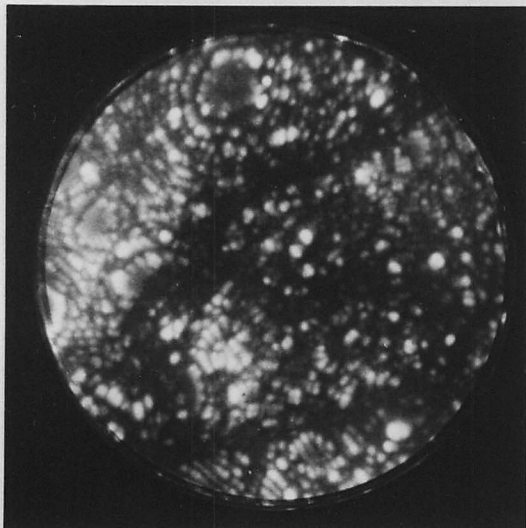


Fig.(3:32a) FIM of A/R + LTHT "A"
patented wire (Ne)

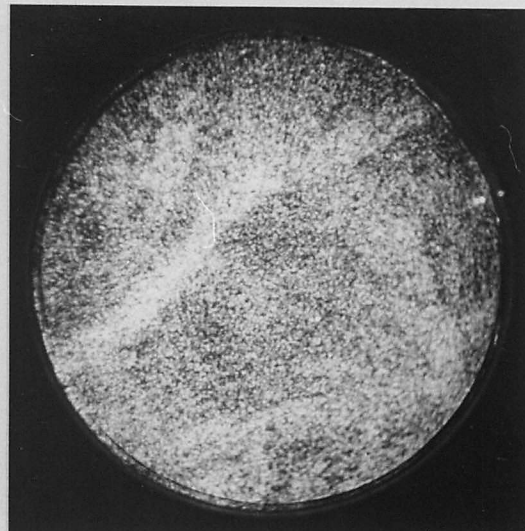


Fig.(3:32b) corresponding Fe²⁺ desorption image



Fig.(3:32c) corresponding C²⁺ desorption
image



Fig.(3:32d) corresponding N⁺ + Si²⁺ desorption
image

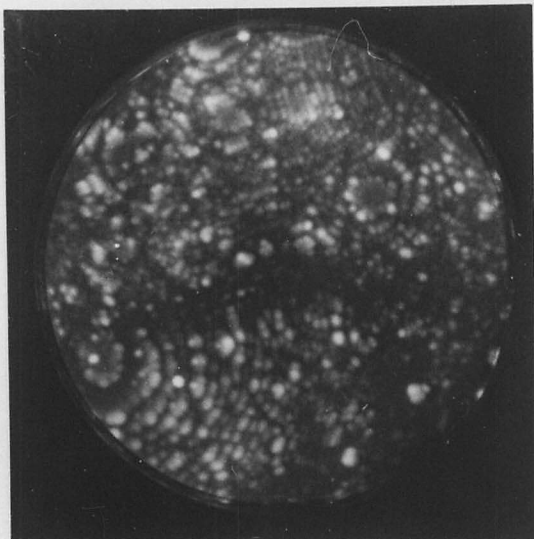


Fig. (3:33a) FIM of A/R + LTHT "A"
patented wire (Ne)

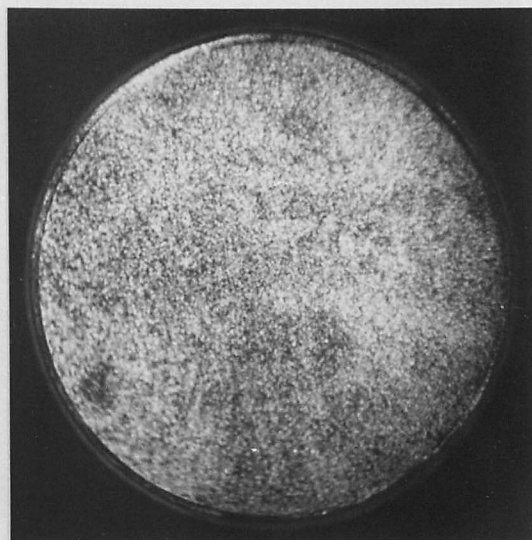


Fig. (3:33b) corresponding Fe²⁺ desorption
image

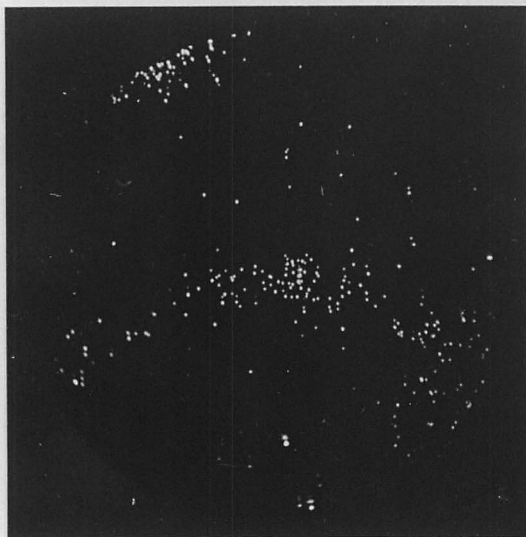


Fig. (3:33c) corresponding C²⁺ desorption
image

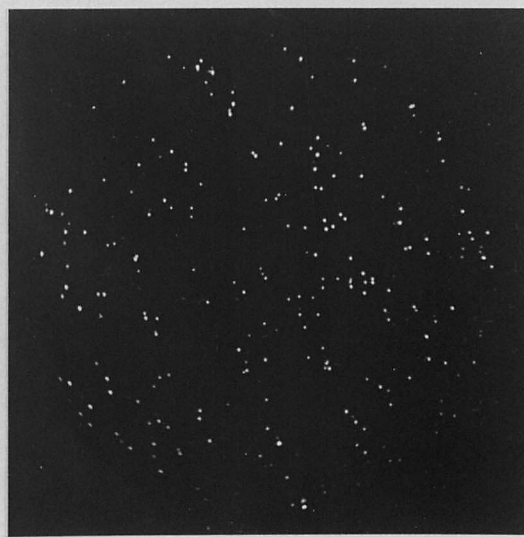


Fig. (3:33d) corresponding N⁺ + Si²⁺ desorption
image

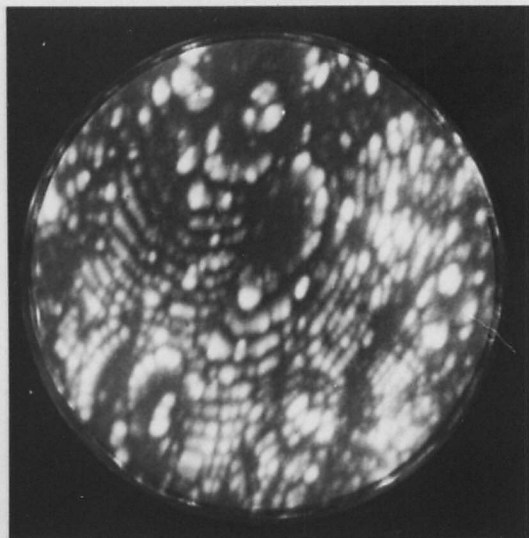


Fig. (3:34) FIM of A/R + LTHT "A"
patented wire
(Ne) (adjacent area to (3:35))

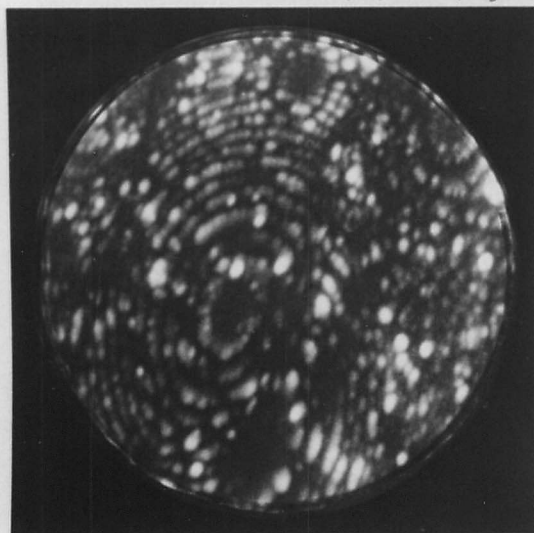


Fig. (3:35a) FIM of A/R + LTHT "A"
patented wire (Ne)

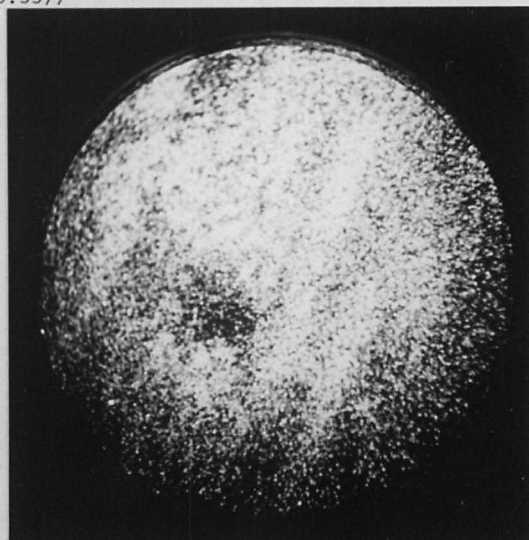


Fig. (3:35b) corresponding Fe^{2+} desorption
image



Fig. (3:35c) corresponding C^{2+} desorption
image



Fig. (3:35d) corresponding $\text{N}^+ + \text{Si}^{2+}$
desorption image

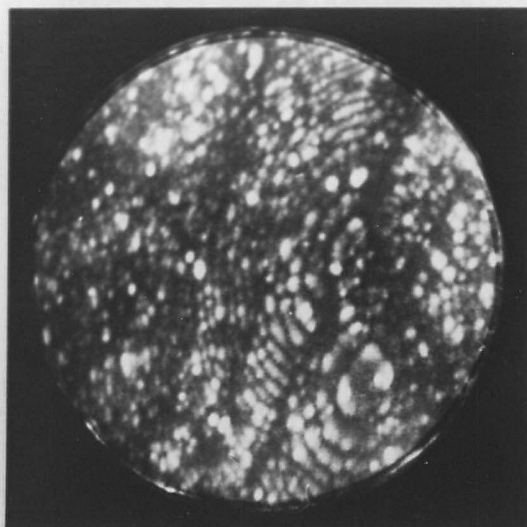


Fig.(3:36) FIM of A/R + LTHT "A"
 patented wire
 (Ne) (similar area to (3:37))

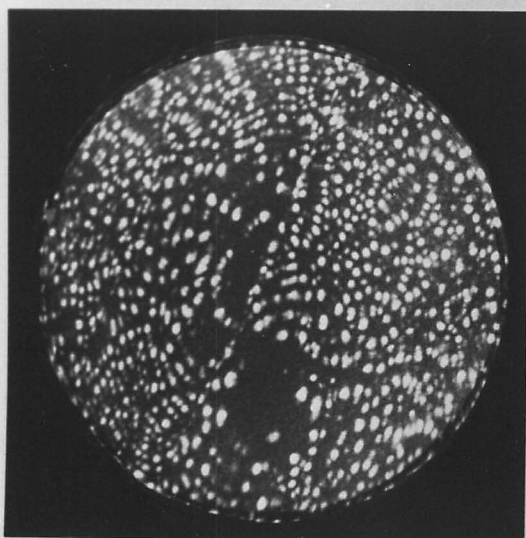


Fig.(3:37a) FIM of A/R + LTHT "A"
 patented wire
 (Ne) (helium cooling)

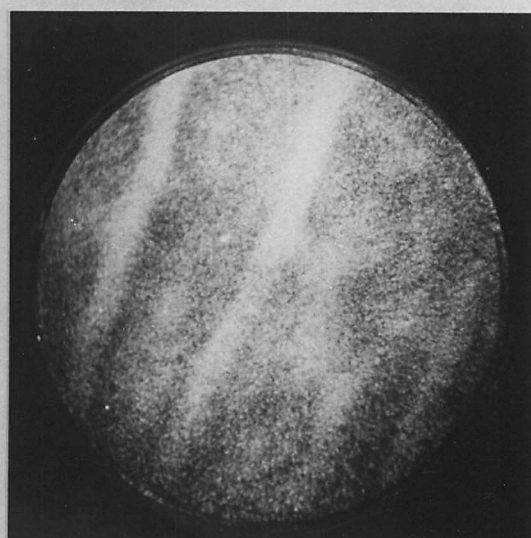


Fig.(3:37b) corresponding Fe^{2+} desorption
 image



Fig.(3:37c) corresponding C^{2+} desorption
 image



Fig.(3:37d) corresponding $\text{N}^+ + \text{Si}^{2+}$ desorption
 image

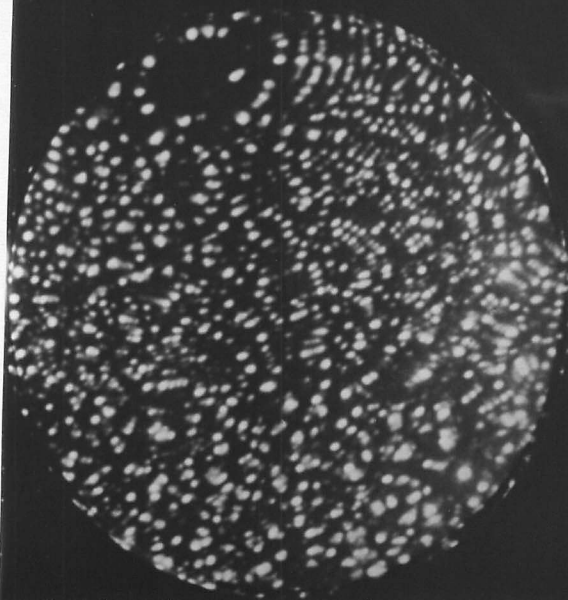


Fig.(3:38a)

FIM

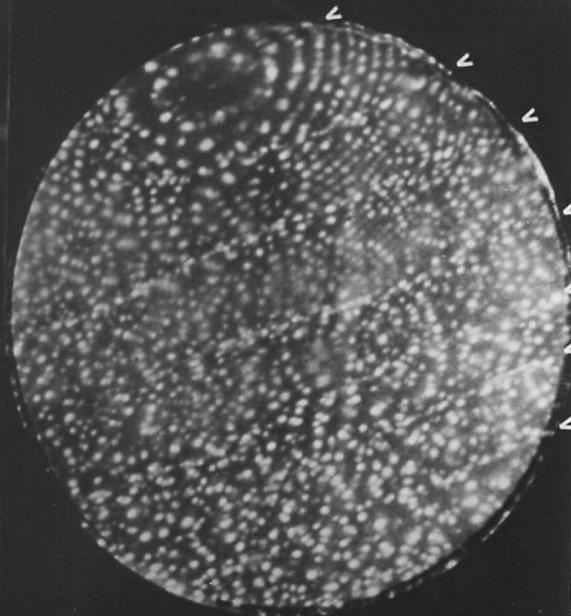


Fig.(3:38b)

FIM

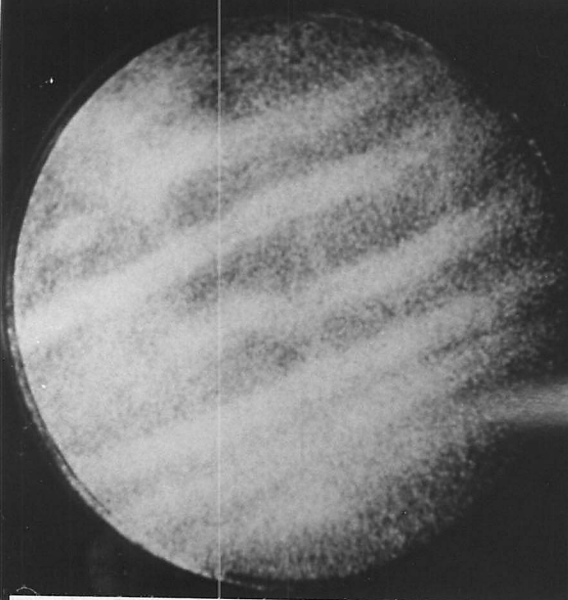


Fig.(3:38c)

Fe²⁺

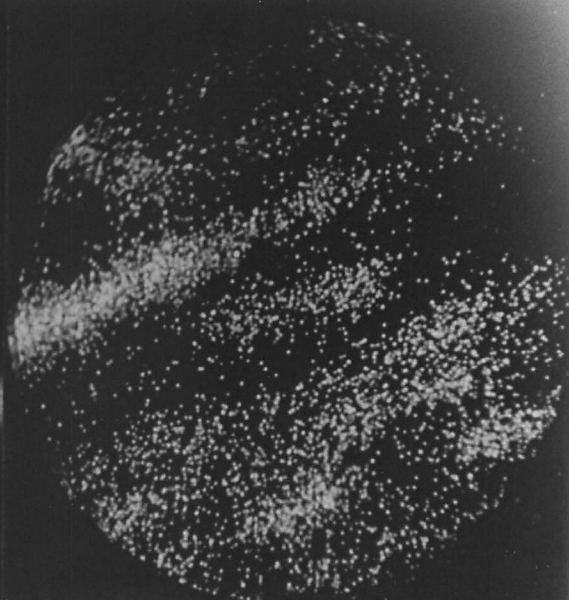


Fig.(3:38d)

C²⁺

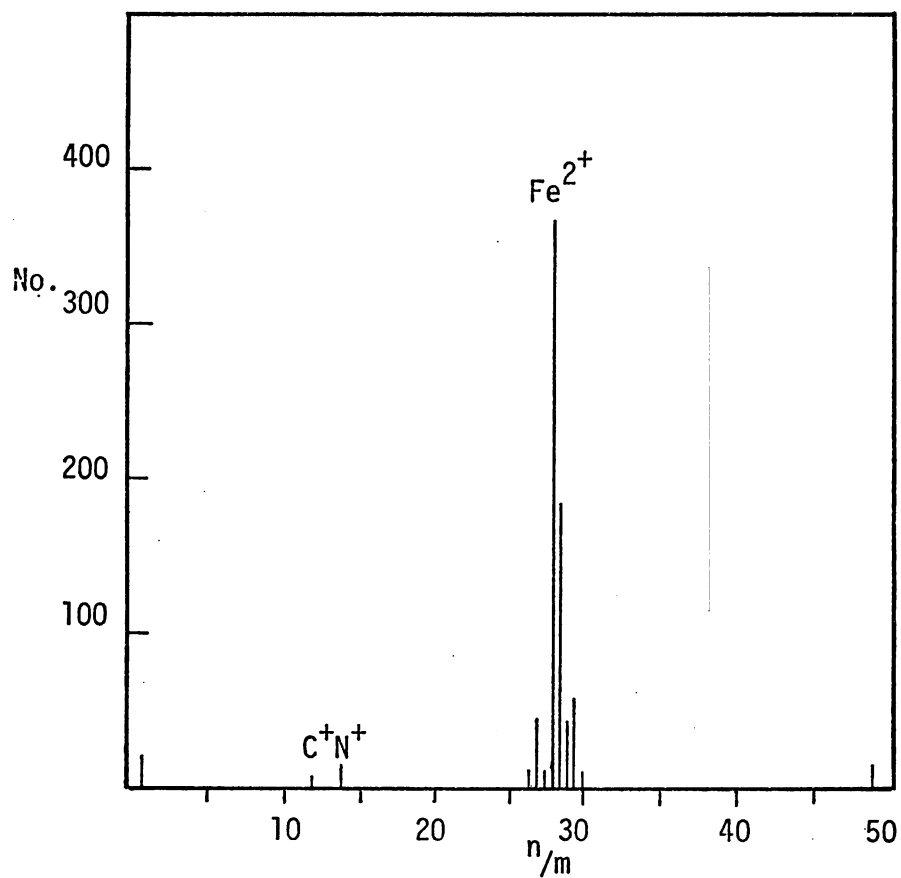


Fig. (3:39a) Spectra from ferrite cell interior (A/R + LTHT "A" patented steel wire, reduction $\approx 98\%$).

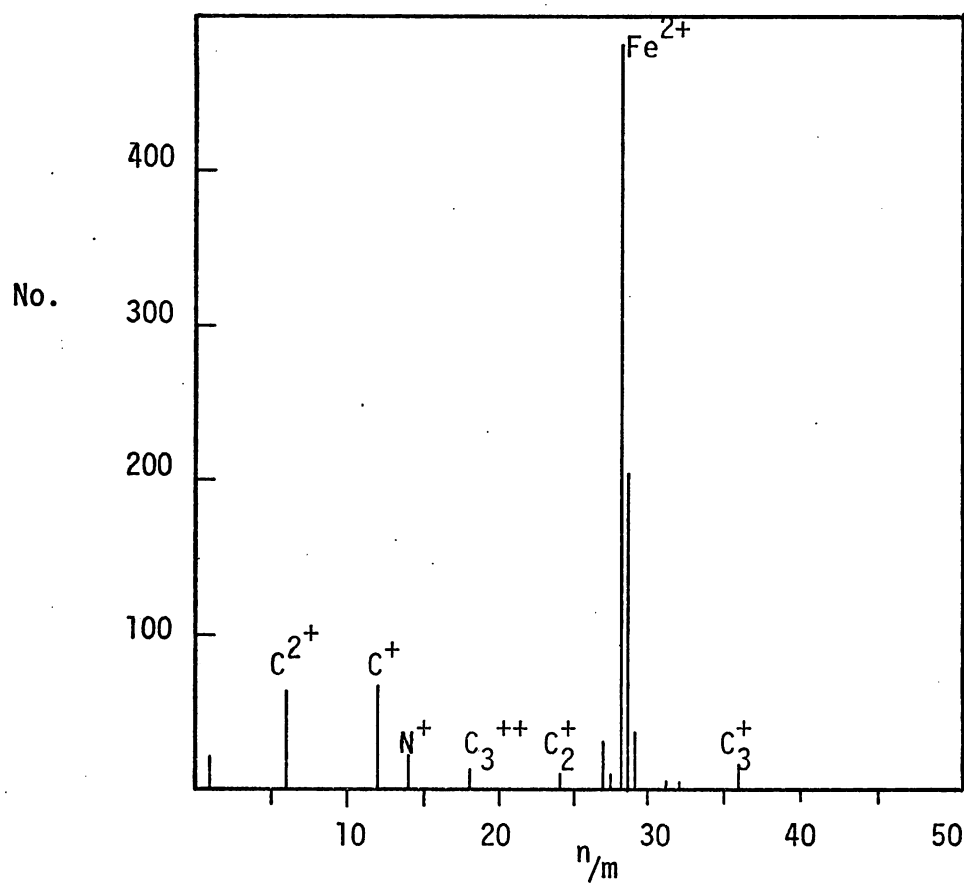


Fig. (3:39b) Spectra from cell wall (A/R + LTHT "A" patented steel wire, reduction $\approx 98\%$).

THE UNIVERSITY OF CHICAGO
LIBRARY

3

THE UNIVERSITY OF CHICAGO
LIBRARY

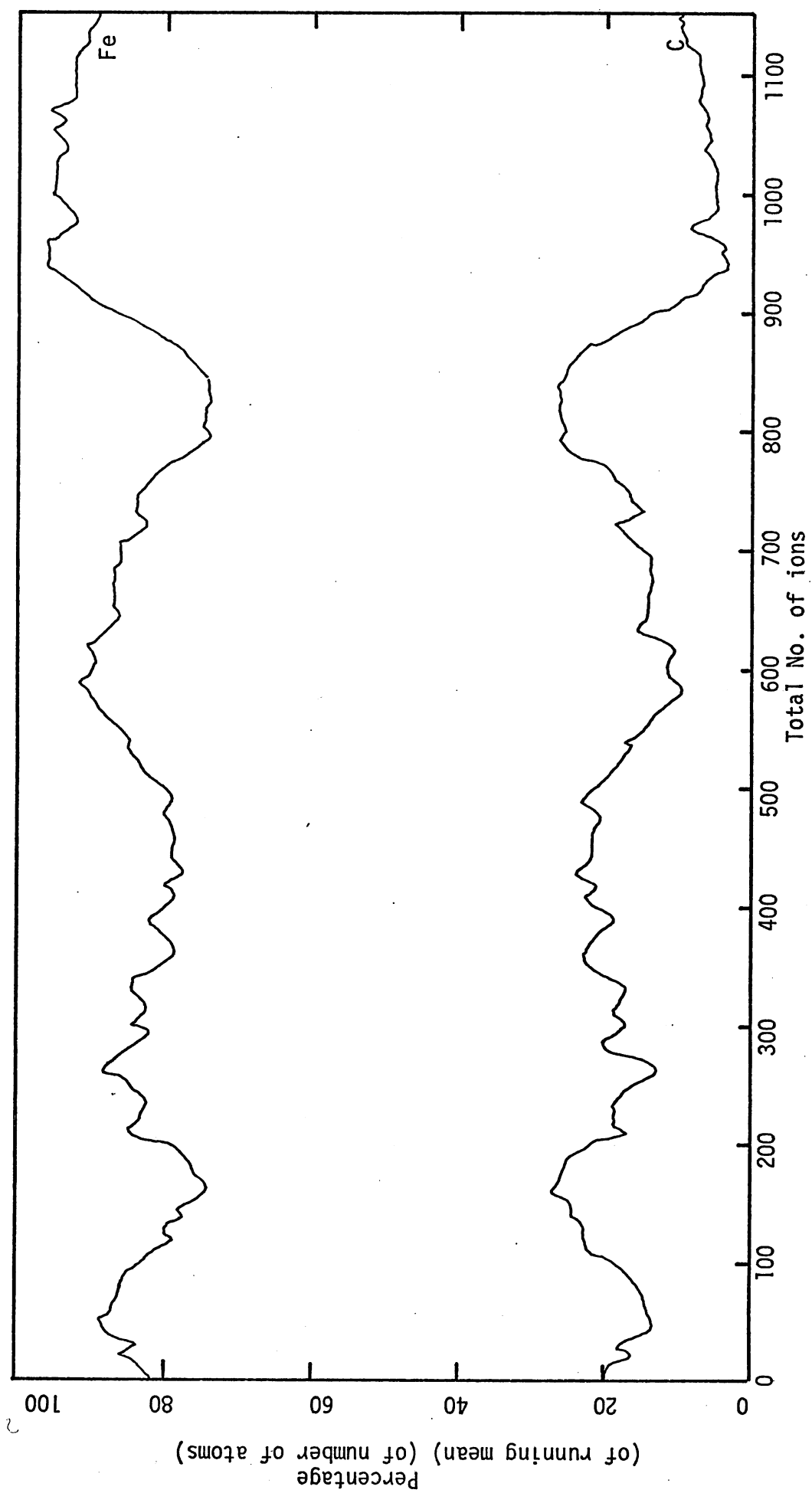


Fig. (3:40) Brenplot trace of Fe and C along an A/R + LTHT "A" patented steel wire specimen, reduction $\approx 98\%$.

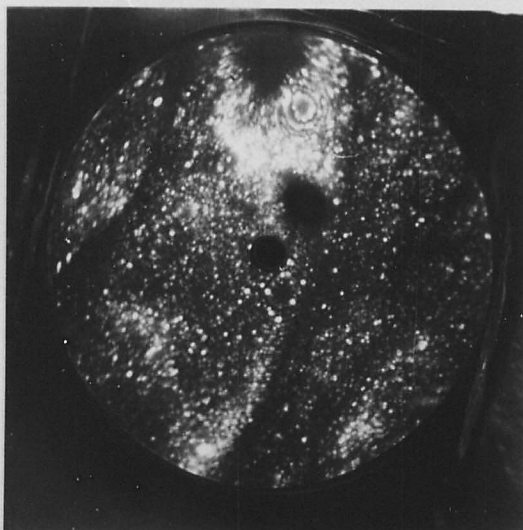


Fig. (3:41) FIM of A/R + LTHT "B"
patented wire (Ne)

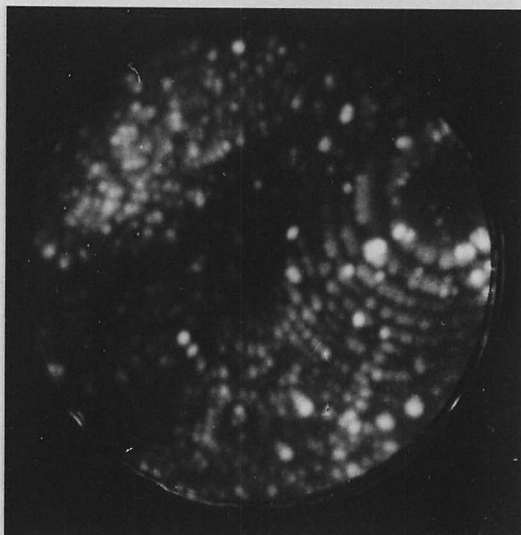


Fig. (3:42a) FIM of A/R + LTHT "B"
patented wire (Ne)

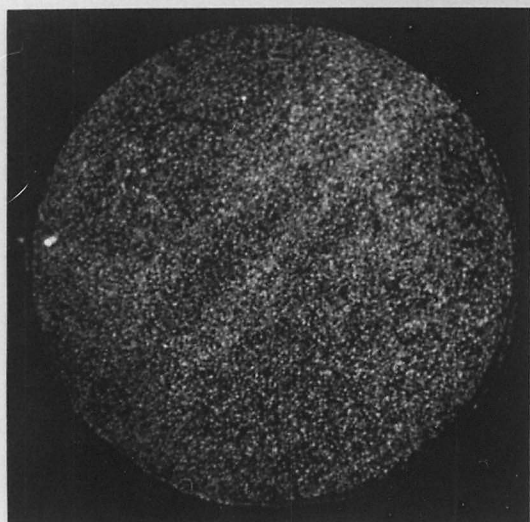


Fig. (3:42b) corresponding F_e^{2+} desorption
image



Fig. (3:42c) corresponding C^{2+} desorption
image

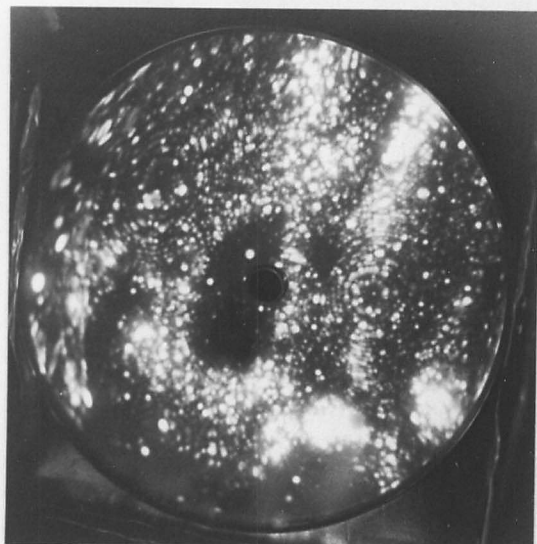


Fig. (3:43a) FIM of A/R + LTHT "B"
patented wire (Ne)

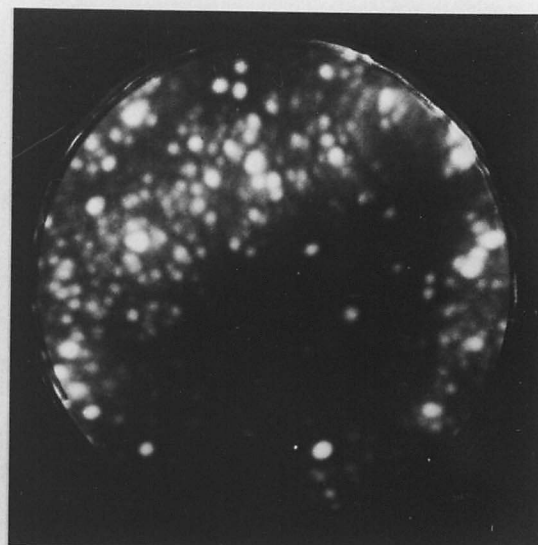


Fig. (3:43b) FIM of A/R + LTHT "B"
patented wire
(Ne) (central portion of (3:43a))

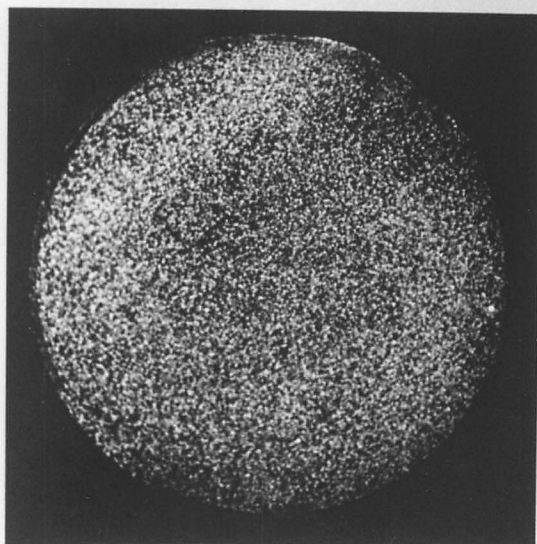


Fig. (3:43c) corresponding Fe^{2+} desorption
image



Fig. (3:43d) corresponding C^{2+} desorption
image

4. Stress Relaxation

4:1. Introduction

The phenomena of stress relaxation has been observed over a wide range of practical situations for many years. In its simplest concept it is recognised by a component which is at constant strain under a system of forces, normally below its yield point, showing a time-dependent plastic deformation giving a stress drop with time, the rate of change of stress decreasing with time. Schematically this can be represented as in fig. (4:1) where $t=0$ represents the initial loading time. When described in this simple manner the phenomenon can be seen to be similar to that of a viscoelastic solid. It can also be seen that, in many ways, it can be closely allied with the process of creep and it is therefore reasonable to expect that similar microstructural changes may occur in the two processes in the same material. For this reason selected comments on the low temperature creep behaviour of steels will be made later.

Stress relaxation along with related behaviour such as creep recovery, internal damping and the ³Ba_uchinger effect are often called "after-effects" of an application of an external load to a sample on its stress-strain characteristics (134). The basic causes of "after-effects" have been assumed to be the removal of variations in such parameters as the internal stress or temperature distributions in the sample by the application of external forces. Goldhoff (134) has given a review of this field, with special reference to creep recovery and he noted the classification of deformation types, table (4:1), and examined certain differences between the concepts of anelasticity and creep recovery.

Table (4:1)

<u>Type of</u>	<u>Time</u>	<u>Stress</u>	<u>Recoverability</u>
<u>deformation</u>	<u>dependence</u>	<u>proportionately</u>	
Elastic	independent	proportional	recoverable
Anelastic	dependent	proportional	recoverable in time
{ Creep recovery }			
{ Plastic }	dependent	not	not
		proportional	recoverable in time

Stress relaxation can be described, in essence, as a process of converting initial elastic deformation into non-recoverable strain by means of inelastic deformation proceeding under decreasing stress. This is not precisely the same as creep under decreasing stress because of the differing behaviour of the recoverable anelastic component in each case (134). Thus,

stress relaxation consists of the specimen being held at constant total strain, after initial loading, and the stress drop shown being due to both plastic and anelastic strain. As a consequence, for this reason alone, a rigorous analytical treatment of relaxation requires a detailed knowledge of the recovery characteristics of the material, which are rarely known. In a recent series of papers, Lloyd & McElroy (135, 136, 137) have attempted to relate these "after-effects". By drawing on their own, in addition to previous work they suggested that high temperature ($>0.3T_m$) stress relaxation and creep recovery were predominantly anelastic processes. In addition, they postulated that internal friction studies (the classic anelastic research technique) can be used to study the above 2 time dependent phenomena. Thus, the more usual strain equation of a stress relaxation test:

$$\epsilon_e + \epsilon_p = \text{const.} \quad 4:1$$

should be replaced by:

$$\epsilon_a + \epsilon_e + \epsilon_p = \text{const.} \quad 4:2$$

where: ϵ_e is the true elastic strain

ϵ_p is the true plastic strain

ϵ_a is the true anelastic strain

They concluded that, in general, the stress relaxation that had previously been observed by a large number of other workers was not, in fact, caused by plastic creep processes but by anelastic recoverable processes (e.g. the bowing of dislocations between pinning points) as in Zener (138) relaxation. Guieu & Pratt (139) have distinguished between these two basic types of relaxation ("plastic" or "anelastic"): the former being recognised as showing a logarithmic change in stress with time, the latter an exponential change. This view appears to be at variance with all other workers who assumed for their tests (whatever the material or test conditions):

$$\epsilon_a = 0 \quad 4:3$$

and this disagreement casts doubt on the validity of assuming that the applied stress can be considered as 2 parts (see later):

$$\sigma = \sigma_i + \sigma^* \quad 4:4$$

where: σ is the applied stress

σ_i is the internal stress

σ^* is the effective stress.

Recent work by Schneibel and Hazzledine (140), using superplastic Pb-Sn eutectic, has indicated that the anelastic component was significant.

Another comment by Lloyd & McElroy, was that the various types of stress relaxation test (see later) were not equivalent, as is normally assumed.

Stress relaxation has been identified as an engineering and metallurgical problem for a considerable period of time (see CPGS (1)) but has only provoked theoretical interest recently, first by Zener (138) and later by many other workers. The stress relaxation characteristics of many engineering materials have been identified in order that the service conditions (of stress, time and temperature) under which an acceptable level of deformation can be expected, are identifiable. Below are listed some of the applications where stress relaxation can be significant.

a) Bolting.

In many situations where bolts are employed, e.g. generator turbine casings, significant relaxation occurs during service after the initial torquing (which is usually carried out to 0.15% strain(141)). It results in the reduction of the holding characteristics, and a re-torquing is necessary: the re-torquing can be repeated a number of times before failure occurs.

b) Wire for pre- or post-stressed concrete.

Normally a high carbon steel wire (such as patented wire) is used in this situation. It is usual (141) to stress the wires to approximately 70% of their tensile strength initially, and this is found to fall to about 60% within a short period of use, partly being due to relaxation in the wire.

c) Welded fabrications.

In this situation, unlike the 2 previous ones, a material which relaxes is an advantage, allowing the reduction of post-welding residual stresses. Such relaxation is aided by a stress relieving heat treatment and anisothermal stress relaxation tests have been performed to evaluate materials for this purpose (this is in contrast to the majority of tests which are isothermal). This general technique of relaxation to remove fabrication stresses is also employed in other fields such as forging, shrink fitting and quenching and tempering (see section 4:3.12).

d) Spring materials.

Stress relaxation has always been of importance in the case of springs of all types, both for static and dynamic applications. The result of the failure is a gradual reduction of the free length (for a helical, compression spring, say) with use. Comparative data for the relaxation behaviour of a wide range of spring materials has been collected (see CPGS 1) and this has enabled a maximum service temperature for each to be defined below which the set-down is regarded as being insignificant. Recent work on spring

materials is reviewed in section (4:2).

From the above comments, it is clear that there has been a division of research in stress relaxation. The first view is from a material standpoint. Empirical work has given information on the behaviour of a wide range of industrial materials allowing a suitable choice to be made for the prevailing service conditions: little attempt has been made to understand the fundamental processes involved beyond assuming their similarity with creep processes under similar conditions. The second approach is that based on a more theoretical aspects, investigating the dislocation processes involved during relaxation and using experimental data from tests with pure materials (often single crystals) to evaluate dislocation dynamics parameters. This work, reviewed in section (4:3), has proved of great value in the understanding of flow processes. The relationships between these materials and industrial alloys is, however, necessarily tenuous and direct comparisons with practical situations are difficult.

4:2. Stress Relaxation of commercial spring wires

The original work on these wires was carried out in the 1920's and 1930's, particularly in the USA (see CPGS (1)). The majority of the research reports and reviews from this country have been produced by the Spring Research and Manufacturers' Association (SRAMA), a summary of the information relevant to this work follows.

The majority of work has considered stress relaxation behaviour along with other important spring qualities; the elastic limit and UTS, the ductility and the fatigue resistance. A comprehensive review of the creep and relaxation research undertaken prior to 1959 has been compiled by Graves (142). A wide range of materials were covered and particular attention was given to the maximum operating temperatures for the alloys considered (table 4:2) as well as comparative relaxation information at various temperatures.

<u>Material</u>	<u>Table 4:2</u>	
	<u>Maximum Operating Temperature °C</u>	
70/30 brass	65	
Phosphor bronze	100	
Hard drawn wire	120	
Music wire	120	
Oil tempered wire	175	
Chromium-vanadium wire	220	
Monel	220	
"K" Monel	230	
Chromium-silicon wire	245	
Duranickel	260	

/Continued

Continued

<u>Material</u>	<u>Maximum Operating Temperature °C</u>
18/8 Stainless steel	290
Inconel	370
Inconel "X"	455

Maximum operational temperatures of various alloys (after Graves 142).

Graves (143) considered in detail the relative relaxation behaviour of BS 1408C and BS 1408D patented wire and BS 2803 oil tempered wire. Relaxation tests were carried out, as in all subsequent work by SRAMA, using helical coil springs (to enhance the effects of relaxation) compressed on Monel bolts. The behaviours at various test temperatures and stresses were obtained and it was noted that corrections to the data due to thermal expansion and creep in the test rig were insignificant in the regime investigated (up to 400°C). It was concluded that the oil tempered springs were slightly superior to those of patented wire (the latter being given a post-coiling low temperature heat treatment, LTHT, of 350°C for 30 minutes), an example of the results are reproduced, fig.(4:2). This work was extended by Graves (144) to further materials: he suggested an order of relaxation resistance the most superior being high speed and stainless steels, followed by the low alloy spring steels, carbon steel and Cu/Be. He noted that hot setting (at 50°C) considerably reduced relaxation in all materials and was correct in his assertion that creep data cannot be generated from relaxation information. He showed that there existed an initial period of rapid relaxation, in the case of carbon and low alloy steel springs 72 hours, while for stainless steels 168 hours approximately. It appeared, certainly for the Cr/Si steel springs, that increasing the LTHT from 300°C to 400°C improved the relaxation behaviour at 200°C significantly. (However, such a LTHT would degrade the tensile properties of patented wire, Section (2:3.4.4.)). Again, with particular reference to the Cr/Si steel, a LTHT of 350°C for only 30 minutes improved the relaxation performance below approximately 200°C. Other, higher temperature materials have been investigated in a similar manner by Graves and Key (145). Gray and Graves (146) performed tests on the mechanical properties of 1408M patented wire (in range 2 of the BS specification, as has been used in the present investigation). They showed that this grade of patented wire was superior in its tensile properties, fatigue and relaxation resistance to the

1408C and 1408D materials. They also noted that the optimum LTHT for relaxation resistance was in the range 175°C to 200°C for 30 minutes, at which temperature a ductility trough was also apparent: fig.(4:3) shows the variation in tensile properties with LTHT and fig.(4:4) shows the relaxation behaviour. As can be seen from the relaxation data the springs that were shot peened (to improve the fatigue performance) were significantly inferior in this respect. Investigations have been carried out by SRAMA on carbon steel wire supplied by Bridon Wire Ltd. to internal specifications UHT2 and UHT3 and these show significant improvements in properties over those of BS 1408M R2. Work by Bird (147) and Gray and Graves (148) on UHT2 and UHT3 has shown that the best tensile and relaxation properties can be achieved by a LTHT of approximately 200°C for 30 minutes, as for BS 1408C/D steels: again shot peening considerably increased relaxation under given test conditions.

Gray (149) has distinguished between static and dynamic relaxation in 3 spring steels. He found that the former is always greater, by a factor of 4 (increasing with decreasing temperature) for the carbon steels. Southward (150) showed that with BS 1408 R3 material the effect of prestressing the test springs on the relaxation properties was negligible.

Bird (151) reported on the effects of LTHT on the properties of BS 5216 : HD3 carbon steel springs. The tensile properties were optimised by a LTHT in the range 175°C to 200°C for 30 minutes while the room temperature relaxation resistance was at its highest value at approximately 350°C for 30 minutes. Shot peening was again shown to be detrimental to the relaxation properties and it was also noted that the "wind-up" of the test springs increased with LTHT temperature unlike the "set-down", which was approximately constant.

4:3. Analytical stress relaxation testing

4:3.1. Introduction

✓ The usefulness of stress relaxation as an analytical tool in the study of fundamental material properties has been explained in section (4:1) The review and analysis which follows of previous work in this extensive field is restricted to relaxation due to plastic flow processes, i.e. irreversible deformation. Most workers who have investigated relaxation of spring materials have regarded this as the main mode of failure in spring materials, rather than anelastic relaxation (a reversible process). It is normal when undertaking relaxation tests to simplify the situation by maintaining as simple a stress state as possible. To enable this,

virtually all tests have been accomplished in uniaxial tension: the few cases where more complex stress states were employed are considered in sections (4:3.11.2), (4:3.11.4).

A number of stress relaxation techniques have been evolved to suit the investigation being undertaken, although there has been some doubt expressed concerning the equivalence of tests (152), (153), (154), (155). The majority of relaxation tests have been undertaken under isothermal conditions for simplicity, as in the present work: a brief review of an isothermal relaxation testing is given in section (4:3.12).

4:3.2. Uses of analytical stress relaxation testing

The first use to which the stress relaxation test was put was in the determination of activation energies and volumes in plastic deformation. The various materials investigated, the initial ones being Cu and α -brass by Feltham, (156) to (159), are fully summarised in section (4:3.11.2).

Subsequent to this early work, the technique has been used by several investigators to gain information on the parameters controlling the dynamics of dislocation motion and to quantify the thermal and athermal components of the flow stress, for example Hull and Noble, (160), Li, (161), and Lloyd and Embury, (162). Again, a summary of this work is given in section (4:3.6).

The work of Guin and Pratt, (139), describes the use of stress relaxation experiments to give reliable measurements of strain rate sensitivity. Noble and Hull, (163), and others have shown that the stress dependence of dislocation velocity can be readily obtained from stress relaxation tests: results correlate well with those from more traditional methods, e.g. Stein and Low, (164).

Hart has completed thorough work on stress relaxation and other related subjects. In his papers, (165) to (168), he has developed the concept of an equation of state for plastic flow along with the allied concepts of hardness states and curves. It is essential that in the measurement of the parameters involved in the hardness state, as little plastic deformation as possible takes place. The stress relaxation test provides this, and given suitable techniques and instrumentation, can be used to great effect. Hart and Solomon, (167), Lee and Hart (168), and Yamada and Che-Yu Li, (169,170) have collected data over a wide range of strain rates to verify the existence of such an equation of state.

The ability of the test to investigate dislocation dynamics involved in deformation, without significantly changing the structure, has been used in creep studies by a number of workers. Oikawa et al, (171), have recently

concluded work on creep in α -Fe and a Fe-Mo alloy which is typical of the methods employed. A particularly complete review of this field along with useful work on the recovery creep of γ -stainless steels, is that by Williams and McLaughlin, (172).

It is clear from the above brief summary, that almost all work has been aimed at the use of stress relaxation in the examination of plastic flow processes of various types. In this context it has already shown itself to be a very powerful technique. In recent years, work on stress relaxation as a source of dimensional instability (as in the present work) has not received much attention. Clearly, what is at present required is a correlation of the results from the considerable effort carried out on the structural and theoretical side to more practical problems, and it is to this object that the present work has been undertaken.

4:3.3. Theoretical considerations

4:3.3.1. Introduction

The methods of analysing stress relaxation data can be divided into 4 basic groups. Although each is often associated with a limited number of workers, the present survey has shown that each has its origins in a wide spectrum of earlier work. For convenience, however, the practice of recent literature in ascribing each after a few workers will be followed.

- a) The largely empirical work due to Feltham in particular, which detected a linear relationship at long times between stress drop and $\log t$.
- b) The analysis due to Li and others based on the assumption that the mean dislocation velocity is proportional to the thermal component of the applied stress to the power m^* .
- c) Sleeswyk has considered an analysis which assumes both:

$$\begin{aligned} \left. \frac{\partial \sigma}{\partial \epsilon_p} \right|_{\dot{\epsilon}_p} &= f(\epsilon_p) \\ &= \text{constant} \\ \text{and } \left. \frac{\partial \sigma}{\partial \ln \dot{\epsilon}_p} \right|_{\epsilon_p} &= \text{constant} \end{aligned}$$

- d) An analysis based on the widely used concept of thermal activation over an energy barrier, has been applied by Guin & Pratt in particular.

There follows selected comments on aspects of dislocation theory relevant to the analyses which are presented later.

4:3.3.2. Dislocation dynamics

Li, (161), has given a concise account of the relationship between dislocation velocity, effective shear stress, temperature and pressure. He also considered the various indirect methods of determining velocity/stress characteristics of dislocations: to do this he relied on previous work,

particularly on that of Johnson and Gilman, (173), Orowan, (174), Gibbs, (175), Gilman, (176), (177), (178), Gilman and Johnson, (179), and Gillis and Gilman, (180), along with his own earlier work, Li, (181), (182).

After Orowan, (174):

$$\dot{\epsilon}_p = w_g |b| \rho_m \bar{v} \quad 4:6$$

where: w_g is a geometric factor,
 b is the burgers vector,
 ρ_m the mobile dislocation density,
 \bar{v} the mean mobile dislocation velocity.

Lloyd and McElroy (136) and McLean (183) have explained that the value of ρ_m is not, in fact, a simple average density. It is necessary to consider segments of dislocations which will move under a particular applied stress. Thus, one should consider a distribution, fig. (4:5), of the number of mobile segments N with stress σ . If the minimum flow stress for any segment is σ_{min} , then:

$$\rho_m = \int_{\sigma_{min}}^{\sigma} l \cdot f(N) dN \quad 4:7$$

where l is the segment length. Normally, however, for stress relaxation situations it is assumed that ρ_m is constant, all segments having the same flow stress.

After Johnson and Gilman, (173) the mean dislocation velocity is given by:

$$\bar{v} = B \tau^{*m*} \quad 4:8$$

where: B is the mobility,
 τ^* is the effective shear stress,
 m^* is a constant.

Alternatively, for high stress applications, after Gilman,

$$\bar{v} = v_c \exp - \left[\frac{\tau'}{\tau^*} \right] \quad 4:9$$

where: v_c is a constant,

$$\text{and } \tau' = m^* \tau^* \quad 4:10$$

Li lists the many applications to which this model has been applied, but points out that the understanding of the underlying processes is not well developed. In addition the variations which exist of the above model are difficult to compare due to the large number of empirical parameters which appear in the dynamic equations.

4:3.3.3. A phenomenological approach

Li, (161), also developed a phenomenological approach to supplement the above model from the basic relationship:

$$d(\ln \bar{v}) = \left. \frac{\partial(\ln \bar{v})}{\partial \tau^*} \right|_{T, Pr} d\tau^* + \left. \frac{\partial(\ln \bar{v})}{\partial T} \right|_{\tau^*, Pr} dT + \left. \frac{\partial(\ln \bar{v})}{\partial Pr} \right|_{\tau^*, T} dPr \quad 4:11$$

From this were derived Maxwell relationships,

$$\text{e.g.} \quad \left. \frac{\partial m^*}{\partial T} \right|_{\tau^*, Pr} = \frac{\tau^*}{kT^2} \cdot \left. \frac{\partial \Delta H}{\partial \tau^*} \right|_{T, Pr} \quad \text{etc.} \quad 4:12$$

Li, (161), considered the velocity-stress relationship for dislocations. The value of the exponent m^* was compared with the exponent m which had been obtained from strain rate cycling tests (see Stein and Low, (164)). Guard (184) explained the difference between m and m^* (the latter obtained from etch pit studies) by a change in the value of ρ_m in the cyclic tests, thus:

$$m = \frac{\partial(\ln \dot{\epsilon}_p)}{\partial(\ln \sigma)} \quad 4:13$$

$$= m^* + \frac{\partial(\ln \rho_m)}{\partial(\ln \sigma)} \quad 4:14$$

Doubts arose to this reasoning, due to the necessarily large changes required in ρ_m . Li and Michalak, (185), and others have overcome this problem by the postulation of a mean internal stress being present. They assumed, in addition, that this internal stress, σ_i , and ρ_m remain constant during the relaxation test.

Thus:

$$\sigma_i = \sigma - \sigma^* \quad 4:15$$

where: σ is the true applied stress,

σ^* is the effective or thermal component of stress

$$As, m = \frac{\partial (\ln \dot{\epsilon})}{\partial (\ln \sigma)} \quad 4:13$$

$$= \frac{\partial (\ln \bar{v})}{\partial \sigma^*} \quad 4:17$$

$$= \left(\frac{\sigma}{\sigma^*} \right) m^* \quad 4:18$$

$$, \sigma_i = \frac{\sigma}{\sigma - \sigma^*} \quad 4:15$$

$$= \sigma \frac{(m + m^*)}{m} \quad 4:19$$

Continuing this reasoning for the stress relaxation tests and following the nomenclature of Noble and Hull, (163), and Hull and Noble, (160), and others: assuming constancy of ρ_m , m^* and the combined modulus of the specimen and machine (see section (4:3.9)), then plotting $\log \sigma$ vs. $\log t$, at long times the slope, s , is such that:

$$s = \frac{1}{1 - m^*} \quad 4:20$$

$$\text{or } m^* = \frac{s - 1}{s} \quad 4:21$$

Alternatively, if s varies with t , then the curvature, s' , of the plot at time t is given by:

$$s' = \frac{d (\log s)}{d (\log t)} \quad 4:22$$

$$m^* = \frac{(s + s' - 1)}{s} \quad 4:23$$

Gupta and Li, (186), (187), further developed the possible plots, along with the theory behind them, that can be used in stress relaxation tests to derive dislocation parameters. Further details on these techniques are given in the following section.

4:3.4. Basic theory and practice of stress relaxation tests

4:3.4.1. Introduction

Details of specific work and theory are given in following sections, here a brief outline of the concepts involved in the phenomenon is attempted: it is drawn from work by a number of authors over the last 15 years.

4:3.4.2. Initial comments on the analysis of the test

One of the most complete analyses of the relaxation test has been given by Guieu and Pratt, (139) who consider that the specimen is deformed in a hard tensile testing machine (for the sake of simplicity)

at a crosshead rate of \dot{y} . At a point on the true stress strain curve σ'_0 , ϵ'_0 the plastic strain rate, $\dot{\epsilon}'_p = \dot{\epsilon}'_0$. If at this point, taken as $t=0$, the crosshead is instantaneously stopped, i.e.

$$\text{Lt}_{(t \rightarrow 0)} \dot{y} \rightarrow 0 \quad 4:24$$

It is found that the specimen continues to deform under decreasing stress and decreasing strain rate. From the load/time record a relaxation curve of the form: $\sigma = \sigma(t)$, can be obtained. This technique is schematically shown in fig. (4:6).

Throughout the relaxation process, the relationship between the stress and strain is determined by the machine characteristics in addition to the geometry and characteristics of the specimen. In hard (position controlled) loading, \dot{y} was assumed to be matched by the elastic and plastic deformation rate of the specimen and the elastic extension of the machine, thus:

$$\dot{y} = \dot{l}_p + \dot{l}_e + \dot{z} \quad 4:25$$

where: \dot{l}_p is the nominal plastic strain rate of the specimen,
 \dot{l}_e is the elastic strain rate of the specimen,
 \dot{z} is the elastic strain rate of the machine.

At $t = 0$, $\dot{y} \rightarrow 0$ (assumed instantaneous),

$$-\dot{z} = \dot{l}_p + \dot{l}_e \quad 4:26$$

If z is given by:

$$S = \frac{dP}{dz} \quad 4:27$$

where: S is the machine stiffness,
 P the applied load.

and converting to strain rates, the deformation for $t > 0$ can be written:

$$\dot{\epsilon}_p + \dot{\epsilon}_e = - \frac{a_0}{l_0 S} \dot{\sigma} \quad 4:28$$

where: $\dot{\epsilon}_p$ is the true specimen plastic strain rate,
 $\dot{\epsilon}_e$ is the specimen elastic strain rate,
 a_0 the specimen cross-sectional area at $t = 0$,
 l_0 the specimen gauge length at $t = 0$

Expressing $\dot{\epsilon}_e$ in terms of the material elastic modulus E,

$$\dot{\epsilon}_e = \frac{\dot{\sigma}}{E} \quad 4:29$$

$$\dot{\epsilon}_p = -M' \dot{\sigma} \quad 4:30$$

where: the combined modulus of the system,

$$M' = \frac{a_o}{l_o S} + \frac{1}{E} \quad 4:31$$

This modulus is assumed constant in the test, on the basis that the plastic strain experienced during the relaxation is small compared with l_o .

The above argument can be considered in terms of shear stresses and strains, in which case the relation can be written:

$$\dot{\gamma}_{pl} = -M\dot{\tau} \quad 4:32$$

where: $\dot{\gamma}_{pl}$ is the shear strain rate,
 $\dot{\tau}$ is the shear stress rate,

and $M = \alpha_3 M'$, α_3 being a numerical constant, considered by Guiu and Pratt, (139) Clough and Demer, (188) and others.

Although the above theory is cast using true stress and strain values, the consideration of the relationships with the practical work where nominal values are measured has been generally overlooked: it appears that those who have briefly considered the problem, e.g. Guiu and Pratt, (139) think the small plastic strains involved make it trivial.

One of the basic assumptions of almost all relaxation work (along with closely related creep work) is that the applied stress, σ can be regarded as the sum of two components, thus:

$$\sigma = \sigma^* + \sigma_i \quad \text{or alternatively} \quad 4:15$$

$$\tau = \tau^* + \tau_i \quad 4:34$$

τ^* is the thermal component or effective stress and describes impedance to flow which can be overcome by thermally activated dislocation motion.

τ_i is the athermal component or long range internal stress, and describes the internal stress fields which are of either a magnitude or extent that dislocation motion is not possible by thermal activation. It is not clear how this component can be correlated with the idea of internal stresses such as residual stresses (see CPGS, A:II).

Further work is required to enable a successful comparison to be made.

Most early workers who considered the problem, regarded τ_i as more or less constant during the relaxation. Guieu and Pratt, (139) considered any change in τ_i could be expressed as:

$$d\tau_i = \theta' d\gamma_{pl} \quad 4:35$$

where: θ' is a work hardening coefficient.

Thus from the above reasoning:

$$d\tau_i = -\theta' M dt \quad 4:36$$

In a hard machine M is of the order of $10^{-4} \text{ mm}^2 \text{ kg}^{-2}$, (139), and so the assumption appeared to the early workers to be justified. An alternative method of considering the internal stress, is to divide it into one component due to the mutual interaction of moving dislocations and another due to immobile dislocations causing work hardening, after Okazaki et al (153), thus:

$$\sigma_i = \beta'' \sqrt{\rho_m} + \theta'' (\epsilon_p - \epsilon_{p0}) \quad 4:37$$

where: β'' , ϵ_{p0} are material constants
 ϵ_p is the plastic strain
 θ'' a work hardening coefficient

These workers have used this model to support their concepts of the processes involved in relaxation (see later). It showed that if the mobile dislocation density decreases, the first term decreases while the second must increase if σ_i is to remain constant.

Assuming that the relaxation is governed by a single thermally activated process, or at least that it is the rate determining process in the flow, then the behaviour can be expressed in the form:

$$\dot{\gamma}_{pl} = A \exp - \left(\frac{\Delta G}{kT} \right) \quad 4:38$$

the Arrhenius equation.

where: ΔG is Gibbs free energy of activation,

A is a factor which contains the mobile dislocation density, a frequency factor and a parameter relating to the geometry of the experiment,

$$\text{i.e., } \dot{\gamma}_{pl} = \dot{\gamma}_0 \exp \left(\frac{-\Delta H}{kT} \right) \quad 4:39$$

where: $\dot{\gamma}_0$ is the pre-exponential constant assuming the entropy of activation to be constant,

ΔH is the apparent activation enthalpy, and may be written as:

$$\Delta H = \Delta H^* - \tau^* A^* |b| \quad 4:40$$

$$\text{or,} \quad = \Delta H^* - \tau^* V^* \quad 4:41$$

where: ΔH^* is the total barrier activation enthalpy,

A^* the activation area - both of these being functions of τ^* ,

b the burgers vector.

The value of $A^* |b|$ is normally taken as the activation volume, V^* .

From the above postulates, expressions connecting the activation enthalpy and area with the test variables were derived, thus:

$$\Delta H = kT^2 \left[\frac{\partial \tau^*}{\partial T} \right]_{\dot{\gamma}_{pl}} \left[\frac{\partial \ln \dot{\gamma}_{pl}}{\partial \tau^*} \right]_{T, \rho_r} \quad 4:42$$

$$\text{and} \quad A^* = - \frac{1}{|b|} \cdot \frac{\partial \Delta H}{\partial \tau^*} \bigg|_{T, \rho_r} \quad (294) \quad 4:43$$

$$= \frac{kT}{|b|} \cdot \frac{\partial \ln \dot{\gamma}_{pl}}{\partial \tau^*} \bigg|_{T, \rho_r} \quad (294) \quad 4:44$$

Similar expressions have been derived by other workers, for example Clough and Demer, (188), such as:

$$\Delta H = kT^2 \left[\frac{\partial (\ln (-\dot{\tau}^*))}{\partial T} \bigg|_{\tau} - \frac{d (\ln m'')}{dT} \right] \quad 4:45$$

where: m'' is the slope of the load vs. total elongation plot.

An alternative approach to the analysis of relaxation data was used by Feltham, (156) to fit his experimental data, (156) to (159). It basically consists of plotting τ or τ^* (τ_i assumed constant) vs. $\log (t + c)$, where c is a constant, i.e. a relationship of the form:

$$\sigma - \sigma' = \lambda' \log c - \lambda' \log (t + c) \quad 4:46$$

$$\text{or} \quad \tau - \tau' = \lambda \log c - \lambda \log (t + c) \quad 4:47$$

where: λ, λ' are constants

$$\sigma = \sigma' \text{ at } t = 0$$

$$\text{and } \tau = \tau' \text{ at } t = 0$$

was assumed. The constant c is chosen so as to give a linear plot from $t = 0$ as shown in fig (4:7).

Noble and Hull, (163), have given a mathematical basis to this technique. From the above assumptions, along with that suggested by Stein and Low, (164), of

$$\bar{v} = \left(\frac{\sigma}{\sigma_o} \right)^{m'} \quad // \quad 4:48$$

they point out that,

$$-\frac{d\sigma}{dt} = A'\sigma^{m'} \quad 4:49$$

where: A' is a test constant.

Integrating and simplifying they show that

$$\sigma - \sigma_0 = f - \log(t + j) \quad 4:50$$

where: f and j are further constants.

It has been pointed out by Kocks, (189), that equation (4:49) is equivalent to the Johnson and Gilman expression, (173) in the form: $\bar{v} = B\tau^{m^*}$ (equation 4:8),

$$\text{thus: } m^* = \frac{V^*\tau^*}{kT} \quad 4:51$$

where: V^* is the activation volume.

4:3.4.3. Consideration of possible dislocation interactions during stress relaxation

One of the usual assumptions in the theory of stress relaxation is that of constant structure, this being mainly based on the small plastic deformations involved. Some consideration has been given to possible errors in this postulate, e.g. strain hardening and recovery.

Sargent et al, (190), considered the strain hardening coefficient θ_1 , where:

$$\theta_1 = \frac{d\sigma}{d\epsilon_p} \quad 4:52$$

from a tensile test and compared it with the coefficient θ_2 where:

$$\theta_2 = \frac{\delta\sigma}{\delta\epsilon} \quad 4:53$$

from a relaxation test as defined in fig. (4:8).

They found that there was good agreement between θ_1 and θ_2 , and expressed θ_1 as:

$$\theta_1 = \frac{1}{2} h' \epsilon_p^{-1/2} \quad 4:54$$

where: h' is a hardening parameter, and they refer to supporting evidence from other work, e.g. Orava et al, (191).

More recent work by White and Smith, (192), has investigated the stress relaxation behaviour in Fe-Ni-Al-Ti alloys. They used the idea, due to Gibbs, (193), that the shape of the relaxation curve initiated at a given effective stress is independent of the manner in which that stress was produced, if there is no change in the dislocation structure.

White and Smith showed that if, after a relaxation, the load was increased again to approximately the same initial stress level, and a further relaxation is performed, the curves do not superimpose, as shown in fig. (4:8). This was taken to indicate the presence of work hardening, i.e. a change in the dislocation structure. The work was continued to obtain a functional form for the hardening. They concluded that linearity in a σ vs. $\log(t)$ plot at large t does not necessarily imply the absence of work hardening.

In the case of high temperature stress relaxation, the further complication of recovery may occur. This has been considered by Solomon et al, (194). They concluded that the level of the mean internal stress is a strongly history dependent function, and that normal recovery events occur, at least during high temperature relaxation. It is to be noted, however, that this conclusion is at variance to those of Cheng and Kocks, (195) who found that the changes in σ_i during relaxation were negligible. Other comments have been made by Grosbras et al (see next section).

4:3.4.4. Summary of analyses and comments

4:3.4.4.1. Introduction

There has, particularly in recent years, been an increasing awareness that the various methods of conducting a stress relaxation test have been considered in isolation and their equivalence has not always been made obvious. Consequently a number of groups of workers have recently considered this aspect of the subject.

An early analysis of the stress relaxation test was due to Guiu & Pratt (139) who, in addition to considering the general analysis, investigated the relation between relaxation and creep (see section 4:3.5)), the effect of machine relaxation and the advantages of the relaxation test as opposed to other analytical tests, e.g. strain rate-cycling. De Batist and Callens (196) have considered the relative merits of Li's (161) analysis and that of Guiu & Pratt (139), and have compared the mathematical expressions for the various theoretical and experimental parameters. They concluded that for small amounts of prior plastic deformation (e.g. as with an annealed material) an exponential relationship between the dislocation velocity, \bar{v} , and the stress (i.e. obeying Guiu & Pratt's analysis) exists. For cold worked material, however, it appeared Li's analysis (i.e. a logarithmic dependence of stress with time) held. They suggested this was

due to a constant internal stress level (during the relaxation) in the latter material.

Aifantis & Gerberich (197) have given a theoretical review of stress relaxation testing and again considered Li's analysis (in their terminology due to Lloyd et al (198)) and a complex analysis due to Sleeswyk (199). In addition to an unusually explicit description of each, they pointed out that in the former case the basic assumptions were that both ρ_m and σ_i remain constant during a test while in the latter $\left. \frac{\partial \sigma}{\partial \ln \dot{\epsilon}} \right|_{\epsilon_p}$ was constant and $\left. \frac{\partial \sigma}{\partial \epsilon} \right|_{\dot{\epsilon}_p}$ was independent of stress.

They concluded that these analyses were consistent and proceeded to support this by reference to tests with iron. In this case, they found that the assumption of ρ_m being constant was invalid near the yield point.

Grosbras et al (200), however, have strongly disagreed with Aifantis and Gerberich in their conclusions. They have insisted that the equivalence of the Li and Sleeswyk analyses was not proved and further suggest that the latter is possibly based on dubious assumptions. They suggested that in many respects the Li and Guin and Pratt techniques are sound but are based on dissimilar basic models and each may be valid in certain circumstances.

Below is given a brief summary of the 3 main analytical techniques of analysing stress relaxation, under the headings which have become usually accepted in recent literature, although notation has been altered in some cases to be consistent within the present work.

4:3.4.4.2. Li's analysis

This is due to a number of authors', notably Li (161), Gupta and Li (186), Noble & Hull (163) and Lloyd et al (198).

Assuming:

$$\bar{y} = B\tau^{m^*} \quad \text{(equation 4:8),}$$

$$\sigma = \sigma_i + \sigma^* \quad \text{(equation 4:15)}$$

and $\sigma_i = \text{const.},$

then $\sigma^* = \sigma$, and it was shown that,

$$\sigma^* = K_1 (t + a)^{-n_1} \quad 4:55$$

$$\text{where } n_1 = \frac{1}{m^*-1}$$

$$K_1 = \left[(m^*-1) \left| \frac{1}{\rho_m} \right| \rho_m B M' w_g \right]^{-n_1} \quad \text{and}$$

a is a constant of integration

From the above analysis, Grosbras et al (200) showed that:

$$\ln (-\dot{\sigma}) = \ln K - (n + 1) \ln K_4 - (n_1 + 1) \ln (K_5 t + a) \quad 4:56$$

and they rewrote this in the form:

$$\ln (-\dot{\sigma}) = K^* - (n_1 + 1) \ln (vt + 1) \quad 4:57$$

where K^* is a constant

Thus if $\ln (-\dot{\sigma})$ is plotted versus $\ln t$, a straight line is predicted for $vt \gg 1$, and its slope, s'' , is given by

$$s'' = \frac{m^*}{1-m^*} \quad 4:58$$

$$\text{or } m^* = \frac{s''}{1+s''} \quad 4:59$$

examples of such plots are given in fig. (4:9). This analysis holds for bcc metals and alloys and ionic and covalent solids. Their technique fails, however, for fcc and hcp metals, see Grosbras et al (200):

Law & Beshers (201) and Rodriguez et al (202) ^{have} considered such failures. For α -Ti, Law & Beshers found that $s'' = -1$, which implies that $m^* = \infty$, and for Al and Cu specimens $s'' < 1$, i.e. $m^* < 0$: clearly both results have no physical meaning. Possible reasons for the failure of the analysis is that fcc and hcp metals may not obey the Johnson & Gilman law (equation 4:6) or that σ_i or ρ_m may not be constant.

• Law & Beshers proposed that an analysis based on a plot of $\log (-\dot{\sigma})$ versus σ would be instructive (e.g. fig. (4:10)) : it can be seen that the bcc material has a negative curvature and the hcp a linear relationship. The Li approach appears to fail for the bcc data because of the rapid variation of ϵ_p with σ^* i.e:

$$\epsilon_p \neq B_1 \sigma^{*m} \quad 4:60 \text{ (from equations 4:6 \& 4:8)}$$

where B_1 is a constant

By considering the relationship:

$$\dot{\epsilon}_p = \dot{\epsilon}_o \exp \left(\frac{-\Delta H}{kT} \right) \quad 4:61$$

Law & Beshers showed that the slopes of their curves, z' , were given by:

$$z' = \frac{|b_v| A^*}{kT} \quad 4:62$$

Thus, the activation volume, V^* , where $V^* = |b_v| A^*$ appears to increase during the relaxation of a bcc material, while decreasing in the fcc case. Kocks (189) regarded the variation of V^* as the most likely cause of failure of the analysis while others, e.g. Rodriguez et al (202),

have suggested that both V^* and ρ_m might vary together. Law and Beshers themselves regarded the cause as probably being due to a rapid variation of σ_i , during a test. Work by Grosbras et al (200) indicated that the last hypothesis may be correct, σ_i varying thus:

$$- \dot{\sigma}_i = B_2 \exp C_1 (\sigma_i) \quad 4:63$$

where B_2, C_1 are constants.

They suggested that this relationship could be explained by recovery during the high temperature relaxation of $\text{Cu-Al}_2\text{O}_3$ and Cu-SiO_2 dispersion hardened materials by self diffusion, although it is not obvious that this mechanism applied to low temperature testing.

4:3.4.4.3. Sleeswyk's analysis

Sleeswyk (199) made the following initial assumptions:

$$\left. \frac{\partial \sigma}{\partial \ln \dot{\epsilon}_p} \right|_{\epsilon_p} = \text{const.} \quad 4:64$$

$$\left. \frac{\partial \sigma}{\partial \epsilon_p} \right|_{\dot{\epsilon}_p} = f(\epsilon_p) \quad 4:65$$

and deformation prior to testing

$$\text{and } \left. \frac{\partial \sigma}{\partial \epsilon_p} \right|_{\dot{\epsilon}_p} = \text{const.} \quad 4:66$$

during the relaxation test. From these he showed that:

$$\begin{aligned} \frac{\partial \sigma}{\partial \ln \dot{\epsilon}_p} &= \text{const.} \\ &= \alpha_4 \text{ say.} \end{aligned} \quad 4:67$$

Integrating:

$$\sigma_o - \sigma = \alpha_4 (\ln \dot{\epsilon}'_o - \ln \dot{\epsilon}'_p) \quad 4:68$$

where σ_o and $\dot{\epsilon}'_o$ are the applied stress and strain^{rate} at $t = 0$. He then produced a relationship between the stress rate and stress during a relaxation of the form:

$$\ln (-\dot{\sigma}) = \ln (M' \dot{\epsilon}'_o) + \frac{(\sigma - \sigma_o)}{\alpha_4} \quad 4:69$$

i.e. a plot of $\ln (-\dot{\sigma})$ versus σ gives a straight line of slope $1/\alpha_4$

Grosbras et al (200) give examples where this approach has been successful, but they also point out that the first assumption (equation 4:64) is rather dubious (at least for fcc materials) and that the second (equation 4:66) implies that work hardening occurs during the

relaxation test at the same rate as during a comparable tensile test. The latter assumption has support from Sargent et al (190) (see figure 4:8).

4:3.4.5.4. Guio & Pratt's analysis

As previously mentioned this analysis (139) was based on the concept of thermal activation aiding dislocation motion past short range obstacles in a relaxation test, (section 4:3.4.2.). In general the mean dislocation velocity can be expressed as:

$$\bar{v} = v' \exp - \left[\frac{\Delta G(\sigma^*, T)}{kT} \right] \quad 4:70$$

where v' is the vibrational frequency of a dislocation segment, and $\Delta G(\sigma^*, T)$ is the Gibbs free energy that has to be supplied for a successful jump. Grosbras et al (200) defined a mean activation parameter \bar{V}^* .

$$\bar{V}^* = \frac{1}{\sigma^*} \int_0^{\sigma^*} V^* d\sigma^* \quad 4:71$$

and pointed out that Guio and Pratt assumed the activation volume, V^* , to be constant during the relaxation test, i.e. $\bar{V}^* = V^*$. This appears to be a reasonable assumption for small σ^* (200).

Using the Orowan relationship the plastic strain rate, $\dot{\epsilon}_p$, can be expressed as:

$$\dot{\epsilon}_p = w_g \rho_m \left| \frac{b}{v} \right| v' \exp - \left[\frac{\Delta G(\sigma^*, T)}{kT} \right] \quad 4:72$$

$$\text{Thus } \Delta G(\sigma^*, T) = -kT \ln \left[\frac{\dot{\epsilon}_p}{v''} \right] \quad 4:73$$

$$\text{where } v'' = w_g \rho_m \left| \frac{b}{v} \right| v'$$

It can be shown that:

$$\left| \frac{b}{v} \right|_{A^*} = V^* = - \left. \frac{\partial \Delta G}{\partial \sigma^*} \right|_T \quad 4:74$$

(See Li (161) or Guio & Pratt (139))

Thus differentiating equation 4:70 with respect to σ^* and using equation 4:74:

$$\frac{\partial \ln \left[\frac{\dot{\epsilon}_p}{v''} \right]}{\partial \sigma^*} = \frac{V^*}{kT} \quad 4:76$$

Assuming σ_i and v'' (i.e. ρ_m) are constant during the relaxation, then equation 4:72 becomes

$$\frac{\partial \ln(-\dot{\sigma}^*)}{\partial \sigma^*} = \frac{\partial \ln(-\dot{\sigma})}{\partial \sigma} \quad 4:77$$

$$= \frac{V^*}{kT}$$

$$= \frac{\left| \frac{b}{v} \right|_{A^*}}{kT} \quad 4:78$$

Grosbras et al (200) pointed out that ΔG could also be expressed as:

$$\Delta G(\sigma^*, T) = \Delta F_0 - \int_0^{\sigma^*} V^* d\sigma^* \quad 4:79$$

where ΔF_0 is the Helmholtz free energy

$$\text{or } \Delta G(\sigma^*, T) = \Delta F_0 - \bar{V}^* \sigma^* \quad 4:80$$

They also pointed out (supported by Wielke in more detail) that the above analysis gave a relationship of the form:

$$\begin{aligned} \sigma_0 - \sigma(t) &= -\Delta\sigma \\ &= \frac{kT}{\bar{V}^*} \ln(1 + a't) \end{aligned} \quad 4:81$$

where a' is a constant of integration.

Thus both the $\ln(-\dot{\sigma})$ vs. σ and $-\Delta\sigma$ vs. $\ln t$ plots (equations 4:17, 4:81) at long t should show linearity, related to V^* (or more correctly \bar{V}^*).

4:3.4.4.5. Comments

The concepts of constant ρ_m and σ_i during a relaxation test has recently been challenged by Okazaki and his co-workers (152 to 155). In their long and complicated analysis they have used an interstitial free iron (Fe-0.056Ti) to examine their theories of stress relaxation at and below room temperature. They suggested that in this alloy the relaxation takes place in 3 stages: the first by a reduction in the mobile dislocation velocity (due to reduction of σ^* on which \bar{v} depends) with constant ρ_m and σ_i ; secondly by the reduction of ρ_m ; thirdly by the reduction of ρ_m and σ_i . They obtained values for all the usual dislocation parameters with test temperature, prior strain, relaxation time and stress loss. It was suggested that the motion of dislocations is generally subject to the control of thermal activation over the Peierls barrier by a process of "kinking". This analysis has not, as yet, attracted adequate comment or criticism (some observations have been made by Smith & Thorpe(203)) and its validity is not certain. Okazaki et al (153) regarded the deformation of this material as homogeneous at all testing temperatures and thought that dynamic recovery was unlikely. They appear to have achieved remarkable experimental accuracies considering the testing equipment used (an Instron type machine) and they attempted to obtain the machine relaxation by the use of a patented wire specimen. Also they regarded as negligible the work hardening of the specimen during relaxation. They showed that the activation volume, V^* , can be obtained by what they term the Feltham-Sargent form:

$$V^* = \frac{M_T kT}{s_1} \quad 4:82$$

where M is the Taylor factor
T

s_1 is the slope of $\Delta\sigma$ versus $\ln(1 + a^*t)$ plot. This analysis assumes, however, the constancy of both ρ_m and σ_i , which Okazaki et al dispute. In a general situation, V^* was shown to vary as a function of the prior strain and of time, figure (4:11), and as a function of $\Delta\sigma$, figure (4:12). They assumed that the variation of V^* was due to a variation in ρ_m during a test, and they proposed the concept of a true activation volume V_F (characteristic of the dominant flow process) by extrapolating the values of V^* to $t = 0$. It is also clear that other problems exist in the determination of V^* . Rhode & Nordstrom (204, 205) obtained different values of V^* for the same material when using an Instron type machine (soft) and a servo-hydraulic machine (hard): Fortes & Proença (206), however, disagree with these results.

Okazaki (152 to 155) used the Li analysis to obtain values of m^* which compared well with some other work. (This approach is apparently relatively insensitive to variations in ρ_m). They did not, however, manage to explain the failures of this approach in some materials (see 4:3.4.4.2.), figure (4:13). They proceeded to use the values of m^* to calculate values of σ^* , figure (4:14). The values of σ_i found for various test conditions are given in figure (4:15) and their suggested variations in the values of σ_m (given as a function of ρ_m/ρ_0 , where $\rho_m = \rho_0$ at $t = 0$) are given in figure (4:16).

These investigations apparently the first co-ordinated attempt at considering the variations in basic parameters during relaxation (earlier workers having assumed their constancy except where mentioned previously): the accuracy of their techniques and the validity of their arguments has still not, however, been considered in detail. It has recently been pointed out that invalid constancy assumptions are not the only basic errors being made. Bengus and Smirnov (207) reviewing the stress relaxation work of Eastern Europe (based on Li's and Guiu & Pratt's work) suggested that non-uniform values of σ_i may be a significant factor in this phenomenon. While this no doubt has a bearing in practical situations, particularly in the deformation of two phase materials such as patented wire, it is clear that the theory requires considerable extension and elaboration before it can accurately be applied to these cases with confidence.

4:3.5 The relationship between creep and stress relaxation

As detailed in section 4:1, this relationship is not obvious because of anelastic components in the relaxation. This point has recently been confirmed by Hammamy et al (208) in a range of materials. An empirical relationship has existed for some time between creep strain and time, (157) thus:

$$\epsilon - \epsilon_0 = -\delta_1 \log g + \delta_1 \log (t+g) \quad 4:83$$

$$\text{or } \gamma_{pl} - \gamma_0 = -\delta_2 \log g + \delta_2 \log (t+g) \quad 4:84$$

where: δ_1, δ_2 and g are constants.

A relationship between δ_2 and λ (equations 4:47 and 4:84) has been derived, (157,209). This work has been summarised by Guiu and Pratt, (139), who concluded that:

$$\lambda = \theta_3 \delta_2 \quad 4:85$$

where: θ_3 is a work-hardening coefficient, and also point out that the strain rate sensitivity measured by either test is the same, with:

$$\begin{aligned} \frac{-d\gamma_{pl}}{d(\log \dot{\gamma}_{pl})} &= \frac{d\tau^*}{\theta_3 d(\log \dot{\gamma}_{pl})} \\ &= \frac{\lambda}{\theta_3} \\ &= \delta_2 \end{aligned} \quad 4:86$$


which has been subsequently verified, (210,211).

4:3.6 Measurement of activation parameters by stress relaxation

In addition to the work detailed in section (4:3.4), a number of workers have used stress relaxation to obtain activation parameters. They have not, however, taken into account the possible shortcomings of the present theory, as suggested by Okazaki and others.

Clough (188) gave the basic theory to obtain the activation energy of the rate controlling process, following on from Guiu and Pratt who showed how to obtain a measure of the activation volume. Clough's technique was to find the effect on $\dot{\sigma}$ of a sudden change in temperature knowing the combined modulus, M' , at each temperature. Okazaki et al (153) considered the problem using earlier work by Li (213) and showed that the value of ΔH decreased with τ^* , fig. (4:17a). They were unable to positively ascribe the values to any particular dislocation model.

Kubát and Rigdahl (214) gave a detailed and clear account of the work on activation volumes for plastic flow processes in a wide range of metals, alloys and polymers. It is interesting to note that they



divide a particular stress relaxation into two parts (an initial exponential part and a subsequent power law part) but it is not clear on what theoretical basis it is done. They also noted that V^* for creep processes are assumed to be constant. Their plots of V^* versus σ^* from the initial parts of relaxation curves of a wide range of materials are given, fig. (4:17b). Wielke (215) has confirmed on a theoretical basis that the activation parameters for the various types of relaxation test are not always comparable.

4:3.7 Measurement of internal stress by stress relaxation tests

The measurement of internal stress of materials of differing compositions, microstructures and thermomechanical histories, has been a field where stress relaxation has shown great usefulness. A common example is the measurement of internal stress during creep. Ahlquist, (216), has given a comparison of experimental techniques for measuring the mean value of the internal stress. It is important to note that most authors have assumed a sinusoidal variation in the internal stress field, (213), (217), (218), (219). This is clearly an oversimplification and a statistical treatment would be a great improvement. In fact, Kocks, (189), has completed some initial work on this idea, although this appears to have been largely ignored.

Partial reviews of this technique have been made by Guieu, Rodriguez, (220), Vlach and Skarek, (221), and Ahlquist and Nix (222). The basic method consists of determining the stress level at which the relaxation rate is zero, (220), or by an incremental unloading or loading of the specimen until no relaxation can be detected, (223), (224). It is argued that when no relaxation occurs (or is observed) the value of $\dot{\epsilon}_p = 0$, and therefore the effective or thermal component of the stress is zero. Guieu, (225), expressed considerable doubts about the validity of this argument, although others, e.g. (221), by alternative methods, have managed to indicate its approximation to the truth.

The debate on the validity of the two types of stress relaxation test has still not been satisfactorily resolved. Further efforts have been made to show experimentally their equivalence, e.g. Lloyd and Embury, (162) or on a theoretical basis (with experimental riders), e.g. Conrad, (226) Cuddy, (227), Hasegawa et al (228), Lloyd and Embury, (229), Cheng and Kocks, (195), Sleeswyk et al, (199), and Aifantis and Gerberich, (197). In fig. (4:18) is given a summary of the main types of relaxation test.

4:3 8 Stress relaxation prior to yield

In the above discussion, relaxation has been started from a post-yield

configuration, i.e. there has been general dislocation motion before relaxation. One of the assumptions on which the theories, (230), are based, the constant density of mobile dislocations (or constant structure), is clearly suspect near yield and this has been used to explain anomalous relaxation behaviour in this region (see, for example, Aifantis and Gerberich, (197)).

Some workers have considered the relaxation properties of a material at various points on the stress-strain curve, including stress relaxation prior to yield. The presence of significant (although small) relaxation in this stress regime seems to imply an additional possible mechanism for the process. Gillis and Sargent, (231), investigated the problem of relaxation in the "elastic region" by analysis with the Johnson and Gilman model, (173), previously mentioned. The shear dependence of the dislocation velocity can be written in the form:

$$\bar{v} = v' \exp - \left(\frac{(D + h'' \epsilon_p)}{\tau} \right) \quad 4:87$$

where: v' is a limiting velocity,

D a characteristic drag stress,

h'' a hardening parameter,

τ the resolved shear stress

This expression implies that plastic flow will occur in a solid at any finite stress, which is not observed. Thus, Gillis and Sargent adopted a cut off stress, below which no plastic flow is observed, to describe the pre-yield region. The resulting mathematical expressions for the relaxation are in the form of exponential integrals, as has been obtained from similar analyses in creep, (278). They appear to fit experimental data from work completed by Shaw and Sargent, (232), in the pre-yield region. In this latter work, the effects of repeated relaxation from a stress below yield on Nb and Mo was observed: the result was to monotonically reduce the magnitude of relaxation on each occasion. This, presumably, indicates significant interaction of moving dislocations during the pre-yield relaxations. A further study by Groh and Conte, (233), has been made into the relaxation of ferrite below and above yield. In fig. (4:19) is given the relative relaxations from the indicated points on the stress-strain curve. Groh and Conte postulate that the small amount of pre-yield dislocation motion is due to the movement of partials involved in interactions at locking points.

4:3.9 Machine problems

As has been described the interaction between the deforming specimen and the tensile machine is of great importance. The general problem of the interaction can be expressed by a displacement equation of the form:

after Gillis & Medrano (234):

$$\int_0^t \dot{y} dt = \frac{\sigma_n a_0}{S} + \frac{\sigma_n l_0}{E} + l_p l_0 \quad 4:88$$

where:

\dot{y} is the crosshead speed,

t the time,

σ_n the nominal stress,

a_0 the initial cross section of specimen,

l_0 the initial gauge length of specimen,

l_p nominal plastic strain in specimen,

S machine stiffness,

E specimen Young's modulus.

The problems involved in applying this form of equation to strain rate tests, including stress relaxation tests, have been considered in detail by Gillis and Medrano, (234). Amongst other points they conclude that the machine stiffness appears to vary not only from test to test but also within a test. They went on to describe a method by which a value for the machine stiffness for a test can be found.

Gillis and Medrano are not alone in the conclusion that the normal tensile testing machine (e.g. a screw Instron) is insufficiently reliable in its stiffness: Lee and Hart, (168), also found that it varied in a series of tests. Fortes and Proença (235) obtained measurements of machine stiffness using stress relaxation tests. They claimed a constant value for a wide range of σ , $\dot{\epsilon}_p$ and specimen dimensions: this view has been opposed by Gillis and Medrano (234) and Hockett and Gillis (236). It is thus doubtful of the validity of such comments however, when such workers as Wielke (215) have found significant variations in the activation energies from equivalent tests on hard and soft machines. A recent investigation by Reed-Hill and Donoso, (237) into the effect of machine relaxation in an internal stress investigation in Ti, suggests a procedure for the removal of this error (assuming a consistent rate of machine relaxation).

One method of determining machine relaxation, is to replace the specimen by a test piece of sufficient bulk to have negligible relaxation. The machine relaxation is often attributed to processes at joints, for example, by Sargent and Shaw, (238). Clough and Demer, (188), however, believe that this effect in their machine (again an Instron TT-C) was due to anelastic relaxation of the epoxy bonded strain gauges in the load cell. This does not appear to have been substantiated by other

workers, but it is clear from the comments of many of the workers who have carried out experimental work in this field, that elastic machine effects can normally be taken into account. Non-linear effects, however, are considerably more difficult to correct for.

The majority of workers have used screw driven Instron machines. While more than adequate for most tensile tests, they have inherent problems for relaxation tests, the above being only one aspect. The finite time (quoted as 2 seconds by Solomon, (239)) required to start or stop the crosshead causes difficulties in allowing for stress transients caused by strain rate changes. This subject has been considered by Guin, (240). These transients can be caused by such phenomena as variation in the mobile dislocation density or Snoek ordering of interstitial atoms. Other tensile machines used include bench Hounsfield tensometers by Feltham, (156), (157), (158), (159), in his early work. These are unsuitable as, in addition to lacking accuracy, it is apparently difficult to determine the machine constants.

A notable advance was made by Solomon, (239), in the adoption of a closed-loop servohydraulic machine. In addition he used an extensometer attached to the grips employing a linear voltage differential transducer (LVDT). Temperature control was obtained with an optical furnace. Although the increase in complexity of the machine has inherent problems, there are a number of advantages:

- (a) the ability to switch instantaneously between various types of mechanical test;
- (b) elimination of interactions between the specimen and machine (the system is inherently hard with position control from the gauge length);
- (c) ability to examine dislocation structure changes subsequent to creep and/or stress relaxation by rapid cooling at constant load;
- (d) ability to study anelasticity as well as stress relaxation with a greater resolution than usual. (Neumann (241) has undertaken a programme to improve the actuator position stability of a closed-loop servohydraulic machine. By careful control of the oil temperature and pressure along with extensive development of oil seals he has obtained a position control of $\pm 0.2\mu\text{m}$, this variation being due to inherent noise in the servo-valve. To improve the control further he has employed a stack of piezo-electric crystals in the loading train and claims a final control of $\pm 10\text{nm}$ as a result). These advantages have apparently not been sufficient to encourage many workers to use such a system; this seems to be due to several factors, including the initial cost and equipment problems, as

well as a general lack of interchange of ideas in this field: Solomon and Nix (217), Solomon, (239), Ahlquist and Nix (222), and Hart and Solomon, (167), have successfully set up such apparatus.

Most workers have used standard paper chart recorders for the collection of stress-time data from stress relaxation tests. Lee and Hart, (168), and Hart and Solomon, (167), have stressed the fact that this form of instrumentation allows a substantial loss of test information. An example is the loss of data at high strain rates, i.e. just after the initiation of the test. The best solution to this problem appears to be the use of a high speed digital recording system as employed by Lee and Hart, (168). Hart and Solomon, (167), went one stage further, by feeding the output into a data logging system to given rapid computation of the required parameters. Thorpe and Smith, (242), have carried out a computer analysis of some stress relaxation data using Li's, (161), theoretical approach (although not his graphical solution). It seems that this more advanced data processing will become more widespread as and when the necessary equipment is available.

4:3.10 Summary of stress relaxation work on some specified materials

4:3.10.1 Introduction

It is rare to find stress relaxation tests being carried out on engineering materials. This is a natural consequence of how this field has tended to develop from the theoretical aspects. Mechanical tests have largely been used to investigate the internal structure of materials rather than to predict mechanical failure.

An outline of relaxation work on specific materials, not previously mentioned as such, is given below.

4:3.10.2 Cu and Cu alloys

The initial work on stress relaxation in recent years by Feltham was carried out on Cu and α -brass, (156), (157), at low temperature. He introduced the idea that the rate determining step was the conservative dragging of jogs. Koppelaar, (243), investigated thermally activated slip mechanisms in neutron irradiated Cu single crystals by a stress relaxation method. In their investigation of dislocation dynamics in the Cu-Sn system, Lloyd et al, (198), used stress relaxation tests to find such parameters as the activation volume of the rate determining step. They also found that m^* varied in a complex manner with the solute content. Cheng and Kocks, (195), investigated and compared stress relaxation, creep and strain rate changes in Cu single crystals. Davies et al, (244), used relaxation experiments to give values for the mean internal stress level during high temperature creep which indicated

that the creep rate $\dot{\epsilon}_c$ can in Cu, Fe and Zn be described by:

$$\dot{\epsilon}_c \propto (\sigma - \sigma_i)^4 \quad 4:89$$

Dolsenko and Landau, (245) considered stress relaxation of polycrystalline Cu in the range 4.2K to 300K. They consider that they found an alternative equation to fit their data more accurately than the usual logarithmic type. They also obtained values for the activation parameters at varying stresses and temperatures: anomalous values at low temperature are explained by the postulation of a zero-point energy phenomenon.

Relaxation in a spring material (Cu-Be) has been recently investigated. Goel, (246), attempted to predict the 40 year relaxation behaviour by the use of temperature accelerated tests, using the formula:

$$\ln t_2 = \ln t_1 + \frac{\Delta H}{R} \left[\frac{1}{T_2} - \frac{1}{T_1} \right] \quad 4:90$$

where: R is the gas constant.

i.e. he compensates for test time t with an increase in test temperature T. Parikh and Shapiro, (247), (248), suggest, however, that this argument may be suspect and may considerably underestimate the remaining stress at long times. Rohde and Nordström, (249), have also carried out work on this material. They again use stress relaxation data to investigate dislocation dynamics of plastic flow.

Fox (250) has considered the effect of heavy cold rolling on the relaxation behaviour of a 5% tin, phosphor-bronze. Using a novel technique (which appears, however, to be unsuitable for analytical work) he showed that the relaxation was greater parallel to the rolling direction (compare with work on drawn Al wire) whatever the test temperature. Annealing at temperatures up to 274°C for 2 hours significantly reduced the relaxation, particularly in the rolling direction so the anisotropy was lost. This anneal did not affect the texture and did not allow recrystallization, suggesting the effect was produced by dislocation movement. Fox (251) extended his work to copper and copper alloy wires giving a comprehensive review of the relaxation properties of many of the copper conductor wires at present in use. He showed that, in general, increasing the cold work applied improved the relaxation performance, although this is probably partly due to its effect on the yield stress of the material. He attempted, by extrapolation of σ versus $\log t$ plots, to predict the relaxation over a 40 year period.

4:3.10.3 Al

Commercially pure Al has been examined by Clough and Demer, (188). They found activation parameters for flow using relaxation data, and were amongst the first to suggest that this method was superior to

creep or other tensile tests for this purpose. Hart and Solomon, (167) used polycrystalline, high purity Al to show the existence of an equation of state in deformation, a concept which has since been used by others. Alden (252) has discussed load relaxation in pure Al single crystals of known orientation and analysed the results after Guin and Pratt. He related the relaxation to recovery creep and suggested that a "hardness of state" concept as suggested by Hart does not exist.

An interesting study on stress relaxation has been made on drawn Al conductor wire by Altermo and Lagneborg (253), who showed that the relaxation properties were anisotropic in hard drawn, recovery annealed (280°C for 7 mins) or fully annealed (320°C for 120 mins) material. In general the relaxation was greater in the transverse as opposed to the longitudinal direction, this being more evident, for the same initial stress, for the hard drawn wire. Full annealing decreased the relaxation substantially, however, there was a concurrent decrease in the yield stress from 193 MPa to 48 MPa, the latter being insufficient for conductor material. The recovery anneal only decreased the yield stress to 120 MPa while the relaxation resistance was improved almost to that of the fully annealed material, fig. (4:20). They pointed out that creep tests are not an efficient substitute for relaxation tests where the latter is the service failure mode. They concluded that the anisotropy was due to a Bauschinger effect rather than to texture and the effect of the recovery anneal was to remove loosely bound dislocations from the hard drawn structure. Herö (254) has also investigated the relaxation of commercial Al wire, but considered the work from a rather more theoretical viewpoint.

4:3.10.4 Fe and Fe-alloys

Feltham, (157), began the relaxation work in α -Fe using similar procedures to those used in his work on Cu alloys. Kelly and Round, (255) used α -Fe as an experimental material to find how the internal stress varied with temperature, and to compare this with the concomitant changes in the dislocation structure. They used a somewhat different analysis to that of Li, (161), enabling them to use the relaxation data at short times to more effect. They also found a linear relationship between $\log \tau^*$ and $1/m^*$.

An important series of tests were carried out by Sugai et al, (256) in two α -Fe samples, one with 155 ppm C and the second quoted with 0.5 ppm C in solution. These were tested at various temperatures

Above 20°C the relaxations varied between the samples: the former showed a more rapid reduction in the relaxation than the low C sample, and also showed a yield drop on further tensile extension. This was taken to imply that dynamic C pinning was reducing the total relaxation under these test conditions, fig. (4:21).

Sarrak and Shubin, (257), used relaxation tests on α -Fe to study the heterogeneity of the internal stress as a function of the dislocation structure. Gupta and Li's work, (186), on α -Fe showed that in the discontinuous yield regime, stress relaxation tests are of little value, presumably due to the varying mobile dislocation density. The varying relaxation in α -Fe for the range 4K to 300K has been investigated by Groh and Conte, (233). They used the data obtained to indicate the various types of thermally activated processes which have a predominant effect.

Yamada and Che-Yu Li, (170), have used Hart's idea of a mechanical equation of state for plastic flow in bcc metals in their tests of monotonically loaded α -Fe and Nb. Yamada and Che-Yu Li, (169), have also considered, by a similar analysis, the relaxation of the fcc materials, 304 and 316 stainless steels: they also refer to further work of a similar nature on Pb, Al, Nb and Ni.

Some work has been carried out on the relaxation which occurs during the tempering of a hardened steel under a load below general yield. Brown and Cohen, (258) and Brown, Rack and Cohen, (259) adopted a novel test method to do this involving wedging open a split eccentric ring of the steel, tempering, removing the wedge and noting the spring-back. Although this is a convenient method, its relationship with the usual techniques is not obvious. Brown, Rack and Cohen noted that the relaxation followed the tempering sequence of the steel and postulated that it was considerably enhanced by the plastic zones formed during carbide precipitation.

Work on the prediction of complex-stress relaxation of some engineering materials, (0.24%C steel, Cu-Al alloys and Mg alloys) at elevated temperatures from simple tensile relaxation tests by Henderson, (260), has shown promise. He showed that combined tension/torsion relaxation test results could be predicted from simple tensile tests with adequate accuracy. This is clearly of great importance when helical spring materials are considered as torsion is their major deformation mode.

4:3.10.5 Other materials

Other materials have been investigated, again usually from the investigation of dislocation dynamics standpoint.

Sargent, (261) (Nb), and Shaw and Sargent, (238) (Nb and Mo), have used relaxation tests to investigate thermal activation, in the latter case prior to yield: relaxation tests were undertaken in the range 77K to 300K. Sargent, (261) gives details of possible pinning interactions in bcc metals which might contribute to the rapid increase in yield stress below room temperature.

The results of stress relaxation tests carried out by Rodriguez et al, (202), on Zr, Ti and their alloys are in agreement with Law and Beshner's results, (201). These papers again throw suspicion onto the Li, (161) and Gupta and Li, (186), (187), analysis. Earlier work had been carried out by Sargent and Conrad, (262) and Sargent, Jones and Conrad, (190) on the thermally activated deformation of Ti and work hardening during its relaxation respectively. More recently, Okazaki and Conrad, (263), have completed relaxation tests on Ti-N alloys at 300K and 400K. They found that m^* increased with nitrogen content and decreasing temperature. Evidence was given that N pinning was the rate controlling process in deformation. Other papers by Okazaki and his co-workers have been described in section (4:3.4.5.5) involving Fe-0.056%Ti.

Feltham, (264), investigated the relation in Cobalt: again, he stated that the rate controlling process was the dragging of jogs, here by basal dislocations.

The only example of stress relaxation tests being conducted on non-metals that has been found in this review, is that due to Gupta and Li, (187), on LiF and NaCl crystals. They found that the relaxation was non-linear with $\log(t)$ but could be described by:

$$\sigma - \sigma_i = K_1(t + a)^{-n_1} \quad (\text{from equation 4:55})$$

where: K_1 , a and n_1 are constants.

This formula can be derived from the Johnson-Gilman analysis (173). It was shown that for LiF, m^* is constant with strain while for NaCl it increases: a value for the mean internal stress, σ_i , was found for each material.

4:3.11 Anisothermal stress relaxation testing

Significant research has been undertaken using analytical anisothermal stress relaxation tests in order to simulate certain industrial situations, e.g. post-welding heat treatment: a review of this field has been given by Tait (265). This worker also undertook such tests on $\frac{1}{2}\text{Cr}\frac{1}{2}\text{Mo}$ V steels using a closed-loop servo-hydraulic testing machine, similar to that employed in the present work. In this material he found significant $\dot{\epsilon}_p$ drops, possibly arising from:

- (a) formation of C-dislocation interactions at 300°C to 400°C;
- (b) formation of C-V-dislocation interactions at 500°C to 600°C.

Ritter and McPherson (266,267) also performed anisothermal tests on $\frac{1}{2}\text{Cr}\frac{1}{2}\text{Mo}$ V steels: they included another review of this work. They pointed out the complications in addition to those found in isothermal relaxation tests and distinguished two regimes of relaxation; before and after yield. They suggested that relaxation of residual stresses could take place by 3 basic mechanisms:

- (a) elastic relaxation, resulting from a decrease in the lattice binding forces with increasing temperature;
- (b) plastic flow, allowing conversion of elastic strain to plastic strain subject to dislocation locking mechanisms (e.g. dynamic strain ageing, alloy carbide precipitation) and grain boundary relaxation;
- (c) phase transformations (e.g. decomposition of retained austenite) leading to relaxation by dilatation and induced local plastic flow.

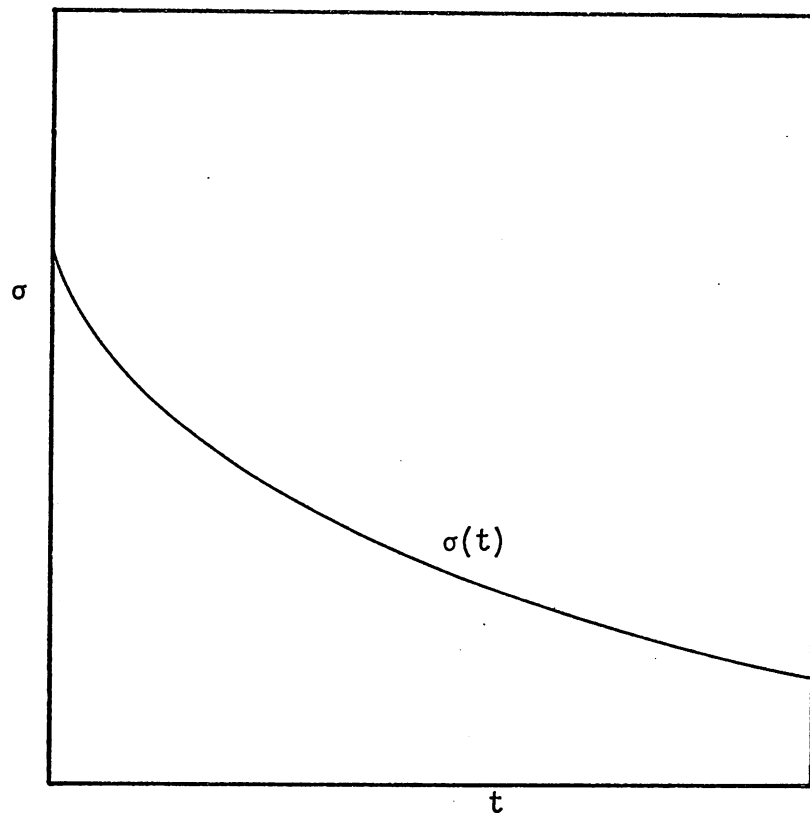


Fig. (4:1) Schematic representation of stress relaxation with time.

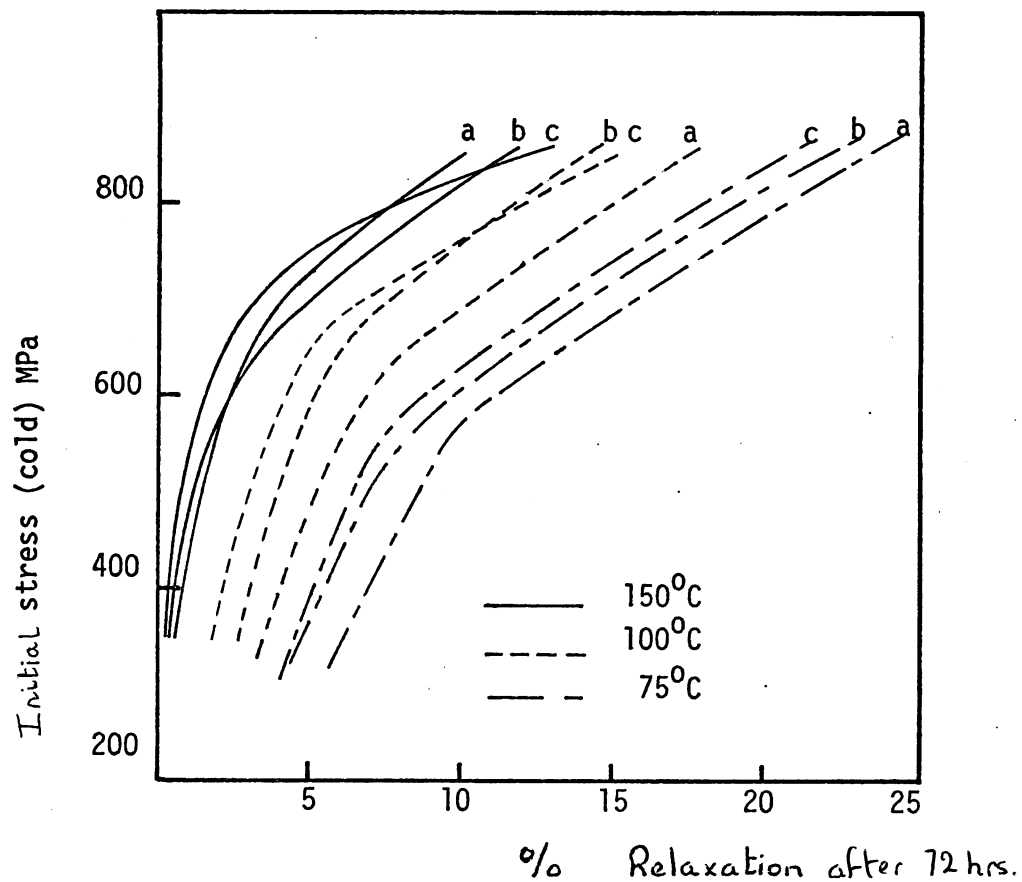


Fig. (4:2) Comparison of stress-temperature relaxation properties of:
a) patented hard-drawn wire; b) En 49D wire; c) oil-tempered wire (143).

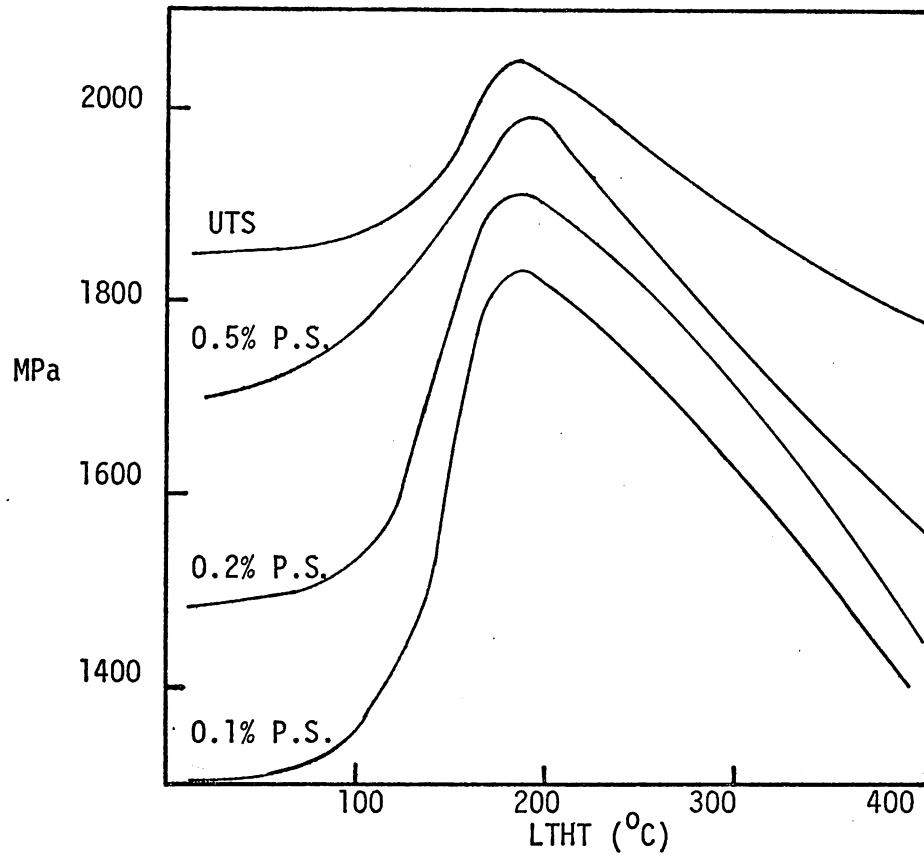


Fig. (4:3) Effect of LTHT on tensile properties of BS 1408M R2 wire, as used in the tensile tests in this work (246).

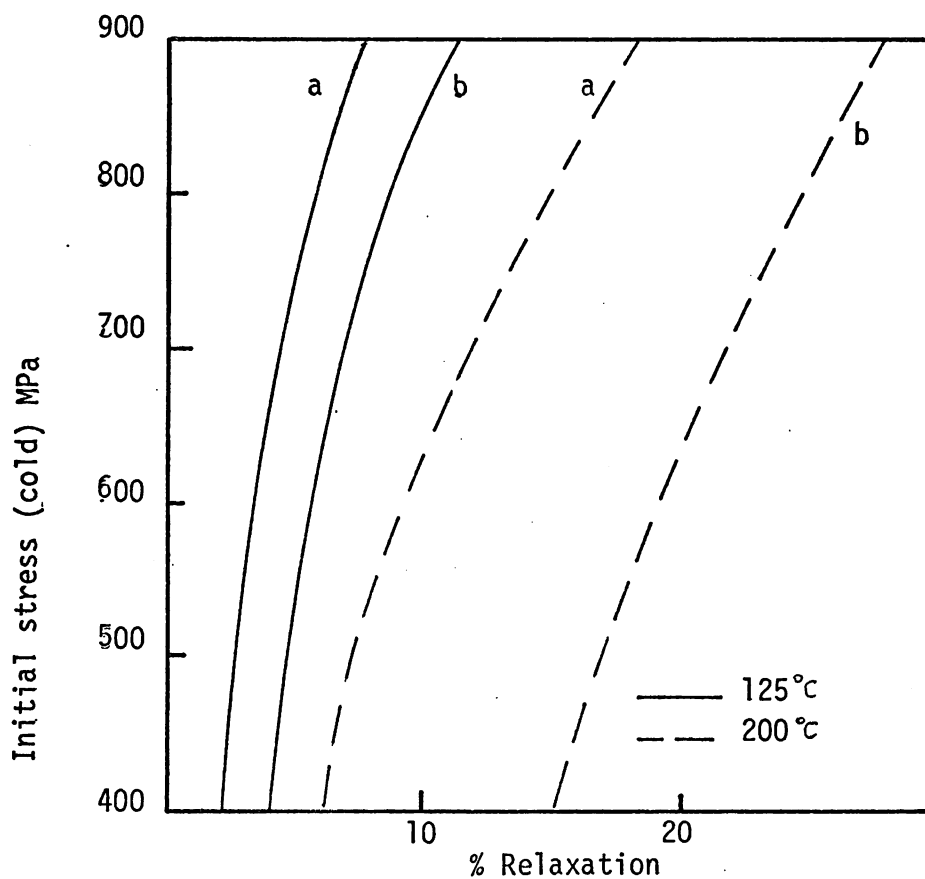


Fig. (4:4) Relaxation behaviour of BS 1408M R2 wire at various test temperatures a) as coiled b) shot-peened (246).

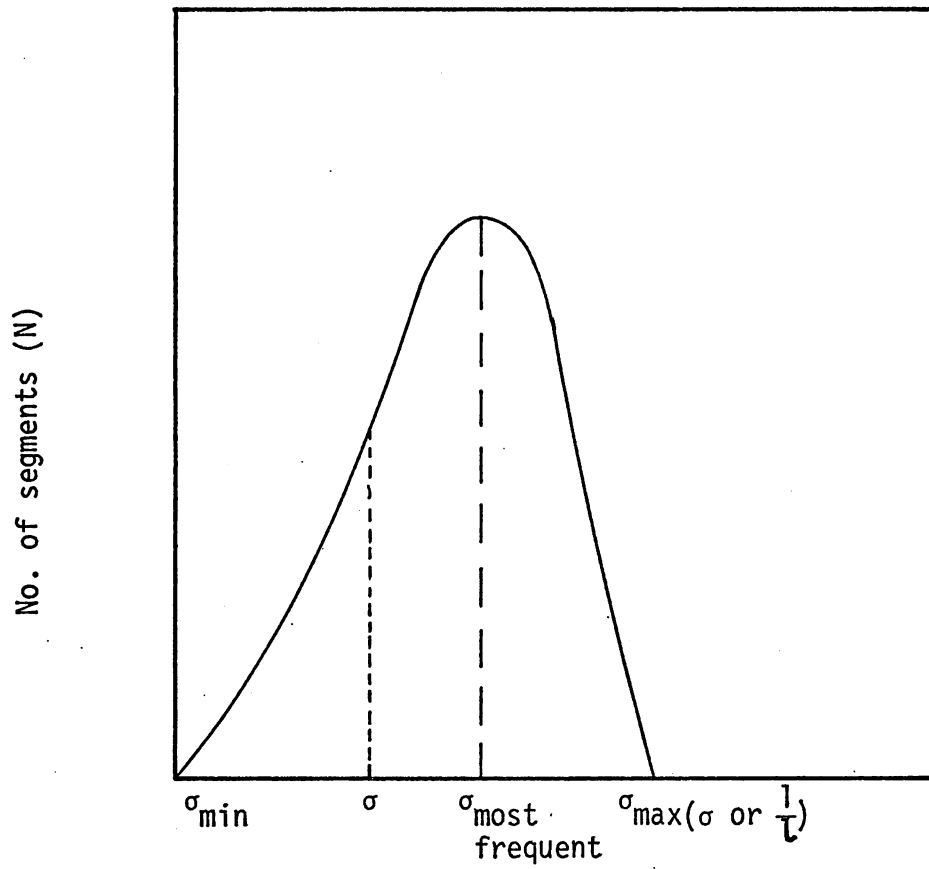


Fig. (4:5) Hypothetical distribution of mobile dislocation segments with applied stress, σ (136).

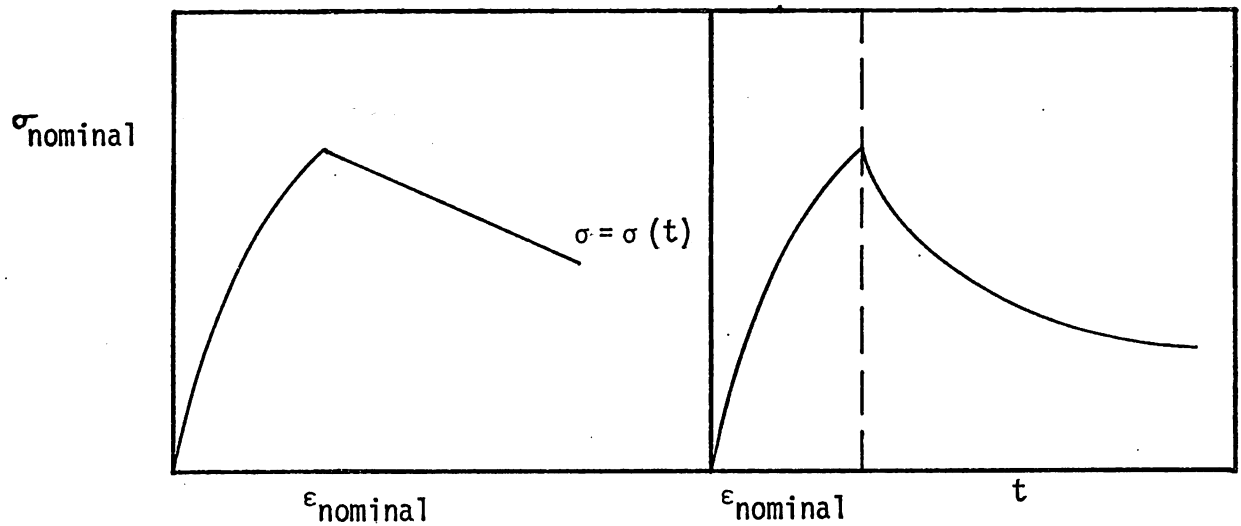


Fig. (4:6) Schematic representation of a relaxation test - stress as a function of strain or time.

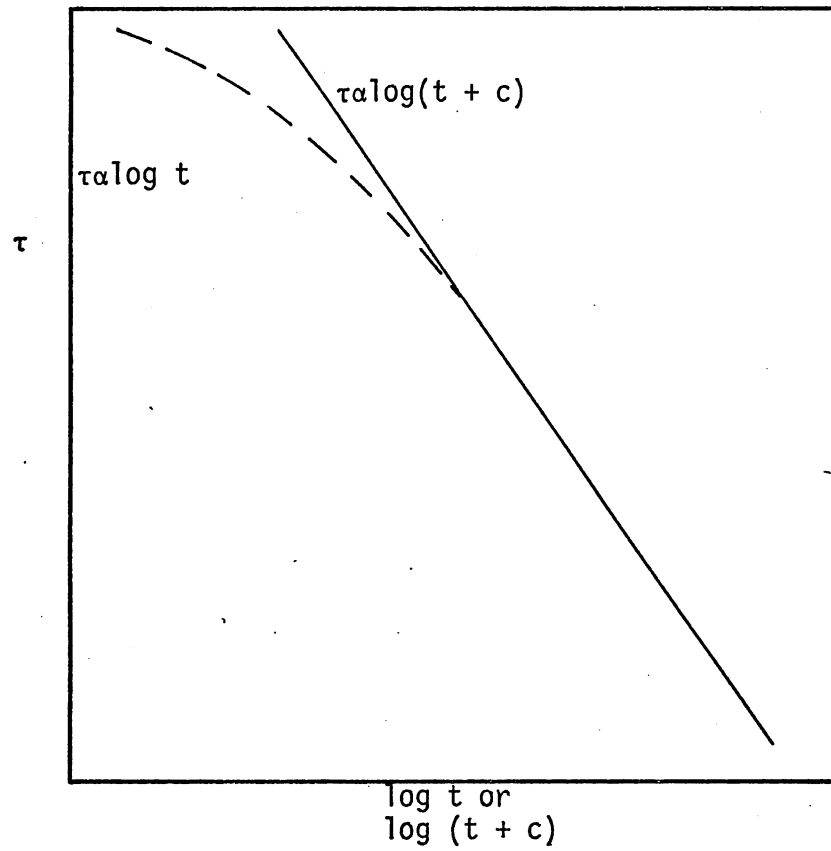


Fig. (4:7) Schematic representation of shear stress with $\log(t)$ or $\log(t + c)$ for a stress relaxation test.

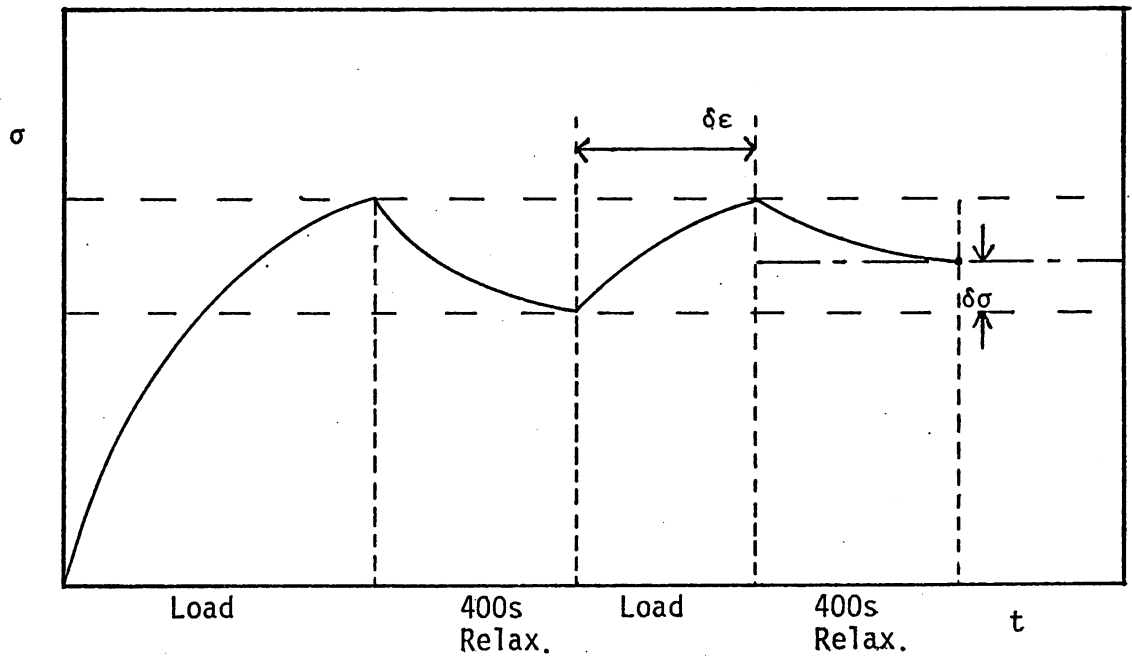


Fig. (4:8) Comparison of a 1st relaxation immediately followed by a 2nd from the same initial stress.

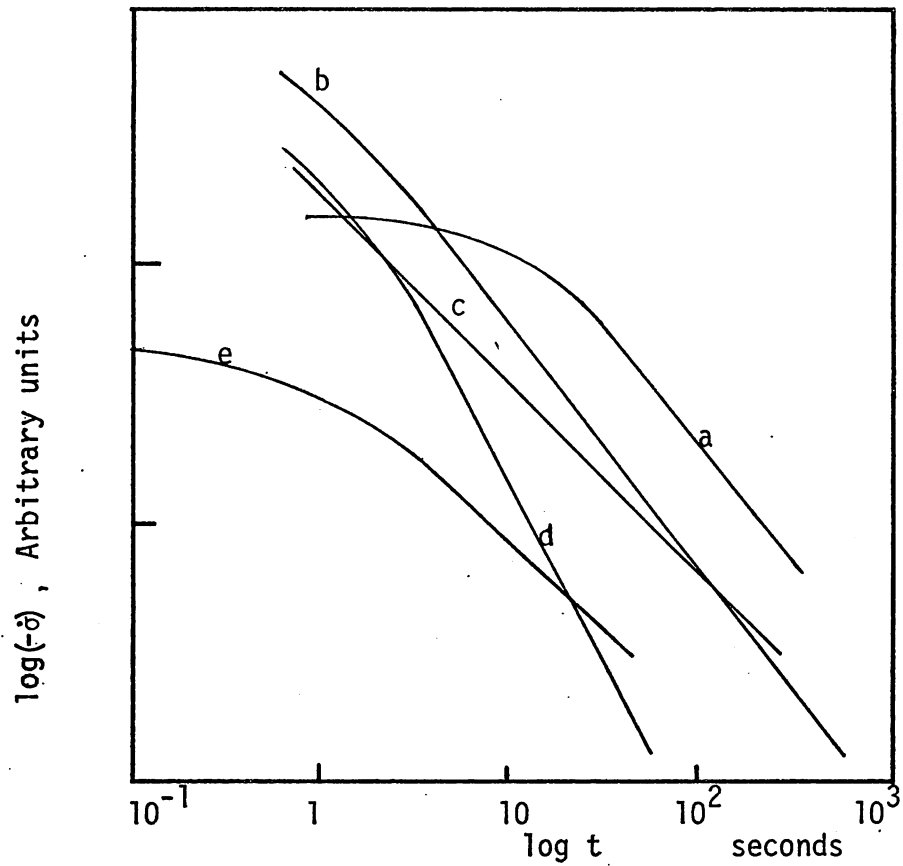


Fig. (4:9) Plot of $\log(\dot{\sigma})$ vs. $\log t$ plots for relaxation tests (201):
a) Ti; b) 6061 Al; c) Cu; d) Fe; e) Al.

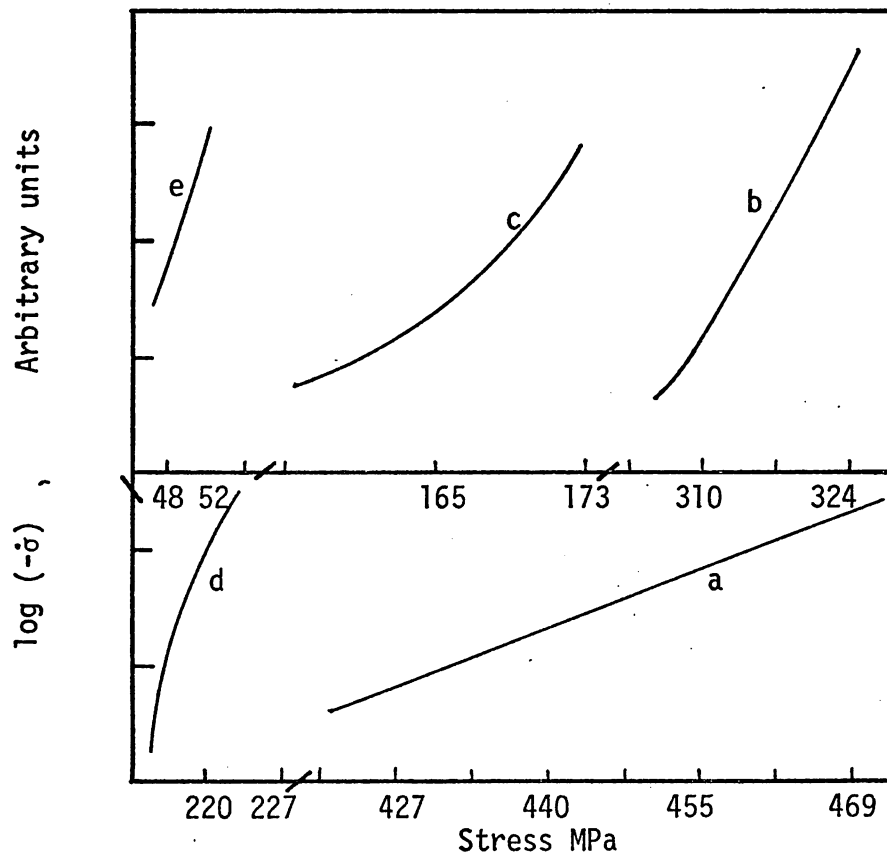


Fig. (4:10) Plot of $\log(\dot{\sigma})$ vs. σ for relaxation tests on materials
in Fig. (4:9) (201)

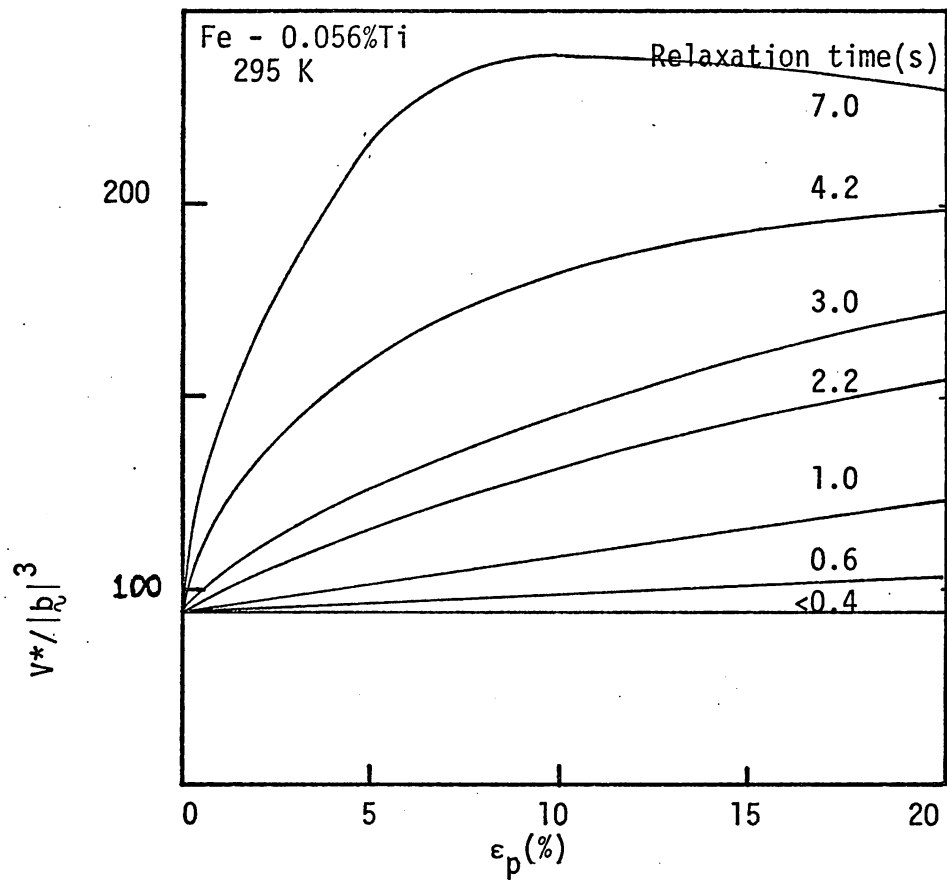


Fig. (4:11) Variation of V^* with prior strain and relaxation time (152).

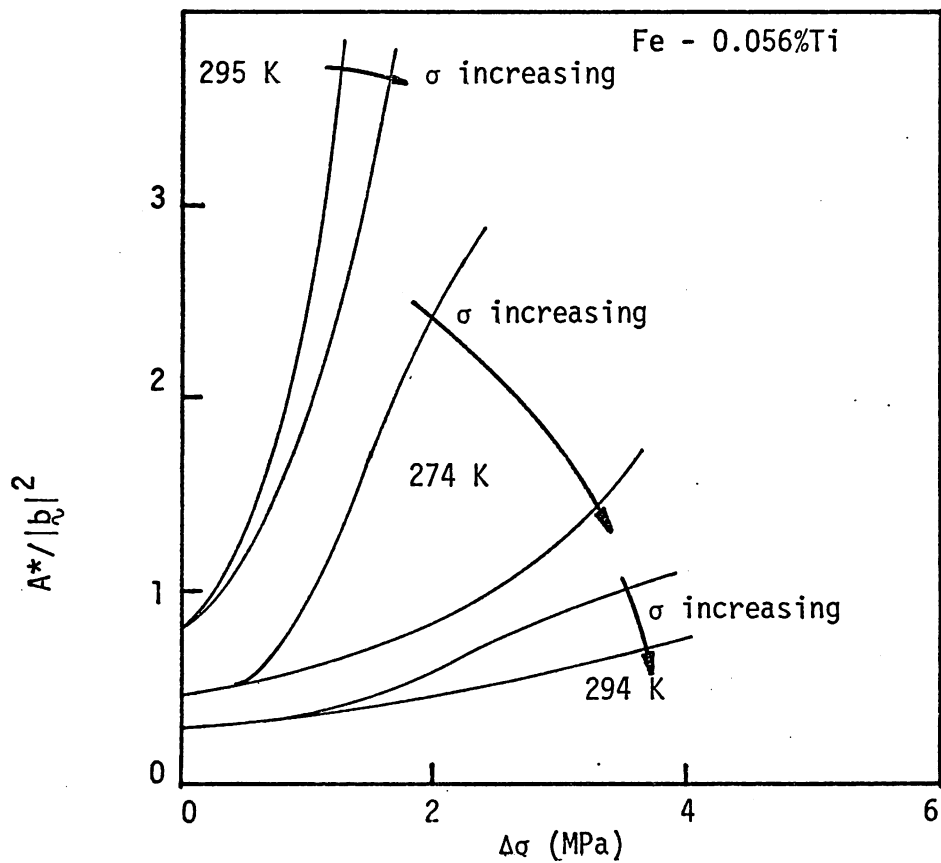


Fig. (4:12) Variation of A^* with initial stress and relaxed stress, ($\Delta\sigma$) and temperature (152, 153).

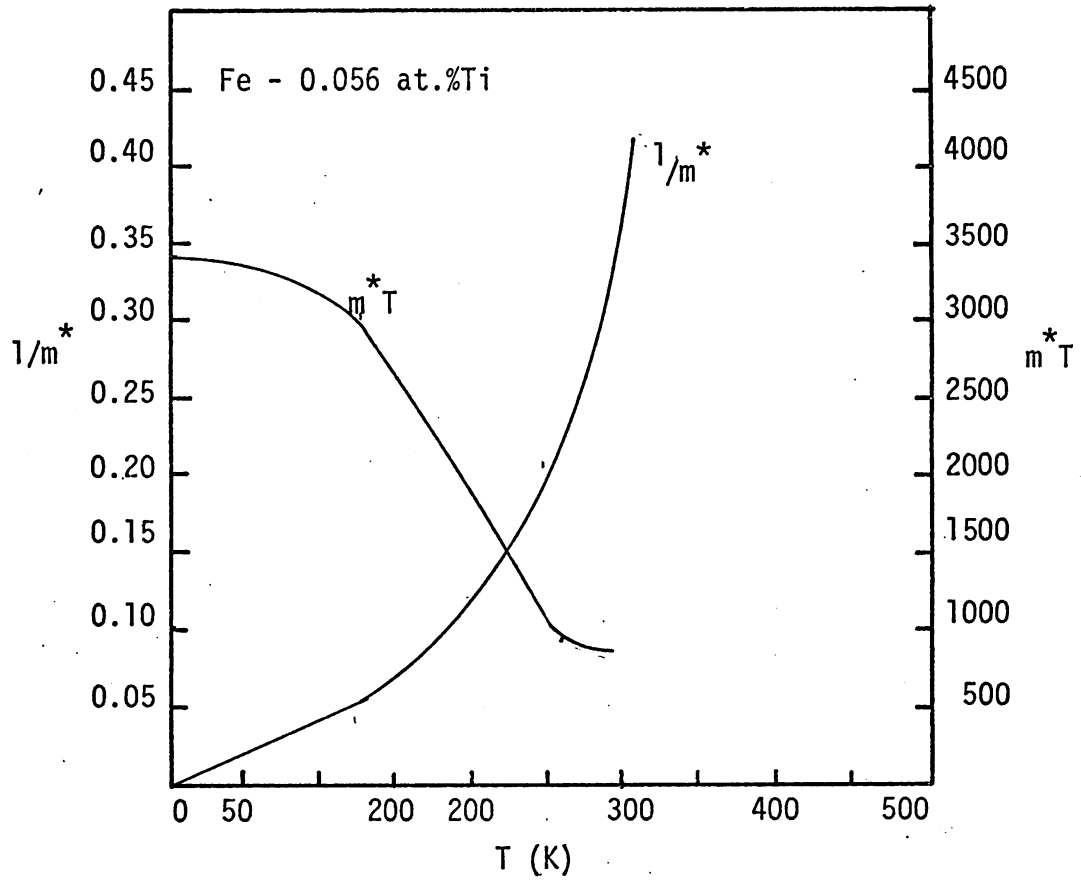


Fig. (4:13) Variation of m^* and m^*T with test temperature (below 150K, m^* is calculated from $m^* = \left[\frac{\sigma^* v^*}{MkT} \right]$ (152).

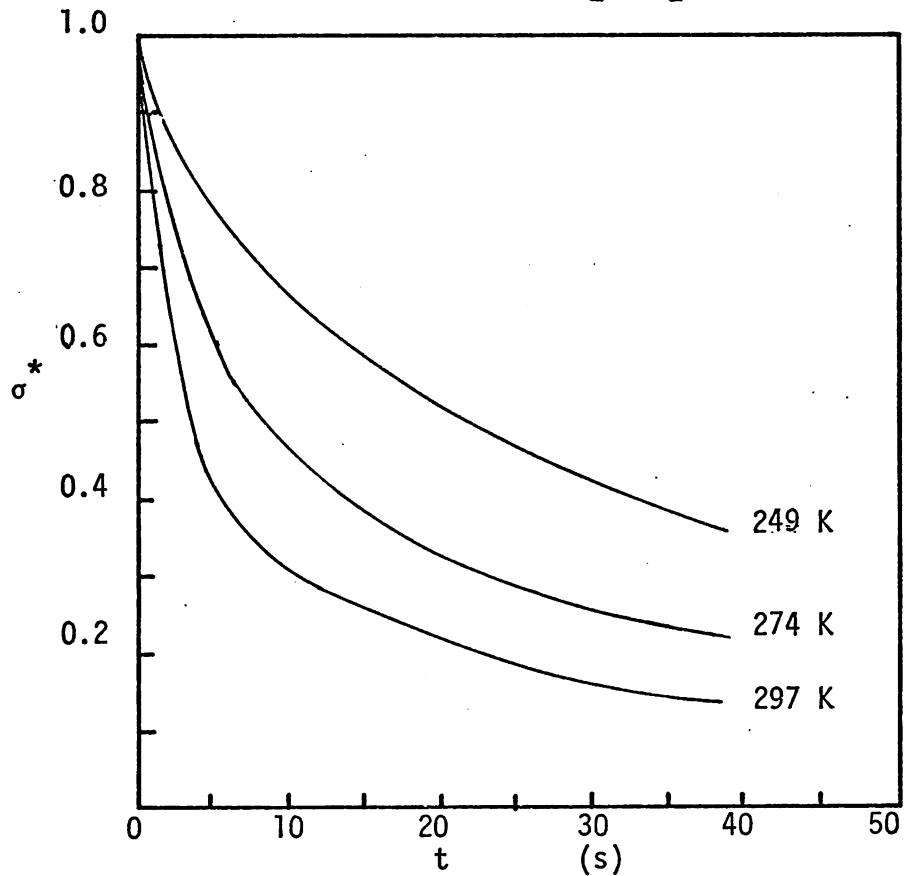


Fig. (4:14) Variation of σ^* (normalised) as a function of relaxation time and test temperature, (Fe - 0.056at.%Ti) (154).

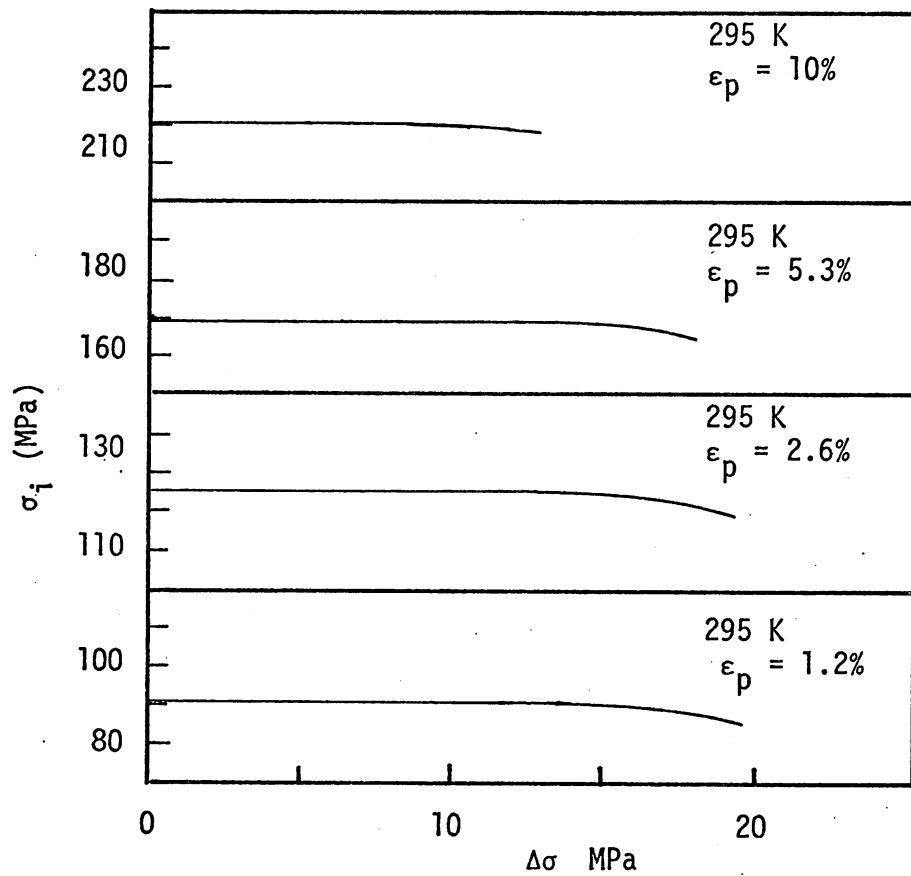


Fig. (4:15) Variation of σ_i as a function of relaxed stress ($\Delta\sigma$) and prior strain, (Fe - 0.056at.%Ti) (153).

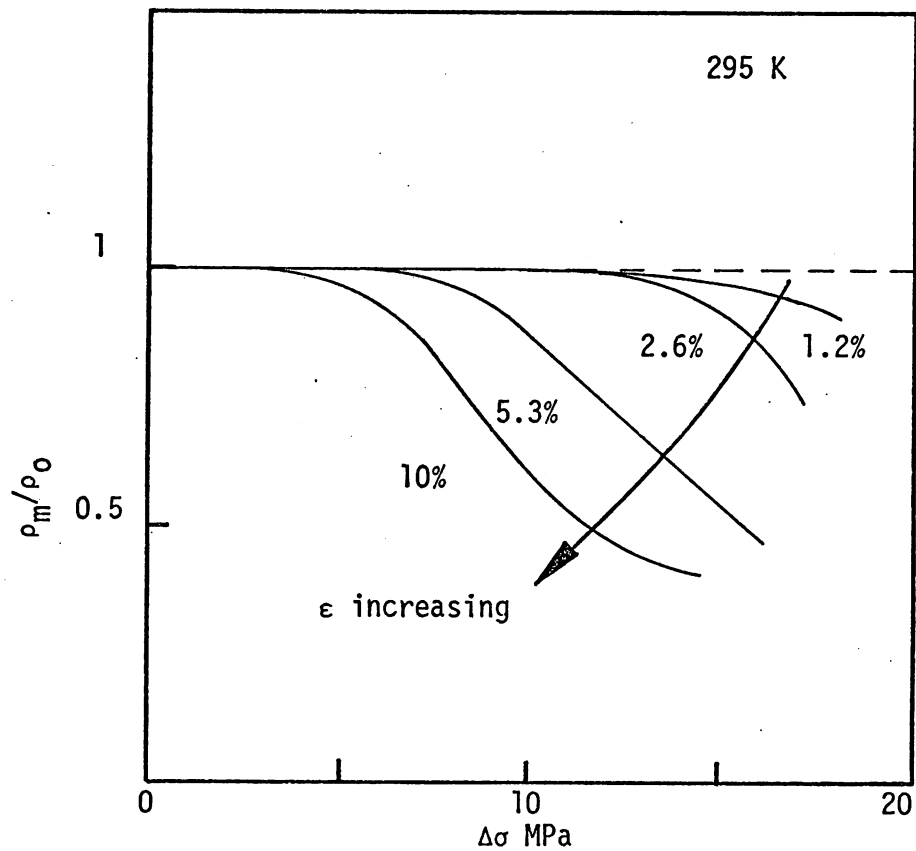


Fig. (4:16) Variation of normalised ρ_m as a function of relaxed stress ($\Delta\sigma$), and prior strain (Fe - 0.056at.%Ti) (153, 154).

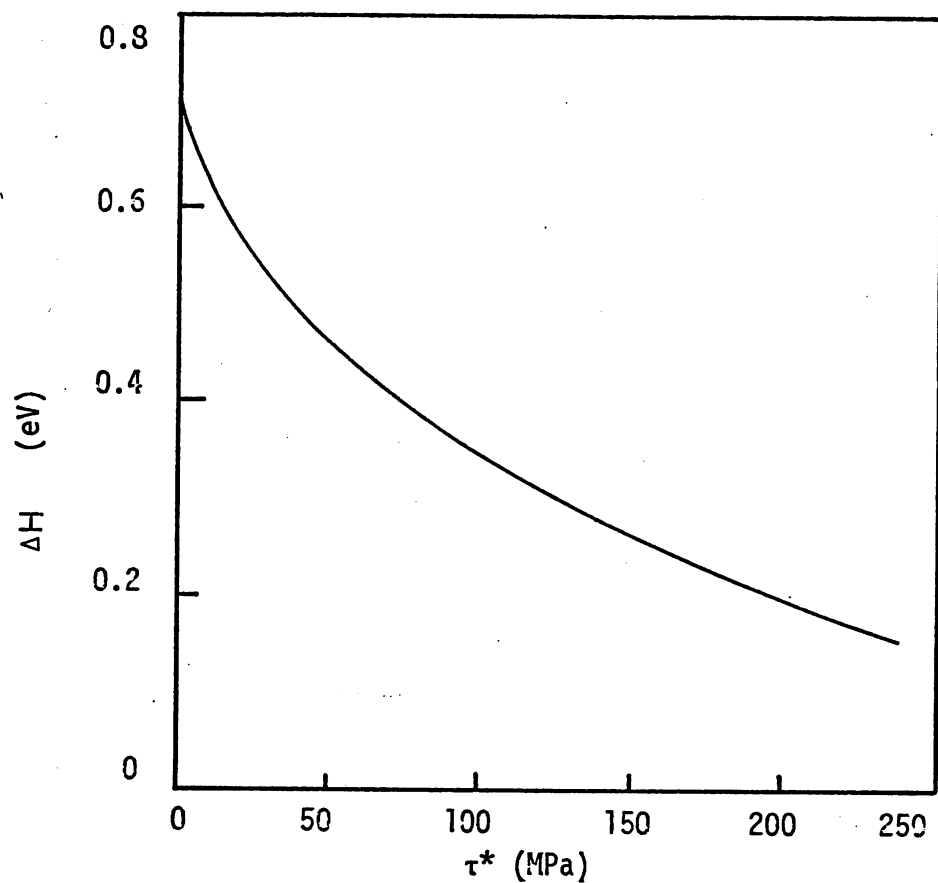


Fig. (4:17a) Variation of ΔH with τ^* during a relaxation, (Fe + 0.056 at.%Ti) (152)

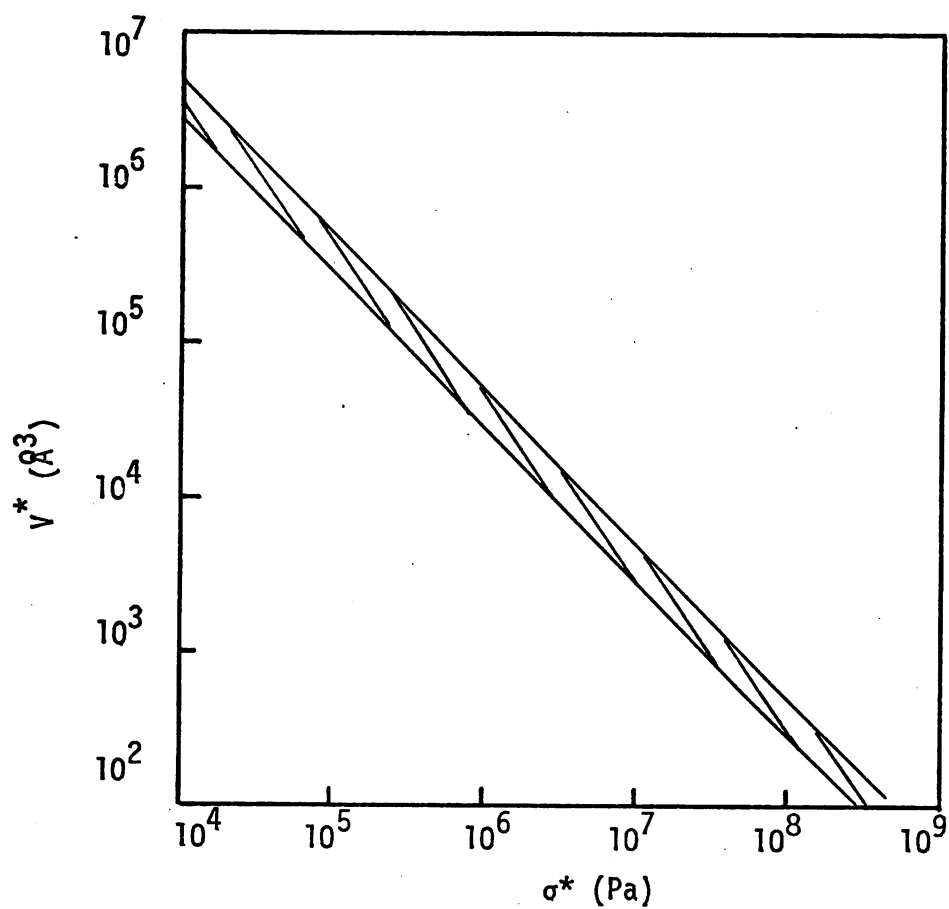
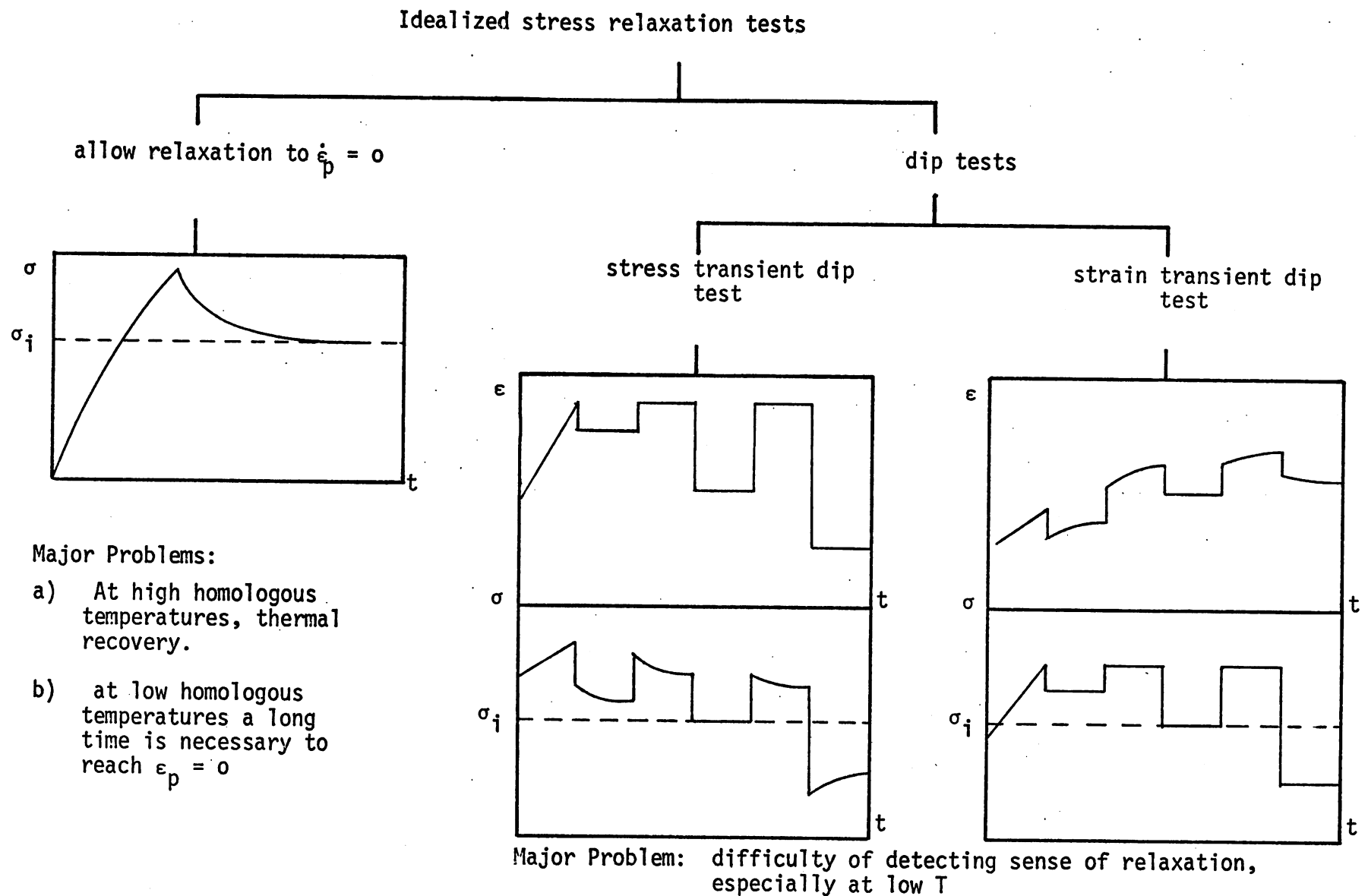


Fig. (4:17b) Variation of V^* with σ^* for various materials (214).

Fig.(4:18) Summary of the types of relaxation test.



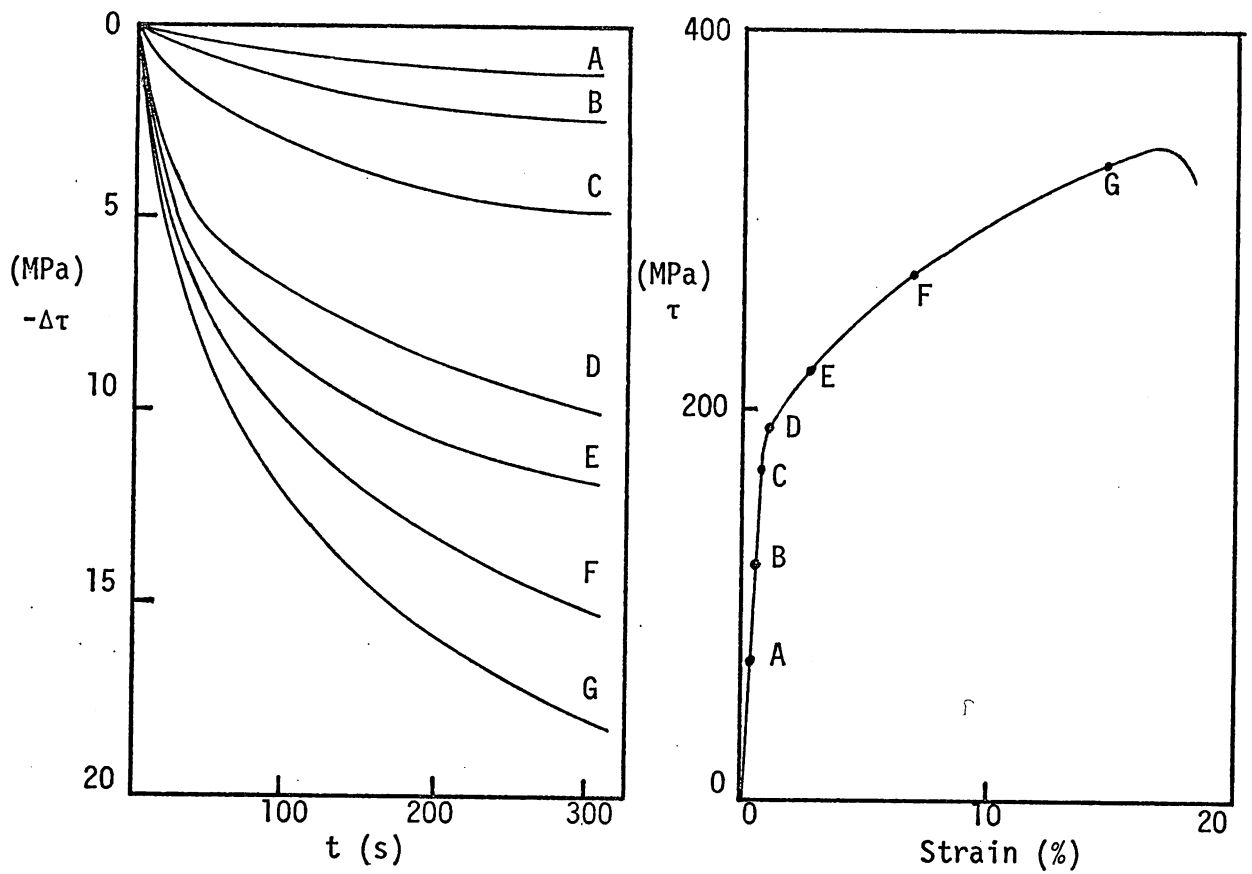


Fig. (4:19) Relaxation tests carried out on ferrite at 100K, at various indicated points on the stress/strain curve (233).

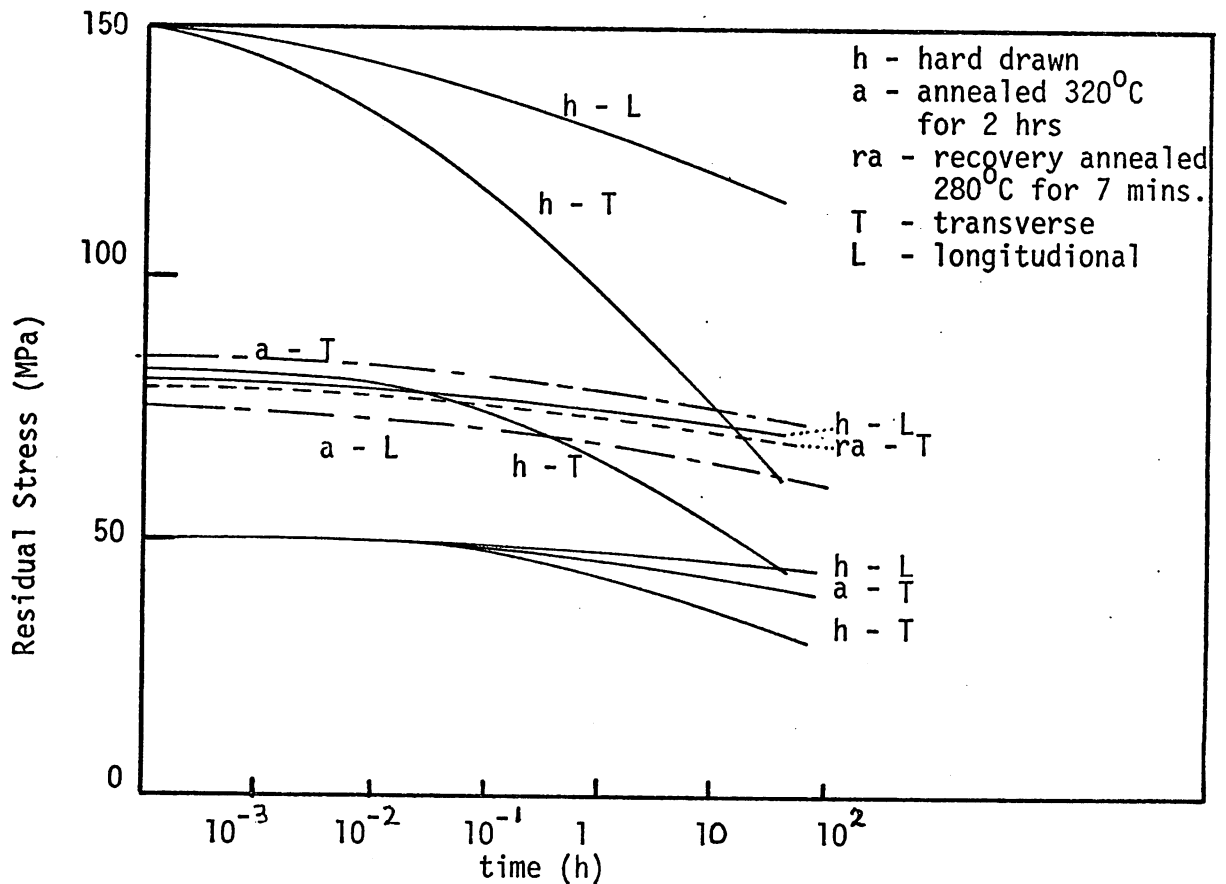


Fig. (4:20) Relaxation of conductor Al wire in longitudinal and transverse directions in various states (253).

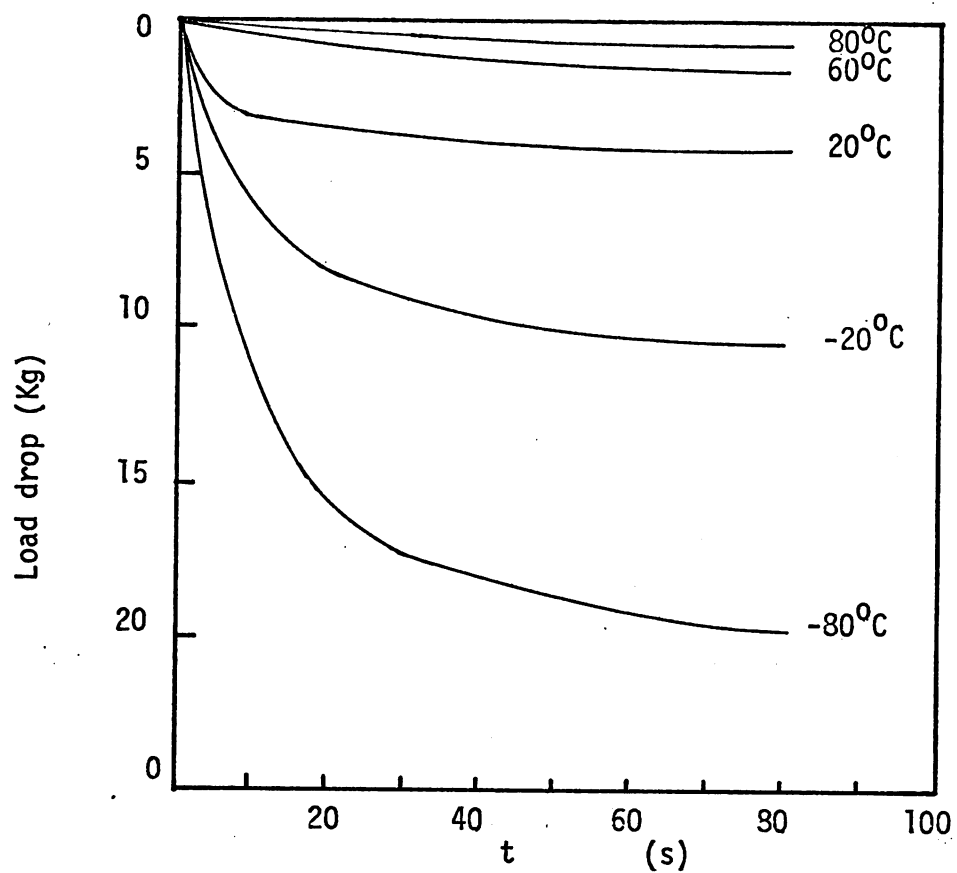


Fig. (4:21a) Relaxation of a Fe - 155 ppm C alloy at various temperatures (256).

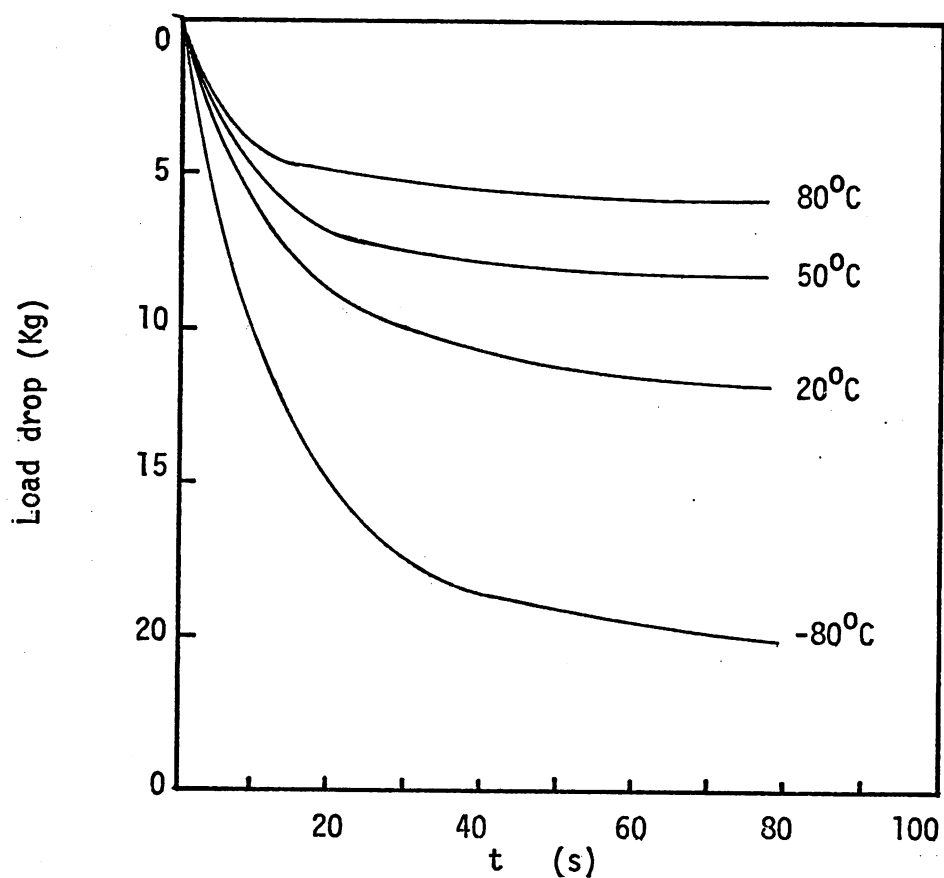


Fig. (4:21b) Relaxation of a Fe - 0.5 ppm C alloy at various temperatures (256).

5. Mechanical Testing

5:1 Introduction

The mechanical testing programme was required to produce significant, high grade data to allow an accurate interpretation of phenomena which have been observed in the spring wires. In addition it would need to generate data in a selection of environments in an attempt to relate the material properties with the industrial spring situation. With these aims, 2 testing programmes were set up: the first required the development of an accurate and reliable series of tests in uniaxial tension, using a closed-loop, servo-hydraulic testing machine. It resulted in specimen, grip and machine designs capable of extremely high resolution and accuracy, allowing a valid study of the relaxation properties of spring wires to be made: these designs also allowed tensile tests to be performed. Details of the design, development and use of the apparatus are given in Appendix A.I. These tests were carried out at room temperature (22°C). The second series of tests were of lower accuracy and were carried out on similar spring wire which had been coiled to form helical springs: details are also given in A.I. This technique enabled tests to be easily accomplished at various temperatures, stress and times, and gave an insight to the materials behaviour in spring applications. The materials which were tested and are discussed in this chapter are the A/R and A/R + LTHT patented wires listed in Ch. 3:1. The spring tests were, however, carried out only on A/R and A/R + LTHT "A" patented wire.

5:2 High accuracy tensile testing

A closed-loop, servo-hydraulic testing machine was employed to obtain accurate tensile data on the wires at room temperature under strain control. It was found that the 2 batches of the as-received wire of identical specification behaved differently on testing with respect to their failure characteristics. One batch showed considerable ductility after reaching its UTS while the second fractured in a macroscopically brittle manner at or before the UTS: the elongations to failure varied widely. Examples of these types of behaviour are given in fig. (5:1) for A/R material: similar behaviour was noted in the 2 batches in the heat treated conditions. The fracture surfaces showed considerable differences, the ductile case exhibiting deep longitudinal fissures along the aligned pearlitic structure which were absent in the less ductile material, fig. (5:2). Possible causes for this variation have been

discussed in Ch.2 and elsewhere. It was noted that microstructures of each were identical (by TEM examination).

A study of typical A/R nominal stress/strain curves (as given in fig. (5:2)), shows a small linear region with a relatively low elastic limit/proof stress value. The work hardening rate steadily decreases to the UTS over a large (as compared with LTHT material) range of strain (typically 2% to 2.5%). In the material showing the greater ductility considerable elongation after necking was often noted (typically 5%). The effect of any of the LTHTs has been shown to be particularly dramatic on the 0.2% proof stress, LTHT "A" typically raising it by approximately 40%: The UTS in this case only being raised by approximately 15%. Typical nominal stress/strain curves for the annealed wires are given in fig. (5:3) for the more ductile material (the less ductile material fracturing at or near the UTS). The long plateau at or near the UTS was found to be characteristic of the annealed material. The changes so brought about on the elastic limit, 0.2% proof stress and UTS are given in fig. (5:4). The UTS was shown to increase with time and temperature of LTHT while the most suitable anneal for optimum values of proof stress and elastic limit appeared to be 200°C for either 30 or 300 minutes.

The effects of prior stress relaxation on the tensile stress/strain characteristics are discussed in section 5:4.

5:3 Spring testing

5:3.1 Introduction

It was originally planned to test springs helically coiled from patented wire at 6 temperatures, 22 °C, 50°C, 100°C, 150°C, and 200°C, using A/R springs and springs-annealed to LTHT "A", and at 250°C with A/R springs. Following initial testing, it was found that the 2 lowest temperatures were impractical with the given spring design, the relaxations observed not being considered significant with respect to the experimental scatter. Springs were compressed to at least 3 set lengths (corresponding to 3 initial stresses, including the solid stress, i.e. the stress level with the spring fully compressed) on stainless steel studding and held at test temperatures for periods up to 240 hours (previous work on this material showed that the majority of relaxation is complete after 72 hours, see Ch.4). Details of experimental technique

and errors are given in A.I, while a consideration of spring deformation and the stresses arising were given in reference 1, the CPGS.

5:3.2 Experimental results

It was found that in all cases there was a rapid relaxation in the initial 2 hours, the resolution of the test not being capable of following the load variation. Each relaxation curve was characterised by an initial period of relatively rapid, but decreasing, relaxation rate followed by an approximately linear relaxation. Details of the loading parameters of each test are given in A.I:1.2. As can be seen in figs.(5:5a to 5:5g) the relaxation rates in both the linear and non-linear periods increased with test stress and temperature for either the A/R or A/R + LTHT "A" material. The effect of the LTHT was only significant in the tests carried out at 150°C where both parts of the curves show significant reductions in the relaxation rate. In tests performed at 100°C, the resolution of the technique, although showing a relaxation in each case, was insufficient to detect improvements brought about by the LTHT "A". This was partly due to the spring design employed which, with the available spring wire, did not allow a solid stress approaching the material yield stress in torsion to be obtained. However, the problems which have been encountered with this technique in the present work must question its acceptability for valid fundamental material investigations.

The 200°C tests again did not show significant variations between the 2 types of spring. In this case, however, this was not entirely unexpected as the LTHT took place at 200°C for only 30 minutes, the effects of which would not have been evident with the testing time intervals chosen. As the effect of the LTHT would be unimportant in the case of the 250°C tests, only A/R springs were investigated.

It was found that relaxation was considerably enhanced over the lower test temperatures, particularly at the solid stress. It was again found, however, that the majority of the relaxation (> 90%) had been completed after 72 hours at all stresses.

No attempt has been made to relate the relation rates with stress time or temperature. These types of analyses would be valuable if their validity could be assumed in such complex testing situations. An example is that the results obtained here indicate that there are at least 2 significantly different, dominant deformation phenomena occurring at

various periods of time during the test, as indicated by the rapid and slower relaxation stages. For example, an Arrhenius type analysis of the relaxation, as can be employed for accurate relaxation data (see Ch.4) does not, when applied to these results, yield consistent activation data at whatever stage during the relaxation is considered. Such a conclusion is not unexpected, not only for the above reason of competing deformation mechanisms, varying in importance with time during a relaxation, but also that there is a likelihood of the mechanisms varying in relative importance with temperature. It is in addition to these fundamental concepts that the complex nature of the stress state (see (1)) and inherent inaccuracy of the test must be viewed. It is clear that although this type of test would, if modifications were introduced, give valuable insight into the behaviour of a finished component, it is extremely unlikely to give insight into fundamental material behaviour during such a failure. A summary of the behaviour of the test springs showing the relaxation after 72 hours with temperature and stress is given in fig.(5:6 a,b).

5:4 High resolution stress relaxation testing

5:4.1 Introduction

The principle reason for the development of a high resolution testing programme was to be able to generate data for a wide range of materials, under various test conditions allowing both comparative and absolute information to be obtained and to investigate the fundamental stress relaxation models which have been developed (see Ch.4). The tensile testing technique employed in the present work has proved itself to be particularly versatile in these respects and a full description of the experimental method is given in A.I:1.1. It has to be understood that these tests are on the material rather than the spring wire as such: this is a necessary consequence of straightening and machining the wire (necessary in order to obtain specimens capable of giving useful data). Such procedures inevitably change the internal macro-stresses, but they are unlikely to change the internal micro-stress variations which are superimposed upon them (see ref.(1)). The micro-internal stress variations will be on the scale, in the drawn patented wire, of the interlamellar spacing (the ferrite being left in compression by the drawing process) and a further variation on the scale of the dislocation cell structure (of more significance in the higher drawing reductions). In order to test spring wire itself it would not only be necessary to test it in its normal

deformation mode (mainly simple torsion, although this can be asymmetric and complicated by bending - see the CPGS (1)) but also to test the wire after coiling and with no gauge length defined or machined: it had to be accepted that, at present, this was not possible. The tensile testing technique, however, can provide an accurate guide to more complicated testing modes (see Henderson (260)) and can show the effects of such procedures as LTHT and repeated relaxation. It can also be used to evaluate the many competing models and analyses which have been detailed in Ch. 4:3. There has been some confusion in previous work over the effect of varying the strain rate and loading times to obtain various initial specimen stresses. It is clear that the relaxation behaviour will not only be dependent on the initial stress (it is not a function of state) but also on the deformation route by which that stress was obtained. For example, as the test specimen is not loaded instantaneously in the present work, nor in any previous work, some relaxation is likely to occur during the loading. This may well explain why various loading rates to the same initial stress can cause a variation in subsequent relaxation behaviour (e.g. 166). No example has been found in the literature where adequate attention has been given to this problem. As part of the consistency evaluation, a series of 30mm gauge length patented wire specimens, with cross sectional areas within $\pm 2\%$ of each other were loaded at various strain rates (i.e. various actuator rates) for various times to obtain the same loads (and stresses to within $\pm 4\%$) and the subsequent relaxations were monitored. It was found that a much wider scatter in relaxations ($\pm 17\%$) was encountered than a similar group of specimens which were loaded under constant conditions ($\pm 4\%$). These results, in themselves indicate the importance of loading under standard conditions. It is not clear whether it would be more accurate to vary the strain rate or time while keeping the other variable constant. Similar tests to chosen loads obtained by varying one of the parameters, were found to give essentially the same relaxation ($\pm 4\%$). It has been outside the scope of the present work, however, to elucidate this problem to any greater depth. For the present work it has been decided to adopt a procedure whereby each specimen is loaded for the same time period (180 seconds) from an initial load of 0.5kN (there being non-linearity below this load). The choice of initial load from which the relaxation was to begin was chosen by the appropriate value (after trials had been

made) of the loading rate. This technique was used as it was regarded to simulate more accurately a service situation. The 180s loading period was found, in practice, to be the most rapid which could be followed by manual adjustment on the chart recorder. This manual adjustment was necessary to give sufficient resolution on the graph trace. The information which has been obtained in the present work has indicated the type of deformation which has taken place (see Ch. 4:1) along with its extent and its dependence on prior deformation and heat treatment: the machine and patented wire behaviour is discussed in the following sections while that of the 17-7 PH stainless spring wire is detailed in Ch.6.

5:4.2 100kN servo-hydraulic Mand behaviour

The choice of a closed-loop, servo-hydraulic machine has been made necessary by factors detailed in 4:3.10. The normal testing equipment employed in this type of investigation has been the Instron type of screw driven machine and there have been doubts expressed on the consistency of the stiffness with load, time, temperature and successive relaxations. It was decided to investigate this problem briefly in the present work with an available Instron TTC machine. This work, which has been described in reference (1), consisted of a comparison of the relaxation of a plastically deformed patented wire specimen with that of an elastic mild steel bar from the same initial stress: the relaxations were not significantly different and further investigation was considered unwarranted within the scope of the present work. A summary of previous work and comments on this important problem is given in (4:3.10) and it is clear that owing to the magnitude and the inability to predict the machine component of a relaxation reliably, previous work using machines of the screw driven Instron type must be regarded with extreme suspicion.

For the above reason it was decided to use a closed-loop, servo-hydraulic machine for accurate tests in uniaxial tension: the advantages of such a system have been explained by Solomon (239). The evaluation, development and use of such a system for use in the present work is described in A.I:1.1. Despite the utilization of such an inherently hard system it was found, by the use of the elastic mild steel specimen, that there was significant relaxation present. An extensive programme of machine calibration was undertaken in order to produce values of machine relaxation for various times and loading rates (to give the required range of initial loads for the 180 second loading period). It was found

You may join the Society now, in which case you will be able to enjoy its facilities immediately. Just complete the attached form and send it together with your subscription to the Chief Clerk.

The life subscription to the Society is £41.60 inclusive, or an annual subscription of £24.20 or a contributing subscription of £5.60 followed by 8 monthly payments of £4.70 by Bankers Order.

analytically the resulting load relaxation data.

relaxations vs. initial load for particular times

relaxation have shown very good linearity: an

r.(5:7). This linearity was present at all times and

tions for other initial loads could be inter-

This technique required considerable calculation

For this reason computer techniques were employed to generate a

3-dimensional array of machine relaxation with time and initial load.

As an investigation of not only a first but also a subsequent relaxation (with the specimen being reloaded to the same initial load) was envisaged, it was necessary to calibrate the machine relaxation for these subsequent tests as well. Machine calibration data is given in A.II.

It was occasionally found, however, despite the precautions taken, that the accuracy of the machine calibrations was inadequate for tests with initial loads giving relatively small specimen relaxation (typically $< 10N$). This problem tended to be more severe for the LTHT wires which showed little relaxation up to higher loads, at which machine relaxation was more significant. As described previously (Ch.4), this machine relaxation is generally thought to be largely due to relaxation in the epoxy bonding in the load cell and it was considered that this problem could only be reduced further by the acquisition of a load cell of radically different design.

No digital data acquisition equipment was available for the present work: this in many ways is unfortunate. Solomon (239) has described the value of data collected at short relaxation times, but without equipment of this type the information must be lost. The method of data collection is described in A.I:1.1.6.2.1. and the techniques employed in its analysis in A.II.

5:4.3 Consistency evaluation:

In addition to the evaluations which have been described above, concerning the nature of the relaxation test itself, consistency tests were undertaken to evaluate the testing system and the adopted procedures once they had been developed to as high an accuracy as possible. This was achieved by relaxation tests on 20, A/R, 30mm gauge length, patented wire specimens, with gauge areas within $\pm 2\%$. Each was loaded under the same strain rate to approximately 5kN, at which load the specimens were showing uniform plastic deformation. It was found that the stresses

attained varied by less than $\pm 1\%$ and that the subsequent 1st and 2nd relaxations varied by less than $\pm 4\%$. It is considered that these accuracies fully justify the detailed analysis of the data which has been undertaken.

5:4.4 Preliminary investigation into the nature of the stress relaxation test

The basic features of the stress relaxation test have been outlined in(4:1); it is characterised by a time dependent stress drop which is not proportional to the applied stress and which is not recoverable. It is clear from any of the relaxation curves shown from the present work, or elsewhere, that the value of $\dot{\sigma}$ is a complex function of, but reduces monotonically with, time. Once the machine had been fully calibrated it was possible to investigate whether the stress relaxation was recoverable when the applied stress was removed. This was achieved by relaxing a standard patented steel wire specimen for a period of 30 minutes from an initial load of 5kN (a stress normally between 1650 and 1700MPa) and noting the load loss (of the order of 500N). The indicated load on the specimen was reduced to approximately 1kN and it was allowed to change for a further 30 minutes and the increase if present was noted. This apparent increase in the load was due to 2 possible anelastic processes: firstly in the machine (particularly the load cell - see 4:10) and secondly in the specimen. The anelastic relaxation in the machine (trials showed it to be fully reversible within 15 minutes of unloading) had been fully documented by the calibration tests, and thus any anelastic behaviour in the specimen could be deduced. In the above investigation the anelastic component of the specimen relaxation was found to be below 10N (the limit of accuracy of a single machine relaxation test over a long time period). In order to verify that anelastic behaviour was not proportionally more important at other stresses, the investigations were extended to lower loads: the result was similar indicating that anelastic behaviour in a relaxation of effectively infinite period in patented wire is negligible. This appears at variance with the comments of Lloyd and McElroy (135 to 137) but is not necessarily relevant to finite frequencies (e.g. as in a damping experiment) where anelastic relaxation are important or possibly dominate the behaviour.

5:4.5 Effect of relaxation on the material under test

It has often been assumed that the deformation which occurs during a relaxation is sufficiently small not to significantly alter the microstructure and properties of a specimen, e.g. Hart (165). If this concept were correct, an immediate repeat relaxation from the same stress as the initial test would yield identical results. Such tests have been undertaken in the present work with all the materials under investigation. Detailed analytical investigation of these, by means of existing relaxation models, are discussed in a following section, while the more obvious differences in the stress time data obtained are examined here.

It was found that, without exception, the total stress relaxation after any chosen time was significantly less for the second relaxation whatever the condition of the material. It has been suggested that this hardening of the material, in the sense of an increased resistance to small scale plastic flow, can be quantified by a graph of $\delta\sigma$ vs. $\delta\epsilon$: $\delta\sigma$ being the difference in stress between the 2 relaxations after 400 seconds (the limit of these standard tests) and $\delta\epsilon$ the strain which had to be applied to return the specimen to the chosen initial stress - see Sargent (261). An example for A/R patented wire is given in fig.(5:8a). As can be seen the correlation between these two variables is poor and it is considered that assigning a value to the Sargent hardening parameter $\delta\sigma/\delta\epsilon$ on this basis would not be sound: similar scatter and range was evident for all materials in the present study. In addition, no satisfactory relationship could be found between either $\delta\epsilon$ or $\delta\sigma$ and the initial relaxation stress. This lack of correlation is not entirely surprising as it assumes $\delta\sigma$ will be a unique function of a single deformation parameter, e.g. σ . As has been previously described, the mechanical state at the onset of the relaxations will not only be dependent on the initial material state and the initial relaxation stress but also, for example, the strain rate and loading time. While Sargent has shown a relationship between $\delta\sigma$ and $\delta\epsilon$, it must be remembered that the magnitudes of the 2 variables appear to have been much greater for reasons which may have included a considerable amount of machine relaxation.

The important information which can be deduced from these observations is that there is a significant strain hardening during a relaxation at this test temperature. Its magnitude can be a significant fraction of the overall relaxation and although the processes involved are no doubt

complex (both strain hardening and recovery may well occur) its presence must cast doubt on the use of this type of test of this duration to investigate the mechanical state of a material after a given deformation has been imposed, which assumes negligible plastic strain (and therefore change in state) during the test, e.g. Hart (165).

It has been shown that the strain hardening continues with further successive relaxations, in the A/R material, fig.(5:8b), the values of $\delta\sigma$ decreasing as shown. (These tests were performed at approximately the 0.2% proof stress: repeated tests above this value often caused failure before $\delta\sigma$ reduced to zero.) Similar although more rapid, reductions in $\delta\sigma$ were observed in the LTHT materials.

The effect of a relaxation on A/R wire at a stress approaching its UTS, immediately preceeding a stress/strain determination has been investigated: a typical result is shown in fig.(5:9). As can be immediately seen the linear region of the curve has been extended to a higher stress (the proof stress has been significantly improved) and the UTS slightly increased. Such features are extremely similar to those produced by the LTHT at 200°C, see fig.(5:14b). It was also noted that if, after relaxation, the specimen was aged at room temperature (see the following section) the stress/strain curve reverted to the A/R material behaviour. Such evidence suggests that the microstructural processes which occur during LTHT at 200°C or relaxation are essentially similar.

5:4.6 Effects on subsequent relaxations of ageing specimens at room temperature

While successive relaxations have been shown to cause significant strain hardening in patented wire it has also been shown that ageing specimens at room temperature causes an increase in the relaxation (after 400s of test). Examples of this phenomenon are given in fig.(5:10), where 2 sets of curves for the 1st and 2nd relaxations are shown for a specimen of A/R material with a period of 24 hours between each set. As can be seen, there was a significant return of the relaxation between the 2nd and 3rd curve. The changes in $\delta\sigma$ (as defined in the previous section) with changing ageing time are given in fig.(5:11a), where the ageing time has been varied between zero and 720 hours. Similar curves for A/R + LTHT "A" are given in fig.(5:11b), in this case $\delta\sigma$ asymptoting to zero over a shorter period. The period over which $\delta\sigma$ fell to $1/e$ of the initial

value (obtained from the curves obtained for each case) for a variety of initial relaxation stresses has been obtained for the A/R material: the values are shown in fig.(5:12) and show good consistency.

5:4.7 Changes in magnitude of relaxation with stress

Information on the relaxation with varying initial stress is of great importance to component designers. Such information is readily extracted from the data analysis developed in the present work (A.II): examples of which are given in the following section and in (6:3.3.2.2) (for the 17-7PH stainless steel).

In fig.(5:13a) are displayed a number of relaxation curves for A/R patented wire at various initial stresses, indicated on the stress strain curve (fig.(5:13b)): the corresponding information for the other micro-structural states of this wire are given in figs.(5:14, 5:15, and 5:16). In order to accentuate the pattern of relaxation with initial load, the stress drop (in MPa) after 400 seconds has been related to the initial stress (in MPa) for the 1st and 2nd relaxations for each material, figs. 5:17 to 5:20. It is clear that the LTHT programme improved the relaxation performance of the patented wire, the best performance being shown by the LTHT "A" and "B" materials. The most extreme heat treatment (LTHT "C") showed a significant deterioration in this property. Another important point was that on heat treatment, the range of initial stresses over which relaxation becomes significant diminished rapidly. It can also be noted, that the stress at which significant relaxation becomes apparent correlated well with the onset of non-linearity in the requisite stress/strain plot (figs.(5:13b to 5:16b)). The above changes also occurred in the appropriate 2nd relaxations, although the effects were not so pronounced. In comparing the behaviour on 1st and 2nd relaxations for the A/R material, the marked reduction in the range of initial stress over which significant relaxation occurred is obvious: such a reduction was not present in the heat treated materials (see 5:4.6).

5:4.8 Relaxations of patented wire specimens over periods exceeding 400 seconds

Relaxations of periods up to 7200 seconds were undertaken on patented wire to compare the behaviour exhibited by A/R and A/R + LTHT "A" material at similar initial stresses. In fig.(5:21a) the stress was chosen to be such as to give significant relaxation in each material, i.e. at a stress

greater than linear part to the relevant stress/strain curve. In fig.(5:21b) the stress was such as to give significant relaxation in only A/R wire while in (5:21c) it was sufficiently low to give small relaxations in each case. It can be seen that at high initial stresses, relaxation of decreasing rate continues over the whole period shown (a feature which has also been demonstrated in the spring tests 5:3). The marked difference in behaviour in the stress chosen in fig.(5:20b) (approximately 520 MPa) indicates the importance of long term tests for material evaluation in this type of failure. In the classification adopted by other workers (see section 4:3), the majority of relaxation, where it is significant, appears to be complete in approximately 2000 seconds. This is to be contrasted with the spring testing programme where a similar measure was 72 hours.

5:4.9 Variation of dislocation parameters during relaxation in patented wire with various initial loads and heat treatments

5:4.9.1 Introduction

The high resolution mechanical testing techniques, allied with the data reduction systems have allowed an evaluation of the various models which have been developed to describe stress relaxation of infinitely long time period. A review and detailed analysis of the available theories has been given in (4:3) and the following comments are based on this work. The data reduction systems developed in the present work (see A.II) not only allowed a rapid and complete presentation of absolute relaxation information for 1st and 2nd relaxations performed on a given specimen, but also provided graphs of various types relating to the main types of relaxation theories previously developed. Thus, for each relaxation the following graphs have been obtained:

- a) Load relaxations (in N) vs. time for the specimen plus machine component, and for the machine alone (for the appropriate initial load);
- b) Stress relaxation (in MPa) vs. time, corrected for machine relaxation;
- c) $\ln(\dot{\sigma})$ vs. $\ln(t)$;
- d) $\ln(\dot{\sigma})$ vs. stress drop, $\Delta\sigma(t)$;
- e) stress drop vs. $\ln(t)$.

It should be noted that in the last 3 cases the vertical scaling can vary for each relaxation: complete information is available in A.II.

It has been impossible to include complete sets of information for

each relaxation in the present work: information has been extracted where required. However, a number of examples (figs. 5:22 to 5:25) have been included in order to exemplify the data format. A set of graphs for each state of the patented wire has been given in these figures, each example chosen showing a significant relaxation, i.e. from an initial stress above that of the linear region of the stress/strain curve. In each case the following comments should be noted:

fig.(a) the machine relaxation is signified by 3 curves, the predicted curve together with curves indicating twice the standard deviation;

fig.(b) the true specimen curve has been given (green) with the highest and lowest curves given by the standard deviation values from the machine relaxation;

fig.(c) values for $\ln(-\dot{\sigma})$ vs. $\ln t$ have been given along with highest lowest values from the above error (all points in red);

fig.(d) values for $\ln(-\dot{\sigma})$ vs. $\Delta\sigma$, the error range points being given in green;

fig.(e) values for $\Delta\sigma$ vs. $\ln t$, the error range points being in black. As can be seen, the errors which are present from the machine relaxation, in the given examples, are negligible.

5:4.9.2. Variations in dislocation velocity exponent, m^* , with test variables

5:4.9.2.1. Introduction

As explained in detail in(4:3.4.4.2), the Li analysis of stress relaxation data is based on the Johnson-Gilman dislocation velocity equation:

$$\bar{v} = B \tau^{m^*} \quad (\text{eq.}^n \quad 4:8)$$

where m^* is the dislocation velocity exponent, and the basic assumptions are (in addition to the validity of the above relationship) that both ρ_m and σ_i are constant during the relaxation. These assumptions lead to the conclusion that the slope s'' of the $\ln(-\dot{\sigma})$ vs. $\ln(t)$ graph at large t is given by

$$s'' = \frac{m^*}{1-m^*} \quad (\text{eq.}^n \quad 4:68)$$

The data reduction systems evolved in the present work allow a comparison of s'' , and therefore m^* to be made with time during a relaxation test, initial load and material heat treatment.

5:4.9.2.2 Behaviour of patented wire

In the A/R material, the plots of $\ln(\dot{\sigma})$ vs. $\ln t$ produced have the characteristic form of those produced in previous work. The linearity should, from the analysis, be present at large t and in the present work this was generally correct for times greater than approximately 3 seconds. The gradient (s'') of the linear region was calculated and is displayed in fig.(5:26a) for both 1st and 2nd relaxations with initial stress: the corresponding graphs of m^* are given in fig.(5:26b). All observed values of m^* were found to be negative with a rapid change in value during the transition period between linearity in the stress/strain curve and general plastic flow. The values for m^* for 2nd relaxations are significantly lower than for the 1st relaxations as indicated by the second curve. Such negative values of m^* do not appear to have physical significance in terms of the Johnson-Gilman equation (eq.ⁿ 4:8) although many materials appear to exhibit such behaviour, e.g. Law and Beshers (201). The values of m^* measured for the similar specimens aged at room temperature for 28 days following the above tests and retested in an identical manner, indicated the same trends in m^* although showing consistently less negative values (by up to approximately 10%).

The general characteristics of the $\ln(\dot{\sigma})$ vs. $\ln t$ graphs for LTHT "A" material were similar to those of A/R wire, the gradients and the changes in gradient with initial stress were, however, different and the values of s'' and m^* are depicted in fig.(5:27a,b). The values of m^* show a smaller range, with a higher initial stress required to show their decrease than was observed in the A/R material. The rate of change of m^* with initial stress was significant, greater than in the A/R material. As with the A/R material, the respective values of m^* for the 1st and 2nd relaxations were significantly lower when retesting followed a 28 day ageing at room temperature.

The trends shown by the shorter heat treatment (LTHT "A") were accentuated in LTHT "B" the values of m^* showing a more rapid decrease with initial stress, figs.(5:28(a,b)). In this material, although the values of m^* for the 2nd relaxations were consistently greater than for the 1st relaxations, the difference cannot be regarded as significant considering the possible errors inherent in the data.

In LTHT "C" material the range of values of m^* were similar to those exhibited in LTHT "B". There was, however, a significant increase in the

range of initial stress over which this change occurred. Again, m^* values for 1st and 2nd relaxations were, in general, similar within experimental error.

5:4.9.3. Variations in behaviour of $\ln(\dot{\sigma})$ vs. $\Delta\sigma$ graphs, with test variables

5:4.9.3.1. Introduction

The use of graphs of the form $\ln(-\dot{\sigma})$ vs. $\Delta\sigma$, have frequently been suggested (see section 4:3.4.4.) although, as was pointed out earlier, the various analyses attribute various qualities to them. From the thermal activation analysis (4:3.4.4.4.) the slope of such graphs are related to $\frac{V^*}{kT}$, or $\frac{|p|A^*}{kT}$. In the case of the present work graphs for the 1st and 2nd relaxations for the various states of the patented wire have been constructed over the widest practical range of initial stresses the modulus of the gradient being $\frac{|p|A^*}{kT}$. Sleeswky et al. (199) in their analysis indicated that if the slope of the graph was α_4 then

$$\frac{1}{\alpha_4} = \frac{\partial \ln \dot{\epsilon}_p}{\partial \sigma} \quad (\text{eq. } 4:67)$$

It is important to remember that these are two completely different approaches: it is also interesting to note that the latter, from its basic assumptions, regards α_4 as being constant during a relaxation, while Grosbras et al. (200) have shown that from equations 4:6 and 4:8 (i.e. using the Li analysis) and assuming $d\sigma_1 = 0$, then:

$$\frac{\partial \sigma}{\partial \ln \dot{\epsilon}_p} = \frac{m^*}{\sigma^*}$$

During a relaxation test σ^* is assumed to be continuously decreasing, so that $\frac{\partial \sigma}{\partial \ln \dot{\epsilon}_p}$ is an increasing function, m^* assumed to be constant.

Law and Beshers (201) have used graphs of $\log(-\dot{\sigma})$ vs. σ to investigate the failure of the Li analysis in hcp and fcc materials (see section 4:3.4.4.2 and fig. 4:10). The individual graphs from the present work can be used to investigate this concept, remembering that for the present graph the curvature is the reverse of that considered by the above workers.

5:4.9.3.2. Behaviour of patented wire

In the A/R wire it was generally found that the graphs of $\ln(\dot{\sigma})$ vs. $\Delta\sigma$ were linear after an initial drop in $\Delta\sigma$. This period of non linearity was found to correspond to that shown in the respective graph of $\ln(\dot{\sigma})$ vs. $\ln t$ to within less than 2 seconds. It was also noted that with decreasing initial stress the period of time over which the gradient was changing was more or less constant although the related value of $\Delta\sigma$ decreased considerably. It was found that the gradient of the $\ln(\dot{\sigma})$ vs. $\Delta\sigma$ graphs decreased from an initial high value to the lower, constant value. (The determinations of gradients in the initial part was found to be inaccurate due to more severe scatter).

Fig.(5:30a) shows the variation in gradient of the linear region for both 1st and 2nd relaxations. In all tests the value of the slope for the 2nd relaxation was more negative than for the 1st, although the amount was small and within the general error band. It can be clearly seen that the gradient becomes more negative with increasing initial stress and this change corresponds to the changes which were noted in the $\ln(\dot{\sigma})$ vs. $\ln t$ graphs and the material's stress/strain behaviour (figs.(5:26a,b and 5:13b)). Fig.(5:30b) shows the variations in value of $|b|A^*$ for the range of initial stresses. It was shown to be consistently larger for the 2nd relaxation at each initial stress and showed a variation between approximately $1.5 \times 10^{-22} \text{ m}^3$ and $6.8 \times 10^{-22} \text{ m}^3$. These values are much larger than those normally quoted for iron, or many other materials in the literature (e.g. see Hanley et al. (290), Balasubramanian and Li (291)). The changes observed on retesting the specimens after 28 days ageing at room temperature were more dramatic than those described in section (5:4.9.2.2.). In all retests except one 2nd relaxation, the values of the slopes were significantly higher than in the initial tests for both 1st and 2nd relaxations. While insufficient evidence is available to draw precise conclusions it was found that the slopes were increased by a factor of between 1.5 and 2.2, with a similar increase for the values of $|b|A^*$.

The corresponding behaviour for A/R + LTHT "A" patented wire is given in fig.(5:31): the LTHT again had a significant effect on the material property. Although the range of values of $|b|A^*$ is similar to the A/R material the range of initial stresses over which the decrease in $|b|A^*$ occurs is considerably reduced in line with reduced range of stress

over which yielding behaviour occurs in the stress/strain graph, fig.(5:14b). Again further testing would have been required to examine in detail the changes which occurred on 28 day, room temperature ageing. It was clear, however, that the marked increases in $|b|A^*$ noted in the A/R material were not indicated.

The effects of prolonging the 200°C heat treatment (LTHT "B") on the values of $|b|A^*$ were similar to those seen before in that their reduction occurred over a smaller range of initial stresses, corresponding to the yielding behaviour (see fig.(5:15b)). The range of magnitudes of $|b|A^*$ were, however, reduced (fig.(5:32b)), although it was interesting to note that the minimum value recorded was found to be similar ($1.5 \times 10^{-22.3} \text{ m}^3$) to those observed in the other heat treatments. The differences between 1st and 2nd relaxations were less evident than in the previous cases, the 2nd relaxation value of $|b|A^*$ not necessarily being higher than that of the 1st relaxation. It was noted in this material state for tests above approximately 1800MPa the $\ln(\dot{\sigma})$ vs. $\Delta\sigma$ graph, significant positive curvature was present during the entire range of $\Delta\sigma$: this is represented in the error margins in fig.(5:32b).

The trends described above were shown to be continued in the more severe heat treatment. The range of initial stresses over which changes in $|b|A^*$ were measured increased (as did concomitant changes in the stress/strain behaviour, fig.(5:16b), and m^* , fig.(5:29b)), i.e. the value of $|b|A^*$ was lower at below approximately 1850 MPa: again the minimum values obtained were similar to those derived from the other materials. A similar positive curvature to that noted in the LTHT "B" material was again detected at higher initial stresses.

5:4.9.4 Variations in behaviour of $\Delta\sigma$ vs. $\ln t$ graphs with test variables

5:4.9.4.1. Introduction

Graphs of this type have been used for a considerable period of time (see reference 1) and extensive use was made by Feltham (157) of an empirical relationship of the form:

$$-\Delta\sigma = \lambda' \log C - \lambda' \log (t + c) \quad (\text{eq}^n \text{ 4:46})$$

where λ' and c are constants, indicating a linear $-\Delta\sigma$ vs. $\ln t$ relationship at large t . Both Guin & Pratt (139) and Grosbras et al. (200) have strengthened the theoretical basis of this type of relationship by means of the thermal activation model. The latter workers showed that:

$$-\Delta\sigma = \frac{kT}{|b|A^*} \ln(1 + at) \quad (\text{eq}^n \text{ 4:81})$$

The graphs of $\Delta\sigma$ vs. $\ln t$ from the present work have been examined on this basis.

5:4.9.4.2 Behaviour of patented wire

The plots of $-\Delta\sigma$ vs. $\ln t$ in the A/R material were of typical form becoming linear at times greater than 20 seconds. This period of non-linearity was considerably greater than that shown by either of the other 2 plotting techniques and was approximately constant with initial stress. Fig.(5:34a) shows the variation in gradient of the linear region with initial relaxation stress for both the 1st and 2nd relaxations. In this case the values for the 2nd relaxation were found to be consistently less than for the 1st, although the experimental scatter did not allow an accurate trend to be ascertained. The corresponding values of $|b|A^*$ are given in fig.(5:34b) and it is instructive to compare them with the values obtained from the $\ln(\dot{\sigma})$ vs. $\Delta\sigma$ plots, fig.(5:30b). The trends in the reduction of $|b|A^*$ with increasing initial stress during the yielding process are very similar except that the magnitudes from this derivation are somewhat greater at lower initial stresses.

The same comments are also valid for the LTHT patented wire: the values of $|b|A^*$ at lower stresses tended to be somewhat higher than those indicated by the previous analysis, at higher stresses this analysis gave results in much closer agreement. The graphs for these materials are given in figs.(5:35, 5:36 and 5:37).

5:4.9.5. Determination of σ_i and σ^* values

Three basic methods of determining the variation of σ^* during a relaxation have been proposed: the first 2 assume that σ_i is constant during a relaxation. Gupta and Li (186) suggested that once m^* had been obtained from $\ln(-\dot{\sigma})$ vs. $\ln t$ plots at large t , the constant a'' in their form of the general equation:

$$\ln(-\dot{\sigma}) = \text{constant} - (n_1 + 1) \ln(t + a'') \quad (\text{eq}^n \text{ 5:1})$$

could be determined by the deviation from linearity. Then, σ_i can be found from 2 points on the curve thus:

$$\left(\frac{\sigma_1 - \sigma_i}{\sigma_2 - \sigma_i} \right) = \left(\frac{t_1 + a''}{t_2 + a''} \right)^{\frac{1}{m^* - 1}} \quad (\text{eq}^n \ 5:2)$$

This approach cannot be used in the present work as the values of m^* being negative, have no physical meaning, thus casting doubt onto the applicability of this theory to this material.

A different approach is to assume that if σ_i is constant during a relaxation, i.e. no strain hardening or recovery occurs, then as $t \rightarrow \infty$ then $\sigma^* \rightarrow 0$ and $\sigma \rightarrow \sigma_i$. Thus the stress/time curve will asymptote towards σ_i . The present work has shown that even after long periods at room temperature relaxation continues at a finite rate. This, of course, may well be evidence to suggest recovery processes being active.

Okazaki et al. (152 to 155) did not assume that σ_i was constant during a relaxation. They suggested that the mean internal stress between 2 time points t_1 and t_2 could be evaluated from the equation:

$$\sigma_{i(1,2)} = \sigma_2 + \frac{(\sigma_1 - \sigma_2)}{\left(1 - \frac{-\dot{\sigma}_1}{-\dot{\sigma}_2} \right)^{1/m^*}} \quad (\text{eq}^n \ 5:3)$$

Again this requires confidence in the value of m^* , which cannot be secured for the materials under investigation in the present work. It has therefore been concluded that values of σ_i and thus σ^* cannot, with the present data, be obtained.

5:5 Comments and Summary

5:5.1 Techniques

The present work has developed a high resolution testing system which has proved itself capable of satisfying the requirements of normal stress strain determinations and also providing valid stress relaxation data. It has been found that the equipment still has certain obvious limitations.

a) Machine relaxation is significant and although in the majority of tests at initial stresses where specimen relaxation is large ($> 10\text{N}$) the extensive calibration programme has proved effective, in some instances it has been found that the acquisition of a new design of load cell (e.g. capacitative or displacive) would be desirable.

(b) The data recording system is at present not sufficiently accurate,

particularly at short times (< 3 seconds). To improve this a digital, data-logging system would be necessary.

c) Within these limitations, however, the equipment has been shown to be exceptionally accurate and reliable by means of a series of consistency tests. The technique of loading in a constant time period (180s) was adopted as being more accurate and more in line with the industrial situation. The techniques employed in these tests can be adapted to many materials and test temperatures.

d) A technique of spring testing was perfected to enable the wires to be evaluated at various temperatures and stresses. By this method the spring wires could be tested under the complex stress configurations brought about not only by drawing and loading, but also by the coiling process itself. Improvements could easily be made with this work if wire of a smaller diameter could be obtained, and springs be coiled from it to a different specification, thus allowing a higher loading stress to be achieved.

e) An accurate and flexible data reduction system has been developed using computer techniques. This has allowed an accurate machine calibration to be produced and has allowed the raw relaxation data to be corrected for this error. A number of plots have been produced for the 1st and 2nd relaxations for all tests, allowing a second interpretation and evaluation of theoretical relaxation models to be made in the course of obtaining dislocation parameters of various types. This data reduction system can be further developed to produce further graphical displays and calculations and could be extended to give higher resolution particularly at short times, and for longer relaxation periods if a digital data logging system were to be available. The machine calibration could also be extended to produce a larger information matrix for the present machine or for any other testing machine which displays the same characteristic relaxation.

5:5.2 Information obtained

5:5.2.1. Tensile testing

(a) The high tensile strength of A/R patented wire was confirmed.

(b) Two batches of otherwise apparently identical A/R wire showed differing ductility.

(c) The main effects of LTHT were to increase the tensile strength slightly and to improve the proportional limit and proof stress dramatically. The

LTHTs "A" and "B" were shown to be the most beneficial to these properties.

5:5.2.2. Spring testing

- (a) Relaxation was found to increase with loading stress.
- (b) The relaxations could all be divided into 2 time periods: the first showing a rapid non-linear relaxation of increasing rate with loading stress (complete after 72 hours), the second a continuing period of approximately linear relaxation which persisted through the remainder of the test and whose rate increased with loading stress.
- (c) Below 100°C the testing technique was not sensitive enough to evaluate the relaxations (mainly due to the low loading stresses).
- (d) At 150°C the LTHT "A" caused a significant improvement in the relaxation behaviour.

5:5.2.3. High resolution stress relaxation testing

- (a) The stress relaxation was not recoverable with time, i.e. the anelastic component was negligible.
- (b) Significant strain hardening occurs during relaxation, although a hardening parameter could not be accurately specified owing to it not being a function of the initial stress alone.
- (c) A prior relaxation has a similar effect to LTHT "A" on subsequent stress/strain behaviour, i.e. the proof stress and proportional limit are dramatically improved.
- (d) The effect of ageing at room temperature was to negate the effect of the above hardening during a relaxation such that the parameter $\delta\sigma$ reduced asymptotically to zero after approximately 720 hours.
- (e) Specimen relaxation became significant at initial stresses which were approximately greater than the proportional limit. The best relaxation resistance was observed in materials with LTHTs "A" and "B".
- (f) At initial stresses significantly above this level, i.e. where general plasticity had occurred, the relaxation was essentially similar for all materials.
- (g) Tests undertaken for periods up to 7200 seconds indicated that relaxation was still continuing, although it was found that the majority of the stress drop occurred approximately within the initial 2000s (a considerably shorter period than was observed in the spring tests).
- (h) The values of m^* were found to be negative for all tests. This, under the original definition, is not possible although such behaviour has been noted elsewhere: possible causes have been advanced. The values of m^*

did, however, show consistent trends, becoming more negative with increasing initial stress for all heat treatments. The effects of LTHT were to reduce the range of m^* values and to reduce the range of initial stresses over which this change occurred, which correlated well with the changes in the stress/strain behaviour. The m^* values for the 2nd relaxations were always significantly less than for the 1st. The effects of a 28 day anneal at room temperature between a first pair of relaxations and a second pair was relatively insignificant.

(i) Values of $|b|A^*$ (often termed V^*) were determined from $\ln \dot{\sigma}$ vs. $\ln t$ plots and were found to be considerably larger than has been observed previously in less complex materials. The differences between the values of $|b|A^*$ for 1st and 2nd relaxations was not significant. It was found that its value decreased as the initial stress was increased from the proportional limit towards general plasticity. LTHT "A" caused this initial stress range to be decreased (correlating with the stress/strain behaviour), while for LTHTs "B" and "C" the range of $|b|A^*$ values was also decreased. In all materials, however, the minimum values of $|b|A^*$ at general plasticity were similar. It was found that the 28 day age at room temperature caused $|b|A^*$ values to be increased by a factor ranging between 1.5 to 2.2, for all materials, depending on initial stress.

(j) Values of $|b|A^*$ were also obtained from plots of $\Delta \sigma$ vs. $\ln t$. The plots showed linearity at times greater than approximately 20 seconds (as compared with approximately 3 seconds in plots discussed in (h) and (i) above). The values of $|b|A^*$ were found to be similar to those obtained in (i) above.

(k) It was found that values of σ_i and thus σ^* could not be determined in the present tests.

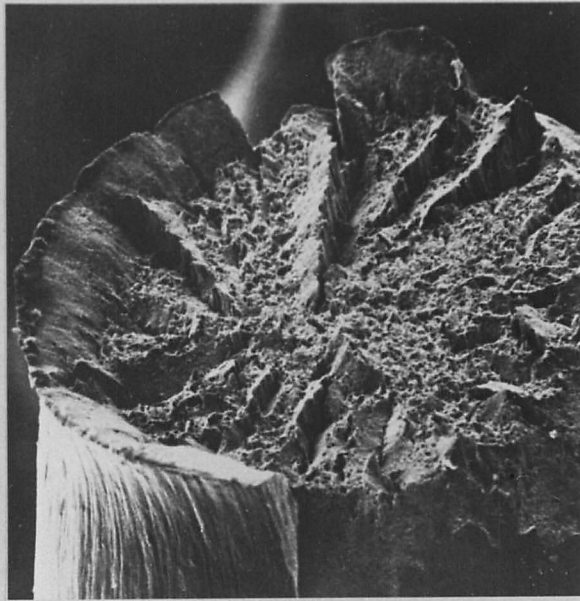


Fig. (5:1a) SEM of more ductile type of
tensile failure x60

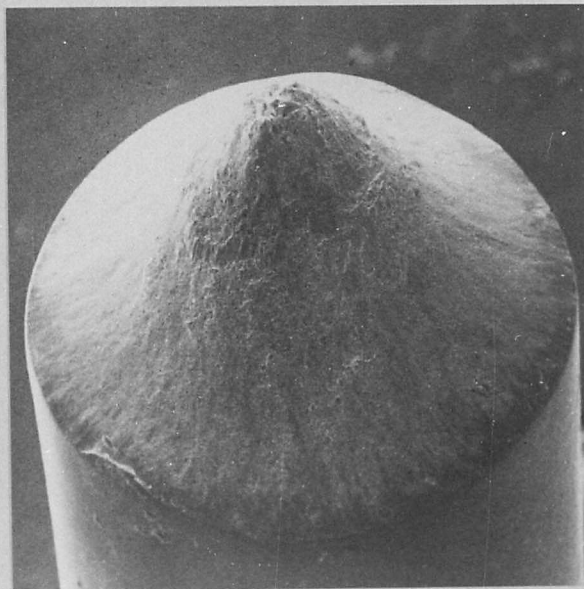


Fig.(5:1b) SEM of less ductile type of
tensile failure x50

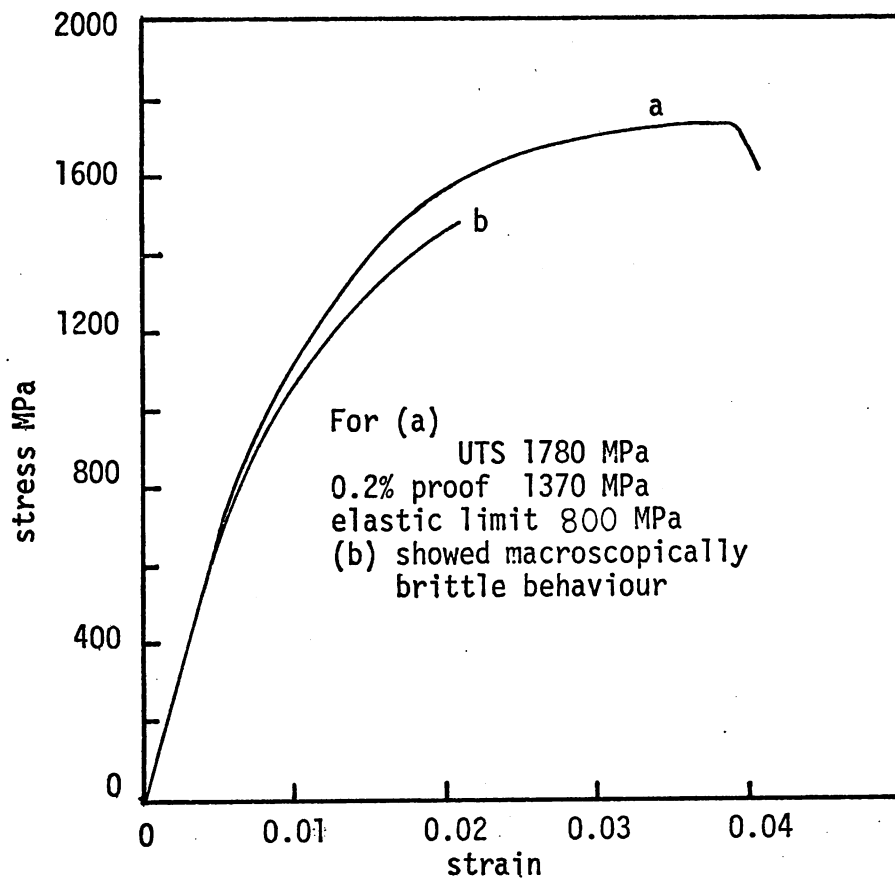


Fig. (5:2) Typical nominal σ/ϵ curves for A/R patented steel wire (reduction $\approx 70\%$).

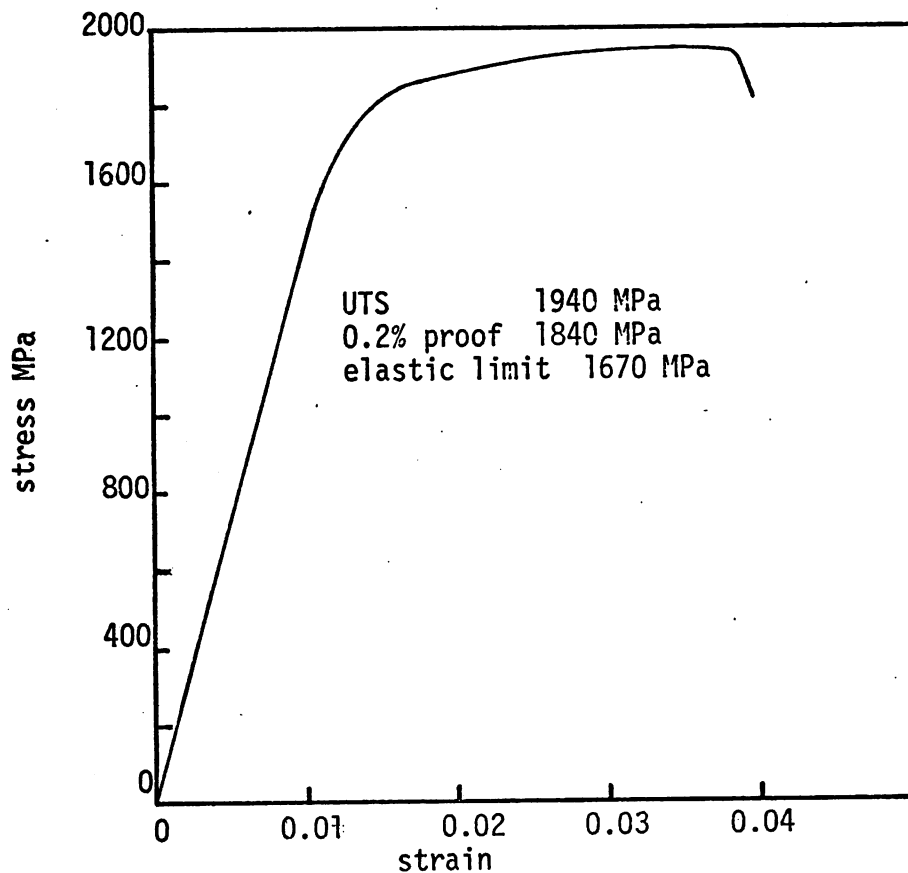


Fig. (5:3) Typical nominal σ/ϵ curve for A/R + LTHT "A" patented steel wire (reduction $\approx 70\%$).

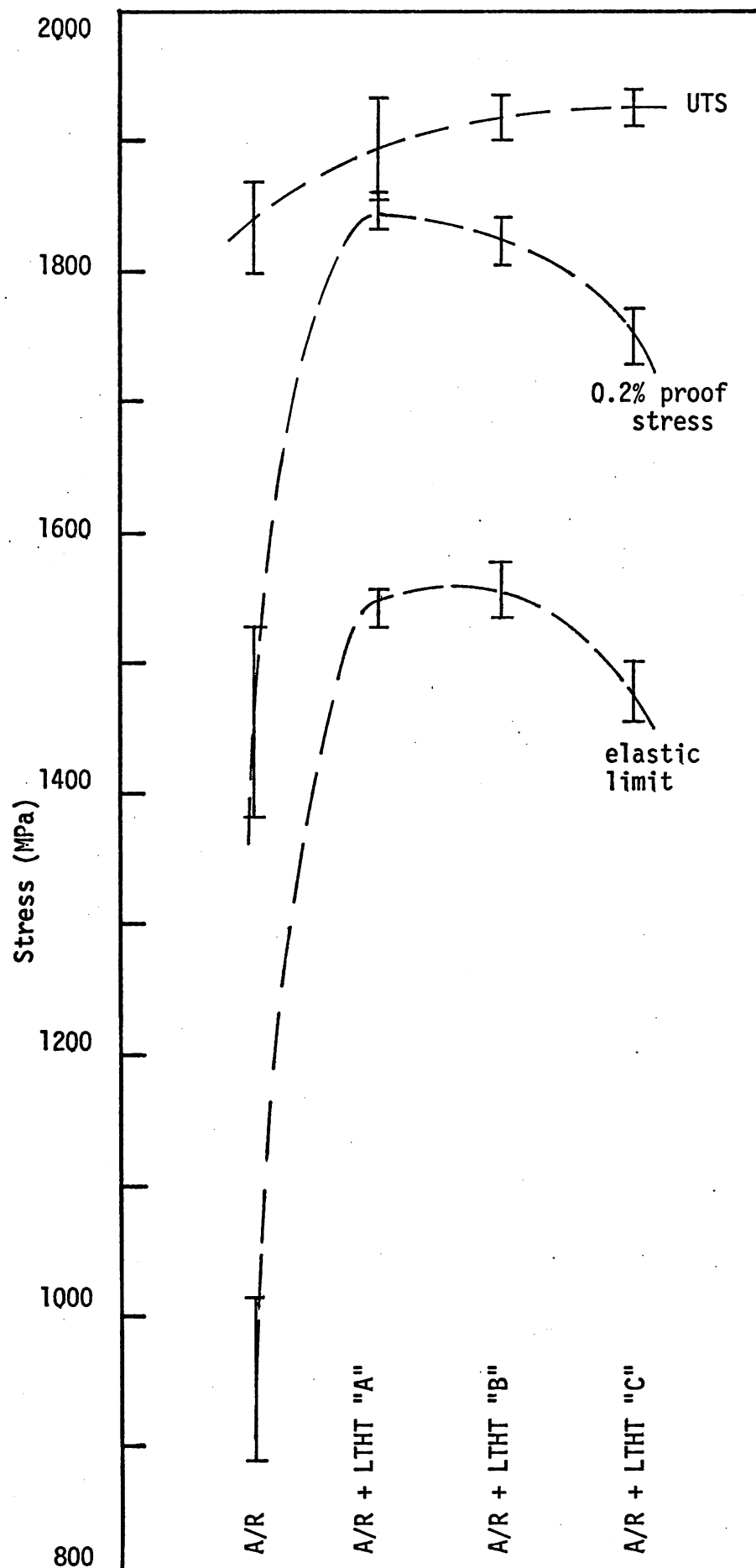


Fig. (5:4) Variation of elastic limit, 0.2% proof stress and UTS with LHTT, of patented steel wire (reduction $\approx 70\%$). Error bars indicate range of values obtained

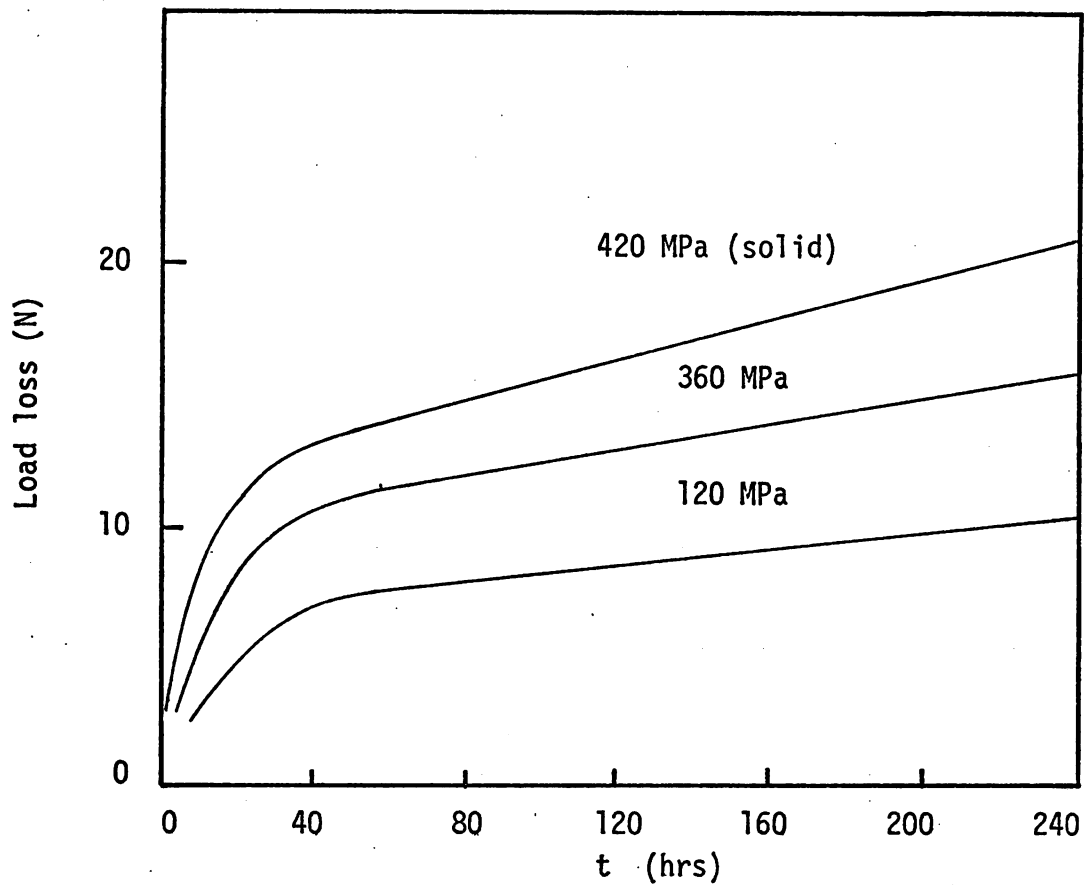


Fig. (5:5a) A/R patented steel wire, spring relaxation curves at 100°C , maximum shear stresses are noted.

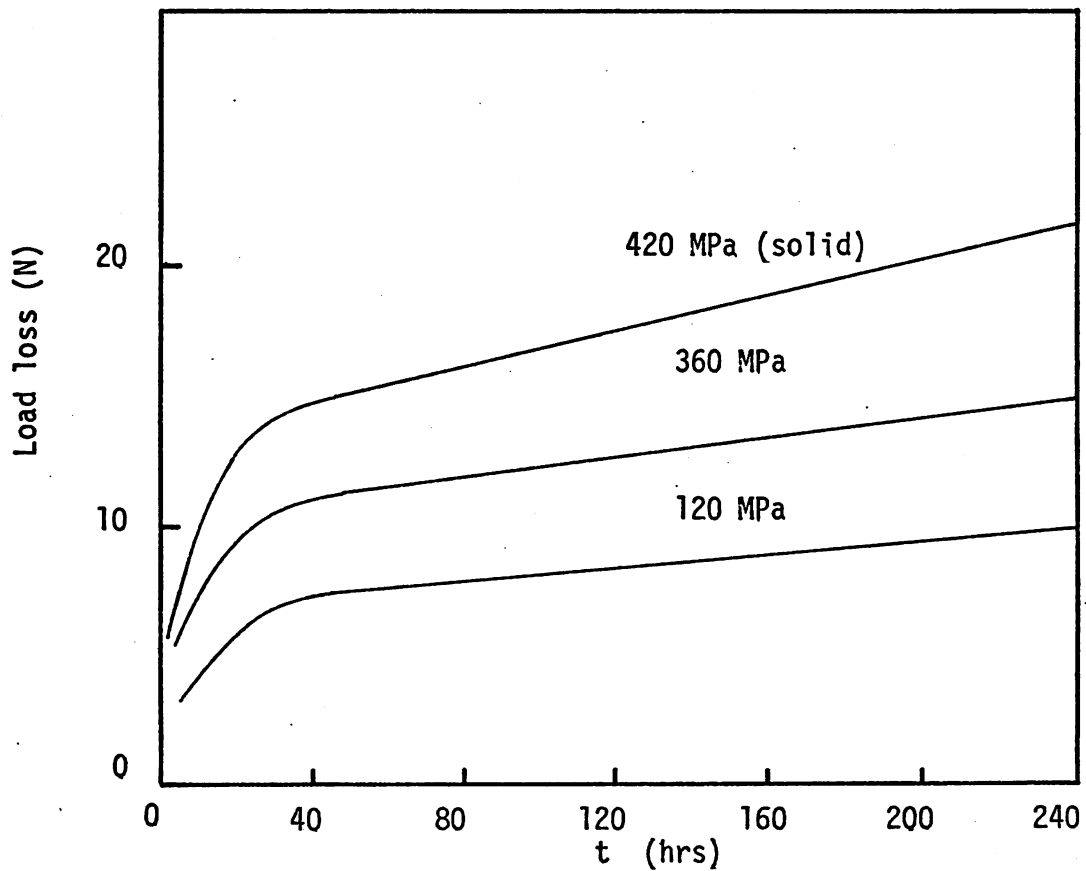


Fig. (5:5b) A/R + LTHT "A" patented steel wire, spring relaxation curves at 100°C , maximum shear stresses are noted.

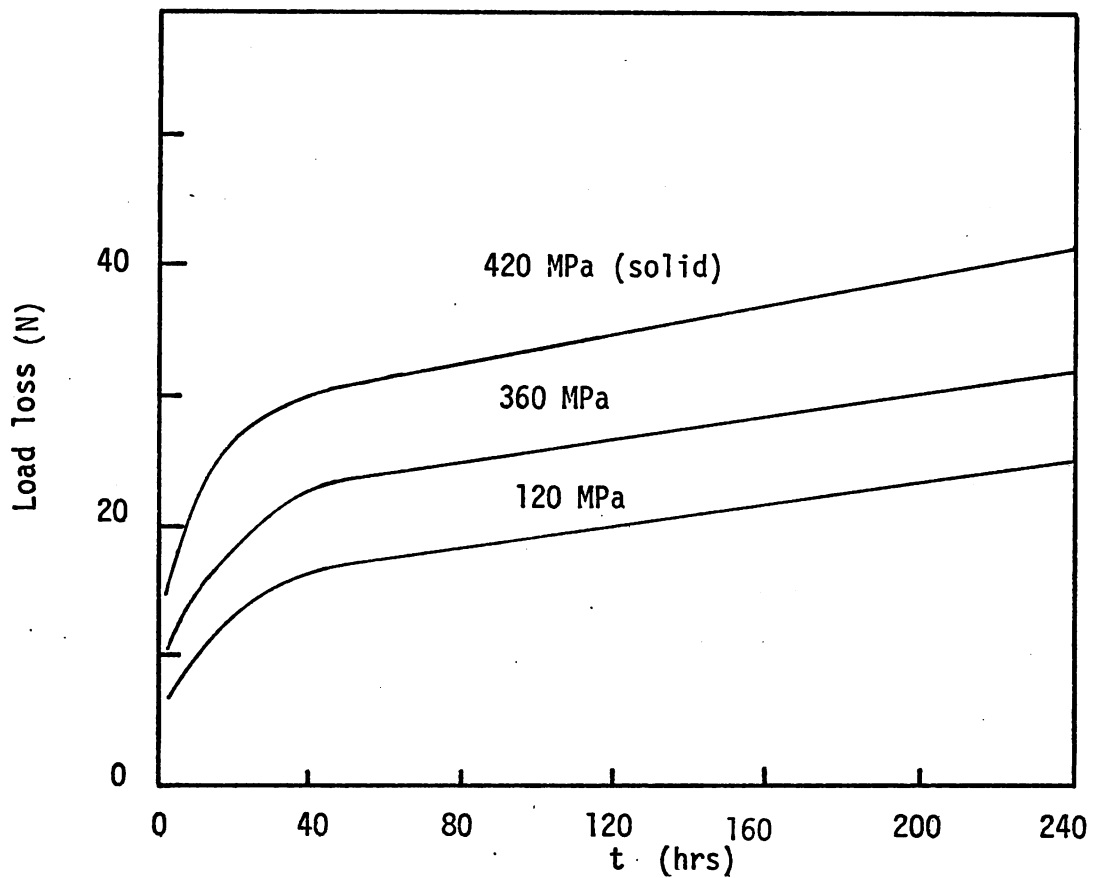


Fig. (5:5c) A/R patented steel wire, spring relaxations at 150°C, maximum shear stresses are noted.

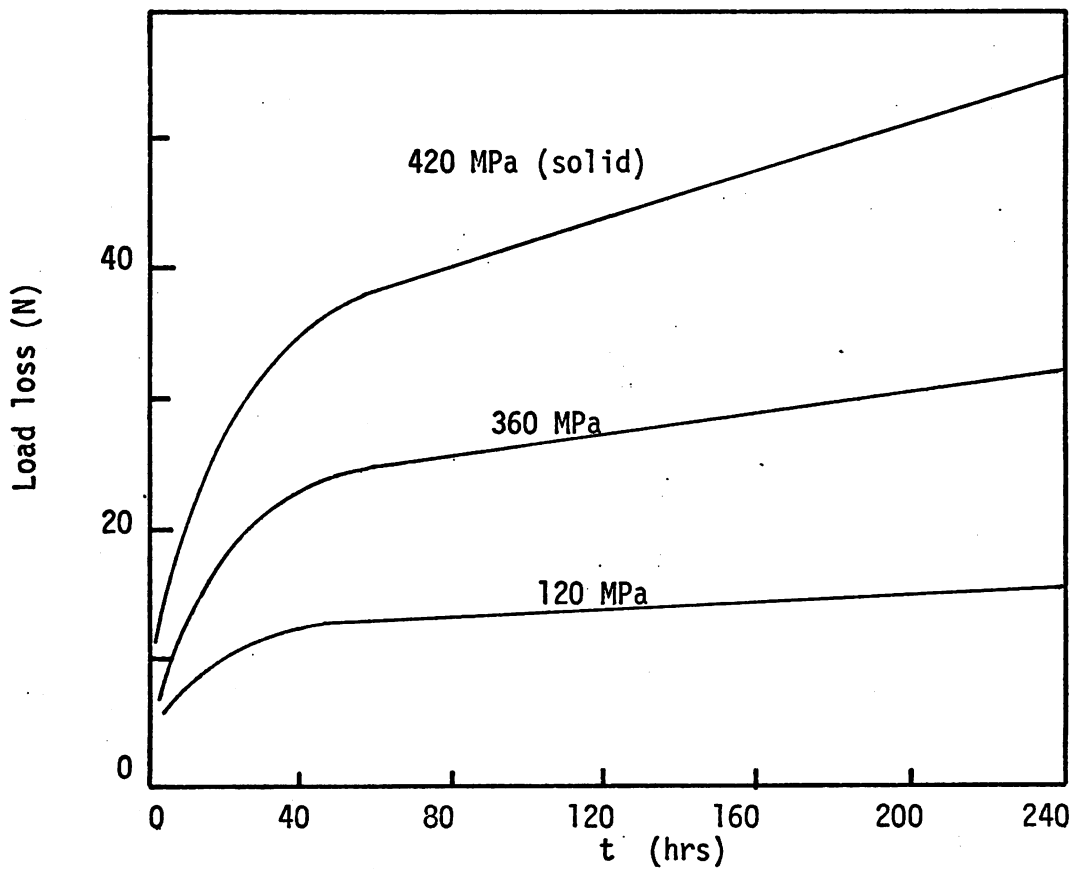


Fig. (5:5d) A/R LTHT "A" patented steel wire, spring relaxation at 150°C, maximum shear stresses are noted.

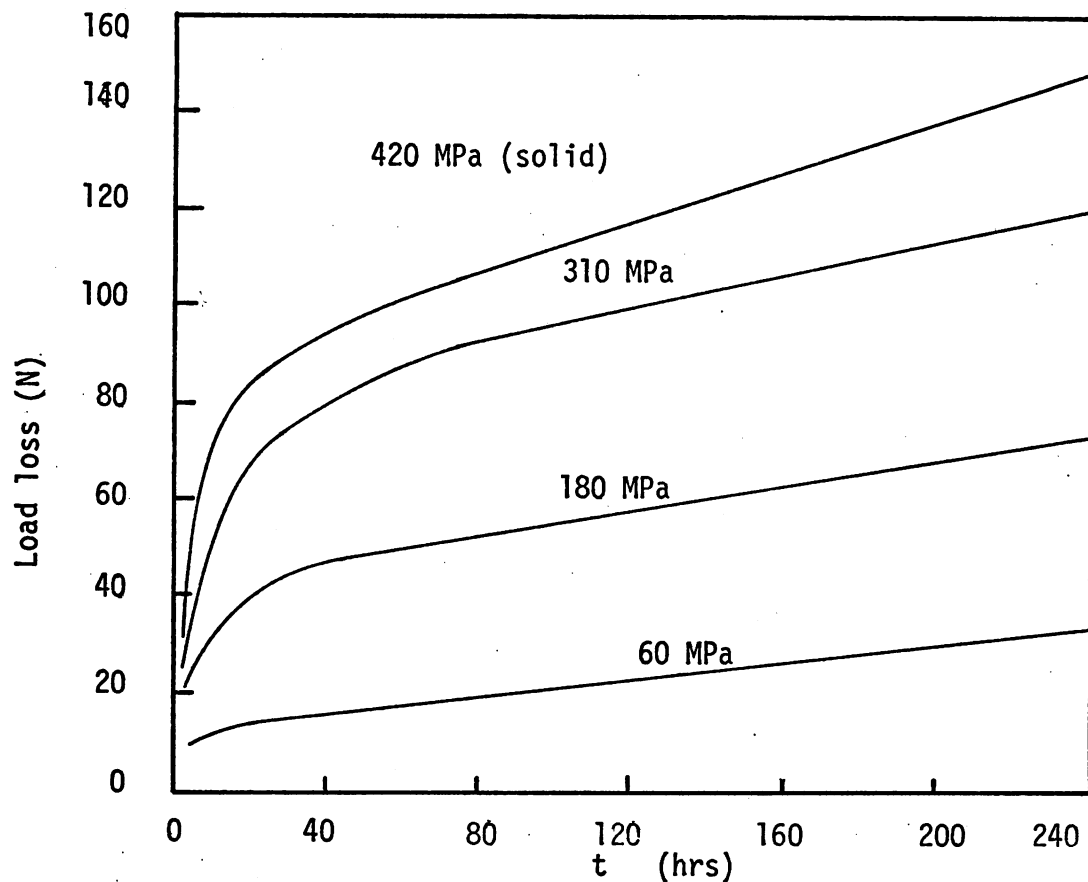


Fig. (5:5e) A/R patented steel wire, spring relaxation curves at 200°C, maximum shear stresses are noted.

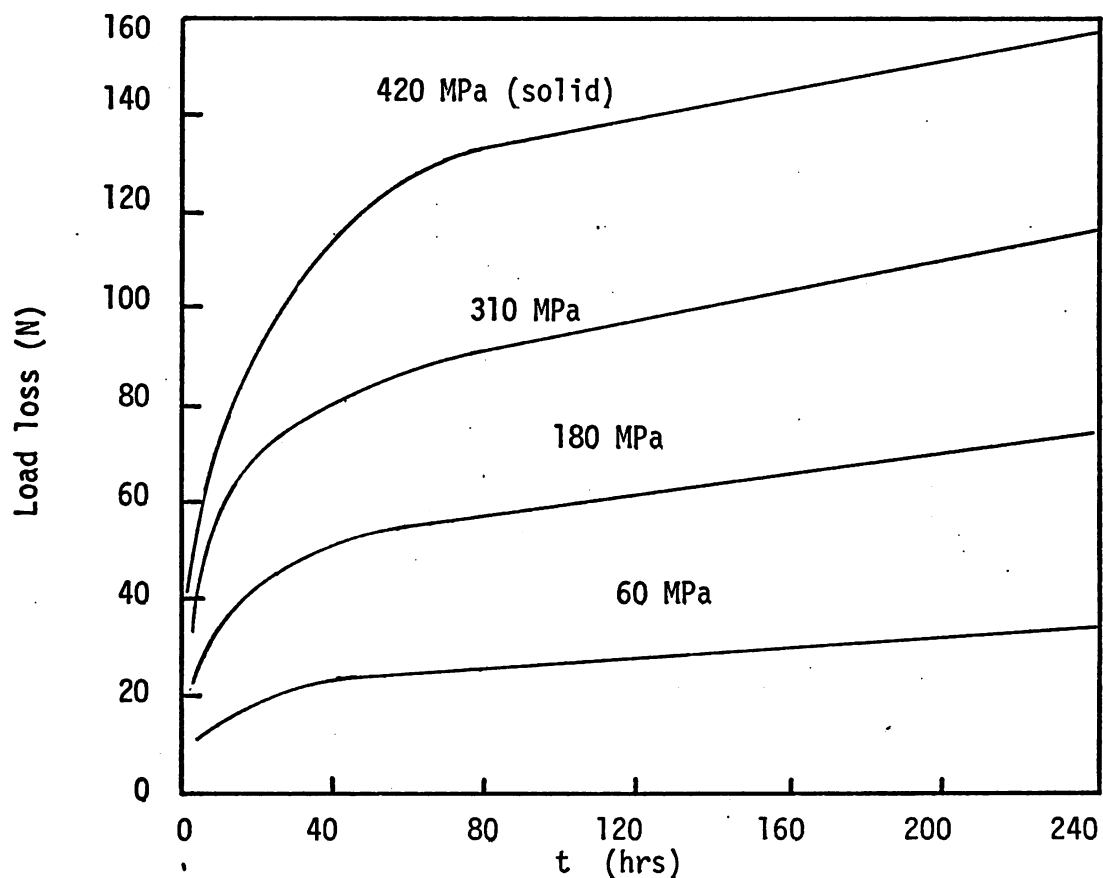


Fig. (5:5f) A/R + LTHT "A" patented steel wire, spring relaxation curves at 200°C, maximum shear stresses are noted.

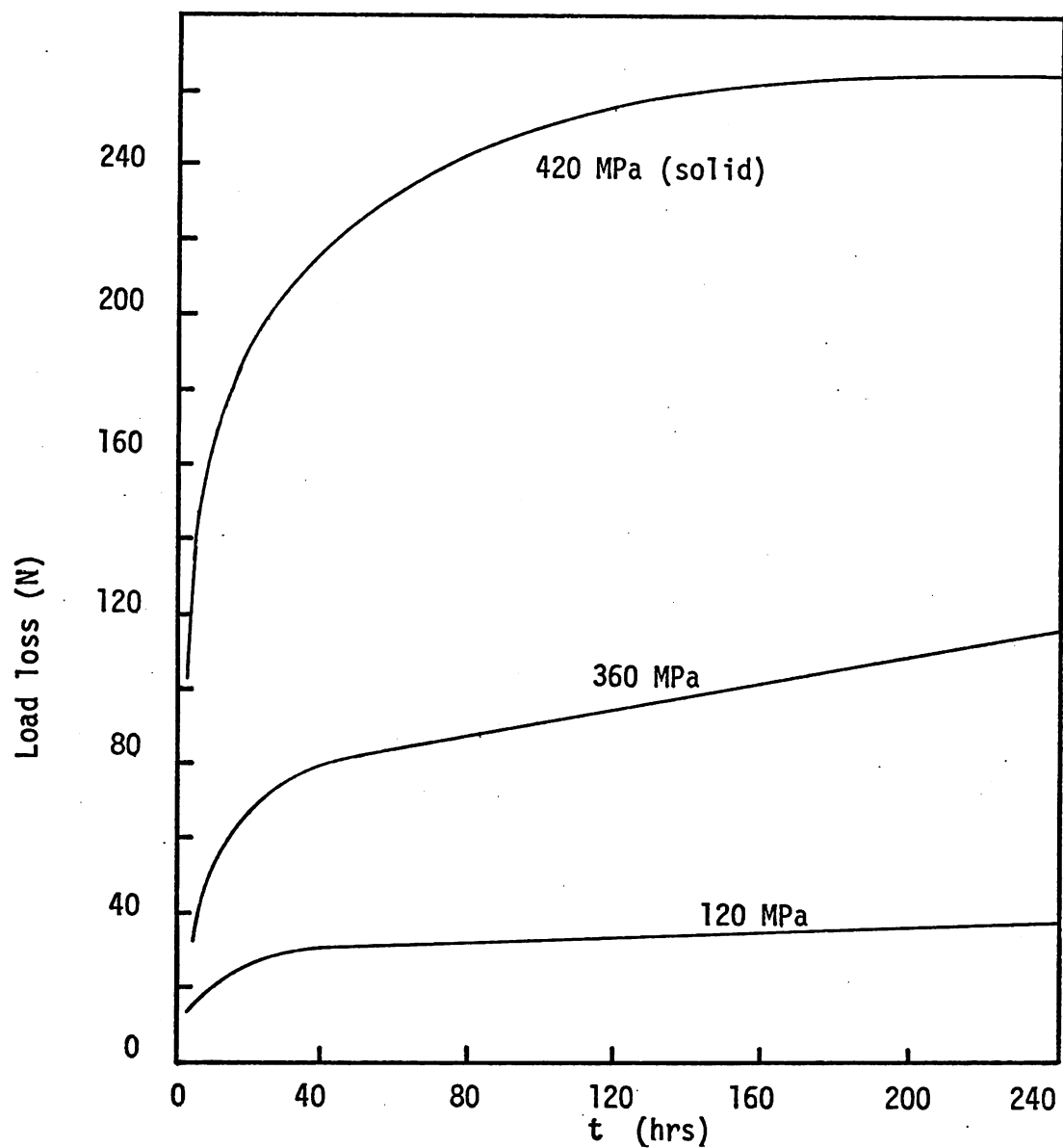


Fig. (5:5g) A/R patented steel wire, spring relaxation curves at 200°C, maximum shear stresses are noted.

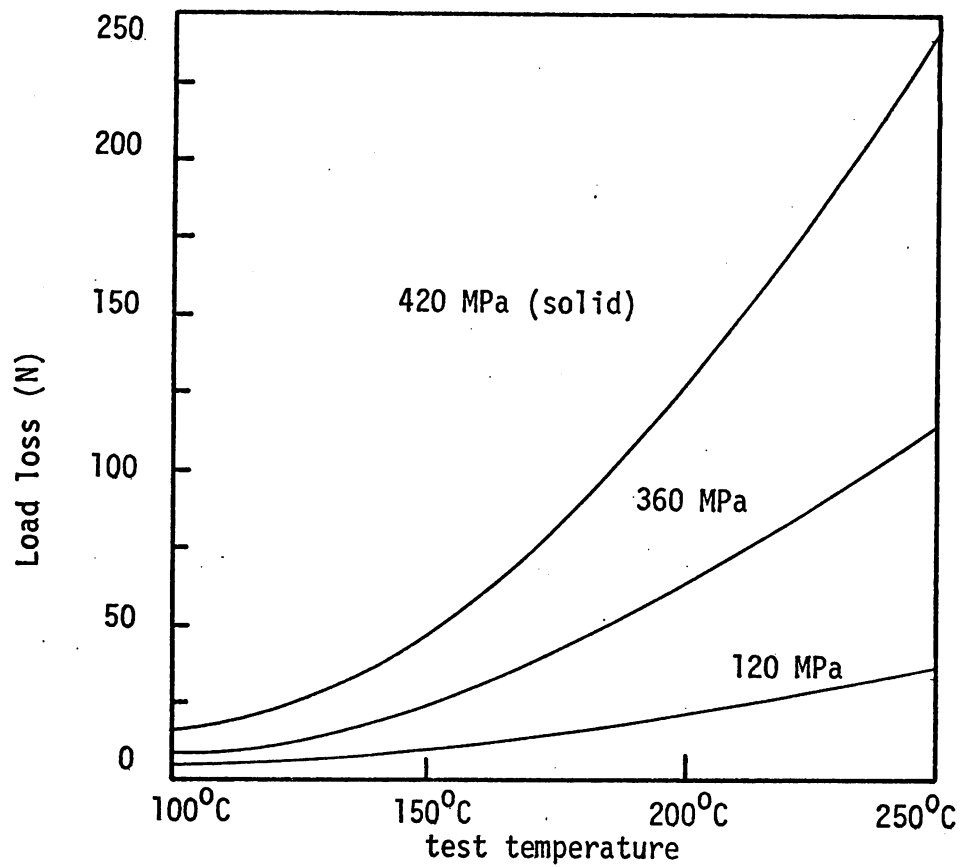


Fig. (5:6a) Relaxation of A/R patented steel wire springs after 72 hours, with temperature and stress.

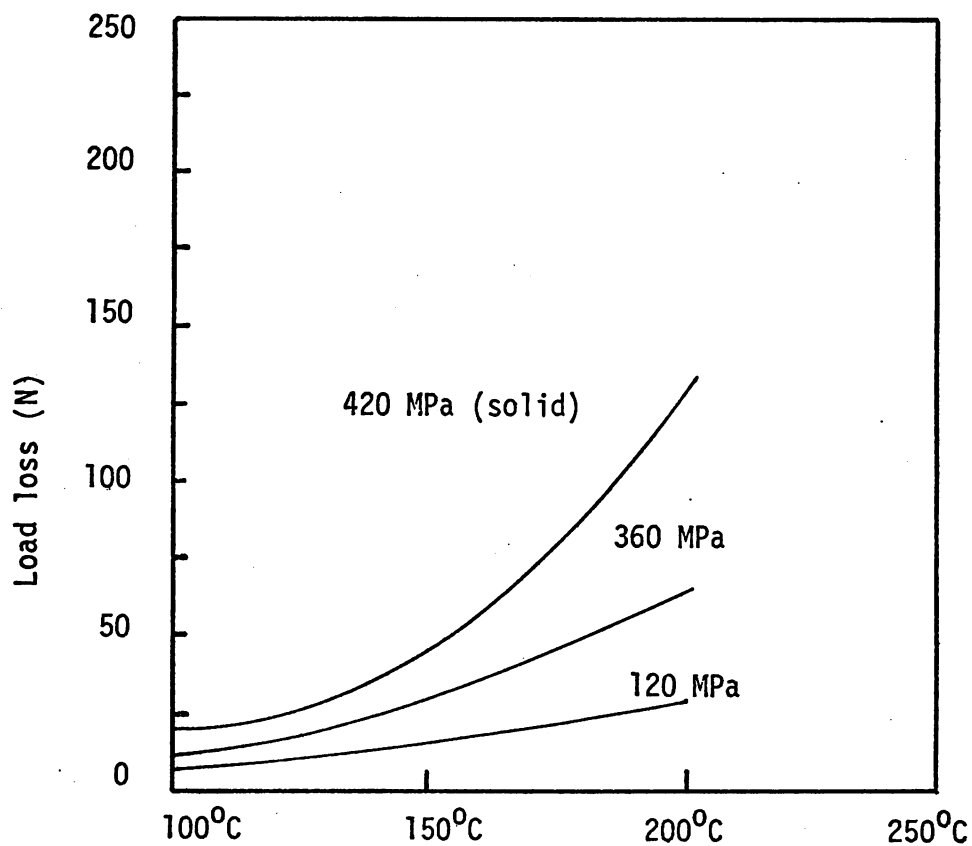


Fig. (5:6b) Relaxation of A/R LTHT "A" patented steel wire springs after 72 hours, with temperature and stress.

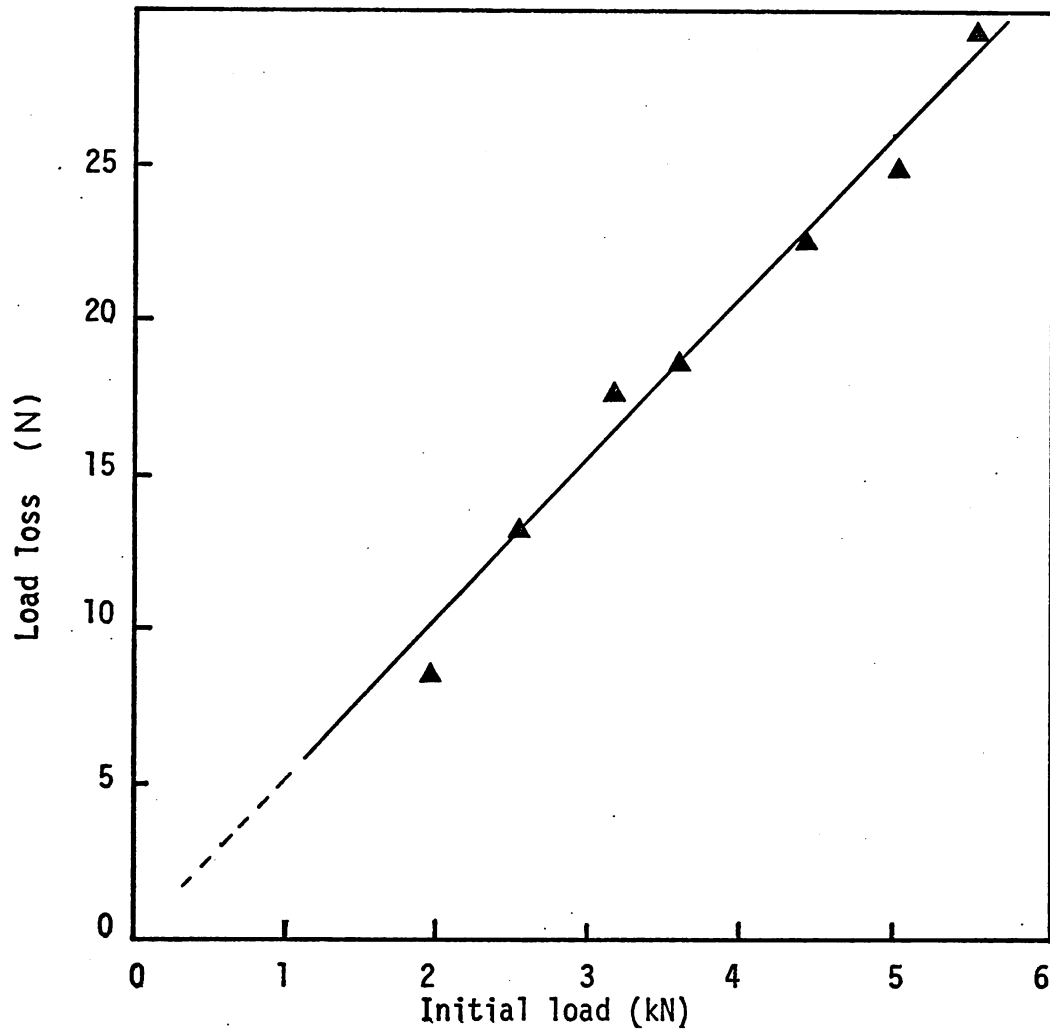


Fig. (5:7) Typical plot of 100kN Mand machine relaxations vs. initial load for a given time during tests.

Loading at various strain rates for 180 seconds to obtain loads. Load loss indicated is that shown after 30 seconds relaxation.

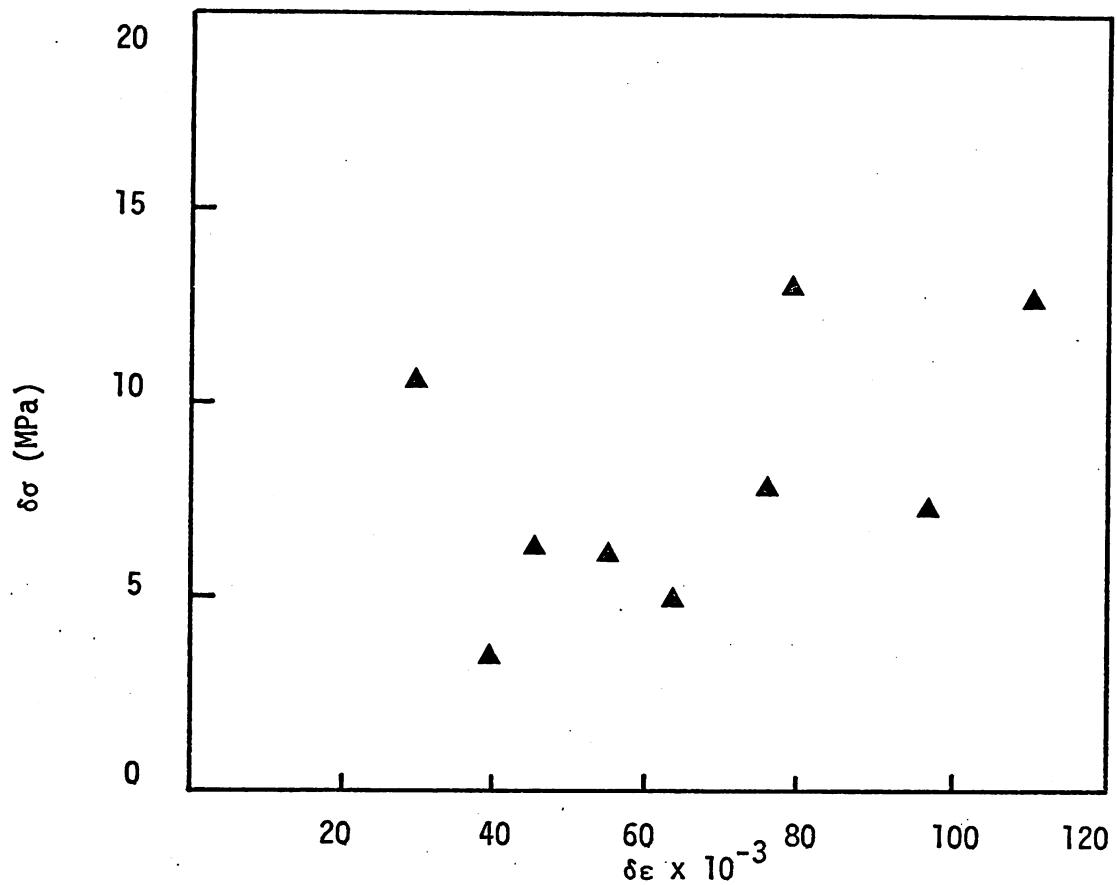


Fig. (5:8a) Plot of $\delta\sigma$ vs $\delta\epsilon$ for A/R patented wire for tests of various initial stresses.

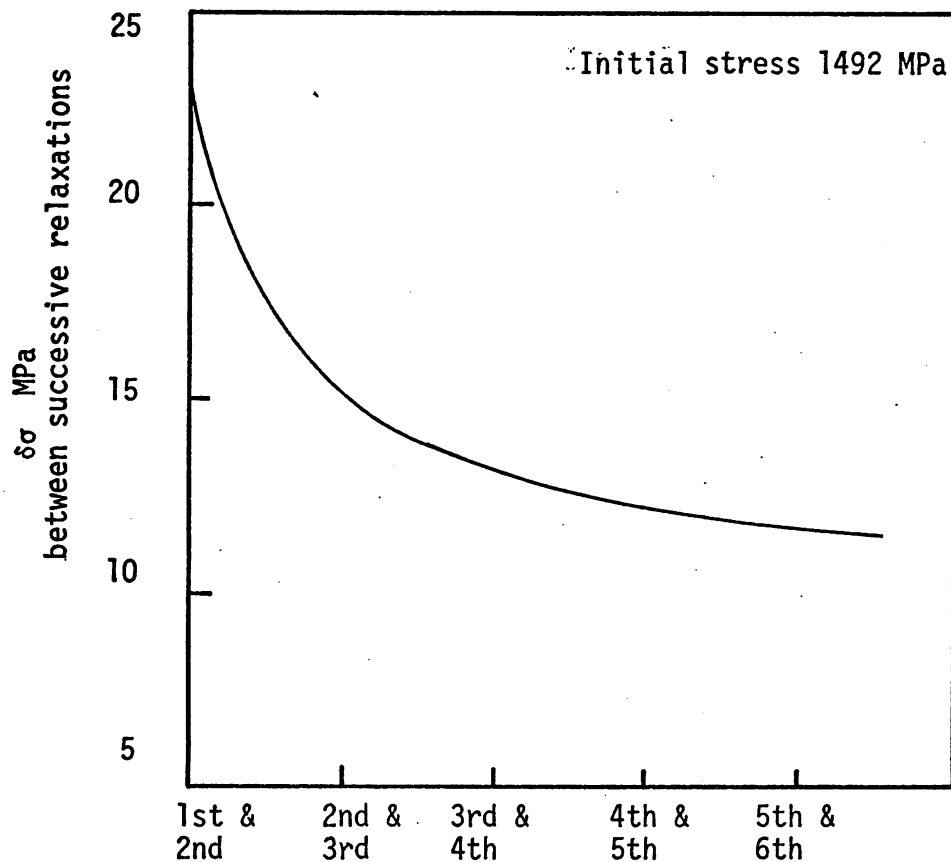


Fig. (5:8b) Plot of $\delta\sigma$ values for successive relaxations performed on A/R patented steel wire at approximately the 0.2% proof stress.

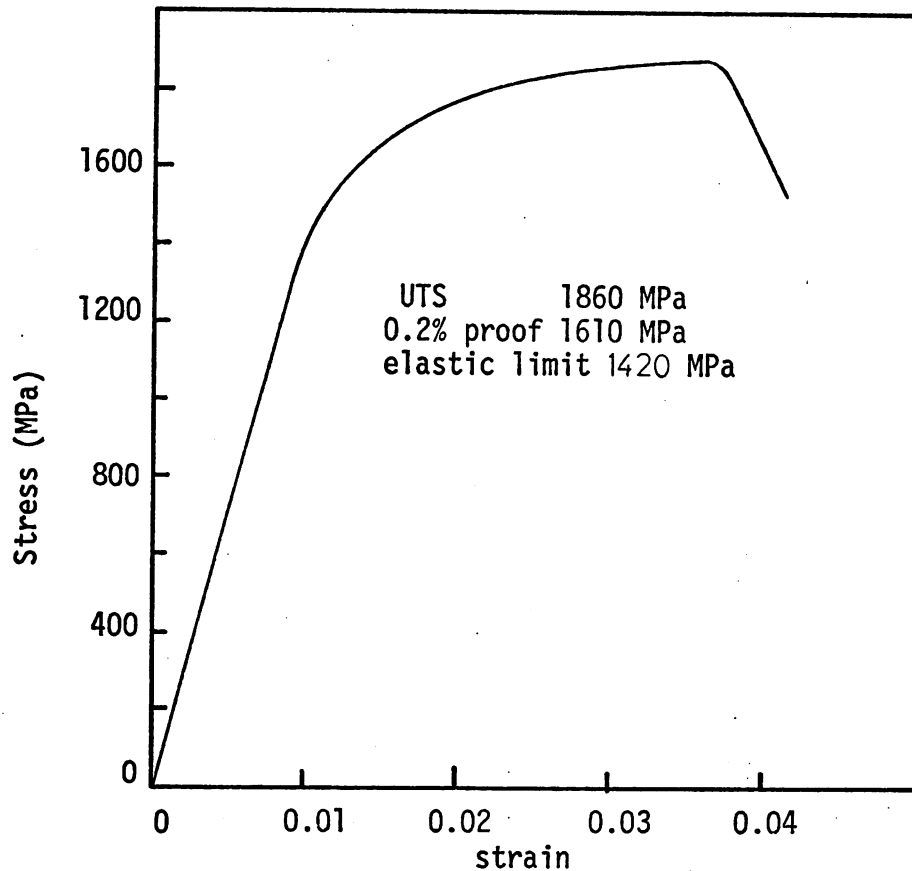


Fig. (5:9) A typical nominal stress/strain curve for A/R patented steel wire which had been preceded by a relaxation near the material's UTS.

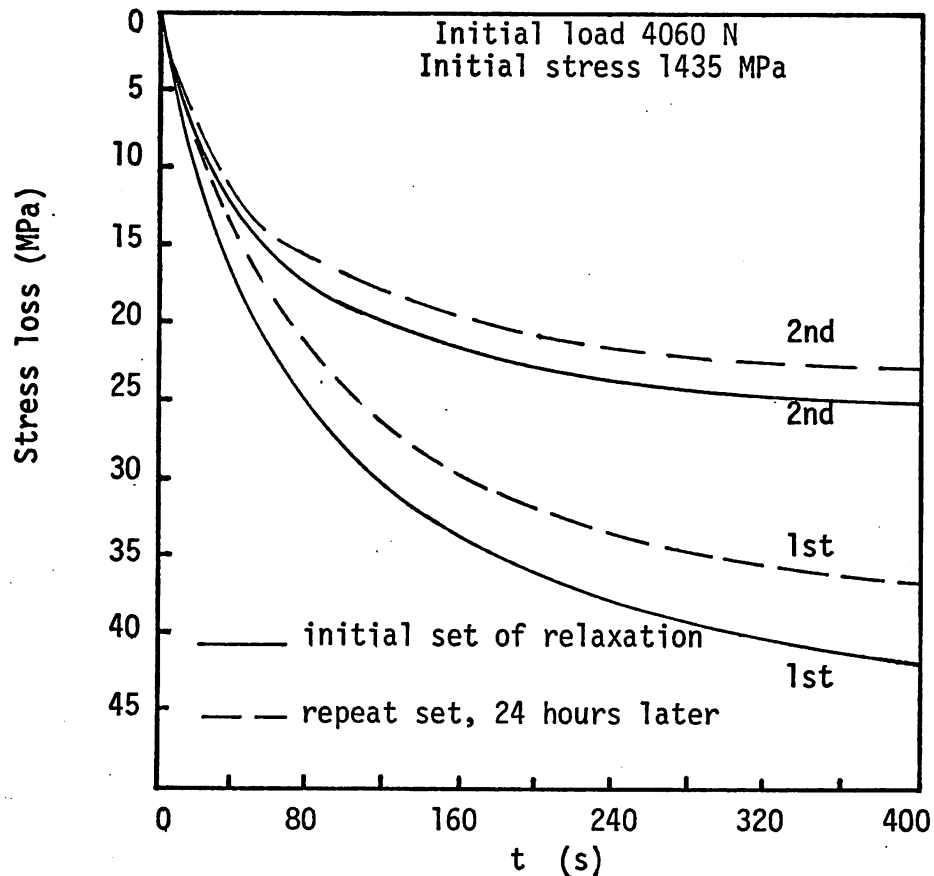


Fig. (5:10) 2 sets of 1st and 2nd relaxation of A/R patented steel wire separated by 24 hours at room temperature.

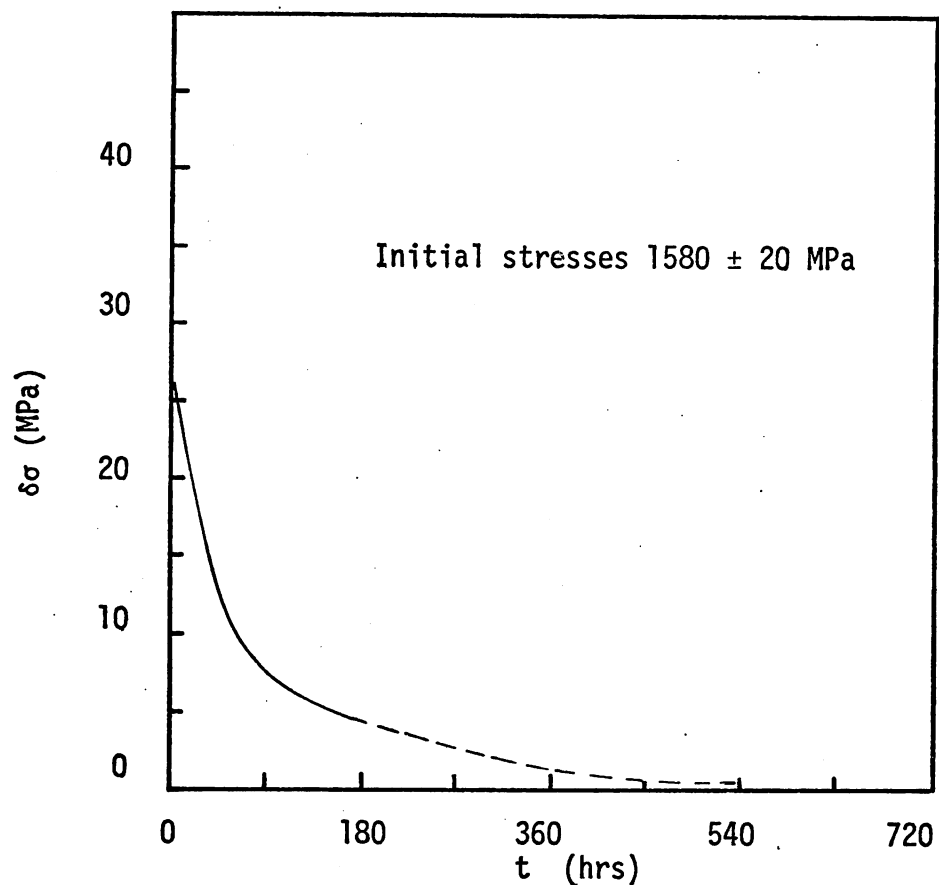


Fig. (5.11a) Changes in $\Delta\sigma$ with ageing time at room temperature between 2 sets of relaxations in A/R patented steel wire.

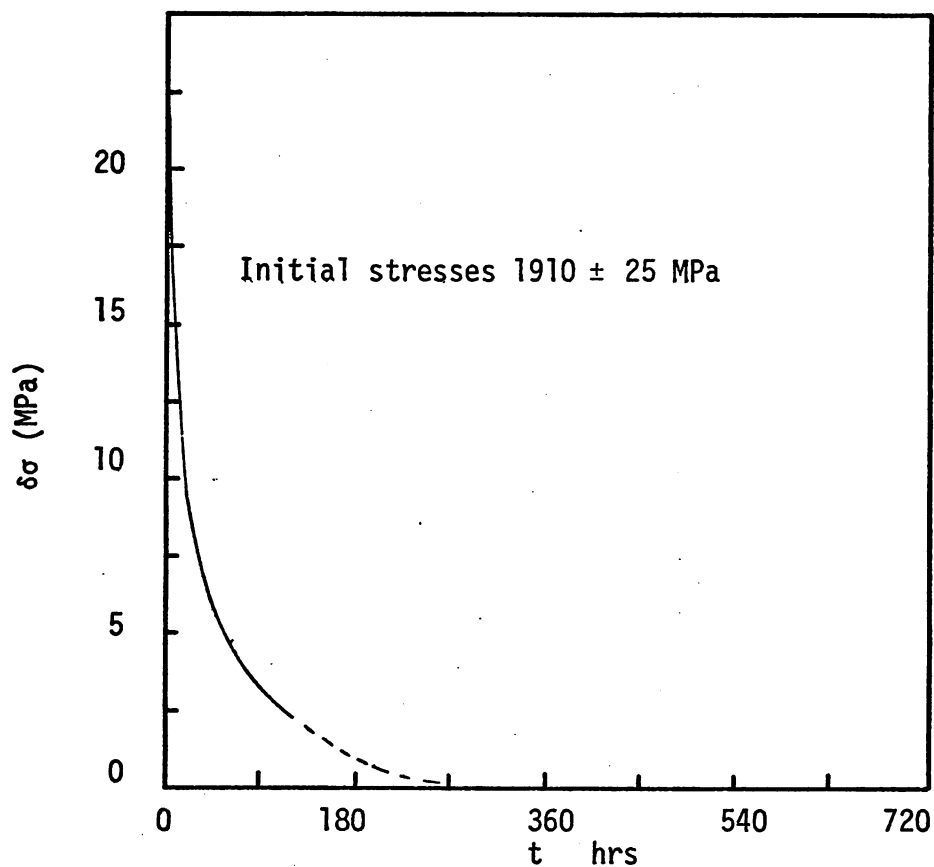


Fig. (5:11b) As above but for A/R + LTHT "A" patented steel wire.

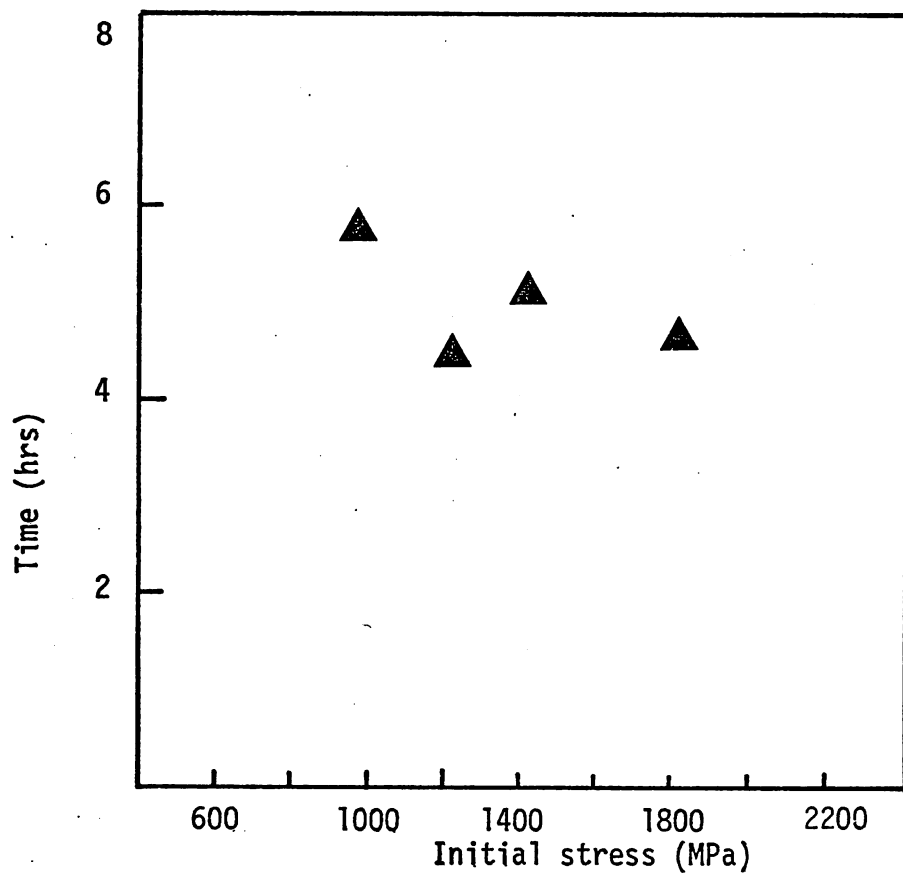


Fig. (5:12) Time required for $\delta\sigma$ to fall to $1/e$ of its initial value for A/R patented steel wire.

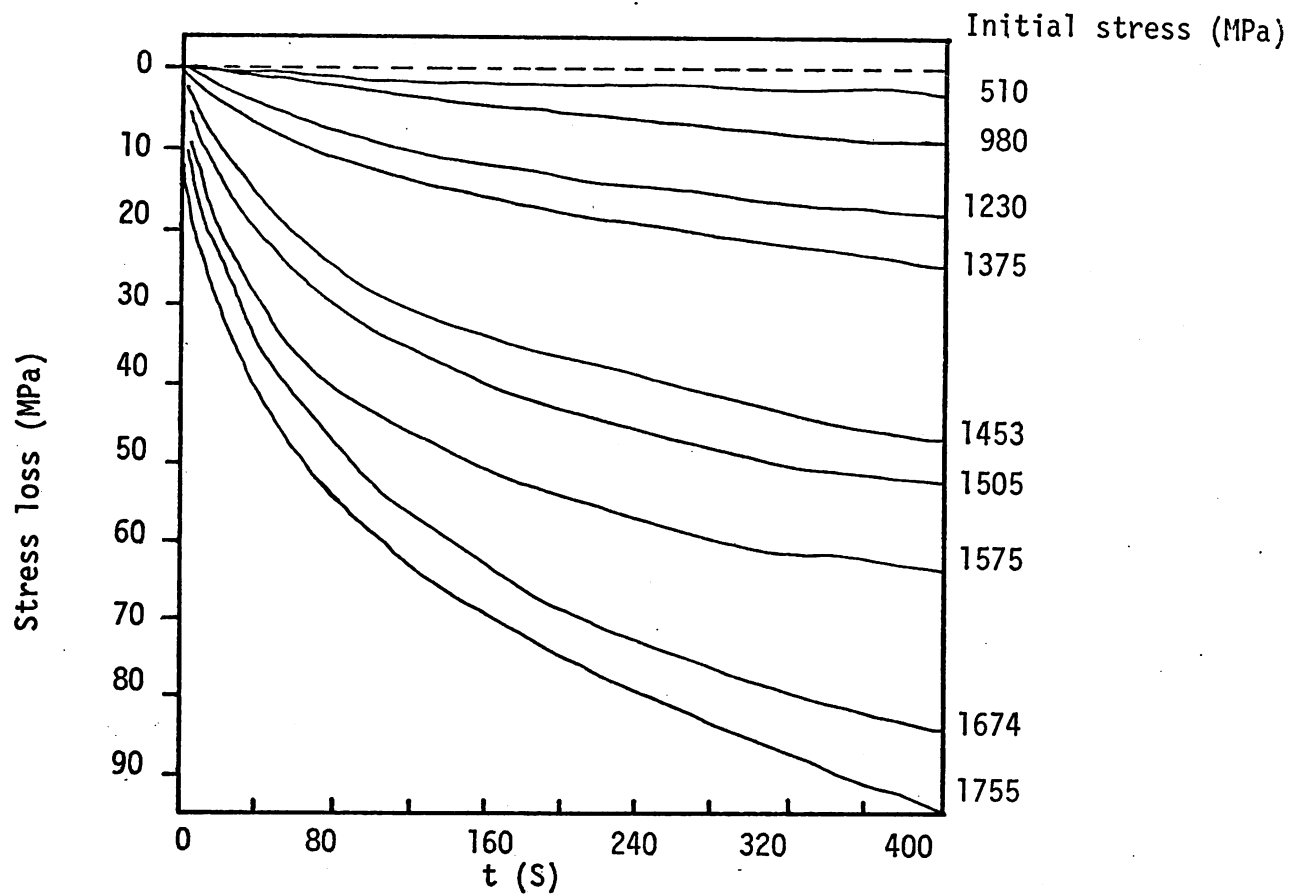


Fig. (5:13a) Relaxation curves for A/R patented steel wire at various initial stresses (see below).

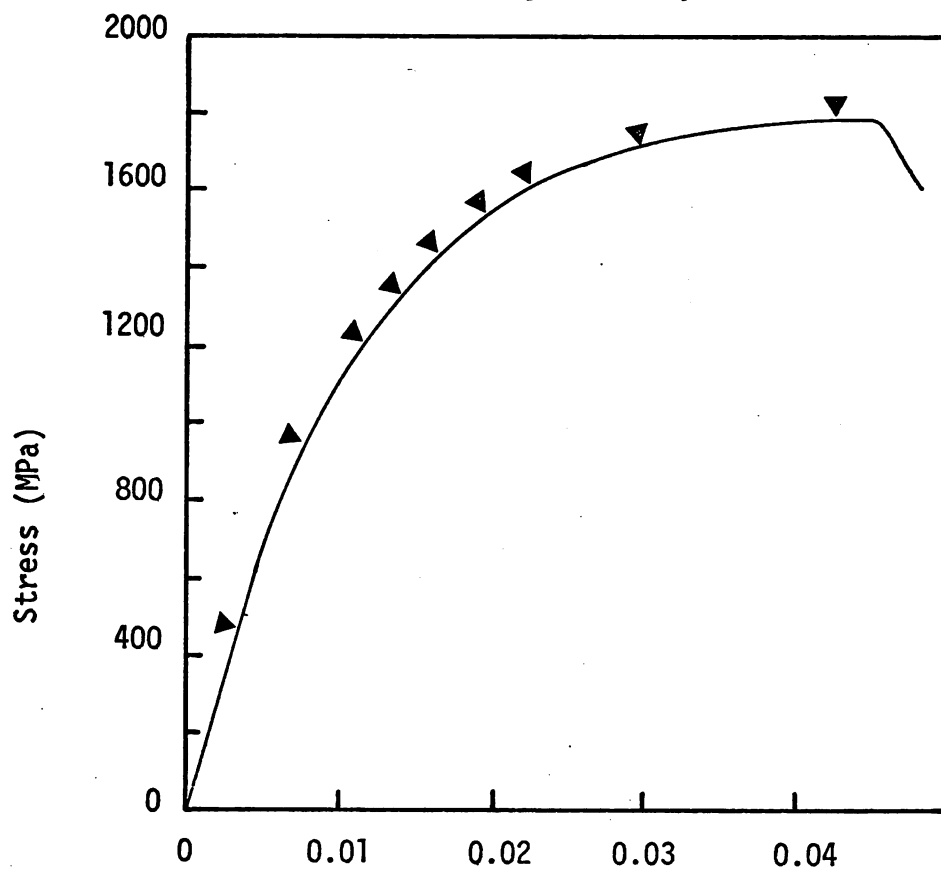


Fig. (5:13b) Nominal σ/ϵ curve for above, showing initial stresses.

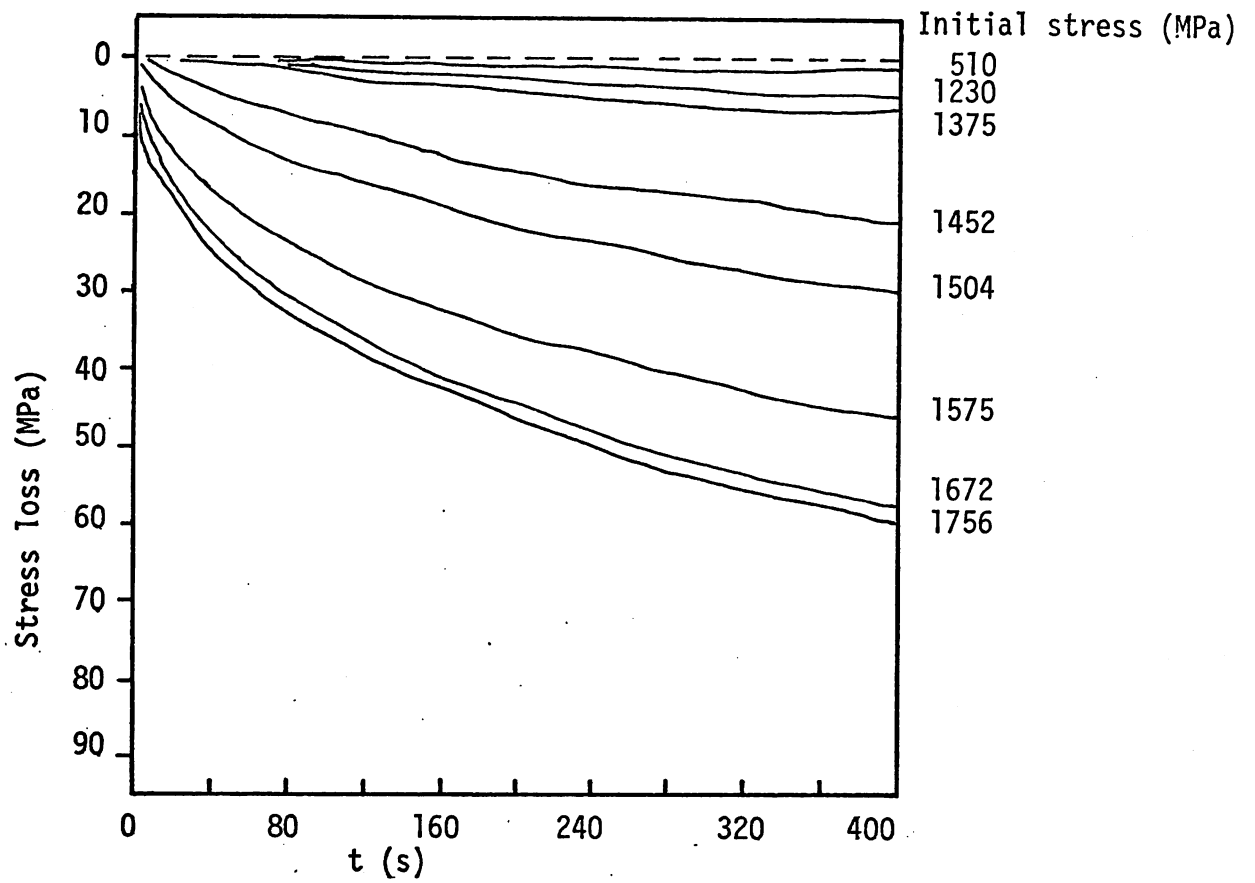


Fig. (5:13c) 2nd relaxation curves for A/R patented steel wire at similar initial stresses

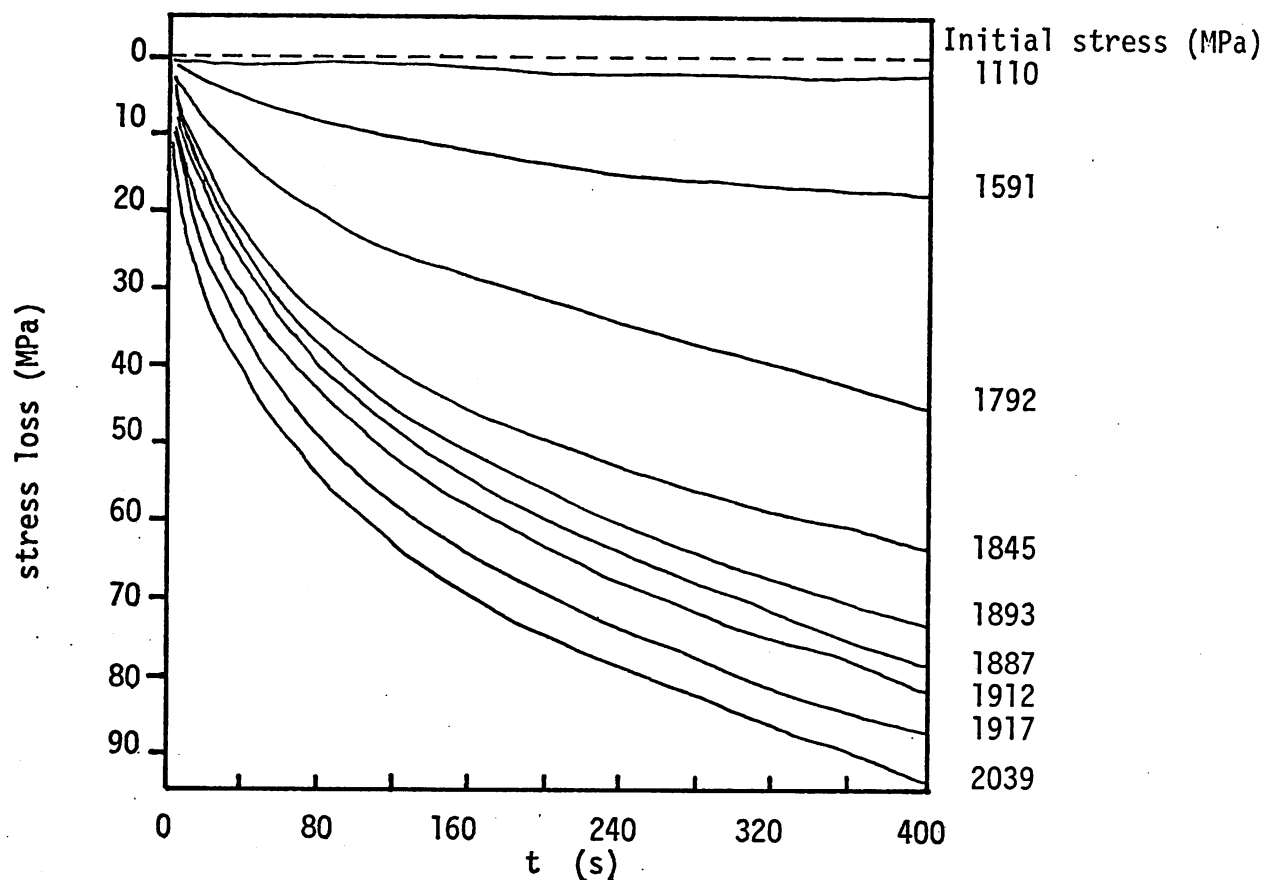


Fig. (5:14a) Relaxation curves for A/R + LHTT "A" patented steel wire at various initial stresses (see below).

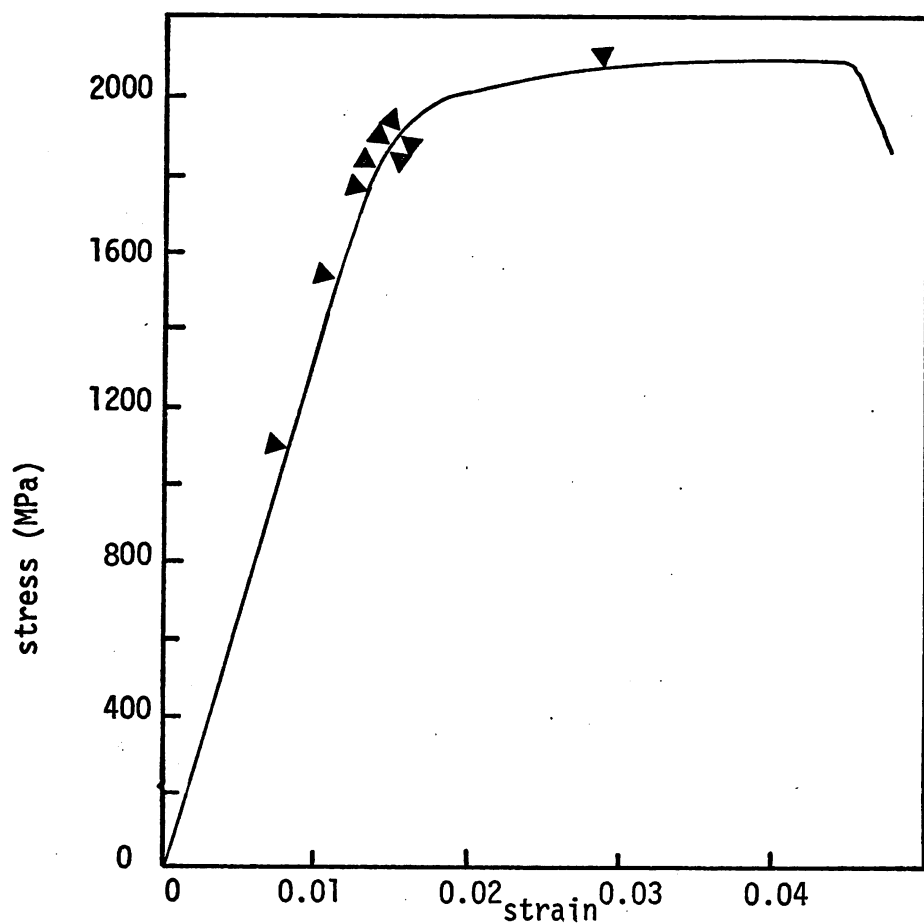


Fig. (5:14b) Nominal σ/ϵ curve for above, showing initial stresses.

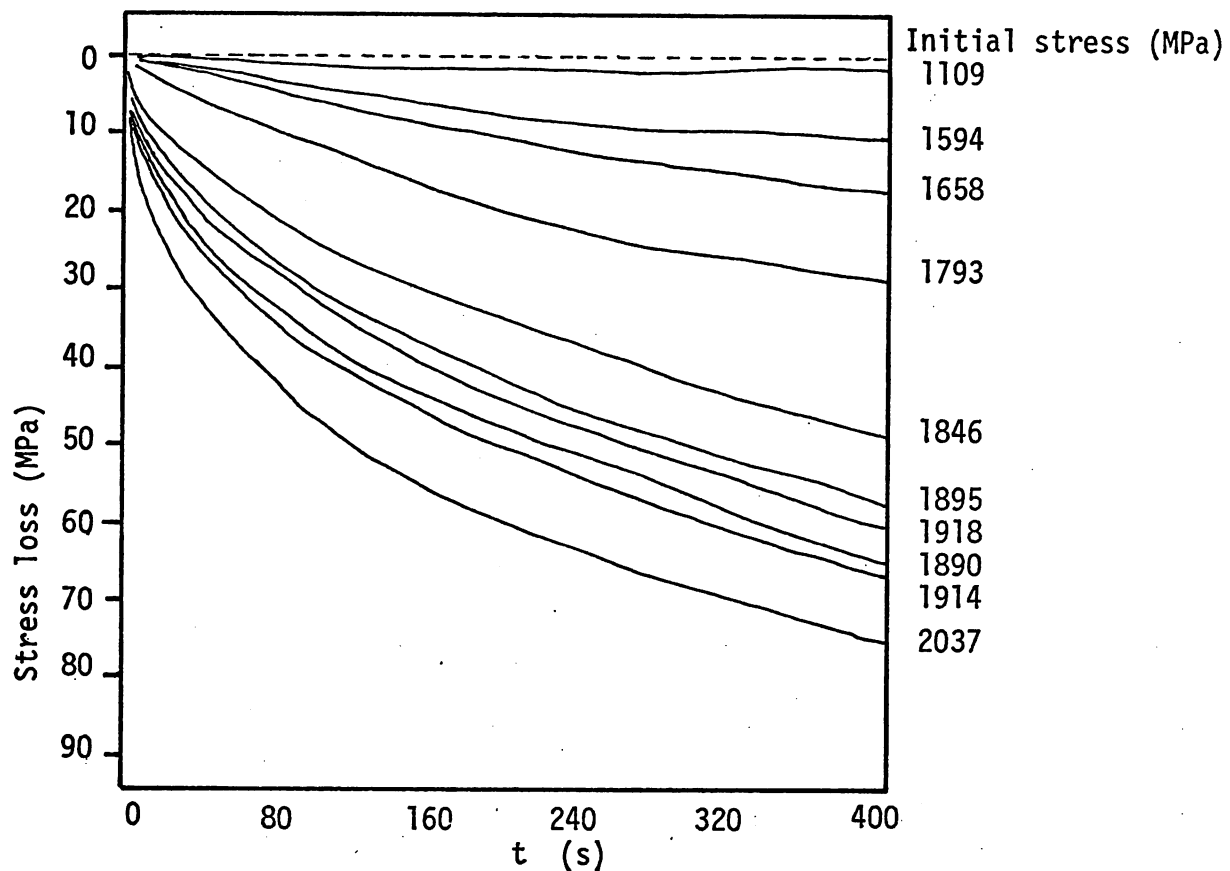


Fig. (5:14c) 2nd relaxation curves for A/R + LTHT "A" patented steel wire at similar initial stresses

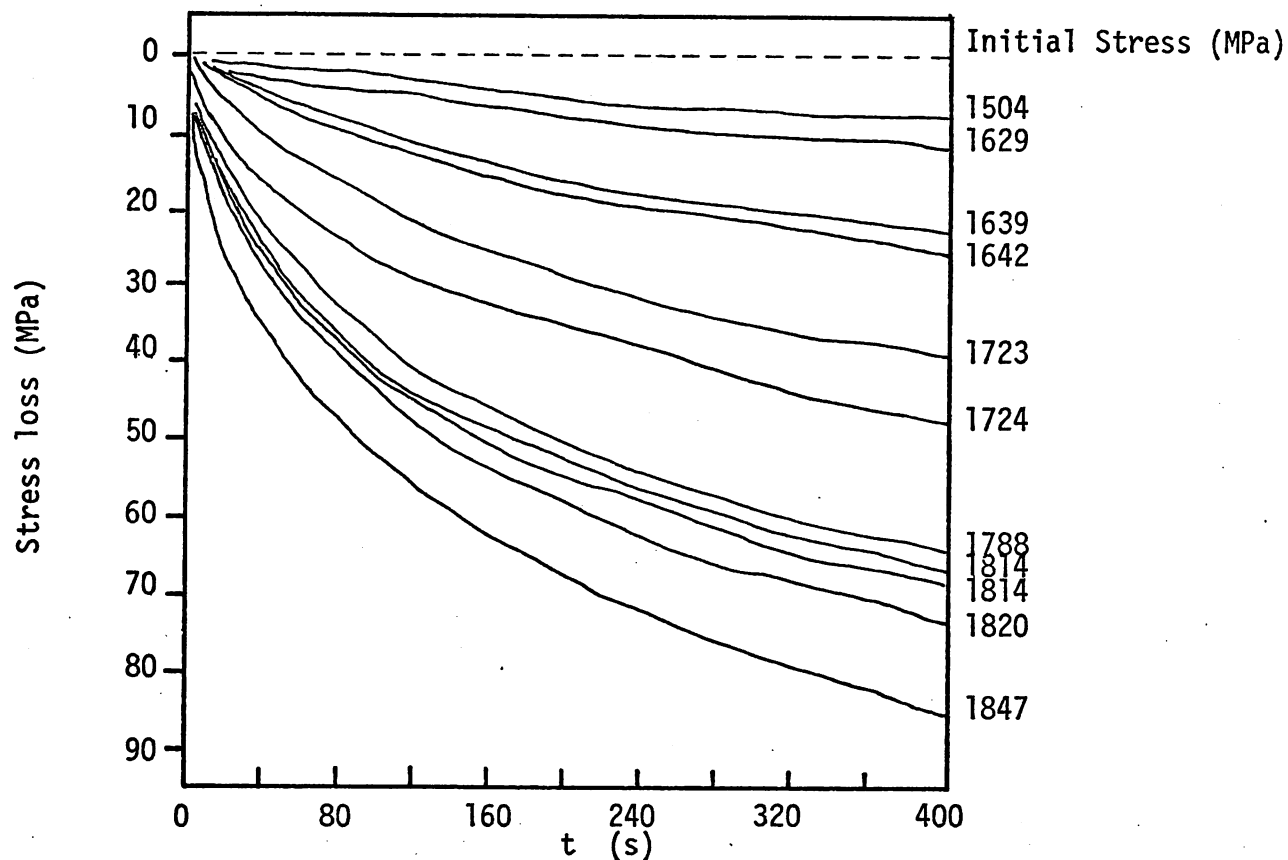


Fig. (5:15a) Relaxation curves for A/R + LTHT "B" patented steel wire at various initial stresses (see below).

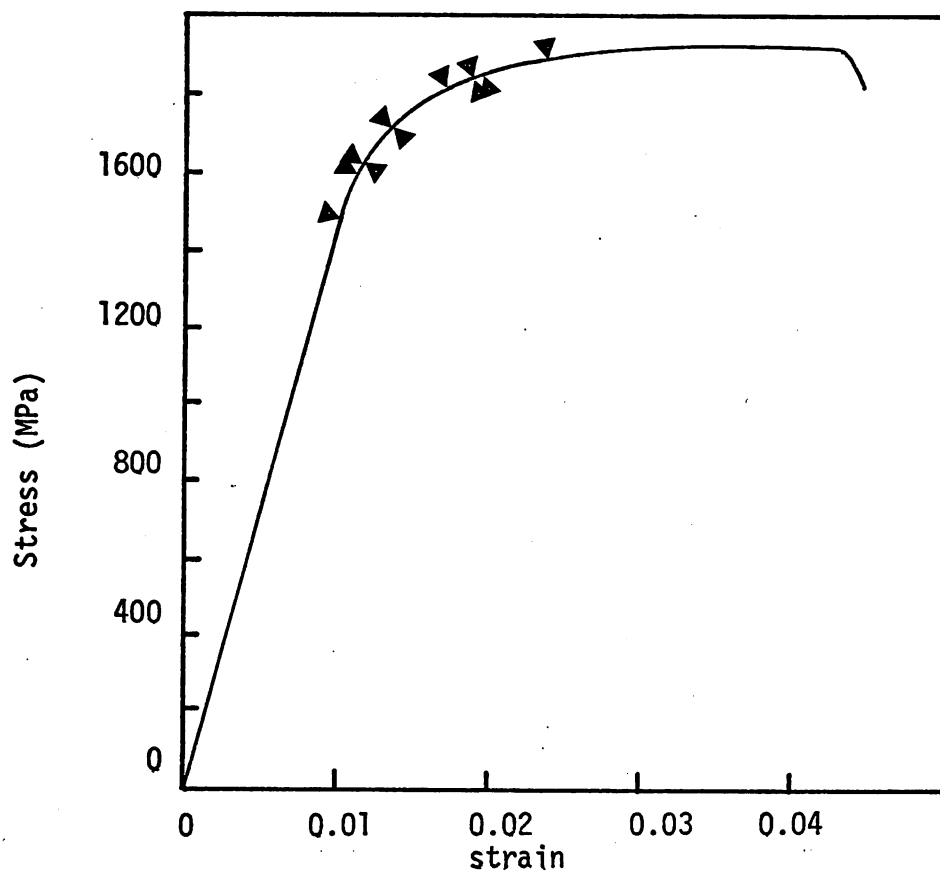


Fig. (5:15b) Nominal σ/ϵ curve for above, showing initial stresses.

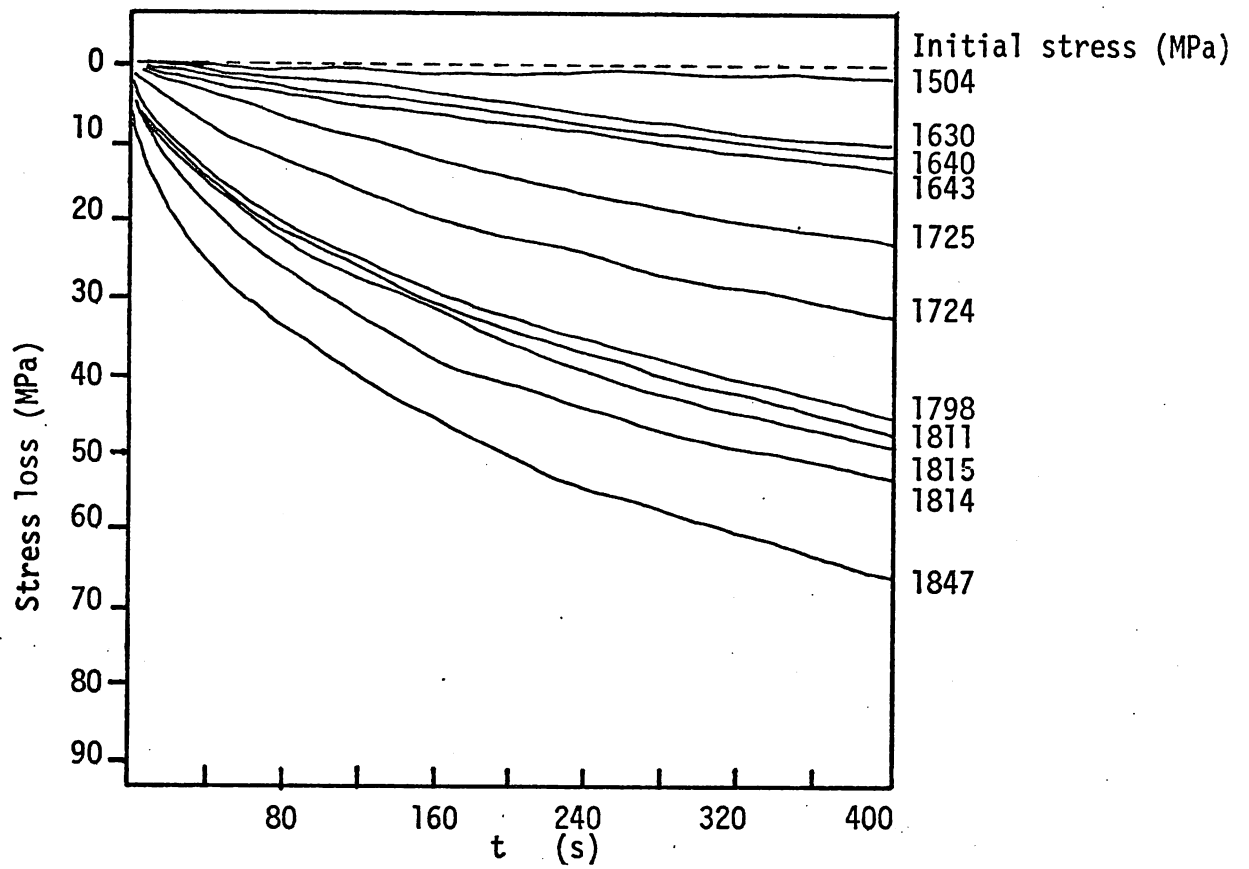


Fig. (5:15c) 2nd relaxation curves for A/R + LTHT "B" patented steel wire at similar initial stresses

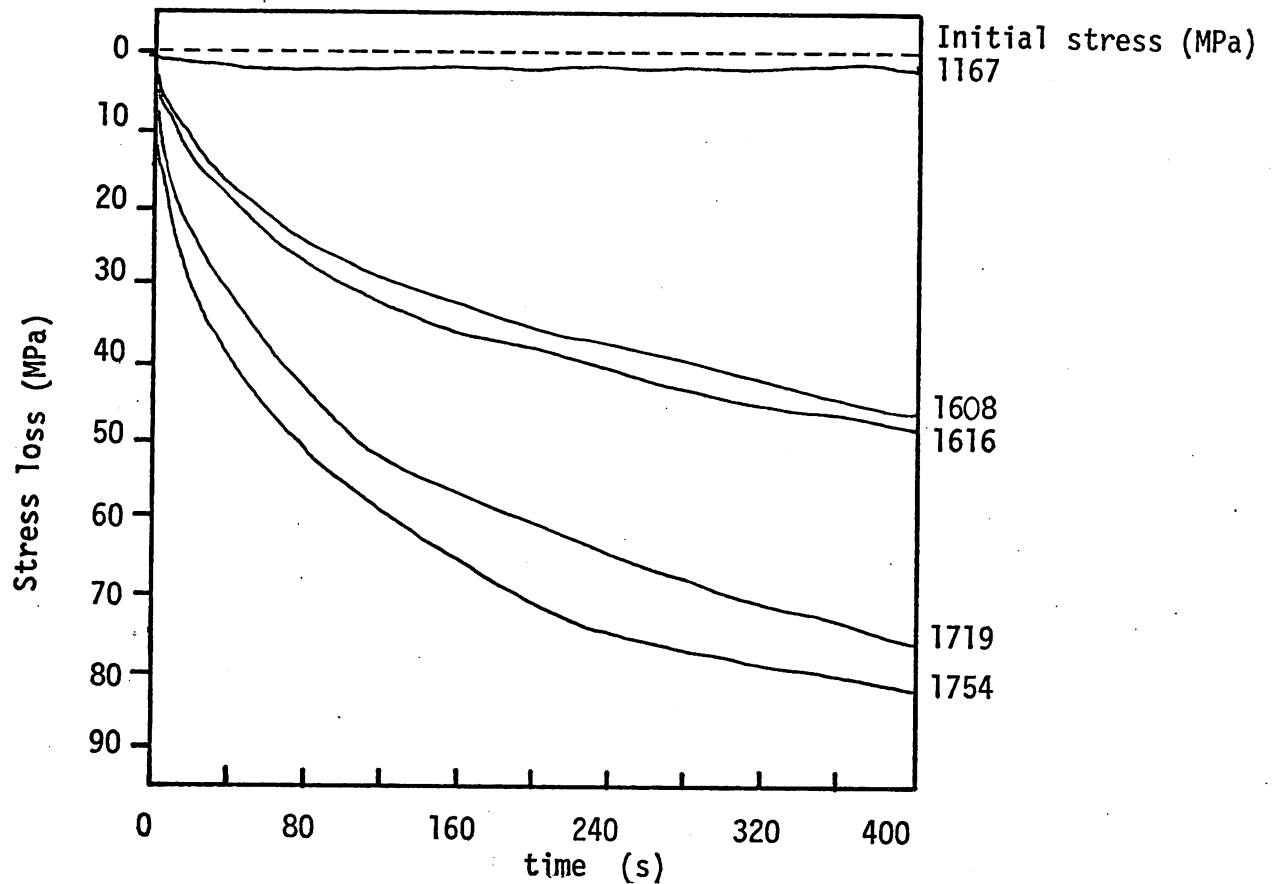


Fig. (5:16a) Relaxation curves for A/R LTHT "C" patented steel wire at various initial stresses (see below).

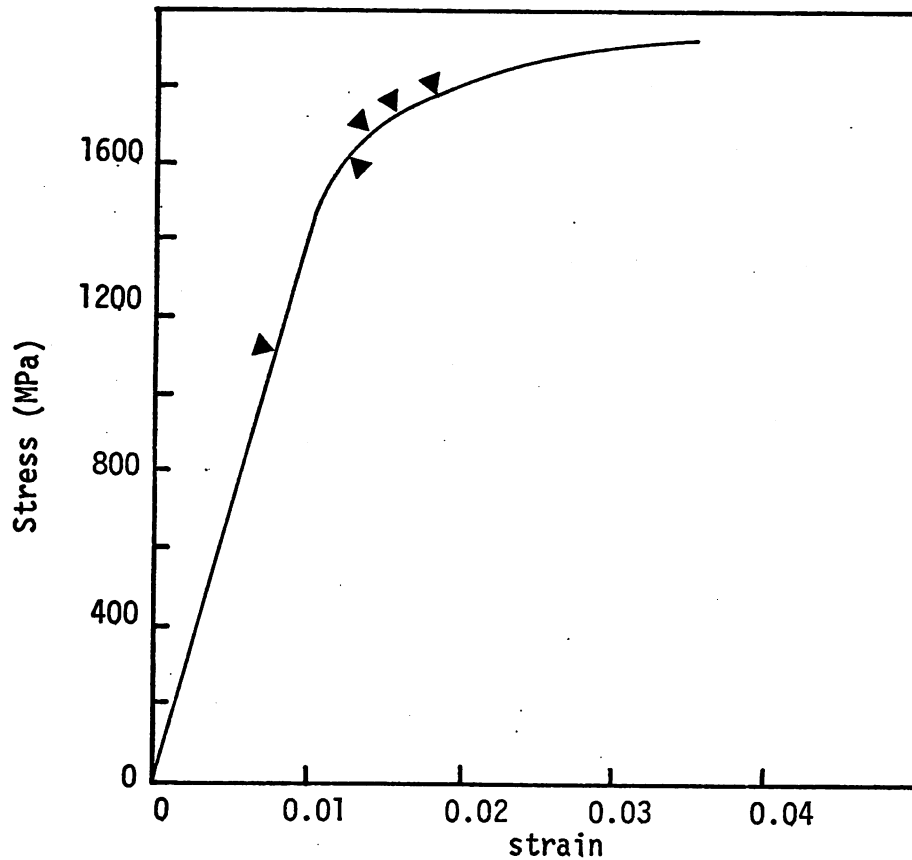


Fig. (5:16b) Nominal σ/ϵ curve for above, showing initial stresses.

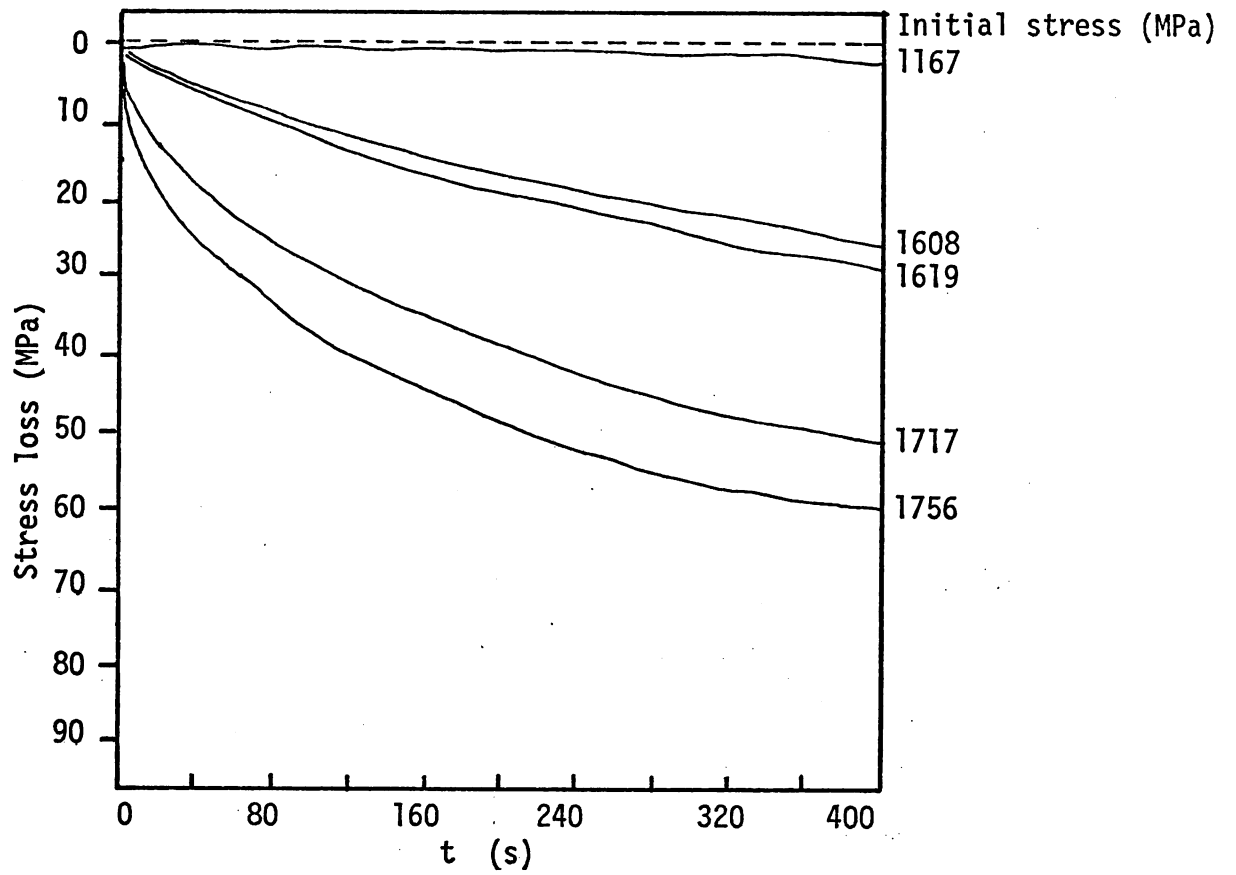


Fig. (5:16c) 2nd relaxations for A/R + LTHT "C" patented steel wire at similar initial stresses

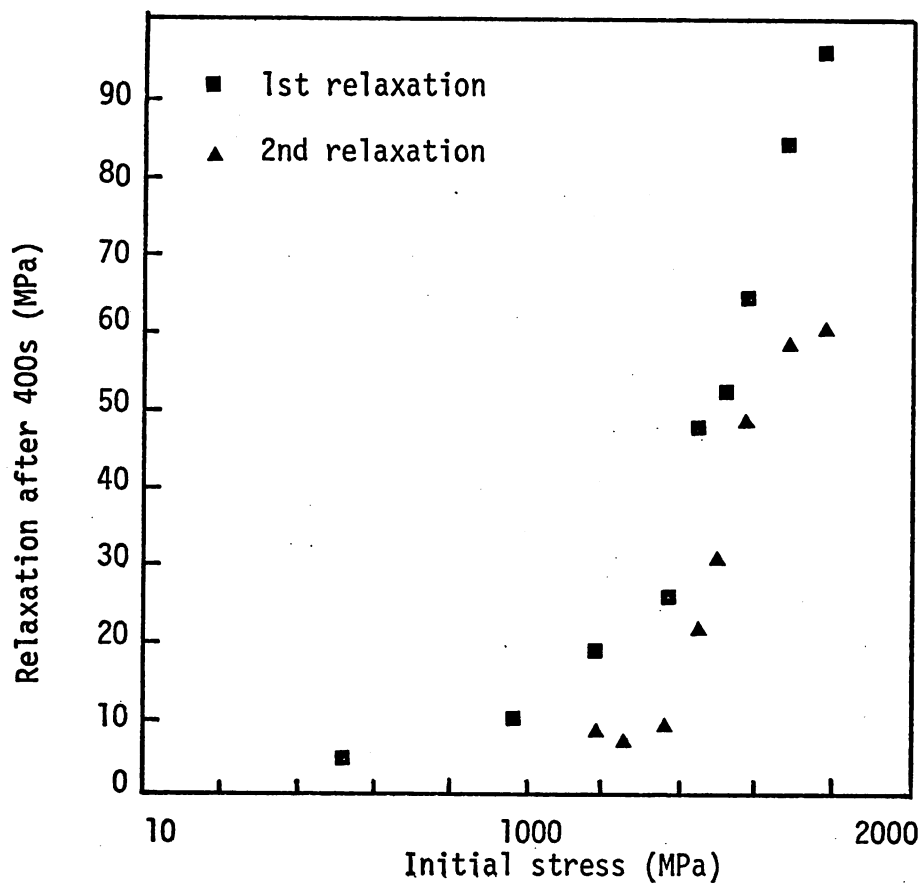


Fig. (5:17) Stress drop for 1st and 2nd relaxations after 400s in A/R patented steel wire, with initial stress.

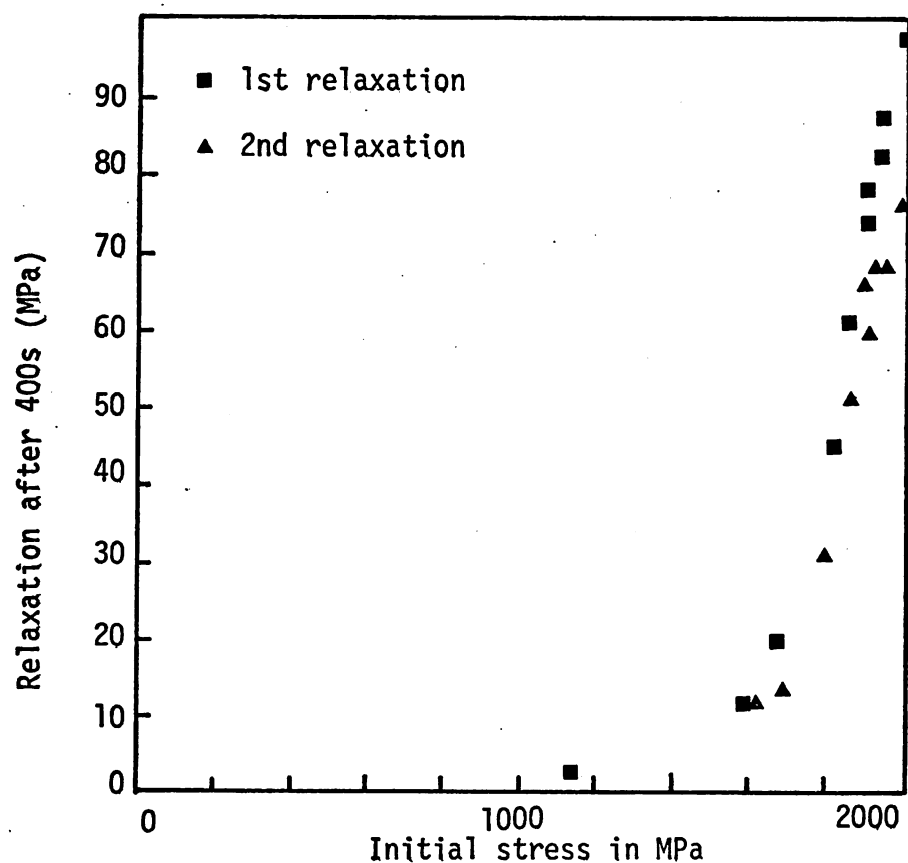


Fig. (5:18) Stress drop for 1st and 2nd relaxation after 400s in A/R + LTHT "A" patented steel wire with initial stress.

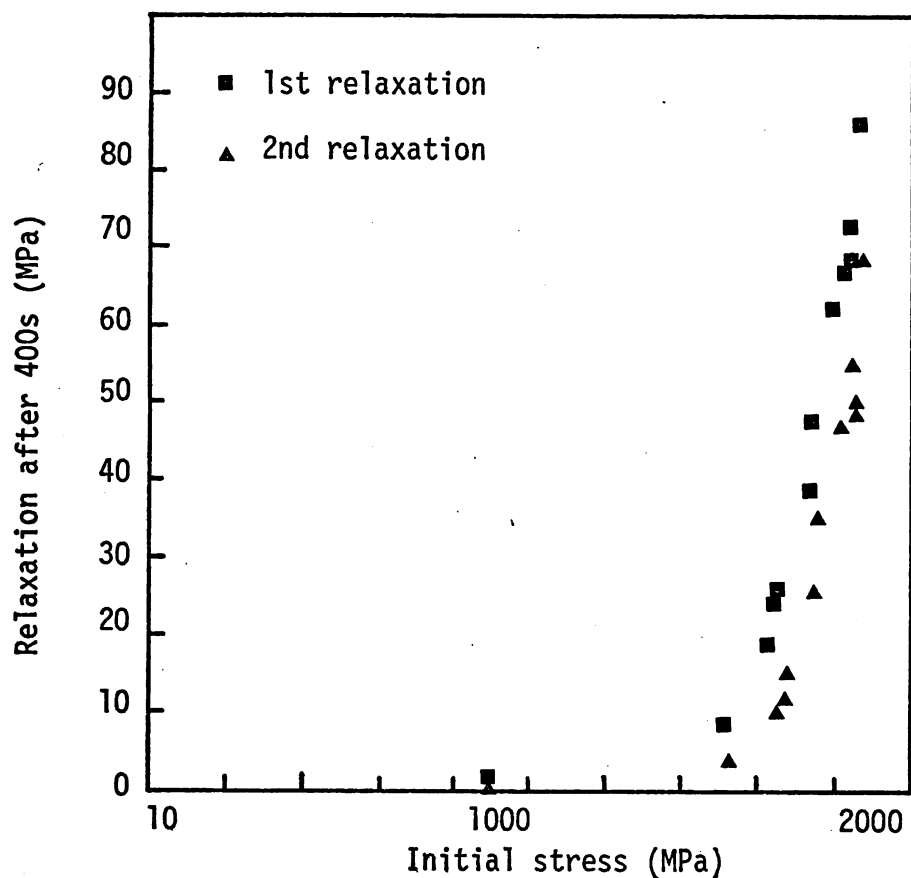


Fig. (5:19) Stress drop for 1st and 2nd relaxation after 400s in A/R LTHT "B" patented steel wire, with initial stress.

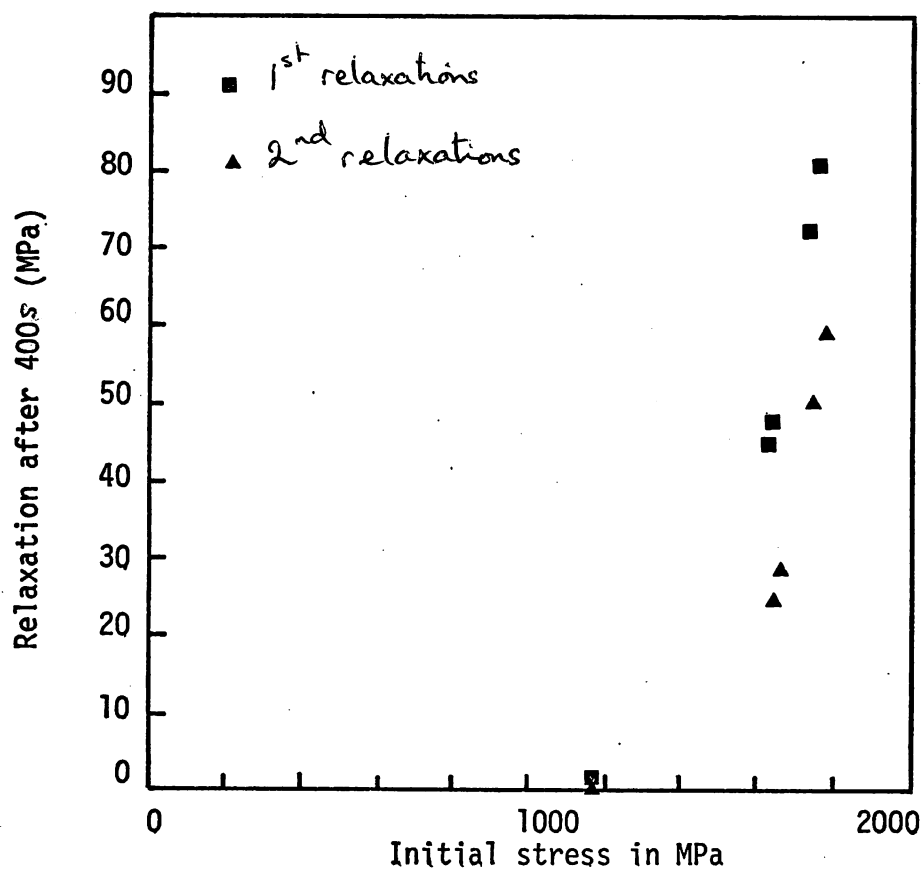


Fig. (5:20) Stress drop for 1st and 2nd relaxation after 400s in A/R + LTHT "C" patented steel wire, with initial stress.

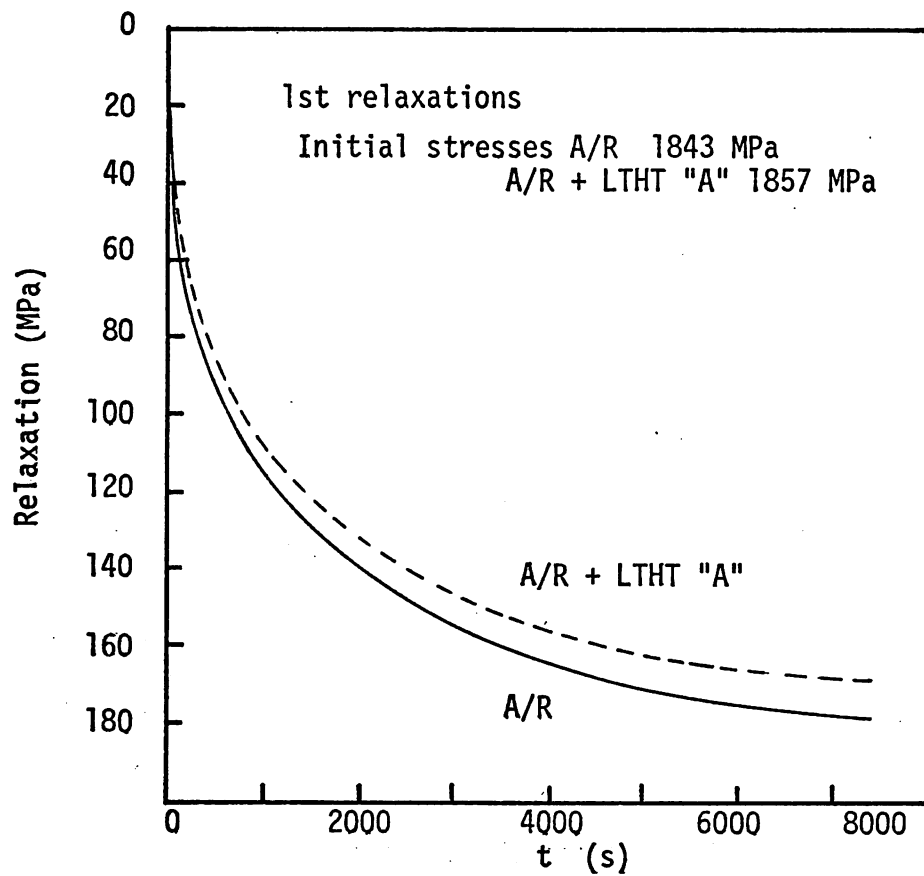


Fig. (5:21a) Long term relaxations for A/R and A/R + LTHT "A" patented steel wire, from ~ 1850 MPa.

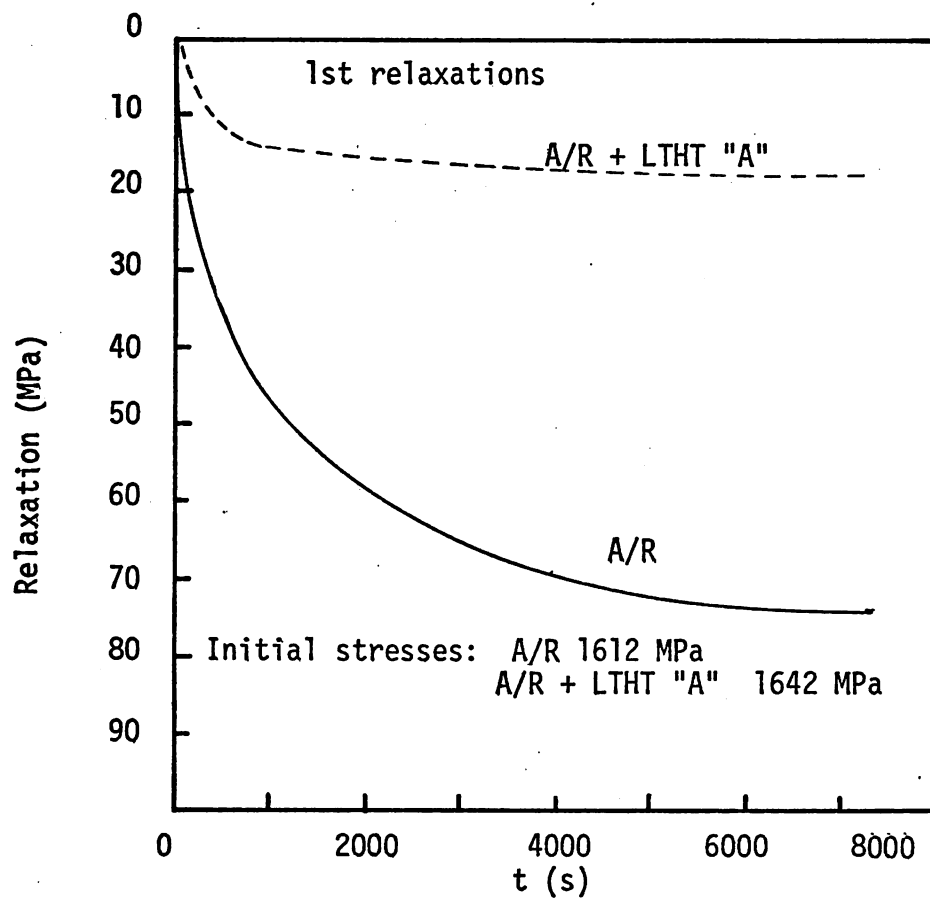


Fig. (5:21b) Long term relaxations for A/R and A/R + LTHT "A" patented steel wire, from ~ 1620 MPa.

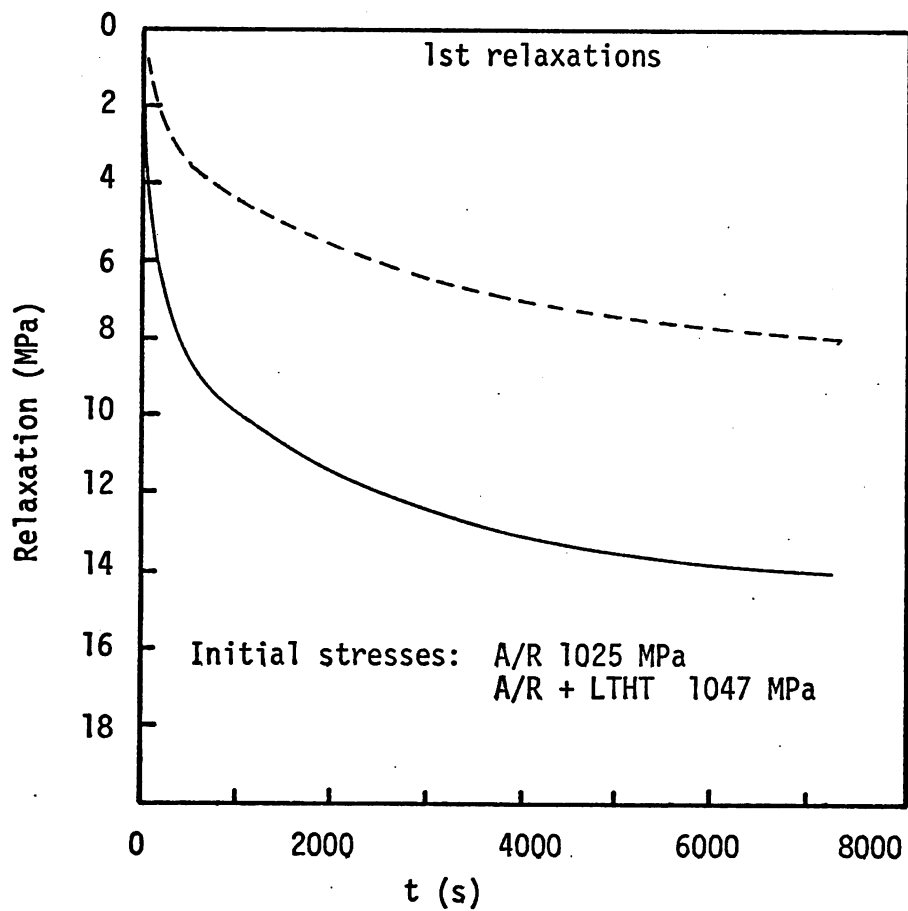
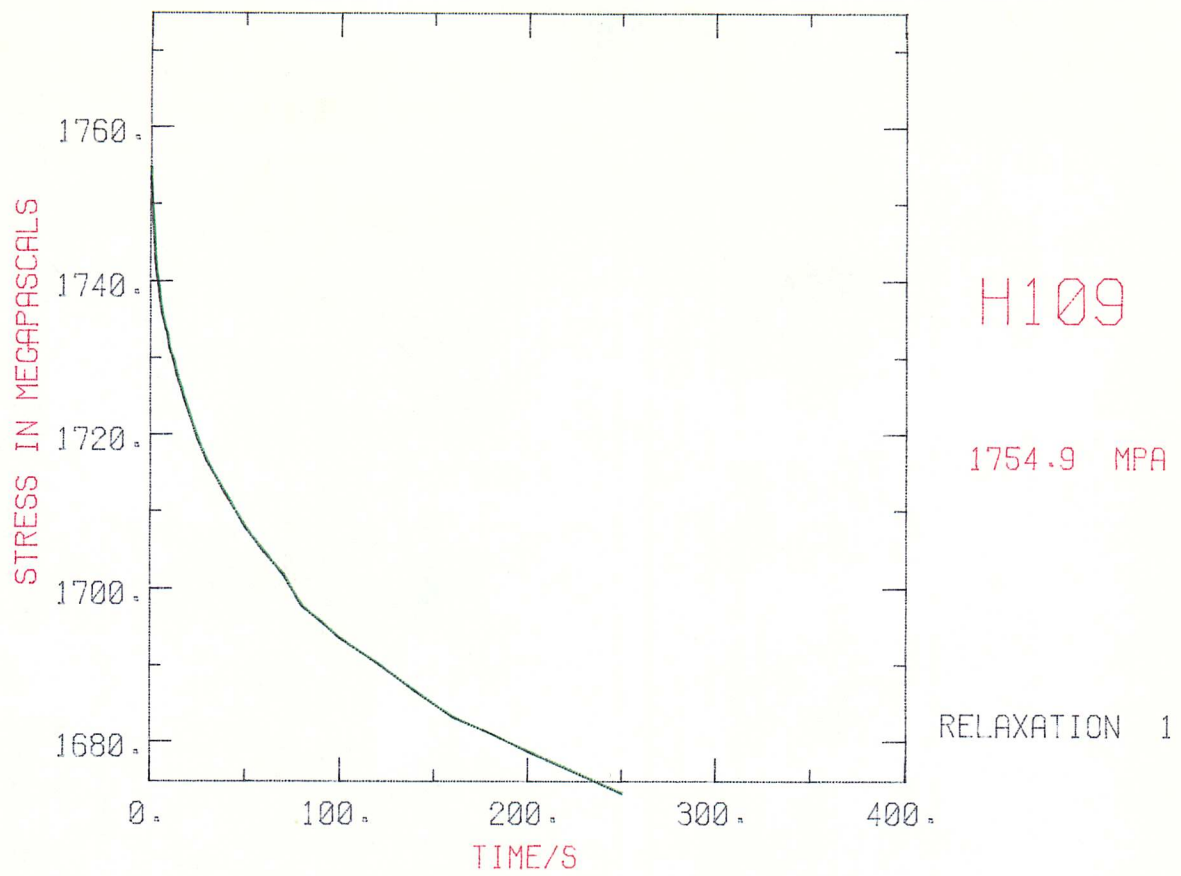
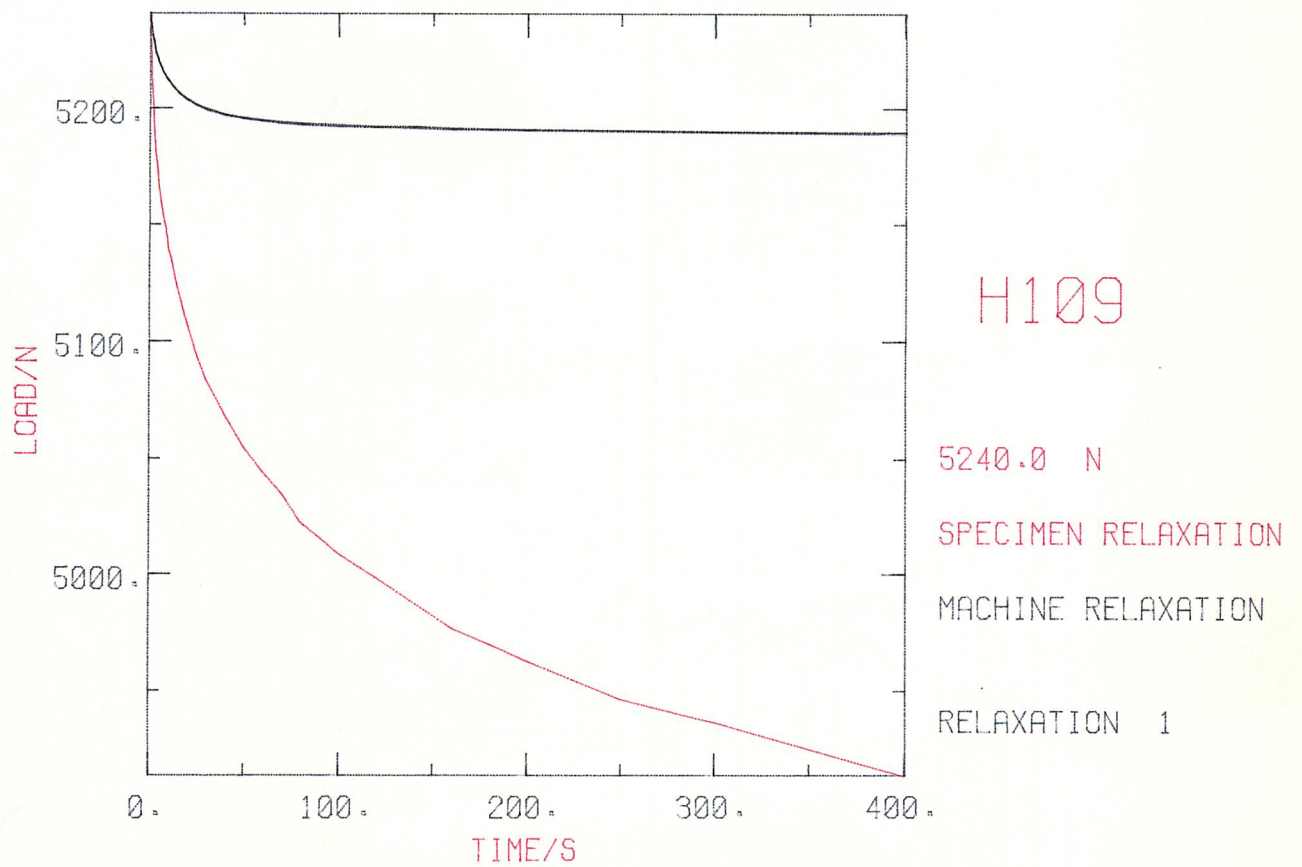


Fig. (5:21c) Long term relaxations for A/R and A/R + LTHT "A" patented steel wire, from ~ 1025 MPa.

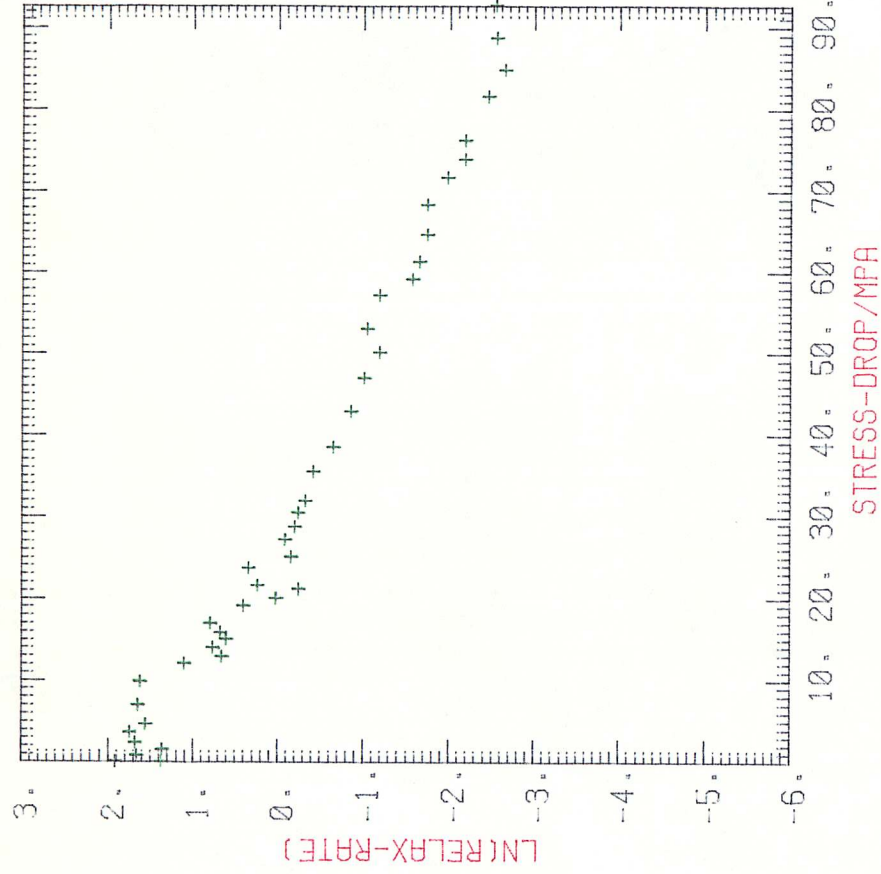
Fig. (5:22, a to e) Examples of IBM output for an A/R patented wire specimen.



LOAD RELAXATIONS



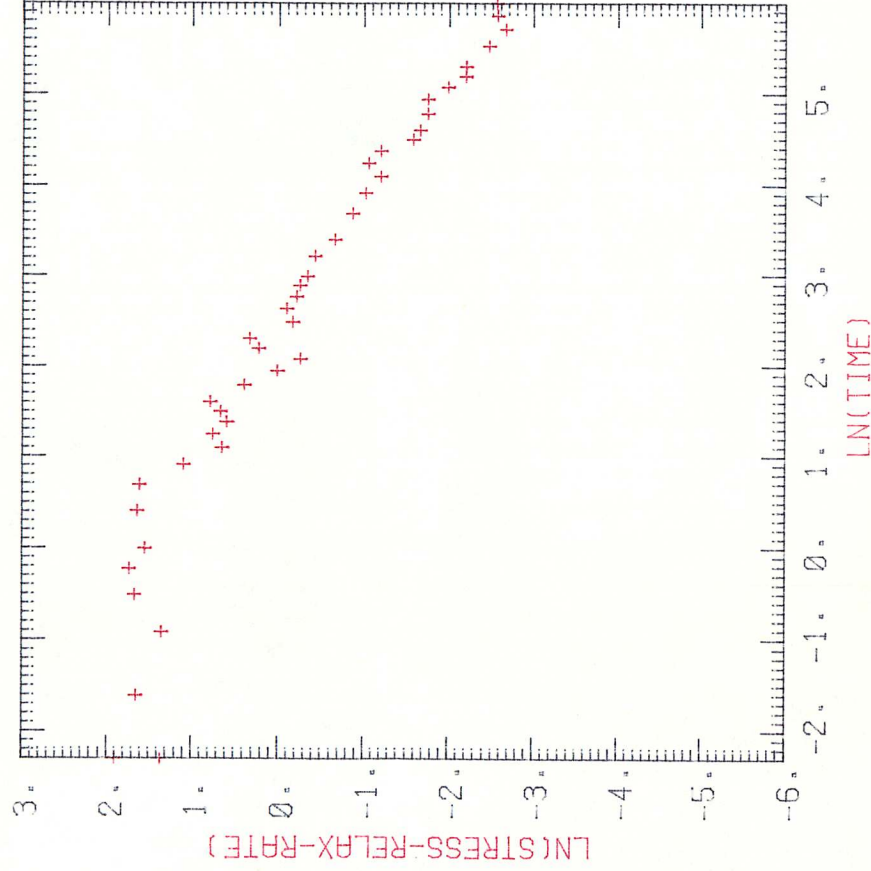
LN(RELAX-RATE)/STRESS-DROP



H109

RELAXATION 1

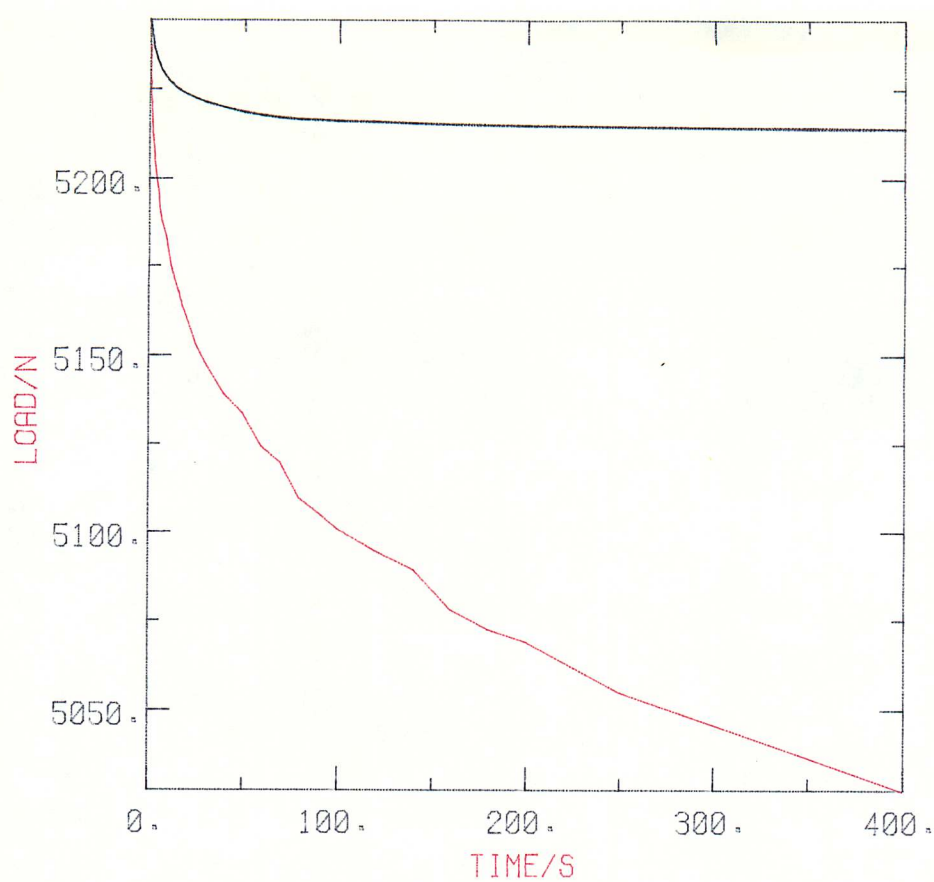
+



H109

RELAXATION 1

+



H109

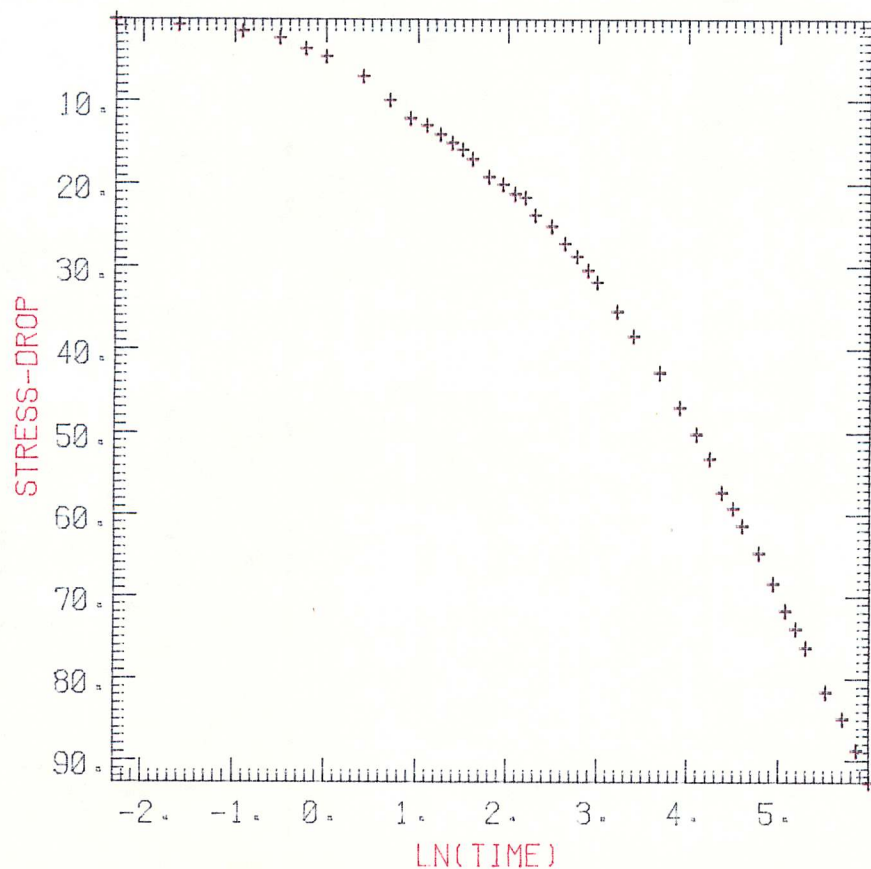
5244.0 N

SPECIMEN RELAXATION

MACHINE RELAXATION

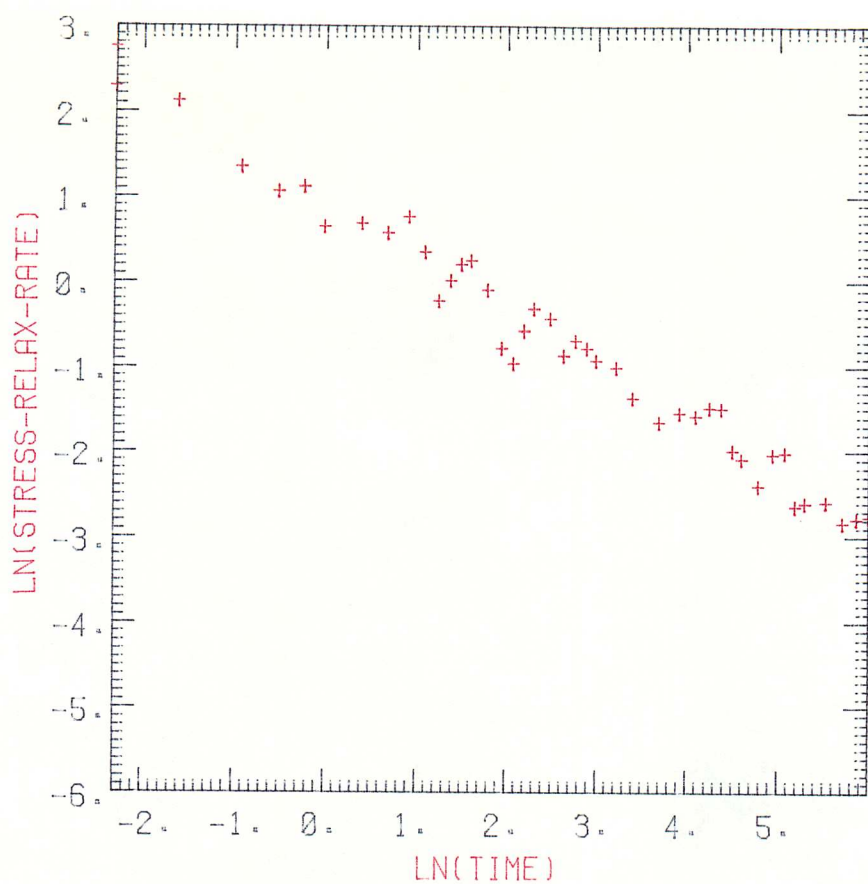
RELAXATION 2

STRESS-DROP/LN(TIME)



H109

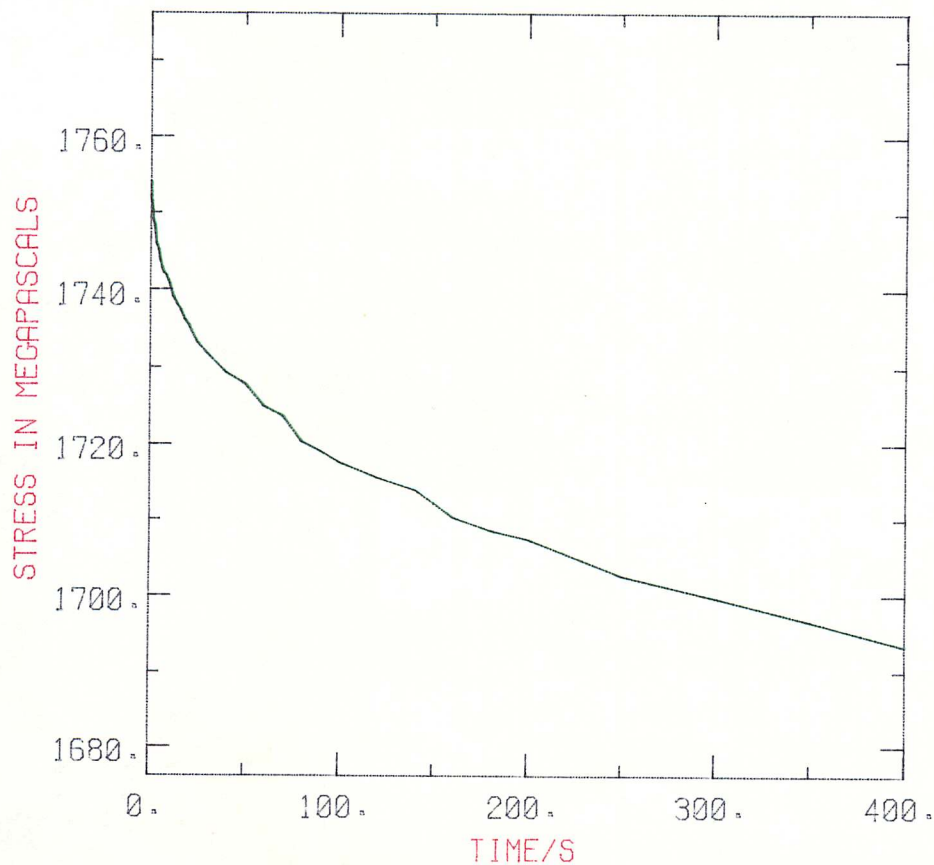
RELAXATION 1



H109

RELAXATION 2

STRESS RELAXATION

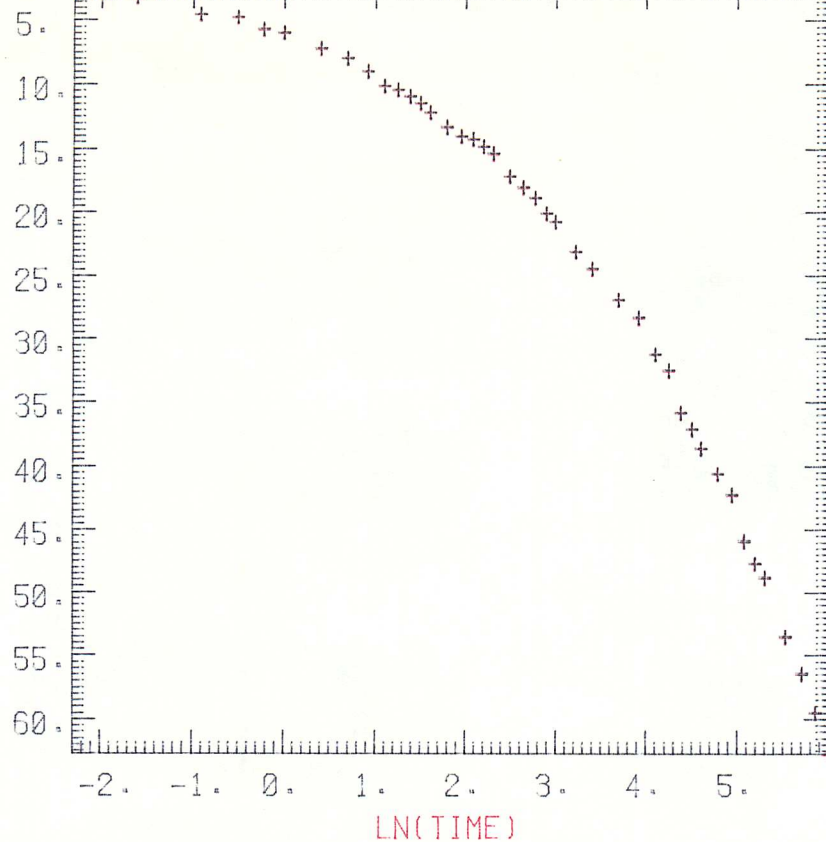


H109

1756.2 MPA

RELAXATION 2

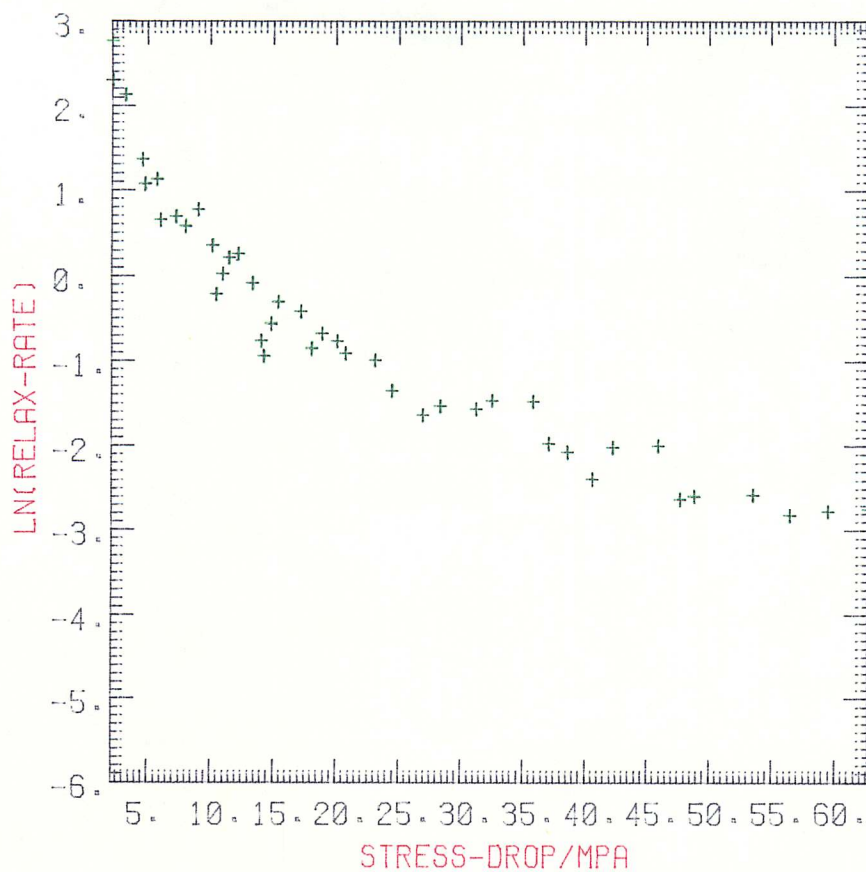
STRESS-DROP



H109

RELAXATION 2

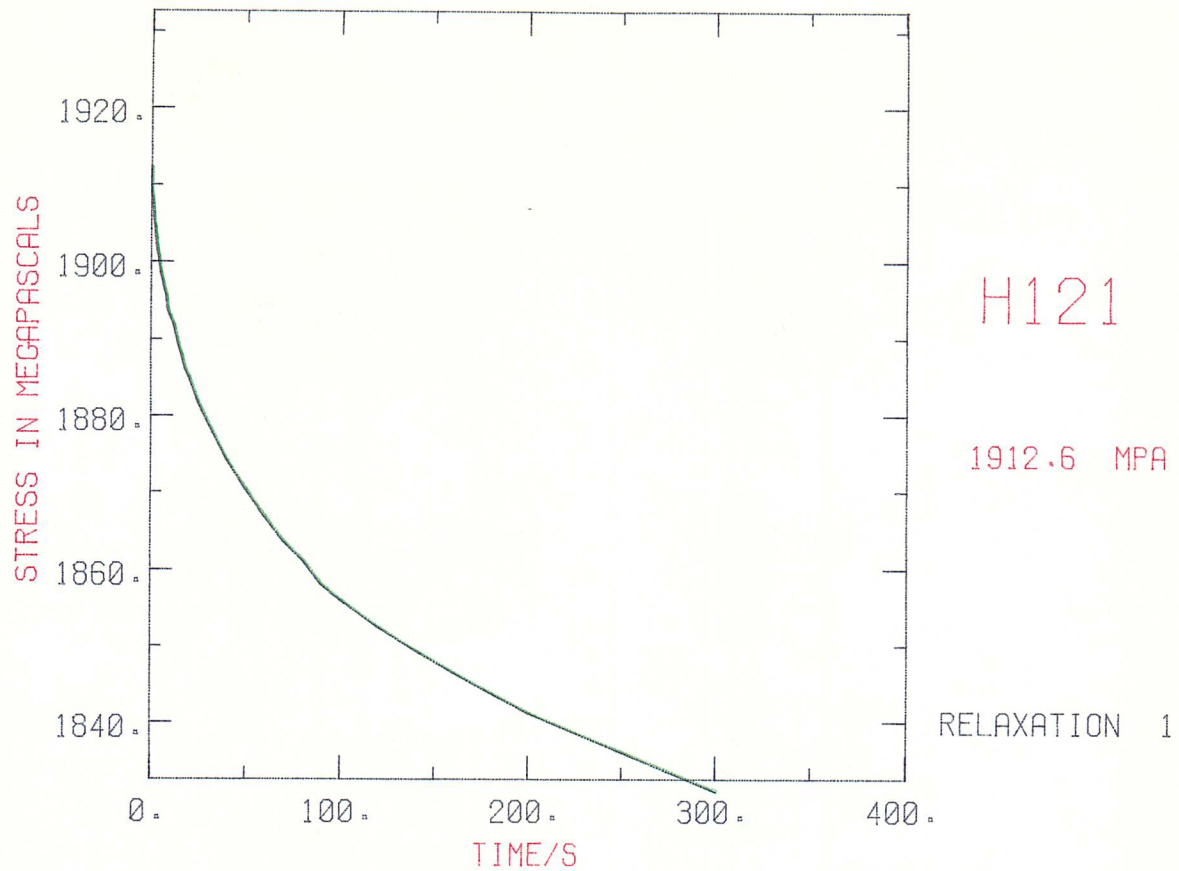
LN(RELAX-RATE)/STRESS-DROP



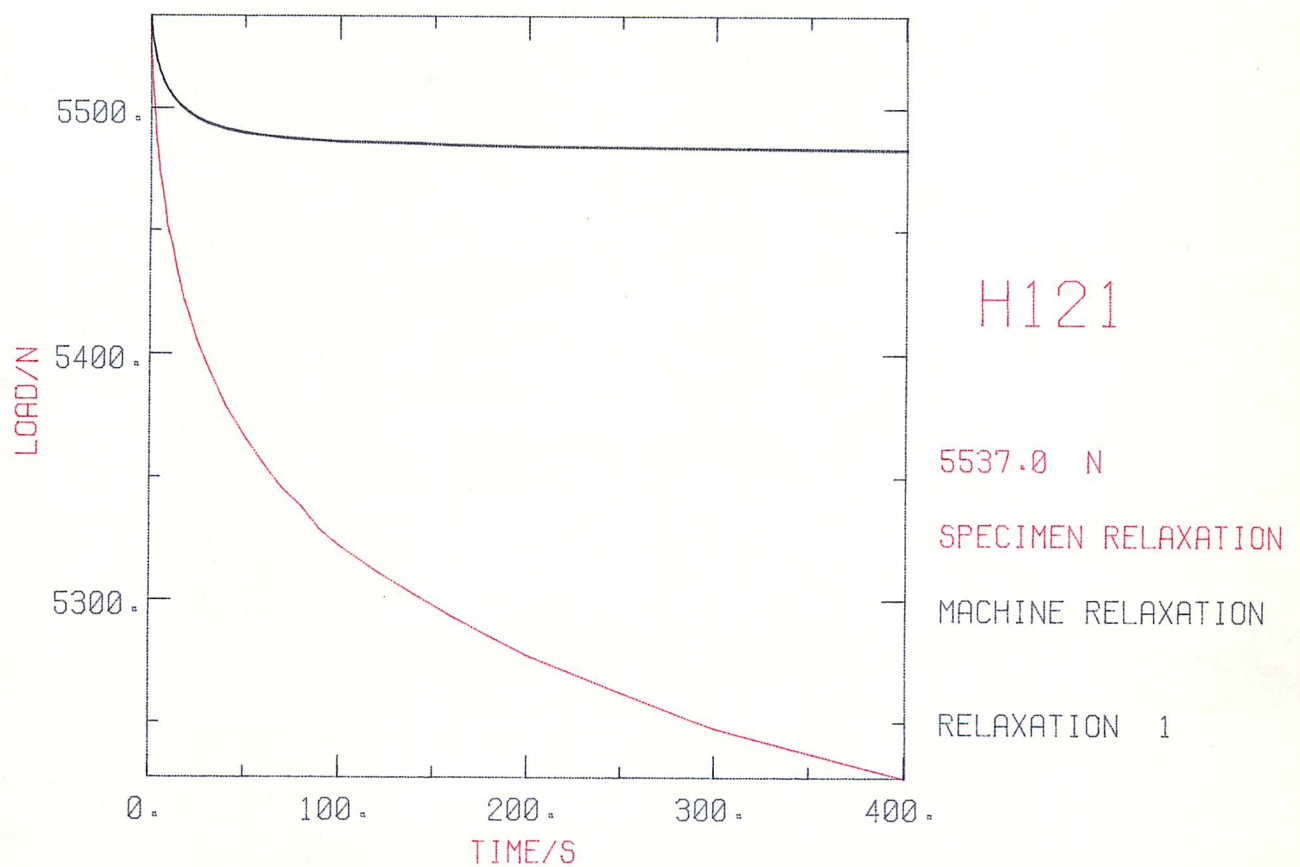
H109

RELAXATION 2

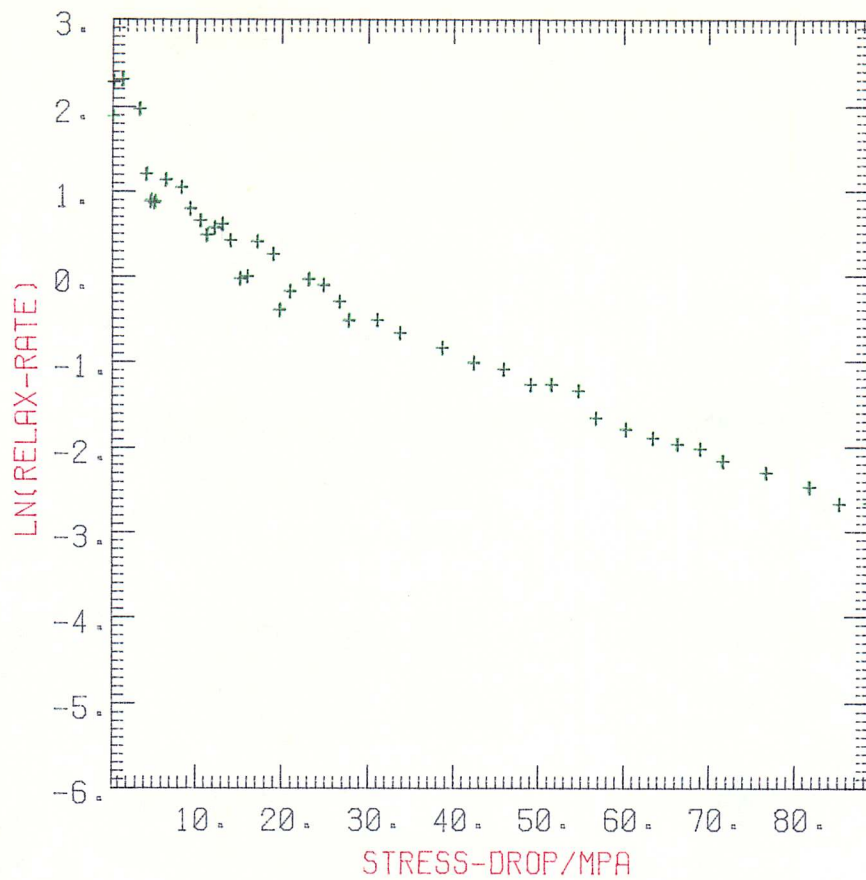
Fig. (5:23, a to e) Examples of IBM output for an A/R + LTHT "A"
patented wire specimen.



LOAD RELAXATIONS

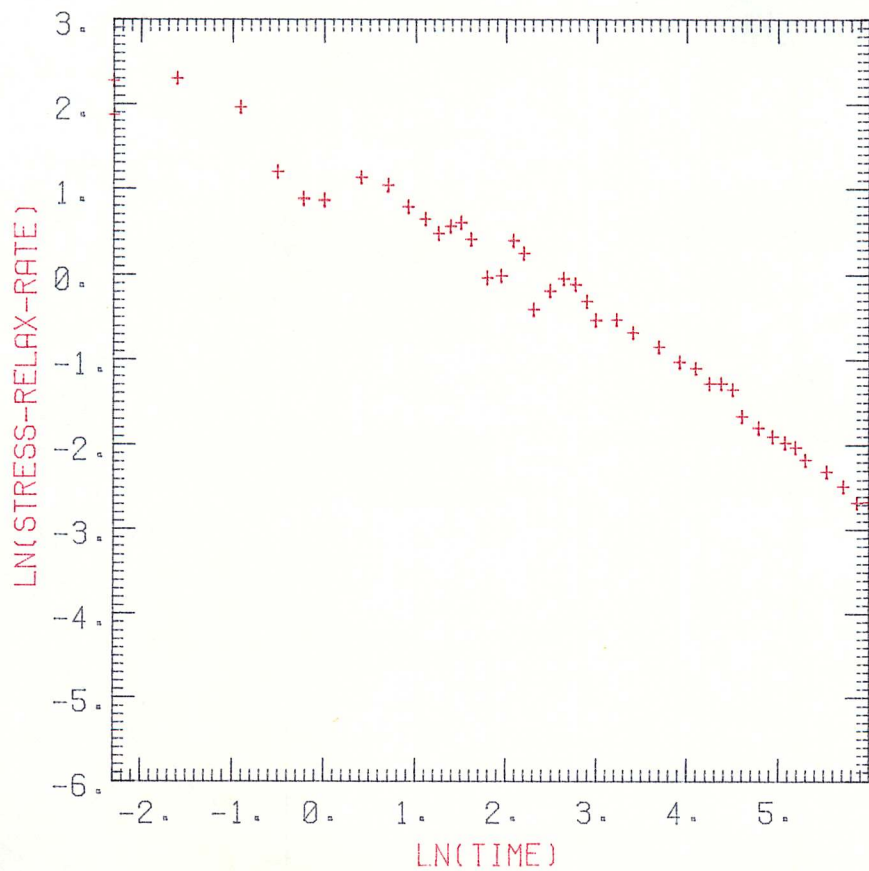


LN(RELAX-RATE)/STRESS-DROP



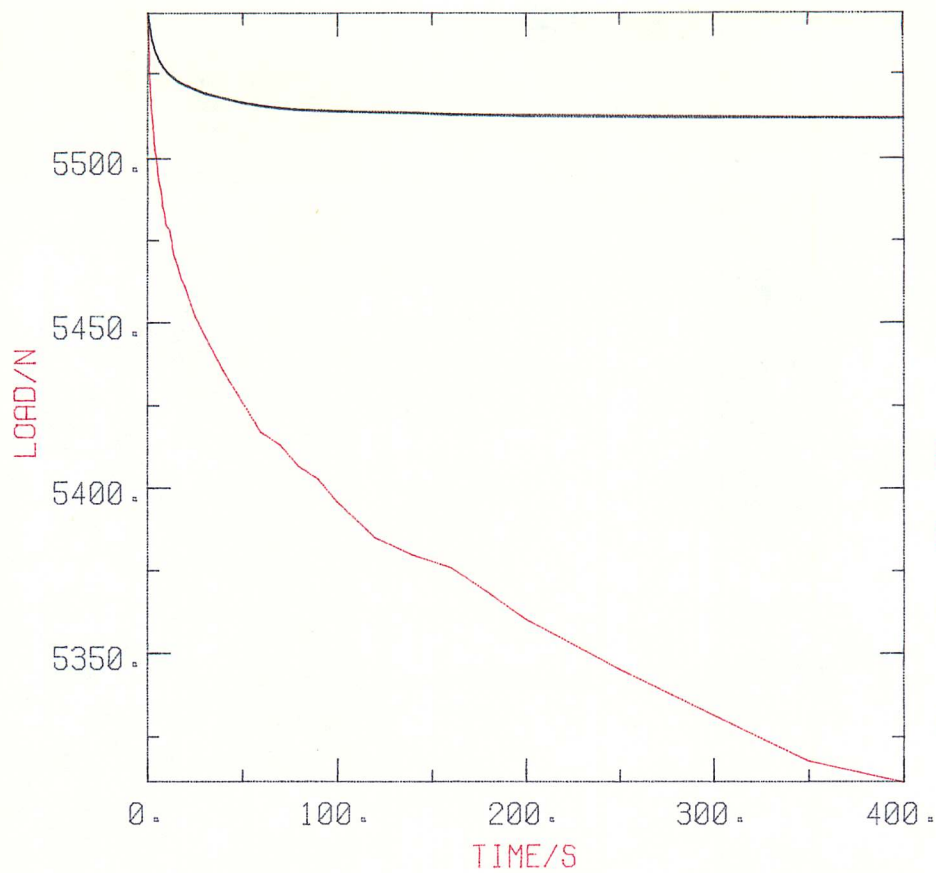
H121

RELAXATION 1



H121

RELAXATION 1



H121

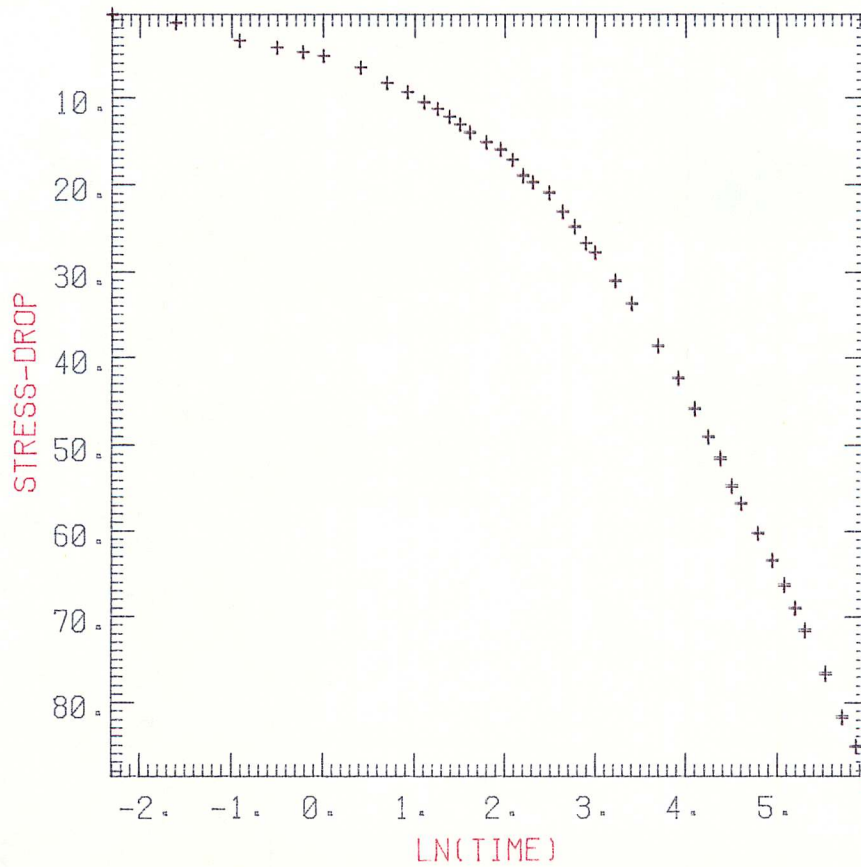
5543.0 N

SPECIMEN RELAXATION

MACHINE RELAXATION

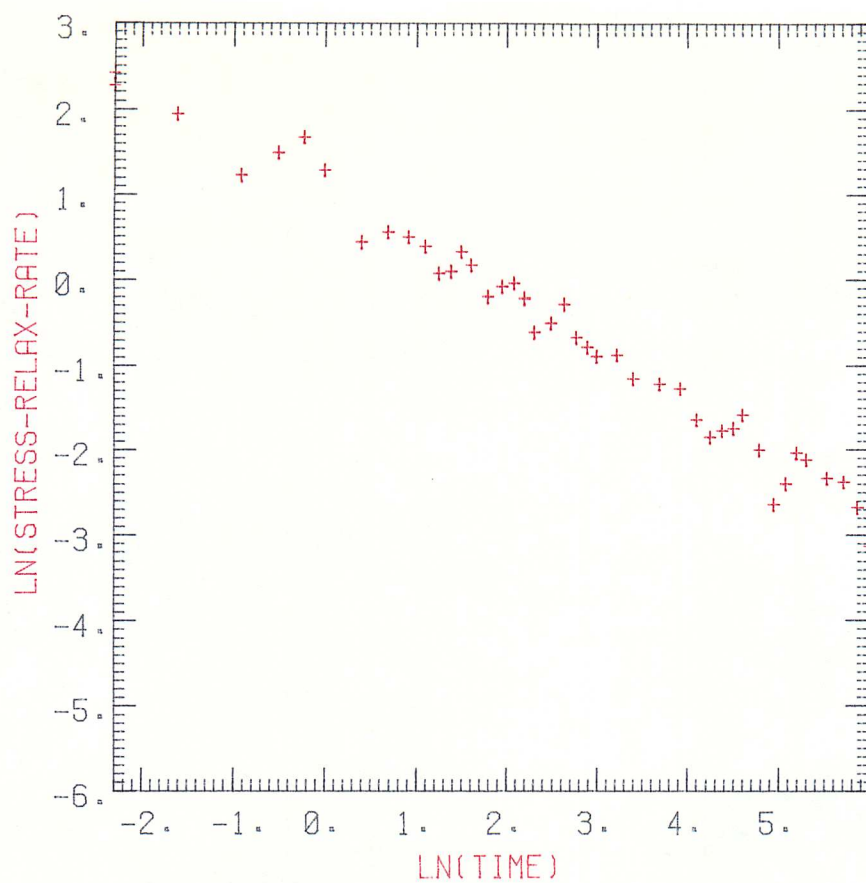
RELAXATION 2

STRESS-DROP/LN(TIME)



H121

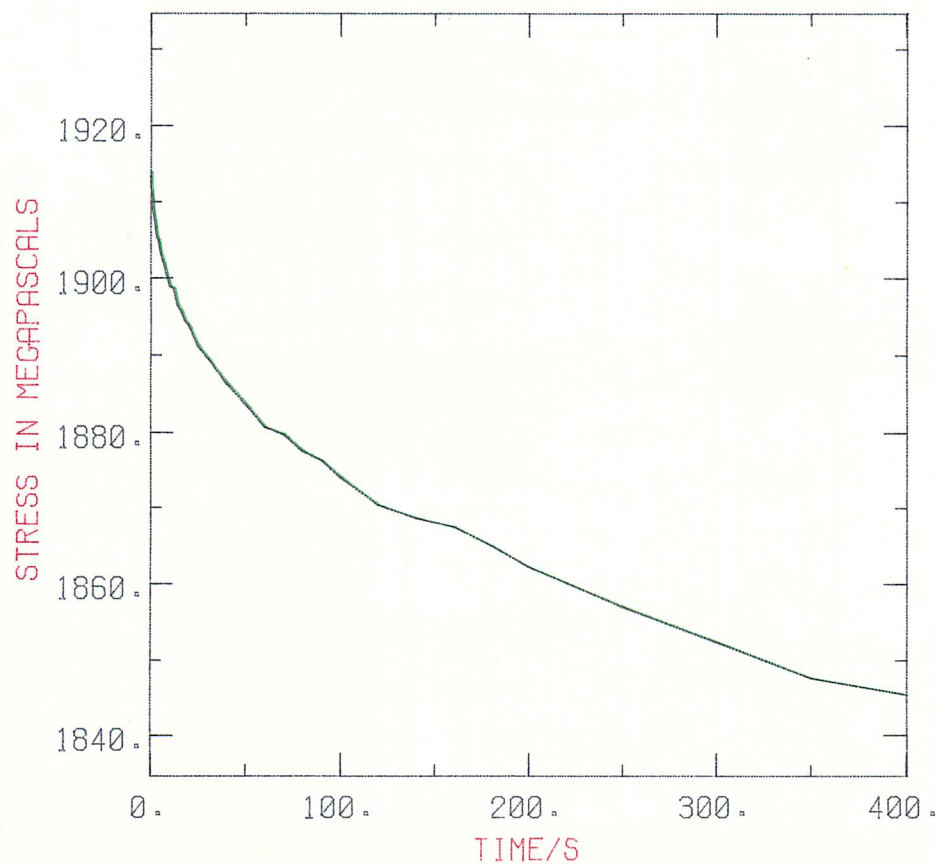
RELAXATION 1



H121

RELAXATION 2

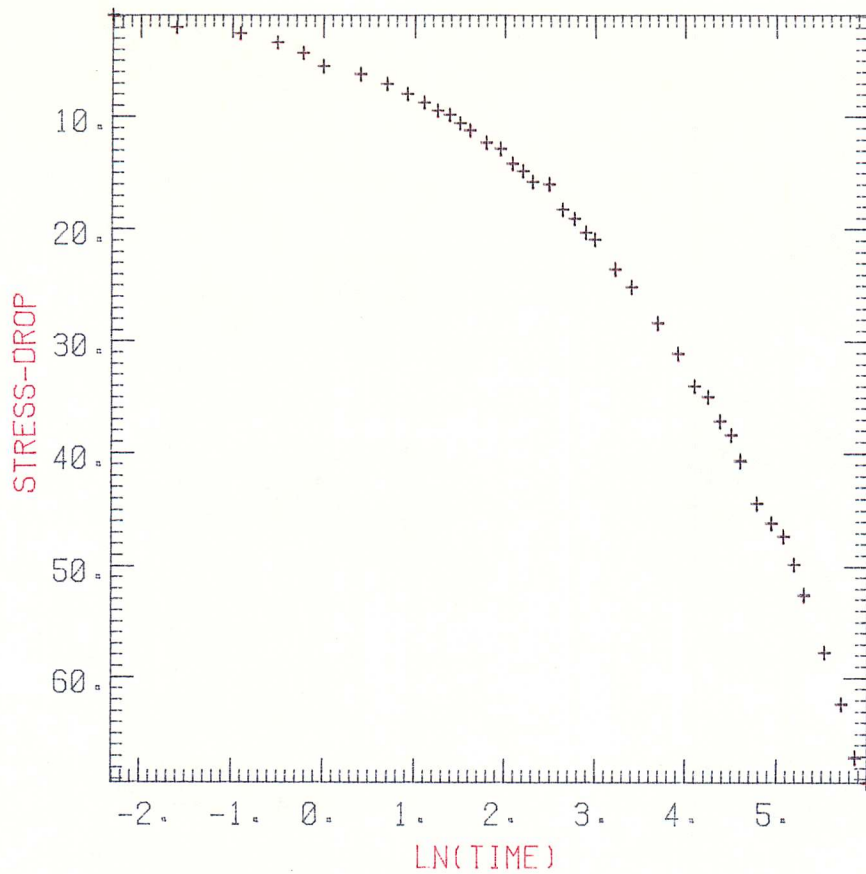
STRESS RELAXATION



H121

1914.7 MPA

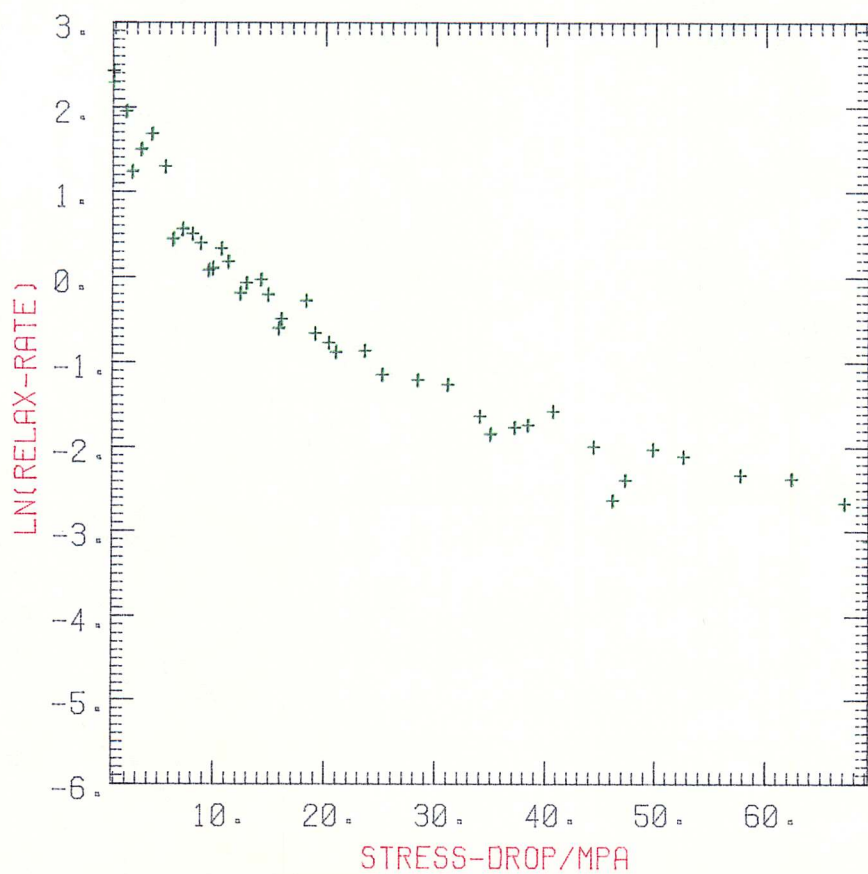
RELAXATION 2



H121

RELAXATION 2

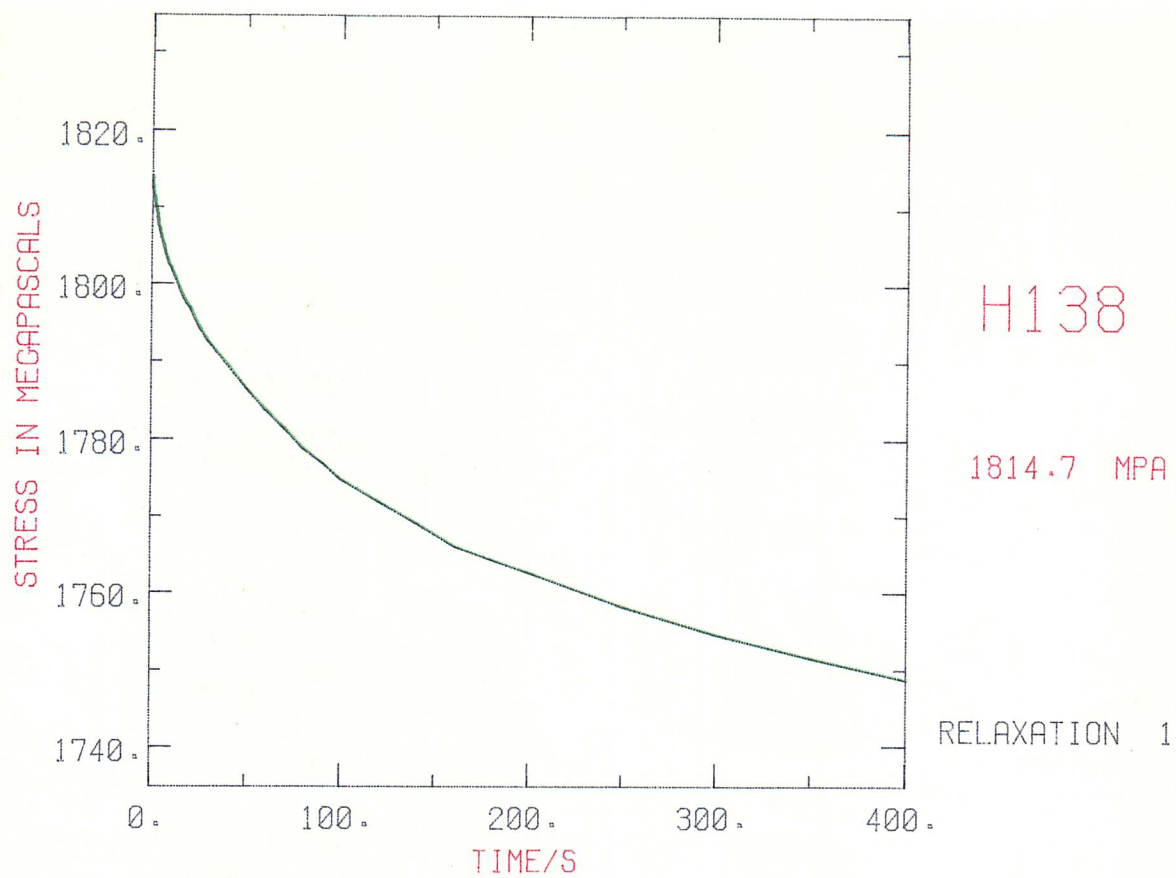
LN(RELAX-RATE)/STRESS-DROP



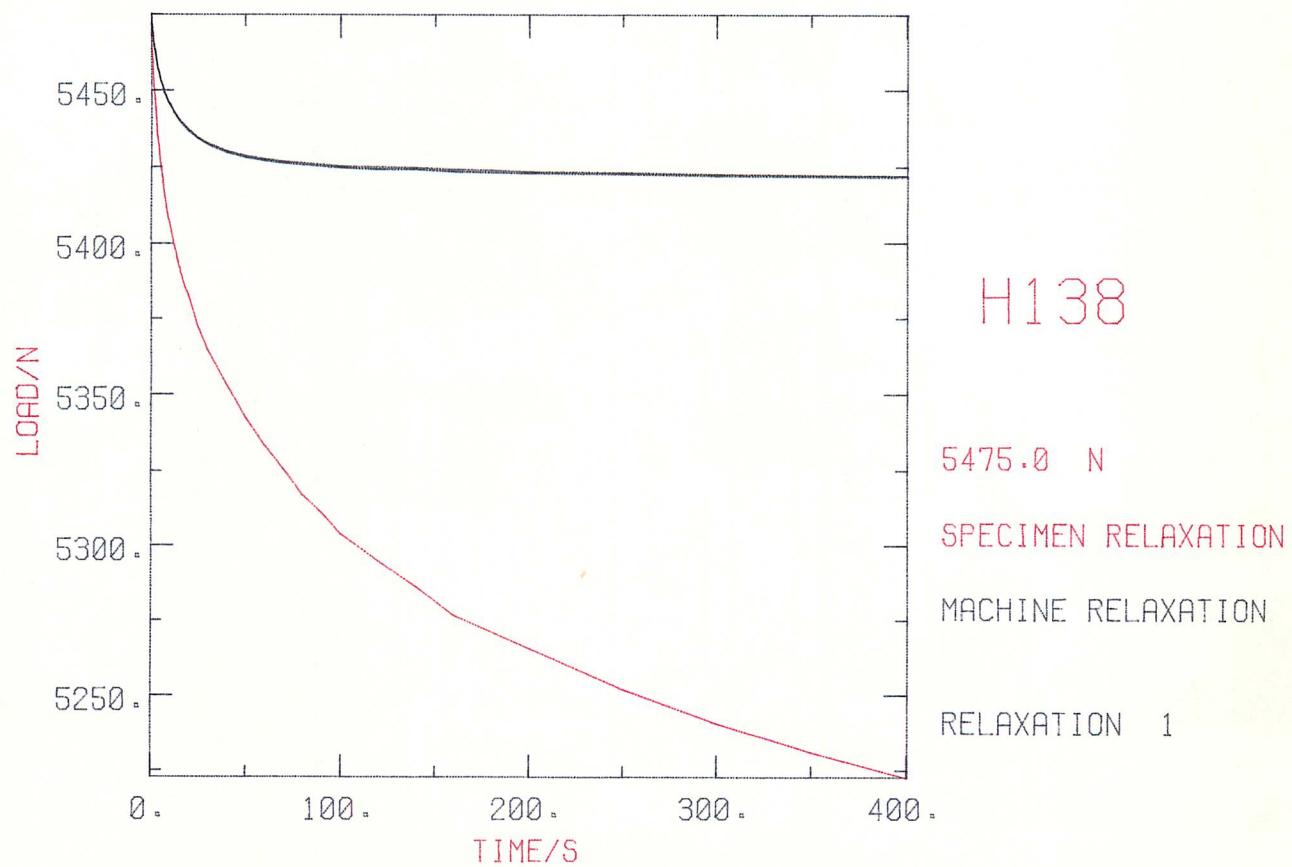
H121

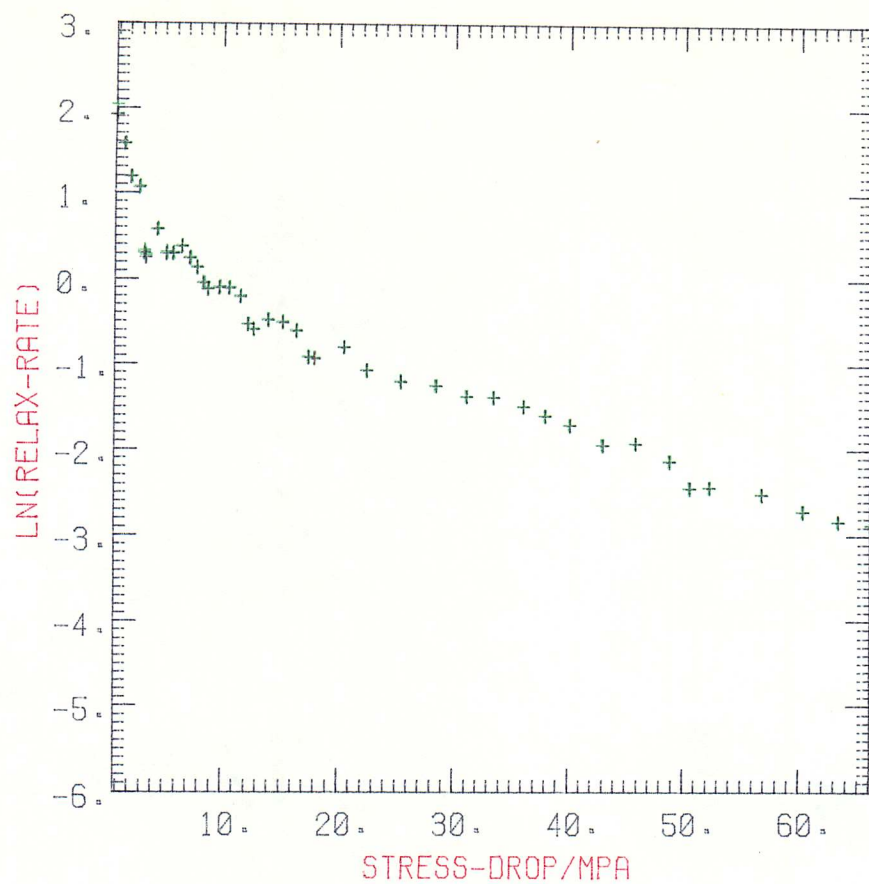
RELAXATION 2

Fig. (5:24, a to e) Examples of IBM output for an A/R + LTHT "B"
patented wire specimen.



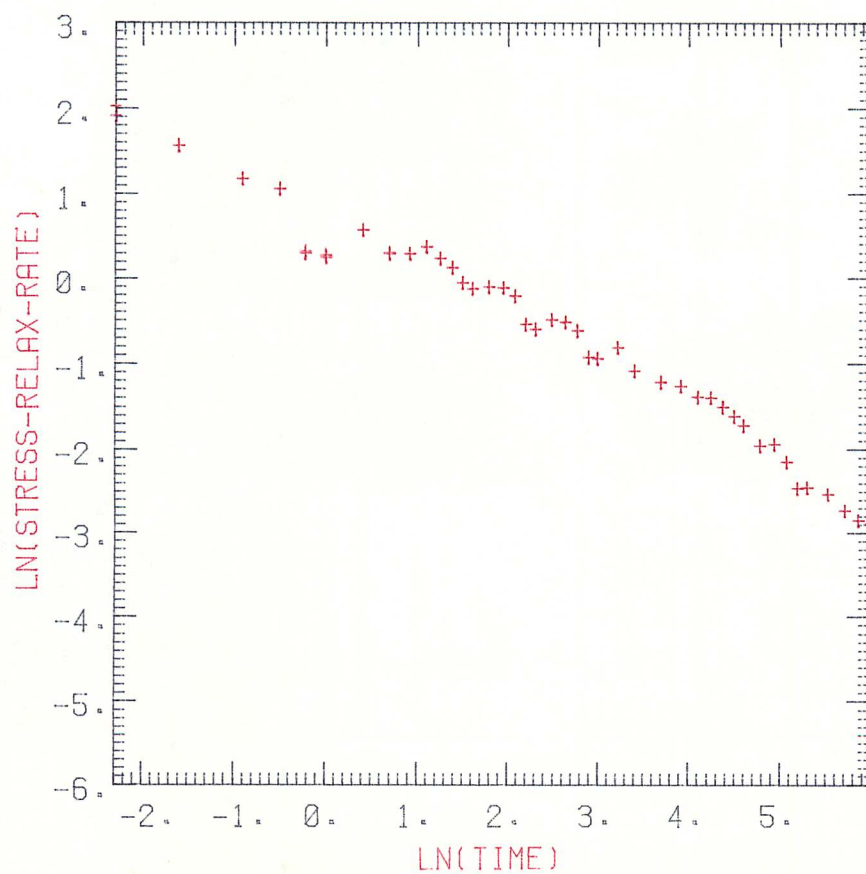
LOAD RELAXATIONS





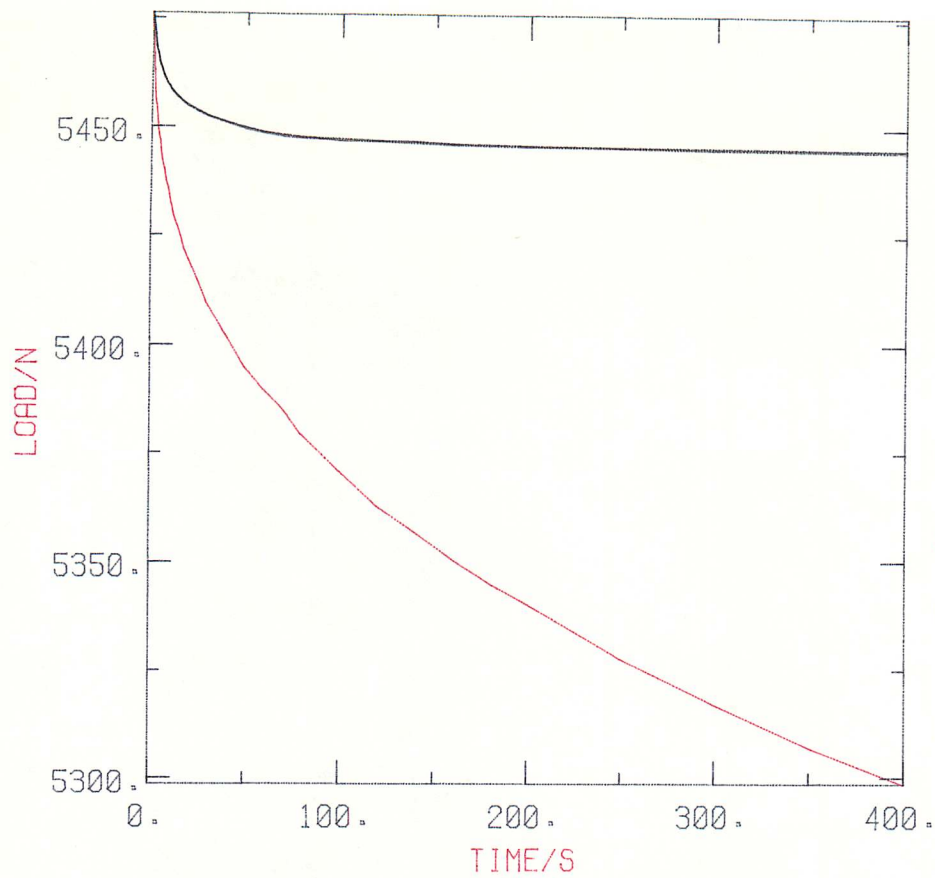
H138

RELAXATION 1

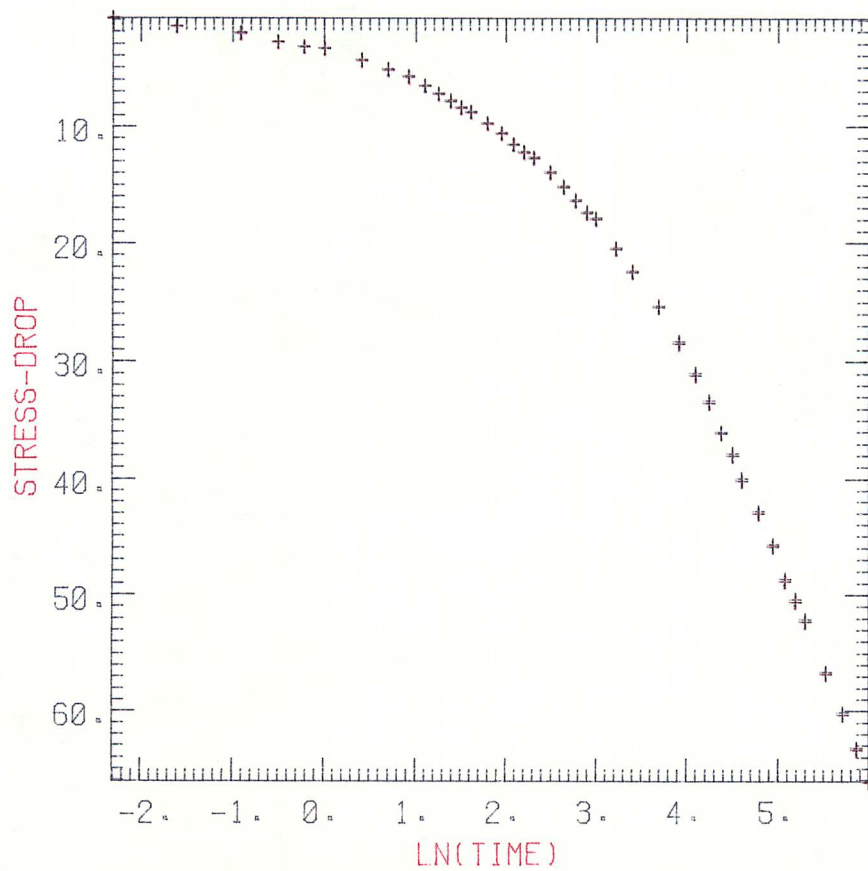


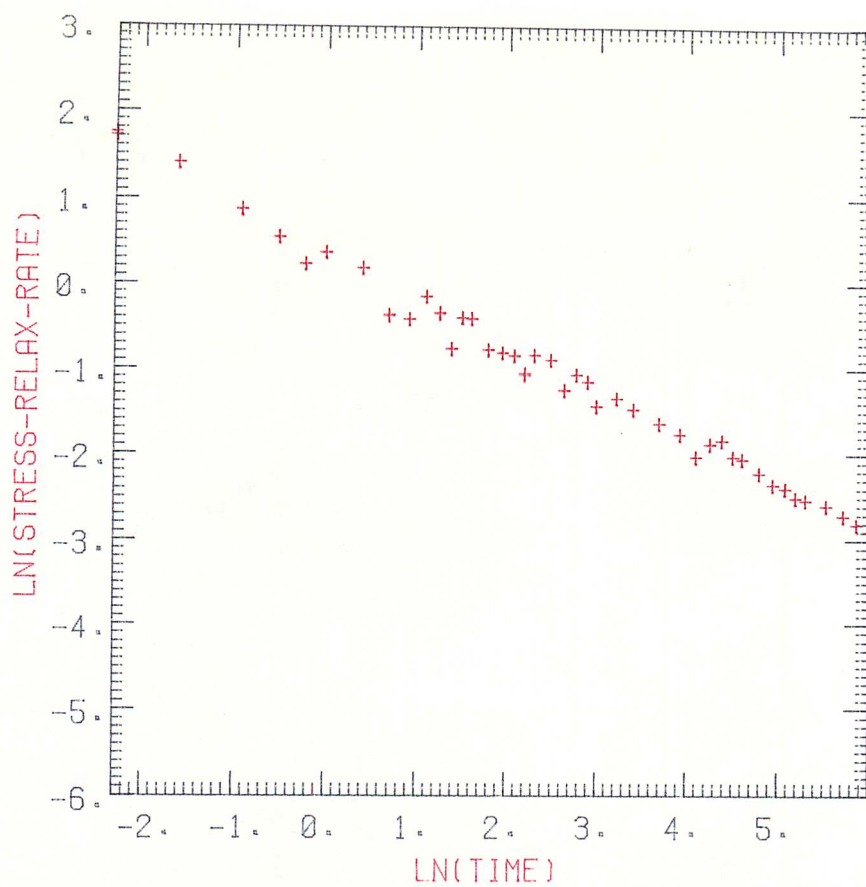
H138

RELAXATION 1



STRESS-DROP/LN(TIME)

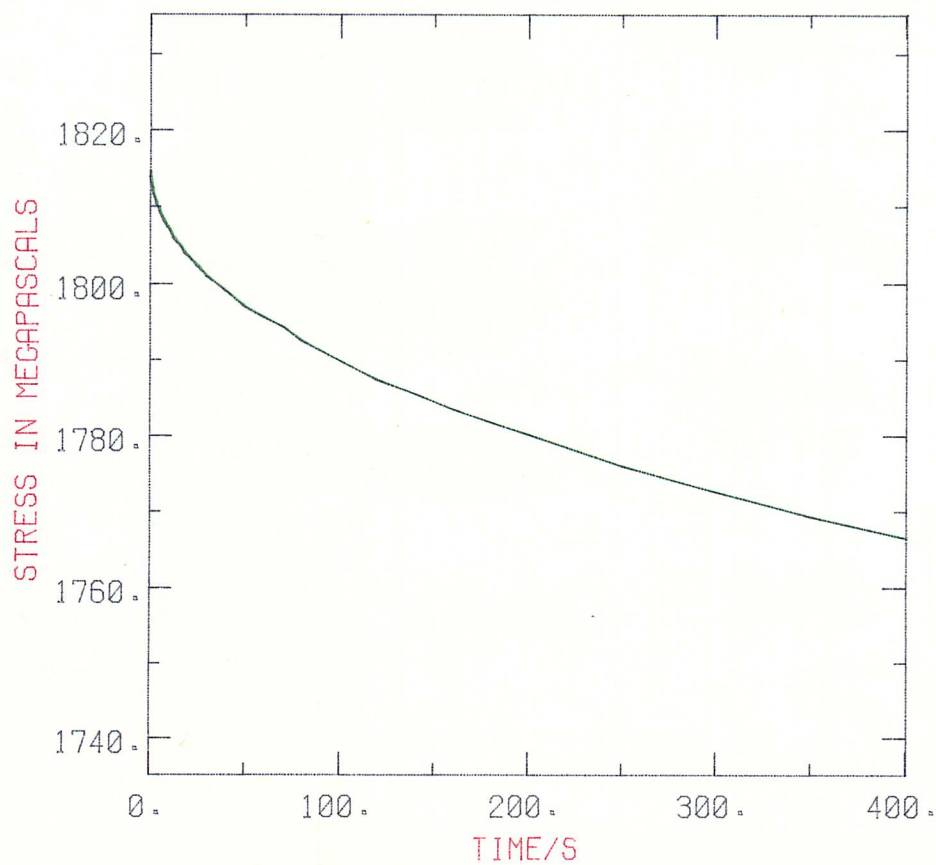




H138

RELAXATION 2

STRESS RELAXATION



H138

1815.0 MPA

RELAXATION 2

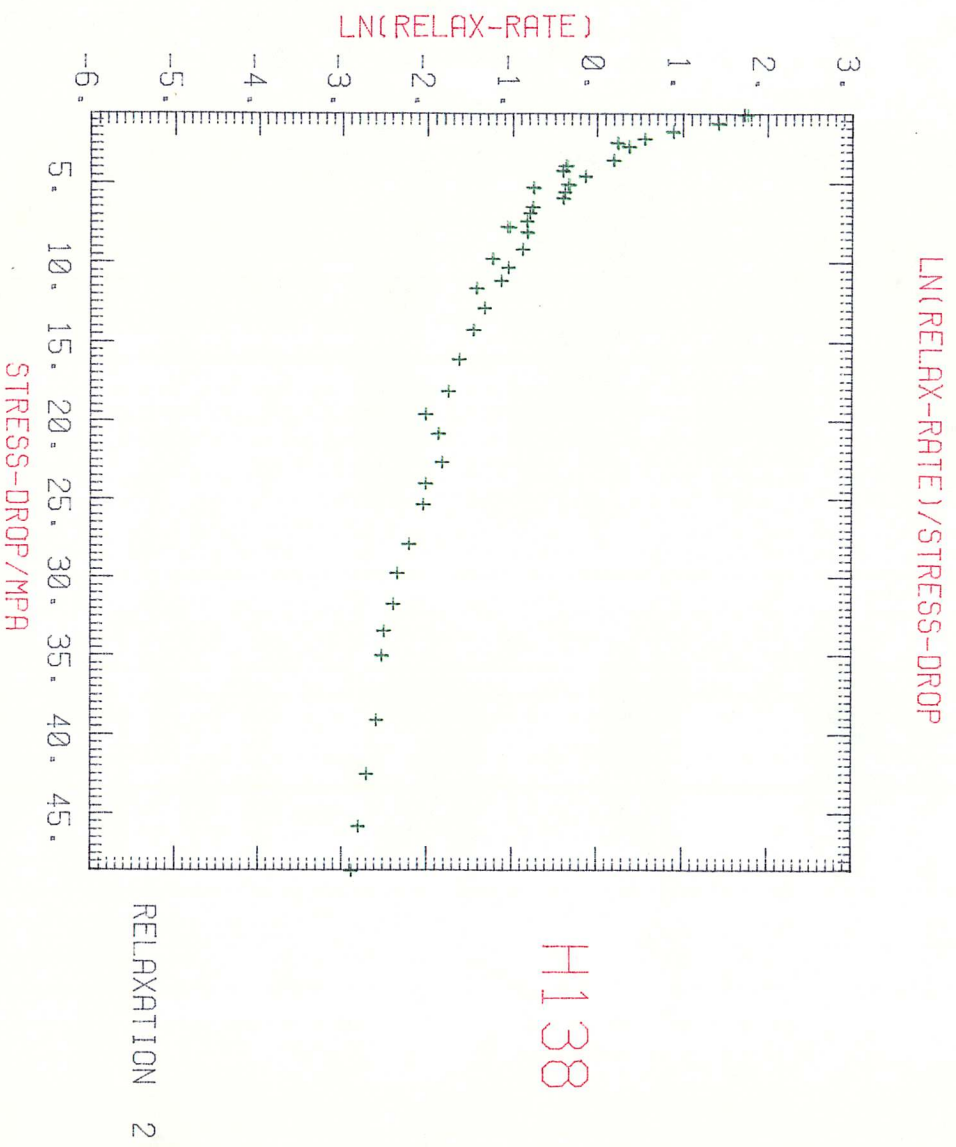
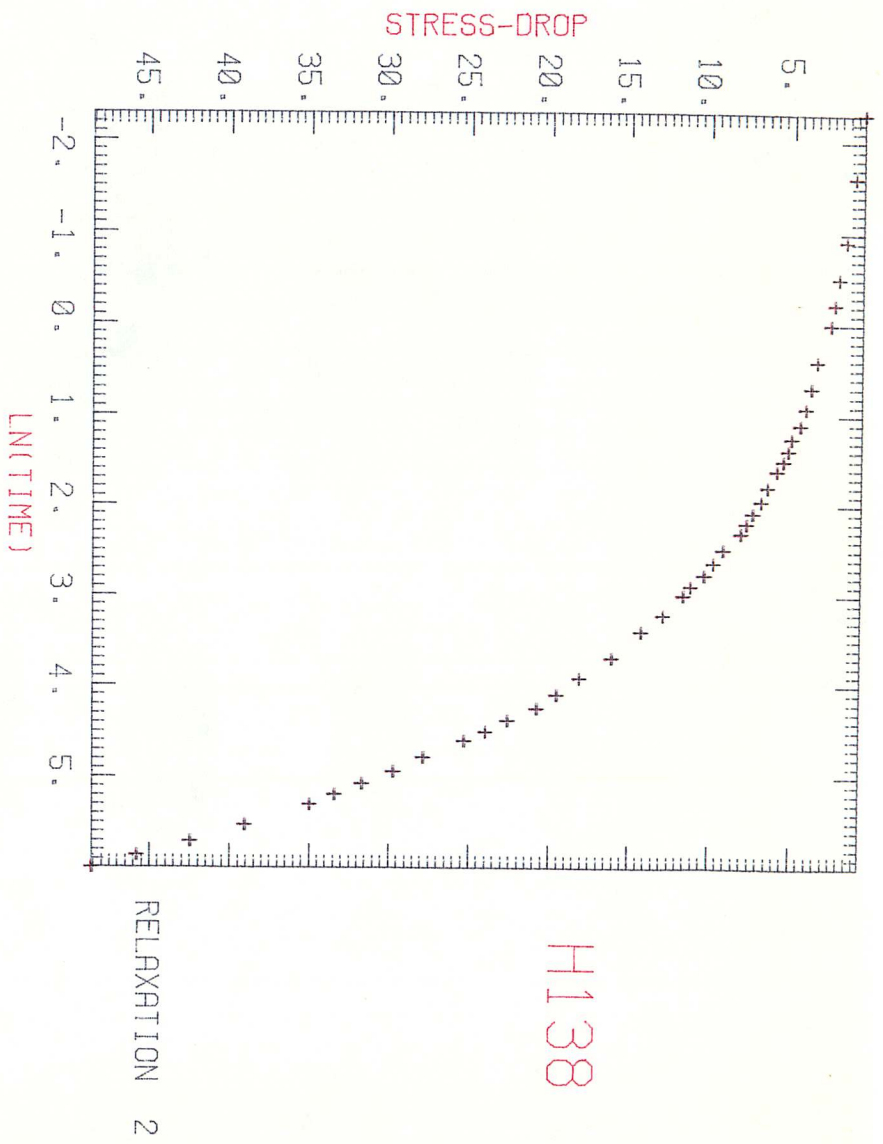
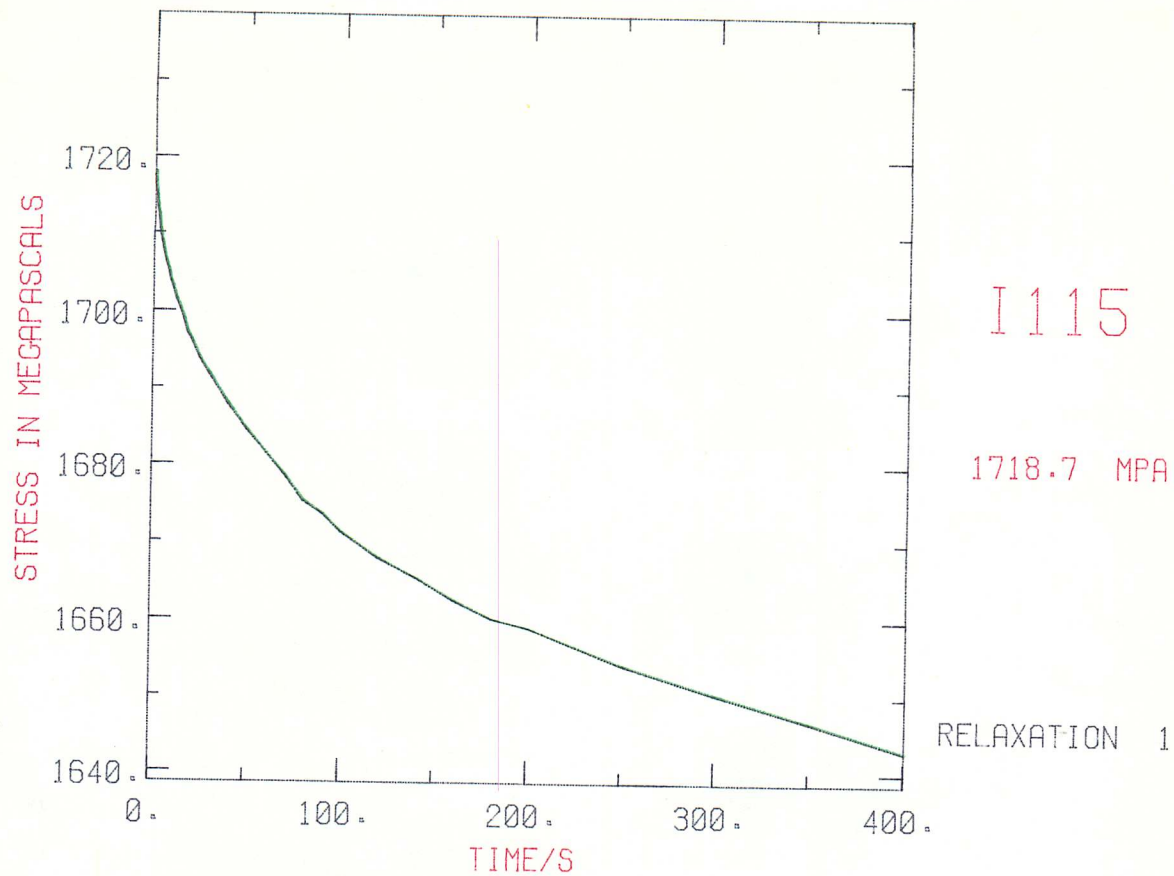
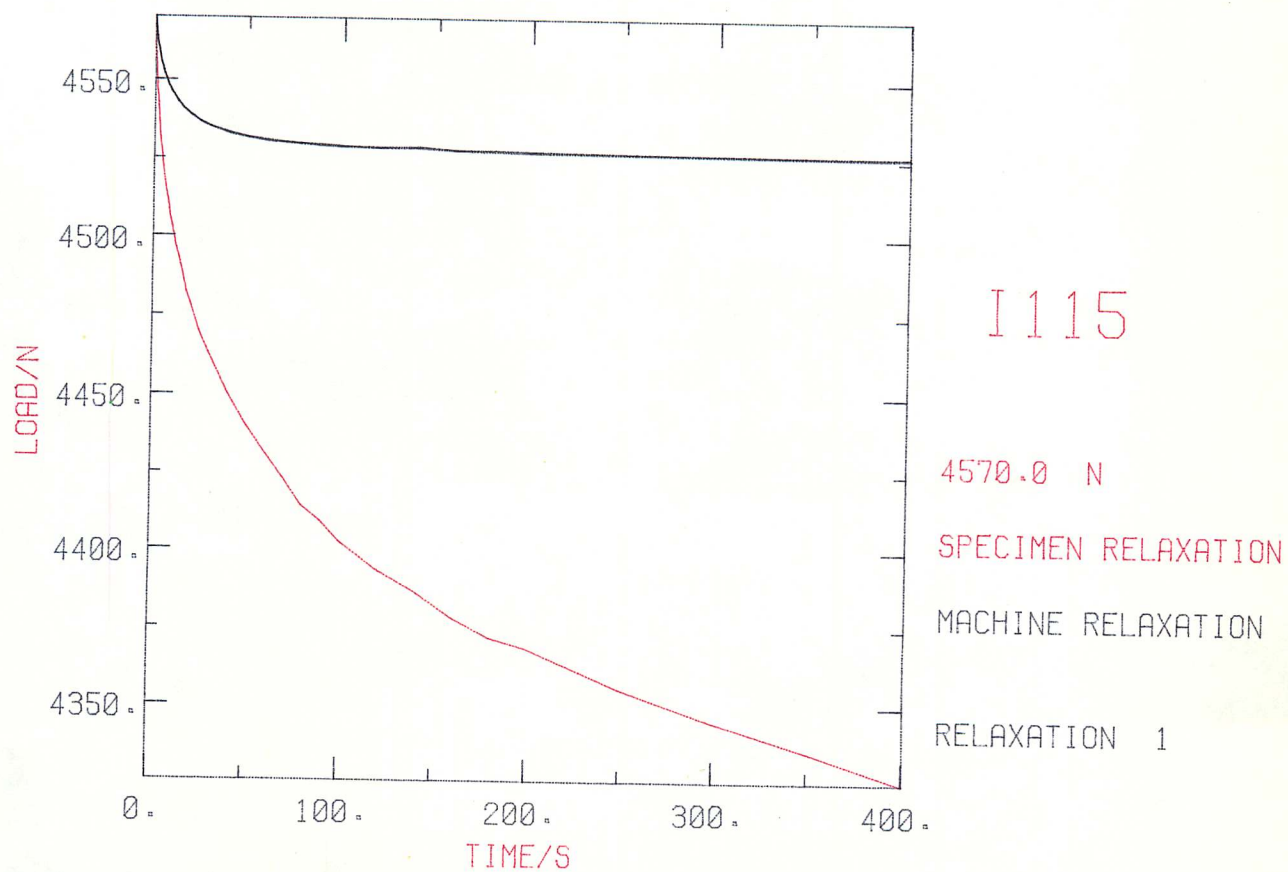
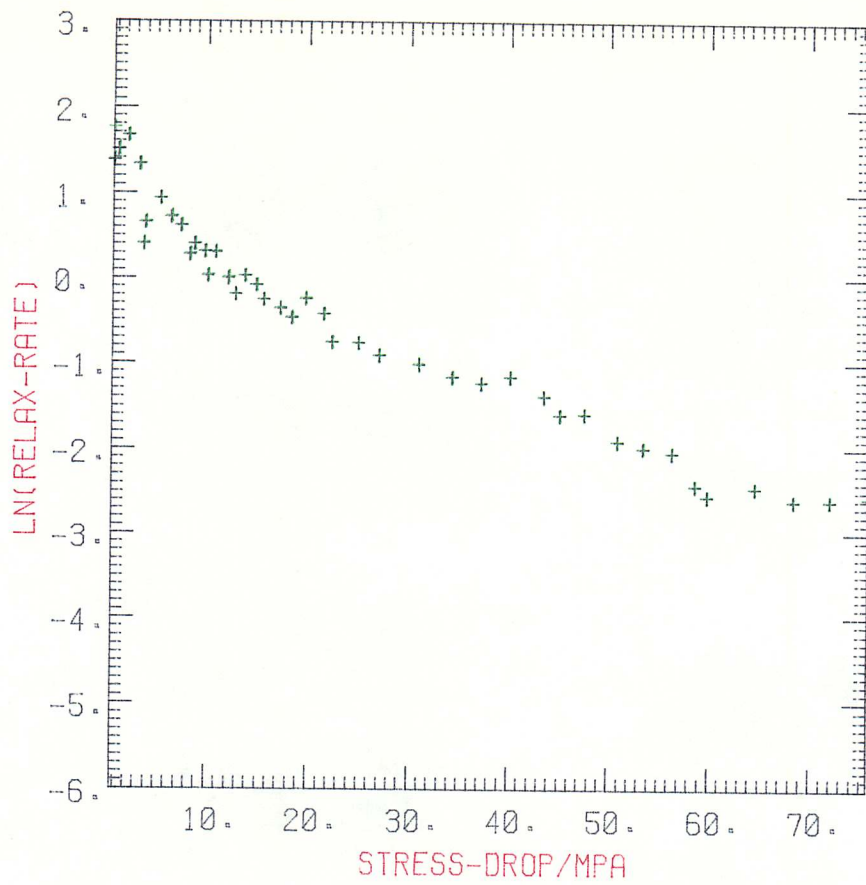


Fig. (5:25, a to e) Examples of IBM output for an A/R + LTHT "C"
patented wire specimen.



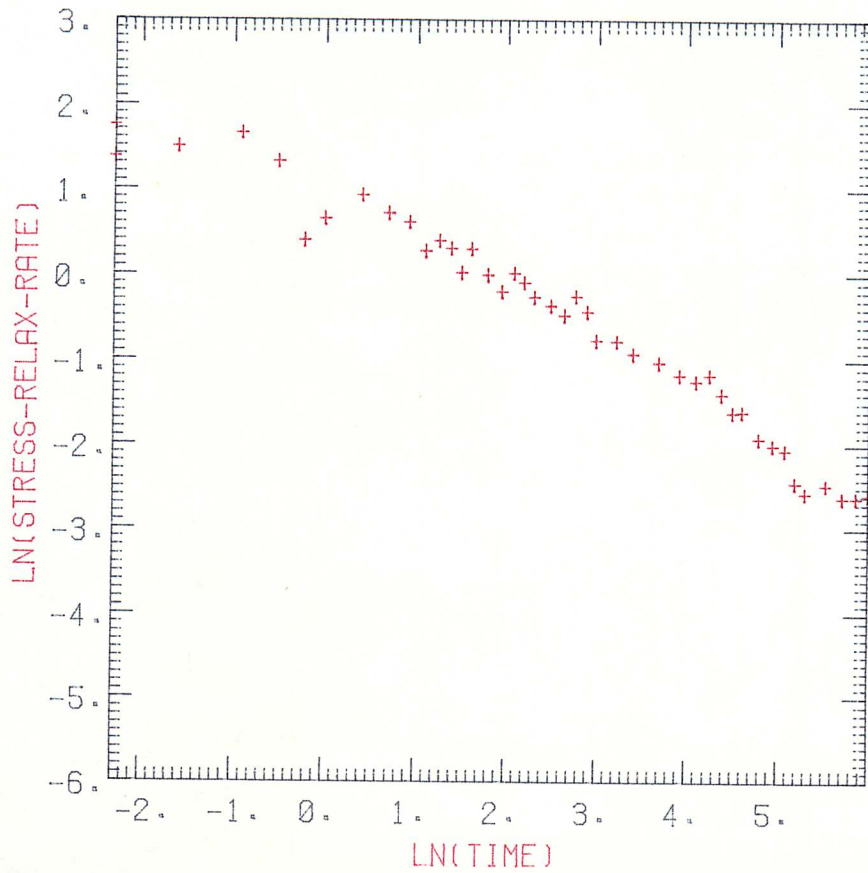
LOAD RELAXATIONS





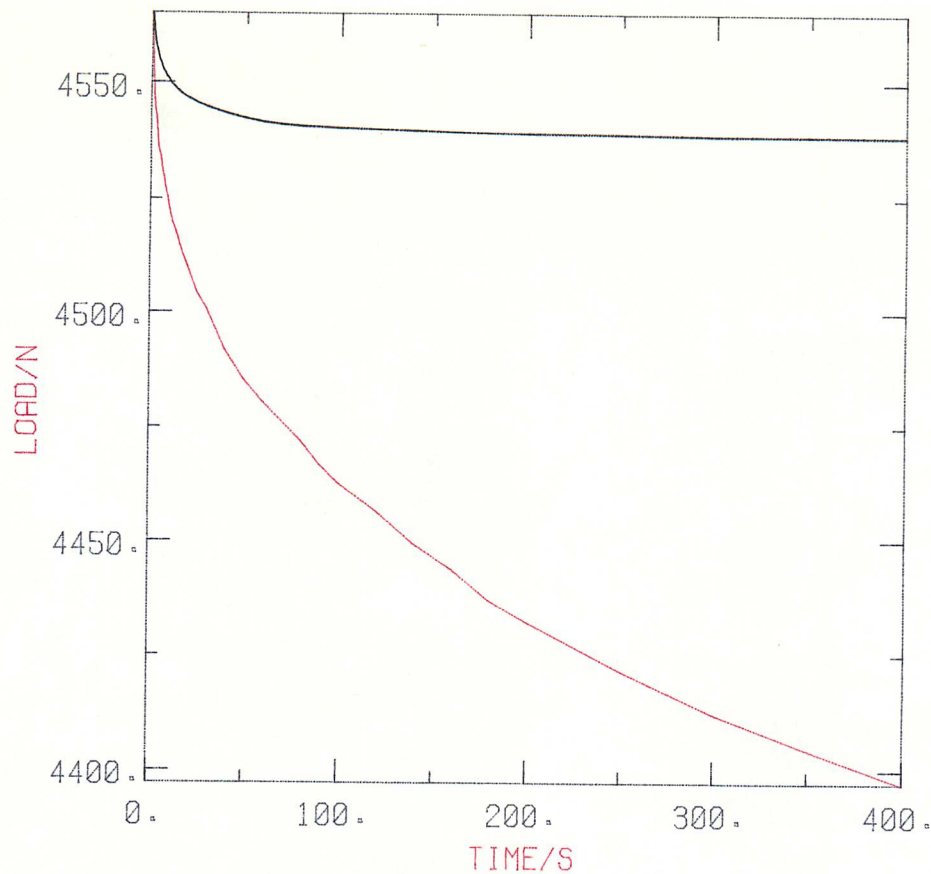
I115

RELAXATION 1



I115

RELAXATION 1



I115

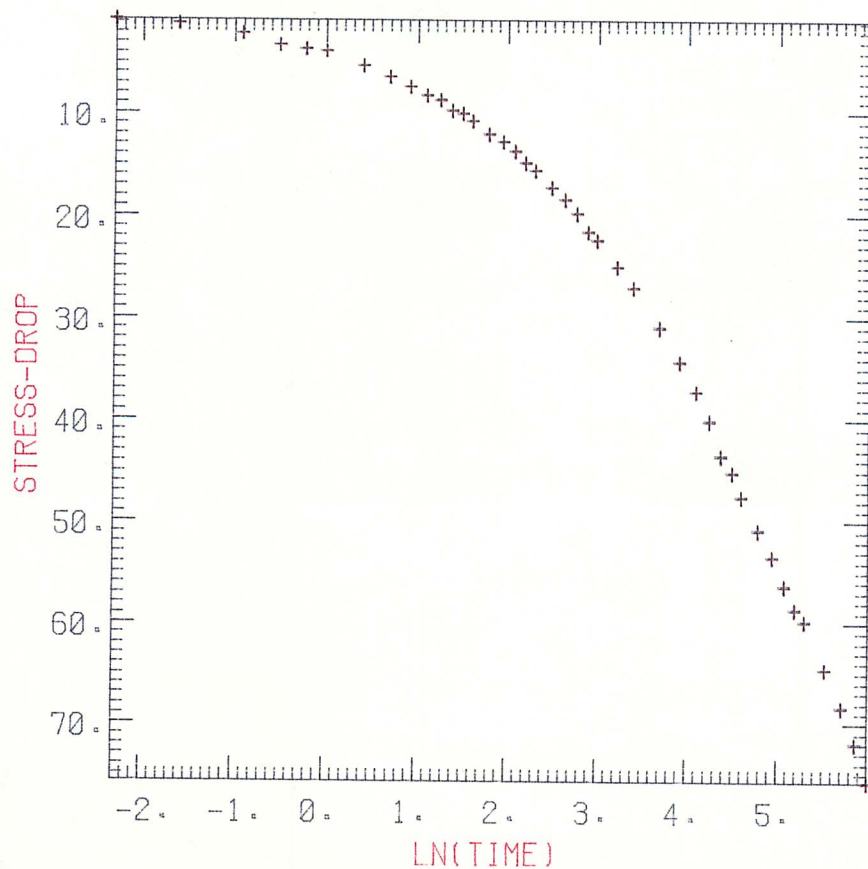
4565.0 N

SPECIMEN RELAXATION

MACHINE RELAXATION

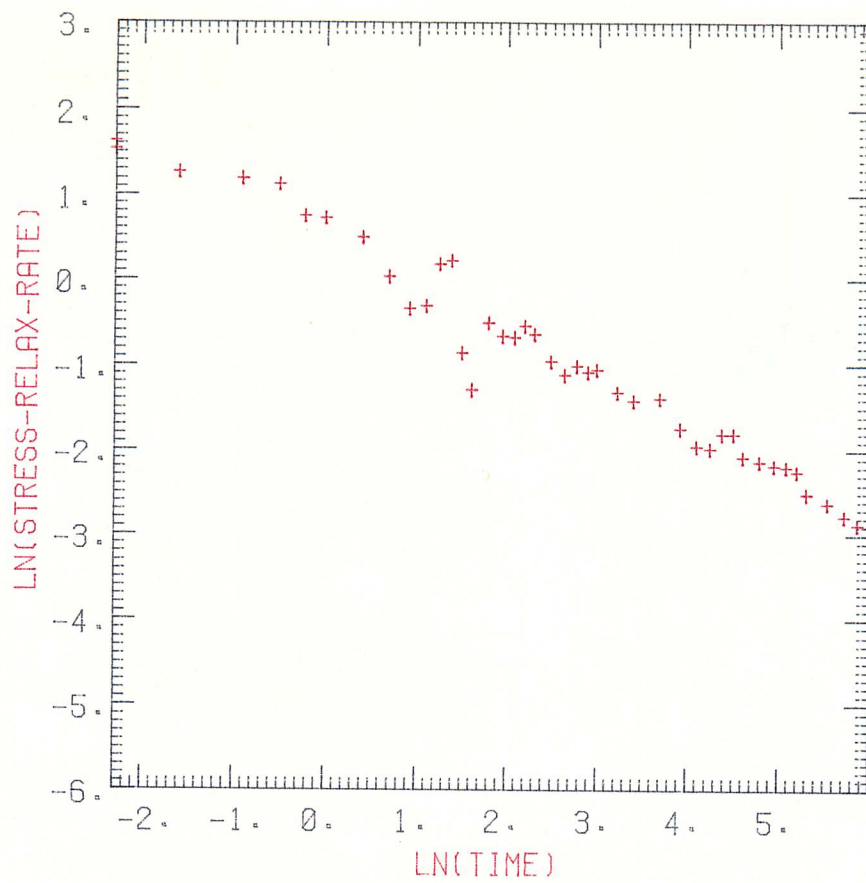
RELAXATION 2

STRESS-DROP/LN(TIME)



I115

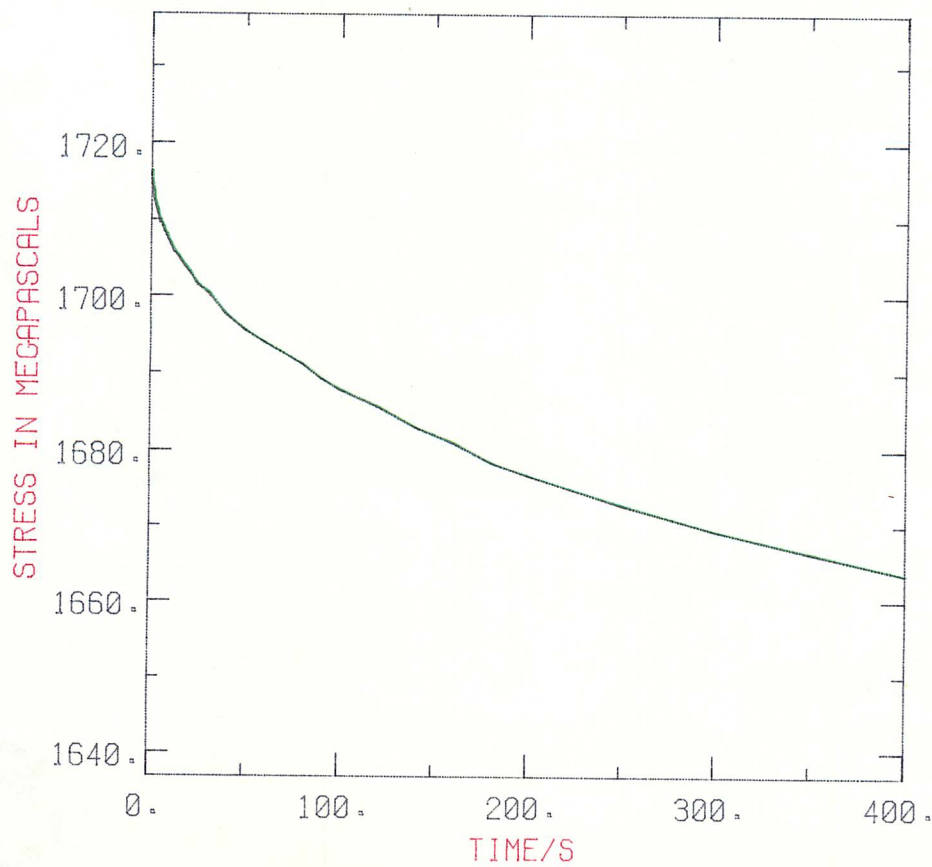
RELAXATION 1



I115

RELAXATION 2

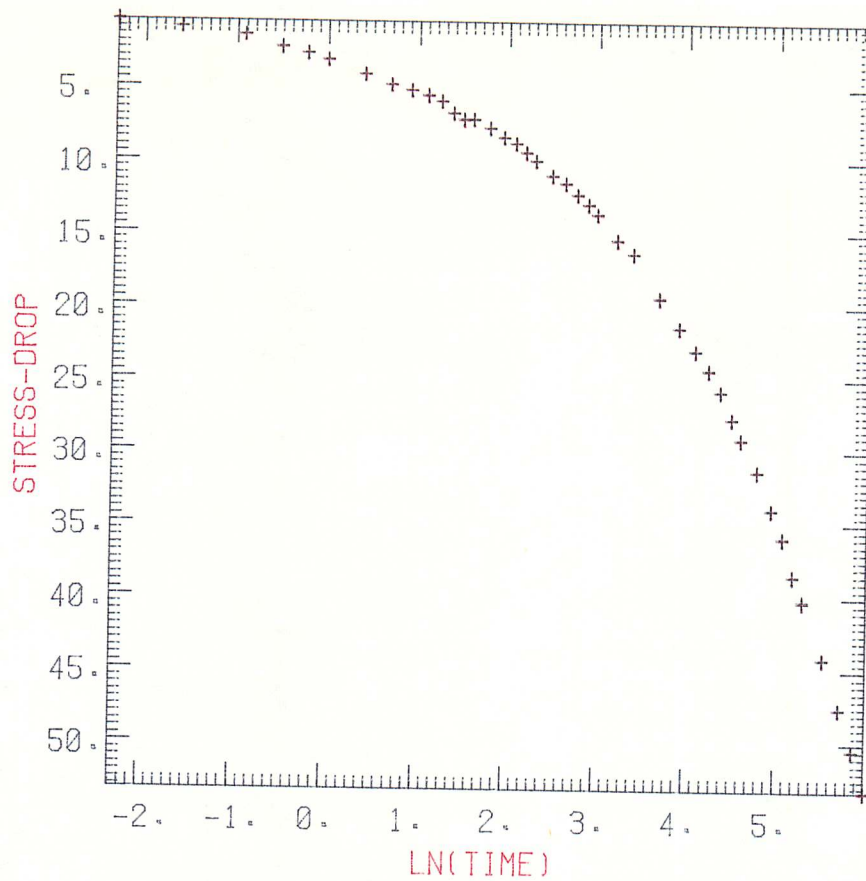
STRESS RELAXATION



I115

1716.8 MPA

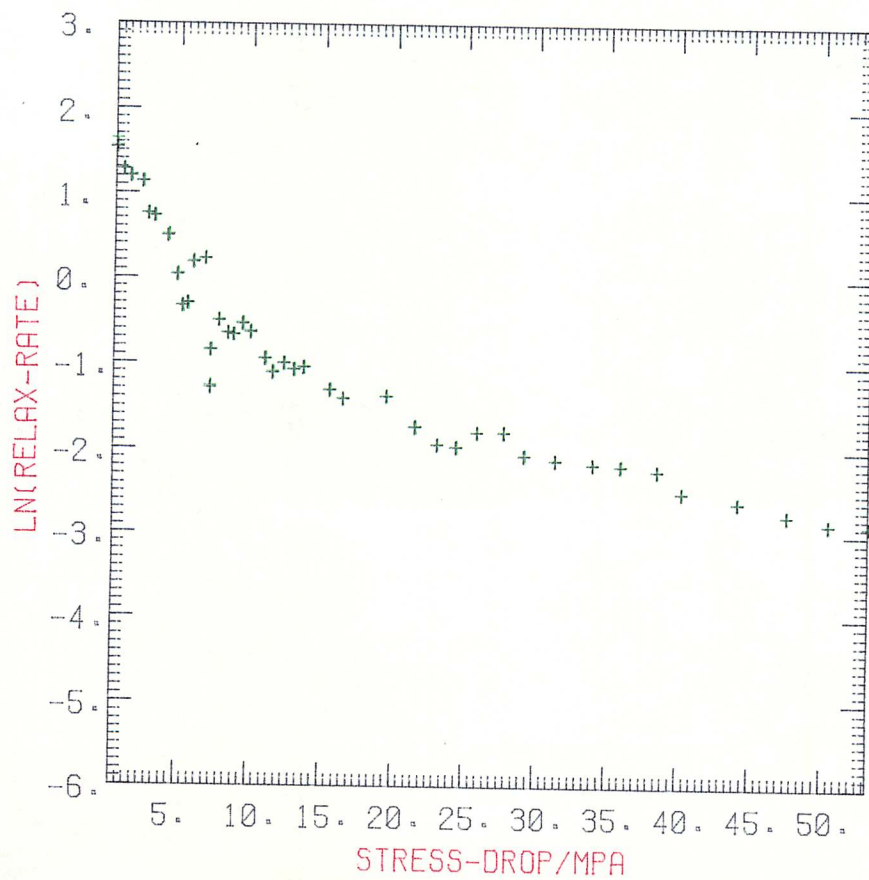
RELAXATION 2



I115

RELAXATION 2

LN(RELAX-RATE)/STRESS-DROP



I115

RELAXATION 2

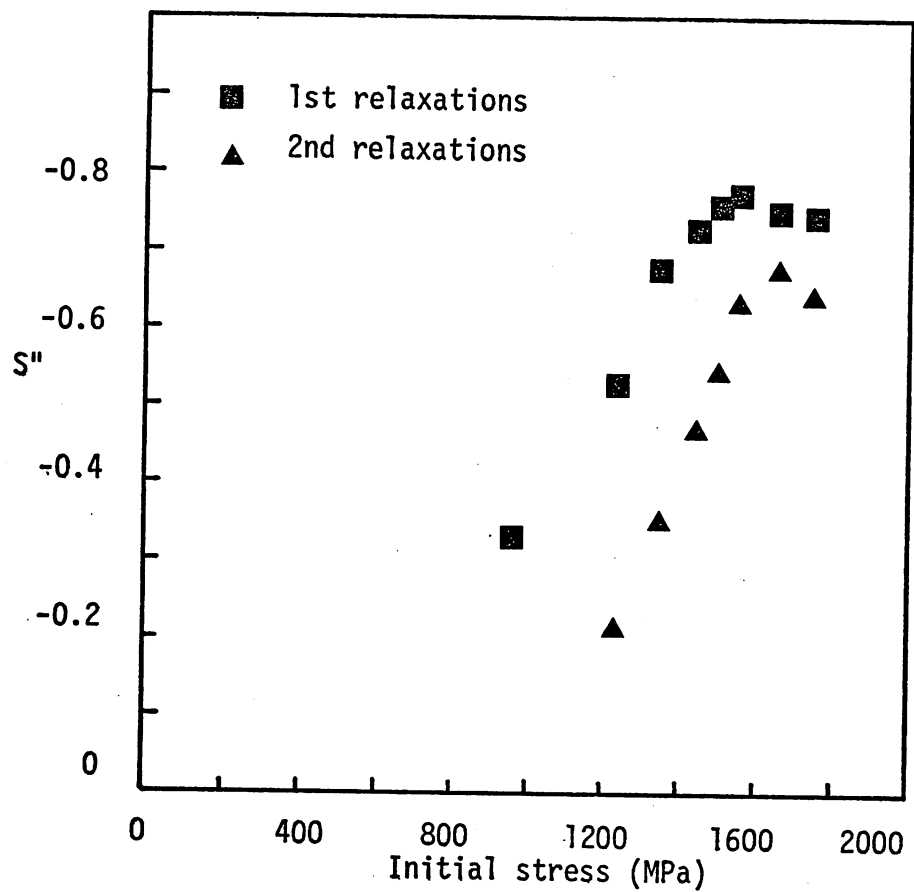


Fig. (5:26a) Values of gradient (S'') of $\ln \sigma$ vs. $\ln t$ graphs for A/R patented steel wire, for both 1st and 2nd relaxations.

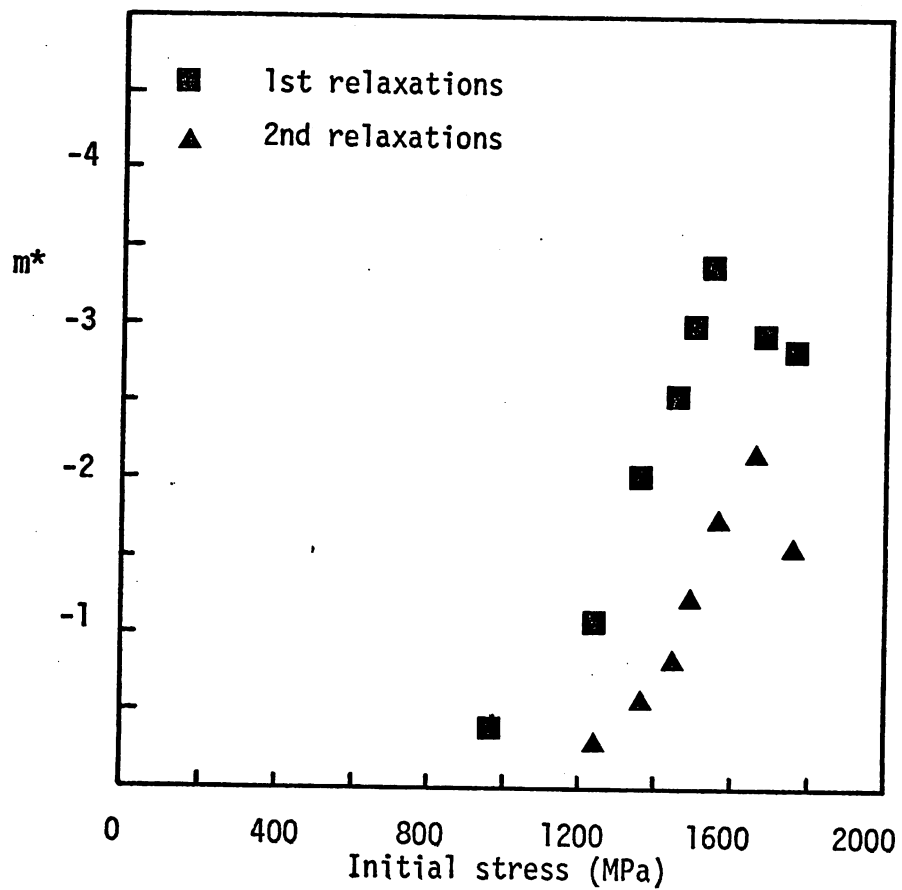


Fig. (5:26b) Corresponding values of m^* .

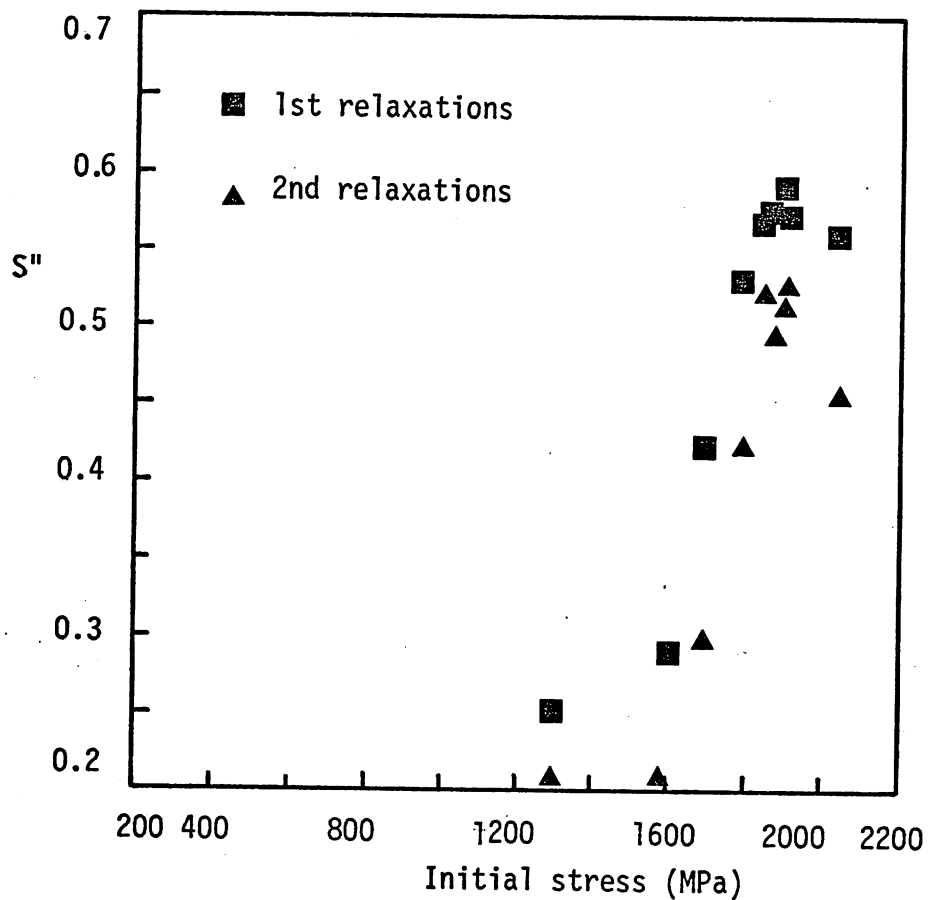


Fig. (5:27a) Values of gradient (S'') of $\ln \sigma$ vs. $\ln t$ graphs for A/R + LTHT "A" patented steel wire, for both 1st and 2nd relaxations.

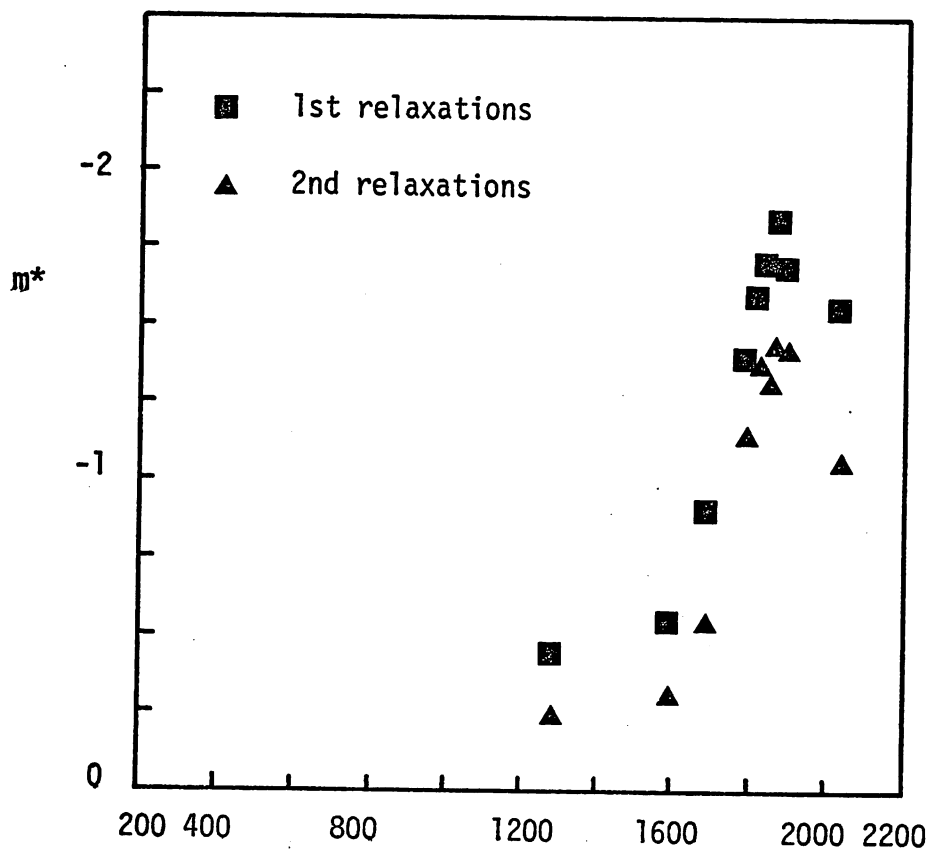


Fig. (5:27b) Corresponding values of m^* .

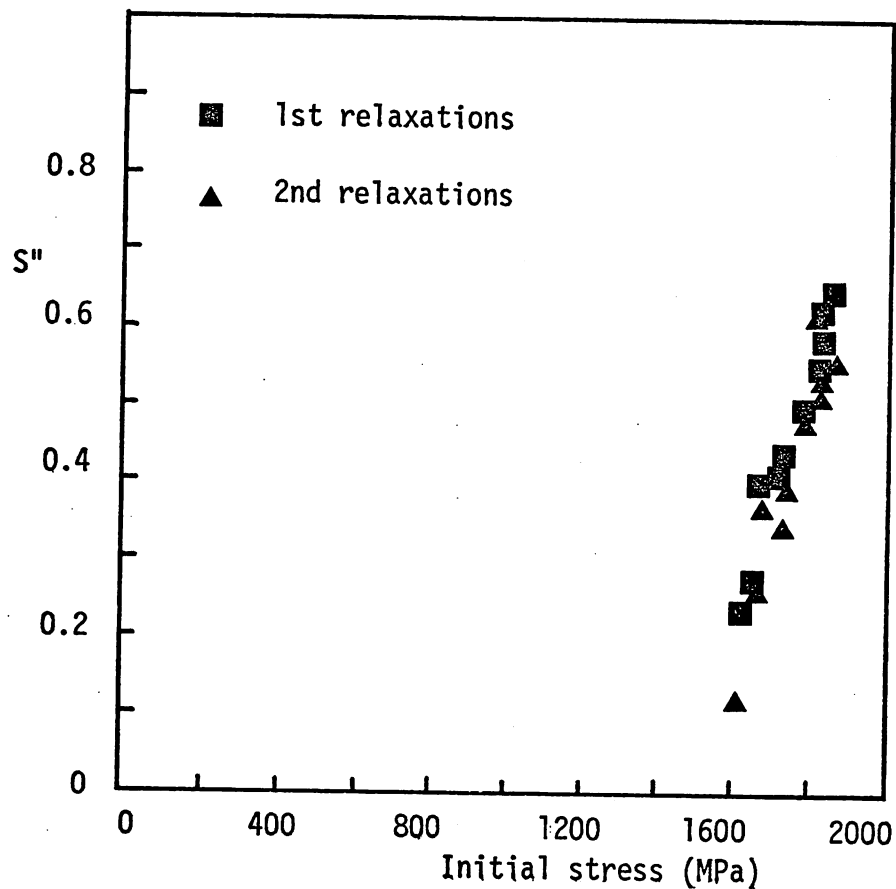


Fig. (5:28a) Values of gradient(S'') of $\ln \delta$ vs $\ln t$ graphs for A/R + LTHT "B" patented steel wire, for both 1st and 2nd relaxations.

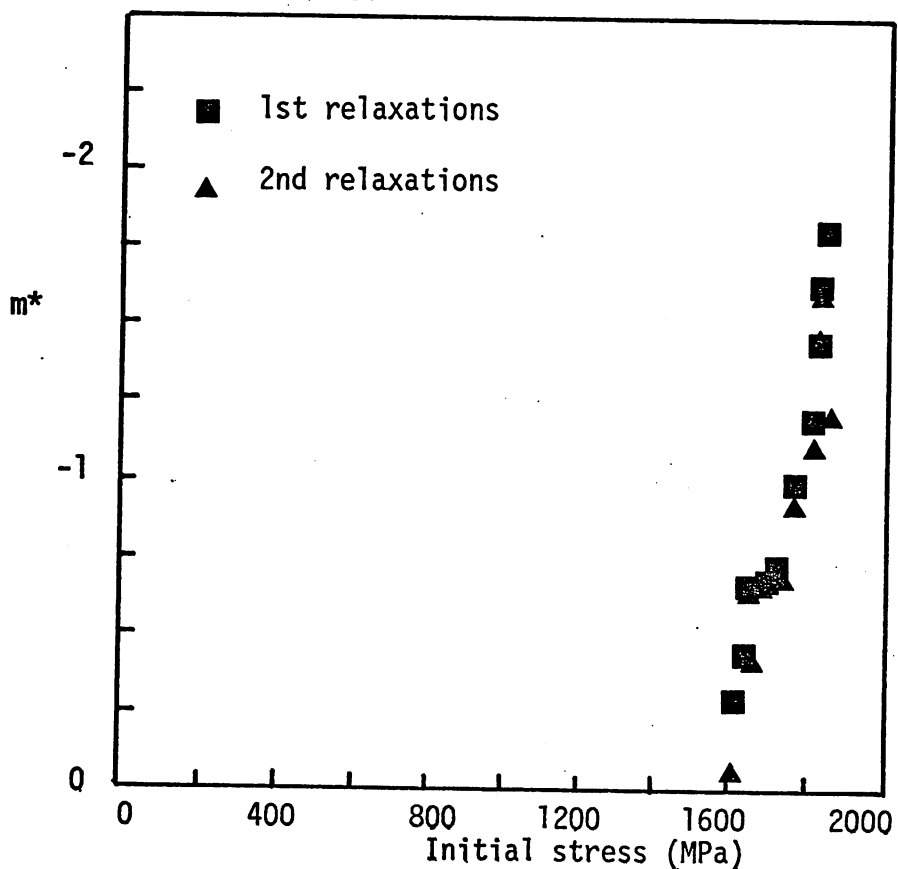


Fig. (5:28b) Corresponding values of m^* .

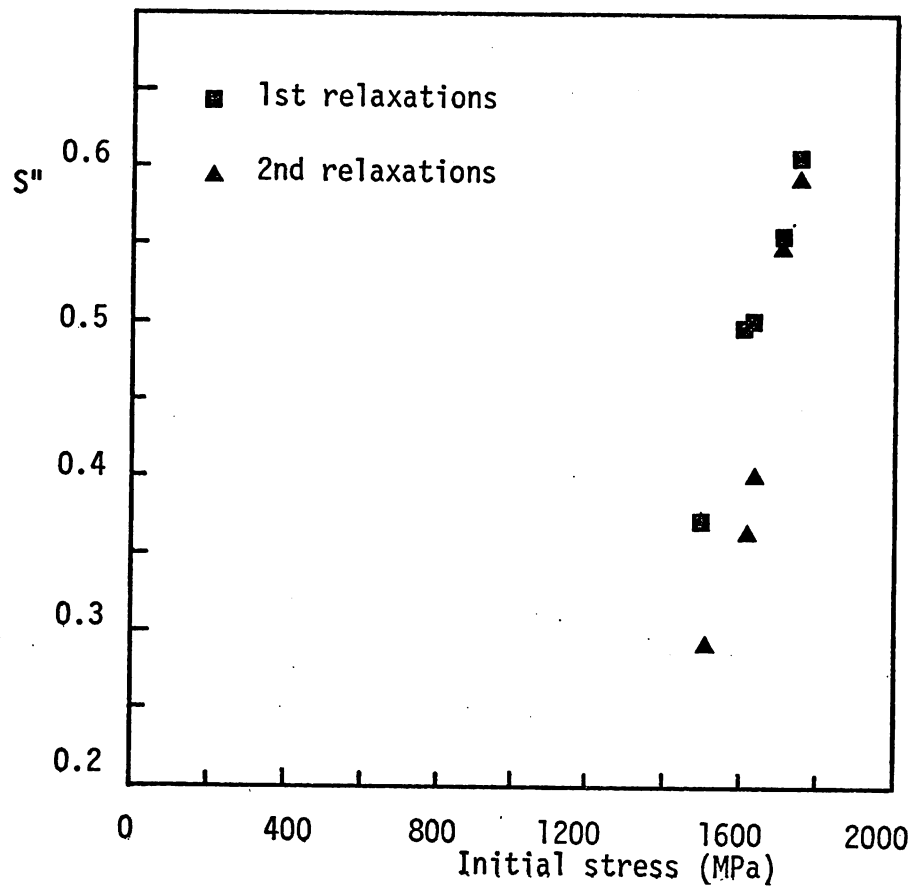


Fig. (5:29a) Values of gradient (S'') of $\ln \sigma$ vs $\ln t$ graphs for A/R + LTHT "C" patented steel wire, for both 1st and 2nd relaxations.

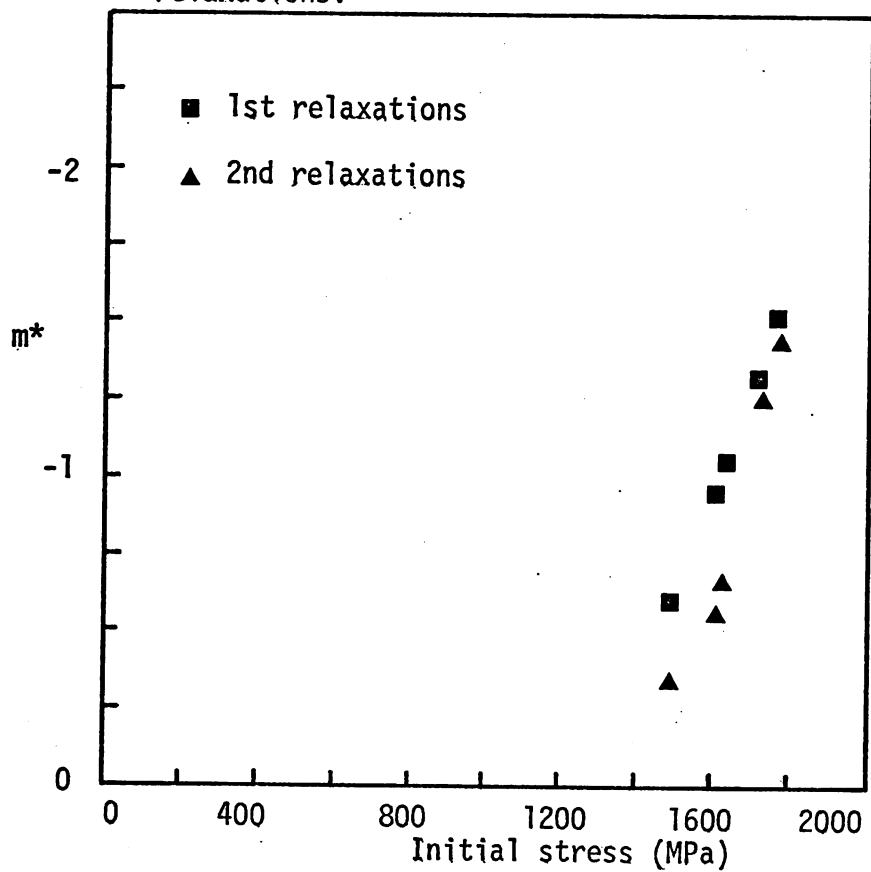


Fig. (5:29b) Corresponding values of m^* .

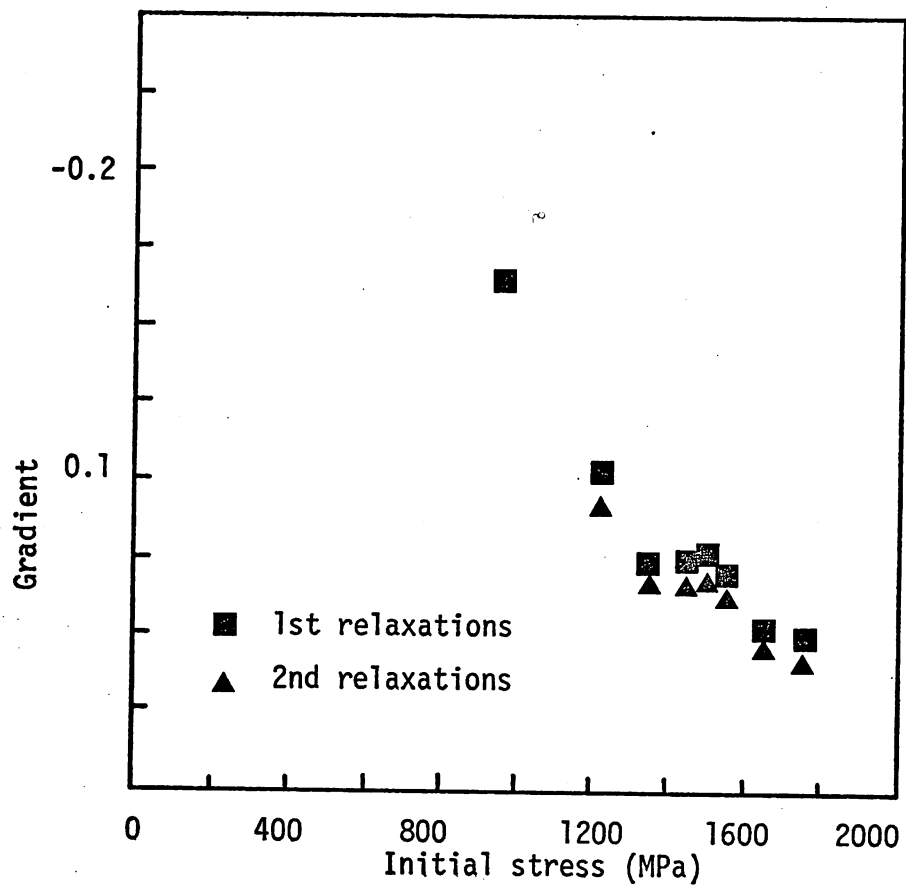


Fig. (530a) Variation in gradient of $\ln\sigma$ vs. $\Delta\sigma$ graphs of A/R patented steel wire, for both 1st and 2nd relaxations.

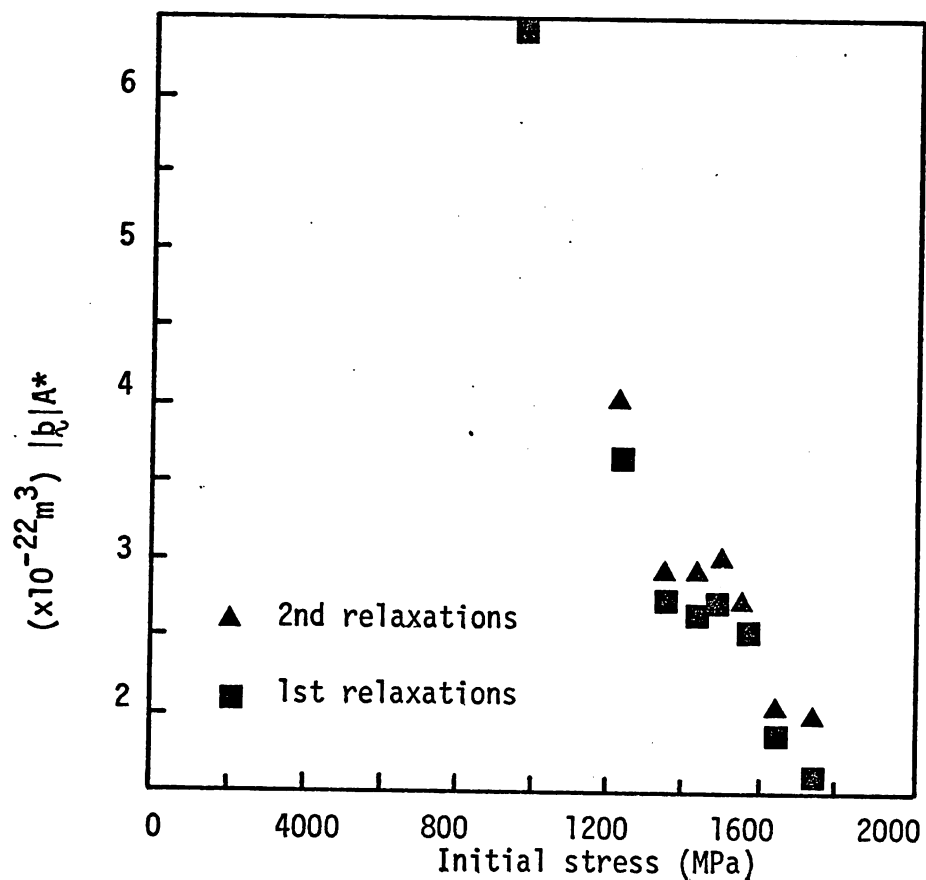


Fig. (530b) Corresponding values of $|b| A^*$.

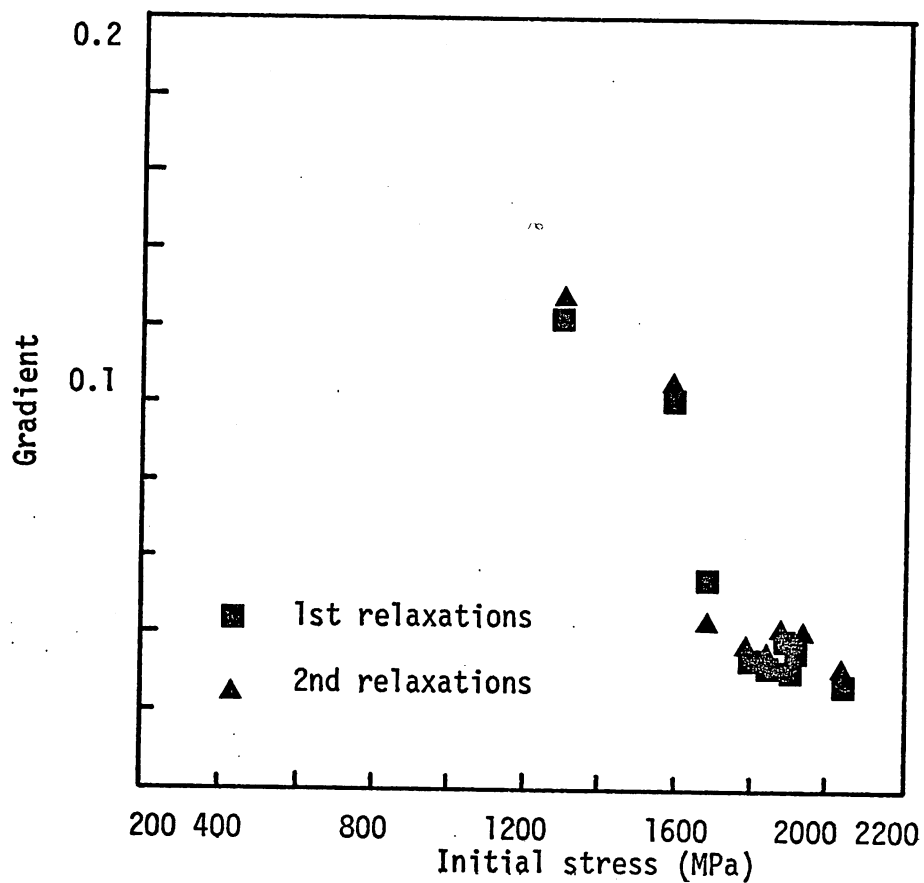


Fig. (5:31a) Variation of gradient of $\ln \dot{\sigma}$ vs. $\Delta \sigma$ graphs of A/R + LTHT "A" patented steel wire, for both 1st and 2nd relaxations.

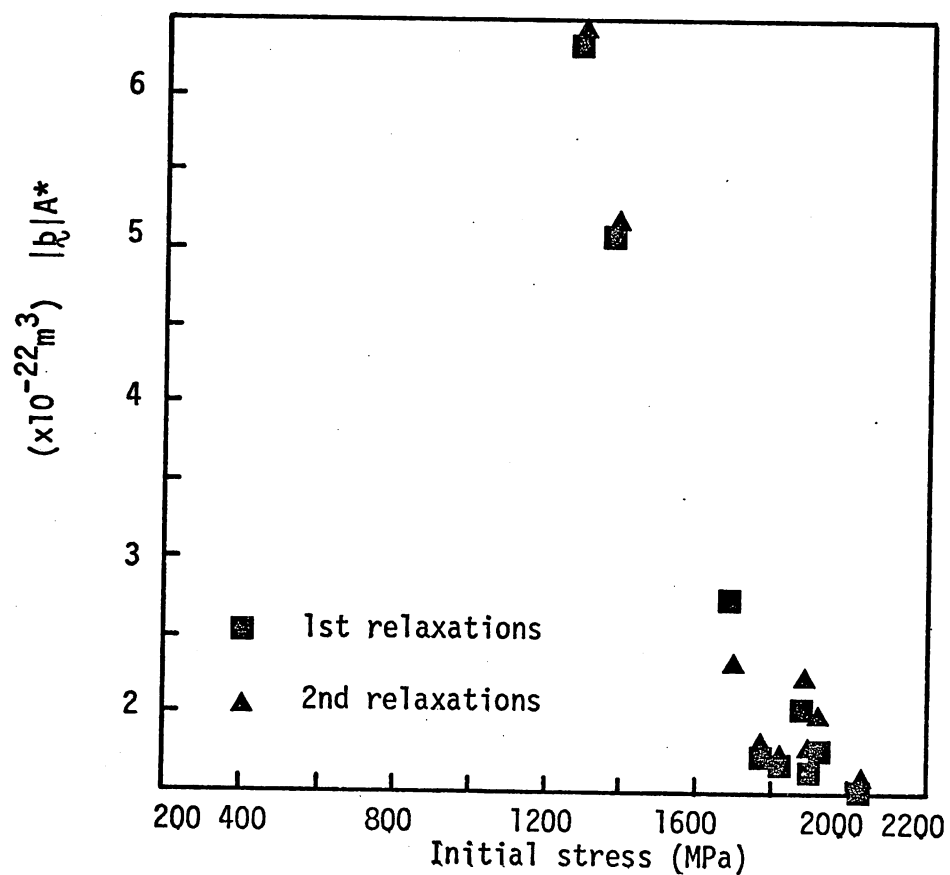


Fig. (5:31b) Corresponding values of $|b|/A^*$.

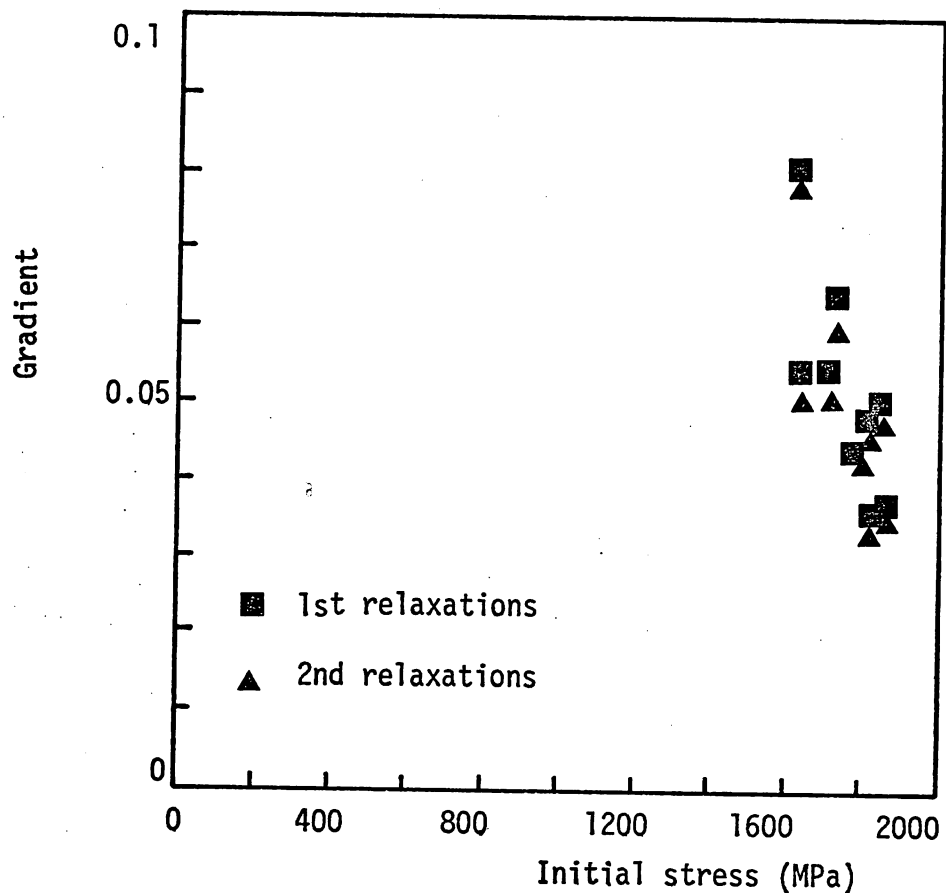


Fig. (5:32a) Variation in gradient of $\ln \sigma \cdot \Delta \sigma$ graphs of A/R+LTHT 'B' steel wire, for both 1st and 2nd relaxations.

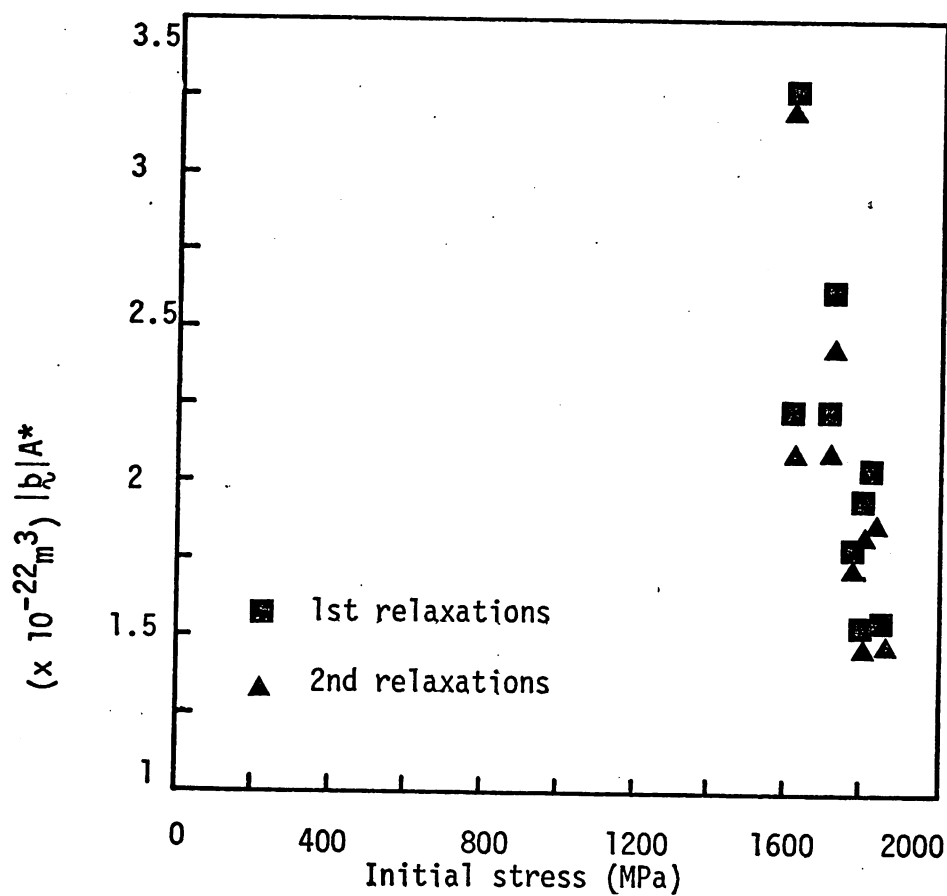


Fig. (5:32b) Corresponding variations in $|b| A^*$.

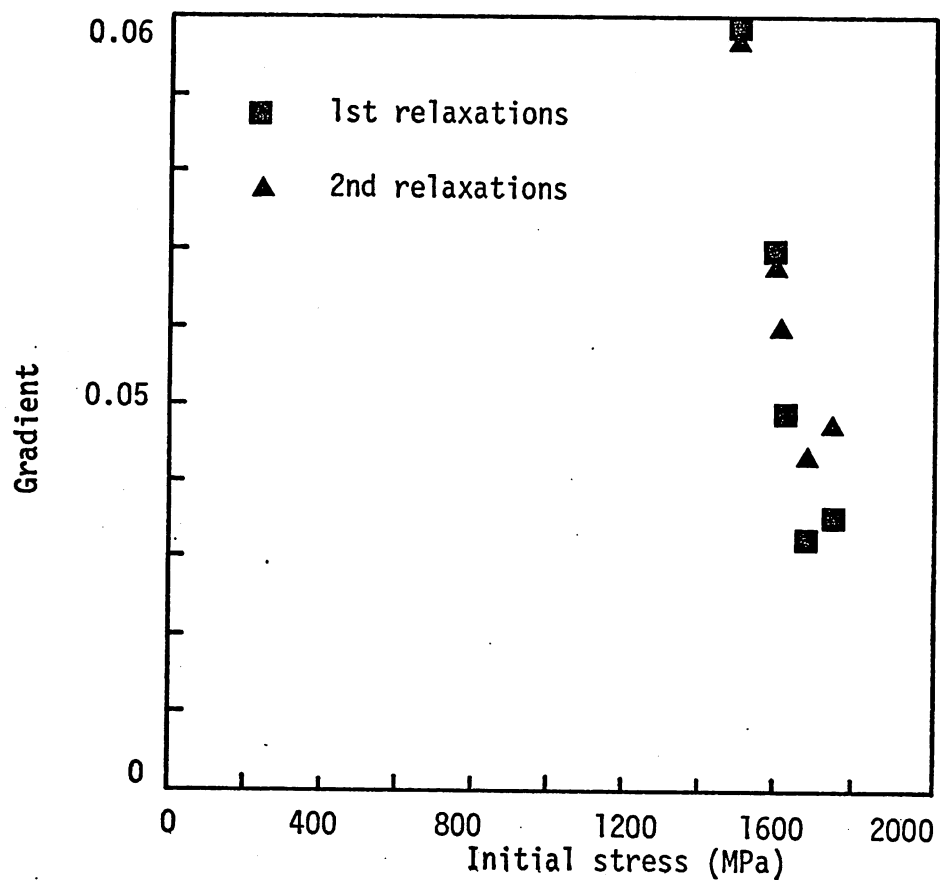


Fig. (5:33a) Variation in gradient of $\ln\sigma$ vs. $\Delta\sigma$ graphs of A/R + LTHT "C" patented steel wire, for both 1st and 2nd relaxations.

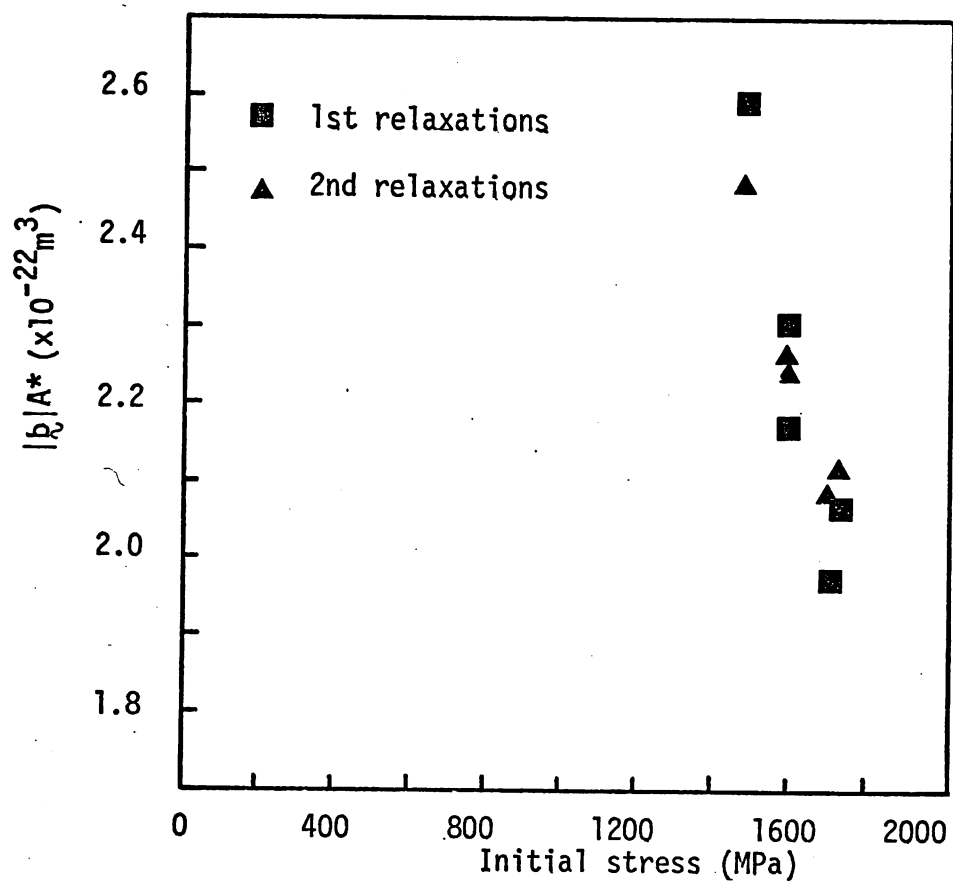


Fig. (5:33b) Corresponding variations in $|b| A^*$

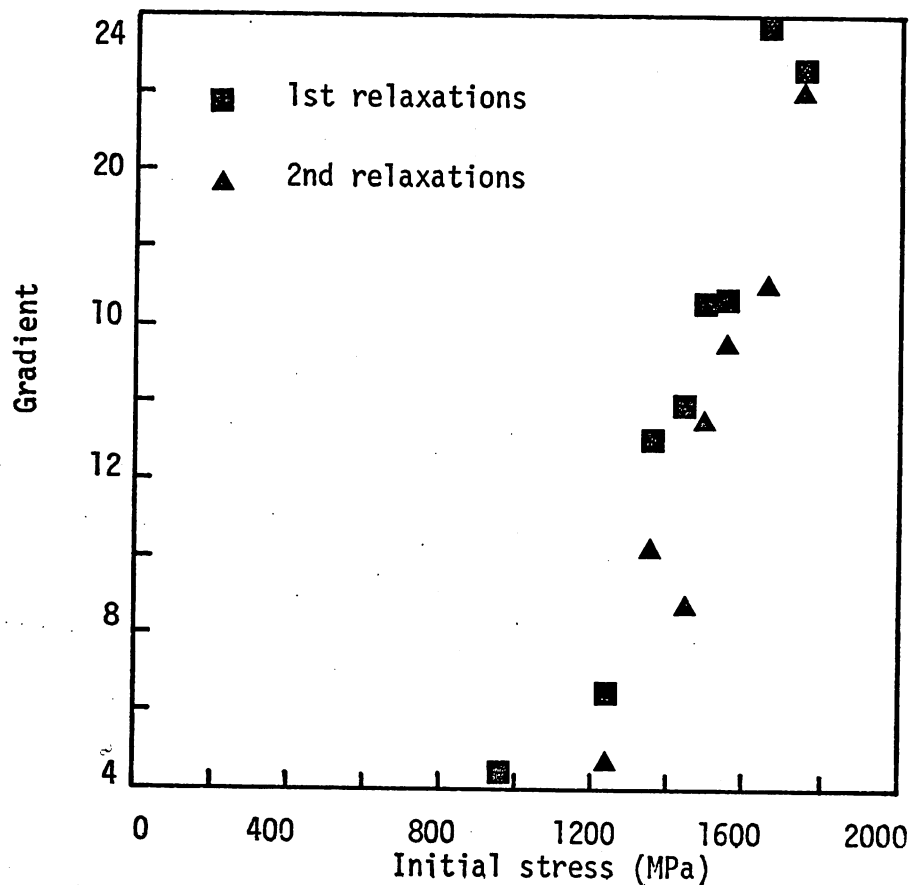


Fig. (5:34a) Variation in gradient of $\Delta\sigma$ vs. $\ln t$ graphs for A/R patented steel wire, for both 1st and 2nd relaxations

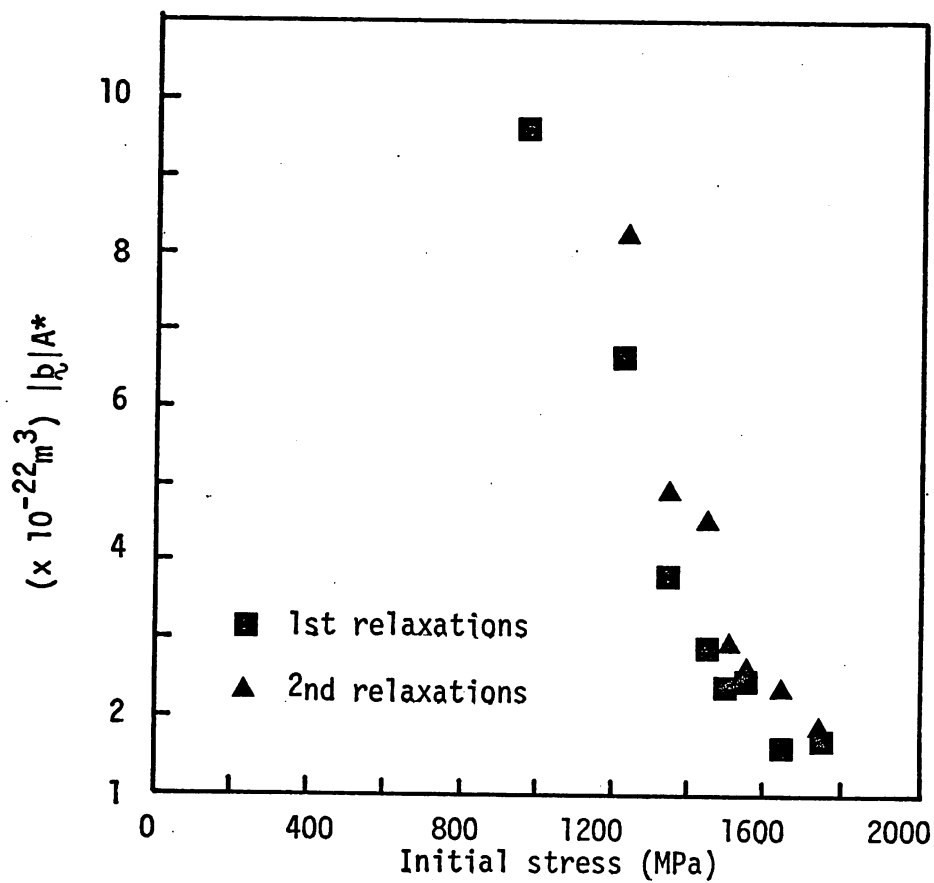


Fig. (5:34b) Corresponding values of $|b|A^*$

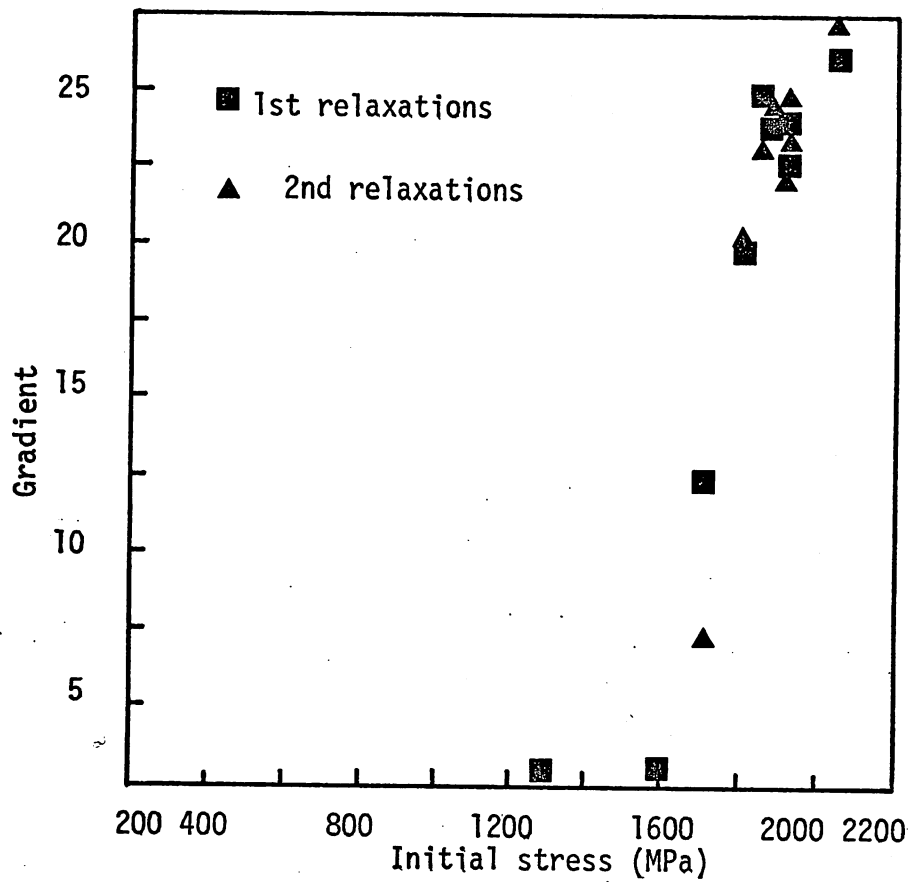


Fig. (5:35a) Variation in gradient of $-\Delta\sigma$ vs. Int graphs for A/R + LTHT"A" patented steel wire, for both 1st and 2nd relaxations.

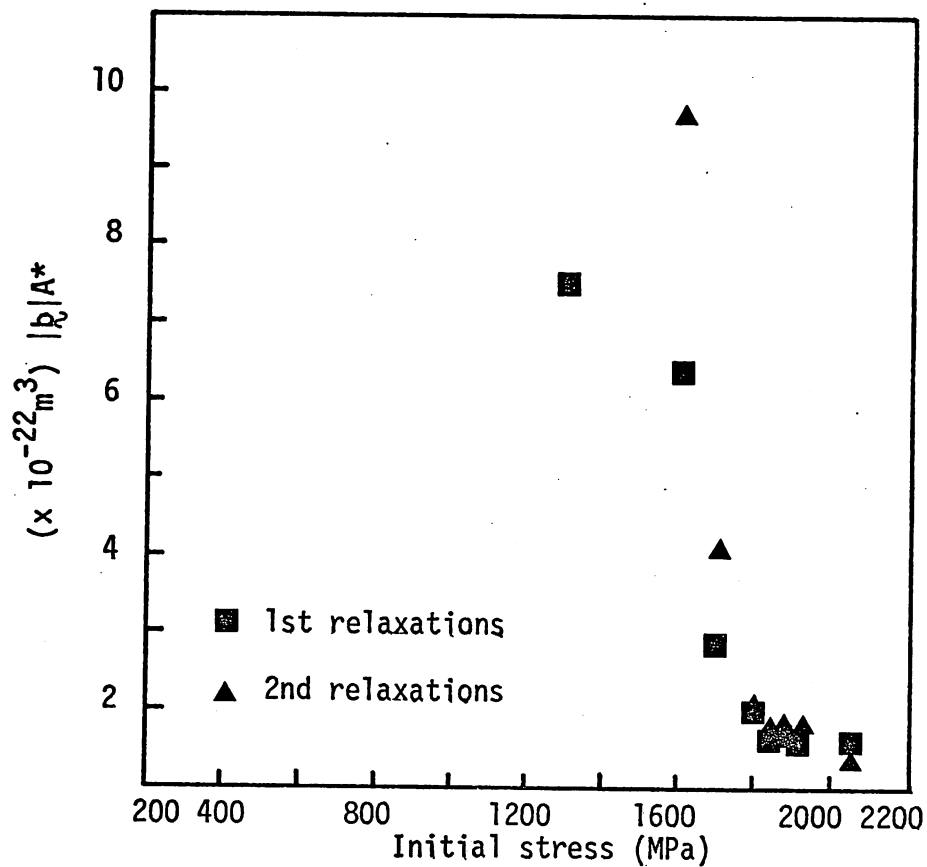


Fig. (5:35b) Corresponding values of $|b|/A^*$.

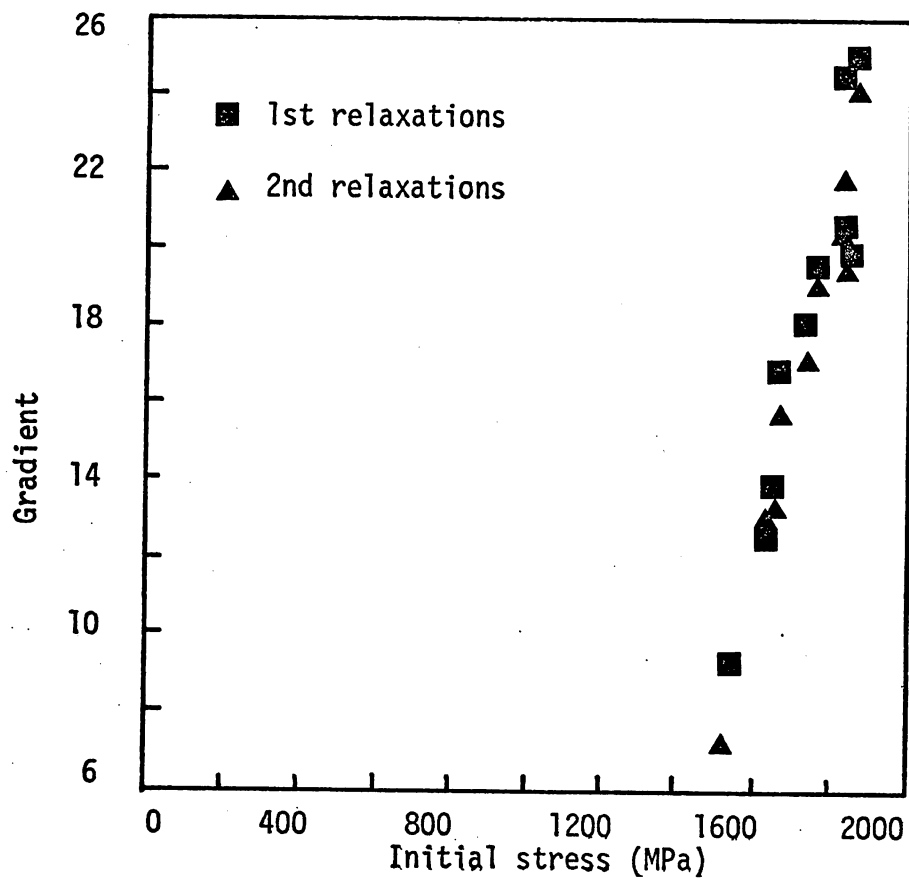


Fig. (5:36a) Variation in gradient of $-\Delta\sigma/\Delta t$ graphs for A/R + LTHT "B" patented steel wire, for both 1st and 2nd relaxations.

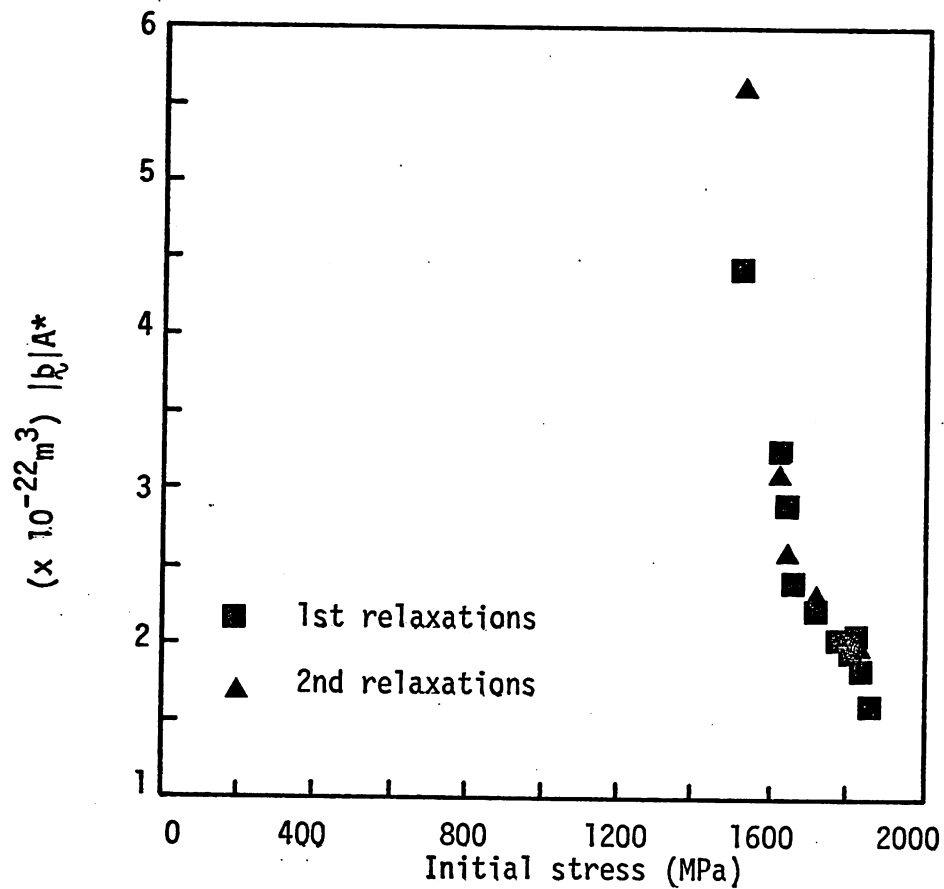


Fig. (5:36b) Corresponding values of $|b|/A^*$.

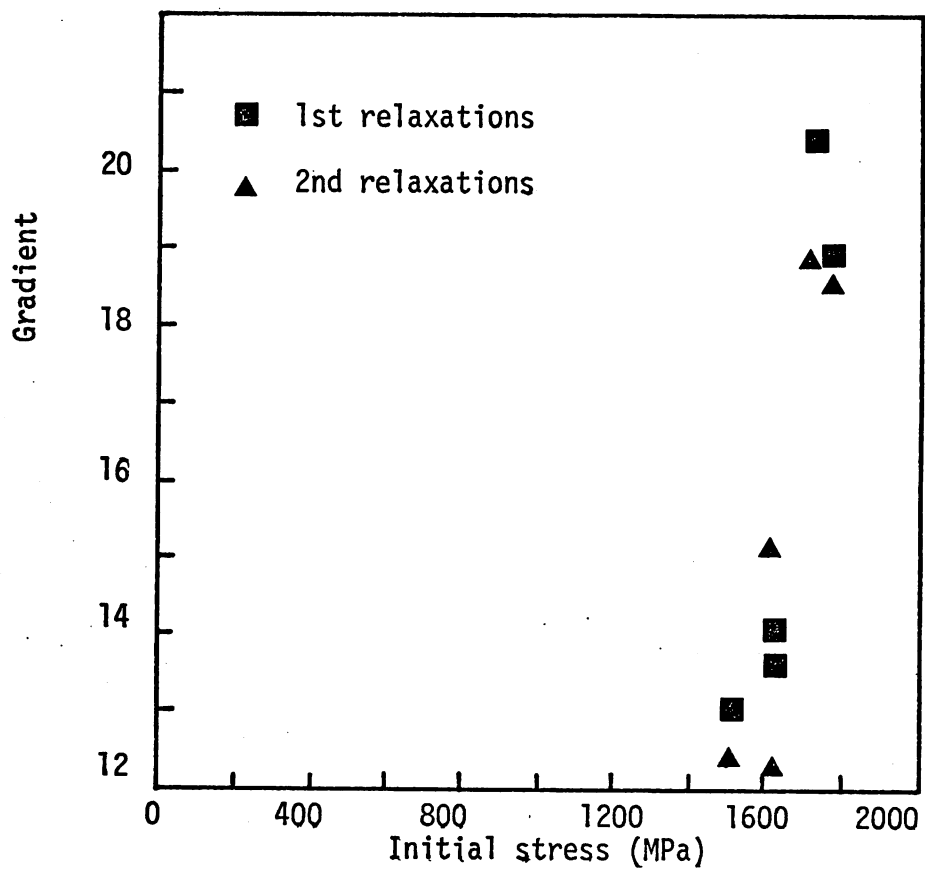


Fig. (5:37a) Variation in gradient of $-\Delta\sigma$ vs. $\ln t$ graphs for A/R + LTHT "C" patented steel wire, for both 1st and 2nd relaxations.

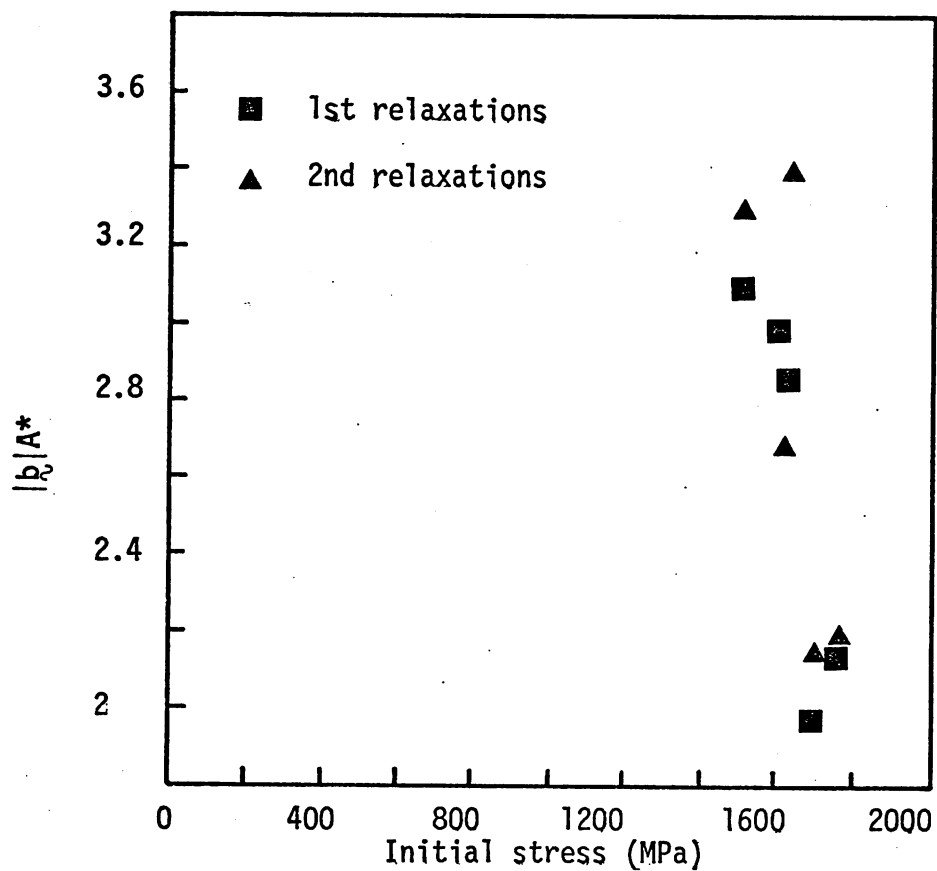


Fig. (5:37b) Corresponding values of $|b_v|/A^*$.

6. Preliminary observations on the microstructure and stress relaxation behaviour of 17-7PH stainless steel

6:1 Introduction

Preliminary investigations have been carried out (in the present work) on the precipitation hardened, 17-7PH stainless steel. In the original spring application, this steel was chosen to replace patented wire in service because of its superior relaxation resistance. There follows a brief description of the precipitation hardenable stainless steels as a general background, followed by more detailed comments on previous work on this particular materials. Further information can be obtained from Pickering (268), Peckner and Bernstein (269) or Colombier and Hockmann (270).

6:2 Previous investigations on controlled transformation and precipitation hardenable stainless steels

6:2.1 Introduction

Many precipitation hardenable stainless steels have been developed in the last 40 years. They are often an extension of the controlled transformation stainless steels which employ the austenite (γ) to bcc martensite (α') transformation as their main strengthening mechanism. The precipitation hardenable stainless steels can use this hardening technique but they all use dispersion hardening to enhance their properties. Both categories exhibit relatively easy fabrication (including welding), good corrosion resistance and impressive strength to weight ratios up to moderately high temperatures. Such properties have made their uses extend from aerospace components to non-magnetic pinballs.

6:2.2 Controlled transformation stainless steels

The basic requirements of these steels have been given by Pickering (268). The characteristics of the production sequence are as follows:

- (a) The stock material is solution treated at approximately 1050°C and air cooled, which retains a largely austenitic microstructure;
- (b) The material is cold worked to its final form with little or no transformation to martensite;
- (c) Transformation to bcc martensite (α') is then achieved by a choice of methods (see later);
- (d) Further precipitation hardening may follow.

It may be noted that:

- (i) M_s must be sufficiently below room temperature to facilitate cold working;

- (ii) A low carbon content is required for formability and resistance to weld decay;
- (iii) There must be sufficient Cr to give good corrosion and stress corrosion resistance;
- (iv) In general the formation of δ -ferrite should be avoided for good formability and strength.

The microstructure given by the air-cool from the solution treatment can be predicted from the Schneider modification of the Schaeffler diagram (271), fig.(6:1). The effects of certain alloying additions (often added for the purpose of precipitation hardening) on the δ -ferrite content have been given by Pickering (268). Clearly for as high a transformation to α' this phase should be avoided. The Ni, Co, Mn or Cu (γ stabilizers) vs. Cr, V, Al, Mo or Si (α stabilizers) balance has to be carefully controlled to ensure that although transformation does not occur on cold working, a simple heat treatment can raise M_s sufficiently to allow a high α' transformation on a final air-cool. This α' transformation can be achieved by one of three methods:

- (a) conditioning or primary ageing at approximately 700°C , this allows the precipitation of $M_{23}C_6$ reducing the Cr and C content and thus reducing the γ stability;
- (b) refrigeration, which can give complete transformation to α' of higher C content than given in (a);
- (c) in some cases M_s can be raised substantially by cold work to give a transformation (this can only conveniently be used for sheet or wire).

As may have been indicated by the above comments, the production of these materials can be difficult and close control over the composition and thermomechanical treatment is essential to obtain optimum properties.

6:2.3 Wrought precipitation hardenable stainless steels

As commented on earlier these steels overlap those discussed in the previous section and the last comment is still pertinent here. There has been defined three basic classes of these materials: austenitic, semi-austenitic and martensitic.

6:2.3.1 Austenitic steels

This type will not be dealt with here at any length. They have good corrosion resistance due to their high Cr content and have high Ni contents to stabilise the γ structure. They are hardened mainly by the addition of

such elements as Al, Ti or P and see service in a wide range of applications from high temperature turbine components to cryogenic plant.

6:2.3.2. Semi-austenitic steels

This class of steels can be regarded as part of the controlled transformation steels, and all comments in section(6:2.2) apply. The solution treatment temperature is usually limited to 1050°C followed by an air-cool and the composition is adjusted to give approximately 5% δ -ferrite - γ microstructure at this stage. The conditioning treatment, if employed, can vary between 700°C and 950°C depending on what change in M_s is required. The aim is to reduce the Cr and C contents of the γ by the precipitation of Cr_{23}C_6 mainly at the δ -ferrite/ γ interfaces which is regarded as being least detrimental to the mechanical and corrosion properties. (It is for this reason that some δ -ferrite is retained). There are dangers if the heat treatment is such as to produce other carbide types, precipitation at other sites (e.g. grain boundaries) or to give continuous carbide films. To avoid such problems the carbon content is kept low (e.g. $< 0.07\text{wt}\%$) and the conditioning temperature at approximately 750°C (see 269 Ch. 4 and 7). This type of treatment is the normal industrial procedure for this type of steel. On cooling from the conditioning temperature, transformation occurs (possibly not to completion) and the final precipitation hardening heat treatment can be undertaken. As one might expect, this heat treatment also stress relieves the martensite to improve the ductility, toughness and corrosion resistance, Further details of the precipitation phenomena will be discussed in(6:3). The most widely used semi-austenitic steels are given in table(6:2), while their main properties, given their usual heat treatments, in table(6:3). The classification of these steels, as elsewhere in this chapter, are derived from the USA where most development has occurred. The transformation technique using refrigeration does not appear to be widely used and that of severe cold working is normally avoided to the extent that warm fabrication may be employed (inhomogeneous properties are likely): this is often despite the fact that such techniques can enhance the properties further, although it is possible only in certain products, e.g. wire or sheet.

The 17-7PH stainless steel is a member of this group and has, in general, shown inferior mechanical properties to those of say PH 15-7Mo, although the causes for these differences are not clear (269, Ch.4). A

detailed comparison between these two alloys is given by Perry and Jasper (269, Ch.7).

6:2.2.3 Martensitic steels

These are probably the most frequently used steels of the precipitation hardenable type, and they are used in a wide range of products. The composition is chosen such that on air-cooling from the solution treatment they transform (except for any δ -ferrite present) to α' . Common steels and some of their properties are given in tables (6:5 and 6:6). Care has to be taken on precipitation hardening as too high a temperature can cause a partial reversion to γ .

6:3 The microstructure and properties of 17-7PH stainless steel

6:3.1 Introduction

From the above description, it can be seen that 17-7PH is described as a semi-austenitic, precipitation hardenable stainless steel. It is, in fact, one of the earlier examples of this class, having now been replaced to a degree, by such alloys as PH 15-7Mo which have a higher strength and can be used at higher service temperatures (480°C against 310°C). In practice, however, the former material appears to be preferred for spring applications, particularly at temperatures below 200°C (272), e.g. coil springs, whip aerials, saw blades and skis. Although the industrial production techniques of these materials are well established, the detailed microstructure at all production stages and the mechanisms involved in the complex changes which occur, are not well understood.

6:3.2 Previous work on the microstructure and properties of 17-7PH stainless steel

All previous work on this steel has been concentrated on the following production route:

- (a) solution treat at approximately 1050°C and air-cool to give a $\gamma + \delta$ -ferrite microstructure;
- (b) condition at approximately 750°C , air-cool to give a $\alpha' + \delta$ -ferrite + retained γ microstructure (sometimes cooling to below room temperature has been employed to increase the extent of transformation);
- (c) precipitation harden at approximately 480°C for 1 hour.

Both the direct refrigeration and cold working routes have not been investigated, despite their superior mechanical properties. The nominal composition of this steel is:

Table 6:1

	C	Cr	Ni	Al	Si	Mn
wt. %	<0.09	17	7	1	<1	<1

It appears to have been assumed that the main precipitation hardening reaction is to form a Ni-Al intermetallic. It is therefore important to ensure an adequate supply of Al for this reaction (excess will stabilize too much δ -ferrite). The Al content of the material can easily be reduced before and during the solution treatment by the nucleation and growth of large AlN grain boundary precipitates. These are extremely detrimental to the drawing, coiling and final toughness and fatigue resistance in addition to their reduction in the strengthening behaviour. Their presence can be avoided by vacuum remelting, to keep the N content low, or by the addition of certain other stabilizing elements. Nitrogen can also be absorbed in the production of carbo-nitrides, e.g. $M_{23}(C,N)_6$ tending to retard its precipitation, and is thought to promote the formation of M_6C . With additions of alloying elements such as Ti, V and Nb, nitrogen can also be stabilized in compounds of the form $M(C,N)$ at the expense of AlN (269, Ch.4). These $M(C,N)$ compounds can precipitate as a fine dispersion which is far less detrimental than the AlN precipitation. Using the conditioning production route, a significant proportion of the C present in the austenite is removed, largely in the form of $M_{23}C_6$ which generally appears at the γ/δ -ferrite interfaces. This type of precipitate is not generally regarded as being detrimental, although the reduction of C in the subsequently induced α' is likely to be a significant factor in this route's lower tensile properties. It also has to be remembered that the use of strong carbide formers will tend, on conditioning, to make the procedure of de-stabilizing the γ less effective. In addition, any alloying changes normally have an important effect on the relative $\gamma - \alpha' - \delta$ stability, see table(6:7).

Krauss and Averbach (273) investigated the γ content of both 17-7PH and 17Cr/4Ni/3Mo steels with heat treatment by means of X-ray techniques. In the former material, the δ -ferrite content remained at approximately 10% while on conditioning the γ content decreased from approximately 70% to 60% (the remainder being α') and precipitation hardening gave no further change. Using the refrigeration technique, the γ content decreased to 13% but increased to 18% on ageing. In both cases a strength increment was noted on final ageing. It was concluded that this steel was strengthened partly by the $\gamma \rightarrow \alpha'$ transformation but also by a precipitation

reaction in the α' . The other steel seemed to depend almost completely on the $\gamma \rightarrow \alpha'$ transformation for its improvement in strength. These factors were taken to support ideas suggesting an Al based precipitation reaction in the α' while in the latter the Mo appeared to strengthen the α' in solid solution form (it is also possible for Mo to enter the $M_{23}C_6$ precipitate or accelerate the formation of M_6C precipitation).

Underwood et al (274) considered the precipitation reaction in 17Cr/7Ni/2Al single crystals: it was assumed to be of an ordered Ni-Al type. It was found that the high Al content tended to stabilize δ -ferrite, and also that when quenched from the solution treatment temperature in water, a fine acicular precipitation was given (with a faster quench this was suppressed). It was suggested that these precipitates were ordered γ' (Ni_3Al). Specimens which were solution treated, cooled in liquid nitrogen and precipitation hardened in the normal way showed peak hardness at ageing times greater than 10 hours. This work indicated that an ordering process occurred during the ageing and it was apparently assumed that this precipitation was also due to ordered γ' .

Hughes, (275) using X-ray analytical techniques on electrolytically extracted precipitated phases, systematically investigated a range of steels with approximately 25wt.%Cr and Ni, Al, Ti, Mn and Si present. In addition to detecting the presence of carbides and nitrides of various types intermetallics were investigated. In the ferritic alloys the latter varied between the NiAl and NiTi compounds (both of the end members being ordered bcc) depending on the steel composition. It was also observed that Fe could replace Ni in the NiAl compound, although this was not investigated in detail. The austenitic alloys investigated again indicated that the intermetallics precipitated showed a range of types depending on the Ti/Al ratio of the alloy. It was clear that the precipitation sequence was not as well defined as in the ferritic steels (probably due to variations in ageing conditions employed in earlier work) but it appeared that although Ni_3Ti was formed at high Ti/Al ratio, NiAl was the stable compound rather than Ni_3Al at low ratios.

Wilkins et al. (276) have studied the precipitation reactions in both 17-7PH and PH 15-7Mo steels using X-ray, TEM and carbon-extraction replica techniques. The microstructures they observed for each were very similar at all stages of the heat treatment sequence employed. On air-cooling from the solution treatment, twinned γ grains of low dislocation density

were observed, with small areas of retained δ -ferrite. The conditioning treatment apparently resulted in a complete transformation of the γ to α' of high dislocation density: the relatively dislocation free δ -ferrite remained, with a decoration of Cr_{23}C_6 precipitates on the δ -ferrite/ α' boundaries. No Mo was observed in the carbide in the PH 15-7Mo steel. Ageing both the alloys at 565°C for 90 minutes appeared to cause a reversion of some α' to γ (rather less evident in the 17-7PH) and no further precipitation was evident despite an increase in hardness noted from that of the conditioned alloy. On ageing at this temperature for longer periods up to 100 hours, the precipitation of NiAl followed by Ni_3Al was noted. (This sequence was retarded in the PH 15-7Mo as compared with the 17-7PH). The sites for this precipitation were not elucidated. Evidence was also found for ordering in the NiAl (B_2 -structure) and Ni_3Al (L_{12} -structure) at ageing times of greater than 6 hours. These workers suggested that these precipitates in an early, disordered form, could have caused the increase in strength with ageing for 90 minutes, although their presence was not detected. Alternatively, a precipitation sequence on the "Gunier-Preston zone model" was proposed, in which peak hardness would have been caused by segregation of Al or Ni to defect sites in the α' structure.

Yukawa et al. (277) have also carried out a TEM study of 17-7PH steel produced by the conditioning route. They investigated a commercial steel and a high purity steel, table 6:8, the latter used to eliminate the effects of the carbide precipitation normally encountered. The steels A and B on quenching from 760°C and 1050°C respectively were both said to form α' with some residual δ -ferrite. Ageing experiments were undertaken at 600°C , at which temperature peak hardness was attained after approximately 10 minutes. This material examined in TEM showed a homogeneous dispersion of "spherical contrasts" of the order of 10nm in diameter. Further ageing at this temperature allowed these precipitates to grow, and they were shown to be an ordered bcc phase, probably NiAl. Similar results, although occurring rather more slowly, were obtained by ageing at 500°C . Particularly at the higher ageing temperature, a reversion to γ was noted, which probably contributed to the softening after peak hardness. In addition to this homogeneous nucleation, a fine lamellar precipitation at the δ -ferrite/ α' interfaces was noted in steel "B" on ageing for 10 minutes at 600°C . It was suggested that the hardening behaviour was entirely due to the fine,

coherent precipitation in the α' .

Pickering (268) and Dulis (278) in their reviews considered the precipitation hardening reactions using Al and Ti in fully austenitic structures. In such steels a nickel content of at least 20% is employed to give γ' precipitates of the form $\text{Ni}_3(\text{Al},\text{Ti})$, which are particularly stable to overageing and Pickering suggested that the initial stage of precipitation was that of fcc zones (N.B. this was at variance with the earlier comments of Hughes (275)). Overageing in steels with Al alone causes a bcc NiAl phase to be formed as Widmanstätten laths. The addition of some Ti resulted in the similar $\text{Ni}(\text{Al},\text{Ti})$ phase being formed while further addition gives first Ni_2AlTi and finally fcc γ' , the latter being of spherical form. In some cases with a high Ti/Al ratio a hcp Ni_3Ti form was suggested which occurs as either Widmanstätten plates or a grain boundary cellular precipitate. Pickering noted that the age hardening effect of such phases are normally largely due to coherency strains which increase with Ti/Al ratio. However, too high a ratio causes the deleterious Ni_3Ti precipitate to be formed. He discussed the effects on alloying changes on the instability of the γ to mechanical working, particularly with its effects on formability. Such factors are not only important in the choice of the original alloy composition but also the strain required to give the wire, say, its final required strength. It was noted that low δ -ferrite^{contents} and large γ grain size help in allowing good ductility and the strain induced α' not only gives a good increase in work hardening rate and apparently does not give rise to the initiation of ductile failure but also, by its nature, it probably reduces ductile void growth. Hard second phase particles, however, such as Cr_{23}C_6 tend to reduce the ductility and so the maximum attainable strength on deformation. In fact this carbide is known to cause hot cracking on rolling in duplex stainless steels in similar situations. (This can be stopped by stabilizing with Ti or Nb to produce a fine, intragranular carbide dispersion.

Precipitation in martensitic stainless steels was also discussed. Although the requirements are rather different in the choice of alloy balance, (a fully martensitic structure is required on air-cooling from the solution treatment) precipitation reactions and their effects on the strength and ductility are often applicable to the precipitation hardenable stainless steels. While precipitation of carbides such as M_7C_3 , M_2C and M_{23}C_6 are not possible in the final heat treatment, hardening by means of other

precipitation has been noted, e.g. Cu, NiAl, NiTi, Mo-Cr-Co R-phase, Fe₂Mo or Fe₂W. Ageing for such precipitation is usually undertaken at approximately 500°C, if peak hardness is required, or at approximately 650°C to 700°C if more ductility is necessary.

In an earlier review by Pickering (279) on precipitation hardening in ferritic steels, precipitation hardening by Al is considered in detail in both low alloy and stainless steels. In the latter it was indicated that the hardening phase was NiAl (with some replacement of Ni by Fe). This precipitation was in the form of a fine homogeneous dispersion of spheroids, probably by spinodal decomposition, when aged at 600°C for 100 hours, although other dispersions could be produced by ageing at higher temperatures and/or for longer times. It was noted that NiAl was ordered bcc with a similar lattice parameter to the ferrite.

6:3.3 Present investigations into the microstructure and properties of 17-7PH stainless steel

6:3.3.1 Introduction

The methods of testing and examination of this material were broadly similar to those employed on the patented wire: limitations of time and material however ensured only a brief, initial investigation. For these reasons no atom-probe work, as yet, has been included. Details of techniques employed are again given in AI.

6:3.3.2 Microstructural information

The optical appearance of the as drawn wire was found to be similar to that noted in previous work (see earlier) with stringers of δ -ferrite, elongated in the drawing direction in a lighter etching matrix. Further details of the matrix microstructure were not visible (fig. 6:3). The optical appearance of the drawn wire which had been precipitation hardened at 485°C for 75 minutes was found to be indistinguishable (fig. 6:4) from that of the as drawn.

The TEM study undertaken on this wire proved to be inconclusive in a number of ways. The high degree of cold drawing (probably greater than 60%) caused difficulties in polishing similar to those encountered in the patented wire, resulting in little electron-optically thin area. While the polishing techniques enabled a survey of the fine scale structure at distinguishing between the various phases which previous work would suggest were present. This was despite the large number of individual specimens prepared and examined. In fig.(6:5a) the typical appearance of the T/S of

the as drawn wire is shown in bright field: numerous low angle boundaries and a very high dislocation density are visible in the low carbon martensite. The discrete nature of the structure is clearly shown in the appropriate SADP, fig.(6:5b): the dislocations produced by the transformation and cold work have formed distinct subgrains within the lath martensite structure. Fig.(6:5c) is a higher magnification, ferrite centred dark-field: dislocation tangles and nets which form the boundaries are clearly visible, along with dislocations within each area of similar ferrite orientation. The appearance of the L/S of the wire was similar showing similar laths with dislocation structure. Fig.(6:5 d,e) shows such a section, many of the boundaries appear rather more distinct than in fig.(6:5a), however this was thought to be due to a sectioning effect.

It was found that one effect of the standard precipitation heat treatment was to allow a higher success rate in specimen preparation. This was presumably due to a reduction in internal stresses. The appearance of the T/S of such wire was similar to the as drawn material, although a slight reduction in dislocation contrast was noted. Such a small reduction in the dislocation density is noteworthy considering the severity of the heat treatment (485°C for 75 minutes). It was also noted that there was a significant increase in the number of dislocation nets visible in the structure (figs. 6:6b,c): it was not clear whether the nets had been formed during this heat treatment or whether they were just more easily visible because of the reduction in general dislocation density. The lath structure was particularly well shown in a L/S, annealed specimen, fig.(6:6d,e). The sharp variations in orientation at some boundaries along with the gradual variations within a martensite lath are well shown in a L/S, ferrite-CDF micrograph, fig.(6:6f). A series of micrographs investigating a subgrain in a lath are given in fig.(6:7), from a L/S. Dislocations can be clearly seen within the subgrain in the α -CDF, the reflection used being shown in the accompanying SADP.

While the general appearance of the microstructure was ascertained, it has not been possible, as yet, to distinguish between the strain induced martensite (α') and the highly deformed δ -ferrite: in fact it is not clear how this can be achieved with any degree of certainty in this alloy. No trace of any retained austenite (γ) was found in either material state although it is likely to be present: the fine scale of the microstructure and the resulting complexity of the diffraction patterns was

probably responsible. It was also found that the precipitation reaction could not be observed. The fine scale of the likely precipitate (NiAl) and the considerable strain contrast already present clearly did not allow unambiguous observation.

6:3.3.3 Mechanical testing information

6:3.3.3.1 Stress/strain behaviour

The as drawn 17-7PH wire was tested in the form of 90mm gauge length, 2mm gauge diameter specimens in a similar manner to the patented wire. Some variability was noted in the series of tests, particularly in the elongation to failure of otherwise identical specimens (a variation in total plastic strain of between 1 and 3% was noted). The mean tensile stress over 5 tests was 1487 ± 37 MPa while the proportionality limit was 1058 ± 29 MPa. The plastic strain to the peak load was relatively consistent, between 0.5% and 0.7%. The form of the nominal stress/strain graph took an interesting form, fig.(6:8). It appears that after the peak load the plastic instability caused the further transformation of retained γ to α' allowing further stable plastic deformation with slight work hardening. When this work hardening had been exhausted final plastic instability to failure occurred.

The improvement of mechanical properties on the precipitation heat treatment were considerable, although not always as dramatic as those seen in the patented wire with a less severe anneal. In the precipitation hardened state the series of 5 specimens showed an ultimate tensile stress of 1833 ± 13 MPa and a proportional limit of 1381 ± 40 MPa: this represented an increase of approximately 23% in the former and 31% in the latter over the as drawn wire. The plastic elongations to failure were in the range 1% to 1.25% while the plastic elongations to peak load varied from 0.6% to 0.7%. It is interesting to note that former generally showed a smaller value due to the inability of the material, after the retained γ had transformed, to work harden, fig.(6:8).

6:3.3.3.2 General comments on relaxation behaviour of 17-7PH stainless steels

Similar, although not as yet as extensive, tests were carried out on the 17-7PH stainless steel as have already been described for the patented wire. It was ensured, in a similar manner, that the relaxation behaviour of this steel was also non-recoverable, i.e. was not due to anelastic

processes. It was found with all test specimens used at loads where significant relaxation was evident that significant hardening occurred during a relaxation, i.e. as with the patented wire the load drop was less for a 2nd, subsequent relaxation than for the 1st. As before (see 5:4.5) no relationship could be found between either $\delta\epsilon$ or $\delta\sigma$ and the initial load and, probably because of the few tests possible, no hardening parameter $\delta\sigma/\delta\epsilon$ could justifiably be specified. It is interesting to note, however that the scatter of values for these quantities were similar to those found for the patented wire specimens. The effects of ageing at room temperature after a pair of relaxation tests, has only been investigated for one initial stress. It was found that in this case there was no significant decrease in $\delta\sigma$ after ageing for 72 hours unlike the behaviour shown by patented wire (5:4.6). This indicates a retardation of recovery processes at this temperature.

The changes of the magnitudes of relaxation with initial stress are given in figs. (6:9 and 6:10) for as drawn and heat treated wire. The approximate positions on the relevant nominal σ/ϵ curves are included. For comparison with patented wire they should be compared with figs. (5:13 to 5:16) (5:4.7). As before, to accentuate the pattern of relaxation with initial load, the stress drop ($\delta\sigma$) after 400 seconds has been related to the initial stresses for both 1st and 2nd relaxations in figs. (6:11) and (6:12). It is clear from these that the relaxation resistance of the heat treated wire was good to a higher initial stress than for the as drawn wire. The initial stress at which significant relaxation occurs correlates well with the onset of non-linearity in the stress/strain behaviour as was true with the patented wire (see figs. 5:17 to 5:20). Relaxations for periods greater than 400s were only performed at high stress with the precipitation hardened material, i.e. at an initial stress showing significant relaxation. The stress chosen was similar to that employed in the examples of patented wire tested at high stress, fig. (5:21a) (see 5:4.8). The relaxation curve for the 17-7PH stainless steel wire is given in fig. (6:13) along with that of patented wire A/R + LTHT "A", relaxed from a similar stress for convenience. As can easily be seen, although the initial relaxation rate of the stainless steel is more rapid, the total relaxation after 7600 seconds is less than that of the plain carbon steel wire. This is due to a more rapid reduction in the relaxation rate in the former such that at the end of this period the rate is approximately 10%

of that of the patented wire.

6:3.3.3.3 Variations in dislocation parameters during relaxation with initial load

The techniques of testing and data processing exactly followed those employed with the patented wire. They again allowed the variation of m^* and $|b|A^*$ to be studied. The review of the theories given in chapter 4 is applicable here, and details of the plots are summarized in the relevant sections of (5:4.9).

It was clear that the Li analysis which was developed to give m^* values from stress change experiments, such as is found in stress relaxation again did not describe the deformation adequately: m^* values were always negative. As with all conditions of the patented wire, m^* showed a variation with increasing initial stress during the yield and plastic flow behaviour of the material, becoming more negative with increasing initial stress. The ranges of values shown by both the as drawn and the precipitation hardened material were similar to those exhibited by the A/R patented wire. The only significant difference in the behaviour of the as drawn and heat treated stainless wire was that the variation in m^* in the former was displaced to lower initial stress values, fig.(6:14).

The evaluation of $|b|A^*$ from plots of $\ln \dot{\sigma}$ vs. $\Delta\sigma$ and $\Delta\sigma$ vs. $\ln t$ (see 5:4.9.3 and 5:4.9.4) again showed a variation as the initial load was increased above the yield stress with values of $|b|A^*$ decreasing with increasing initial stress. The values obtained tended to be greater than those exhibited by the patented wire, especially in the LTHT conditions. The as drawn stainless wire showed a slightly greater variation in $|b|A^*$ as compared with the heat treated material. The slopes obtained from the computed plots and the resulting values of $|b|A^*$ are given in figs.(6:15 and 6:16).

It was found that the linear portions of the computed graphs and the differences in parameters between the 1st and 2nd relaxations from the same initial stress were similar to those of the patented wire. It was noticed, however, that the scatter in values obtained was slightly greater.

6:4 Comments and Summary

6:4.1 Techniques

It has been shown that the mechanical testing techniques which had previously been applied to the patented steel wire could also be used to

investigate 17-7PH stainless steel wire. The only limitation shown in the present work was due to lack of specimens, as each could only be tested once.

TEM, while showing a basically martensitic structure with high dislocation density, failed to show the presence of retained γ or (although the difference between it and the α' in this material has not been documented) δ -ferrite. In addition no significant change in the micro-structure could be detected: the dislocation content remained very high, the strain fields of which presumably masked those of the very fine precipitation which would have occurred.

6:4.2 Information obtained

The tensile testing programme clearly showed the beneficial effect of the precipitation heat treatment on both the proportional limit and UTS. While the effect on the former parameter was rather greater than on the latter, the change in proportional limit to UTS ratio was not as dramatic as that shown by the patented wire, on being subjected to LTHT "A". The hardening heat treatment was sufficient to improve the room temperature, tensile properties of the stainless wire to approach those of the patented wire in its optimum condition. These properties, in addition to those of relaxation resistance, are clearly of great importance when making a materials choice for light weight, high strength springs.

The high resolution relaxation testing programme indicated that although the initial relaxation rate was faster, the rate decreased more rapidly than that shown of the patented wire in any of its conditions. This behaviour was particularly noticeable during the long term relaxations, although the differences were also evident by examination of the computed curves for the 400 second relaxations. The effects of the precipitation hardening appeared to be solely on the range of initial stresses over which the change in the m^* or $|b|A^*$ parameters occurred, i.e. for the as drawn material the changes occurred at lower initial stress levels, which correlated well with the yielding behaviour as shown by the nominal stress/strain curves. It is thus clear that, as with the patented wire, relaxation in this material becomes significant when the initial stress is increased beyond the proportional limit: above this level relaxation increases rapidly. The divergence of total stress loss during a relaxation between this material and the patented wire (in their respective service conditions)

has been shown to be due to a more rapid decrease in the value of σ in the former case. Such a change can have great significance over the service life of a spring component.

TABLE 6:2. Nominal Chemistry of Selected Semiaustenitic Precipitation-hardenable Stainless Steels (Peckner & Bernstein (269))

Grade	C	Mn	Si	Cr	Ni	Mo	Al	N
17-7PH*	0.07	0.50	0.30	17.0	7.1		1.2	0.04
PH 15-7Mo*	0.07	0.50	0.30	15.2	7.2	2.2	1.2	0.04
PH 14-8Mo+	0.04	0.02	0.02	15.1	8.2	2.2	1.2	0.005
AM-3501§	0.10	0.75	0.35	16.5	4.25	2.75		0.10
AM-3501§	0.13	0.85	0.35	15.5	4.25	2.75		0.12

* 17-7PH and PH 15-7Mo are registered trademarks of the Armco Steel Corporation

+ PH 14-8Mo is a trademark of the Armco Steel Corporation

§ AM 350 and AM 355 are trademarks of the Allegheney Ludlum Steel Corporation

TABLE 6:3. Typical Mechanical Properties of Selected Semiaustenitic Precipitation-hardenable Stainless Steels (Peckner & Bernstein (269))

<u>Grade</u>	<u>Condition</u>	<u>Form</u>	<u>0.2% yield strength</u> (MPa)	<u>Ultimate tensile strength</u> (MPa)	<u>Elongation</u> in (50.8 mm) (%)	<u>Hardness, (R_c)</u>
17-7PH	TH-1050	Sheet	1276	1379	9	43
PH 15-7Mo	RH-950	Sheet	1551	1655	6	48
PH 15-7Mo	CH-900	Sheet	1793	1827	2	49
PH 14-8Mo	SRH-950	Sheet	1482	1586	6	48
AM-350	SCT-850	Sheet	1207	1420	12	46
AM-355	SCT-850	Sheet	1248	1510	13	48

TABLE 6:4 Standard heat treatments for Armco 17-7PH and PH15 7Mo (Peckner and Berstein(269))

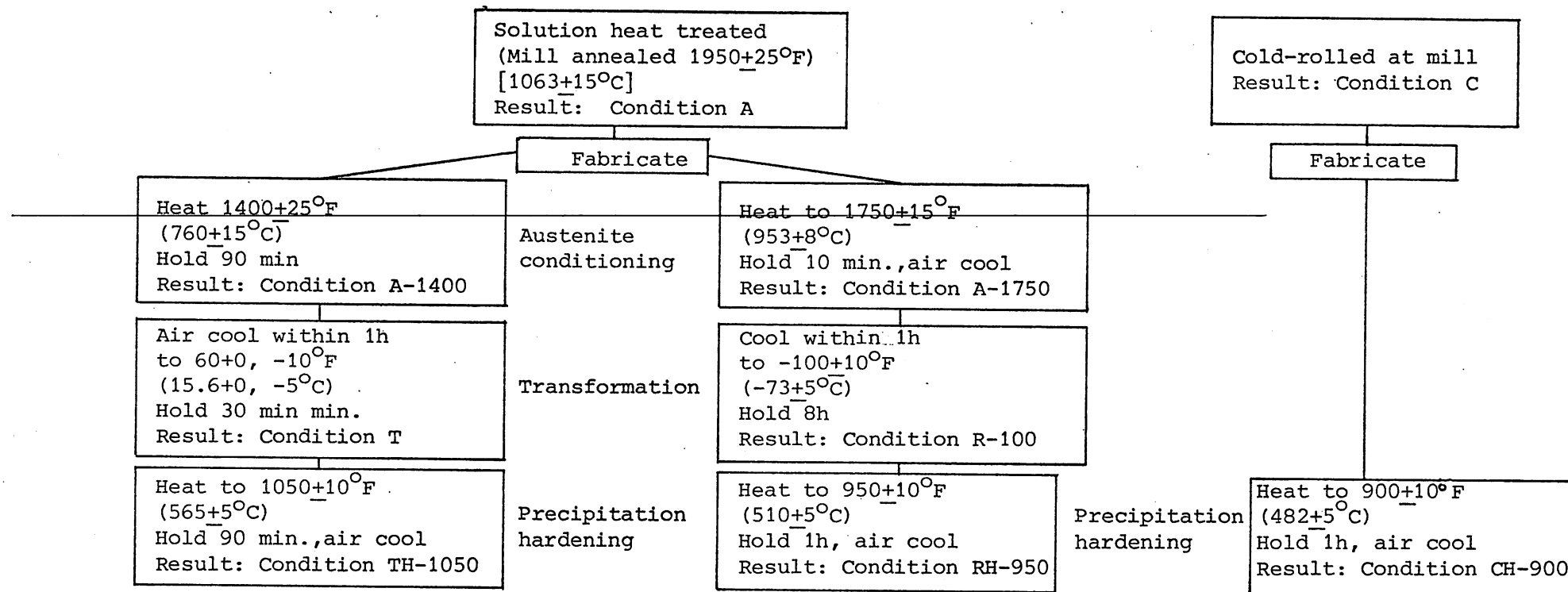


TABLE 6:5 Nominal Chemistry of Selected Martensitic Precipitation-hardenable Stainless Steels (Peckner & Bernstein (269))

Grade	C	Mn	Si	Cr	Ni	Mo	Al	Cu	Ti	Cb
MODERATE STRENGTH										
17-4PH*	0.04	0.30	0.60	16.0	4.2			3.4		0.25
15-5PH*	0.04	0.30	0.40	15.0	4.5			3.4		0.25
Custom 450+	0.03	0.25	0.25	15.0	6.0	0.8		1.5		0.3
Stainless W\$	0.06	0.50	0.50	16.75	6.25		0.2		0.8	

HIGH STRENGTH										
PH 14-8Mo*	0.04	0.03	0.03	12.7	8.2	2.2	1.1			
Custom 455+	0.03	0.25	0.25	11.75	8.5			2.5	1.2	0.3

*17-4PH 13-8Mo and 15-5PH are registered trademarks of the Armco Steel Corporation

+Custom 450 and Custom 455 are trademarks of the Carpenter Technology Corporation

\$Stainless W is a trademark of the United States Steel Corporation

TABLE 6:6 Typical Mechanical Properties of Selected Precipitation-hardenable Stainless Steels (Peckner & Bernstein (269))

Name	Condition	Form	0.2% yield strength (MPa)	Ultimate tensile strength (MPa)	Elongation in (50.8 mm) (%)	Reduction (%)	Hardness (R _c)
MODERATE STRENGTH							
17-4PH	H-925	Bar	1207	1310	14	54	42
15-5PH	H-925	Bar	1207	1310	14	54	42
Custom 450	H-900	Bar	1269	1351	14	60	42
Stainless W	H-950	Bar	1241	1345	10		42
HIGH STRENGTH							
PH 13-8Mo	H-950	Bar	1448	1551	12	50	47
Custom 455	H-900	Bar	1620	1689	10	45	49

TABLE 6:7 Effect of alloying elements on constitution and M_s temperature of controlled transformation steels (Pickering 268)).

Element	Change in percentage of delta ferrite per wt-%	Change in M_s , $^{\circ}\text{C}$ per wt-%
N	-200	-450
C	-180	-450
Ni	-10	-20
Co	-6	+10
Cu	-3	-35
Mn	-1	-30
W	+8	-36
Si	+8	-50
Mo	+11	-45
Cr	+15	-20
V	+19	-46
Al	+38	-53

TABLE 6:8 (277)

	C	Cr	Ni	Al	Si	Mn	Fe
Steel A	0.072	16.53	7.72	1.25	0.44	0.84	bal
Steel B	0.004	16.16	7.45	1.48	0.07	0.01	bal

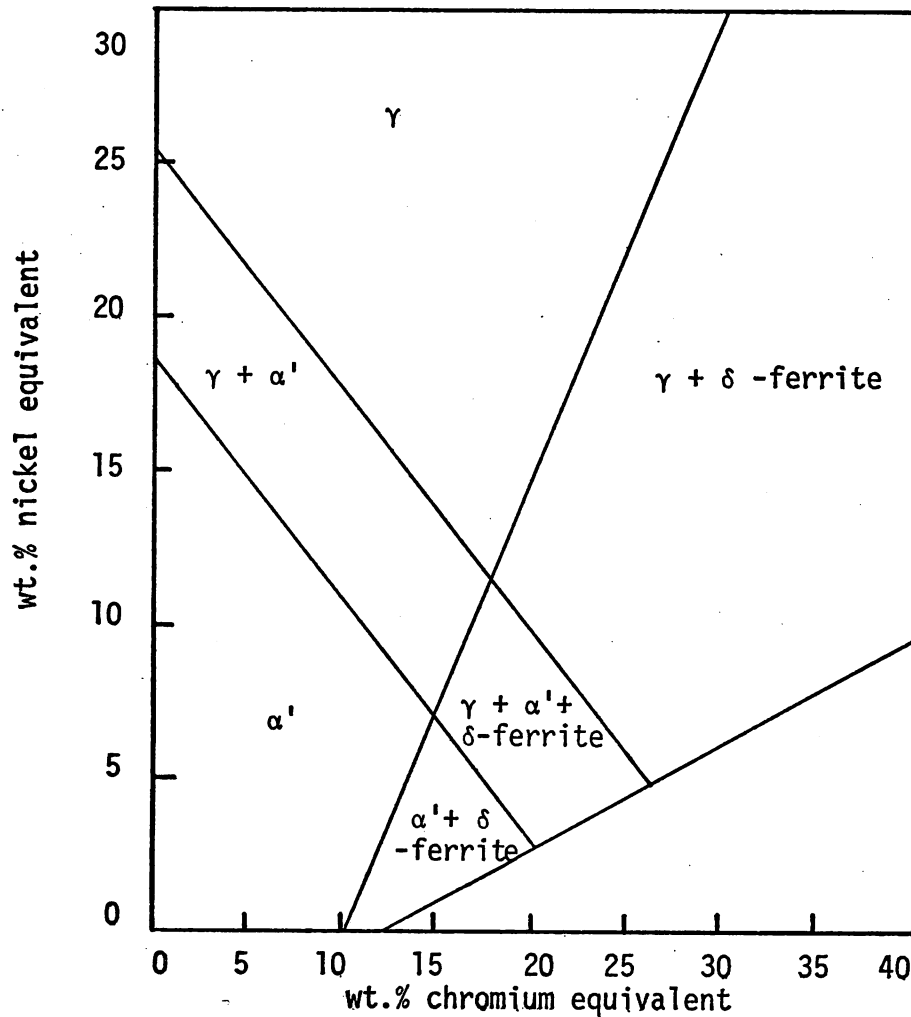


Fig. (6:1) The Schneider modification of the Schaeffler diagram.

$$\text{Nickel equivalent} = \%Ni + \%Co + 0.5\%Mn + 30\%C + 0.3\%Cu + 25\%N$$

$$\begin{aligned} \text{Chromium equivalent} &= \%Cr + 2\%Si + 1.5\%Mo + 5\%V \\ (\text{wt.}\%) &+ 5.5\%Al + 1.75\%Nb + 1.5\%Ti \\ &+ 0.75\%W \end{aligned}$$

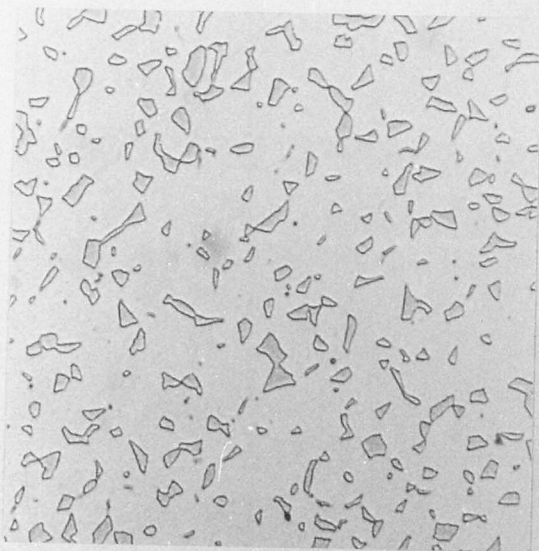


Fig. (6:3a) Optical micrograph of T/S of A/R,
17-7PH stainless steel wire
(NaOH electrolytic etch) X 400



Fig. (6:3b) Optical micrograph of L/S of A/R,
17-7PH stainless steel wire
(NaOH electrolytic etch) X 400

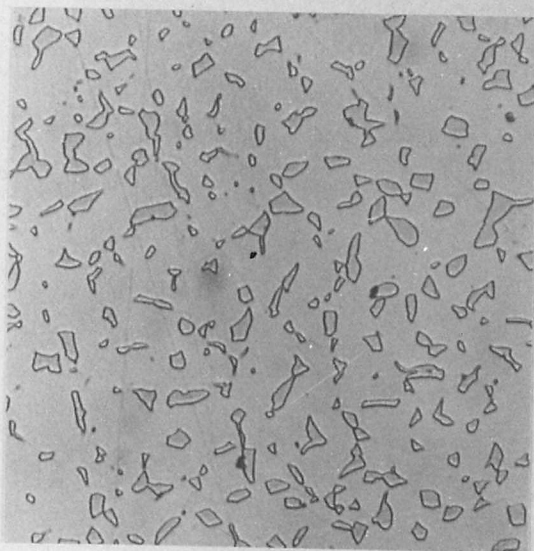


Fig. (6:4a) Optical micrograph of T/S of A/R +
HT, 17-7PH stainless steel wire
(NaOH electrolytic etch) X 400

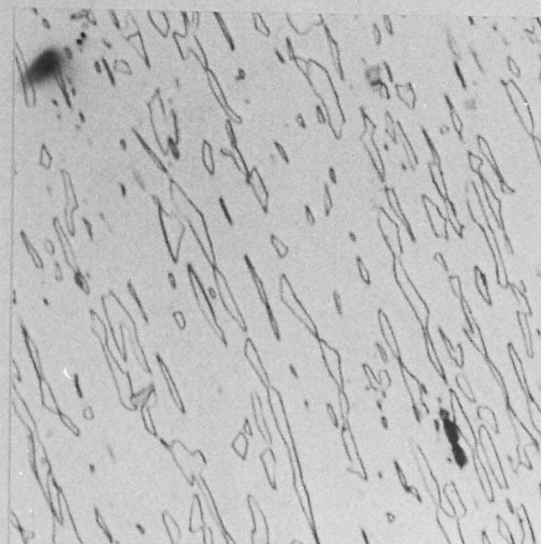


Fig. (6:4b) Optical micrograph of L/S of A/R +
HT, 17-7PH stainless steel wire
(NaOH electrolytic etch) X 400

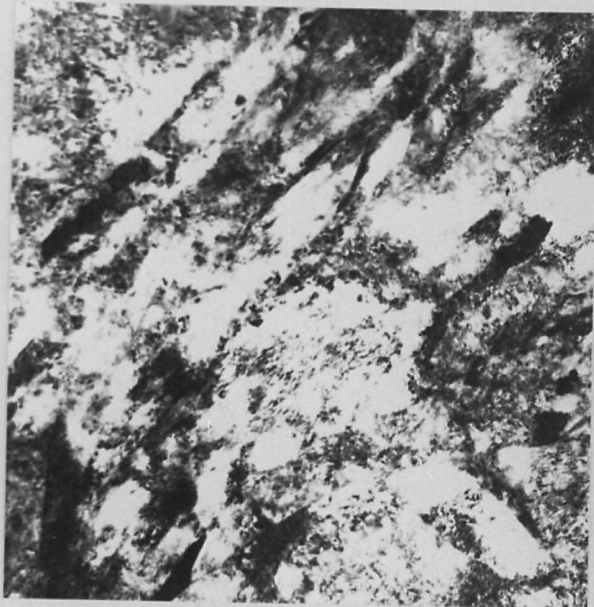


Fig. (6:5a) TEM of T/S of A/R, 17-7PH
stainless steel wire
(BF) X60,000

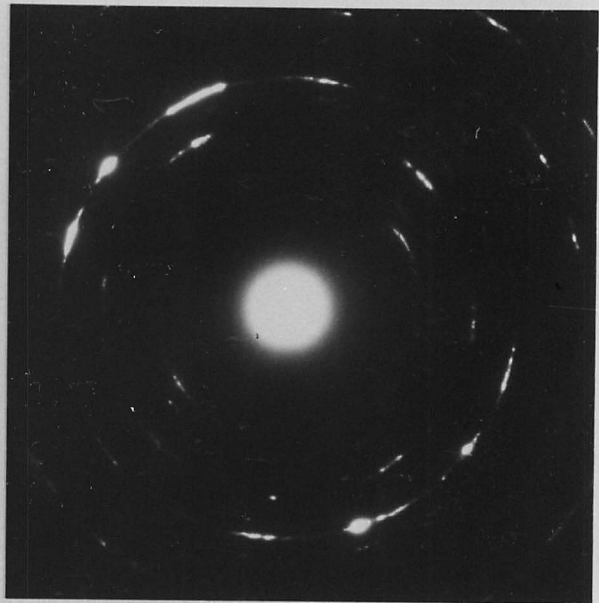


Fig. (6:5b) TEM of T/S of A/R, 17-7PH
stainless steel wire
(SADP for (6:5a))

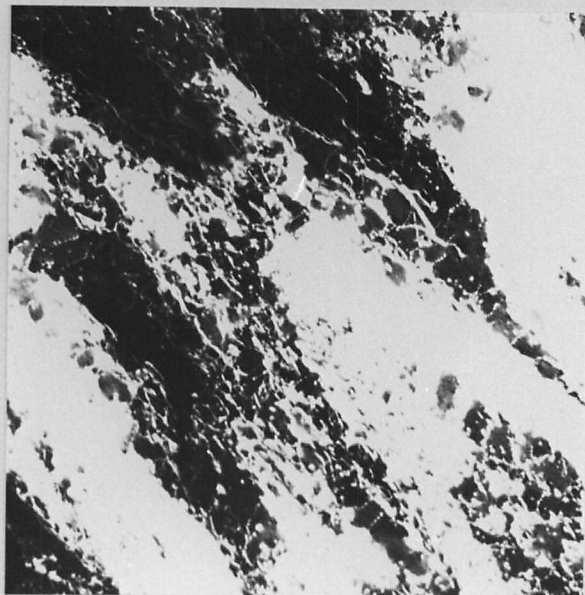


Fig. (6:5c) TEM of T/S of A/R 17-7PH
stainless steel wire
(BF) X180,000



Fig.(6:5d) TEM of L/S of A/R, 17-7PH
stainless steel wire
(BF) X60,000

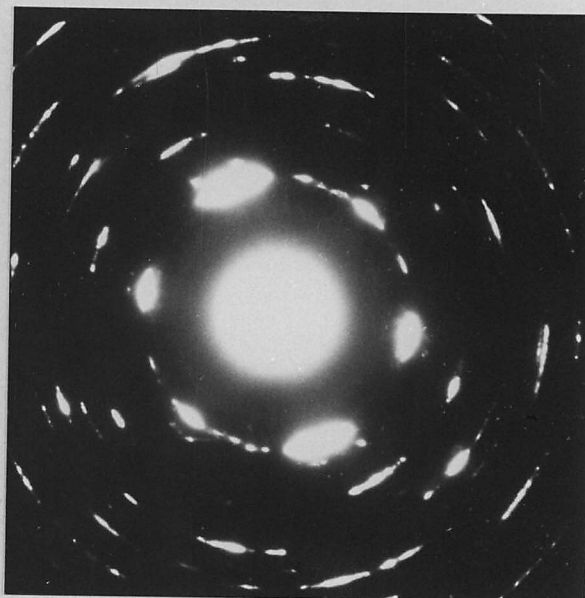


Fig.(6:5e) TEM of L/S of A/R, 17-7PH
stainless steel wire
(SADP for (6:5d))

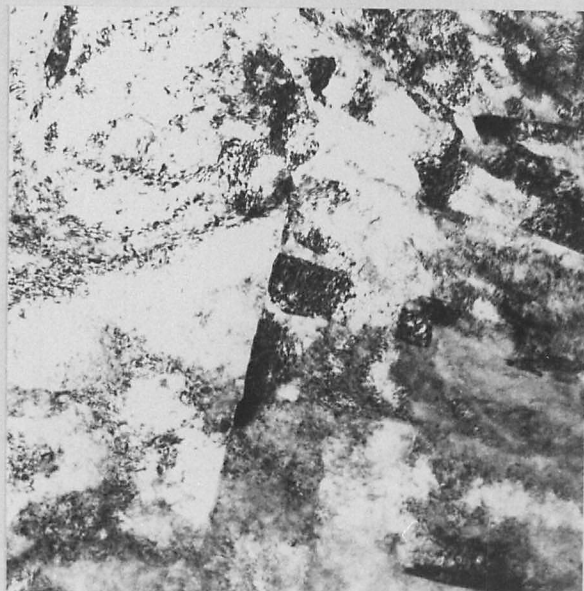


Fig. (6:5f) TEM of L/S of A/R, 17-7PH
stainless steel wire
(BF) X60,000



Fig. (6:6a) TEM of T/S of A/R + HT, 17-7PH
stainless steel wire
(BF) X60,000



Fig. (6:6b) TEM of T/S of A/R + HT, 17-7PH
stainless steel wire
(BF) X180,000



Fig. (6:6c) TEM of T/S of A/R + HT, 17-7PH
stainless steel wire
(BF) X180,000



Fig. (6:6d) TEM of L/S of A/R + HT, 17-7PH
stainless steel wire
(BF) X60,000

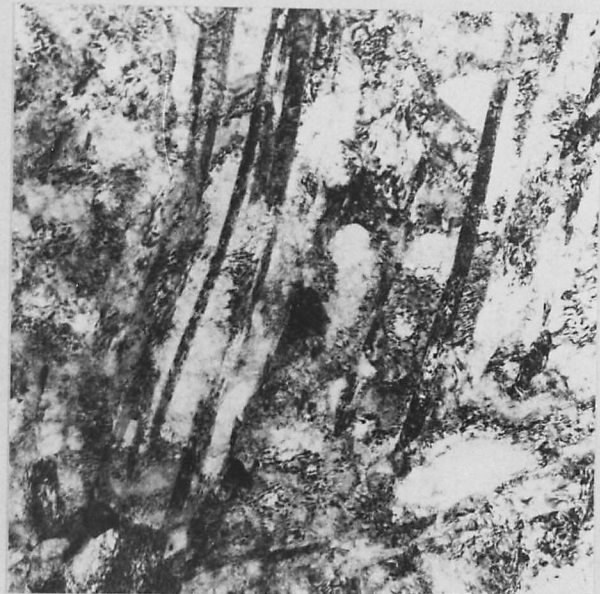


Fig. (6:6e) TEM of L/S of A/R + HT, 17-7PH
stainless steel wire
(BF) X60,000

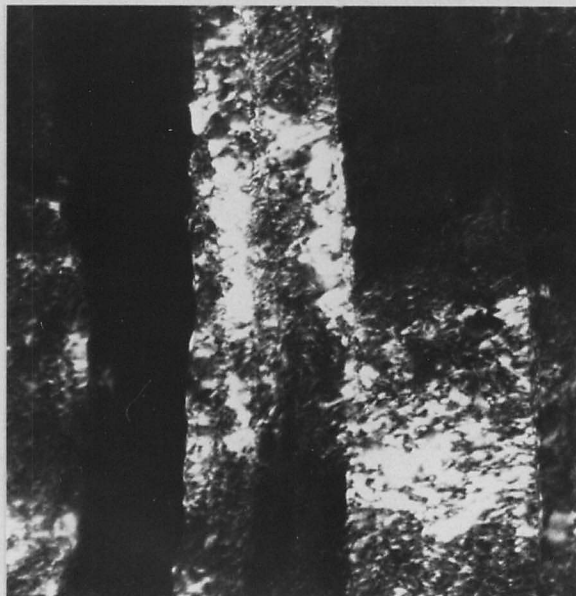


Fig. (6:6f) TEM of L/S of A/R + HT, 17-7PH
stainless steel wire
(α CDF) X180,000

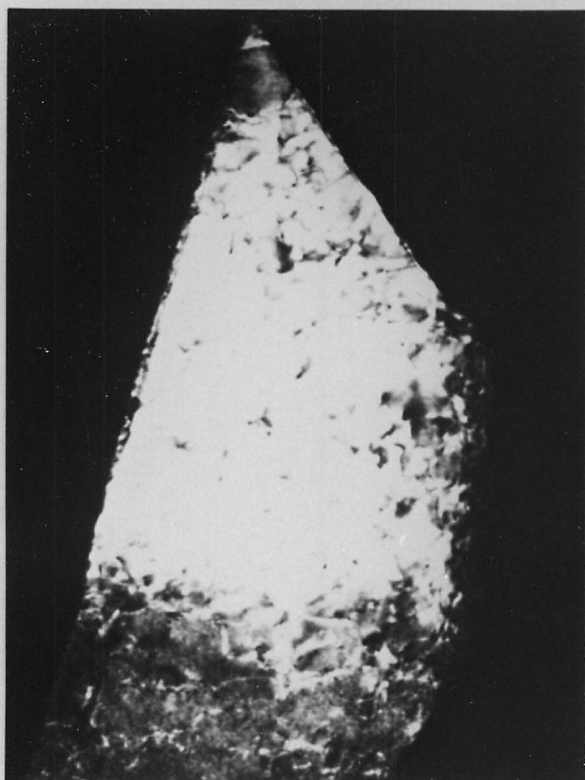


Fig. (6:7a) TEM of L/S of A/R + HT, 17-7PH
stainless steel wire
(α CDF) X180,000

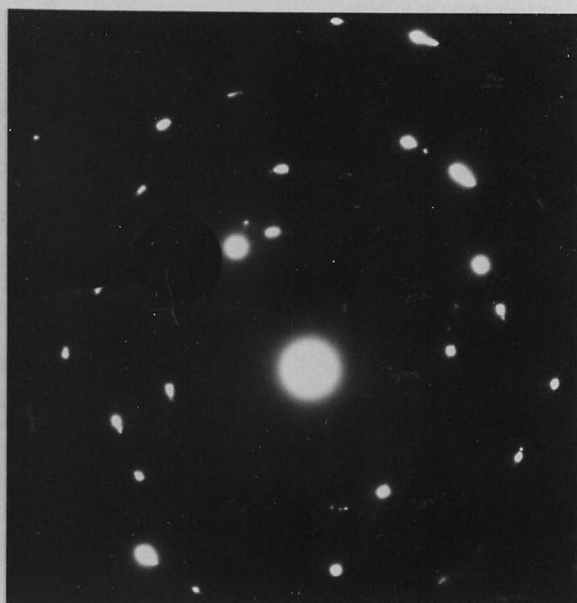


Fig. (6:7b) TEM of L/S of A/R + HT, 17-7PH
stainless steel wire
(SADP for (6:7a))

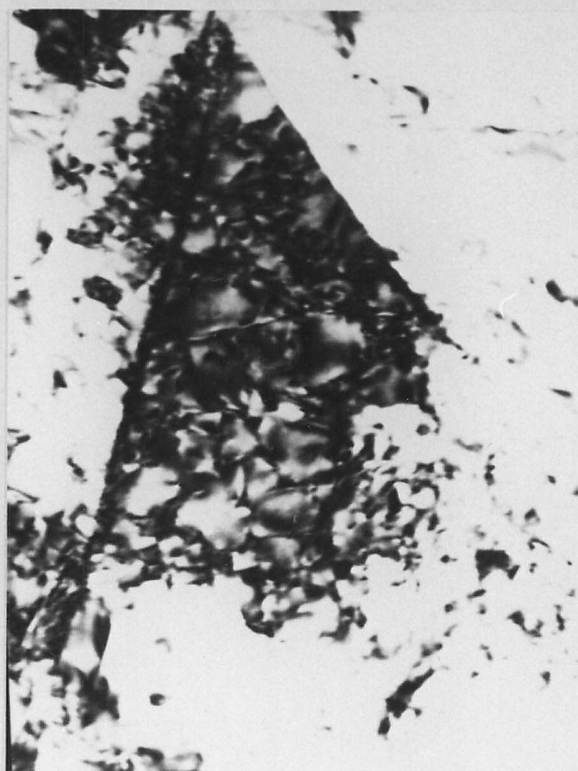


Fig. (6:7c) TEM of L/S of A/R + HT, 17-7PH
stainless steel wire
(BF) X180,000

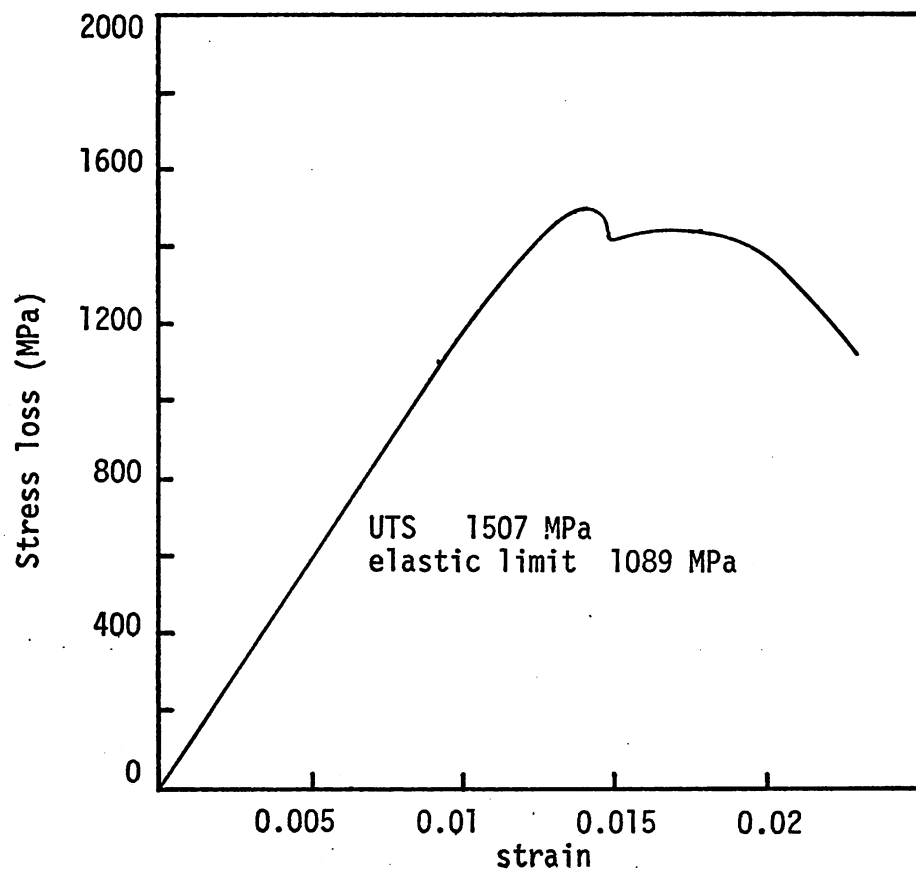


Fig. (6:8a) Nominal σ/ϵ graph for A/R, 17-7PH stainless steel.

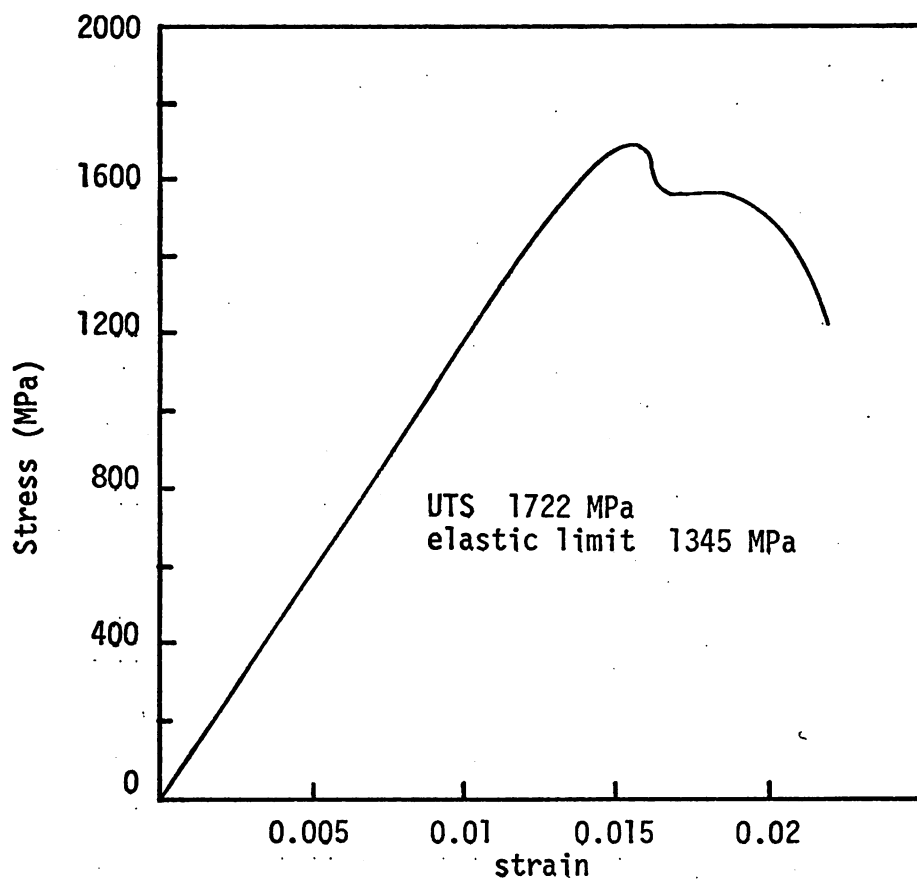


Fig. (6:8b) Nominal σ/ϵ graph for A/R + HT, 17-7PH stainless steel.

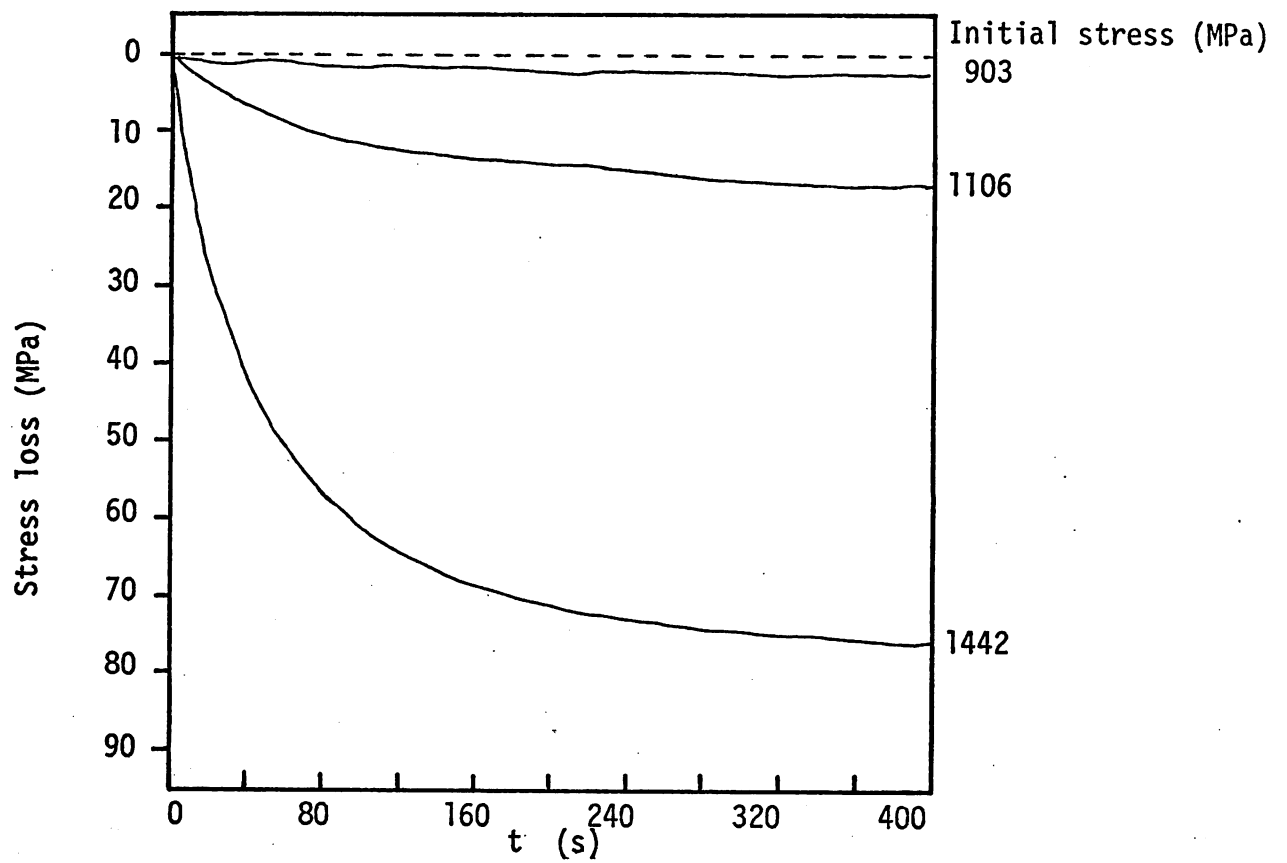


Fig. (6:9a) Relaxation curves for A/R, 17-7PH stainless steel wire at various initial loads (see below)

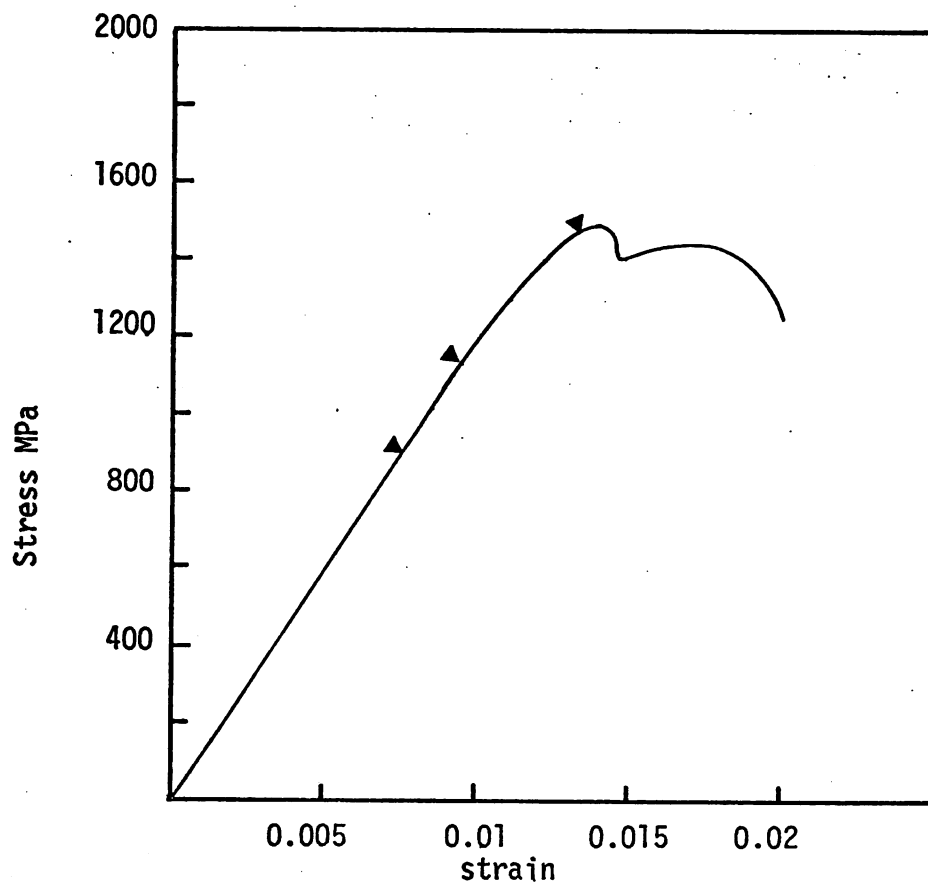


Fig. (6:9b) Nominal σ/ϵ curve for above, showing initial stresses

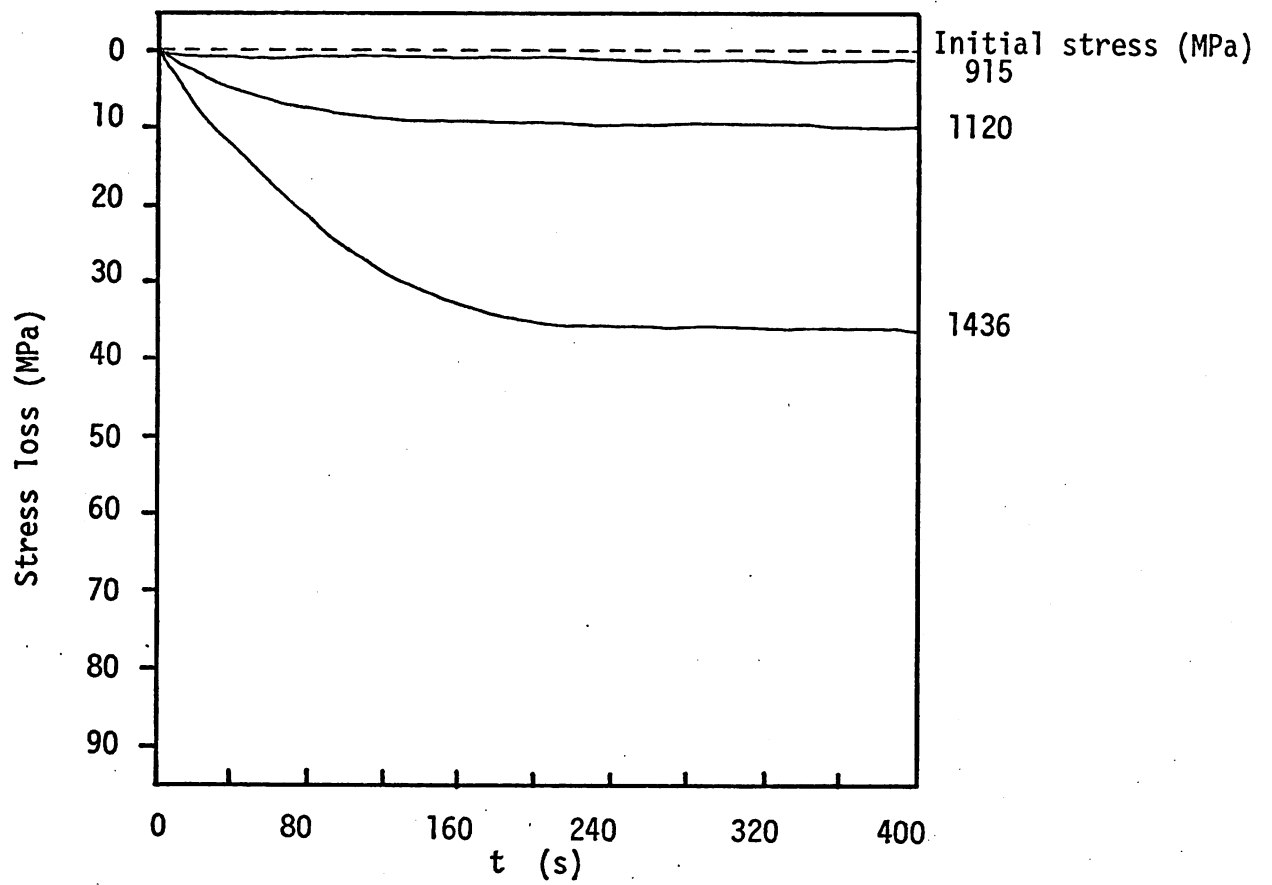


Fig. (6:9c) 2nd relaxation curves from similar stresses

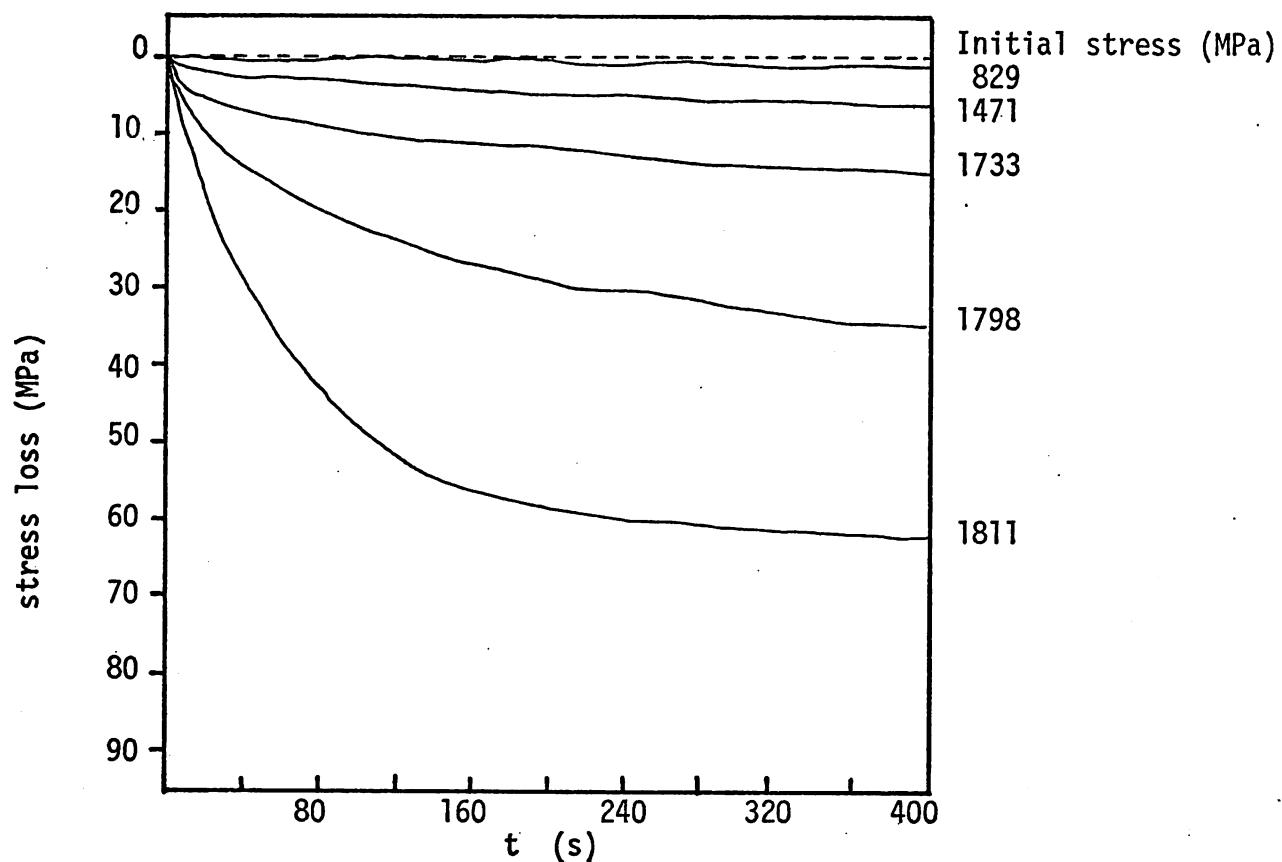


Fig. (6:10a) Relaxation curves for A/R + HT, 17-7PH stainless steel wire at various initial loads.

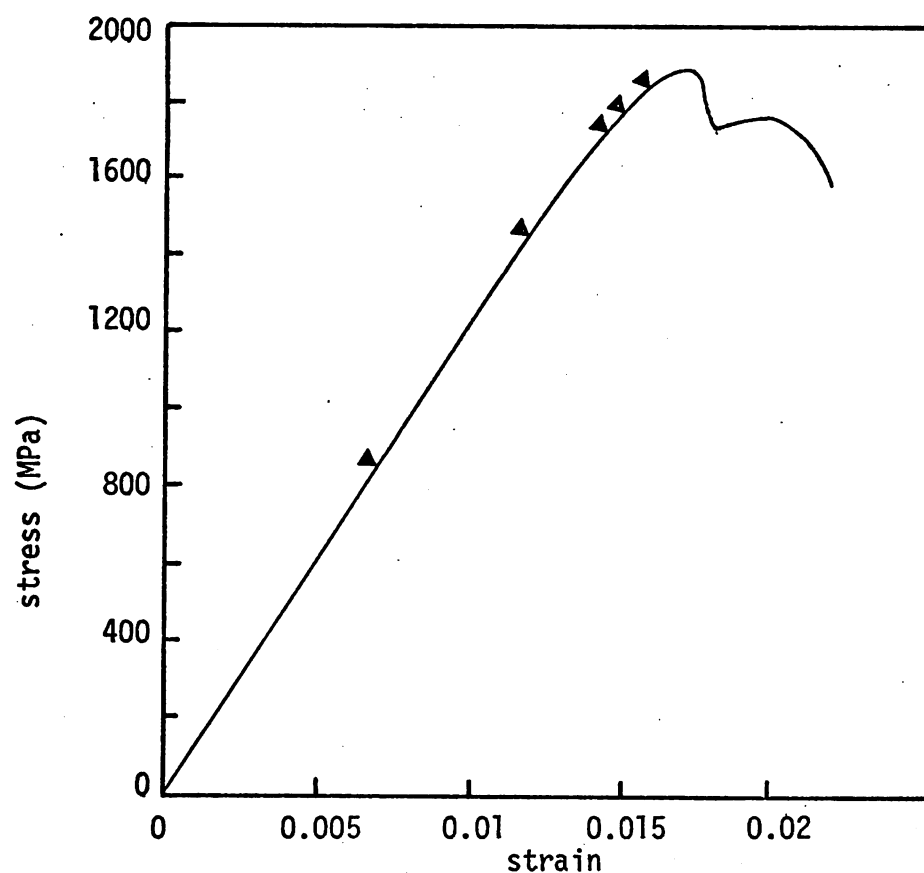


Fig. (6:10b) Nominal σ/ϵ curve for above, showing initial stresses.

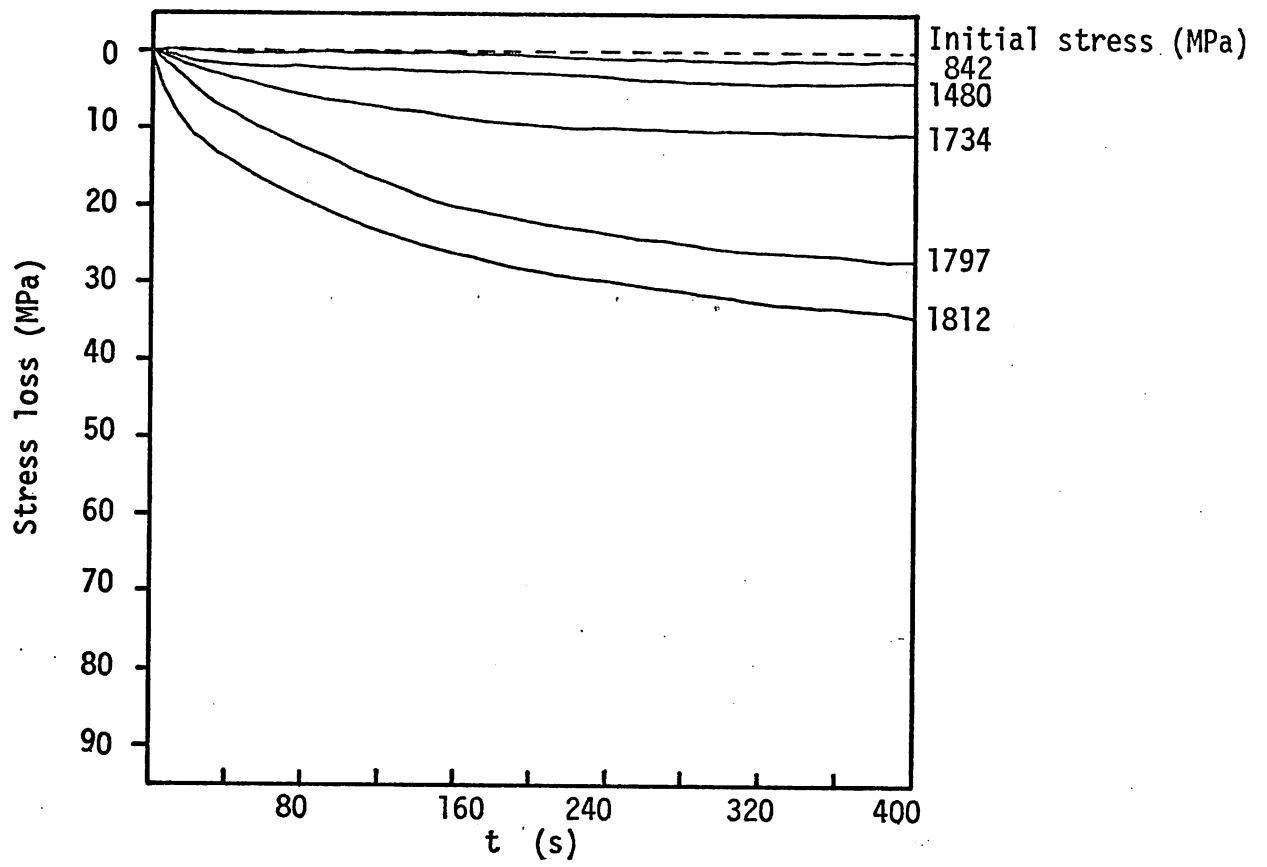


Fig. (6:10c) 2nd relaxations from similar stresses

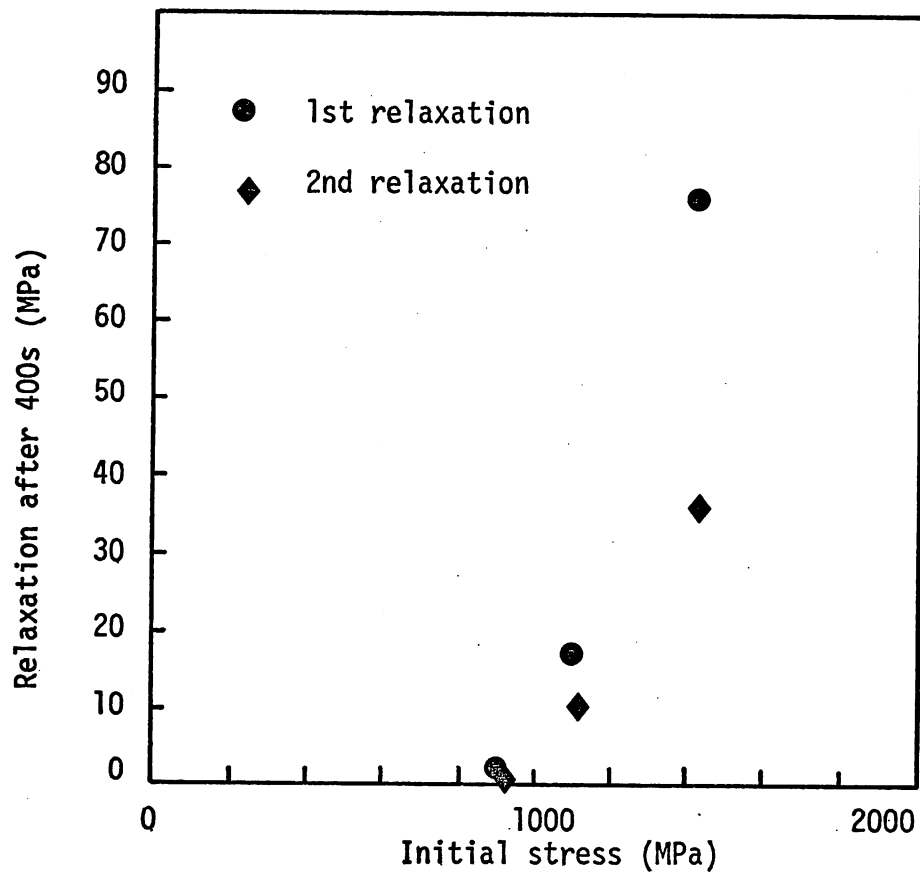


Fig. (6:11) Stress drop for 1st and 2nd relaxations after 400s in A/R, 17-7PH stainless steel wire, with initial stress.

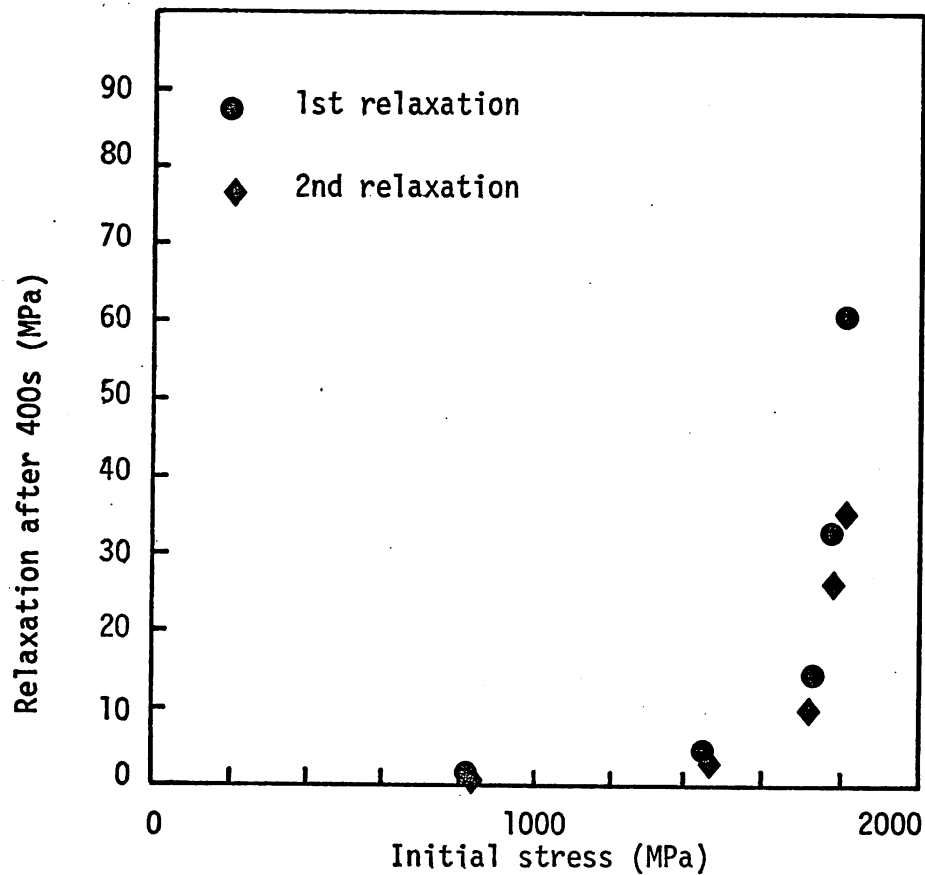


Fig. (6:12) Stress drop for 1st and 2nd relaxation after 400s in A/R + HT, 17-7PH stainless steel wire, with initial stress.

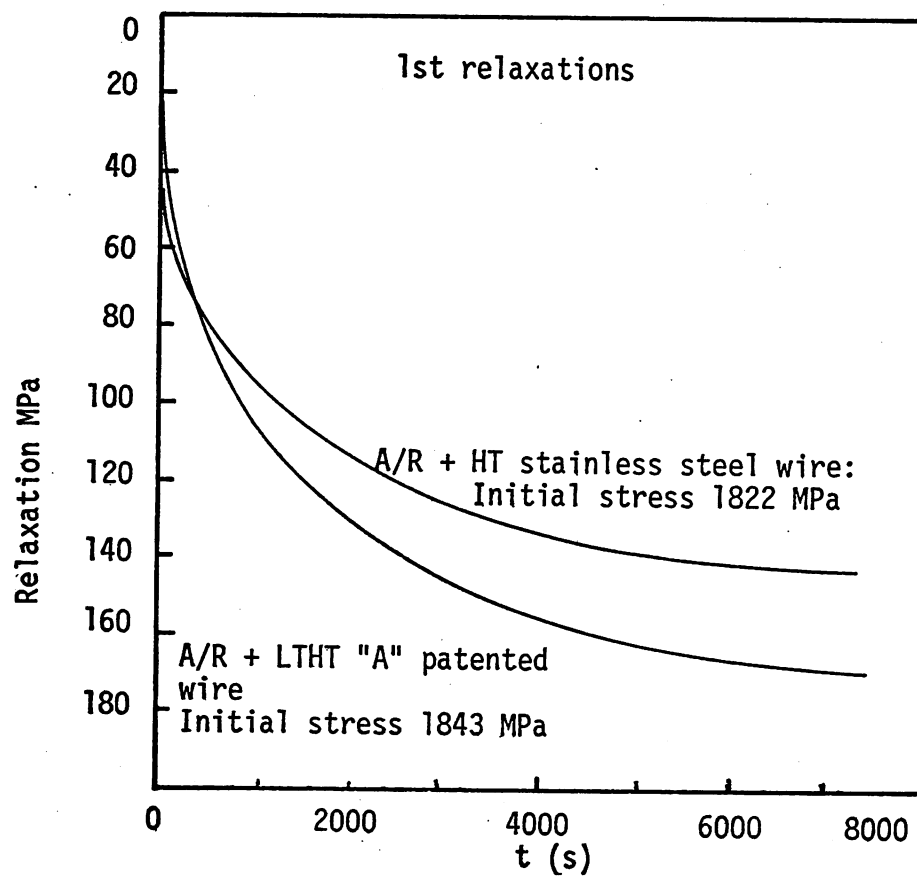


Fig. (6:13) Long term relaxations for A/R + HT stainless steel wire with that of an A/R + LTHT "A" patented steel wire specimen for comparison.

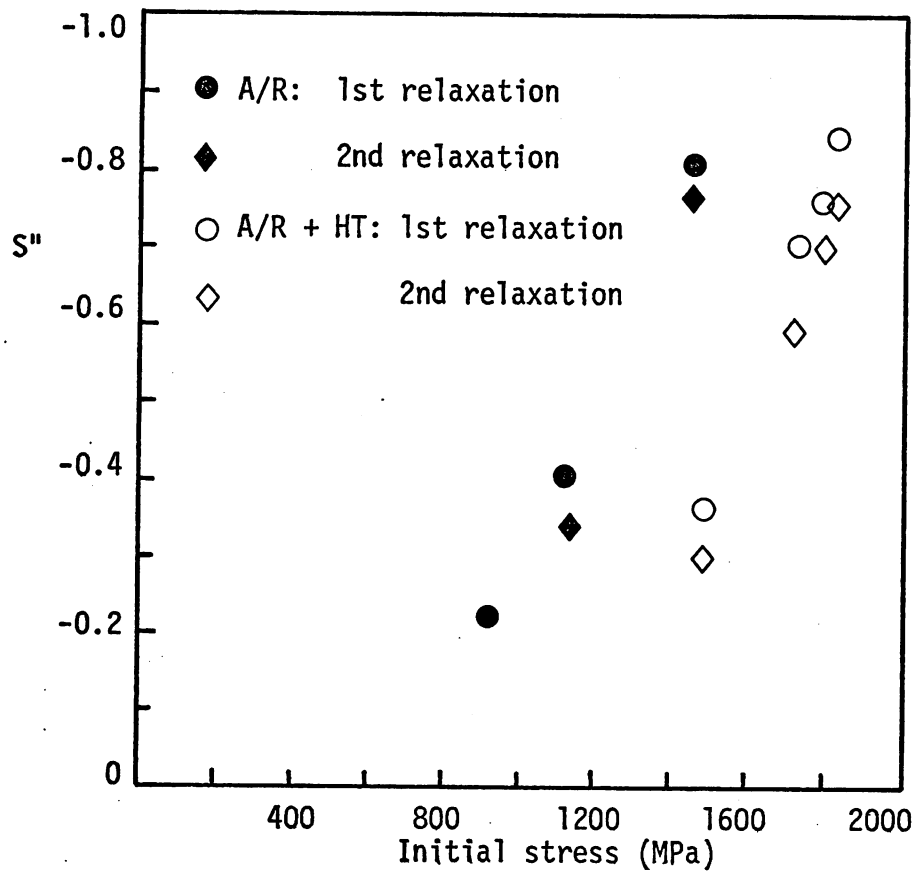


Fig. (6:14a) Values of gradient (S'') of $\ln \sigma$ vs. $\ln t$ graphs for A/R and A/R + HT, 17-7PH stainless steel.

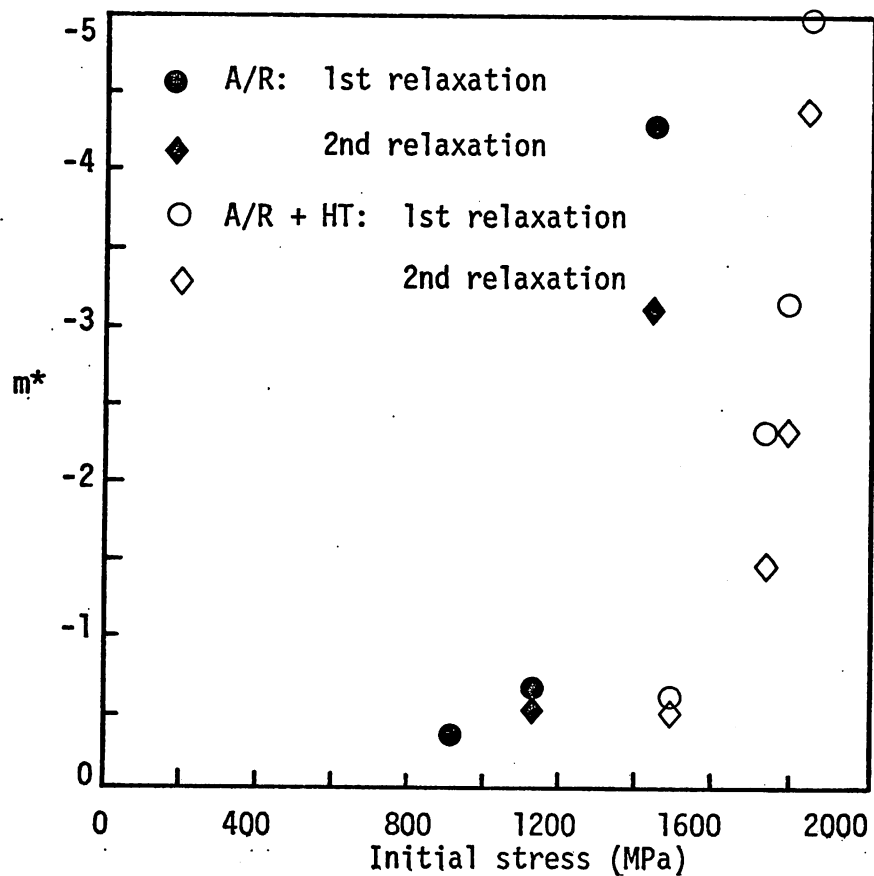


Fig. (6:14b) Corresponding values of m^* .

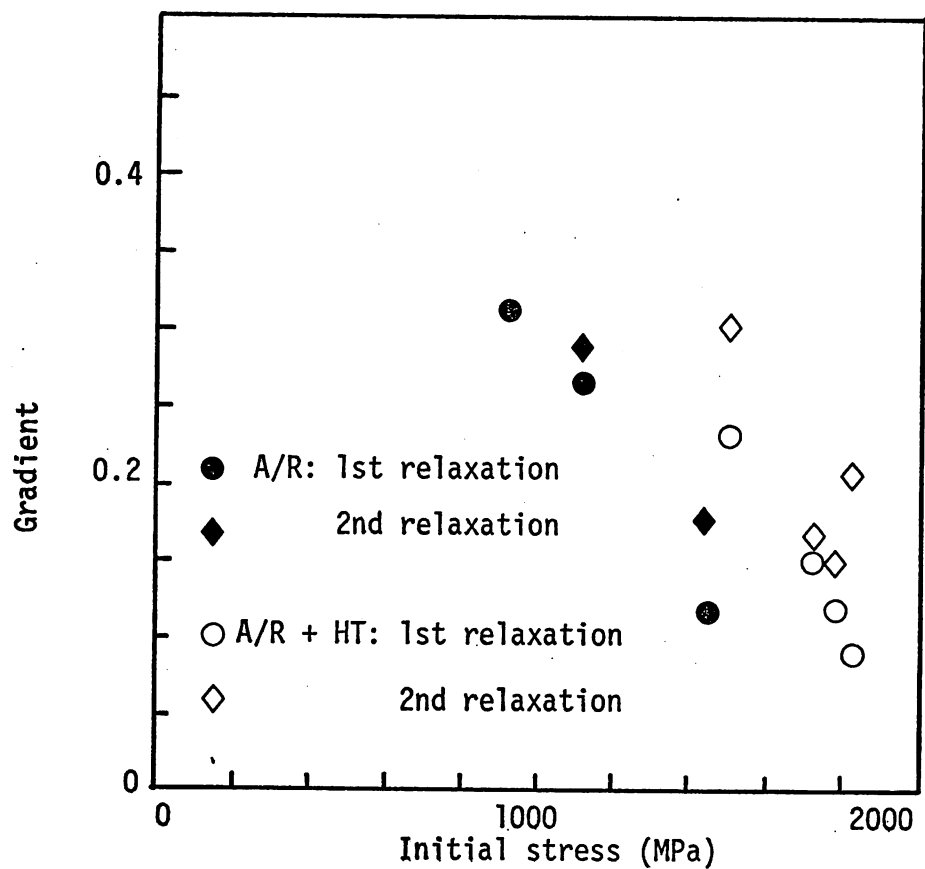


Fig. (6:15a) Values of gradient of $\ln \sigma \Delta \sigma$ graphs for A/R and A/R + HT, 17-7PH stainless steel wire.

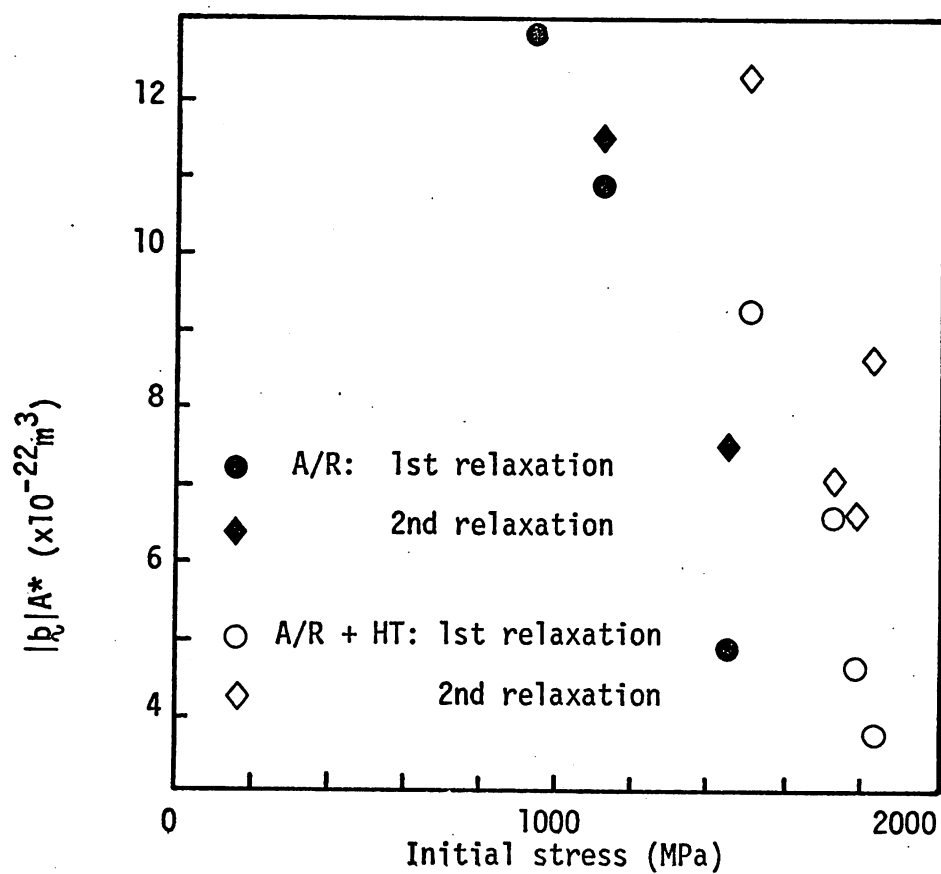


Fig. (6:15b) Corresponding values of $|b|/A^*$.

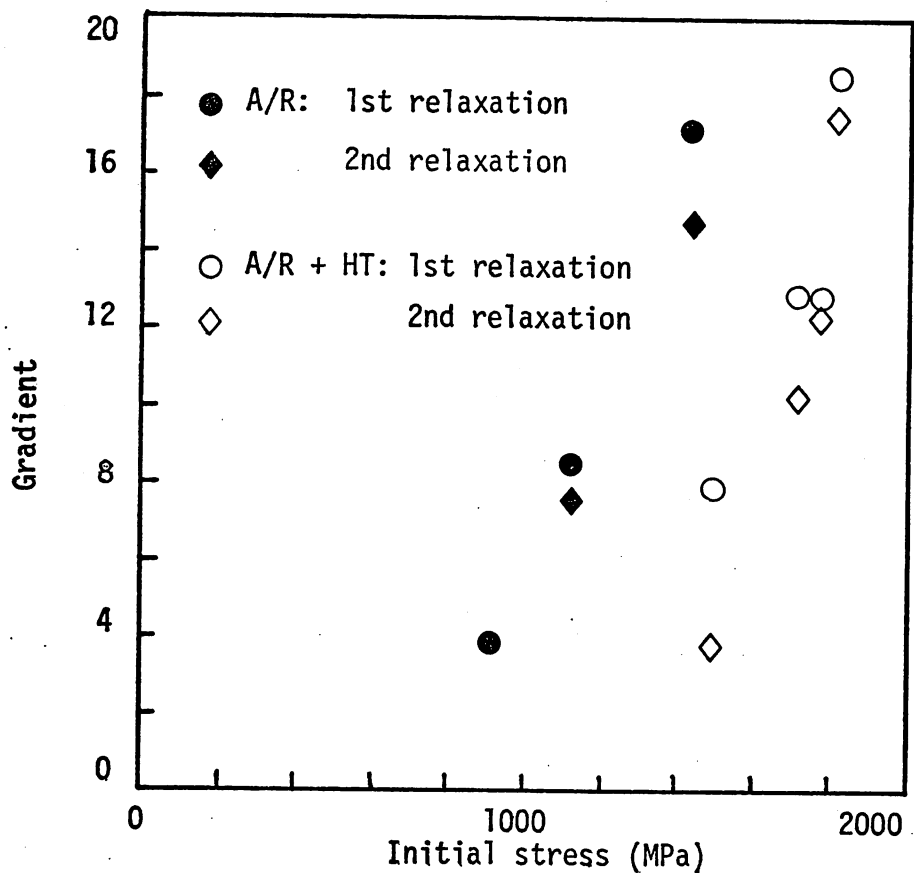


Fig. (6:16a) Values of gradient of $\Delta\sigma$ vs. $\ln t$ graphs for A/R and A/R + HT, 17-7PH stainless steel wire.

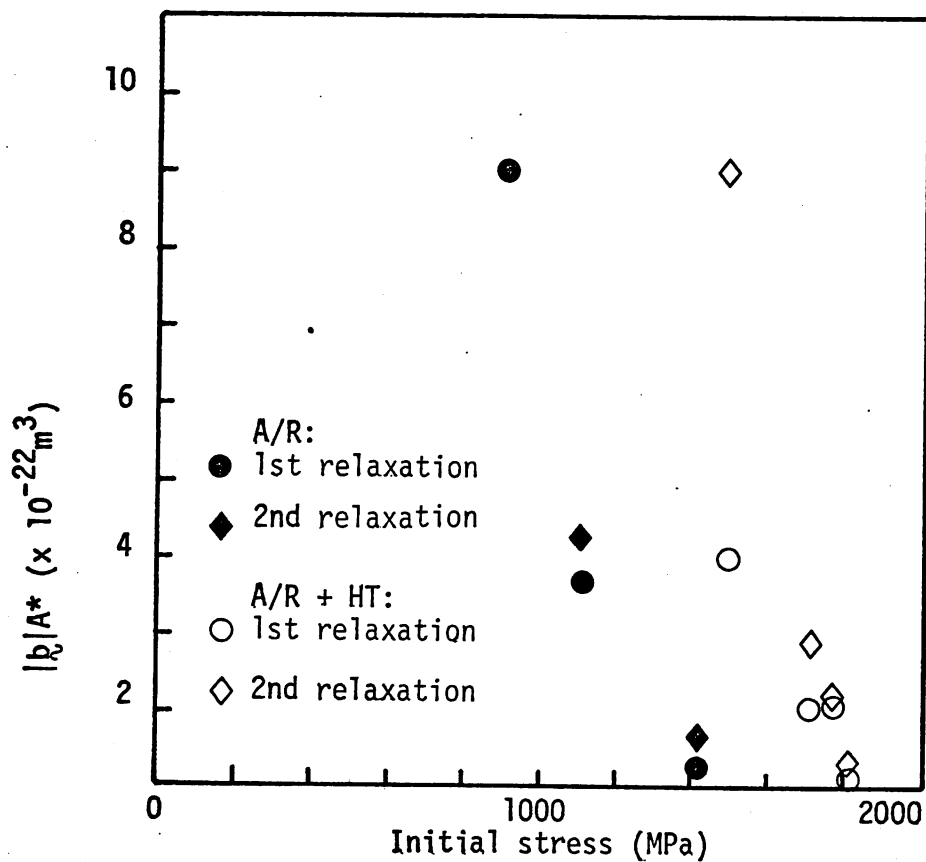


Fig. (6:16b) Corresponding values of $|b|/A^*$

7. General discussion

7:1. Introduction

As previously described (1) there are many requirements for a material which is to be used as a spring: these are often complex, and include not only the physical properties of the final article but also those which allow its production in a suitable form. Probably the most important, however, (at least in static service requirements) is that of high proof stress or elastic limit. It is this which ultimately controls the possible specific energy density which a spring can sustain. It is common practice to use as high a service stress as possible to enable light-weight springs to be used. The value of the stress levels attained in the spring are generally assessed from the applied loads (e.g. ref.1, AI) without taking into account internal, residual stresses which may have been introduced during production. The residual stresses have normally been regarded as being of little significance when considering the maximum working stresses.

The present investigation has, however, shown that a number of workers regard the residual stresses present in the final spring as being important in type of failure known as stress relaxation. This failure is well known within the spring industry (amongst others) and the remedies or palliatives which are employed have been discussed at length in chapter 4. Of particular interest are the methods which are employed in the reduction of stress relaxation in patented wire, spring steels.

7:2. Patented wire and 17-7PH stainless wire: their microstructures, strengthening mechanisms and their general stress relaxation behaviour

The present work has extended the microstructural information on this material in a number of areas. As described in chapter 4, the consensus of previous work indicated that the main strengthening mechanism in patented wire is that due to the presence of dislocation cells in the ferrite, it being assumed that the ferrite will undergo general plastic deformation before the cementite. A major role of the latter phase has been assumed to be the stabilization of these ferrite cells to give a small final size, and so dislocation mean free path, on extensive cold drawing. This ferrite dislocation substructure thus enhances the inherent strength of the softer phase to such an extent that extremely high yield and tensile strengths can be obtained in these wires at high drawing reductions.

The present work confirms this basic concept, but also provides further insight into the structure/property relationships. All the samples of 4.25mm patented wire (having undergone a wire reduction of approximately 70%)

appeared similar in the TEM study, indicating the subtle effects the LTHT's cause in the microstructure. In this material the lamellar microstructure was highly aligned along the wire axis (as shown in both the transverse and longitudinal sections) with little evidence of significant fragmentation of the cementite lamellae and no evidence of void formation. It was also seen to be essentially uniform across the wire section except for a surface decarburized layer. The dislocation substructure in the ferrite was characterised in detail despite observational problems. It was shown to consist of dislocation cells, bounded by low angle boundaries, which extended across several ferrite lamellae. They were generally of similar size in the longitudinal and transverse section. Such behaviour has not been noted previously in this material and is indicative that the deformation processes during drawing must occur in small units of the structure as postulated by Langford (35). It is instructive to relate the cell sizes observed for these 2 reductions to their flow stresses (taken as the 0.2% proof stresses) and correlate these to those obtained by Embury, Keh & Fisher (66). The values for the fine wire agree well with the drawn pearlite line (fig.7:1). However, the values for the larger diameter wire are in poor agreement. This discrepancy can be understood in that in this case the dislocation barrier spacing is of the order of the mean ferrite lamellar width not the mean cell diameter. This supports the view that in the finer wire the typical dislocation mean free path is of the size of the ferrite cell size whereas in the larger diameter wire it is of the order of the ferrite lamellar width. It was also observed in the current work, that a dislocation substructure on an extremely fine scale exists in the lamellar cementite. Such features have not previously been noted, and as this substructure could not be studied in detail, its relationship with previous observations of defects in cementite has not, at present, been pursued (see chapter 2).

The patented wire which has been investigated using atom-probe techniques, was similar to the above wire except that it had undergone a much higher wire reduction (approximately 98%). These techniques proved to be extremely powerful in elucidating the dislocation substructure in the ferrite and in segregation phenomena, the latter being discussed later. It was found in this case that the typical transverse cell size was smaller than the interlamellar spacing. The LTHT's caused the cell walls to become more regular and well defined and often aligned with the lamellae. It was also noted that the density, in the cell interiors, of

defects which were not securely pinned (for example to a cell wall or a ferrite/cementite interface) was significantly reduced. Typical misorientations across cell walls were similar to those observed in the larger diameter wire. It was found that no significant changes occurred in LTHT to the distribution of solute, in particular that of carbon and nitrogen; this point is discussed further below. It is clear that the significant effect of the LTHT's, is to allow a reduction in the complexity and stored strain energy of the dislocation substructure and the removal of weakly pinned dislocation segments (see chapters 3 and 4). The driving force for such processes is likely to be the residual stresses present in the as drawn material, which as a result are reduced in magnitude (see chapter 4). These stress distributions, present in such wires, were unable to be investigated in the present work. Previous work (see 1) has only considered the macro-residual stress distribution in this material. This is due to the anisotropic deformation in wire drawing across the wire which can result in either tensile or compressive stresses in the outer layers of the wire depending on the exact mode of deformation. Residual stress variations must also be present on the scale of the interlamellar spacing, due to the widely different mechanical properties of ferrite and cementite. This would result, after drawing, in the ferrite being left in compression with respect to the adjacent cementite lamellae. A further stress distribution may well occur on a sub-lamellar scale if dislocation cells exist on a scale finer than the lamellar width. Such modifications of the macro-residual stress distributions have not been investigated and it is therefore unknown what relative effect LTHT's have on each distribution. It is likely, however, that as such macro-distributions are considerably reduced by similar stress relieving heat treatments (1) the micro-distributions would also be extensively modified.

The effects of the LTHT's on the tensile properties of the 4.25mm wire have been shown to be significant and have allowed a convenient correlation with their respective relaxation properties. Tests undertaken have shown that the A/R wire yields in a gradual manner showing a low proportional limit/UTS ratio. The effect of a LTHT (e.g. 200°C for 30 minutes) was seen to be particularly dramatic on the proportional limit, although the UTS was also raised, thus the ratio increased. This gave the wire a more rapid yielding behaviour with strain. These changes can be well understood in terms of the previously described microstructural changes in the closely similar wire. As will be described later in this chapter, significant

relaxation was only found at initial stresses which were above the proportional limit. It is in this sense that the tensile strength of a spring material has been shown to be not necessarily an adequate guide to its relaxation resistance.

Similar investigations have been initiated on the service replacement for patented wire in light-weight springs, viz. 17-7PH stainless steel. Limitations of time have, however, only allowed an initial investigation. A TEM study has not been able to distinguish between α' and the heavily dislocated δ -ferrite which should be present. In addition, no retained γ was detected. Again this technique could not distinguish between the A/R and HT materials (the heat treatment being designed to give a fine intermetallic precipitation). This HT does, however, improve the mechanical properties, in this material the proportional limit/UTS ratio remaining approximately constant. An interesting feature of the wire in both conditions, is that sensitivity of the load became positive after the UTS is passed the strain-rate again in the tensile test, indicating stress induced transformation of retained γ to α' . A general comparison with the LTHT patented wire (of similar tensile properties) for relaxation resistance showed that at similar initial stresses the HT 17-7PH wire initially showed a more rapid relaxation rate but it decreased more rapidly than the LTHT patented wire, so that after a certain time the load loss became progressively smaller in the former material. It is important to note at this stage that the HT given to the 17-7PH wire was significantly more severe than any of the LTHT's for the patented wire. This is likely to result (additional to precipitation phenomena) in a more complete rearrangement of dislocations present (the precipitation would tend to stabilise the substructure) and a lower final level of residual stresses.

As the tensile strength of the spring material appears to be a rather unreliable indicator of the relaxation resistance it might be valuable to try to correlate it with other documented properties. A popular and obvious choice would be the low temperature creep resistance. Previous workers (e.g. 208) have attempted to relate the 2 properties in a quantitative manner without much success. Reasons for such problems have been discussed in chapter 4, but a few points will be reiterated here. Whether the deformation is anelastic or plastic has to be considered in each case (all material relaxations in the present work have been shown to be plastic in nature within experimental limits). The idea of considering stress relaxation to be creep under a decreasing effective stress is appealing

but as commented on previously, there are difficulties inherent in this argument. For example, it is unlikely that the dislocation processes are identical for each situation as the plastic strains occurring (and so the dislocation interactions) in each type of test are of completely different magnitudes. It is true, however, that materials with good creep resisting properties tend to have good relaxation properties which can, when allied with the influences of free dislocations and residual stresses present, be useful in the selection of materials. In addition it is instructive to analyse the possible dislocation processes which have been identified in creep failures which also may occur in stress relaxation: this is explored in a later section in this chapter.

7:3. Analytical stress relaxation

7:3.1. Introduction

A detailed description and analysis of the concepts involved in all aspects of analytical stress relaxation has been presented in chapter 4. In the following section comments pertinent to the present work are discussed and developed.

7:3.2. Testing problems

It is clear that the simplest form of analytical relaxation test involves a complex interaction between the specimen and testing machine. It is for this reason alone that such testing is more difficult to perform than comparative steady state creep tests. As previously pointed out, it is only recently, by relatively few workers, that the necessity of the use of a closed-loop testing system with strain control has been realised. Only such a system can ensure the constant strain criterion during a test. Despite the comments of numerous workers using screw driven testing machines that either machine effects were negligible or that they were constant and predictable, the present work using patented wire specimens has shown this to be, at the very least, a highly dangerous supposition. The relatively large machine relaxation found in a floor model Instron machine supports the comments of the few workers who have insisted on the use of closed-loop machines (166,167). The effects of these doubts on much of the earlier work cannot be ascertained but it is clear that the results of such research should, initially, be treated with caution,

The present work has also shown that machine relaxation cannot be ignored in a closed-loop machine. Unlike the machine component which has frequently been observed (which is possibly due to thread attachment effects) it appears that this relaxation is due to a load cell effect (possibly the

relaxation of the epoxy bonding of the strain gauge network). An extensive calibration programme on the machine employed in this work has shown that this relaxation is reproducible and could be accurately characterized to allow a correction to be performed on the test data. It was noted that it was "anelastic" in general behaviour, i.e. it was totally recoverable (over a period of time) on removal of the applied load. It was also noted that the machine relaxation occurred over a relatively short initial period (which depended on initial load) after loading, after which it was relatively constant.

It appears likely that as the machine component of either or both the two above types appears difficult to avoid totally, it may well be responsible for much of the confusion and argument over the analysis of strain rate testing, a specific problem being the poor correspondence between continuous stress relaxation and stress and strain dip tests (see chapter 4 and ref. 1). Such problems are unlikely to be as significant in creep testing where the system soon attains a "steady-state". This difference may account for some of the problems of relating stress relaxation to comparable creep data.

The above, accurate machine calibration was only made possible by the adoption of a standard time to load the system, of in this case 180 seconds. The use of constant crosshead rate to load gave unreliable values. In addition to this reason, the loading method adopted was thought to be more closely allied with service conditions (see chapter 5). The importance of loading rate is not confined to its effect on the microstructure (and therefore, possibly, on its flow characteristics) but also to relaxation behaviour which will occur before the actuator is stopped. As the present work has shown, relaxation can occur at relatively low stresses, and dislocation movements in the loading process are highly probable. This problem has been totally ignored by previous workers and will require considerable further effort to elucidate. It is possible that the effect of this error may be merely to change the total relaxation, that is in effect to "lose" the first part of the relaxation curve. The analysis of stress relaxation due to Li and Guin and Pratt (see chapter 4) is unlikely to be affected but that due to Sleswyk may, however be suspect, as suggested by Grosbras et al. (200), because of the effects on his initial assumptions.

It was found in the present work that the recording techniques available were by no means the best suited to the problem (see A.I. In order to obtain a sufficiently accurate recording on the chosen X-Yt

recorder during the relaxation, the sensitivity had to be high. This not only imposed operating difficulties (the input had to be manually backed-off during each loading to the correct level) but it also made difficult the recording of the total stress/time behaviour during the whole of the test. In addition, the recorder had to be set to a single time-base value for a test. This was a compromise between obtaining the whole of the test information (normally up to 400 seconds) and the requirement of accurate stress or stress rate/time information (the latter needing a fast time base). The present work has shown that such a data acquisition system is not entirely adequate for this type of investigation: significant information was lost and errors introduced at short times. The use of a digital recording system with a high sampling rate would enable all these problems to be circumvented, and in addition, the subsequent manipulation of the information by computer analysis would be made considerably easier.

7:3.3. Comments on stress relaxation analyses and the concepts introduced by them

A number of concepts have been introduced by previous workers which have proved useful in the dislocation kinetics of stress relaxation and other forms of plastic flow situations. It can generally be noted that they all adopt a continuum approach to varying degrees. At one end of the spectrum are the phenomenological approaches which ascribe macroscopic behaviour to generalized flow processes (see Hart (166) and others), ranging through the approach of Sleeswyk to the thermally activated dislocation concepts. It is the latter type which have often proved most instructive and better able to explain and predict phenomena in various materials. Such analyses postulate the thermal activation of mobile dislocations between pinning positions under the action of the effective (or thermal) component of the applied stress, σ^* . Thus the applied stress, σ , is taken to be composed thus:

$$\sigma = \sigma^* + \sigma_i$$

The internal (or thermal) component, σ_i , is assumed to be due to long range interaction forces within the microstructure, i.e. caused by dislocation barriers which cannot be overcome by thermal activation due to their scale.

The components of the applied stress are often considered in terms of shear stresses which is rather more convenient when considering dislocation interactions on a slip plane. Thus:

$$\tau = \tau^* + \tau_i$$

It appears normal to assume that the Taylor factor, M_T , is 2, i.e.

$$\tau^* = \frac{\sigma^*}{2}, \text{ rather than } 2.7 \text{ for bcc materials and}$$

3.06 for fcc ones. It has also been noted (Li, 213) that a periodically varying internal stress field (as is inevitable with defects in the structure) will have the effect of increasing the values of A^* , m^* , ΔG in the activation behaviour. Recovery process or work hardening during the deformation are thought to affect only σ_i (e.g. see Solomon, Ahlquist and Nix, 194) and are often assumed to be negligible during stress relaxation, i.e. $\sigma_i = \text{constant}$. It is therefore postulated that as relaxation proceeds, σ^* will gradually decrease and the thermally activated processes will also decrease until at long times, $\sigma = \sigma_i$. Disagreements with this assumption have been detailed in chapter 4 (e.g. the use of stress dip tests to find σ_i , but note the above objection put forward from the present work). It is interesting to note in this context that Gibbons (293) has related the value of σ_i to the 0.2% proof stress in some creep resistant alloys. Long term relaxations on patented wire, and wire in spring form, at room temperature, have indicated that relaxation apparently continues at significant rates indefinitely even at relatively (below macroscopic yield) low stresses, thus strongly suggesting the activation of recovery processes. In addition the universal observation in this work that a 2nd relaxation from the same initial load immediately following a 1st relaxation indicates the impact of work hardening. (This may partly be due to some plastic flow during the reloading even though it was noted that after relaxation the tensile specimen would continue on the same stress/strain curve as was being followed during the initial loading. The behaviour of 17-7PH stainless steel investigated in the present work was, in general, similar except that long term tensile relaxation tests indicated that recovery occurred at a much slower rate. It is possible that in materials such as spring wires the large residual stresses due to drawing, forming or phase changes on heat treatment, may influence the flow behaviour, e.g. in a very simplified form

$$\sigma = \sigma^* + \sigma_i + \sigma(\text{res})$$

Unfortunately little is known of the detailed nature of the residual stresses, for example, whether they can be regarded as thermal or athermal in nature. In the case of patented wire discussed previously the 3 scales of the residual stress distribution may have different effects, complicating

the problem further. However, from the above simple concept it can be seen that $\sigma(\text{res})$ may reduce the value of σ_i such that σ^* and so the driving force for relaxation will dramatically increase. It is possible that this may also help to explain the far better relaxation resistance of 17-7PH stainless steel over patented wire in the finished product, the former being far more effectively stress relieved by the far more severe heat treatment. Attempts have been made in the present work by using a simplified macro-residual stress profile, to predict the overall tensile stress/strain and relaxation behaviour of patented wire by assuming its effect on the deformation processes. This has proved largely unsuccessful mainly due to theoretical inadequacies already described. It is possible, however, to suggest qualitatively that the gradual yielding behaviour may be caused by these residual stresses. This concept is however, unlikely to be valid in this particular situation, as the LTHT employed for the patented wire is regarded as being insufficient to reduce significantly the macro-residual stresses.

It is interesting to note in this context, the comments of previous workers who have touched on this problem. Brown, Rack and Cohen (259) noted that relaxation was considerably enhanced in their steels during the precipitation hardening process. They postulated that the "enhanced plasticity" around each growing precipitate may cause this. This could be explained by the production of mobile dislocations at the interface of a growing precipitate and/or by the change of residual stress levels around each. Another example comes from the work of Ritter and McPherson (267) who investigated anisothermal relaxation in Cr-Mo-V steels. In addition to effects due to dynamic strain ageing and precipitation processes they noted that the induced transformation of retained austenite significantly increased the relaxation. An example from spring materials has also been commented on in chapter 4: that of shot peening finished springs. This is often done to improve the fatigue properties but it was found that the relaxation properties deteriorate significantly. This implies that causing compressive macro-residual stresses in the wire surface (and so necessarily reducing similar stresses in the wire core) will have this effect. The reasons why such a reduction in relaxation resistance is caused by a reduction in the peak tensile and compressive macro-residual stresses is not clear, but it points out that techniques employed in manufacture, not obviously connected with relaxation, may have significant effects on it. A significant investigation was undertaken by Altermo and Lagneborg (253) on the anisotropic stress relaxation behaviour of pure aluminium wire:

they tested wire in hard drawn (by 96.5%) recovery annealed (at 280°C for 7 min.) and fully annealed (at 320°C for 2 hours). It was found that in the hard drawn state the wire relaxed at the same or a faster rate than in the fully annealed condition. This was in spite of the higher yield strength and creep resistance of the former. It was found that the relaxation properties of the hard drawn wire were anisotropic, showing considerably greater relaxation in the transverse as opposed to the longitudinal direction. It was also shown that the recovery anneals' transverse relaxation properties were improved to the level of that of the annealed material with little loss of yield strength. These workers ascribed the anisotropic properties to a Bauschinger effect brought about by the wire drawing process rather than a texture effect (which was the same for the drawn and annealed materials). (see Fig. (4:20)).

Despite the uncertainties, it can be seen from the above comments that it is important that residual stresses and their effects should be far better understood in many cases. In addition it is important to realise when considering the components of the applied stress, that σ_1 cannot be simply related to residual stresses and it would be sensible in these problems not to refer to residual stresses as "internal" stresses, as is often done in the literature.

Common parameters used in thermally activated analyses are A^* and V^* where:

$$A^* \left| \frac{p}{V} \right| = V^*$$

It is, in fact, incorrect to use the term activation volume in this context (it is correctly, the derivative of the free energy with respect to pressure) as the definition used in this theory involves the derivative of the free energy with respect to τ^* (see Li, 213). The correct term is therefore, activation area which is the area on a slip plane which is swept out by a thermally activated event under the action of an effective stress τ^* . Thus if $A^* \left| \frac{p}{V} \right|$ for a process is of the order of the atomic volume, the rate determining process would be the diffusion of vacancies (e.g. Nabarro-Herring creep). If the process is some dislocation movement, $A^* \left| \frac{p}{V} \right|$ would be characteristic of the area swept out by dislocations being activated over a free energy barrier between two low energy configurations. Commonly known theory can then be used to calculate the activation rate (and therefore the deformation rate) of dislocations under an effective stress τ^* over such barriers. Normally activation against the stress is taken as negligible and an exponential dependence of the strain rate with free energy results. Developing the

above ideas (again see Li, 213) it can be shown that $|b|A^*$ is strongly dependent on the effective stress, whereas not very dependent on the temperature, crystal structure, or composition (at least at relatively high values of τ^*), see Babsubramian and Li (291). Kubát and Rigdahl (214), Conrad and Hayes (294) and Arsenault (295). In fact, and quite surprisingly, the values of the logarithms $\log A^*$ for many materials show a similar linear relationship to the logarithms of τ^* . Christian (296) has also noted that the values of $A^*|b|$ for many materials are insensitive to work hardening. To some degree the apparent similarity in behaviour of $|b|A^*$ is possibly a little misleading, as a close examination of the original published data has indicated that it was common practice to use information obtained at widely varying test temperatures to cover various parts of the τ^* spectrum.

The general behaviour of the tests undertaken in the present work concurs with the above comments. Also the behaviour of all the investigated materials at the various initial stresses showed similar trends. It was found during a relaxation, after the initial few seconds of a test, the value of $|b|A^*$ was usually constant. However, the value of $|b|A^*$ was found to be a strong function of the initial stress, decreasing with increasing initial stress. The effect of the heat treatments on both the patented wire and the 17-7PH stainless wire was to reduce the range of initial stresses over which these changes occurred and to push them to higher overall values in close agreement to the previously described changes in the yielding behaviour of these materials. On the basis of the thermal activation theory, these changes would tend to indicate that the value of τ_i was being increased by the heat treatment. This is a plausible argument in the case of the stainless steel, where precipitation is occurring, but seems unlikely in the case of the patented wire where major changes in precipitation have not been observed. In the latter case this apparent inconsistency may well be explained by the suggestion, as described earlier in this chapter, that dislocation rearrangement occurs so as to remove easily activated elements of the substructure, i.e. the remaining dislocation networks ensure a higher value of τ_i in the structure.

It is also interesting to note that the range of $A^*|b|$ obtained for all the materials tested, under varying initial stresses were similar: typical values being 1.5 to $8.5 \times 10^{-22} \text{ m}^3$. They correspond to values of A^* of between approximately 60 and $380 \times 10^{-14} \text{ m}^2$. These are of several orders of magnitude greater than those observed for pure iron (e.g. see ref. 294), where activation over the Peierls-Nabarro barrier is taken to be the rate determining

step (see later). However, the values obtained here are consistent with the area swept out by an activation event being across a dislocation cell, although this hypothesis does not fully explain the variations with initial stress.

The second, common approach to the analysis of this type of plastic deformation (which can also be applied to other types) is that which assumes a relationship between the mean dislocation velocity and the effective stress of the form

$$\bar{V} = B \tau^{m^*}, \text{ i.e. a power law.} \quad (\text{eq}^n \text{ 4:8})$$

The theory, after Li (161) and others, has been given in detail in chapter 4. It allows an analysis of the data to find m^* , which is assumed constant. In previous work the analysis has been seen to hold for bcc alloys but not for fcc or hcp ones. In the latter, values of m^* of ∞ or <0 were obtained which are clearly impossible. Law and Beshers (208) proposed reasons for the failure, such as the inability of the Johnson-Gilman equation (eqⁿ. 4:8) to model the system, the power law not holding in these situations or the variation of ρ_m or τ_i during a test.

In the present work it was found that all values of m^* obtained were negative, despite the fact that the deforming phases were largely bcc. It is true that precipitation hardened bcc phases containing a very fine dislocation substructure have not been examined previously by these techniques. While this further failure of the application of the power law is clear, the reasons are again not obvious. It can be noted, however, that in the present series of tests m^* varied in a continuous manner with initial stress the variation again correlating with the yielding behaviour, i.e. it occurs over a much narrower initial stress range in the heat treated materials.

The above analyses both assume the constancy of σ_i (which is discussed above) and ρ_m . In general the latter is assumed to be true (see chapter 4). Raghuraman and Arsenault (297) have undertaken a theoretical study of the effect of a variation of ρ_m on τ_i , τ^* and τ_{fl} and concluded that, in general, any effects were minor. Other workers, however, disagree, e.g. White and Smith (192), and it is obvious that considerable clarification is required. Most workers (see chapter 4) agree that ρ_m is likely to vary during the onset of plastic deformation, which is the situation often present during tests undertaken in the present work. Bernstein (298) in particular, regards the main variation in this stress regime to be the variation in dislocation velocity.

Suggestions have been made that the rather unpredictable failures of

the present dislocation kinetic theories may largely be due to the simple division of dislocations into mobile and immobile populations. Work on such problems has been slow to develop, the initial statistical ideas being put forward by Kocks (299). The ideas have been developed, somewhat, in papers by Lagneborg, Forsén and Wiberg (300) and Lagneborg and Forsén (301) who have regarded the dislocations present in a material as being a 3 dimensional network with a distribution or spectrum of link sizes. Thermal activation can release some of the links (depending on their size) to form loops which are then pinned and so form further links. Recovery is postulated to occur by climb controlled shrinkage of these networks. Thus these ideas replace mobile and immobile dislocations with mobile and immobile links. Such concepts have particular attractions when considering dislocation substructures as have been examined in the present work. Some links will be tightly bound in the cell walls and precipitate/matrix interfaces, while others will be less so and, by means of thermal activation, could expand across a cell. The effect of a heat treatment would be to lower the energy of the system by activation of these weakly pinned links and their absorption into a more tightly bound position. These links would not then be available to move during a relaxation situation. This argument could explain why an anneal, such as is given to patented wire, can impart relaxation resistance in environments approaching the anneal temperature and why hot setting (see chapter 2) is also so effective due to the effect of the imposed stress on τ_i .

7:3.4. Particular comments on the work of Okazaki et al. - a case study

Effort has been made in this work to emphasis the assumptions made in the analyses as previously used in relaxation testing, such as constancy of ρ_m and σ_i . Recent papers by Okazaki et al. (152,153,154,155) have indicated the first concerted effort to analyse relaxation data without these assumptions. As described in detail in chapter 4, they considered that in a relaxation test, ρ_m drops after an initial period of stability to be later followed in a drop in σ_i , and they put forward plausible mechanistic arguments to give support. Attempts have been made to analyse the present data in the light of these ideas, and have been totally unsuccessful. A number of weaknesses in their analysis can be put forward, although it is not clear how important each are. Their testing machine was of a screw driven type which apparently showed remarkable accuracy, although they appear, in general, to have ignored the defects inherent in the system. They do appear, in later work, to have ascertained whether machine relaxation was important. Surprisingly they suggested it was negligible although this

may not be unexpected as they used patented wire test specimens for the purpose. Also their data recording technique was of the paper graph type and so of not particularly good accuracy considering the weight they put on their data. A further problem with the experimental work is that they, as have other workers, ignored relaxation which occurs before the crosshead was stopped. It is interesting to note with this in mind, that they attempted to extrapolate to $t=0$, i.e. when the crosshead was stopped, to obtain "true" values of V^* and σ^* . The theoretical analysis they used is of standard type, assuming both the Orowan and Johnson and Gilman flow equations. They obtained values of m^* (assumed constant for a test) by a standard procedure and then calculated values of V^* : σ_i , σ^* and ρ_m at various times during a test by a novel technique using data from two adjacent points on the relaxation curve. As discussed by Smith and Thorpe (203) this analytical technique is open to criticism, and it may be due to inherent failings in it that some of the results obtained are rather surprising (e.g. the more rapid relaxation observed at lower testing temperatures). Thus, while this type of critical approach to the generally accepted stress relaxation theory is now required, it is unlikely that an adequate theory has been (as yet) devised.

7:4. Previous research on the concepts of rate controlling deformation processes - general examples

It is instructive to consider the rate controlling processes indicated by previous work which has special relevance to the low temperature deformation of both patented wire and 17-7PH stainless steel. The thermally activated low temperature deformation of pure bcc metals has been ascribed various mechanisms, including:

- a) overcoming the Peierls-Nabarro stress,
- b) non conservative motion of jogs in screw dislocations,
- c) overcoming solute atom pinning,
- d) overcoming interstitial atom precipitates.

Conrad and Hayes (294) concluded in a wide ranging survey that (a) was the most likely solution in the form of a double kinked dislocation where the kinks can move freely. Arsenault (295) in consideration of iron between 123 and 253K suggested that the pinning of jogs was not likely to be important due to their low density. He also thought that because of the variation of $|b|A^*$ with impurity content, pinning by such "clusters" was also unimportant ($|b|A^*$ was far too small). He supported the idea that the double kinked dislocation model was the critical effect on the

basis of a number of reasons. This mechanism was further explored by Dorn and Rajnak (302) who showed how it could explain much of the deformation behaviour of pure bcc materials. In a little reported work by Wray and Horne (303), relaxation was used to study the deformation of pure iron at 77K. They noted that:

- a) The relaxation mechanism was apparently the same as for yielding and creep .
- b) The relaxation rate was highly stress dependent in the micro-yield region but less so above macroyield.
- c) Appreciable stress relaxation only occurs when there are lengths of the dislocations in an unlocked condition. These dislocations can be locked at room temperature, probably by impurity atmospheres, and no appreciable stress relaxation is then observed. They can also be locked at 77K, perhaps by "nascent" point defects, and are only freed after a short time period at high stress.
- d) A species of defect that is mobile at 77K is produced by plastic deformation of iron at that temperature.

Recent work on the thermal activation of pure iron has been given by O'D Hanley et al. (290). They suggested that there are two successive activation barriers: the first the Peierls-Nabarro mechanism and the second the dragging of the kinks produced due to point defects. In more complex systems it is often rather more difficult to ascertain rate controlling steps. By means of stress relaxation testing, Jack and Guin (304) have, for instance, showed that in a Fe-Si-Ti alloy the rate determining step was surprisingly unaffected by the presence of precipitates.

7:5. Previous research on the concepts of the rate controlling processes - with particular relevance to the present work

It has been known for some time that solutes, in the form of dislocation atmospheres, are particularly effective in restricting low temperature creep processes. Woodhead and Quarrel (305) suggested that at low temperatures, alloy strain ageing in steels (e.g. by Mo) is important. Irvine and Pickering (306) noted that N segregation to dislocations is useful (although Allen and Hopkins disagreed (307)) as well as that of C and B. In 316 stainless steel, Alden and Aronsson (308) regarded that C was not as important as N or Mo in controlling dislocation movement, possibly through Cr-N or Cr-Mo interactions. Threadgill and Wilshire (309) regarded creep in an austenitic stainless steel as being controlled by the γ' precipitation, although it should be noted this effect was above room temperature.

In the present work a survey of the segregation to the dislocation substructure in the ferrite of the patented wire was undertaken. In view of the above work it seemed possible that the dramatic changes in the tensile behaviour along with concurrent changes in the relaxation resistance on LTHT may have been due to segregation or precipitation phenomena (i.e. strain ageing): this is discussed in detail in chapter 4. The atom-probe technique proved ideal for this study the results of which are presented in chapter 5. It was found that although there were significant changes in the dislocation distribution on LTHT, the segregation of C and N did not significantly alter. N was, within the limits of detection, found not to segregate to the substructure, whereas the C heavily decorated it. It was also noted that the C segregation was not uniform along the line of the cell walls but patchy, the concentration reaching as high as 25 at.% in some areas. Although the apparent lack of N segregation is surprising (see for example the work of Keh and Wriedt (310)) a consideration of the temperatures achieved in "cold" drawing (at least 140°C), the scale of the structure and the abundance of solute sources (the cementite) can allow the full decoration of the substructure with carbon to be explained (Yamada (36) has dealt with the case of segregation of solute in high carbon steels while Wilson and Russell (311) with low carbon ones). It is useful to remember that even small concentrations of C can affect the relaxation of ferrite. This was shown by Sugai (256) by means of a very low C content material and one with a slightly high concentration. Below approximately 20°C relaxation were present in both materials. Above this, however, in only the higher carbon material, relaxation at the stress levels investigated were not significant.

7:6 Summary of the present work

a) TEM examination of the A/R 4.25mm patented wire showed a very fine pearlitic microstructure with strong alignment of the lamellae along the wire axis. This indicated the considerable ductility in both phases during the wire drawing operation. In this wire, a dislocation cell structure, composed of low angle (typically 5° to 10°) cell walls with low dislocation density interiors, was observed in the ferrite. It was found that the transverse dimension was of the order of several ferrite lamellae widths (e.g. $\approx 200\text{nm}$), the longitudinal length being of a similar order. In favourable circumstances, the dislocation substructure in a cell wall was visible, although the generally high dislocation density (mostly within the walls) made such observations difficult. A dislocation cell substructure was observed in the cementite lamellae on a finer scale (e.g. $\approx 5\text{nm}$), the scale and problems encountered in thinning this phase, not allowing further investigation in the present work. No significant variations in the microstructure (except for a surface decarburized layer) was found across the wire section (see Chapter 3).

b) No significant changes could be found in the TEM examination between the above, A/R, wire and wire which had undergone a LTHT "A" (30 minutes at 200°C). It is considered that this was due to limitations of technique in such a complex material (see Chapter 3).

c) Atom-probe studies of a patented wire, drawn to a greater degree than the wire described in (a) and (b) $\approx 98\%$ at opposed to $\approx 70\%$ reduction, were undertaken. It was found in this case, that in the A/R wire the transverse ferrite cell size was less than the ferrite lamellae width. The typical misorientation across each cell wall was again 5° to 10° . In this condition the cell walls tended to be irregular in outline with indications of a significant defect density within the cell interiors. Using the atom probe, a solute segregation study was made of this material. No evidence of N segregation was observed but strong C segregation was present at the cell walls. The latter was found to be "patchy" in nature varying from 1 at.% to 25 at.% (see Chapter 3) in concentration.

d) The effect of LTHT on the ferrite cell substructure was shown to be significant, using the atom-probe technique. It was found that considerable alignment of the cell walls to the lamellar structure occurred along with a decrease in defect density in the cell interiors. No significant change was found in solute segregation in the microstructure (see Chapter 3).

e) The microstructure of the 17-7PH stainless steel has not, as yet, been examined in detail. The TEM investigation failed to elucidate the largely martensitic microstructure in detail due to the high dislocation density nor did it detect changes on HT, although the mechanical properties were significantly altered (see Chapter 6).

f) The mechanical testing programme was undertaken in two parts, spring

testing and uniaxial testing. Although it was found that the results obtained could not be related in great detail (largely due to the spring design and manufacture), the former series of tests indicated that the LTHT "A" could give a significant improvement in the relaxation properties. They also showed that after an initial period of rapid relaxation (\approx 72 hours for the 4.25mm patented wire) relaxation continued for an indefinite period at a reduced rate (see Chapter 5).

g) The development of a reliable uniaxial testing techniques with allied data reduction facilities allowed accurate testing to be undertaken. This work is considered to have serious implications for previous work in this field (A.I., chapter 4, chapter 5).

h) Uniaxial stress/strain curves for the patented wire in all its conditions (A/R and LTHT) were obtained. In the A/R condition the material had a low proportional limit/UTS (or proof stress/UTS) ratio: yielding occurred in a gradual manner with increase in strain. In the majority of specimens considerable ductility was shown although in some cases it was significantly less, possibly due to a high notch sensitivity and poor quality specimen (see Chapter 5).

i) The stress/strain characteristics of the LTHT wire were noticeably different from the A/R material, the main change being a dramatic increase in the proof stress/UTS ratio. The changes between the various LTHT's were found to be slight (see Chapter 5).

j) The change of the proof stress/UTS ratio on HT in the 17-7PH stainless wire was not as great as in the patented wire, although in both there was a useful increase in the UTS values (see Chapter 6).

k) High resolution, uniaxial, stress relaxation tests on the patented wire showed that all the relaxation observed were not recoverable with time, i.e. was plastic in nature (see Chapter 5).

l) Specimen relaxations only became significant in the patented wire at initial stress levels above the proportional limit. Thus, the effect of the LTHT's were apparently largely allied to their impact on the proportional limit. Initial stresses at which general yielding had occurred showed similar relaxation properties. Thus, in the range of initial stresses over which yielding was occurring, there was the most rapid change in the relaxation properties (see Chapter 5).

m) Significant strain hardening was found to occur between a first and subsequent relaxation which was immediately undertaken from the same initial stress. If, however, room temperature ageing between the two relaxations

was allowed, it was found that recovery would reduce this effect (see Chapter 5).

n) Long term, uniaxial relaxations (up to 7200s) indicated that initial relaxation (up to ≈ 2000 s) was rapid, and was followed by a slower but indefinite relaxation (see Chapter 5).

o) The relaxation behaviour of the 17-7PH stainless wire was essentially similar to that of the patented wire in character. It was found that significant relaxation only occurred at initial stresses above the proportional limit. If general yielding had occurred, the relaxation did not show any further significant increase (see Chapter 6).

p) The important effect of the HT on the 17-7PH steel was to improve the proportional limit, thus increasing the initial stress below which relaxation was negligible (see Chapter 6).

q) It was found, particularly in long-term relaxations, that although the initial relaxation rate of the A/R 17-7PH steel wire was similar or greater than LTHT patented wire at the same initial stress, the rate decreased at a faster rate. Thus for relaxation behaviour at long times (e.g. greater than a few hours) the 17-7PH would show an important improvement in relaxation resistance over the patented wire (see Chapter 6).

r) The high accuracy, tensile testing programme allowed an analysis of dislocation theories concerning stress relaxation. It was found that for all materials, in all tests, the value of the dislocation velocity exponent m^* was negative. This is unacceptable on the basis of the theories available and indicates some of their inadequacies. It was, however, noted that the values of m^* varied systematically as the initial stress was increased through the yielding regime. The effects of LTHT's on the patented wire and HT on the 17-7PH wire were only particularly significant in their effects on the respective yielding behaviours (see Chapters 4,5,6)

s) Values of $|b| A^*$ were obtained by two different methods, which, in general, agreed well. The values obtained for A^* were much greater than those previously obtained for less complex materials (e.g. pure bcc iron). They indicated, for the patented wire, that the area swept out by an activation event was of the order of that of a dislocation sweeping across a cell (the slip distance limited by the cementite lamellae). It has been shown that the value of $|b| A^*$ uniformly decreased with increasing initial stress as the yielding regime proceeded. The effect of the LTHT's on the patented wire was again mainly limited to that of the reduction in range of initial stresses over which this change in behaviour was observed. The values of

$\frac{b}{b_0}$ A* for the 17-7PH stainless wire were found in general to be somewhat greater than those observed in the carbon steel material.

7:7 Conclusions from the present work

- a) The proof stress of patented wire is dependent on the nature of the dislocation cell substructure in the ferrite lamellae. This was found to be greater in transverse size than the lamellae width for a $\approx 70\%$ reduction wire but smaller for a $\approx 98\%$ reduction wire. In considering the rate determining dislocation barrier it is necessary to consider this change in microstructure.
- b) The optimum LTHT for the patented wire investigated was "A", i.e. 200°C for 30 minutes. This gave the best relaxation resistance which could be obtained in this material.
- c) The effect of LTHT is a reduction in the complexity and energy of the dislocation network by means of thermal activation of weakly pinned dislocation links under the influence of micro-residual stresses. Thus, there is a removal of the weakly pinned links which can affect later deformation.
- d) The LTHT does not significantly alter the solute distribution in the ferrite. Previous work suggesting further pinning of the dislocation network by C and N on the LTHT is not true in this case. N segregation is not significant while C segregation to the cell walls is found to be "patchy". The high concentrations of C (up to 25 to %) are at intervals along the walls which may (considering the angular misorientation) be the sites of dislocations which form the boundary.
- e) The relaxation properties of the various forms of patented wire can be related to the stress/strain behaviour. Insignificant relaxation was found below the proportional limit in each case, becoming rapidly more important as the initial stress is increased. It is probable, considering the effect of the LTHT, that this effect is due to the production of weakly pinned dislocation links which can move under the combined effects of residual stresses and applied stress by thermal activation.
- f) The analysis of the relaxation data indicates the rate determining factor is that of movement of dislocations across the cells present: this is not greatly affected by the LTHT's.
- g) The long term relaxation properties of the patented wire are not only affected by a rapid initial relaxation but also by a slower subsequent relaxation. The latter may be due to recovery processes occurring in the material, lowering σ_i .

h) In general similar behaviour was noted for the 17-7PH steel wire to that of the patented wire. It is therefore probable that the basic dislocation interactions causing the plastic strain during relaxation are similar. It has been shown that the relaxation rate does, however, decrease more rapidly possibly indicating a greater resistance to recovery. This may be due to the more severe heat treatment producing a more stable dislocation structure with lower micro-internal stresses or the fine γ' precipitates stabilizing the microstructure or a combination of the two.

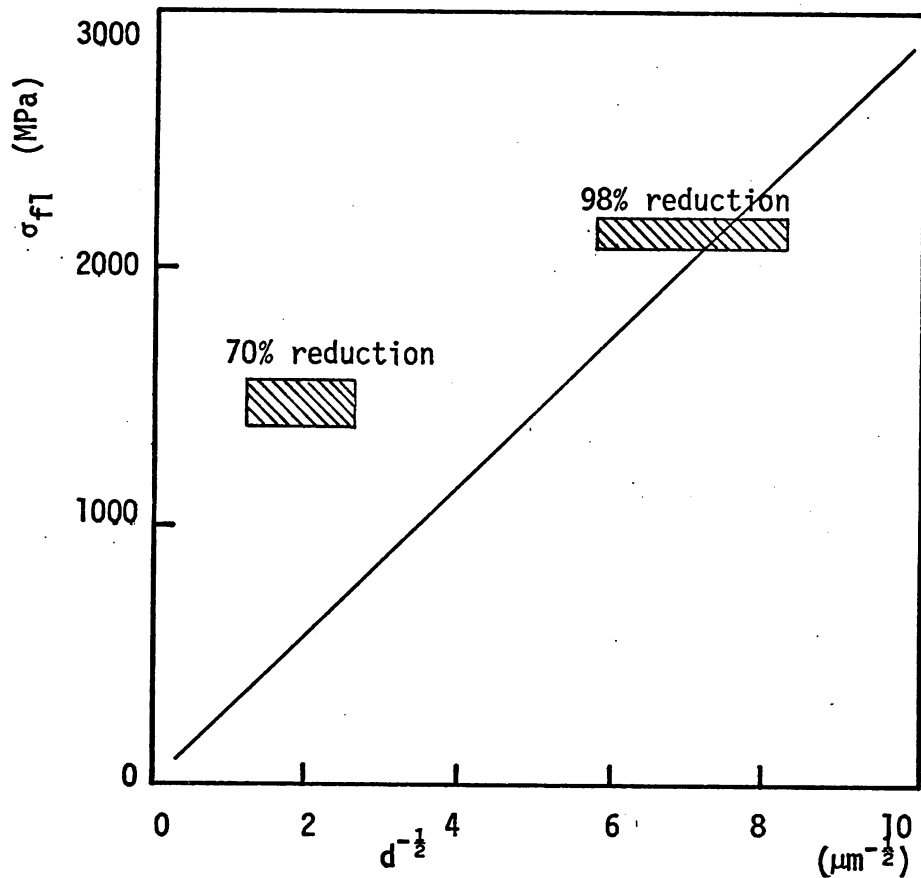


Fig. (7:1) Correspondence of transverse cell sizes of patented wire found in this work with those given by Embury, Keh and Fisher (66).

- N.B. a) Flow stress values for the two A/R materials investigated in the present work are taken as twice the standard error of the 0.2% proof stress ranges obtained.
 b) The error bars for the T/S cell sizes are twice the standard error values for each material.

8. Further Work

8:1 Introduction

By the nature of the present wide ranging investigation, considerable further work can be immediately suggested in the practical field. It will be clear from comments already made, that extensive further effort is also required in developing adequate analytical theories for this, and allied, work. This work can only, however, flourish on the basis of accurate and reliable data, the type which the present work has allowed possible.

8:2 Microstructural work

- a) The use of low temperature (He cooled) atom-probe work to investigate in more detail the dislocation substructure in the ferrite lamellae of patented wire in wide selection of heat treatments, and by similar means investigate the relationship of the substructure to the cementite lamellae.
- b) The same atom-probe can be employed at low temperature to investigate, in further detail solute segregation in the above materials.
- c) Atom-probe techniques can be used, initially with N cooling, and later at low temperatures to investigate the detailed microstructure of 17-7PH stainless wire. As in the case of the patented wire the dislocation substructure could be studied and also, using the analytical facility, the precipitation sequence on HT (485°C for 75 minutes) could be studied on an extremely fine scale. An extended HT could be used to accentuate the phenomena involved (remembering that the precipitates might alter in character).
- d) Using a heating stage the effects of LTHT on patented wire and HT on the stainless steel might be investigated in situ in TEM. This might help to elucidate the apparently subtle changes which occur, particularly in the former. (Caution would have to be used to gauge the influences of foil surface effects.)
- e) The use of atom-probe techniques could be employed to investigate the changes in ferrite dislocation substructure with wire drawing reduction. (Specimens would have to be carefully cut from the wire with standard methods.)
- f) Similar techniques could be used to investigate the changes in substructure in the ferrite (and possibly in solute segregation) at LTHT's other than have been used in the present work, e.g. at 200°C for times less than 30 minutes.

8:3 Mechanical Testing

- a) A spring testing programme of improved design could give better information than the present work into the relationship between relaxation in this complex mode and that in uniaxial tension.
- b) Uniaxial, tensile relaxation tests should be carried out in far more detail with the 17-7PH stainless steel in both A/R and HT conditions at room temperature.
- c) Tensile, relaxation tests should be carried out on the patented wire described in 8:2(f).
- d) A wide ranging, systematic programme of tensile, relaxation tests ought to be carried out on both patented wire and 17-7PH stainless steel in A/R and LTHHT or HT conditions at temperatures above room temperature. For this purpose it would be necessary to construct more suitable grips with a heating facility, and possibly the acquisition of a suitable wire extensometer.
- e) The investigation of the materials studied for their relaxation properties to elucidate the residual stresses present in the wire. In the case of the long wire specimens, the longitudinal stresses would be of greatest importance. The macro-residual stresses could possibly be studied by means of a successive etching technique using a dilatometer, with normal specimen heating facilities. Micro-residual stresses could best be studied by an extensive Bauschinger test programme, possibly using grips required for 8:3(d).
- f) The designing and building of an apparatus to investigate the stress/strain and relaxation properties of the previously described wires in torsion. It might be possible to adapt the facilities of the 100 kN Mand, previously developed, to carry this out. Specimens suitable for 8:3(f) (the Bauschinger tests) could be adapted for this purpose. This investigation would greatly help the comparison between the tensile data and the spring data, although as has been previously explained, detailed analysis of the torsion deformation mode is not simple.
- g) The study of other spring materials might give further insight into relaxation deformation processes e.g. additions such as B could be made to the basic patented wire to attempt more effective pinning of the dislocation substructure. The possible use of an alloy carbide dispersion in the pearlitic ferrite may also be of interest, although it is possible that the material is unlikely to draw.
- h) While the present testing equipment is adequate for much of the proposed work, it must be again repeated that the acquisition of a digital,

data logging system would be of considerable value in a number of previously described ways.

i) A valuable study of the detailed dislocation substructure in the ferrite could be made in the spring materials by means of modern microdiffraction techniques. Such analysis may well also prove useful in the elucidation of the deformation processes which occur in the wire drawing of pearlite.

8:4 Theoretical Work

It is clear that the theoretical work on which much relaxation data has been analysed is not too soundly based. Such concepts of the constancy of ρ_m , σ_i and the applicability of various basic flow equations, is in question and considerable further work is required. It seems likely that the simplicity of much of the dislocation theory may be a considerable handicap, and it appears profitable at the present time to develop the statistical theories described in Chapter 7. It is also clear that it is just as important to employ high quality testing techniques in such investigations, again not necessarily relying on dubious assumptions which are extremely difficult to substantiate.

A.I. Appendix 1: Experimental Techniques

A.I:1. Mechanical Testing

A.I:1.1 High Resolution Testing

A.I:1.1.1. Introduction

The initial objective in the high resolution mechanical testing programme was to develop techniques to give useful and accurate relaxation data in tension on material supplied in the form of wire of 4.0 mm to 4.25 mm diameter. The majority of previous work on stress relaxation has been carried out in this deformation mode, the most obvious reason being, that the more common types of mechanical tests are accomplished in this manner and testing equipment is therefore readily available. It was found necessary to devote considerable care to the design of the grips, and also to the choice and development of the testing equipment.

A.I:1.1.2. Design of the tensile specimens

The general design of the tensile specimen employed is given in fig. (A.I:1). This non-standard specimen was chosen for several reasons. It was found that the as-received wire was too hard for normal machining (the Vickers hardness for 50 kg load was found to be 528 ± 10 for the patented wire and 460 ± 10 for the as-received 17/7 PH stainless steel wire). Alternative machining techniques were investigated including electrochemical machining (which would not have introduced further internal stresses but would have required considerable development). The most acceptable technique was found to be grinding. It was originally carried out on a Universal grinding machine, but it was found advantageous to introduce centreless grinding for later specimens. This technique necessitated the adoption of a simple cross-section and this precluded the use of a threaded grip attachment. The section includes a 30° taper to the gauge length to give an acceptable contact area with the grips. This reduced the possibility of deformation of the specimen outside the well-defined gauge length, while giving secure positioning of the specimen in the grips.

Considerable problems were at first encountered in the grinding operations due to the wire being received in coiled form. This wire was straightened, as far as possible, by hand, prior to grinding. During machining, however, as material under stress was removed, the wire tended to bow, causing barrel shaped and tapered gauge lengths. Although some improvement could be gained by hand polishing, the maximum gauge length was limited to 30 mm. It was felt advantageous to increase this in order

to reduce testing errors due to inaccuracies in the machine actuator control. This was achieved by first having the wire straightened (by a spinneret) and by the adoption of centreless grinding. By such means it was possible to increase the gauge length to 9 cm for the final series of patented wire specimens. All 17/7 PH stainless specimens were of this gauge length. Mechanical machining techniques introduce surface residual stresses, and it was decided to machine the specimens 100 μ m oversize in all dimensions and then remove the surface stressed layer by the use of a chemical polish for the patented wire and by means of an electrochemical polish for the stainless steel, details of which are given below.

Chemical polish

10% distilled water

85% H_2O_2

5% HF (40% by wt.)

The HF was added to the other components. Frequent renewal of the solution was required to obtain a good finish and considerable care was taken to avoid overheating.

Electrochemical polish

10% Perchloric acid operated at ~5V

20% glycerol

70% ethanol at room temperature

To ensure consistent polishing, the stainless steel specimens were suspended in a beaker equidistant from a cylindrical stainless steel cathode. The solution was stirred vigorously and care was taken to avoid overheating.

After polishing, heat treatments were given if required by means of a fluidized bed with temperature held constant to $\pm 5^\circ\text{C}$.

The mean gauge diameter of each specimen was obtained from 3 pairs of micrometer values taken at right angles, the gauge length was recorded with vernier calipers.

A.I:1.1.3. Design of the inner grips

The inner grip design is given in fig. (A.I:2). The split inserts were machined from NSOH steel to give a heat treated Vickers hardness of 720. These inserts were designed to fit tightly into 2 selected sets of Hounsfield grips, an initial design requirement being the simple attachment

to existing tensile testing equipment. The backing set screw was included to reduce possibility of the specimen slipping back into the taper during a load reduction (e.g. during relaxation). From the evidence of load/extension curves taken with and without these setscrews, such slippage appears to be apparent only below 0.5 kN under optimum test conditions. Thus to ensure validity, all tests were conducted with tight set screws and timed loading commenced from 0.5 kN.

All machining of grips was accurate to better than 25 μm .

A.I:1.1.4. Design of the outer grips

The choice of outer grips was determined by the testing machine used. For use with the Instron TT-C machines, outer grips were already in existence. Mand servohydraulic machines required the manufacture of their own outer grips due to variation in attachment, not only between machines, but also between the upper and lower fixing points on 2 of the 3 machines available. The design of the outer grips for the 100 kN Mand is given in fig. (A.I:3), again manufactured to an accuracy of 25 μm or better. After due consideration of the stresses involved, and expected operating environments, mild steel was accepted as adequate for these components.

A.I:1.1.5. Evaluation of tensile machines for high resolution stress relaxation testing

Extensive comments have already been made (CPGS 1) concerning the choice of testing machine for this type of mechanical test. It is on the basis of these that the following points are made.

Although used for earlier work, e.g. (Feltham 156), the Hounsfield Tensometer was considered inadequate for the tests to be undertaken (CPGS 1). In addition to incompatibility with the designed grips, the problems of flexing in the apparatus along with the inadequate data recording system, make their use impossible.

Floor model Instron TT-C, screw driven machines were available and have been extensively used for normal tensile testing. Noting comments (e.g. Solomon 239) on the use of such machines for stress relaxation tests, acceptance trials were carried out on a short frame machine. These were achieved by initially relaxing a 3 cm patented wire specimen from a set load, and repeating with a "hard" (i.e. a fully elastic) 2.5 cm diameter, mild steel test piece from the same initial load and with the same loading time. The result is given in figure (A.I:4). As can be seen the difference in relaxation is small, and it was considered that it would be unreliable to remove the machine relaxation component by such a calibration

process, although this is a method which has been adopted by some other workers (see Ch.4). In addition doubts have been expressed on the consistency of this type of machines relaxation (see Ch.4.3.10).

As closed-loop, servo-hydraulic Mand testing machines were available, it was decided to utilize these, as has been advocated by other workers (e.g. Solomon 239). Tests were undertaken to ascertain the machine most suited to the present testing requirements. The advantages of such a system have been described (Ch.4:3), the most important factors being the inherent hardness of the frame, the rapid and accurate position response and the ease of the use of strain control, to help eliminate machine effects.

The 250 kN Mand proved unreliable, and was apparently incapable of controlling the position channel under relatively low loads, e.g. 10 kN. The 50 kN Mand was specifically designed as a high frequency (e.g. >100 Hz) testing machine, employing 2 Moog valves in the hydraulic control. For this reason it was unsuited to very low frequency work, such as monotonic relaxation. The third Mand available was a 100 kN, 4-post machine, and further development was undertaken after initial tests had shown that sufficient accuracy and reproducibility could be obtained.

A.I:1.1.6. Description and use of 100 kN, 4-post Mand, with specific reference to tensile stress relaxation tests

A.I:1.1.6.1. General description of a closed-loop, servo-hydraulic testing machine

A schematic representation of the operation of such a machine is given in fig.(A.I:5). There is an essential choice between operating in position, strain or load control at one time, although it may be possible to change the control mode during a test. The closed-loop mechanism refers to the actuator position being controlled in response to an error signal being detected between a set voltage, on the control channel, and the output of a sensing device which refers to that control, e.g. the load cell for load control. The error is corrected, at a rate, which is dependent on the loop gain and damping factors which are chosen prior to testing, by means of an appropriate actuator movement.

A.I:1.1.6.2. Mand 100 kN machine

A.I:1.1.6.2.1. General comments

The general layout of this machine is given in fig (A.I:6). The crosshead can be raised or lowered to accommodate various testing rigs by means of untorquing the 10 clamping bolts and using hydraulic rams, controlled by 2 valves on the machine's base. It is important to note, that when either valve has been shut, the crosshead tends to settle by a

significant amount, and also it is essential to clamp both sets of bolts together, otherwise the crosshead and actuator tends to skew, causing gross misalignment.

In addition to the main testing frame, the Mand consists of a hydraulic power-pack (water and air-cooled) and a control console. The console includes: 2 digital-voltmeters (DVMs) for load, position or strain display; control modules for each servo-amplifier channel (to allow switching between channels during a test); a ramp generator to vary the set-point voltage on the chosen control channel; a function generator and a number of error detectors and interlocks. Recording devices fitted are a Bryans 29000 Y-Xt recorder and a Bryans 28000 XX-t recorder: other recorders can be used via the 3 output modules fitted. Detailed procedures which were found necessary in addition to normal operating practice are described in a later section.

A.T:1.1.6.2.2. Modifications and improvements introduced to Mand
100 kN machine

- a) Although care was taken to set the crosshead horizontal, it was found that the actuator was permanently misaligned. The design of the grips did not allow for such an error and the actuator housing was re-machined.
- b) The ram surface was found to be scored; it was removed and re-chromium plated. This helped to ensure the friction between ram and seals was as small as possible to give best position resolution.
- c) A low flow-rate, high resolution Moog valve was fitted to improve the position resolution.
- d) A pair of grade A1, ± 5 mm range linear voltage displacement transducers (LVDT's), matched with a transducer amplifier was used. This enabled the actuator position to be controlled by the strain across the specimen, reducing machine and grip effects. The electrical noise level was also reduced as the position transducer has a ± 50 mm range.
- e) It was calculated that only a low load range (less than 10 kN) would be required for relaxation tests. A 10 kN, mechanically guarded load cell was acquired, again decreasing the inherent electrical noise to an acceptable level.
- f) A thorough check of all electrical modules was undertaken; in particular, noisy potentiometers (e.g. on module set-points) were replaced and amplifier circuits checked to ensure no drift in set-point valves.
- g) After a series of trials, it was decided to use, for most purposes, the Y-Xt recorder fitted to the machine, which was provided with a fly-back

facility. It was found that this recorder had a sufficiently rapid response, while allowing relatively simple operation combined with flexibility. For some long-term tests (up to 6 hours) a XX-t recorder was employed, but it was found that it was not manually possible to operate both simultaneously during a relaxation test.

It would have been a considerable advantage to have a digital data-logging facility available. This has been used to considerable effect by some workers (e.g. Solomon 239) as it allows very rapid data collection over a wide range of both load and time variables with high resolution and in addition considerably simplifies data analysis via an interface with a processing facility.

It was felt necessary to undertake these changes and improvements with some care to ensure that sufficient resolution was obtained. A series of acceptance tests was carried out to give a survey of the machine performance. With the 100 kN Mand under ± 5 mm strain control with optimal control settings (see later) and the actuator position held constant, the performance is summarised below.

- a) Typical strain variation across the outer grips was $\pm 0.2 \mu\text{m}$. (This strain gave a calculated load variation with a 90 mm wire specimen of $\pm 2.9\text{N}$ (using a value for $E = 21.19 \times 10^{10} \text{ Nm}^{-2}$). In practice a variation of $\pm 2.5\text{N}$ was observed under optimum conditions, indicating that the strain across the specimen is the same as that shown across the outer grips). This load error represents a $\pm 0.1\%$ error in a total load of 6 kN or a $\pm 2\%$ error in a 150N relaxation.
- b) The load cell was accurate to better than 0.1% over its entire range (better than grade A1) when tested with a NPL proving ring.
- c) Relaxation of the load cell (presumably due to relaxation of the epoxy bonding of the strain gauges) was found to be significant during the period of specimen relaxation. The cell relaxation was measured by loading an elastic test piece (a 2.5 cm diameter mild steel bar) to a set load in a chosen time. These relaxations were found to be reproducible (Ch.4) and a simple numerical correction was therefore valid for the wire relaxation tests.
- d) The transducers were grade A1 (better than $\pm 0.1\%$) and proved to be accurate to 0.05% in the range ± 2 mm. For this reason tests were conducted within this strain range.
- e) Consistency tests were undertaken as described before (Ch.4) by means of relaxing a series of 30 mm gauge length patented wire specimens from

the same stress. The variation in relaxation behaviour of $\pm 4\%$ indicated not only the adequacy of the testing procedure, but also the preparation of the test specimens.

f) With optimum operating procedures, the actuator drift under strain control was found to be less than $0.05 \mu\text{m/hr}$ over a 5 hour test. This corresponds to a drift using a 90 mm patented wire specimen, of 0.7 N/hr which is less than the random electrical noise level inherent in the load output.

A.I:1.1.6.2.3. Procedure for tensile relaxation tests

A. Initial setting up of test rig

The crosshead was initially raised sufficiently to allow easy access to the attachment threads. The lower attachment apparatus was manufactured specifically to allow for fine alignment of the loading position. It was, initially, lightly attached to the machine base by 6 set screws. The load cell was screwed onto the upper attachment point, seating onto spacing rings and a pair of spiral wedges (fig. (A.I:7)). The outer grip (No.128) was secured to the load cell via 2" BSF studding, again seating on spacing rings and a set of spiral wedges. The second outer grip (No. 62) was attached to the lower fixing thread via a spacing ring and spiral wedges which had been turned down to allow access to the set screws while in position. The crosshead was lowered and clamped in such a position that when the actuator was run to the highest point of its travel, a wire specimen, complete with inner grips could be inserted; lowering the actuator would then force the lower inner grip into its respective outer grip and the 5/16" pins could be inserted.

Having clamped the crosshead, the two outer grips were accurately aligned, by moving the lower, to ensure that no turning moment was applied to the test specimen. The lower attachment was clamped down by means of the set screws. A 1" diameter, hard test piece was inserted and pinned in the upper outer grip with the actuator at its highest point. Control of the actuator under position control was best obtained on the $\pm 5 \text{ mm}$ range using the minor range control for rough positioning while the set point control on the servo amplifier was used for fine control. By these means the test piece was positioned, pinned and loaded to 8 kN in tension (i.e. above any load the system would be subjected to during testing). By means of "C-spanners" the spiral wedges were tightened and the specimen unloaded and removed. Thus it was ensured that the contact surfaces in the loading train remained fully in compression during testing, eliminating a possible source of error.

B. Safety interlocks and their use

The 100 kN Mand is provided with a series of interlocks which have to be checked before hydraulic pressure can be obtained. In addition there are provided a number of trips which may operate during use, causing a loss of hydraulic pressure. It was found essential to avoid such trips during a test as the actuator tended to move a significant distance (typically 20 mm) at such times, and thus a large force could be exerted on specimens and transducers.

A trip was provided on the cycle counter; this was generally not used, the control being set to "hold". Using this, the cycling control could be stopped after a sufficient time during a warm-up period. Both compression and tension trips are provided on the load trip module. These can be set to any percentage of the full range: for relaxation tests these were set to 100% tension and 40% compression.

Servohydraulic testing machines are inherently more dangerous than their screw driven counterparts. This is because the rapid position response of the machine over a large distance of the actuator travel. An attempt has been made to combat this problem by the inclusion of an error detector module. This error refers to the difference between the set-point and the control output voltage. Whenever the Mand was testing, the error detector was set to a low value (e.g. 0.25V) on trip. However, it was necessary to switch this to hold when the actuator was moved manually due to noise on the potentiometers. Other power supply transients could trigger this error detector at such a low setting: these were internal in origin and mains transients were not significant in these tests. Internal transients could be produced by either switching on or off the Wavetek function generator or either of the chart recorders or by switching either of the DVM selectors from load input to either strain or auxiliary.

It was found essential to protect the 240V mains supply to the console (if interruption was expected, testing was suspended) as power failure caused all control of the hydraulic supply to be lost.

C. Procedure for setting up relaxation tests

i) To eliminate drift in the electronics at least a 4 hour warm-up period was required. This process was aided by the use of a 24-hour time switch on the 240V mains supply. The hydraulic system was found to require only a 1 hour warm-up to remove the majority of thermal drift. The remainder of the drift could have been eliminated by the use of the integrator on the servovalve driver module, however, it was found that this caused a significant actuator position transient if the actuator motion was required

to stop rapidly. By allowing the hydraulics to run for a further 2 hours, it was found that actuator drift could be reduced to less than 0.25 μm in a 5 hour test. The hydraulic warm-up period was accomplished using a sine wave output from the Wavetek under ± 50 mm position control, all trips being in operation when running.

ii) Optimum control settings were obtained by means of extensive testing with both 30 mm wire specimens and elastic, 1" test specimen (to amplify errors). The results of this programme are summarised below:

a) DVM's

I/P	Left strain (range $\pm 5\text{mm}$)	Right load (range ± 10 kN)
strain zero } suppressor }	0	0
Mode	Normal	Normal

b) Position Transducer Amplifier

Range ± 5 mm

(Thus the minor range potentiometer gave a $\pm 50\text{mm}$ actuator range)

c) Extensometer Amplifier

Set up as detailed below

d) Load Cell Amplifier

Range ± 10 kN

Zero (see later)

e) Load trips

Tension	100%	Trip
Compression	40%	Trip

f) Servo Amplifiers

Modules were in the rack under the position transducer amplifier and the extensometer amplifier. Each module's loop gain was set to 9.8×10 (i.e. to give a rapid response) and testing was performed with the cyclic amplitude potentiometers at zero. (The input voltage from the Wavetek was varied by means of these potentiometers). The control channel required was selected by activating (the control being then illuminated) either module.

g) Servo driver module

Damping 0 (for rapid position response)

Dither 2 (to stop the actuator "sticking" while the position was being held constant)

Integrator off

h) Ramp generator

Ramp level initially set to a low level (e.g. 1).

Ramp rate to choice with the filter set to the same or greater (to give a rapid response on stopping the generator) value.

i) Function generator,

a.c. - off

j) Cycle counter,

off

k) Error detector,

set to 0.25v, operated on trip when testing or when specimen or transducers were being manually positioned

l) Oscilloscope

used to monitor the strain and load (a.c. inputs) on maximum Y sensitivity.

m) Recorders

only the Y - Xt recorder was generally used due to operational difficulties, for relaxation tests the scales were

10mV/cm	}	for load recording
or 25mV/cm		
1mV/cm		for strain, or position recording
2s/cm		for short relaxations
50s/cm		for long relaxations

The Y channel was always used on the calibrated setting and the electronic filters were not used when the load or strain was rapidly varying, e.g. when the actuator was stopped during a relaxation test.

iii) After the machine was fully warmed-up, a 2.5 cm diameter, elastic, mild steel test piece was inserted as before, to load the test rig to 6 kN (i.e. above any test load) for 30 minutes: this effectively removed any prior mechanical history. On unloading, the rig was left for 15 minutes to allow the load cell to relax back to a stable state. The load cell amplifier (i.e. the load reading on the right DVM) was zeroed. This was taken to be the standard machine state from which all tests were initiated.

iv) Machine relaxation data was mainly obtained by using the same elastic test piece and loading by means of various ramp rates to selected final loads. As it had been decided to load all tests for 180 seconds (Ch.4) the same procedure was adopted for the calibration relaxations. Thus, a large number of machine relaxation curves were obtained at various loads from 0.5 kN to 6 kN. This data enabled graphs of relaxation with time for

a range of initial loads, and graphs of relaxation (load loss) against initial load at various times after the actuator had been stopped, to be constructed. The latter has been shown to exhibit a linear behaviour of adequate accuracy up to within 0.5 kN of the preload level (fig.A.I:8). Thus for any wire relaxation obtained, the machine component could be removed by a simple numerical process.

v) Wire tensile specimens were loaded in the inserts in the inner grips (fig.A.I:9) and a Hounsfield ring was used to hold one of the inner grips together. The other was held in a clamp (fig. A.I:10) designed to allow its removal once the assembly was in place in the loading train. The set screws could then be tightened behind the specimen ends without gross wedging of the grips. The Hounsfield ring was removed and the inner grip inserted into the appropriate outer grip and pinned. The actuator was lowered to force the second inner grip home, gradually withdrawing the clamp, which was removed after pinning. The transducers were positioned in the upper clamps ensuring that this did not impair their smooth action. With the extensometer amplifier on transducer A, the appropriate steel rod clamped to the lower outer grip (the rod being fitted with a glass cover slip for the transducer to bear onto, to reduce contact friction) was positioned so that the A strain output (shown on left hand DVM) indicated approximately $-.15 \text{ mm}$, thus ensuring the transducer would be used in the centre of its range. This process was repeated with transducer B. The extensometer amplifier was set to $\frac{A+B}{2}$ to reduce possible errors. (N.B. The zero adjustment was set to approximately 5) (fig.A.I:11).

Using the set point on the strain channel, the error signal was zeroed and the control mode was changed to strain control (pressing activate). The specimen could then be loaded in a controlled manner either by use of the strain set point, or by the ramp generator control.

vi) Load/extension curves were plotted generally using a 0.6V/min ramp rate (equivalent to $\dot{\epsilon} = 0.0001 \text{ s}^{-1}$). Outputs of strain and load were taken from two of the output modules to the Y - Xt recorder, zeroing being affected by use of the zero offset potentiometers.

vii) Examples of the loading curves for both 90 mm patented wire specimens and the elastic test piece for various ramp rates, loaded for 180s are given in fig. (A.I:12).

viii) With the specimen at zero load, the zero offset fitted to the load

cell amplifier was used to zero the indicated load (shown on the right hand DVM): the calibration of the load cell was checked, a load value of 6.51 (N.B. The load cell trips were not required to be set to warn), and the zero was rechecked.

ix) In the case of the wire relaxation tests, the specimens were manually loaded (with the set-point) to 0.5 kN, as all significant non-linear behaviour appeared below this level. The specimen was loaded at the chosen ramp rate for 180s. The increase in the load was followed on the right hand DVM and also by manually adjusting the zero offset on the load output module to keep the chart recorder pen on scale. In this period the chart recorded input load filter was set to off. A few second before loading was to stop the chart recorder pen was engaged at a suitable point on the Y scale to enable the whole of the relaxation to be recorded. (In all but the largest relaxations a load scale of 10mV/cm, i.e. 10N/cm, was adequate.). After 180s the actuator was stopped and the relaxation recorded. Normally 5 sequential traces were recorded (corresponding to approximately the first 350s of relaxation) utilizing the recorder's automatic fly-back facility.

After this period, a second relaxation curve from the same initial load was obtained by reloading with the ramp generator and repeating the above procedure. An absolute measure of the load was conveniently made on one of these traces with reference to the load DVM. The specimen was unloaded using the set point or ramp generator to zero load. The control was returned to the position channel and the transducers and pins could be removed. The specimen was removed using the minor range position control to raise the actuator. Between the testing of each specimen, the load cell was allowed to relax back to its standard state condition, i.e. with zero indicated load.

x) While the cell was returning to its standard state, the ramp generator set point was re-set to a low value and the ramp rate was set to the value required by the following test. The accuracy of the rate multiplier proved to be rather poor, and also, when varied between X1 and X2.5, it had the effect of moving the actuator a significant amount.

xi) The Mand testing machine was operated in an air-conditioned room thus reducing temperature variations to a minimum. Screening around the test rig was also employed. All relaxation tests were performed at $22^{\circ}\text{C} \pm 2^{\circ}\text{C}$. The typical variation in specimen temperature during a typical 5 hour test using the above precautions was found by means of a spot welded Cr/Al thermocouple

on the gauge length. The maximum change measured was $\pm 0.25^{\circ}\text{C}$, which would give a load change, with a wire specimen, of ± 5 N.

xii) The gauge diameter of each specimen was measured before each test and while at the test stress. Thus the nominal and true (up to instability) stresses could be measured.

A.I:1.2 Lower resolution testing (spring testing)

A.I:1.2.1 Introduction

The spring tests were designed to fulfill a number of experimental functions. In the present series of high resolution tests it was not possible to perform relaxations at above room temperature. It was considered advantageous to generate data, although of lower resolution, in this regime since in the service application under investigation it is probable that such springs reach 100°C for some time. It was also considered necessary to relate the relaxation data produced in the tensile mode (a relatively simple deformation) to that caused by the deformation of a spring.

A.I:1.2.2 Experimental details

Spring relaxations were carried out using 4.25 mm 1408M2 Patented wire supplied by Bridon Wire Ltd. in coil form. This wire was coiled into straight, helical compression springs by Entex Ltd. with the following design parameters:

Mean wire diameter	(d_w)	4.25±0.05 mm
Mean spring diameter	(R_s)	40.0±0.5 mm
Number of active coils	(n_c)	9.0
Total number of coils	(n'_c)	11.1
Solid length	(l_c)	45.0±1.0 mm
Free length after grinding		100.0±1.0 mm
Solid stress		420±5 MPa

To allow the above springs to undergo relaxation, they were loaded on 0.5 m lengths of 18/8 stainless, 3/4" UNC studding. This allowed 3 springs to be loaded to 3 lengths (i.e. 3 stresses) on each length of studding. Each spring's free length was measured before loading (coding on the loading nuts allowing identification) as variations proved significant in the calculations for tests at 100°C, such relaxations being small (<20N). Sorting of the springs by free length aided experimentation and it was found the use of Mo₂S lubricant significantly improved the reproductibility of data when used between the ground spring ends and the stainless steel washers.

The testing programme was designed to investigate relaxations from 3 spring loads for both as received and LTHT (200°C for 30 minutes) specimens over a period of 10 days. The lengths of studding with springs were held at one of the 4 test temperatures (100°C, 150°C, 200°C or 250°C) in an air oven, with circulating fan, accurate to ±1°C over the test period. After

holding at temperature, the sets of studding were quenched and the springs removed.

The spring characteristics of both as coiled springs in the A/R and LTHT states and springs after testing were investigated by loading in machined cups (fig. A.I:13) in the Mand, an actuator loading rate of 0.5 mms^{-1} being employed. By this means each spring was loaded to the length at which it underwent testing. From the load/extension graphs of the tested and untested springs, the relaxation during the test was evaluated.

The effects of the changes in stress due to thermal expansion of the stainless steel studding and the spring are regarded as being insignificant in this type of test (151). Consequently no corrections were applied in the above tests.

A.I:2 Structural Investigations

A.I:2.1 Transmission Electron Microscopy (TEM)

Specimens of both patented steel wire and 17/7 PH stainless steel wire were examined by TEM. The patented steel was received in coil form from Bridon Wire Ltd. as 4.25 mm or 4.0 mm diameter bright drawn wire. The 17/7 PH stainless steel was obtained from Wasa (Garphytte) Ltd. as 4.0 mm diameter wire. By use of a water/oil lubricated, SiC cutter, 0.25 mm sections of these wires were prepared in both transverse and longitudinal sections. In the latter case it was found necessary to initially cut short (10 mm) lengths of the wire otherwise longitudinal slitting caused the sections to break out of the epoxy mount.

3 mm diameter discs were obtained from the cut sections by spark machining. To allow this, the sections were attached to a brass plate with a conducting glue (Durofix and graphite). It was found that if care was taken the 3 mm discs remained attached to the plate. These were subsequently removed by soaking in acetone. This preparation route ensured that the material was not subjected to significant thermal or mechanical processes. The 3 mm discs were thinned by grinding on 600 grade, water lubricated, SiC paper using a holder. This was essential to reduce the "magnetic-mass" of the final thin foil and also to enhance the possibility of a good foil profile being obtained. The discs (ground to approximately 50 μm) were electrochemically thinned to perforation in a Fischione twin-jet polisher which was provided with an up-graded fibre-optics and photo-diode perforation detection system. A number of polishing solutions were used with varying success rates; generally the best solution was "B" (see later) for both the patented and 17/7 PH steel wires. Further details on electrolytic polishing solutions have been given by Thompson-Russell and Edington (280) and Goodhew (281). The optimum polishing conditions

were found to vary with solution batch, solution age and many other, not always well defined, variables. It was found that optimum conditions could best be found by polishing an un-ground disc, removing the foil frequently and observing the surface in reflected light. The polishing potential was adjusted such that etching (first noticed in the centre of the foil) was just avoided.

Polish "A"

5% Perchloric Acid

95% 2-butoxyethanol

This solution was only used for the patented wire. Although it appeared to polish the ferrite and cementite phases at similar rates, little thin area was produced probably due to the rapidly varying internal stresses.

Optimum conditions: 75V at -10°C
10V on pump motor

Polish "B"

10% Perchloric Acid

20% Glycerol

70% Ethanol

This solution tended to polish the ferrite faster than the cementite, leaving the latter in relief on the surface. It did, however, produce more extensive thin areas on foils than polish "A". If a slower polish was required the amount of perchloric acid was reduced, balancing with an increase in the glycerol content (the polishing potential was then increased). This polish was also used for the 17/7 PH stainless steel wire.

Optimum conditions: For patented wire 20V at 20°C
For stainless steel 40V at -5°C
both with 8.5V on the pump motor.

Polish "C"

100 g anhydrous sodium chromate
in 500 ml glacial acetic acid

The solution appeared to polish both the ferrite and cementite phases in the patented wire at the same rate but did not give sufficient thin area for examination. The reason for this was that the solution rapidly became opaque and perforation could not be detected.

Optimum conditions: 100V at 40°C
4.2V on pump motor

Polish "D"

250 ml glacial acetic acid

14 ml water

50 g chromic oxide

Similar problems to those found for solution "C" were encountered. The water content appears to be critical so the hygroscopic nature renders this solution unstable.

Polish "E"

Orthophosphoric acid saturated with chromic oxide

Similar problems to those of solution "D" were encountered.

As soon as perforation was indicated the foil was removed, thoroughly washed in clean methanol, dried and stored in a vacuum desiccator. Despite these precautions the usable life of the carbon steel foils was of the order of a few hours; the stainless steel foils remained in good condition for considerably longer.

The technique of ion-beam thinning was also employed in attempts to improve foil quality. Both thinning from the 50 μm thick discs and back-thinning foils perforated by electropolishing was used for this. Ionized argon gas was used as the thinning agent at a 6kV potential, directed at both sides of the disc, which was rotated and inclined at approximately 60° to the gas beam. It has been reported (Goodhew 281) that this technique is not subject to composition or internal stress variations of the disc. When it was employed on patented wire, however, little thin area was produced.

All foils were examined using either Philips EM 300, EM 301 or EM 400 machines using either standard double or single tilt stages.

A.I:2.2 Field-Ion Microscopy (FIM) and Atom-Probe Analysis

A.I:2.2.1 Introduction

An outline of the development of field-ion microscopes and atom probes has been given (Ch. 2), further details can be obtained from the references given. The 2 FIM/Atom-probes used in this investigation are described in detail in the literature (282,283), a broad outline of each is given below along with the experimental techniques employed.

A.I:2.2.2 Time-of-flight atom-probe

Müller (284,285) first combined a FIM with a time-of-flight, mass spectrometer (known as an atom-probe) to distinguish between chemical species on a FIM tip. The apparatus used in the present work is shown schematically in fig. (A.I:14). The fine wire specimen (0.5 mm in diameter) is spot welded to a nickel tube and a suitably profiled tip (see later) is polished. The tip is mounted on a manipulator in the specimen chamber, entry to which is by means of a pre-pumped specimen exchanger. The position of the specimen can be adjusted to vary the magnification and to examine various portions of the tip. The image is

formed, after intensification, on a phosphor screen if a suitable image gas is present. Holes in the centre of the channel plate, phosphor screen and inclined mirror allow evaporated ions (produced by pulsing the specimen potential) from an area of interest to pass down a flight tube to strike a detector of single-ion sensitivity. If the time of flight is known, along with the ion energy and flight path length, the mass to charge ratio of any ion can be calculated. Normally the pulse height is of the order of 2 to 5 kV (i.e. in addition to the d.c. "image-voltage" imposed on the specimen). It is estimated by Waugh (283) that the mass resolution of this machine is of the order of $\pm 1/3$ at $m_i/n_i=60$ (where m_i is the ion mass, n_i the ion charge). To avoid specimen contamination the apparatus is constructed to ultra-high vacuum standards in stainless steel with ion-pump, titanium sublimation pump and mercury diffusion pump. Before use the microscope is baked at 500K to desorb gas from the system. Specimen cooling is via a jacketed cryostat and copper braid to allow liquid nitrogen, liquid nitrogen under reduced pressure or helium cooling. Measurement of flight times can be displayed on a fast scanning, storage oscilloscope. A more accurate method is to use a high frequency timer with the flight times stored on punched tape. This tape, along with experimental parameters, are processed on an IBM 370 computer to give spectra of the number of ions recorded during a suitably long test period against mass to charge ratio, thus allowing ionic species to be distinguished.

Applications of this type of microscope are diverse and have been summarized by Turner et al

A.I:2.2.3 Imaging atom-probe

Panitz (286) has described an alternative type of atom-probe microscope which allows the chemical composition of a large area of the tip to be displayed at one time, while maintaining the spacial resolution of the time of-flight microscope. The imaging atom-probe used in this work (developed by Waugh 283) differs somewhat in detail from the original design and a schematic diagram is shown in fig. (A.I:15). Ions from the specimen surface are field evaporated by a high voltage pulse of nanosecond rise time on the specimen, and drift at a rate determined by their mass to charge ratio, in a manner similar to the first type of atom-probe, towards a planar channel plate intensifier. The intensifier is gated on by a pulse which is set to a variable delay from the initial pulse. Ions which reach the intensifier during the second pulse are detected on the phosphor screen. The variable delay allows ions of chosen mass to charge ratio to be detected.

Again extremely high quality design and construction are required and the apparatus is of similar construction to the first atom-probe.

This microscope was operated in two modes for the present work. Firstly, if an adequate d.c. bias was applied to the specimen, a FIM image was obtained with an image gas introduced. Secondly, pulsing the specimen and detector, with a delay between, allowed a spacial distribution of a selected mass to charge ratio species to be displayed. Fine adjustment of this delay is possible by the observation of a known species, e.g. Fe^{2+} , and calibrating accordingly. A high detection efficiency is possible (Waugh 283) due to the mode of operation of the channel plate. Damage occasionally occurs to the channel plate, often due to fragmenting specimens; such spurious images are easily recognised. A mass resolution for this instrument of $\Delta m_1/m_1 = 1/25$ has been calculated while the spacial resolution is of the order of 0.5 nm to 1.0 nm (Waugh). One of the most serious problems affecting the latter, is that due to etching at high energy sites on the FIM tip (e.g. at sub-boundaries); this causes a focussing effect in such regions. This problem was considerably reduced in the present investigations by the cooling of the specimens to 20K.

A.I:2.2.4 Preparation of FIM specimens

A sample of 1408M2 patented wire drawn to 0.5 mm was obtained from RARDE and was comparable in composition and thermomechanical history to the 4.25 mm patented wire used in the tensile testing programme, except that it had undergone a much higher drawing reduction (approximately 98%). This fine wire was used as it was of suitable diameter to polish to a well-profiled tip. Also the high deformation ensured a fine scale microstructure, and thus there was a reasonable probability of finding the two phases and dislocation structures present at any given tip.

The polishing technique employed was first developed by Brandon and Ralph (287) and later improved by Morgan (288) and Davies (289). It was based on a thin layer technique where a layer of a suitable electrolyte is floated on carbon tetrachloride. The specimen, about 10 mm long, with its nickel mount was vertically lowered so it just protruded into the carbon tetrachloride. A d.c. potential was applied between the specimen and a stainless steel cathode in the container and the specimen polished where it was in contact with the electrolyte and progressively necked to failure. Removal of the specimen at this time sometimes produced a tip

of suitable radius (i.e. between 20 and 200 nm), the observation of which was carried out under bright illumination with a microscope. The perchloric acid/2-butoxyethanol solution (polish "A" - A.I:2.1) used at room temperature at 6V proved suitable. This polishing was rather slow and on occasions a pre-polish of the lower half of a specimen in a 30% acetic acid/70% perchloric acid solution at 4V and room temperature was carried out, before final necking as above. Further details are given by Morgan and Dury (125). Tips were inspected for suitability either optically or in the Philips EM 300, the best ones showing a uniform taper of 10° to 30° .

A.I 2.2.5 Selected details of operation of atom-probes

Both atom-probes were provided with prepumped specimen airlocks to facilitate rapid changes. Both instruments were pre-baked to obtain a background vacuum of better than 5×10^{-10} torr to reduce spurious data. Super-pure neon gas at a pressure of approximately 10^{-4} torr was used as the image gas in all cases. Both nitrogen under reduced pressure and cold helium gas were used for specimen cooling. The d.c. potential required for neon imaging of ferrite varied with temperature and tip radius. It was generally found that the best image field was of the order of 3.5 V/\AA (Dury 125) for the ferrite, while that of the cementite was somewhat greater. At fields significantly greater than this value, the probability of the tip disintegrating (flashing) increased, so field evaporation had to be undertaken with some care.

It became general practice to investigate a specimen in the imaging atom-probe, initially, and obtain both FIM and desorption images of suitable areas. If particularly interesting features were found, the tip was transferred to the time-of-flight atom-probe for quantitative analysis. Two problems were inherent in this procedure: firstly, the difficulty in finding the area of interest again and secondly, that the specimens appeared to undergo significant deterioration during transfer, sufficient to cause failure on re-applying the imaging potential. These problems are being overcome by the modification of the imaging atom-probe to include a time of flight detector (Waugh 283). In both microscopes it was necessary to obtain a stable FIM image to find areas suitable for examination. In the case of the imaging atom-probe, this was followed by obtaining desorption images of suitable ions (after calibration), while in the time of flight atom probe the FIM image was used to ensure the precise alignment of the probe hole over the selected area. Sufficient ions (normally greater than 1000) were detected to give an adequate spectrum (the image gas

normally being pumped out during a run, but periodically being re-admitted to check alignment).

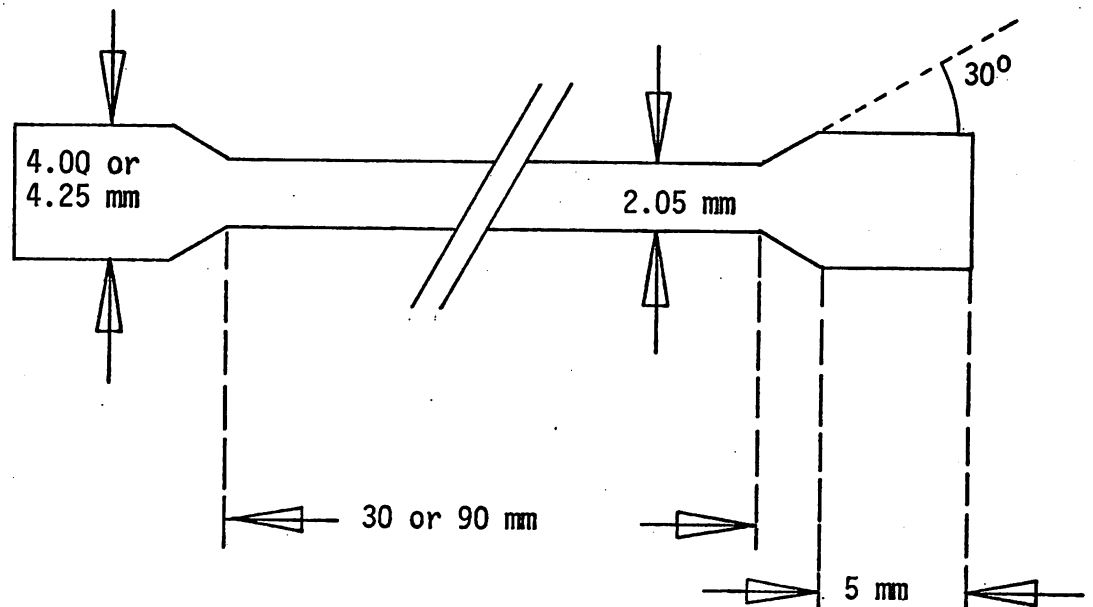


Fig. (A.I:1) Design of the tensile specimens (before polishing)

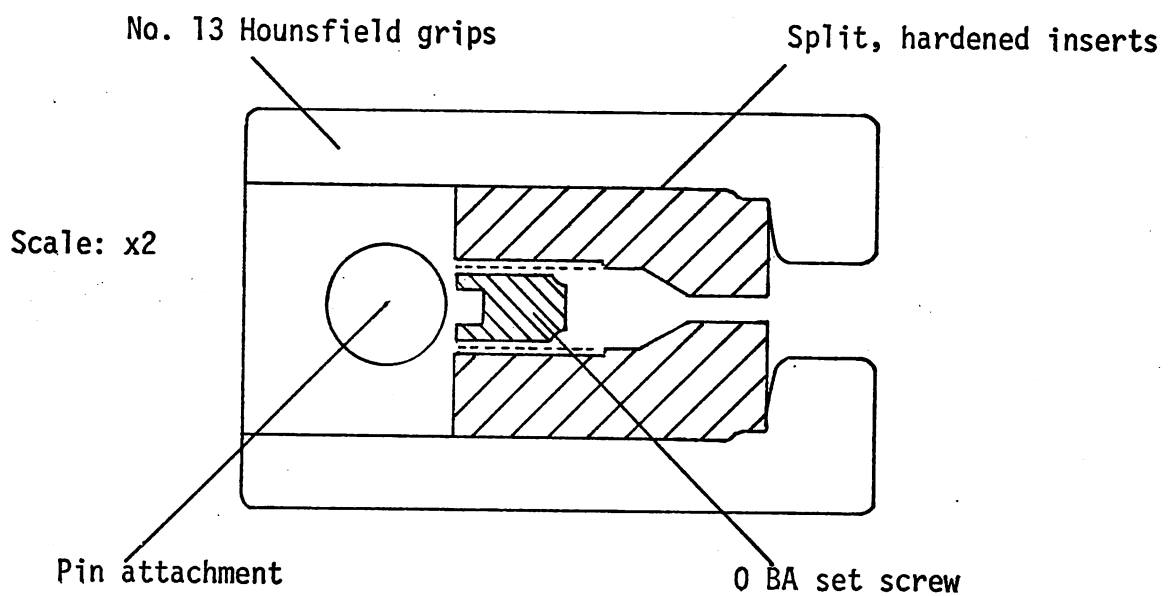


Fig. (A.I:2) Design of the inner wire grips (NSOH steel inserts).

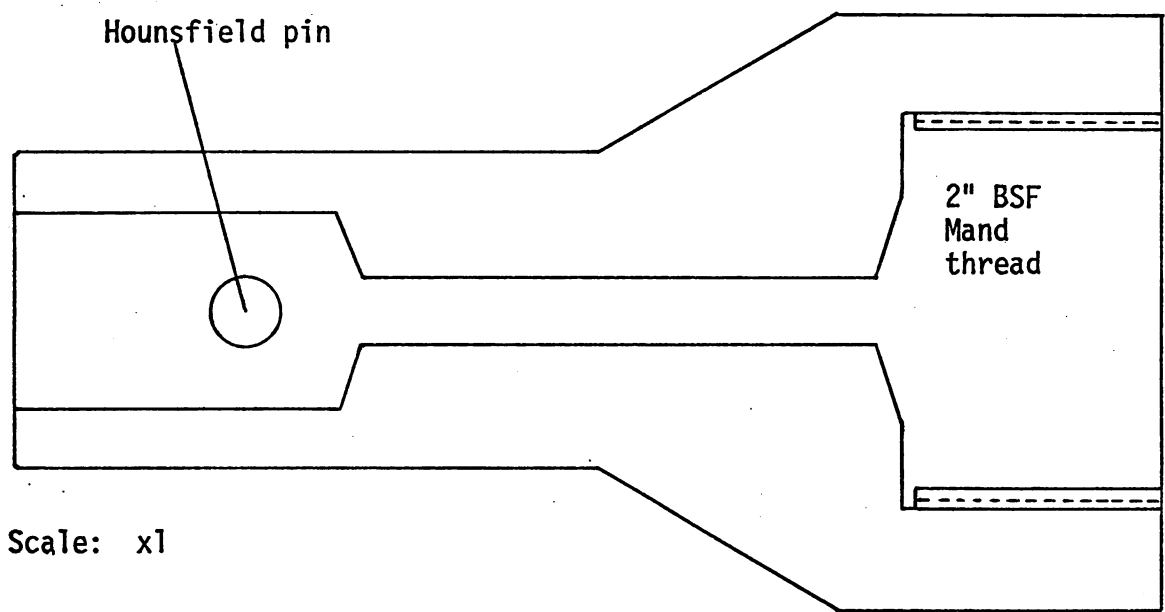


Fig. (A.I:3) Design of 100kN Mand outer grips. (mild steel).

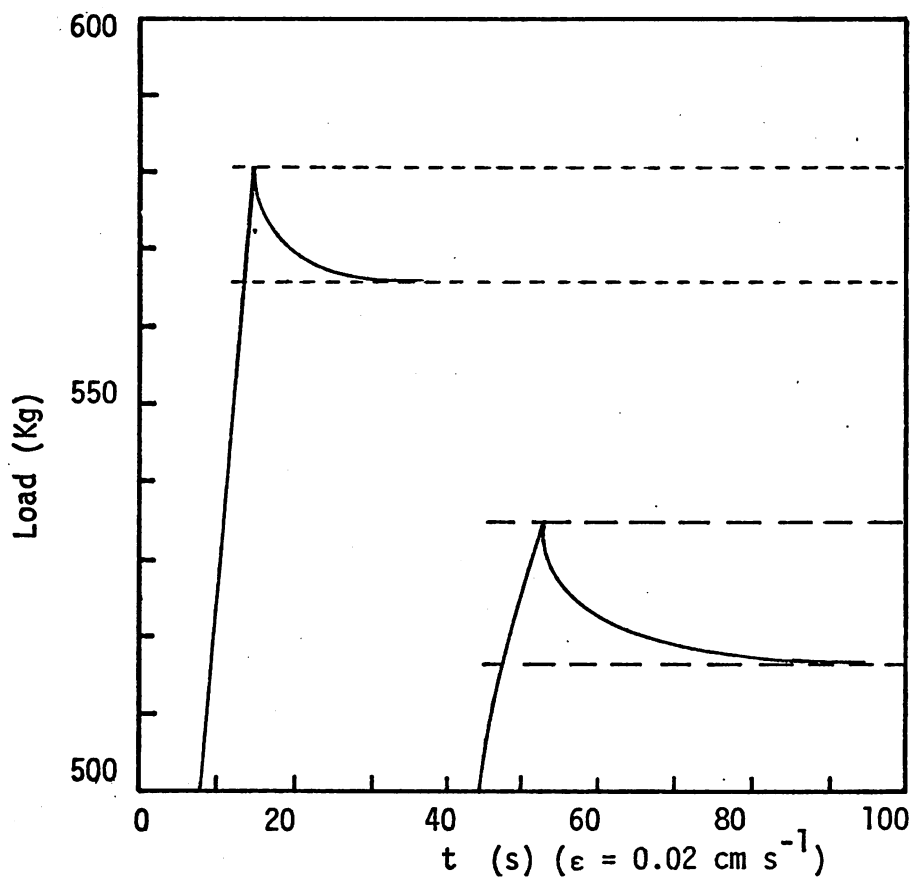


Fig. (A.I:4) Relaxation recorded on a screw-driven Instron TT-C machine for (a) patented wire specimen, (b) fully elastic specimen.

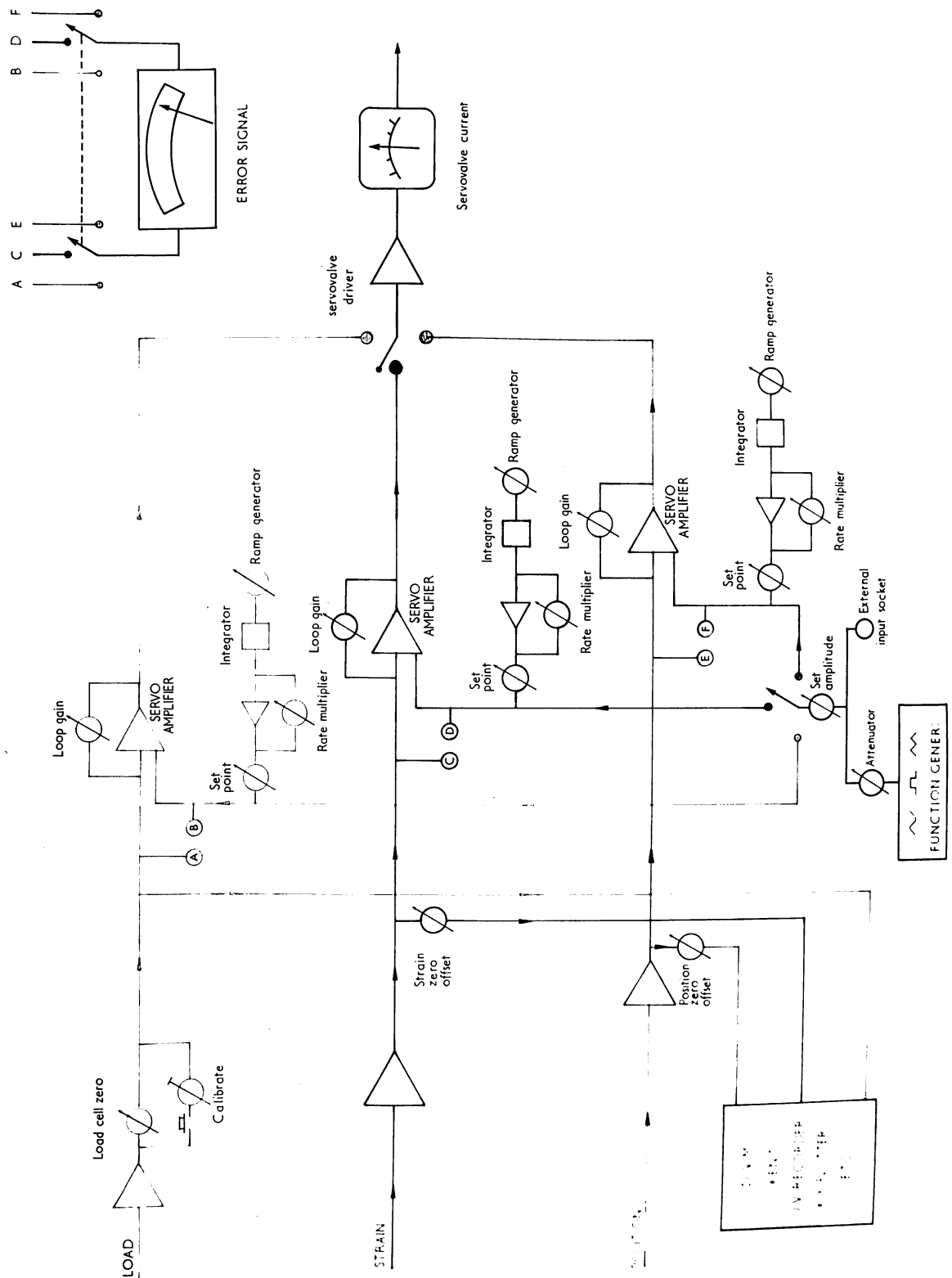


Fig. (A.I:5) Schematic representation of a typical closed-loop servo-hydraulic machine (courtesy of Mr. S.D. Charter).

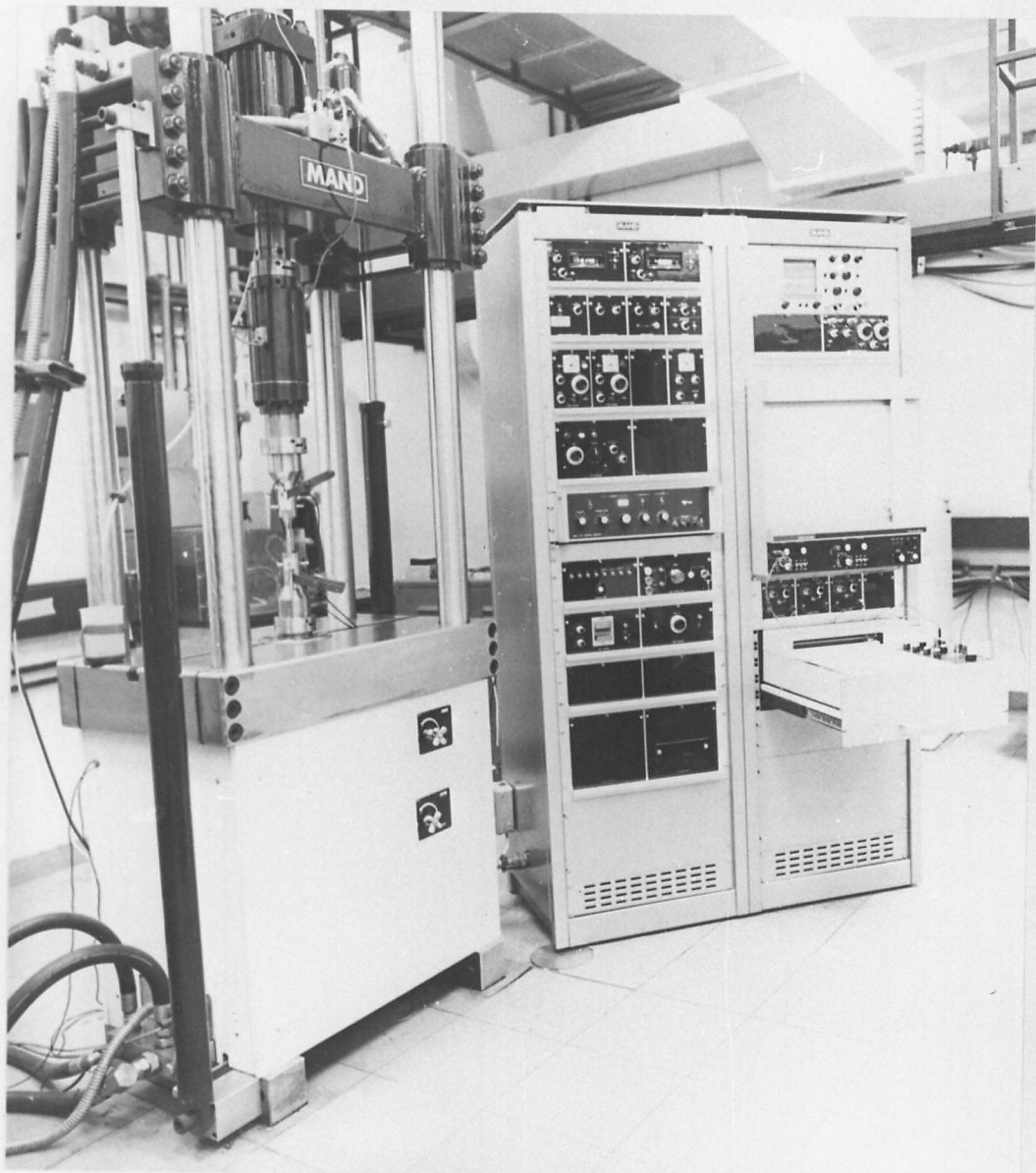


Fig. (A.1:6) General appearance of
Mand 100kN, closed-loop, servohydraulic
testing machine

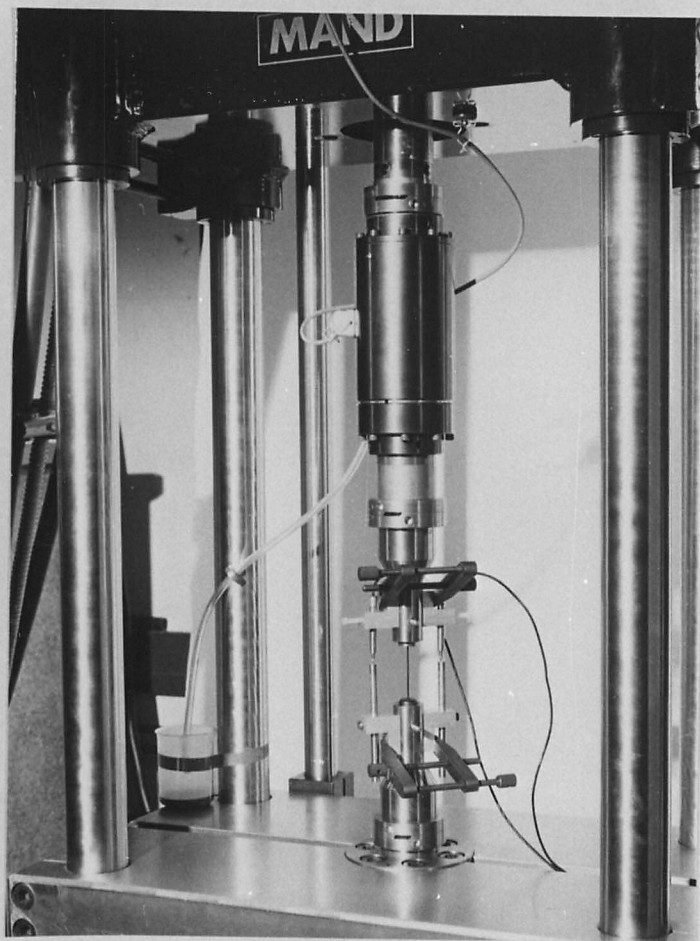
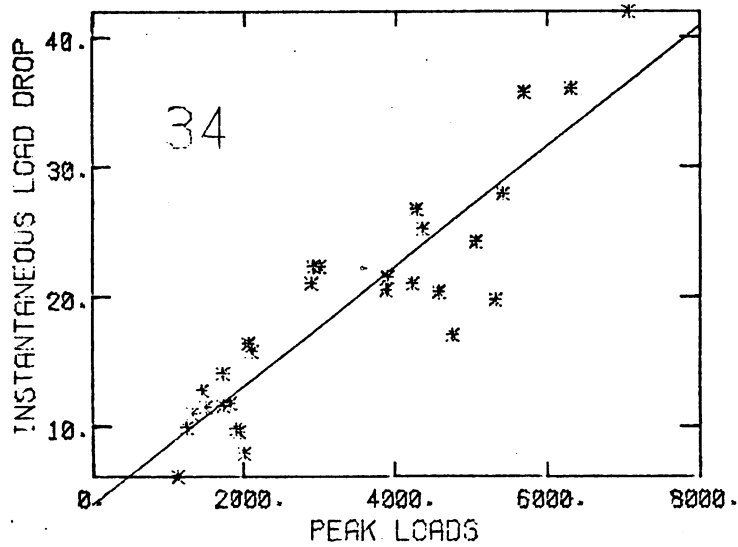


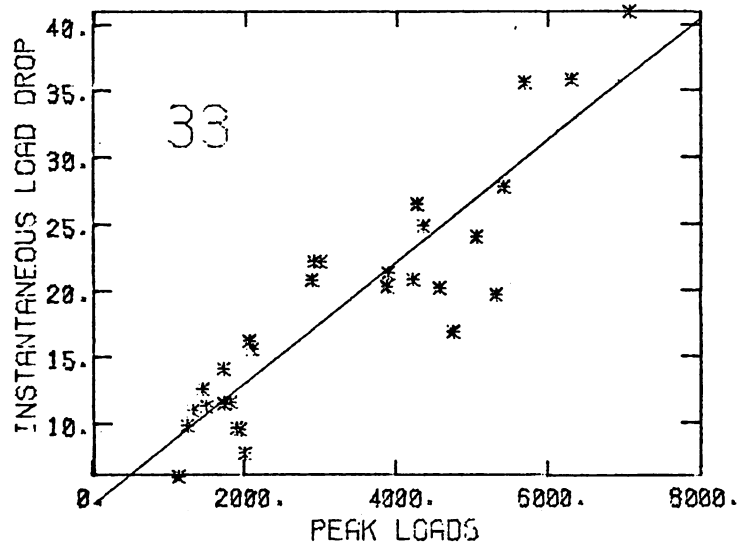
Fig. (A.1:7) Appearance of upper loading train used on Mand 100kN machine in high resolution tests

Fig. (A.I:8) Examples of 100kN Mand machine relaxation data (IBM output).



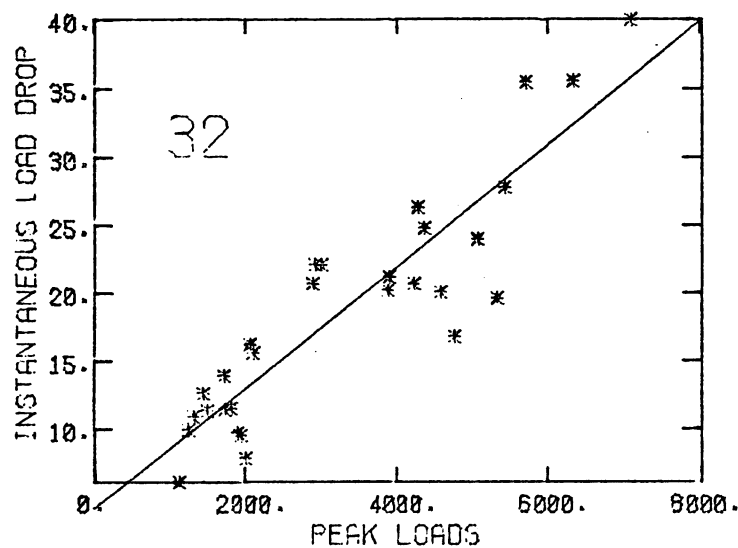
120.00
SECONDS

SLOPE= 0.995E+00
INTERCEPT=-0.386E+01



100.00
SECONDS

SLOPE= 0.995E+00
INTERCEPT=-0.389E+01



90.00
SECONDS

SLOPE= 0.995E+00
INTERCEPT=-0.396E+01

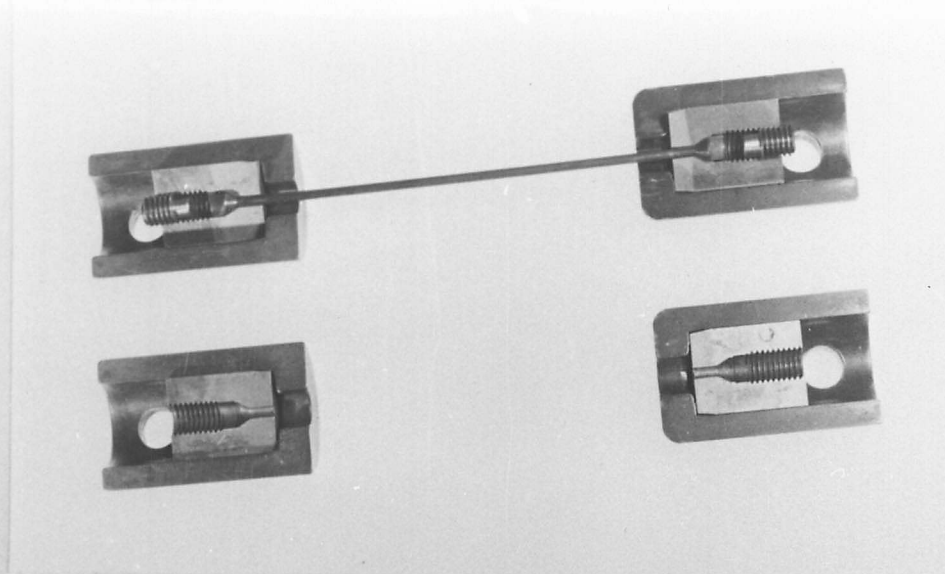


Fig. (A.1:9) Appearance of wire specimen and inner grips

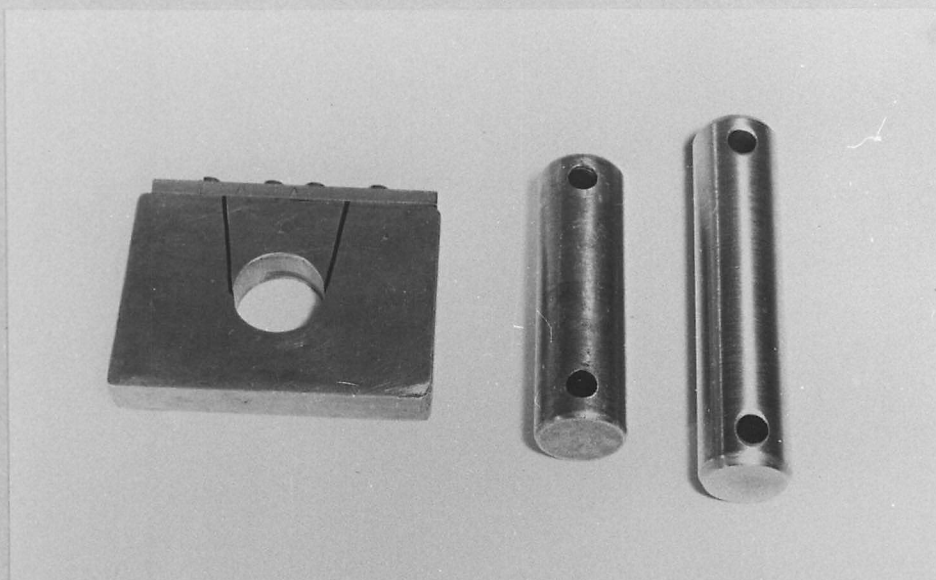


Fig. (A.1:10) Appearance of clamp used in securing inner grip

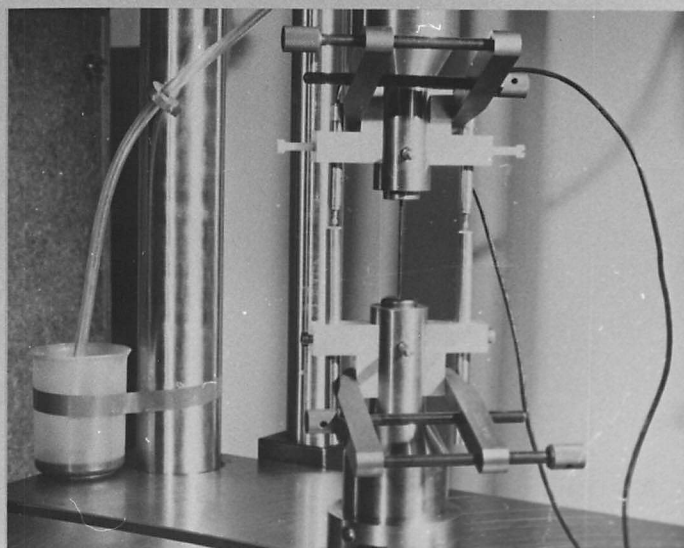


Fig. (A.1:11) General appearance of specimen, grips and transducers in testing position

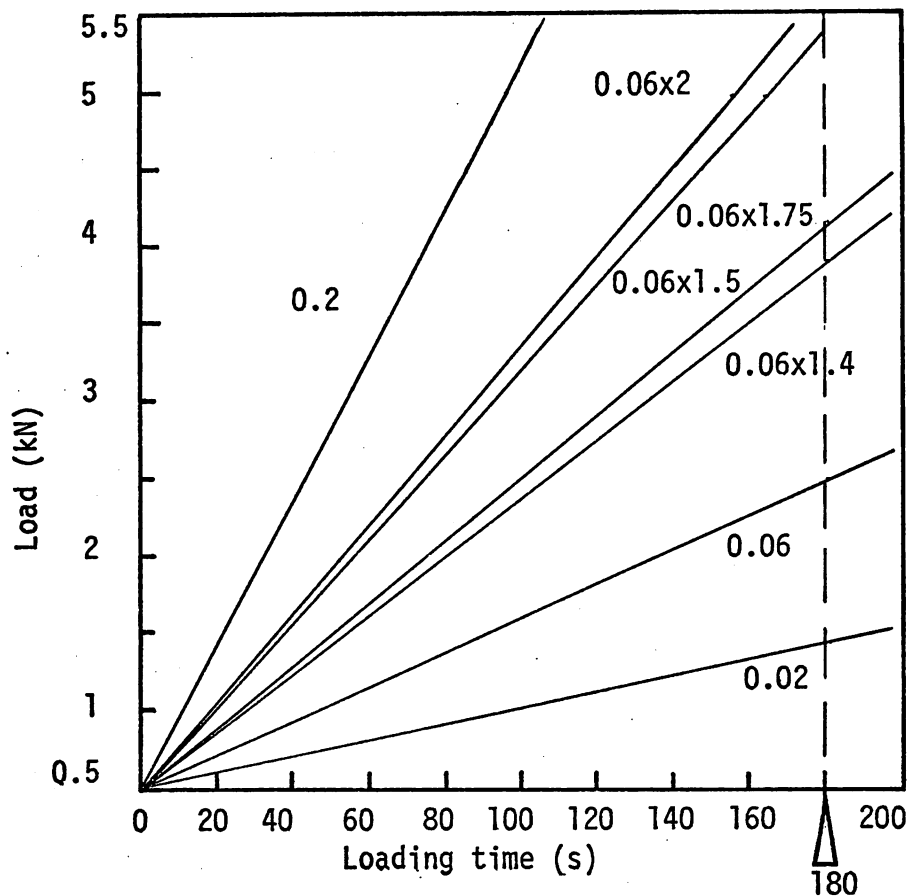


Fig. (A.I:12a) Loading graphs for elastic test specimen.
(ramp rates are given in V/min).

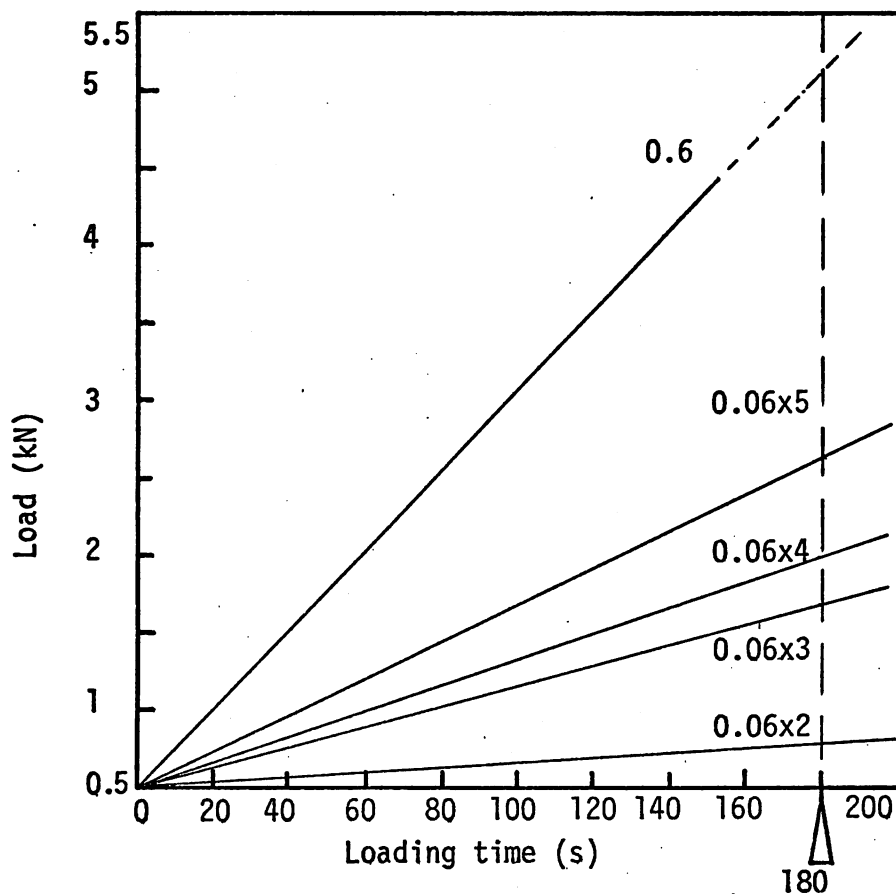


Fig. (A.I:12b) Loading graphs for 90mm patented steel wire specimens.
(ramp rates are given in V/min)

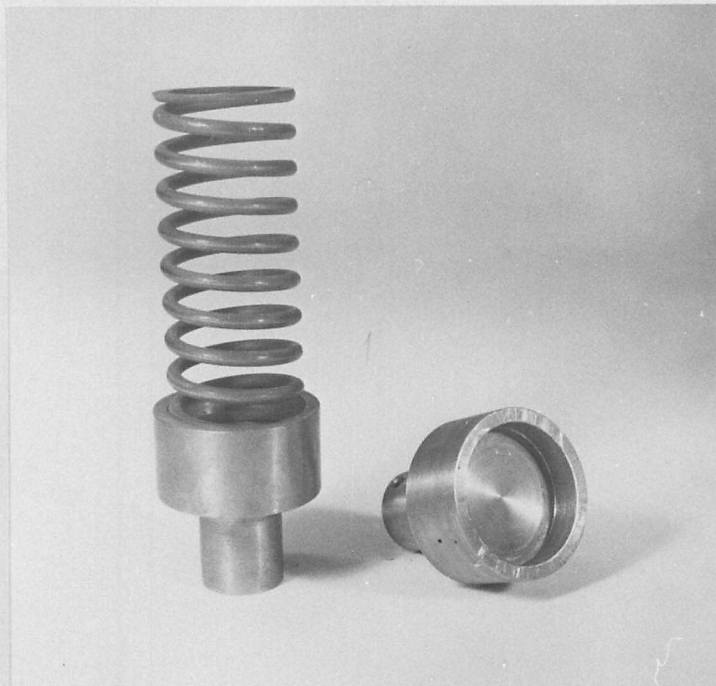


Fig. (A.1:13) Appearance of cups used
to load springs

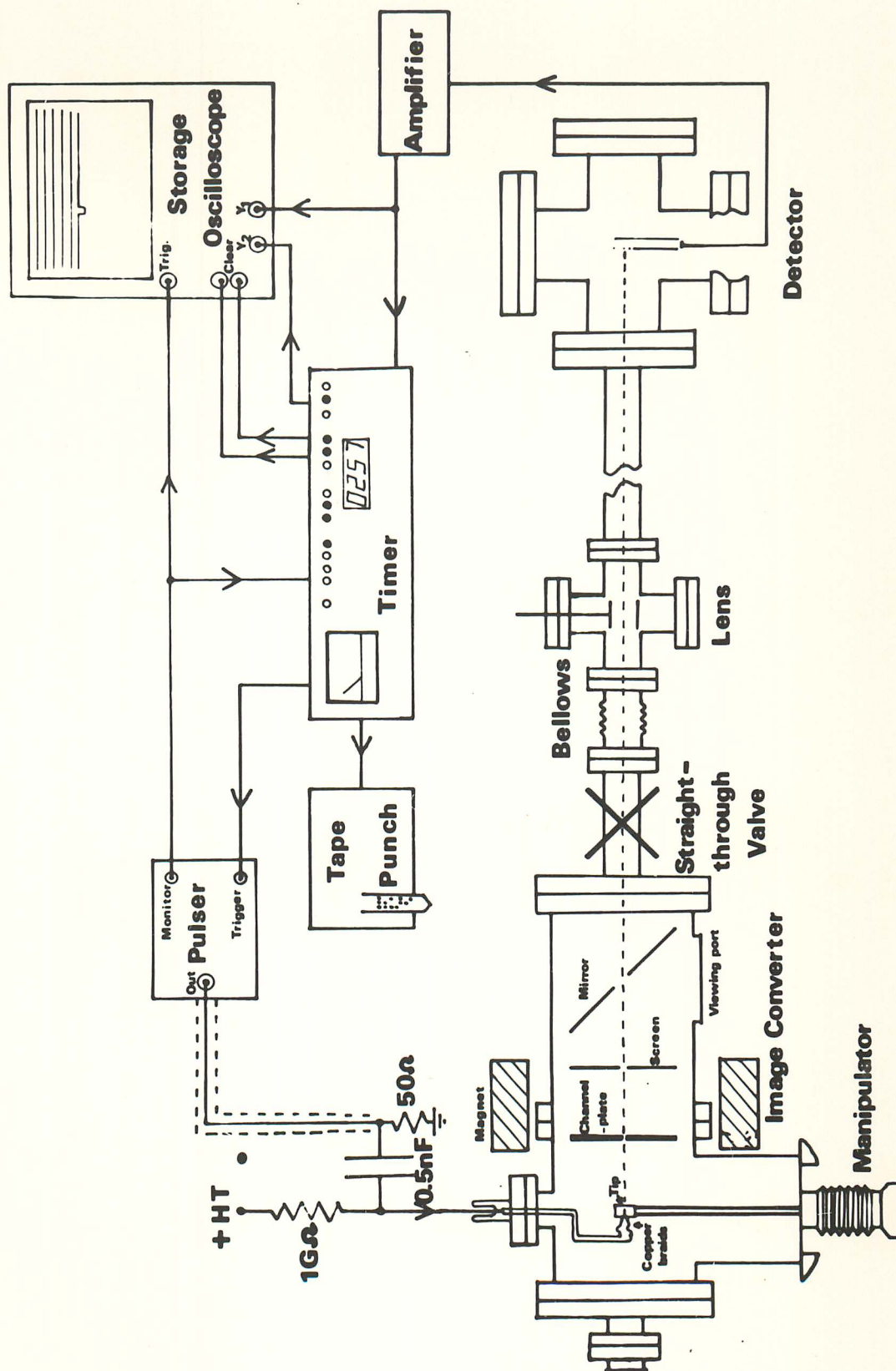


Fig. (A.I:14) Schematic representation of the time-of-flight atom-probe (Courtesy Mr. P. Mills).

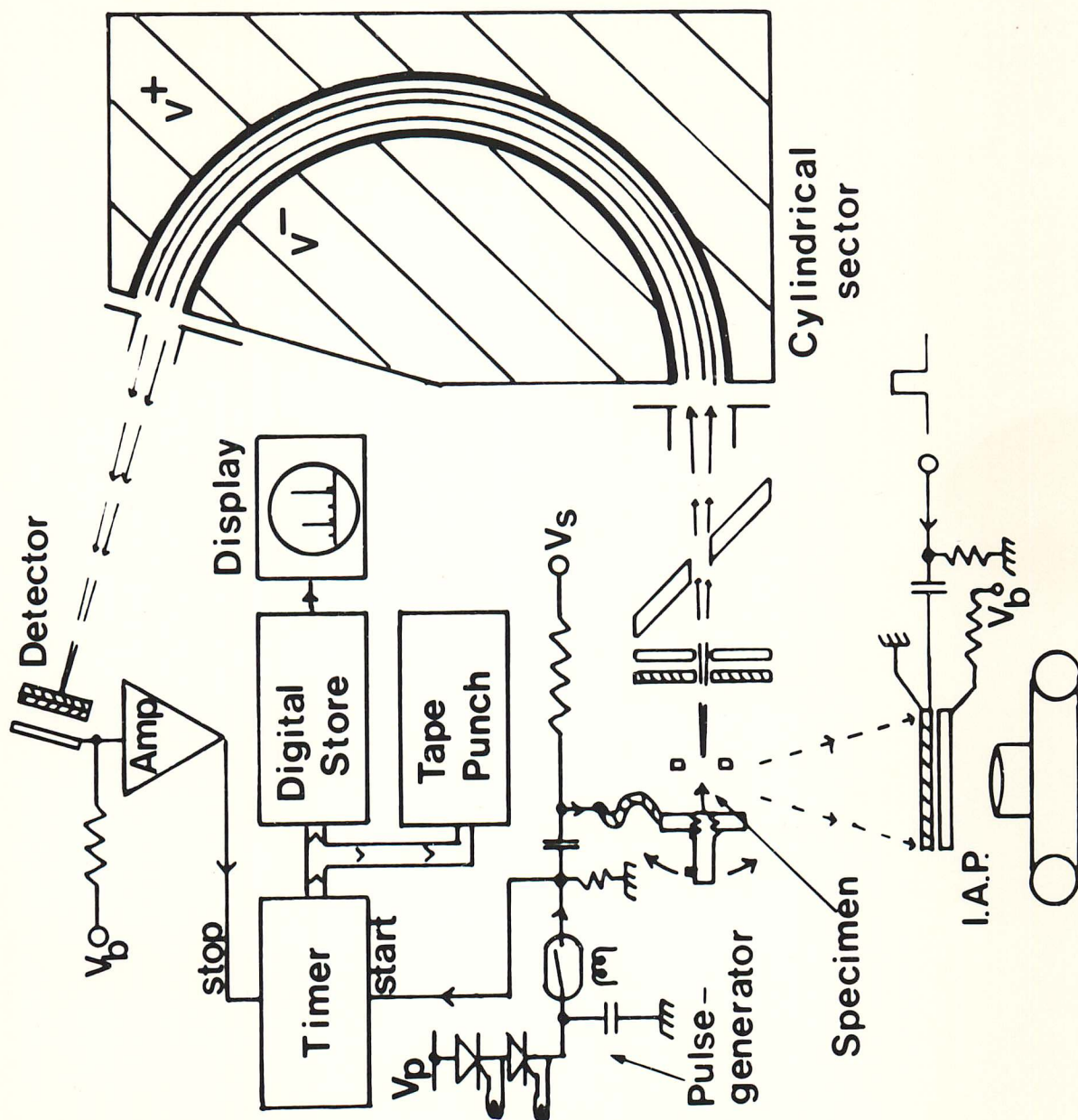


Fig. (A.I:15) Schematic representation of the imaging atom-probe (Courtesy Dr. A.R. Waugh).

A.II. Appendix II. Mechanical testing data reduction

A.II:1. Introduction

As described in A.I. the majority of the high resolution stress relaxation data was recorded on A3 plotting paper by a Bryans X-Yt recorder. This recorder was fitted with an automatic fly-back facility which enabled a pen speed of 2 cms^{-1} to be possible for a 180s test. Although data could be obtained and manually processed to produce the required information, it rapidly became clear that due to the large number of relaxation curves to be analysed the time involved would inevitably become excessive. It was therefore decided to develop computer programs for use with the Cambridge University Computer Syndicate IBM 370/165 machine. This machine has been particularly developed as a versatile interactive system and has a wide range of peripherals including 3 colour, high speed Benson plotters which were particularly useful in the present work.

In order to do this the stress relaxation graphs were digitised using a D-mac machine (type SP/100X100) on to 8-track paper tape. This storage medium was chosen in preference to magnetic tape for ease of checking. The D-mac was provided with a keyboard which enabled a job description to proceed the data for each specimen which enabled the information to be read into the correct file. The information itself for a pair of relaxations (i.e. 1st and 2nd relaxation) had the following format:

- a) A specimen code;
- b) The specimen cross-section (in mm^2) at test load (to obtain true stress);
- c) The peak load (in N);
- d) A scaling factor (this enabled various load scales to be accommodated, e.g. 0.1 for 1 Nmm^{-1} or 0.25 for 2.5 Nmm^{-1});
- e) a double column of figures, the first column is the X value of the D-mac cursor for each point (ignored in the programs) and the second is the Y value of the D-mac cursor (in mm) which corresponded to the load at that point. After the data for the 1st relaxation, the peak load for the 2nd relaxation (in N) was given, followed by the information from that relaxation. The last statement on the tape was an end code.

The times during each relaxation at which the load was recorded was chosen to reflect the rate of change of load, i.e. there was a higher sampling rate at low times. The total number of data points for each 400 second relaxation was chosen to be 42 which was found to give optimum performance within a reasonable amount of computing time. The same timing

marks were used to collect in a similar manner the load-time relaxations of the machine as described in A.I. There follows a brief description of each program used and how they are operated.

A.II:2. How to make it work

There are two fortran programs, in files sp13. interp and sp13.substract, and four pheonix programs in the partitioned file sp13.c: members intgo, subgo, subgo2 and forxlib, and this documentation: member doc, which is in "roff input" format. The partitioned file sp13. data contains load relaxation data measured from chart recorder output using the D-mac and the file sp13. calib holds machine relaxation data for calibration and the definition of the timing marks used by INTERP and SUBTRACT. The partitioned file sp13.lib has one member, a compiled version of sp13. substract called SUBTRACT. The system is completed by the file sp13. lines which is produced by INTERP and read by SUBTRACT.

The pheonix command sequences send messages to the user when the jobs reach the head of the job queue. Messages are sent when the job begins and when it ends, they also say how it ends, either "OK" or "bleah". For details of how jobs are submitted and timetabled on the Cambridge 360/165 it is essential to consult the documentation produced by the University Computing Service.

The individual command sequences will now be described, whenever "<" is written it should be interpreted as "carriage return".

A.II:2.1. Program Intgo

This command-file submits a job which compiles and runs the fortran program sp13. interp using sp13. calib as data and producing sp13. lines as output. To run the command-file type "c sp.13.c: intgo <" at a phoenix terminal.

A.II:2.2. Programs Subgo and Subgo2

These command-files submit jobs which run the program SUBTRACT. Subgo uses the precompiled version in the library sp13.lib whereas subgo2 compiles the program afresh each time from sp13.subtract, this is used for debugging the fortran program after changes have been made. For production runs subgo should always be used, after first making sure that the library contains the object code from the latest version of SUBTRACT (see forxlib).

To run the command-file type "c sp13.c: subgo <" or "c sp.13.c:subgo 2 <" at a pheonix terminal, it will reply "data?" at which point the name of the member of the partitioned file sp13. data which contains the set of data to be run should be typed, e.g. "A123 <". The job will then be submitted to

the job queue and it will type "data?" again. When all the sets of data have been submitted simply type "stop <" instead of the member name.

A.II:2.3. Program Forxlib

This command-file submits a job to the job queue to compile the fortran source from sp13. subtract and to put the resulting object code in sp13.lib: subtract. This command-file uses the IBM H-extended compiler whereas subgo2 uses the G-1 compiler. The former compiler produces more efficient code than the latter, but is more "expensive" to run. It is better, therefore, to use the H-extended version for production runs when the compilation only needs to be done once and the saving in faster object code is worthwhile.

To run the command-file type "c sp13.c: forxlib <" at a pheonix terminal.

A.II:2.4. Program INTERP

This program reads in a set of timing marks from unit 5 (sp13.calib) which are then used as the basis for calculating load relaxation in the machine (this program) and in the specimen (program SUBTRACT) e.g. .5, 1, 3,5,10, ... 400 seconds. After the timing marks a large number of machine relaxation curves are read in. These all begin with the peak-load (in Newtons) followed by a list of the load-drops from this peak at each of the timing marks (see section 4.1). Each test was repeated using nearly the same peak-load and these are termed first and second relaxations.

The sets of machine relaxations cover the complete range of peak-loads that are used in the specimen relaxation experiments. The purpose of this program (INTERP) is to provide an estimated machine relaxation curve for any peak-load in the calibration range. This is achieved by assuming that for each and every time slot the amount by which the load has dropped due to machine relaxation is linearly related (i.e. by a straight line interpolation) to the value of the peak-load. Thus for each time slot a straight line is fitted to the loads at that time (y-axis) against the peak-loads (x-axis). The gradient, intercept, correlation coefficient etc. for the fit for each time slot is output to unit 1 (file sp13. lines) after a copy of the time-slot information. The program also produces plots of the gradient and the intercept of the fitted line against times as a check that enough data has been gathered for a smooth calibration to be made. If these plots, and they are done for both first and second relaxations, are not monotonic curves then more, and more accurate, calibration data should be collected.

There follows a line by line listing of some of the comments in the program.

NTIMES The number of time slots
 TIMES (NTIMES) Array holding the time slots in seconds
 LOADSC(NSETS) The initial peak load for each relaxation set
 RELAXC(NSETS,NTIMES) 20 array holding the load for each relaxation set and for each time slot. Initially these are read as load drops.
 GRAD the gradient of the straight line for a particular time slot
 INTERC the intercept of the straight line for a particular time slot. The straight line is fitted using initial loads:
 LOADSC(NSETS) as the x-axis, and the actual loads at that time slot: RELAXC(NSETS,GO) as the y-axis.

Initialise the plotting routines
 Read the timing marks
 There are two groups of relaxations, 1st and 2nd.
 Read the machine relaxation curves, there are NSETS sets of them.
 For each time slot (GO) compute the interpolating line
 Calculate the means

Now calculate the regression parameters
 Plot the data and straight line for each time slot, load at time slot/peak load, correcting the scale each time to show the spread of the data clearly
 Plot the points
 Plot the line
 Plot the box & title
 Set the plot transformation
 Plot the gradient and intercept values against time

A.II:2.5. Program SUBTRACT

This program calculates the correct machine relaxation to subtract from the experimental relaxation. The parameters concerning the machine relaxation it gets from unit 1 (sp13.lines) and the experimental relaxation it gets from unit 5 (sp13.data). The experimental specimen load relaxations have the format: peak-load followed by load drops, but the format is different from that of the machine relaxations (in sp13.calib) because they come from the paper tape output of the data digitiser.

There follows a line by line listing of the comments in the program.

 Do almost the entire program twice, for the first and second relaxations
 Read in the data, for each time slot calculate the machine relaxation and subtract it from the given relaxation to get the specimen relaxation. Now plot the experimental specimen load relaxations, the interpolated machine relaxations (SUB) & 2* standard-error limits (SUBHI & SUBLO), and the corrected specimen relaxation (SREL) and limits (SRELHI & SRELLO):
 Initialise
 Plot the tear-off marks
 Plot a label
 Plot the lines themselves
 Plot the box & title

Now convert the loads to stresses in MPa ($= N/mm^2$)

Now plot the stress relaxations (means and 2*ste. range):
 Initialise
 Now plot tear-off marks
 Now plot a label
 Now plot the stress relaxation curves
 Plot the box & title

Now calculate the gradients, stress against time, (arranged so that they are +ve) for the mean and 2*ste. range:
 Now convert to log (stress relaxation rate) and produce an array of log (times)

Now plot a graph of lg(stress-relaxation-rate) against lg(time):
 Initialise
 Now plot the tear-off crosses
 Now plot a label
 Plot the graphs
 Plot the box & title

Now put the stresses in terms of 'stress drop'

Now plot the lg(stress-relaxation-rate) against the stress drop, do this for mean/mean, high/low and low/high estimates:
 Initialise
 Now plot the tear-off marks
 Now do a label
 Now plot the graph
 Plot the box & title

A.II: 3. The Data Formats

The calibration data is in a single sequential file (sp13.calib) and the test data is in a partitioned file (sp13.data) because the test data sets need to be accessible individually whereas the calibration data is only used all at once.

A.II:3.1. The Data File CALIB

The first set of numbers is the definition of the timing marks. Since this is the same file as the machine calibrations different timing marks can be used for different machines. First is the number of marks followed by the times in seconds in 5F5.0 format, e.g.

7

0.5 1. 2. 9. 17.
 50. 150.

Then follow all the first relaxations together, followed by all the second relaxations. These two sets can have different numbers of relaxations but they should nearly always be the same; if, however, the first relaxation goes perfectly, but the second is interrupted by some external factor (e.g. lunchtime) then there may be more first, than second relaxations. Each relaxation is in 5F5.0 format, except for the peak load which must only contain a decimal point, and must contain the same number of readings as there are timing marks as given above.

The peak load is given first (in Newtons) followed by the load drops (also in Newtons) from that peak at the relevant timing mark. Thus in the example below in the first relaxation the peak load is 5002.6 N and 9 seconds later it is 4992.6, a drop of 10 N.

In this example there are four first and three second relaxations, there must always be at least three relaxations in each group.

```

4
5002.6
  0.2   2.   5.  10.  15.
  20.  22.
4010.5
  0.1   1.   4.   8.  11.
  15.  17.
2986.4
  0.07  0.2   .8  1.2  3.
  9.   10.
2007.6
  0.05  0.17  .5  1.   2.
  8.0  9.5

```

Now follow the second relaxations:

```

3
4996.0
  0.2   2.   3.   8.  10.
  11.  11.6
4008.0
  0.1   1.   2.   6.   8.
  10.6  11.
1989.1
  0.05  0.16  0.3  .87  1.1
  3.5  3.7

```

The set of calibrations actually used for processing the data had 42 timing marks (up to 400 seconds) and 35 and 29 sets of first and second relaxations from 1130 to 7080 N.

A.II:3.2. The Data File DATA

Each member of the file sp13.data is identified only by the member name and this is the identifier which appears on the output and in the messages subgo to the terminal.

Each member contains just two relaxations, first and second, from one specimen. The format is the peak load first, followed by a scaling

factor, and then a double column of figures. The first column is rubbish produced by the digitiser and the second is the load drops. When these figures from the second column are multiplied by the scaling factor (which was always 0.1 for this data) they load drops in Newtons. The peak load is given in Newtons directly:

```
3520.5
  0.1
5798 0002
6327 0012
6356 0052
8527 0102
9216 0130
0013 0216
0146 0250
```

Now the second relaxation, which uses the same scaling factor:

```
3514.0
1127 0002
1526 0011
1756 0049
1192 0099
2100 0119
2272 0123
2391 0131
```

A.II:4. Calibrating Several Machines

If the experimental testing is extended to be run on two mechanical testing machines, or several jigs or specimen holders are employed, then each configuration must be individually calibrated.

The same programs INTERP and SUBTRACT can be used without any change, as can the command-files intgo, subgo, subgo2, forxlib. A different calibration file is required, e.g. sp13.mc2.calib, and INTERP should be run thus:

```
"c sp13.c: intgo calib=sp13.mc2.calib lines=sp13.mc2.lines <"
```

which will produce the appropriate file sp13.mc2. lines to be used by SUBTRACT. Subgo, or subgo2, should be run thus:

```
"c sp13.c: subgo data file=sp13.mc2. data lines=sp13.mc2.lines <"
```

where the appropriate data is in the new partitioned file sp13.mc2.data. Any number of machines and jigs can be calibrated concurrently in this way.

If different timing marks are to be used for different machines or jigs that presents no problem, the first section of the calibration file is altered accordingly, but if only one, or more than two, relaxations are to be calibrated, then sp13. subtract and sp13.interp must be edited. Only a single line of fortran need be altered in each (a "DO loop" statement), and then the program can be used as above.

A.III. Appendix III: Nomenclature

Notes

1. It has been attempted in this thesis to maintain the nomenclature used in previous work when referencing it or when expanding on it. It has, however, become clear that this is not always possible as previous workers have made little attempt to adopt standard terminology and it is clearly necessary to keep to this principle within this work. This has necessarily involved the use of a complex nomenclature here and also has required alterations to that used in the CPGS (1). For the readers convenience the symbols used in this thesis and their counterparts from the CPGS (1, Appendix V), where they existed, are given in the following list.
2. In this work where stress or strain values are used they refer, unless explicitly stated, to the true values. In many previous investigations this has not been stated, it normally being assumed that they are true values. For the case of stresses and strains during a stress relaxation test this irregularity is particularly prevalent, it being assumed that the plastic strains being sufficiently small to ensure that the true and nominal values measured are indistinguishable. (This problem is discussed in 4:3.4.3. and by (Guiu & Pratt (163)).
3. If a particular terminology employed here was due to certain workers in particular, their reference is given.
4. Where a symbol used in this work which applies to a particular derivation, the equation in which it is first employed is given.

Symbol in this thesis	Counterpart symbol in the CPGS (where applicable)	Comments	eqn. in this thesis	ref.
a	-	a constant of integration	4:55	-
a'	-	a constant	4:81	-
a''	-	a constant	5:1	-
a _o	a _o	initial specimen cross section in tensile test	4:28	-
at%	at%	atomic percent	-	-
A	-	pre-exponential factor, involving ρ_m , frequency factor and geometry	4:38	-
A'	-	a constant in equation	4:49	-
A*	A*	activation area	4:40	-
A/R	A/R	as received material (as drawn)	-	-
$ b $	$ b $	modulus of burgers vector	2:19	-
$b_{\sqrt{cm}}$	$b_{\sqrt{cm}}$	burgers vector in cementite	2:16	-
$b_{\sqrt{\alpha}}$	$b_{\sqrt{\alpha}}$	burgers vector in ferrite	2:16	-
B ^{α}	B ^{α}	dislocation mobility factor	4:8	-
B ₁	-	material constant	4:60	-
B ₂	-	material constant	4:63	200
B ₂ -structure	-	ordered b-c structure, c.f. CsCl	-	-
BS 5216	-	British Standard Institute Specification for patented cold drawn carbon steel wire for mechanical springs, replaces BS 1408, N.B. HD3, R2, C, D following the title refer to sections of the specification.	-	-
c	c	a constant (units of time)	4:46	-
C ₁	-	material constant	4:63	200
d	-	cell or grain size in generalized Hall-Petch equation	2:15	-
\bar{d}	\bar{d}	mean cell size	2:20	-
\bar{d}_b	-	generalized mean barrier intercept on slip plane	2:11	-
\bar{d}_g	-	mean grain size	2:20	-
\bar{d}_1	\bar{d}_o	mean initial pearlite inter- lamellar spacing before wire drawing	2:8	-
\bar{d}_o	-	mean initial barrier spacing for dislocation motion before wire drawing	2:13	-

\bar{d}_ϵ	\bar{d}_ϵ	mean pearlite interlamellar spacing after drawing to a true strain ϵ	2:8	-
D_o	D_o	initial wire diameter before drawing	2:8	-
D_ϵ	D_ϵ	wire diameter after drawing to true strain ϵ	2:8	-
D	D	characteristic drag stress on dislocation motion	4:87	173
E	E	Young's modulus of specimen	-	-
E_c	-	FIM specimen ionization field	3:1	-
f	-	a constant	4:50	-
g	-	a constant	4:83	-
g	-	reciprocal lattice vector (reflection)	-	-
G	-	Bulk Modulus	2:25	-
h	-	dislocation spacing	2:19	-
h'	h	hardening parameter	4:54	190
h''	-	hardening parameter	4:87	173
j	-	a constant	4:50	-
K	K	Kelvin	-	-
K'	K'	Hall-Petch plot slope	2:11	-
K''	-	a constant in modified Hall-Petch plot	2:14	69
K_1	-	a constant	4:55	-
K_2	-	a constant	-	-
K_3	-	a constant	2:29	-
K_4	-	a constant	4:56	197
K_5	-	a constant	4:56	197
K^*	-	a constant	4:57	-
k	k	Boltzmann's constant	-	-
k'	-	a constant	2:13	-
k_1	-	a constant in Ludwig relationship	2:18	-
k_2, k_3, k_4	-	constants	2:25, 2:29, 2:27	-
k_{FIM}	-	material constant (between 5 and 10) in FIM specimen	3:1	-
l_e	l_e	elastic strain rate of specimen during tensile loading	4:25	-
l_p	l_p	plastic strain rate of specimen during tensile loading	4:25	-
L/S	L/S	longitudinal section of specimen wire	-	-

LTHT"A"	-	low temperature heat treatment of A/R patented wire: 30 minutes at 200°C.	-	-
LTHT"B"	-	low temperature heat treatment of A/R patented wire: 300 minutes at 200°C.	-	-
LTHT"C"	-	low temperature heat treatment of A/R patented wire: 30 minutes at 300°C.	-	-
L ₁₂ -structure	-	ordered fcc structure, c.f. NaCl	-	-
m	m	$m = \frac{\partial (\ln \dot{\epsilon}_p)}{\partial (\ln \sigma)}$ $= m^* + \frac{\partial (\ln \rho_m)}{\partial (\ln \sigma)}$ i.e. dislocation velocity exponent modified for changes in ρ_m	4:13	184
m'	-	stress exponent	4:49	164
m"	-	slope of load vs total elongation plot	4:45	188
m _i	-	mass of ion		
m*	m*	dislocation velocity exponent	4:8	-
M	M	combined modulus of specimen and tensile testing system for shear stress calculation	4:32	-
M'	M'	combined modulus of specimen and tensile testing system for tensile stress calculation	4:32	-
		$M = \alpha_3 M'$ $M' = \frac{a_0}{1/S} + \frac{1}{E}$		
M _T	-	Taylor factor	4:82	153
M _S	-	martensitic transformation start temperature	-	-
n ₁	-	exponent, $n_1 = \frac{1}{m^*-1}$	4:55	-
n'	-	strain hardening coefficient	2:5	-
n _p	-	exponent in pearlite growth	2:1	15
N	-	number of mobile segments of a dislocation	4:7	136
p	p	pearlite	-	-
p'	-	exponent in generalized Hall-Petch equation	2:30	-
P	-	applied load	4:27	-
Pr	P	external pressure	4:11	-
Q	-	activation energy	2:1	-
R	R	gas constant	-	-

r_{tip}	-	radius of FIM specimen tip	3:1	-
R-phase	-	a Cr-Mo-Co rich phase	-	268
\bar{s}	\bar{s}	slope of $\log \sigma$ vs. $\log t$ plot at large t , $s = \frac{1}{1-m^*}$ $m^* = \frac{s-1}{s}$	4:20	163
s'	s'	curvature of $\log \sigma$ vs. $\log t$ $s' = \frac{d(\log s)}{d(\log t)}$ $m^* = \frac{s+s'-1}{s}$	4:22	163
s''	s''	slope of $\ln(-\dot{\sigma})$ vs. $\ln t$ plot at large t , $s'' = \frac{m^*}{1-m^*}$	4:58	161
s_1	-	slope of $\Delta\sigma$ vs. $\ln(1+a't)$ $s_1 = - \frac{kT}{ b A^*}$	4:82	157
S	S	machine stiffness	4:27	-
t	t	time	-	-
T	T	absolute temperature	-	-
T_e	-	eutectoid temperature (in K)	2:1	-
T_m	-	melt point (in K)	-	-
T_t	-	a transition temperature (in K) for temperature dependence of yield stress	-	78
T/S	T/S	transverse section of wire specimen	-	-
UHT2	-	Bridon Ltd. internal specification for music wire	-	-
UHT3	-	Bridon Ltd. internal specification for music wire, of higher strength than UHT2.	-	-
\bar{v}	\bar{v}	mean dislocation velocity	4:6	-
v'	v'	limiting dislocation velocity	4:87	-
v_c	-	a constant in dislocation velocity equation	4:9	176
V^*	V^*	activation volume $V^* = A^* b $	4:41	-
\bar{V}^*	-	mean activation volume	4:71	200
V_{EHT}	-	electric potential applied to FIM specimen	3:1	-

V_f	V_f	fibre volume fraction in composite	2:9	-
V_F	-	true activation volume, i.e. V^* extrapolated to $t=0$	-	152
V_p	-	growth velocity of pearlite	2:1	15
W_g	W_g	geometric factor	4:6	174
Y	Y	tensile testing machining crosshead rate	4:24	-
z	z	elastic strain rate of tensile testing machine	4:25	-
z'	z_s	slope of $\log(-\dot{\sigma})$ vs σ $z' = \frac{ b A^*}{kT}$	4:62	201
α	α	ferrite	-	-
α'	α'	bcc martensite	-	-
α_1	-	a constant	2:17	-
α_2	-	a constant	2:26	-
α_3	α''	a constant, $M'\alpha_3 = M$	4:32	-
α_4	-	slope of $\ln(-\dot{\sigma})$ vs σ plot	4:67	199
β	β	a constant	2:14	60
β'	-	a constant	2:17	53
β''	-	a constant	4:37	153
γ	γ	austenite	-	-
γ'	-	fcc $Ni_3(Al,Ti)$	-	-
γ_{pl}	γ_{pl}	true plastic shear strain	4:35	-
$\dot{\gamma}_{pl}$	$\dot{\gamma}_{pl}$	true plastic shear strain rate	4:32	-
$\dot{\gamma}_o$	-	pre-exponential factor	4:39	-
δ	-	bcc, δ -ferrite	-	-
δ_1	δ_1	a constant	4:83	-
δ_2	δ_2	a constant	4:84	-
$\delta\epsilon$	$\Delta\epsilon$	strain required to return specimen to initial stress after 1st stress relaxation test	-	-
$\delta\sigma$	$\Delta\sigma$	difference in stress after 400 seconds between 1st and subsequent relaxations (see 5:4.5)	-	-
$\frac{\Delta m_i}{m_i}$	-	mass resolution of atom probe	-	-
ΔF_o	-	Helmholtz free energy associated with dislocation movement	4:79	200
ΔG	ΔG	Gibbs free energy associated with dislocation movement	4:38	-
ΔH	ΔH	activation Enthalpy associated with dislocation movement	4:12	-

ΔH^*	ΔH^*	total barrier activation Enthalpy for dislocation movement	4:40	-
$\Delta \sigma$	-	stress drop after time t during a relaxation test	-	-
ϵ_a	-	anelastic tensile strain	4:2	-
ϵ_c	ϵ_c	true tensile creep strain	4:89	244
ϵ_e	-	elastic strain	4:1	-
$\dot{\epsilon}_e$	-	elastic strain rate	4:28	-
ϵ_{\max}	ϵ_{\max} (drawing)	maximum possible true strain at one wire drawing pass	2:5	-
ϵ'_{\max}	ϵ_{\max} (tensile)	maximum possible true strain in a tensile test	2:6	-
ϵ_o	-	pre-exponential factor	4:61	-
ϵ'_o	-	true strain of tensile specimen at initiation of stress relaxation test ($t=0$)	4:24	-
ϵ_p	ϵ_t	generalized true plastic strain	-	-
$\dot{\epsilon}_p$	$\dot{\epsilon}_t$	generalized true plastic strain rate	-	-
ϵ_{p_o}	-	a material constant	4:37	153
η	η	wire drawing efficiency term	-	-
θ	-	angular misorientation between cells or subgrains	2:19	-
θ'	-	strain hardening coefficient	4:35	139
		$\theta' = \frac{d\tau_i}{d\gamma_{p1}}$		
θ''	-	a work hardening coefficient	4:37	153
θ_1	θ'	a work hardening coefficient from a tensile test	4:52	190
		$\theta_1 = \frac{d\sigma}{d\epsilon_p}$		
θ_2	-	a work hardening coefficient from a stress relaxation test	-	190
		$\theta_2 = \frac{\delta\sigma}{\delta\epsilon}$		
θ_3	-	a work hardening coefficient	4:84	139
λ	λ	a constant	4:47	-
λ'	λ'	a constant	4:46	-
λ_α	-	dislocation mean free path in ferrite	2:17	53
μ	-	ferrite shear modulus	2:17	53
ν	-	a constant	4:57	-
ν'	-	pre-exponential factor	4:70	-

v''	-	a constant, $v'' = \rho_m b v'$	4:73	-
ρ	-	general dislocation density	-	-
ρ_c	ρ_c	critical dislocation density for cell formation	-	79
ρ_m	ρ_m	mobile dislocation density	4:6	-
ρ_o	-	initial dislocation density in ferrite before deformation	2:17	-
ρ_w	-	dislocation density in cell walls	2:26	-
σ	σ	true applied tensile stress, $\sigma = f(t)$	4:4	-
σ''	-	true stress of tensile specimen at initiation of stress relaxation test ($t=0$)	4:46	156
σ^*	σ^*	effective (thermal) component of σ	4:4	-
σ_c	σ_c	true composite failure stress	2:9	-
σ_f	σ_f	true fibre failure stress in composite	2:9	-
σ_{fl}	σ_{fl}	tensile flow stress	2:11	-
σ_i	σ_i	internal (athermal) component of σ	4:4	-
σ_m	σ_m	true matrix failure stress in composite	2:9	-
σ_{min}	-	minimum flow stress for a dislocation segment	4:7	136
σ_n	-	nominal applied tensile stress	4:88	-
σ_o	-	apparent friction stress	2:11	-
σ_o^*	-	effective (thermal) component of σ at initiation of stress relaxation test	4:55	-
σ	-	applied tensile stress at time t_1 during a stress relaxation test	5:2	-
$\dot{\sigma}$	-	stress rate at time t_1 during a stress relaxation test	5:3	-
σ_2	-	applied tensile stress at time t_2 during a stress relaxation test	5:2	-
$\dot{\sigma}_2$	-	stress rate at time t_2 during a stress relaxation test	5:3	-
τ	τ	true applied shear stress, $\tau = f(t)$	4:34	-
τ''	-	true shear stress at initiation of stress relaxation test	4:47	156
$\dot{\tau}$	$\dot{\tau}$	true shear stress rate	4:32	-
τ'	τ'_o	$\tau' = m\tau^*$	4:9	-
τ^*	τ^*	effective (thermal) component of τ	4:34	-
τ_{fl}	τ_{fl}	shear flow stress	2:15	-
τ_i	τ_i	internal (athermal) component of τ	4:34	-

τ_o	-	shear friction stress	2:15	-
ψ	ψ	generalized exponent in Hall-Petch equation	2:24	-
$\left(\frac{\partial \sigma}{\partial \epsilon}\right)_{tr}$	-	true value of quantities	2:17	53

A.14. Appendix 4: References

1. S. Paetke, CPGS: thesis submitted for Certificate of Post Graduate Study, Cambridge, October 1976.
2. BS 5216: 1975.
3. J.R. Vilella, G.E. Guellich and E.C. Bain: Trans. ASM 24 (1936) 225.
4. F.C. Hull and R.F. Mehl: Trans. ASM 30 (1942) 381.
5. N.T. Belaiew: J.I.S.I. 60 (1922) 201.
6. G.F. Pelliser, M.F. Hawkes, W.A. Johnson and R.F. Mehl: Trans. ASM 29 (1942) 1049.
7. F.C. Hull, R.A. Colten and R.F. Mehl: J.I.S.I. 50 (1942) 185.
8. U.F. Zackay and H.I. Aaronson, eds.: "Decomposition of Austenite by Diffusional Processes:", New York Interscience, (1962).
9. M.P. Puls and J.S. Kirkaldy: Met. Trans. 3 (1972) 2777.
10. A.R. Marder and B.L. Bramfitt: Met. Trans. 6A (1975) 2009.
11. A. McNeill: Ph.D. thesis, Cambridge (1975).
12. T. Gladman, I.D. McIvor and F.B. Pickering: J.I.S.I. (Dec. 1972) 916.
13. M. Gensamer, E.B. Pearsall and G.V. Smigh: Trans. ASM 28 (1940) 380.
14. M. Gensamer, E.B. Pearsall, W.S. Pellini and J.R. Low Jr.: Trans. ASM 30 (1942) 983.
15. B.S. Mellor: Ph.D. thesis, Cambridge (1973).
16. A.R. Marder and B.L. Bramfitt: Met. Trans. 7A (1976) 365.
17. F.B. Pickering: I. & S. (March 1965) 110.
18. K.W. Burns, F.B. Pickering: J.I.S.I. (Nov. 1964) 899.
19. L.E. Miller and G.C. Smith: J.I.S.I. (Nov. 1970) 998.
20. B.S. Mellor and D.V. Edmonds: Met. Trans. 8A (1977) 773.
21. B.S. Mellor and D.V. Edmonds: Met. Trans. 8A (1977) 763.
22. B.L. Bramfitt and A.R. Marder: Met. Trans. 4 (1973) 2291.
23. R.J. Dippenaar and R.W.K. Honeycombe: Proc. Royal Soc. Lon. A333 (1973) 455.
24. W. Pitsch: Acta Met. 10 (1962) 79.
25. W. Pitsch and A. Schrader: Arch. Eisen. 29 (1958) 485.
26. T. Cahill and B.A. James: "Continuous heat treatment of wire" I.S.I. Publication No. 113 (1968) 3.
27. D. Payne and B.F. Smith: "Continuous heat treatment of wire" I.S.I. Publication No. 113 (1968) 28.
28. J.D. Embury and R.M. Fisher: Acta Met. 14 (1966) 147.
29. T. Cahill and B.A. James: Wire and Wire prod. (1968) 64.
30. H. Hirano, E. Takahashi and Y. Yamada: J. Met. Soc. J. 3 (1968) 238.
31. B.M. Armstrong and T.G. Taylor: "Continuous heat treatment of wire", I.S.I. Publication No. 113 (1968) 32.

32. G. Langford and M. Cohen: Trans. ASM 62 (1969) 623.
33. H.J. Rack and M. Cohen: Mat. Sci. & Eng. 6 (1970) 320.
34. G. Langford, P.K. Nagata, R.J. Sober and W.C. Leslie: Met. Trans. 3 (1972) 1843.
35. G. Langford: Met. Trans. 8A (1977) 861.
36. Y. Yamada: Trans. I.S.I.J. 17 (1977) 515.
37. J.G. Wistreich: Met. Rev. 3 (1958) 97.
38. G.D.S. MacLellan: J.I.S.I. 158 (1948) 347.
39. G. Sutton: "Wire Drawing" taken from "Cold Prod. of Steel" I.S.I. (1972).
40. Bridon Wire Ltd.: private communication.
41. E.A. Choynowski, W.J. McG Tegart: Met. Sci. 2 (1968) 14.
42. D.F. Lupton and D.H. Warrington: Met. Sci. 6 (1972) 200.
43. E. Ho and G.C. Weatherly: Met. Sci. 11.4 (1977) 141.
44. H. Paqueton and A. Pineau: J.I.S.I. (Dec. 1971) 991.
45. J. Gil Sevillano: Mat. Sci. & Eng. 21 (1975) 221.
46. K.L. Maurer and D.H. Warrington: Phil. Mag. 15 (1967) 321.
47. A.S. Keh: Acta Met. 11 (1963) 1101.
48. A. Inoue, T. Ogura and T. Masumoto: Trans. J.I.M. 17 (1976) 149.
49. A. Inoue, T. Ogura and T. Masumoto: Met. Trans. 8A (1977) 1689.
50. A. Koréeda and K. Shimizu: Phil. Mag. 17 (1968) 1083.
51. T.E. Davidson and G.S. Ansell: Trans. ASM 61 (1968) 242.
52. S. Karashima and T. Sakuma: Trans. J.I.M. 9 (1968) 63.
53. T. Takahashi and M. Nagumo: Trans. J.I.M. 11 (1970) 113.
54. T.C. Lindley, G. Oates and C.E. Richards: Acta Met. 18 (1970) 1127.
55. J.E. Pepe: Met. Trans. 4 (1973) 2455.
56. H.G. Bowden and P.M. Kelly: Acta Met. 15 (1967) 105.
57. K.E. Easterling and D.A. Porter: Scand. J. Sci. 7 (1978) 55.
58. V.M. Kardonskii, G.V. Kurdyumov and M.P. Perkass: Met. Sci. and Heat Treat. 2 (1964) 64.
59. M.A.P. Dewey and G.W. Briers: 204 (1966) 102.
60. G. Langford: Met. Trans. 1 (1970) 465.
61. W.F. Hosford Jr.: TMS-AIME 230 (1964) 12.
62. J.F. Peck and D.A. Thomas: TMS-AIME 221 (1961) 1241.
63. E.S. Meieran and D.A. Thomas: TMS-AIME 233 (1964) 937.
64. E. Aernoudt and J. Gil Sevillano: J.T.S.I. 211 (1973) 718.
65. V.K. Chandok, A. Kasak and J.P. Hirth: Trans. ASM 59 (1966) 288.
66. J.D. Embury, A.S. Keh and R.M. Fisher: Trans. Met. Soc. AIME 236 (1966) 1252.
67. G.A. Chadwick: Met. Sci. 9 (1975) 300.

68. B. Karlsson and G. Linden: Mat. Sci. and Eng. 17 (1975) 153.
69. H.J. McQueen: Met. Trans. 8A (1977) 807.
70. R.J. McElroy and Z.C. Szkopiak: Met. Rev. 17 (1972) 175.
71. A.W. Thompson: Met. Trans. 8A (1977) 833.
72. J.C.M. Li: Acta Met. 8 (1960) 563.
73. J.C.M. Li: Trans. TMS-AIME 227 (1963) 239.
74. G. Langford and M. Cohen: Paper 14.5, 2nd. Inter. Conf. on strength of Metals & Alloys, Asilomar 1970, ASM.
75. H. Conrad, S. Feuerstein and L.H. Rice: Trans J.I.M. 9 (1968), supplement 401.
76. C.M. Young and O.D. Sherby: J.I.S.I. 211 (1973) 640.
77. J.P. Hirth: Acta Met. 22 (1974) 1023.
78. K. Schlaubitz, O. Müller and A. Güth: Paper 14.7, 2nd. Int. Conf. on strength of Metals & Alloys, Asilomar 1970, ASM.
79. S. Karashima, K. Maruyana and N. Ono: Trans. J.I.M. 15 (1974) 4.
80. D.L. Holt: Paper 14.6, 2nd. Int. Conf. on strength of Metals and Alloys, Asilomar 1970, ASM.
81. D.L. Holt: J. App. Phys. 41 (1970) 3197.
82. Y. Bergstrom: Mat. Sci. & Eng. 5 (1969) 193.
83. Y. Bergstrom: Met. Trans. 1 (1970) 1029.
84. R. Sandström: Acta Met. 25 (1977) 897.
85. R. Sandström: Acta Met. 25 (1977) 905.
86. M.M. Myshlyaer, I.M. Aristova and V.A. Likhachev: Acta Met. 26 (1978) 453.
87. J.D. Baird: I. & S. (May 1963) 186.
88. J.D. Baird: I. & S. (June 1963) 326.
89. J.D. Baird: I. & S. (July 1963) 368.
90. J.D. Baird: I. & S. (Aug. 1963) 400.
91. J.D. Baird: J. & S. (Sep. 1963) 450.
92. J.D. Baird: Met. Rev. 16 (1971) 1.
93. B.J. Brindley and P.J. Worthington: Met. Rev. 15 145 (1970) 101.
94. V.A. Phillips: Trans. ASM 56 (1963) 600.
95. R.F. Vyhal and S.V. Radcliffe: Acta Met. 20 (1972) 435.
96. H.J. Kleemola and Kuusisto: Scand. Met. J. 5 (1976) 151.
97. R.H. Doremus: Acta Met. 6 (1958) 674.
98. W.C. Leslie: Acta Met. 9 (1961) 1004.
99. J.L. Peterson: Trans. ASM 56 (1963) 304.
100. Y. Yamada: J.I.S.I. 16 (1976) 425.
101. A. Szombatfalvy: Bany. es Kohaszati Lopok (Kohaszat) 108.4 (1975) 145.
102. O.D. Sherby, R.H. Klundt and A.K. Miller: Met. Trans. 8A (1977) 843.

103. J.C.M. Li and Y.T. Chou: Met. Trans 1 (1970) 1145.
104. J.P. Hirth: Met. Trans. 3 (1972) 3047.
105. M.F. Ashby: Phil. Mag. 21 (1970) 399.
106. A.W. Thompson, M.I. Baskes and W.F. Flanagan: Acta Met. 21 (1973) 1017.
107. H.J. McQueen and J.E. Hockett: Met. Trans. 1 (1970) 2997.
108. A.K. Miller and O.D. Sherby: Scripta Met. 10 (1976) 311.
109. C.M. Young, S.L. Robinson and O.D. Sherby: Acta Met. 23 (1975) 633.
110. C.M. Young and O.D. Sherby: J.I.S.I. 211 (1973) 640.
111. D.J. Abson and J.J. Jonas: Met. Sci. J. 4 (1970) 24.
112. D.J. Abson and J.J. Jonas: J. Nuc. Mat. 42 (1972) 73.
113. L. Annand and J. Gurland: Met. Trans. 7A (1976) 191.
114. L. Annand and J. Gurland: Acta Met. 24 (1976) 901.
115. G. Langford and M. Cohen: Met. Trans. 1 (1970) 1479.
116. M.R. Staker and D.L. Holt: Acta Met. 20 (1972) 569.
117. M.N. Bassin and D. Kuhlmann-Wilsdorf: Phys. Stat. Sol. 19a (1973) 335.
118. D.H. Warrington: J.I.S.I. 201 (1963) 610.
119. J.J. Irani: J.I.S.I. 206 (1968) 363.
120. E.H. Chia and E.A. Starke Jr.: Met. Trans. 8A (1977) 825.
121. E.W. Müller: Z. Physik 126 (1951) 131.
122. E.W. Müller and T.T. Tsong: Field Emission Symposia, Elsevier 1970.
123. R.F. Hochman, E.W. Müller and B. Ralph, eds.: "Applications of Field ion microscopy", Georgia Tech. Press, (1969).
124. B. Ralph: "Tools and Techniques in Physical Metallurgy, Vol.2" ed. F. Wernberg, pub. Marcel-Dekker (1970) 515.
125. B. Dury: Ph.D. thesis, Cambridge (1970).
126. M. Drechsler and P. Wolf: 4th Int. Conf. on Electron Microscopy, Berlin 835, Springer-Verlag, (1958).
127. P.J. Turner, P. Cartwright, M.J. Southon, A. van Oostrom and R.W. Manley: J. Phys. E., J. Sci. Inst. 2 (1969) 731.
128. A. Youle: Ph.D. thesis, Cambridge (1972).
129. R. Morgan and B. Ralph: J.I.S.I. 206 (1968) 1138.
130. B.L. Dury and B. Ralph: J.I.S.I. 210 (1972) 422.
131. M.K. Miller and G.D.W. Smith: Met. Sci. (July 1977) 249.
132. G.D.W. Smith, D.A. Smith and K.F. Easterling: Paper 16 3rd Int. Conf. on strength of materials, (1972) 75.
133. M.K. Miller, R.J. Lewis, P. Beavan, M.N. Chandrasekhariah and G.D.W. Smith: Paper C19, Grain boundary Conf. Jersey (1976) C19.
134. R.M. Goldhoff: "Advances in Creep Design", Ch.6 81.
135. G.J. Lloyd and R.J. McElroy: Acta Met. 22 (1974) 339.
136. G.J. Lloyd and R.J. McElroy: Phil. Mag. 32.1 (1975) 231.

137. G.J. Lloyd and R.J. McElroy: *Acta Met.* 24 (1976) 111.
138. C. Zener: "Elasticity and Anelasticity in Metals", University of Chicago Press (1948).
139. F. Guiu and P.L. Pratt: *Phys. Stat. Sol.* 6 (1964) 111.
140. J.H. Schneidel and P.M. Hazzledine: *Scripta Met.* 11 (1977) 953.
141. J. Glen: "The Problem of Creep of Materials". Murex Ltd. (1968).
142. G.B. Graves: SRAMA Report No. 113 (1959).
143. G.B. Graves: SRAMA Report No. 115 (1959).
144. G.B. Graves: SRAMA Report No. 143 (1963).
145. G.B. Graves and T. Key: SRAMA Report No. 194 (1971).
146. S.D. Gray and G.B. Graves: SRAMA Report No. 246 (1975).
147. G.C. Bird: SRAMA Report No. 241 (1974).
148. S.D. Gray and G.B. Graves: SRAMA Report No. 245 (1975).
149. S.D. Gray: SRAMA Report No. 218 (1973).
150. M.R. Southward: SRAMA Report No. 233 (1974).
151. G.C. Bird: SRAMA Report No. 277 (1976).
152. K. Okazaki, M. Kagawa and Y. Aono: *Z. Metall.* 67 (1976) 47.
153. K. Okazaki, Y. Ono and M. Kagawa: *Acta. Met.* 24 (1976) 1121.
154. K. Okazaki and Y. Aono: *Z. Metall.* 68 (1977) 368.
155. K. Okazaki, M. Kagawa and Y. Aono: *Scripta Met.* 12 (1978) 407.
156. P. Feltham: *J. Inst. Met.* 89 (1961) 210.
157. P. Feltham: *Phil. Mag.* 6 (1961) 259.
158. P. Feltham: *Phil. Mag.* 6 (1961) 847.
159. P. Feltham: *Phys. Stat. Sol.* 3 (1963) 1340.
160. D. Hull and F.W. Noble: *Dis. Faraday Soc.* 38 (1964) 288.
161. J.C.M. Li: *Can. J. Phys.* 45 (1968) 493.
162. D.J. Lloyd and T.D. Embury: *Phys. Stat. Sol.* 43b (1971) 393.
163. F.E. Noble and D. Hull: *Acta Met.* 12 (1964) 1089.
164. D.F. Stein and J.R. Low: *J. Appl. Phys.* 31 (1960) 362.
165. E.W. Hart: *Acta Met.* 15 (1967) 351.
166. E.W. Hart: *Acta Met.* 18 (1970) 599.
167. E.W. Hart and H.D. Solomon: *Acta Met.* 21 (1973) 295.
168. D. Lee and E.W. Hart: *Met. Trans.* 2 (1971) 1245.
169. H. Yamada and Che-Yu Li: *Met. Trans.* 4 (1973) 2173.
170. H. Yamada and Che-Yu Li: *Acta Met.* 22 (1974) 249.
171. H. Oikawa, K. Ichihashi and S. Karashima: *Scripta Met.* 10 (1976) 143.
172. K.R. Williams and J.R. McLauchlin: *J. of Mat. Sci.* 5 (1970) 1063.
173. W.G. Johnson and J.J. Gilman: *J. Appl. Phys.* 30.2 (1959) 129.
174. E. Orowan: *Proc. Phys. Soc. Lon.* 52 (1940) 136.
175. G.B. Gibbs: *Phys. Stat. Sol.* 10 (1965) 507.

176. J.J. Gilman: Aust. J. Phys. 13 (1960) 327.
177. J.J. Gilman: J. App. Phys. 36.10 (1965) 3195.
178. J.J. Gilman: J. App. Phys. 36.9 (1965) 2772.
179. J.J. Gilman and W.G. Johnson: J. App. Phys. 31.4 (1960) 687.
180. P.P. Gillis and J.J. Gilman: J. App. Phys. 36.11 (1965) 3370.
181. J.C.M. Li: J. of Aust. Met. 8.2 (1963) 206.
182. J.C.M. Li: Trans. Met. Soc. AIME 233 (1965) 219.
183. D. McLean: Can. J. Phys. 45 (1967) 973.
184. R.W. Guard: Acta Met. 9 (1961) 163.
185. J.C.M. Li and J.T. Michalak: Acta Met. 12 (1964) 1457.
186. I. Gupta and J.C.M. Li: Met. Trans. 1 (1970) 2323.
187. I. Gupta and J.C.M. Li: Mat. Sci. and Eng. 6 (1970) 20.
188. R.B. Clough and L.J. Demer: Phys. Stat. Sol. 36 (1969) 221.
189. U.F. Kocks: Phil. Mag. 13 (1966) 541.
190. G. Sargent, G. Jones and H. Conrad: Scripta Met. 3 (1969) 481.
191. R.N. Orava, G. Stone and H. Conrad: ASM Trans. Quart. 50 (1966) 171.
192. M.G. White and I.O. Smith: Scripta Met. 8 (1974) 1153.
193. G.B. Gibbs: Phil. Mag. 13 (1966) 317.
194. A.A. Solomon, A.H. Ahlquist and W.D. Nix: Scripta Met. 4 (1970) 231.
195. C.Y. Cheng and U.F. Kocks: Paper 10.1, 2nd. Int. Conf. on strength of metals and alloys, Asilomar (1970) ASM.
196. R. de Batist and A. Callens: Phys. Stat. Sol. 21.a (1974) 591.
197. C.C. Aifantis and W.W. Gerberich: Mat. Sci. & Eng. 21 (1975) 107.
198. D.J. Lloyd, P.J. Worthington and J.D. Embury: Phil. Mag. 22 (1970) 1147.
199. A.W. Sleeswyk, G.H. Boersma, G. Hut and D.J. Verel: Paper 10.7, 2nd.Int. Conf. on strength of metals and alloys, Asilomar (1970) ASM.
200. M. Grosbras, E. Dedieu and M. Cahoreau: Phys. Stat. Sol. 42a (1977) 449.
201. C.C. Law and D.N. Beshers: Scripta Met. 6 (1972) 635.
202. P. Rodriguez, P. Dasgupta, J.L. Mannan, S.S. Vagarali and K.G. Samuel: Scripta Met. 7 (1973) 671.
203. I.O. Smith and W.R. Thorpe: Scripta Met. 12 (1978) 403.
204. R.W. Rhode and T.V. Nordstrom: Scripta Met. 7 (1973) 317.
205. R.W. Rhode and T.V. Nordstrom: Scripta Met. 7 (1973) 1227.
206. M.A. Fortes and J.G. Proença: Scripta Met. 7 (1973) 1149.
207. V.Z. Bengus and S.N. Smirnov: Mat. Sci. & Eng. 27 (1977) 73.
208. A.K. Hammamy, W. Dubofsky and H.D. Stüwe: Z. Metall. 68 (1977) 417.
209. O. Buck: Phys. Stat. Sol. 3 (1963) 1903.
210. H. Conrad, L. Hamp, G. Schoek and H. Wiedersich: Acta Met. 9 (1961) 367.
211. D. Keefer and C. Wert: Acta Met. 11 (1963) 489.
212. R.B. Clough: Phys. Stat. Sol. 17 (1966) K175.
213. J.C.M. Li: "Kinetics and Dynamics in Dislocation Plasticity" from "Dislocation Dynamics" eds. A.R. Rosenfeld, G.T. Hahn, A.L. Brement Jr. and R.I. Jaffee, McGraw-Hill (1968) 89.

214. J. Kubát and M. Rigdahl: Mat. Sci. & Eng. 24 (1976) 223.
215. B. Wielke: Scripta Met. 11 (1977) 87.
216. C.N. Ahlquist: Scripta Met. 5 (1971) 185.
217. A.A. Solomon and W.D. Nix: Acta Met. 19 (1971) 373.
218. H.S. Chen, J.J. Gilman and A.K. Head: J. App. Phys 35 (1969) 2502.
219. W.D. Nix, W.A. Coughlan and C.R. Barrett: J. Mat. Sci. Eng. 4 (1969) 98.
220. P. Rodriguez: J. Mat. Sci. 3 (1968) 98.
221. B. Vlach and J. Skarek: Scripta Met. 4 (1970) 433.
222. C.N. Ahlquist and W.D. Nix: Acta Met. 19 (1971) 373.
223. G.B. Gibbs: Phil. Mag. 13 (1966) 317.
224. S.R. MacEwan, O.A. Kupcis and B. Ramaswami: Scripta Met. 3 (1969) 441.
225. F. Guiu: Scripta Met. 3 (1969) 753.
226. H. Conrad and K. Okazaki: Scripta Met. 4 (1970) 259.
227. L.J. Cuddy: Met. Trans. 1 (1970) 395.
228. T. Hasegawa, Y. Ikeuchi and S. Karashima: Met. Sci. J. 6 (1972) 78.
229. D.J. Lloyd and J.D. Embury: Met. Sci. J. 4 (1970) 6.
230. M. Boček and W. Schneider: Z. Metall. 4 (1971) 302.
231. P.P. Gillis and G.A. Sargent: Mat. Res. Bull. 6 (1971) 451.
232. B.J. Shaw and G.A. Sargent: Acta Met. 12 (1964) 1225.
233. P. Groh and R. Conte: Acta Met. 19 (1971) 895.
234. P.P. Gillis and R.F. Medrano: J. Mat. Sci. 6 (1971) 514.
235. M.A. Fortes and J.G. Proença : J. Test. & Eval. 4.4 (1976) 248.
236. J.E. Hockett and J.J. Gillis: "Mechanical Testing Machine Stiffness, Part I", Int. J. of Mech. Sci. 13 251.
237. R.F. Reed-Hill and J.R. Donoso: Scripta Met. 9 (1975) 1305.
238. G.A. Sargent and B.J. Shaw: Acta Met. 14 (1966) 909.
239. A.A. Solomon: Rev. Sci. Inst. 40 (1969) 1025.
240. F. Guiu: Scripta Met. 3 (1969) 489.
241. P. Neumann: private communication.
242. W.R. Thorpe and I.O. Smith: Scripta Met. 7 (1973) 123.
243. T.J. Koppenaal: Acta Met. 15 (1967) 681.
244. D.W. Davies, G. Nelves, K.R. Williams and B. Wilshire: Met. Sci. 7 (1973) 87.
245. V.I. Dotsenko and A.I. Landau: Mat. Sci. Eng. 22 (1976) 101.
246. R.P. Goel: J. of Test and Eval. 3.1 (1975) 62.
247. P.D. Parikh and E. Shapiro: J. of Test and Eval. 4.2 (1976) 161.
248. P.D. Parikh and E. Shapiro: "Stress Relaxation in Bending", from ASTM Symposium on "Recent advances in mechanical testing" Montreal (1975).
249. R.W. Rhode and T.V. Nordstrom: Mat. Sci. & Eng. 12 (1973) 179.
250. A. Fox: J. of Mat. 6.2 (1971) 422.
251. A. Fox: J. of Test Eval. 2.1 (1974) 32.

253. T.H. Alden: Met. Trans. 8A (1977) 1675.
253. R. Altermo and R. Langeborg: Met. Tech. (1974) 462.
254. H. Herö: Scripta Met. 9 (1975) 1121.
255. P.M. Kelly and J.M. Round: Scripta Met. 3 (1969) 85.
256. T. Sugai, H. Mimura and S. Kritani: Acta Met. 13 (1965) 1095.
257. V.I. Sarrak and V.N. Shubin: Phys. of Met. and Metallog. 25.1 (1968) 149.
258. R.L. Brown and M. Cohen: Metal Prog. (1962) 66.
259. R.L. Brown, H.J. Rack and M. Cohen: Mat. Sci. & Eng. 21 (1970) 25.
260. J. Henderson: Met. Tech. (1974) 338.
261. G.A. Sargent: Acta Met. 13 (1965) 663.
262. G.A. Sargent and H. Conrad: Scripta Met. 3 (1969) 43.
263. K. Okazaki and H. Conrad: Trans. J.I.M. 14 (1973) 368.
264. P. Feltham: Phil. Mag. 8 (1963) 989.
265. R.A. Tait: Ph.D. thesis, Cambridge (1976).
266. J.C. Ritter and R. McPherson: J.I.S.I. (1970) 935.
267. J.C. Ritter and R. McPherson: J.I.S.I. (1973) 123.
268. F.B. Pickering: Int. Met. Rev. No. 211 (Dec. 1976) 227.
269. D. Peckner and I.M. Bernstein eds: "Handbook of Stainless Steels" McGraw-Hill (1977).
270. L. Columbier and J. Hockmann: "Stainless Steels and Heat Resisting Steels" Edward Arnold (1967).
271. H. Schneider: Found. Trade J. 108 (1960) 562.
272. Nickel Topics 31.3 pub. International Nickel Ltd.
273. G. Krauss and B.L. Averbach: Trans. ASM 52 (1960) 434.
274. E.E. Underwood, A.E. Austin and G.K. Manning: J.I.S.I. (Aug. 1963) 642.
275. H. Hughes: J.I.S.I. (Oct. 1965) 1019.
276. J.C. Wilkins, R.E. Pence and D.C. Perry: from "Advances in the Technology of Stainless Steels and related alloys" ASTM special publication No. 369 (1965) 331.
277. N. Yukawa, M. Mizutani and H. Saka: "6th International Congress for Electron Microscopy" Kyoto (1966) 403.
278. E.J. Dulis: I.S.I. Special Report No. 86 "High Alloy Steels" (1964).
279. F.B. Pickering: I.S.I. Special Report No. 114 "Low Alloy Steels" (1968).
280. K.C. Thompson - Russell and J.W. Edington: "Monograph 5 of Practical Electron Microscopy in Materials Science - Electron Microscope Specimen Preparation Techniques in Materials Science" Philips Technical Library, pub. Macmillan (1977).
281. P.J. Goodhew: "Part I of Practical Methods in Electron Microscopy Vol. I. - Specimen preparation in Materials Science", ed. A.M. Glauert, pub. North-Holland (1972).
282. P.J. Turner, B.J. Regan and M.J. Southon: Vacuum 22 (1972) 4043.
283. A.R. Waugh: J. Phys. E., Sci. Inst. 11 (1978) 49.
284. E.W. Müller, J.A. Panitz and S.B. McLane: Rev. Sci. Inst. 39 (1968) 83.
285. E.W. Müller: Naturwissenschaften 57 (1970) 222.

286. J.A. Panitz: J. Vac. Sci. Tech. 11 (1974) 206.
287. D.G. Brandon and B. Ralph: 3rd International Conference on Electron Microscopy, Prague (1964) 303.
288. R. Morgan: Ph.D. thesis Cambridge (1967).
289. D.H. Davies: Ph.D. thesis Cambridge (1970).
290. T. O'D Hanley, A.S. Krausz and D. Maheshwori: Mat. Sci. & Eng. 16 (1974) 155.
291. N. Balasubramanian and J.C.M. Li: J. Mat. Sci. 5 (1970) 434.
292. TTT diagrams from "Atlas of Isothermal transformation diagrams of Bs En steels", ISI special report No. 56 (1956).
293. T.B. Gibbons: Scripta Met. 12 (1978) 749.
294. H. Conrad and W. Hayes: Trans. ASM 56 (1963) 249.
295. R.J. Arsenault: Acta. Met. 12 (1964) 547.
296. J.W. Christian: Acta. Met. 15 (1967) 1257.
297. S. Raghuraman and R.J. Arsenault: Scripta Met. 12 (1978) 753.
298. J.M. Bernstein: Acta Met. 17 (1969) 249.
299. U.F. Kocks: Mat. Sci. & Eng. 27 (1977) 291.
300. R. Lagneborg, B.-H. Forsén and J. Wiberg: from "Creep strength in steel and high temperature alloys" p.1, Met. Soc. London (1974).
301. R. Lagneborg, B.-H Forsén: Acta Met. 21 (1973) 781.
302. J.E. Dorn and S. Rajnak: TMS-AIME 230 (1964) 1052.
303. P.J. Wray and G.T. Horne: Phil. Mag. 13 (1966) 899.
304. D.H. Jack and F. Guieu: J. Mat. Sci. 10 (1975) 1161.
305. J.H. Woodhead and A.G. Quarrel: JISI (1965) 605.
306. K.J. Irvine, J.D. Murray and F.B. Pickering: from "Structural processes in Creep" ISI and Inst. of Metals, London, (May 1961) p.246.
307. N.P. Allen and L.M.T. Hopkin: as ref. 304. p.323.
308. G. Aldén and B. Aronsson: as ref. 300. p.67.
309. P.L. Threadgill and B. Wilshire: as ref. 300. p.8.
310. A.S. Keh and H.A. Wriedt: TMS-AIME 224 (1962) 560.
311. D.V. Wilson and B. Russell: Acta Met. 8 (1960) 468.